



IRAC Instrument Handbook

Spitzer Heritage Archive Documentation
IRAC Instrument and Instrument Support Teams
Version 4.0 (Final), September 2021



Table of Contents

IRAC Instrument Handbook	1
1 Introduction	1
1.1 DOCUMENT PURPOSE AND SCOPE	1
1.2 BASIC DEFINITIONS.....	2
1.3 IRAC ESSENTIALS	2
1.4 STANDARD ACKNOWLEDGMENTS FOR IRAC PUBLICATIONS	3
1.5 HOW TO CONTACT US.....	3
2 Instrument Description	4
2.1 OVERVIEW	4
2.2 DESCRIPTION OF OPTICS	6
2.2.1 <i>Field of View (FOV)</i>	6
2.2.2 <i>IRAC Image Quality</i>	7
2.2.3 <i>Spectral Response</i>	9
2.2.4 <i>Distortion</i>	13
2.3 DETECTORS	13
2.3.1 <i>Design</i>	13
2.3.2 <i>Linearity</i>	14
2.4 ELECTRONICS.....	16
2.4.1 <i>Hardware</i>	16
2.4.2 <i>Fowler Sampling</i>	16
2.4.3 <i>Exposure Time and Frame Time</i>	17
2.4.4 <i>Calibration Lamps</i>	18
2.4.5 <i>Firmware</i>	18
2.5 SENSITIVITY AND SATURATION	19
2.5.1 <i>Sensitivity Model</i>	19
2.5.2 <i>Saturation</i>	29
3 Operating Modes	32
3.1 READOUT MODES AND FRAME TIMES	32
3.2 PCRS PEAK-UP OBSERVATIONS.....	34
3.3 MAP GRID	35
3.4 DITHERING PATTERNS	35
4 Calibration	40
4.1 DARKS	40
4.1.1 <i>Shutterless Skydarks</i>	40
4.1.2 <i>Closed Shutter Campaign</i>	41
4.2 FLAT-FIELDS	44
4.3 PHOTOMETRIC CALIBRATION.....	45
4.4 COLOR CORRECTION	48
4.5 ARRAY LOCATION-DEPENDENT PHOTOMETRIC CORRECTIONS FOR COMPACT SOURCES WITH STELLAR SPECTRAL SLOPES	54
4.6 PIXEL PHASE-DEPENDENT PHOTOMETRIC CORRECTION FOR POINT SOURCES	57
4.7 IRAC APERTURE PHOTOMETRY CORRECTIONS.....	58
4.8 PHOTOMETRIC VARIATIONS IN DATA TAKEN WITH FULL ARRAY, SUBARRAY, DITHERING AND STARRING MODES	59
4.9 IRAC POINT SPREAD AND POINT RESPONSE FUNCTIONS	62
4.9.1 <i>Core PRFs</i>	66
4.9.2 <i>Extended PSFs</i>	67
4.10 CALCULATION OF IRAC ZMAGS	69
4.11 ASTROMETRY AND PIXEL SCALES	70

4.11.1	<i>Optical Distortion</i>	70
4.11.2	<i>Pixel Solid Angles</i>	71
4.12	POINTING PERFORMANCE	72
4.12.1	<i>Pointing Accuracy</i>	72
4.12.2	<i>Target Acquisition Accuracy</i>	74
4.12.3	<i>Pointing Glitches</i>	75
4.12.4	<i>Jitter, Drift, and Wobble</i>	75
4.13	INSTRUMENT PERFORMANCE TRENDING	84
4.13.1	<i>Photometric Stability</i>	84
4.13.2	<i>Skydark Bias Offsets</i>	85
4.13.3	<i>Radiation Hits</i>	87
5	Pipeline Processing	89
5.1	LEVEL 1 (BCD) PIPELINE.....	89
5.1.1	<i>SANITY DATATYPE (parameter checking)</i>	89
5.1.2	<i>SANITY CHECK (image contents checking)</i>	89
5.1.3	<i>TRANHEAD (header processing)</i>	89
5.1.4	<i>INSBPOSDOM (InSb array sign flipping)</i>	92
5.1.5	<i>CVT12R4 (byte type changing)</i>	93
5.1.6	<i>Wraparound Correction: IRACWRAPDET and IRACWRAPCORR</i>	94
5.1.7	<i>IRACNORM (Fowler sampling renormalization)</i>	95
5.1.8	<i>SNESTIMATOR (initial estimate of uncertainty)</i>	96
5.1.9	<i>IRACEBWC (limited cable bandwidth correction)</i>	96
5.1.10	<i>Dark Subtraction I: FFCORR (“first frame effect” correction) and LABDARKSUB (labdark subtraction)</i> 98	
5.1.11	<i>MUXBLEEDCORR (electronic ghosting correction)</i>	101
5.1.12	<i>DARKDRIFT (“readout channel” bias offset correction)</i>	102
5.1.13	<i>FOWLINEARIZE (detector linearization)</i>	103
5.1.14	<i>BGMODEL (zodiacal background estimation)</i>	104
5.1.15	<i>Dark Subtraction II: SKYDARKSUB (sky “delta-dark” subtraction)</i>	104
5.1.16	<i>FLATAP (flat-fielding)</i>	105
5.1.17	<i>IMFLIPROT</i>	105
5.1.18	<i>DETECT-RADHIT (cosmic ray detection)</i>	106
5.1.19	<i>DNTOFLUX (flux calibration)</i>	106
5.1.20	<i>Pointing Transfer (calculation of pointing information)</i>	107
5.1.21	<i>PREDICTSAT (HDR saturation processing)</i>	107
5.1.22	<i>LATIMFLAG (residual image flagging)</i>	108
5.2	THE ARTIFACT-CORRECTED BCD PIPELINE	108
5.2.1	<i>Stray Light</i>	108
5.2.2	<i>Saturation</i>	109
5.2.3	<i>Sky Background Estimation</i>	110
5.2.4	<i>Column Pull-down</i>	110
5.2.5	<i>Banding Correction (Channels 3 and 4)</i>	110
5.2.6	<i>Muxstripe Correction (Channels 1 and 2)</i>	111
5.3	LEVEL 2 (POST-BCD) PIPELINE	112
5.3.1	<i>Pointing Refinement</i>	113
5.3.2	<i>Superboresight Pointing Refinement</i>	113
5.3.3	<i>Mosaicking and Coaddition</i>	114
6	Data Products.....	116
6.1	FILE CHARACTERISTICS	116
6.2	FILE-NAMING CONVENTIONS.....	116
6.3	IRAC SPECIFIC HEADER KEYWORDS.....	119
7	Data Features and Artifacts.....	123
7.1	DARKS, FLATS, MISSING DATA, AND BAD PIXELS.....	123
7.1.1	<i>Bad Pixels</i>	125

7.1.2	<i>Flat-field</i>	127
7.1.3	<i>Missing Data</i>	127
7.2	ELECTRONIC ARTIFACTS	128
7.2.1	<i>Saturation and Nonlinearity</i>	128
7.2.2	<i>Muxbleed (InSb)</i>	130
7.2.3	<i>Bandwidth Effect (Si:As)</i>	132
7.2.4	<i>Column Pull-Down/Pull-Up</i>	133
7.2.5	<i>Row Pull-Up</i>	134
7.2.6	<i>Full-Array Pull-Up</i>	135
7.2.7	<i>Inter-Channel Crosstalk</i>	135
7.2.8	<i>Persistent Images</i>	136
7.3	OPTICAL ARTIFACTS	144
7.3.1	<i>Stray Light from Array Covers</i>	144
7.3.2	<i>Optical Banding and Internal Scattering</i>	148
7.3.3	<i>Optical Ghosts</i>	150
7.3.4	<i>Large Stray Light Ring and Splotches</i>	152
7.4	COSMIC RAYS AND SOLAR PROTONS	154
8	Introduction to Data Analysis	157
8.1	POINT SOURCE PHOTOMETRY	157
8.2	EXTENDED SOURCE PHOTOMETRY	158
8.2.1	<i>Best Practices for Extended Sources</i>	160
8.2.2	<i>Extended Source Aperture Correction</i>	160
8.2.3	<i>Low Surface Brightness Measurements and the Maximum Scaling Factors</i>	163
8.2.4	<i>Caveats & Cautionary Notes</i>	163
8.2.5	<i>Faint Surface Brightness Behavior</i>	164
8.3	IRAC HIGH PRECISION TIME SERIES PHOTOMETRY	167
8.3.1	<i>Time-Correlated Noise</i>	168
8.3.2	<i>Spacecraft Motion</i>	169
8.3.3	<i>Repeatable Pointing</i>	170
8.3.4	<i>Mapping Intrapixel Gain</i>	172
8.3.5	<i>Residual Nonlinearity</i>	176
8.3.6	<i>Time-varying Bias in Point Source Data</i>	180
8.3.7	<i>IRAC's Photometric Stability</i>	182
8.3.8	<i>Persistent Images</i>	187
8.3.9	<i>Removing Correlated Noise – Repeatability and Accuracy</i>	188
8.3.10	<i>Measuring Noise Reduction</i>	191
8.4	POST-BCD DATA PROCESSING	193
8.4.1	<i>Pointing Refinement</i>	194
8.4.2	<i>Overlap Correction</i>	194
8.4.3	<i>Mosaicking of IRAC Data</i>	194
8.4.4	<i>Source Extraction</i>	196
8.5	THINGS TO CHECK AND IMPORTANT NOTES FOR DATA ANALYSIS	197
	Appendix A. Pipeline History Log	200
	S19.2 (WARM MISSION ONLY; PROCESSING STARTED ON 2015 JUNE 15)	200
	S19.1 (WARM MISSION ONLY; 2015 AUGUST 29)	200
	S18.25 (CRYOGENIC MISSION FINAL PROCESSING; 2012 MARCH 15)	201
	S18.18 (WARM MISSION ONLY; 2010 MAY 27)	201
	S18.18 (2010 MAY 27)	201
	S18.14 (2010 DECEMBER 10)	202
	S18.5 (2008 DECEMBER 1)	202
	S18.0 (2008 JUNE 12)	203
	S17.0 (2007 DECEMBER 5)	203
	S16.0 (2007 APRIL 9)	204
	S15.0 (2006 NOVEMBER 28)	204

S14.0 (2006 MAY 3).....	204
S13.0 (2005 OCTOBER 27)	205
S12.0 (2005 MAY 9).....	206
S11.0 (2004 NOVEMBER 30)	206
S10.5 (2004 JUNE 2).....	207
S10.0 (2004 MAY 7).....	207
S9.5 (2004 MARCH 1)	207
S9.1 (2004 JANUARY 22).....	208
S9.0 (2004 JANUARY 14).....	208
S8.9 (2003 DECEMBER 8).....	208
Appendix B. Performing Photometry on IRAC Images.....	211
A. POINT SOURCE PHOTOMETRY ON A MOSAIC	211
B. POINT SOURCE PHOTOMETRY ON A MOSAIC	213
Appendix C. Point Source Fitting IRAC Images with a PRF.....	217
C.1 USE OF THE FIVE TIMES OVERSAMPLED PRFS OUTSIDE OF APEX	218
C.2 MODIFICATIONS TO THE IRAC PRFS FOR USE WITH APEX	219
C.3 RESULTS OF TESTS WITH PRF FITTING.....	220
C.3.1 <i>Test on Calibration Stars</i>	220
C.3.2 <i>Subpixel Response in Channels 1 and 2</i>	221
C.3.3 <i>The Serpens Test Field</i>	224
C.3.4 <i>The GLIMPSE Test Field</i>	227
C.3.5 <i>Photometry of Moderately-Resolved Sources</i>	228
C.3.6 <i>Positional Accuracy</i>	229
C.3.7 <i>A How-To-Guide for IRAC Point Source Photometry with APEX</i>	229
C.3.8 <i>Pixel Phase</i>	231
Appendix D. Time Series Photometry Supplement	234
D.1 DATA FEATURES.....	234
D.1.1 <i>Header Keywords</i>	234
D.1.2 <i>Skydark Change in the Middle of an Observation</i>	235
D.1.3 <i>Background modulation</i>	236
D.1.4 <i>Noise Pixel Spikes</i>	238
D.1.5 <i>Timing</i>	238
D.1.6 <i>58th Frame in Subarray Datasets</i>	239
D.1.7 <i>Corrupted Header</i>	240
D.1.8 <i>Position Jumps Due to Reaction Wheel Speed Change</i>	240
D.1.9 <i>Pointing History File Change</i>	241
D.1.10 <i>Effects of Cosmic Rays on Centroiding Algorithm</i>	242
D.1.11 <i>Pattern noise (horizontal striping)</i>	244
D.2 TIME SERIES PHOTOMETRY TOOLS	245
Appendix E. IRAC BCD File Headers.....	247
E.1 CRYOGENIC MISSION CHANNEL 1.....	247
E.2 CRYOGENIC MISSION CHANNEL 2.....	251
E.3 CRYOGENIC MISSION CHANNEL 3.....	256
E.4 CRYOGENIC MISSION CHANNEL 4.....	261
E.5 WARM MISSION CHANNEL 1	265
E.6 WARM MISSION CHANNEL 2.....	271
Appendix F. Acronyms.....	277
Appendix G. Acknowledgments	281
Appendix H. List of Figures.....	292
Appendix I. Appendix List of Figures.....	299

Appendix J. List of Tables 300
Appendix K. Appendix List of Tables..... 301
Appendix L. Version Log 302
Bibliography 304
Index..... 307

1 Introduction

1.1 Document Purpose and Scope

The IRAC Instrument Handbook is one in a series of documents that explain the operations of the Spitzer Space Telescope and its three instruments, the data received from the instruments and the processing carried out on the data. The Spitzer Space Telescope Handbook gives an overview of the entire Spitzer mission and it explains the operations of the observatory, while the other three handbooks document the operation of, and the data produced by, the individual instruments (IRAC, IRS, and MIPS). The IRAC Instrument Handbook is intended to provide all the information necessary to understand the IRAC standard data products, as processed by the online pipeline system, and which are retrievable from the Spitzer Heritage Archive (SHA). Besides the detailed pipeline processing steps and data product details, background information is provided about the IRAC instrument itself, its observational modes, and all aspects of IRAC data calibration. It should be stressed that this Handbook is not intended to support interactive data analysis. For data analysis advice and suggested data processing procedures, please refer to the separate documentation available at the InfraRed Science Archive (IRSA) documentation website

<https://irsa.ipac.caltech.edu/data/SPITZER/docs/irac/> ,

including the Spitzer Data Analysis Cookbook. This Handbook serves as the reference for both the processing as well as the correct interpretation of IRAC data as available from the Spitzer Heritage Archive. Note that all the earlier versions of the IRAC Instrument Handbook are now obsolete, and IRAC data users should use the current version of the Handbook.

In this document we present information on:

- the IRAC instrument (Chapter 2) and its operating modes (Chapter 3),
- the calibration of the instrument (Chapter 4),
- the processing steps carried out on the Level 0 (raw) data (“pipeline description,” Chapter 5),
- the final IRAC archival data products (Chapter 6),
- the artifacts, features, and uncertainties in the data (Chapter 7), and
- the IRAC data analysis (Chapter 8).

Several appendices are attached to give more detailed information on the topics briefly covered in the chapters mentioned above.

The Digital Object Identifier or DOI for this document is <https://doi.org/10.26131/irsa486>, and it should be used when quoting this document in articles or journal papers.

1.2 Basic Definitions

This section contains a description of the most commonly used terms in this Handbook. A complete list of acronyms can be found in Appendix F.

An Astronomical Observation Template (AOT) is the generic list of parameters for a distinct Spitzer observing mode. There was one possible IRAC AOT for the cryogenic mission, and one for the warm mission. A fundamental unit of Spitzer observing was the Astronomical Observation Request (AOR), also referred to sometimes as an “observation.” It was an AOT with all of the relevant parameters fully specified. Each AOR is identified in the Spitzer Heritage Archive by a unique observation identification number known as AORKEY. An AOR consists of several Data Collection Events (DCEs), which can be thought of as single frame exposures. The data products consist of Level 0 products (“raw data”) and Level 1 data products that are also called Basic Calibrated Data (BCD), which were derived from the DCEs after pipeline processing. See Chapter 5 for more information about pipeline processing. BCDs (or in the case of IRAC, corrected BCDs or CBCDs; see Section 5.2 for more information about BCDs vs. CBCDs) were designed to be the most reliable data product achievable by automated pipeline processing, and should be the starting point for further data processing. The pipeline also produced Level 2 data products or Post-BCD products, which were derived from data from the whole AOR (i.e., combination of several CBCDs). See Chapter 6 for more information about the data products.

1.3 IRAC Essentials

The most relevant software for IRAC data reduction is MOPEX (mosaicking and point source extraction; Makovoz & Khan 2005 and Makovoz & Marleau 2005). Documentation for it can be found in the data analysis section of Spitzer’s documentation website at IRSA:

<https://irsa.ipac.caltech.edu/data/SPITZER/docs/dataanalysis/tools/> .

See Chapter 8 for a brief introduction into IRAC data analysis. The separate Data Analysis section of the documentation website provides access to tools, user guides and data analysis recipes.

Before you start using IRAC data, we recommend that you familiarize yourself very carefully with this document, and specifically Chapter 7, which discusses the various artifacts in IRAC data. Several of these artifacts are at least partially corrected in the pipeline, but you should still be aware of them. The CBCD frames contain the artifact-corrected observations, and should usually be a starting point for your further data reduction and analysis. However, you always have the option of going back to the BCD frames if you are not happy with how artifacts were corrected in the CBCDs, and perform your own corrections.

Without additional corrections to the photometry, point source flux density measurements from IRAC images are only accurate within about 10%. The additional corrections are discussed in Chapter 4. It is possible to achieve down to a few percent absolute flux density accuracy by carefully performing all the corrections to the data (ultimately limited by the uncertainties in the

spectra of calibration stars). Specifically, we urge the reader to read Chapter 4 carefully to understand why point source photometry should be performed with aperture photometry, unless the targets lie in an area of sky that has an extremely high surface density and/or a strongly spatially varying background. Chapter 4 also emphasizes that the pixel size (the area of sky subtended by a pixel) varies across the arrays and, therefore, flux density measurements off the (C)BCDs require corrections. Chapter 4 and Appendix B give much more information on how to best perform point source photometry on IRAC images. An IRAC data user should note that IRAC images are calibrated in surface brightness units. However, extended emission flux densities, and especially surface brightness, are not nearly as well calibrated as point sources. The user should read the caveats about measuring them in Chapter 8 and think carefully before publishing any results about extended emission flux density and surface brightness.

1.4 Standard Acknowledgments for IRAC Publications

Any paper published based on Spitzer data should contain the following text: “This work is based [in part] on observations made with the Spitzer Space Telescope, which was operated by the Jet Propulsion Laboratory, California Institute of Technology under a contract with NASA.” If you received NASA data analysis funding for your research, you should use one of the templates listed under <https://irsa.ipac.caltech.edu/data/SPITZER/docs/spitzermission/publications/ackn/>. We also ask that you cite at least the fundamental IRAC paper (Fazio et al. 2004) in your research paper, and other IRAC-related papers, as appropriate.

1.5 How to Contact Us

A broad collection of information about IRAC and IRAC Data Analysis is available at IRSA’s Spitzer Documentation website, accessible via

<https://irsa.ipac.caltech.edu/data/SPITZER/docs/irac> .

In addition, you may contact us at the IRSA helpdesk at

<https://irsasupport.ipac.caltech.edu/> .

2 Instrument Description

2.1 Overview

The InfraRed Array Camera (IRAC) was built by the NASA Goddard Space Flight Center (GSFC) with management and scientific leadership by the Smithsonian Astrophysical Observatory (SAO) under principal investigator Giovanni Fazio. The information in this Handbook is based on the design requirements and on the characterization of the flight instrument in pre-flight ground tests and on in-flight performance, including the In-Orbit Checkout (IOC)/Science Validation (SV) in 2003 August – November and the IRAC Warm Instrument Characterization (IWIC) in 2009 May – July.



Figure 2.1: IRAC Cryogenic Assembly model, with the top cover removed to show the inner components.

A brief, high-level summary of IRAC for astronomers appeared in the ApJS Spitzer Special Issue, specifically the paper by Fazio et al. (2004) entitled “The Infrared Array Camera (IRAC) for the Spitzer Space Telescope” and in the paper by Hora et al. (2004) entitled “In-flight performance and calibration of the Infrared Array Camera (IRAC) for the Spitzer Space Telescope.” Links to these papers are available at IRSA’s Spitzer/IRAC documentation website, accessible at

<https://irsa.ipac.caltech.edu/data/SPITZER/docs/irac> .

IRAC was a four-channel camera that provided simultaneous $5.2 \text{ arcminute} \times 5.2 \text{ arcminute}$ images at 3.6, 4.5, 5.8, and 8.0 μm . Two adjacent fields of view were imaged in pairs (3.6 and 5.8 μm ; 4.5 and 8.0 μm) using dichroic beamsplitters. All four detector arrays in the camera were 256×256 pixels in size, with a pixel size of $\approx 1.2 \text{ arcseconds} \times 1.2 \text{ arcseconds}$. The two short wavelength channels used InSb detector arrays and the two longer wavelength channels used Si:As detectors. The IRAC instrument was designed to address the four major scientific objectives defining the Spitzer mission. These were (1) to study the early universe, (2) to search for and study brown dwarfs and superplanets, (3) to study ultraluminous galaxies and active galactic nuclei, and (4) to discover and study protoplanetary and planetary debris disks. The utility of IRAC was in no way limited to these objectives, which we only mention to explain the scientific drivers for the instrument design. IRAC was a powerful survey instrument because of its high sensitivity, stability, large field of view, mapping capabilities, and near simultaneous four-channel imaging.

IRAC consisted of the Cryogenic Assembly (CA) installed in the Multiple Instrument Chamber (MIC) in the Cryogenic Telescope Assembly (CTA), and the Warm Electronics Assembly (WEA) mounted in the spacecraft. Harnesses connected the detectors and the calibration subsystem in the CA to the WEA. The WEA communicated with the spacecraft over three RS-422 serial lines that allowed receiving commands from, and sending acknowledgments and image data to, the spacecraft Command & Data Handling (C&DH) computer.

The IRAC Cryogenic Assembly, depicted in Figure 2.1, consisted of the following major subassemblies: the Pickoff Mirrors; the Shutter; the Optics Housings, which held the doublet lenses, beamsplitters, filters, and cold stops; the Focal Plane Assemblies (FPAs) that included the detector arrays and associated components; the Transmission Calibrator with its Source and Integrating Spheres; and the Housing Structure, consisting of the Main Housing Assembly and the wedge-shaped MIC Adapter Plate.

IRAC operated both during the cryogenic mission and during the warm mission. During the cryogenic mission (or “cryo mission”), the channel 1 and 2 InSb arrays were operating at about 15 K and the channel 3 and 4 Si:As arrays were cooled down to about 6 K. On May 15, 2009, the cryogenic coolant ran out and Spitzer warmed up to 27.5 K. Consequently, the operation of the channel 3 and 4 arrays became impossible because of greatly enhanced thermal noise, but channels 1 and 2 could still be operated with about the same sensitivity as in the cryogenic mission. The temperatures and biases were adjusted. The bias of the channel 1 array was adjusted from 750 mV to 500 mV and the temperatures for the two operating arrays were set to 28.7 K. After the IRAC Warm Instrument Characterization (IWIC) period in 2009 May – July, the warm mission (or “warm IRAC”) operations started on 2009 July 25. The last temperature changes were made on September 18, 2009. The data taken in campaigns PC(post-cryo)1 until the early part of PC4 were taken while the temperatures were still settling and changing, and require the use of specific flux calibration. In general, we caution the user to be extremely careful when using data from PC1 – early PC4 campaigns. The calibration of data from the latter part of the PC4 campaign (which ran 2009 September 10 – 23) onwards is stable.

2.2 Description of Optics

2.2.1 Field of View (FOV)

The IRAC optical layout is shown in Figure 2.2 and Figure 2.3. Light from the telescope was reflected into the IRAC structure by the pickoff mirrors for the two fields of view (FOVs). Each pair of channels had a doublet lens which re-imaged the Spitzer focal plane onto the detectors. A beamsplitter reflected the short wavelength light to the InSb detectors (channels 1 and 2) and transmitted the longer wavelength light to the Si:As detectors (channels 3 and 4). Channels 1 and 3 viewed the same patch of sky (within a few pixels), while channels 2 and 4 viewed a nearby patch of sky simultaneously. The nearest edges of the two IRAC fields of view were separated by approximately 1.52 arcminutes, with no overlap on the sky. The IRAC pixel scale was nearly the same in all channels (≈ 1.2 arcseconds per pixel), providing a $5.2 \text{ arcminutes} \times 5.2 \text{ arcminutes}$ FOV.

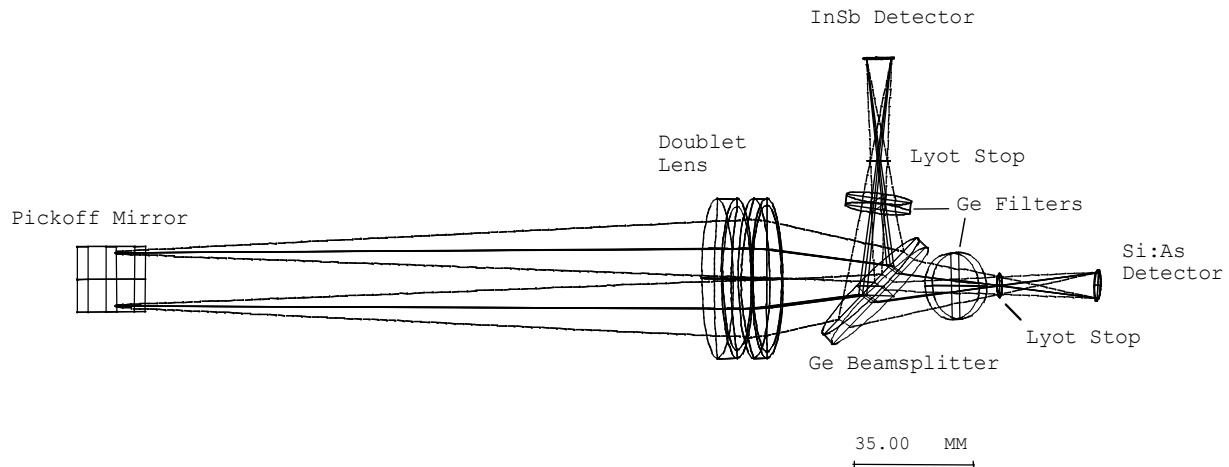


Figure 2.2: IRAC optical layout, top view. The layout was similar for both pairs of channels; the light entered the doublet and the long wavelength passes through the beamsplitter to the Si:As detector (channels 3 and 4), and the short wavelength light was reflected to the InSb detector (channels 1 and 2).

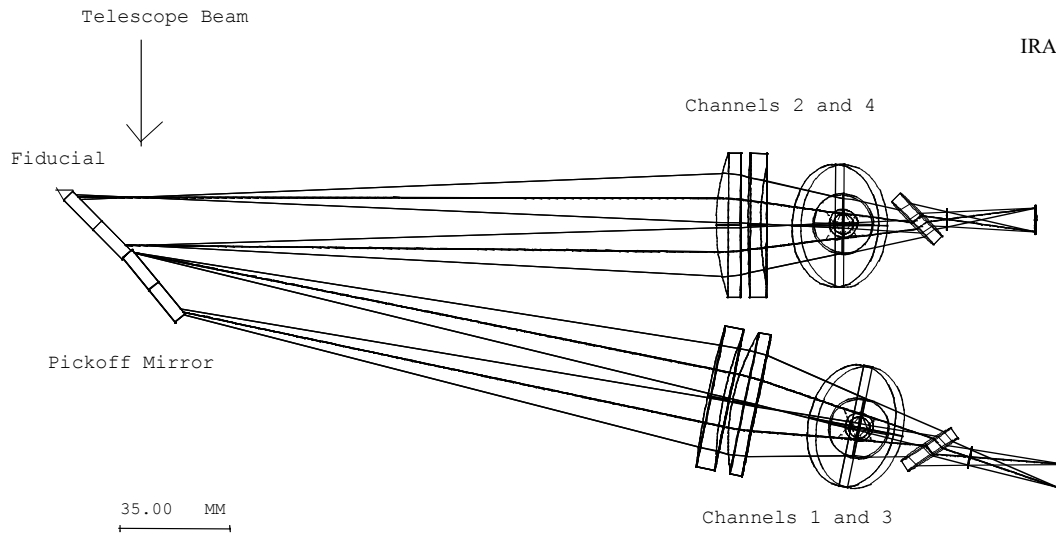


Figure 2.3: IRAC optics, side view. The Si:As detectors are shown at the far right of the figure. The InSb arrays are behind the beamsplitters.

2.2.2 IRAC Image Quality

The IRAC optics specifications limited the wavefront errors to $< \lambda/20$ in each channel. IRAC provided diffraction-limited imaging internally, and image quality was limited primarily by the Spitzer telescope. The majority of the IRAC wavefront error was a lateral chromatic aberration that was most severe at the corners of the IRAC field. The aberration was due to the difficulty of producing an achromatic design with a doublet lens over the large bandpasses being used. The effect was small, with the total lateral chromatic dispersion less than a pixel in the worst case. The sky coordinates of each pixel were accurately measured in the cryogenic mission using an astrometric solution from the ultra-deep GOODS Legacy data (PI Mark Dickinson), resulting in distortion coefficients that are in the world coordinate system of each image. The main effect was that the PSF (point spread function) and distortion may be slightly color-dependent, which may be detectable for sources with extreme color variation across the IRAC channels. See Section 2.2.4 below for more information about the distortion correction in the cryogenic and warm mission images.

A large variation in the flux of sources measured in different parts of the array is due to the filters, which led to a different spectral response in different parts of the field of view. The flat-field calibration was done with the zodiacal light, which was relatively red; blue sources have a flux variation of up to 10% from one side of an array to the other (see Section 4.5 in this Handbook for more details). This is called the “array location-dependent photometric correction” in the IRAC documentation.

Table 2.1: IRAC image quality properties. The second set of numbers for channels 1 and 2 are for the warm mission, and the rest of the numbers are for the cryogenic mission. Noise pixels are defined in Section 2.2.2.

Channel	Noise pixels (mean)	FWHM (mean; ")	FWHM of centered PRF (")	Central pixel flux (peak; %)	Pixel size (")	Maximum distortion (pixels relative to square grid)
1	7.0/7.22	1.66/1.95	1.44/1.78	42/37	1.221	1.3
2	7.2/7.33	1.72/2.02	1.43/1.80	43/34	1.213	1.6
3	10.8	1.88	1.49	29	1.222	1.4
4	13.4	1.98	1.71	22	1.220	2.2

Table 2.1 shows a few properties of the IRAC image quality. The cryogenic numbers were derived from in-flight measurements of bright stars during the cryogenic mission. PRF is the ‘‘Point Response Function,’’ further discussed in Section 4.9. The warm mission values were determined from the ≈ 4000 observations (0.4 second frames) of the calibration star that was used for the PRF/focus measurements in the warm mission after the final biases and temperatures were set. In the warm mission, the FWHM values were obtained from a Gaussian fit to the PRF profile, and the peak central pixel fluxes were the average of stars that were within 0.09 and 0.15 pixels from being centered, in each channel.

The noise pixels column in Table 2.1 gives the equivalent number of pixels whose noise contributes to a linear least-squares extraction of the flux of a point source from a $13 \text{ pixel} \times 13 \text{ pixel}$ portion of an unconfused image, assuming the PRF is perfectly known. The quantity is derived as follows: let the PRF in pixel i be P_i and the intensity of an image in pixel i be I_i . If a point source with flux F is present in the image, then $I_i = FP_i$. If we do a least-squares fit to determine F , then we minimize

$$\chi^2 = \sum \frac{(I_i - FP_i)^2}{\sigma_i^2} \quad (2.1)$$

where σ_i is the measurement uncertainty in pixel i . We will assume here that σ_i is independent of pixel and set $\sigma_i = \sigma$. Now we take the derivative of χ^2 with respect to the source flux and set it to zero to find the optimum value. We find

$$0 = \sum (I_i - FP_i)P_i \quad (2.2)$$

solving for F , we find

$$F = \frac{\sum I_i P_i}{\sum P_i^2} \quad (2.3)$$

Now we derive the uncertainty in the flux. Using the well-known theorem for the propagation of errors

$$\sigma_F^2 = \sum \left(\frac{dF}{dI_i} \right)^2, \quad (2.4)$$

and applying it to the result above, we find that

$$\sigma_F^2 = \sum \left(\frac{P_i}{\sum P_i^2} \right)^2 \sigma^2 = \frac{\sum P_i^2 \sigma^2}{(\sum P_i^2)^2} = \frac{\sigma^2}{\sum P_i^2}, \quad (2.5)$$

or, equivalently, $\sigma_F = \sigma \sqrt{N}$ where $N = \frac{1}{\sum P_i^2}$, which is the definition of noise pixels.

There are two columns for the full width at half-maximum (FWHM) of the PRF in Table 2.1. The mean FWHM is from observations of a star at 25 different locations on the array. The FWHM for the “centered PRF” is for cases where the star was most closely centered in a pixel. The fifth column in Table 2.1 is the fraction of the flux in the central pixel for a source that is well centered in a pixel. It was determined from the images of the focus star (after the telescope was focused) that were the most symmetric and concentrated. These values for the flux in the central pixel can be used in the saturation predictions (see Section 2.5.2 below). The flux in the central pixel for a random observation is likely to be lower, because the Spitzer PRF was undersampled at the IRAC pixel scale.

2.2.3 Spectral Response

The IRAC system throughput and optical performance was governed by a combination of the system components, including the lenses, beamsplitters, filters, mirrors, and detectors. The system parameters are summarized in Table 2.2. The system response was based on measurements of the final in-flight system, including the beamsplitter, filter, ZnS & ZnSe coating transmissions, mirror reflectance, BaF2 and MgF2 coating transmissions, and detector quantum efficiency.

Table 2.2: IRAC channel characteristics.

Channel	Effective λ (μm)	Bandwidth (μm)	Average transmission (η)	Minimum in- band trans- mission	Peak trans- mission
1	3.551	0.750 (21%)	0.426	0.339	0.465
2	4.493	1.010 (23%)	0.462	0.330	0.535
3	5.730	1.420 (25%)	0.150	0.119	0.170
4	7.873	2.930 (37%)	0.280	0.199	0.318

At each wavelength, the spectral response curve gives the number of electrons produced in the detector per incoming photon. While the curves provided are best estimates of the actual spectral response, it is recommended that the curves are used in a relative sense for color corrections, and the supplied photometric scaling (implicit in Level 1 products [“BCDs”] and described in Reach et al. 2005 and updated in Carey et al. 2012) is used for absolute photometric calibration. Tests during the IOC/SV showed that the out-of-band leaks were less than the astronomical background at all locations, for sources of any temperature detectable in the IRAC channels.

The spectral response curves presented below in Figure 2.4 reflect our best knowledge of the telescope throughput and detector quantum efficiency. The response curves used measurements of the filter and beamsplitter transmissions over the range of angles of incidence corresponding to the distribution of incident angles across the fields of view of the IRAC detectors (Quijada et al. 2004).

We provide three sets of curves for each IRAC channel: an average response curve for the entire array, an average curve for the subarray (see Section 3.1) field of view, and a data cube of the response curves on a per pixel basis. The average curves are useful for making color corrections to photometry of well-dithered (four or more dithers) observations. The response cubes can be used for more rigorous color corrections on per instance basis. For most purposes, the average curves are sufficient. A more detailed discussion of the spectral response curves is given by Hora et al. (2008). IRSA’s Spitzer/IRAC section web page

<https://irsa.ipac.caltech.edu/data/SPITZER/docs/irac/calibrationfiles/spectralresponse/>

contains links to the tabulated spectral response curves.

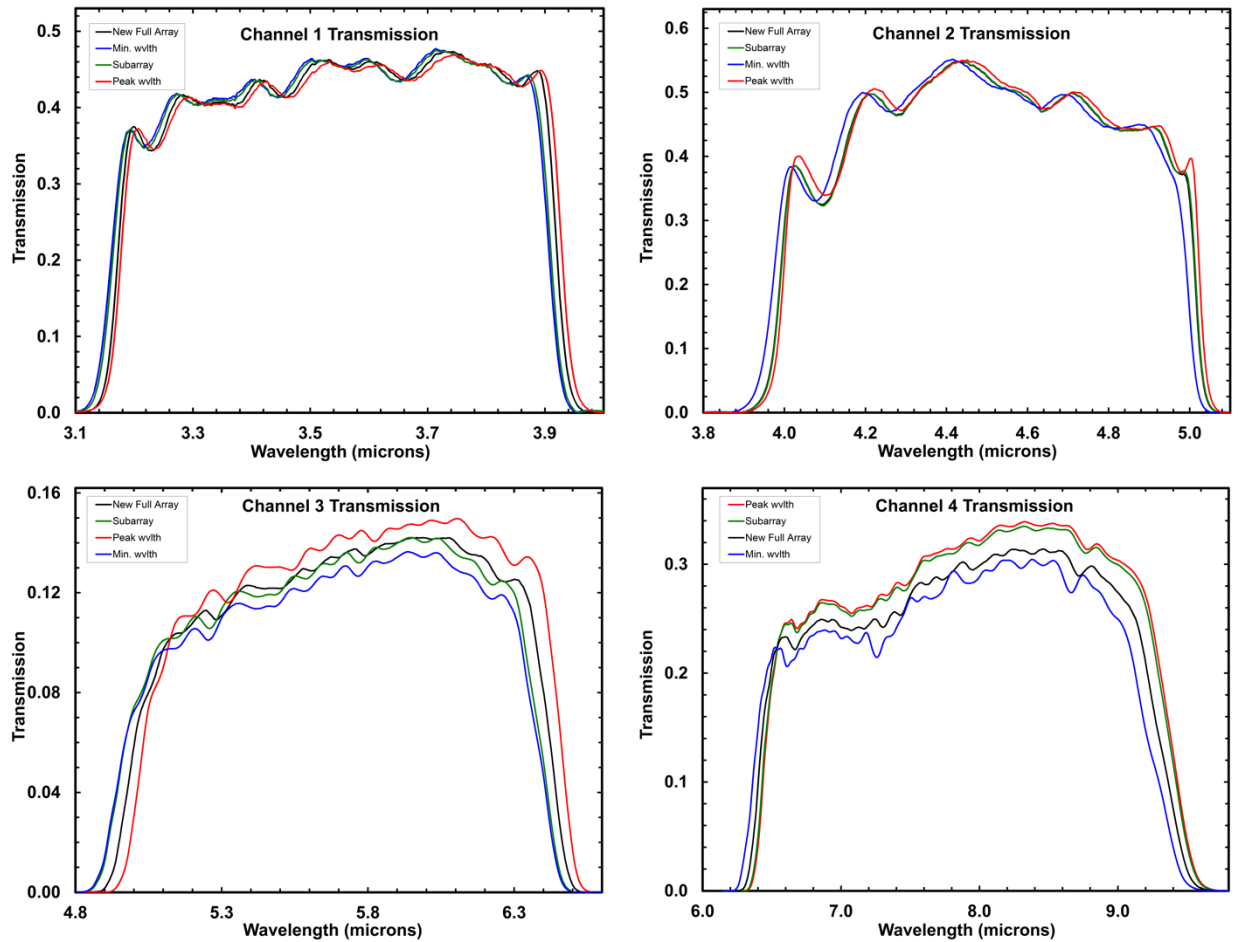


Figure 2.4: Spectral response curves for all four IRAC channels. The full array average curve is displayed in black. The subarray average curve is in green. The extrema of the full array per-pixel transmission curves are also shown for reference. The red curves are for the pixel in the array with the highest nominal wavelength bandpass and the blue curves for the pixel in the array with the lowest nominal wavelength bandpass. For definition of the “nominal wavelength” see Hora et al. (2008). The spectral response curve data are available at <https://irsa.ipac.caltech.edu/data/SPITZER/docs/irac/calibrationfiles/spectralresponse/>.

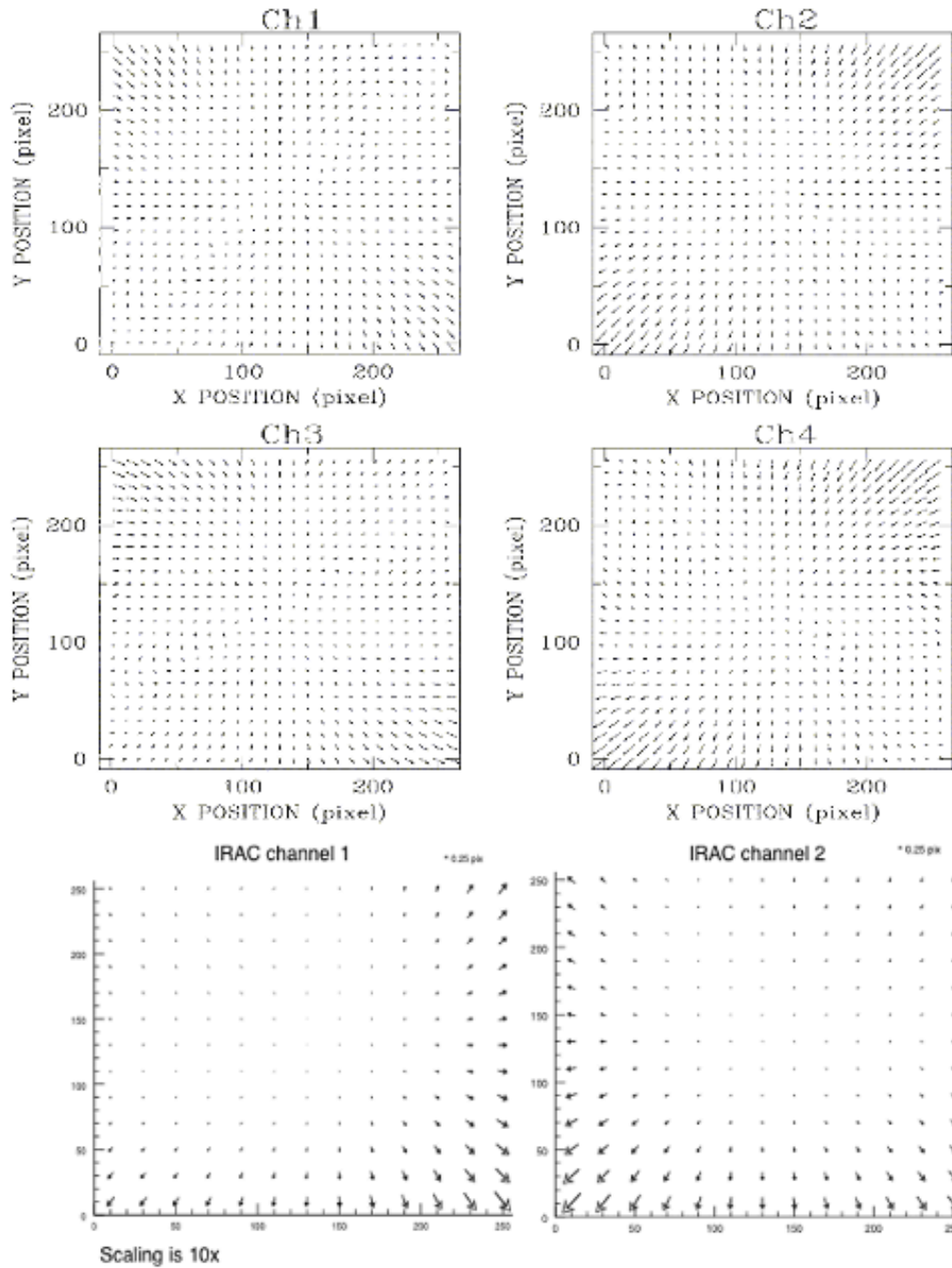


Figure 2.5: Optical image distortion in IRAC channels in the cryogenic mission (above) and warm mission (below). The panels show the image distortions as calculated from a quadratic polynomial model (above) and a fifth-order polynomial (below) that was fit to in-flight data. The magnitude of the distortion and the direction to which objects have moved from their ideal tangential plane projected positions is shown with arrows. The length of the arrows has been increased by a factor of ten for clarity. The maximum positional deviations across the arrays for this quadratic distortion model are less than 1.3, 1.6, 1.4, and 2.2 pixels for channels 1 – 4, respectively. The derivation of the pixel scales that are listed in Table 2.1 fully

accounted for the quadratic (cryogenic data) and fifth order (warm data) distortion effects shown here.

2.2.4 Distortion

Due to the off-axis placement of IRAC in the Spitzer focal plane, there was a small amount of distortion over the IRAC FOV (there would have been some distortion even if the IRAC FOV had been centered in the Spitzer focal plane). The maximum distortion in each IRAC channel was < 2.2 pixels (compared to a perfectly regular grid) over the full FOV. Figure 2.5 shows the distortion across all four IRAC channels in the cryogenic mission, as determined from data taken during the IOC/SV. It also shows the fifth order distortion in the warm mission.

The warm mission distortion correction improved the accuracy by using a fifth order polynomial. Using cluster observations and relative astrometry, the new correction has an uncertainty less than 30 milliarcseconds. The new distortion correction was verified by, and agrees with, two other independent derivations using independent data sets. For more information, see Lowrance et al. (2016).

Table 2.3: IRAC read noise. The second set of numbers in channels 1 and 2 are for the warm mission.

Ch.	Read noise for frame with specified frame time (electrons)											
	Subarray (frame time in seconds)				Full array (frame time in seconds)							
	0.02*	0.1*	0.4*	2*	0.4	0.6	1.2	2	6	12	30	100
1	25.4	16.9/ 13.4	10.8	10.8	22.4	22.4	22.4	11.8/ 16	16	9.4/ 15	7.8/ 14.6	8.4/ 21
2	23.7	16.8/ 12.1	9.4	9.4	23.7	23.7	23.7	12.1/ 12.1	10	9.4/ 10.4	7.5/ 10.4	7.9/ 16
3	-	9.0	-	-	-	-	-	9.1	-	8.8	10.7	13.1
4	-	8.4	-	-	-	-	-	7.1	-	6.7	6.9	6.8 **

* Per single subframe (one of the 64 planes in the BCD cube).

**Per 50 second frame.

2.3 Detectors

2.3.1 Design

The IRAC detector arrays were developed by the Raytheon/Santa Barbara Research Center (SBRC) in Goleta, CA, under contract to SAO (Hoffmann et al. 1998; Estrada et al. 1998). In the cryogenic mission, channels 1 (FPA desig. 48534/34 UR) and 2 (48975/66 GSFC) used InSb

arrays operating at ≈ 15 K, and channels 3 (30052/41 ARC) and 4 (30219/64 ARC) used Si:As detectors operating at ≈ 6 K. In the warm mission, the channel 1 and 2 InSb arrays were operating at about 30 K. Both array types used the CRC744 CMOS readout circuit, and the same physical pixel size of 30 μm . The arrays were anti-reflection coated with SiO (channels 1, 2, and 3) and ZnS (channel 4). The power dissipation for each array was < 1 mW. The quantum efficiencies were 87%, 86%, 37% and 61% for channels 1 – 4, respectively. The quantum efficiencies and the well depths (below) are from pre-flight laboratory measurements of similar arrays and antireflection coatings. The operability, or the percentage of the pixels that are within usable specifications, was 99.97%, 99.9%, 99.99%, and 99.75% for channels 1 – 4, respectively, during the cryogenic mission and 99.01% and 99.97% for channels 1 and 2, respectively, during the warm mission. The well depths were 145000, 140000, 170000, and 200000 electrons in channels 1 – 4, respectively, during the cryogenic mission. During the warm mission, they were 110000 and 125000 in channels 1 and 2, respectively.

Table 2.3 gives the read noise values for IRAC channels 1 – 4 during the cryogenic mission, and for channels 1 and 2 during the warm mission.

2.3.2 *Linearity*

Both types of detectors had measurable nonlinearity. The InSb arrays were nearly linear until they reached saturation. The Si:As detectors were somewhat nonlinear over most of their operating range, and, above half-well capacity, this contributed noticeably to the total error budget. However, all of the arrays were linearized to better than 1% up to approximately 90% of their full-well capacity (defined in electrons above, with the gain listed in

Table 2.4, corresponding typically to 45000 – 60000 Data Numbers; DN). The detector linearity was measured during ground testing and in flight. The laboratory linearity measurements, with the flight instrument, are shown in Figure 2.6. The arrays were illuminated with a constant flux, and successively longer exposures were taken. For a perfectly linear system, the flux would be directly proportional to the exposure time, and the graph would show a straight line. In fact, the arrays were driven past their saturation levels, and the shape of the curve up to 90% of the saturation level was fitted with a polynomial in the pipeline’s linearization module.

During IWIC, it was found that the non-linearity and well depth varied as both a function of applied voltage on the arrays and the array temperature. Therefore, the voltage and temperature were recalibrated during warm operations. Unfortunately, it was extraordinarily difficult to reach the accuracy of the ground-based cryogenic linearization while in flight. Therefore, the warm mission linearity calibration was derived using a combination of staring observations of bright galactic nebulae, and from the photometry of sources observed by the SERVS Exploration Science program, vs. the same sources observed by the SWIRE Legacy Science program during cryogenic operations. The warm mission linearity solution was found to be accurate at the level of better than 0.5%.

IWIC results indicated that the non-linearity at 27 – 28 K temperatures (warm mission) was more severe than at 15 K (cryogenic mission). Using the cryogenic calibration provided at least a partial correction. Note that the flux calibration was based on standard stars that were usually near 1/3 – 1/2 full well. Targets that were near this well depth will always have correct fluxes. The other change in the warm linearization was the well depth that is defined by the point at which the pixel DN peaks, and it was roughly 30000 DN in both channels in the warm mission, whereas it was closer to 44000 DN in the cryogenic mission.

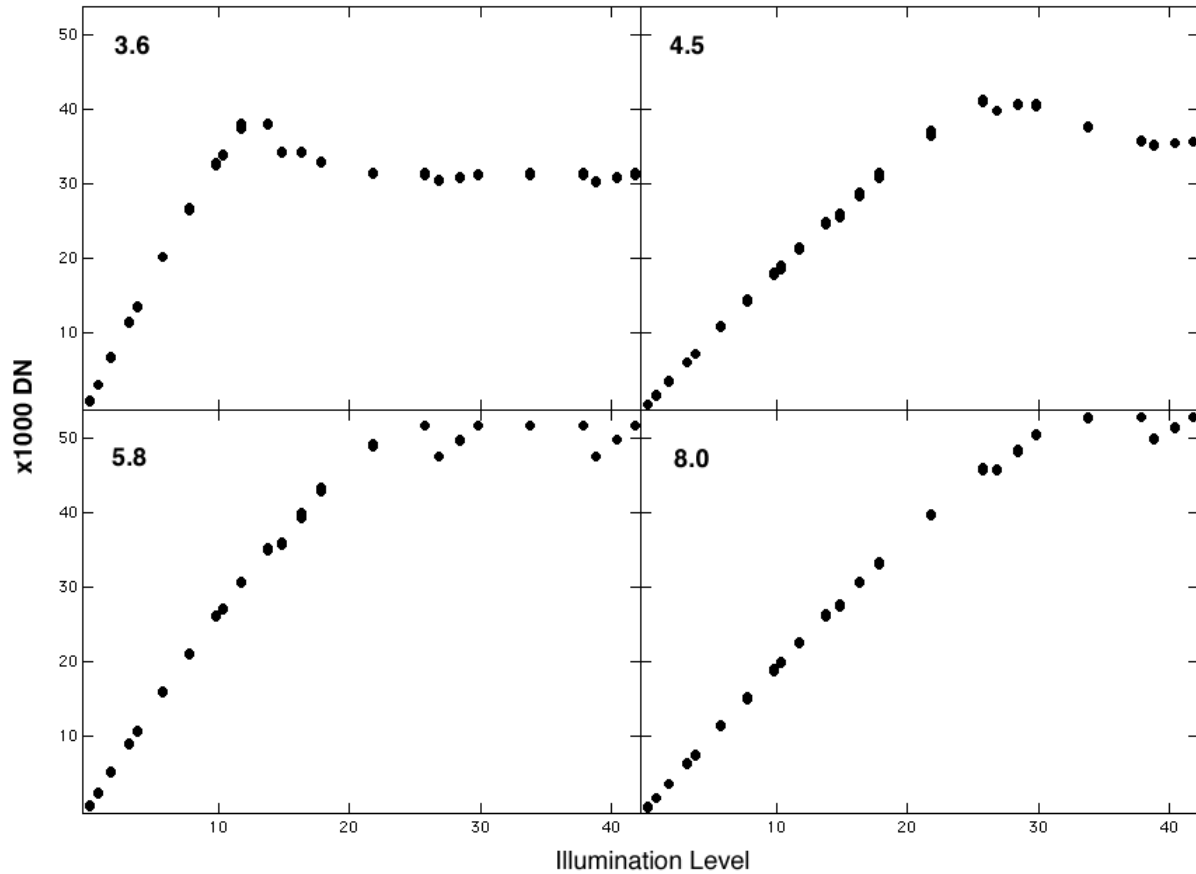


Figure 2.6: Cryogenic linearity curves for the IRAC detectors. As noted in text, the warm detectors were roughly linear to 30000 DN.

2.4 Electronics

2.4.1 Hardware

IRAC had no moving parts (other than the shutter, which was not operated in flight until the last 72 hours of the mission). The instrument took data by staring at the sky and sampling the arrays between resets. IRAC was capable of operating each of its four arrays independently and/or simultaneously. All four arrays were used during normal, full array operation.

2.4.2 Fowler Sampling

Multiple (Fowler) sampling was used to reduce the effective read noise. This mode of sampling consisted of taking N non-destructive reads immediately after the reset, and another N non-destructive reads near the end of the integration. Differencing was performed in the IRAC electronics to generate one integer value per pixel per exposure to store on the spacecraft and transmit to the ground. The Fowler N used for an observation depended on integration time, and was selected to maximize the SNR, based on in-flight performance tests.

2.4.3 Exposure Time and Frame Time

The relationship between the exposure time (T_{ex}) and frame time is shown in Figure 2.7. The exposure time is defined as the time elapsed between the first pedestal sample and the first signal sample. The Fowler samples were taken consecutively at 0.2-second (full array) or 0.01-second (subarray; see Section 3.1 for definitions of the full array and subarray modes) intervals in each group (pedestal and signal samples). The frame time ($T_f - T_i$) is the total time elapsed between resets, which could include multiple reads and dead time before and after Fowler sampling. The frames were commanded by specifying the number of Fowler samples for the pedestal (N_f) and the number of wait ticks in between the pedestal and signal frames (N_w); then the frame time was $T_f = (2N_f + N_w)\tau$, where τ is the readout time (0.2 seconds for full array, 0.01 seconds for subarray mode). T_{ex} is simply $T_f - N_f\tau$. N_f values can be found in Table 2.6. The (C)BCD FITS headers of the individual frames contain the information in keywords FRAMTIME (frame time), AFOWLNUM (N_f), and AWAITPER ($N_w\tau$).

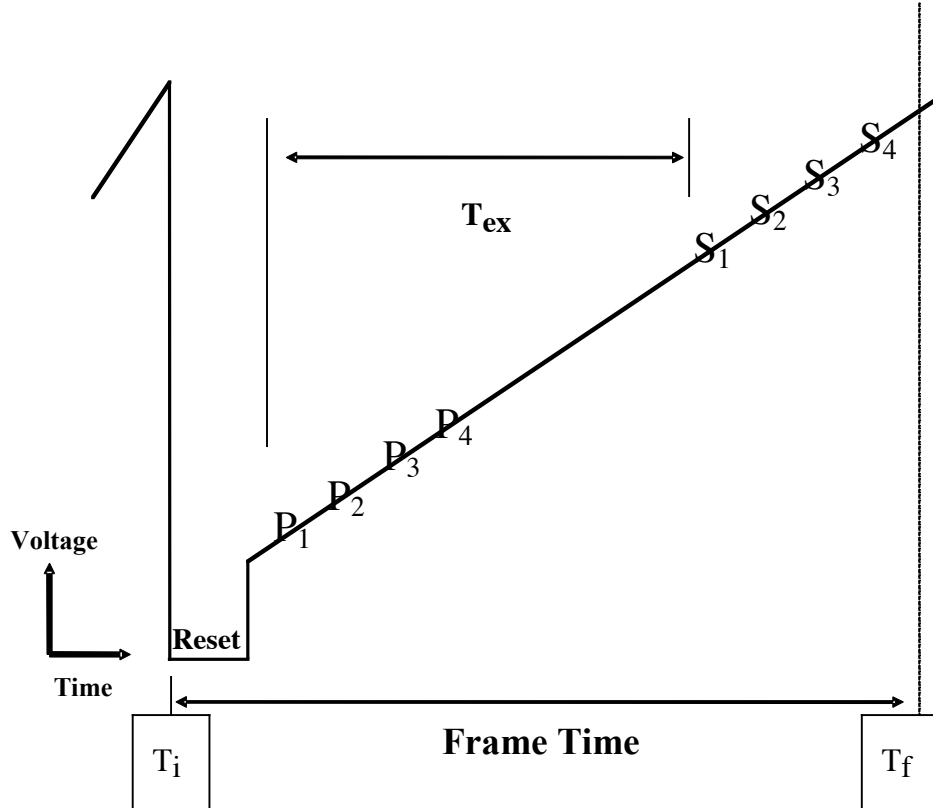


Figure 2.7: Fowler sampling times for one pixel (Fowler $N=4$). The P_n ($n=1,2,3,4$) show the “Pedestal” readouts, and the S_n show the “Signal” readouts. T_{ex} is the effective exposure time, and $T_f - T_i$ is the “frame time,” or total time to obtain one IRAC image. The reset part of the sketch is not at the same time and voltage scale as the rest of the figure.

2.4.4 Calibration Lamps

IRAC contained two types of internal calibration lamps. The first type was the flood calibrators that individually illuminated each detector. Each lamp could be controlled individually, and could be used whether the shutter was open or closed. The flood calibrators were operated at the end of each IRAC campaign in the cryogenic mission and used as a consistency check. The flood calibrators were not operated during the warm mission. Calibration of IRAC is discussed in detail in Chapter 4. The second type of calibration lamps was the transmission calibrator lamps, designed to illuminate all four arrays to provide an internal responsivity measurement. There were two transmission calibrator spheres, each of which contains two lamp elements. To illuminate the arrays, the shutter needed to be closed, a transmission lamp turned on, and the light from the transmission lamp would reflect off a mirror on the back of the shutter. Note that because the shutter was not operated during the nominal operations except for the last 72 hours, the transmission calibrators were not used in flight.

2.4.5 Firmware

The IRAC firmware controlled the focal plane assemblies, calibration electronics, and warm electronics boards. Apart from autonomous fault protection, the IRAC firmware responded only to commands sent by the Spitzer Command & Data Handling (C&DH) computer. The C&DH sent setup commands to configure the electronics, requests for each telemetry packet, and integration commands to generate images. IRAC responded to each command with an acknowledgment. In the case of a command that requested telemetry, the acknowledgment consisted of the telemetry packet, which was sent on the low-speed connection between IRAC and the C&DH. There were two types of engineering data: special engineering data, which were collected every four seconds, and housekeeping data, which were collected every 30 seconds. Special engineering data were used for onboard communication between IRAC and the C&DH, while housekeeping data were used on the ground to monitor instrument performance. A command that generated images from the arrays was acknowledged on the low-speed line, and when the frame was complete, the data-ready signal was sent on the high-speed line. The frames (together with their ancillary data) were then transferred one at a time to the C&DH. The rate of transfer was two seconds per frame, which limited the data collection rate to a maximum of four frames every eight seconds for IRAC observations with all four arrays.

Autonomous fault protection ensured that the instrument would not be damaged or a significant amount of cryogen be lost if the monitored voltages or currents entered into a red limit. Fault protection was performed by comparing the voltages sampled in the housekeeping data to the red limits that were stored in IRAC memory. For example, if a voltage in the focal plane assembly went into a red limit that persisted for three housekeeping cycles, IRAC would turn off the affected focal plane array. (The individual pixel values were not monitored, so a bright astronomical source did not trigger a red limit.) The command sequences would continue to execute; therefore, it was possible for a normal completion of an IRAC observing campaign to occur with only three of the four arrays returning data. If a second focal plane assembly had a telemetry datum go into a red limit, then IRAC would send the C&DH (via the special engineering data on the low-speed line) a

request to be turned off. If a telemetry point other than one affecting a single focal plane went into a red limit, IRAC would also send the C&DH a request to be turned off.

2.5 Sensitivity and Saturation

2.5.1 Sensitivity Model

To estimate the sensitivity of IRAC in flight, where possible we use the measured properties of Spitzer and IRAC from the IOC/SV and IWIC; otherwise we use the required performance based on the design specifications. The sensitivity (σ) to point sources (in flux density units) is based on the following formula:

$$\sigma = \frac{\sqrt{N_{pix}}}{ST_{ex}f_p} \sqrt{BT_{ex} + (BT_{ex}v_F)^2 + R^2 + DT_{ex}} \quad (2.6)$$

where the scale factor is

$$S = \frac{Q\eta_T\eta_I A\Delta\lambda}{h\lambda}, \quad (2.7)$$

the background current is

$$B = SI_{bg}f_S\Omega_{pix}f_{ex}, \quad (2.8)$$

and the effective exposure time is

$$T_{ex} = T_F - 0.2N_F \quad (2.9)$$

In these equations, the spectral resolving power $\lambda / \Delta\lambda$ is from Table 2.2 ; the detector quantum efficiency Q (electrons per photon) is 0.87, 0.86, 0.45, and 0.70 in channels 1 – 4, respectively; the instrumental throughput η_I is from Table 2.2; the telescope throughput $\eta_T = [0.889, 0.902, 0.908, 0.914]$ for channels 1 to 4, respectively (with Be primary, Al-coated secondary, and 50 nm ice contamination); the telescope area (including obstruction) $A = 4636 \text{ cm}^2$; the equivalent number of noise pixels N_{pix} is from Table 2.1 (and defined in Section 2.2.2); h is the Planck

constant; I_{bg} is the background surface brightness in MJy/sr; $f_S = 1.2$ is the stray light contribution to the background; the dark current D is $< 0.1, 0.28, 1,$ and 3.8 e-/second for channels 1, 2, 3, and 4, respectively; the read noise R is from Table 2.3; Ω_{pix} is the pixel solid angle (see Table 2.1); f_p is the in-flight estimated throughput correction for point sources (Table 2.4); f_{ex} is the in-flight estimated throughput correction for the background (Table 2.4); T_F is the frame time from Table 2.6 and N_F is the Fowler number from Table 2.6. Table 2.4 lists some useful combinations of IRAC instrument parameters. The quantity v_F is the flat-field pixel-to-pixel variance, which depends on the observing strategy. In what follows, we will set $v_F = 0$, which would apply strictly in the case of stable detectors with perfect flat-field measurements, and should apply practically for highly-dithered observations.

The “throughput corrections” f_p and f_{ex} were determined by comparing the observed to expected brightness of stars and zodiacal light. Stars were measured in a 10-pixel radius aperture, and the zodiacal light was measured in channels 3 and 4 for comparison to the COBE/DIRBE zodiacal light model. (This measurement was not possible in channels 1 and 2 because we could not use the shutter for absolute reference.)

Early in the mission, we found that the throughput in channels 3 and 4 was lower than expected, both for the extended emission and point sources (but more so for point sources). Measurements of diffuse Galactic emission confirmed the deficit, and measurements of the PRF using bright stars showed that a considerable amount of stellar flux was being spread all across the arrays. The deficit in throughput from the diffuse emission was due to the fact that the quantum efficiency (QE) of the arrays had been overestimated. No reliable measurements of the QE existed for channels 3 and 4, so the QE was based on a theoretical model that incorrectly assumed that all the flux was reflected at the front of the detector diode chip (the detector arrays are backlit). Some of the light that passed through the detector was scattered widely across the array. Measurements on a sister array confirmed this internal scattering, and showed that it was strongly wavelength dependent. There was considerable evidence that the “loss” of the QE and the scattered light were not due to contamination, or damaged optical coatings, etc.

Table 2.5 gives the background brightnesses, in useful units, for three nominal observing directions. The low-background model applies near the ecliptic pole; the high-background case is in the ecliptic plane; and the medium-background case is intermediate. The background model includes contributions from emission and scattering from the zodiacal dust and emission from the Galactic dust. The near-infrared cosmic infrared background radiation is not included because it was partially resolved by Spitzer.

Table 2.4: Useful quantities for IRAC sensitivity calculations. The second set of numbers in channels 1 and 2 are for the warm mission.

Wavelength	3.6 μm	4.5 μm	5.8 μm	8.0 μm
Conversion factor (electrons/seconds)/(MJy/sr)	25/29.5	29/25.3	14	29
S (electrons/seconds)/(μJy)	0.77/0.84	0.89/0.73	0.42	0.91
Gain (electrons/DN)	3.3/3.7	3.7/3.7	3.8	3.8
f_p (throughput correction for point sources)	1.06/1	0.84/1	0.45	0.61
f_{ex} (throughput correction for background)	1	1	0.72	0.88

Table 2.5: Background brightness in IRAC channels. The second set of numbers in channels 1 and 2 are for the warm mission. $I_\nu f_s$ is the expected background brightness on the detectors, F_ν^{BG} is the flux density on each pixel due to the background brightness, and B is the background brightness on the detectors in electrons per second units, using the FLUXCONV values given in Section 4.3 of this Handbook, and the Gain values in Table 2.4.

	3.6 μm	4.5 μm	5.8 μm	8.0 μm
low background model				
$I_\nu f_s$ (MJy/sr)	0.093	0.32	1.7	6.6
F_ν^{BG} (μJy)	3.2	11	57	220
B (electrons/second)	2.5/2.7	9.9/8.9	18	184
medium background model				
$I_\nu f_s$ (MJy/sr)	0.15	0.44	2.3	9.3
F_ν^{BG} (μJy)	5.1	15	79	320
B (electrons/second)	4.1/4.4	14/11	25	260
high background model				
$I_\nu f_s$ (MJy/sr)	0.52	1.0	5.6	22
F_ν^{BG} (μJy)	18	35	190	750
B (electrons/second)	14/15	32/26	60	620

An observation with no dithering is limited by correlated noise. The accuracy of a flat-field derived from a single observing campaign was measured as 2.4%, 1.2%, 1.0%, and 0.3% in channels 1 –

4, respectively, by comparing flats in several campaigns. Using combined flats (“superskyflats”) from the entire cryogenic (warm) mission, the estimated v_F was 0.14% (0.17%), 0.09% (0.09%), 0.07%, and 0.01% in channels 1 – 4, respectively. Using these values for v_F in equation 2.6, single frames were dominated by background and read noise. When combining multiple frames to generate a mosaic, the background and read noises averaged down (as square root of the number of frames), while the flat-field noise only averaged down for dithered observations. For N undithered observations on the medium background, flat-field noise dominated when the total exposure time, $N \times T_{ex}$, exceeded approximately 420 seconds (using individual campaign flats) or 2.5 hours (using the superskyflat). For dithered observations, the flat-field noise also averaged down, and was only important for the very deep observations of high background fields.

For the frame times used in IRAC operations in flight, Table 2.6 gives the readout mode and Fowler number. For full array readout mode, only the 2, 12, 30, and 100 second (and initially 200 second) frame times could be chosen in the IRAC AOT in the cryogenic mission. In the warm mission, 0.4 and 6 second frame times were added. The 0.6 and 1.2 second frame times came as part of the High Dynamic Range (HDR; see Section 3.1) sequences. The 0.4 second full frame time was only available for channels 1 and 2 in the Stellar Mode (see Section 3.1) in the cryogenic mission, but it was available in the regular full array mode in the warm mission. The 2 second subarray frame time was only available in the warm mission. The frame sets that were taken for each pointing in the HDR mode are shown in Table 2.7. Long frame times at 8.0 μm were background-limited. Therefore, there was a maximum frame time of 50 seconds at 8.0 μm , and the 100/200 second frames were automatically converted into two/four repeats of 50 second frames in channel 4. The last column, T_h , gives the extra time spent taking the HDR frames (used in the observing time estimate equation below).

Table 2.6: Fowler numbers for IRAC frames. The numbers in parentheses are for channels 1 and 2 in the warm mission if different from the cryogenic values. Wait ticks are defined in Section 2.4.3.

Frame Time (seconds)	Exposure Time (seconds)	Readout Mode	Fowler Number	Wait Ticks
200	193.6 (187.2/193.6)	Full (not 8.0 μm)	32	936
100	96.8 (93.6/96.8)	Full (not 8.0 μm)	16 (32/16)	468 (436/468)
50	46.8	Full (8.0 μm only)	16	218
30	26.8 (23.6/26.8)	Full	16 (32/16)	118 (86/118)
12	10.4	Full	8	44
(6)	(4.4/4.4)	Full	(8/8)	(14/14)
2	1.2	Full	4	2
2	(1.92/1.92)	Subarray	(8/8)	(184/184)
1.2	1.0 (0.8/0.8)	HDR	1 (2/2)	4 (2/2)
0.6	0.4	HDR	1	1
0.4 ^a	0.2	Stellar/Full	1	0
0.4	0.32 (0.36/0.36)	Subarray	8 (4/4)	24 (32/32)
0.1	0.08	Subarray	2	6
0.02	0.01	Subarray	1	0

^a available only in the stellar photometry mode in the cryogenic mission, full array in the warm mission.

Table 2.7: IRAC High Dynamic Range (HDR) framesets.

Long Frame Time	List of frames taken	T_h (seconds)
200	0.6, 12, 200	15
100	0.6, 12, 100	15
30	1.2, 30	3
12	0.6, 12	2
6 [*]	0.6, 6	2

* Warm mission only.

The sensitivities for the four IRAC channels (for each of the three background models) are shown in Table 2.8, Table 2.9, and Table 2.10 and Figure 2.8, Figure 2.9, and Figure 2.10. The sensitivities in the tables are for point sources extracted from single images (but perfectly flat-fielded). In the figures, the sensitivities are for point sources extracted from coadded images (perfectly registered). We do not include “confusion noise” (due to overlapping images of distant galaxies or other sources of background structure) in the sensitivity estimates. The detectors were assumed to perform according to the ground-based IRAC detector measurements of read noise, dark current, and quantum efficiency. The first eight rows in each table show the sensitivity for full array readouts, and the last four rows show the sensitivity for subarray readouts.

Table 2.8: IRAC point-source sensitivity, based on Equation (2.6), low background (1σ , μJy). The second set of numbers in parentheses for channels 1 and 2 are for the warm mission.

Frame Time (seconds)	3.6 μm	4.5 μm	5.8 μm	8.0 μm
200	0.40	0.84	5.5	6.9
100	0.60 (0.86)	1.2 (1.25)	8.0	9.8
30	1.4 (2.2)	2.4 (2.5)	16	18
12	3.3 (4.9)	4.8 (5.0)	27	29
6	(12.2)	(9.8)	-	-
2	32 (44)	38 (39)	150	92
0.6 ^a	180 (185)	210 (222)	630	250
0.4 ^b	360 (369)	430 (443)	1260	450
2 ^c	(19)	(21)	-	-
0.4 ^c	81 (102)	89 (102)	609	225
0.1 ^c	485 (552)	550 (566)	2010	690
0.02 ^c	7300 (8374)	8600 (8447)	25000	8100

^aavailable only in the high dynamic range (HDR) mode.

^bavailable only in the stellar photometry mode in the cryogenic mission, and full array in the warm mission.

^csubarray mode (set of 64 32×32 images). Sensitivity is per frame, not the sensitivity of a 64-frame coadd.

Table 2.9: Same as Table 2.8 but for medium background (1σ , μJy).

Frame Time (seconds)	3.6 μm	4.5 μm	5.8 μm	8.0 μm
200	0.49	0.97	6.4	8.2
100	0.73 (1.0)	1.4 (1.44)	9.3	12
30	1.6 (2.5)	2.8 (2.9)	18	21
12	3.6 (5.2)	5.3 (5.5)	31	34
6	(12.4)	(10.4)	-	-
2	32	38	150	110
0.6 ^a	180 (185)	210 (222)	640	260
0.4 ^b	360 (370)	430 (443)	1260	460
2 ^c	(19)	(21)		
0.4 ^c	82 (102)	89 (103)	610	250
0.1 ^c	490 (553)	550 (567)	2020	720
0.02 ^c	7300 (8374)	8600 (8447)	25000	8100

^aavailable only in the high dynamic range (HDR) mode.

^bavailable only in the stellar photometry mode in the cryogenic mission, and full array in the warm mission.

^csubarray mode (set of 64 32 \times 32 images). Sensitivity is per frame, not the sensitivity of a 64-frame coadd.

Table 2.10: Same as Table 2.8 but for high background (1σ , μJy).

Frame Time (seconds)	3.6 μm	4.5 μm	5.8 μm	8.0 μm
200	0.89	1.5	9.8	12
100	1.3 (1.48)	2.1 (2.16)	14	18
30	2.5 (3.3)	4.1 (4.2)	27	32
12	4.8 (6.1)	7.1 (7.4)	44	52
6	(13.4)	(12.8)	-	-
2	34 (45)	41 (42)	180	156
0.6 ^a	180 (186)	220 (224)	660	330
0.4 ^b	360 (370)	430 (445)	1280	540
2 ^c	21	24	-	-
0.4 ^c	84 (104)	93 (106)	650	340
0.1 ^c	490 (555)	560 (569)	2100	860
0.02 ^c	7300 (8375)	8600 (8848)	25000	8200

^aavailable only in the high dynamic range mode.

^bavailable only in the stellar photometry mode in the cryogenic mission, and full array in the warm mission.

^csubarray mode (set of 64 32×32 images). Sensitivity is per frame, not the sensitivity of a 64-frame coadd.

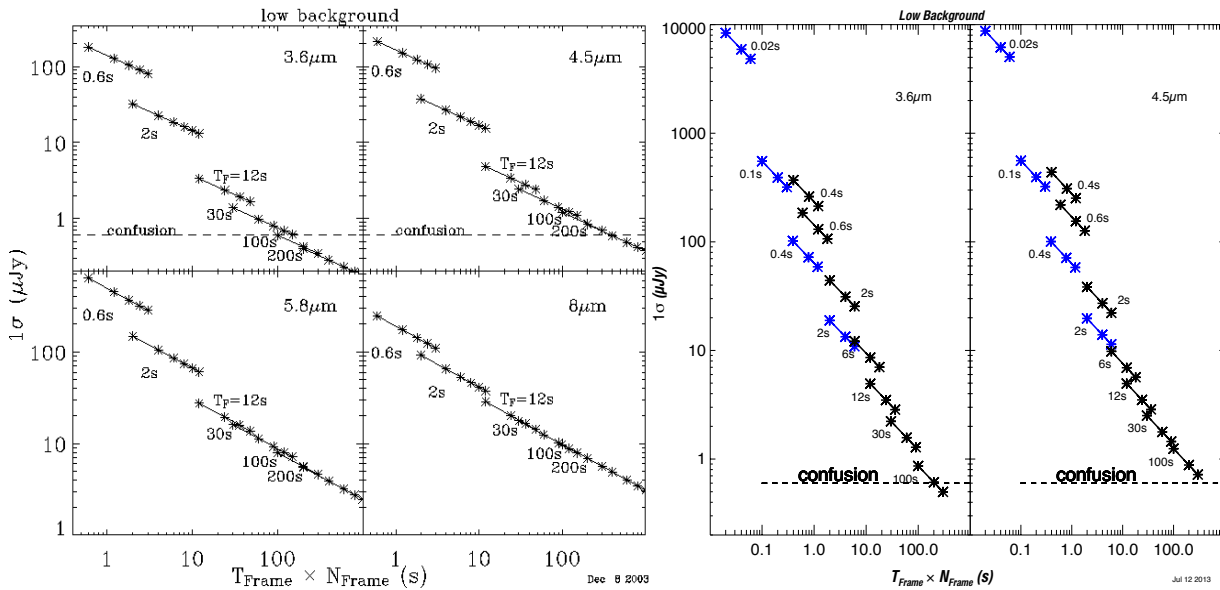


Figure 2.8: IRAC point source sensitivity as a function of frame time, for low background. The cryogenic values are on the left, and the warm mission values are on the right. To convert to MJy/sr, see equation (2.13). Subarrays are plotted in blue.

Figure 2.8, Figure 2.9, and Figure 2.10 show the point source sensitivity as a function of the integration time for each background model. The bottom axes in the plots represent the frame time for the images, which does not include time for moving the telescope. The IRAC full array frame times were 0.4, 0.6, 2, 6, 12, 30, and 100 seconds (0.4 and 6 second frames were available only in the warm mission; 200 seconds was also available in the early mission). Other times plotted are assumed to use multiple exposures of those fixed times.

For bright sources, shot noise due to counting statistics in electrons from the source itself became the dominant source of noise. One could estimate the total noise by adding the shot noise in quadrature, so that

$$\sigma_{tot} = \sigma \sqrt{1 + (F / F_b)} \quad (2.10)$$

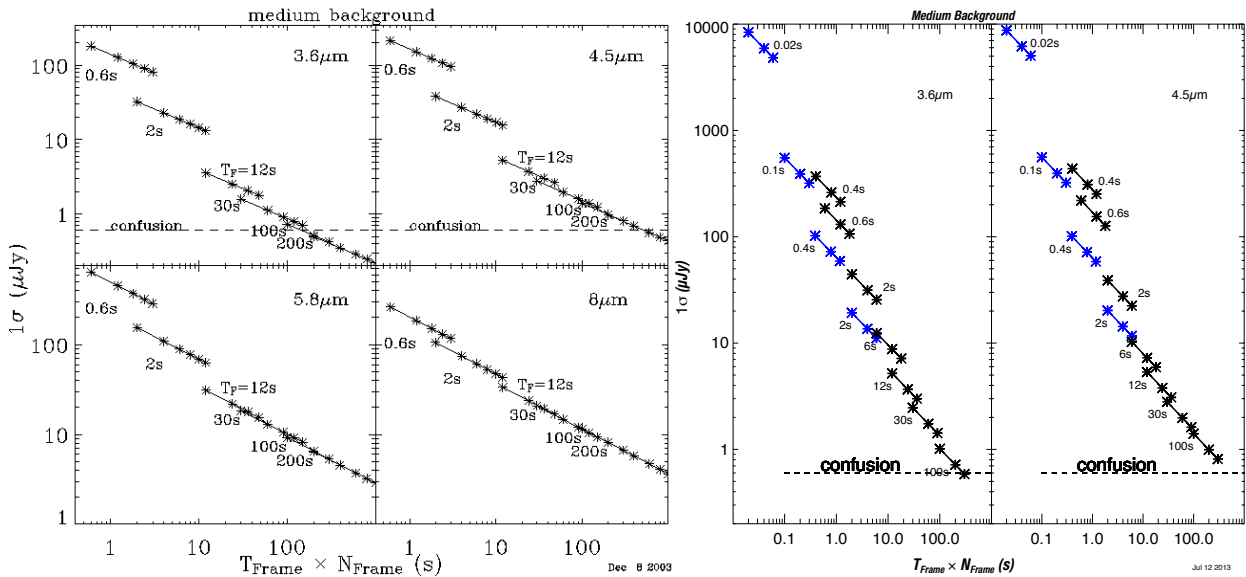


Figure 2.9: Similar to Figure 2.8, but for medium background.

where σ is the noise from Equation 2.6 and

$$F_b = f_p S T_{ex} \sigma^2. \quad (2.11)$$

In the bright source limit, $F \gg F_b$, the signal-to-noise ratio became

$$S/N = \sqrt{f_p S T_{ex} F}. \quad (2.12)$$

If the exposure time is in seconds and the source flux is in μJy , then for IRAC channels 1, 2, 3, and 4, respectively, the SNR was 0.88 (0.86), 0.95 (0.85), 0.65, and 0.95 times $\sqrt{T_{\text{ex}} F}$. Warm mission values are in parentheses.

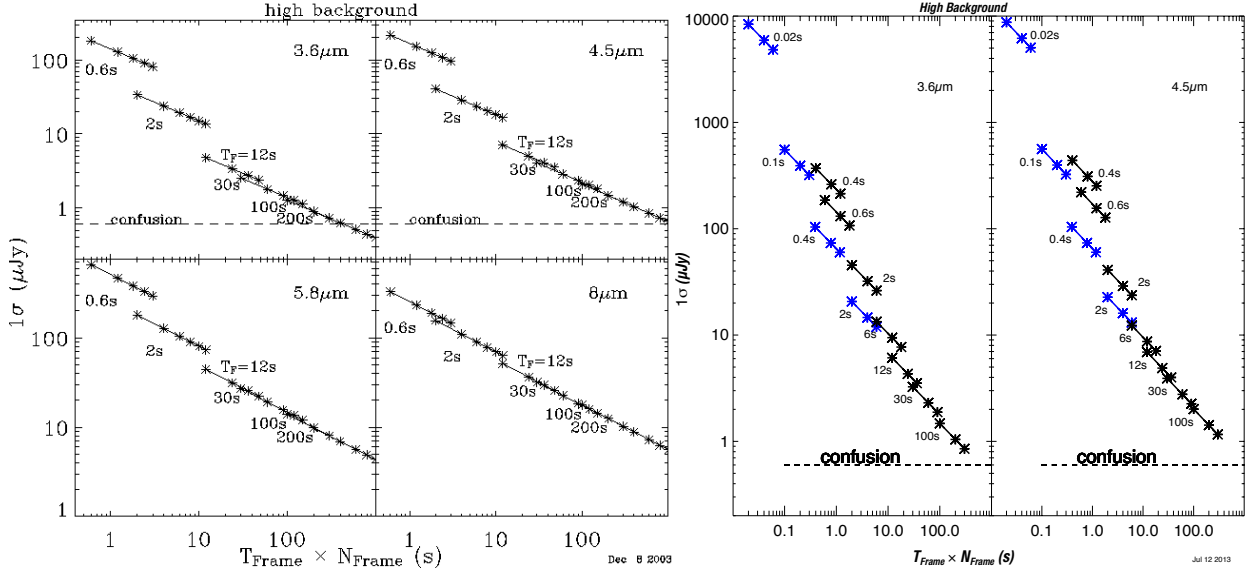


Figure 2.10: Similar to Figure 2.8, but for high background.

In the sensitivity figures, the dashed line at $0.6 \mu\text{Jy}$ is the confusion limit predicted by Franceschini et al. (1991). This does not represent a hard sensitivity limit, but rather indicates where source confusion affected the reliability of source extractions for low background regions. Data from the IOC/SV showed noise decreasing as \sqrt{N} to $0.25 \mu\text{Jy}$ (channels 1 and 2) or $0.6 \mu\text{Jy}$ (channels 3 and 4). Moderately deep source counts indicated that a source density equivalent to 36 beams/source was reached at 20.5 mag, or 1.8 and $1.1 \mu\text{Jy}$ at 3.6 and $4.5 \mu\text{m}$, respectively (Fazio et al. 2004). The confusion estimates by Franceschini et al. and Fazio et al. are for low background, extragalactic observations only. For observations of higher background or more dense regions (such as the Galactic Plane), the confusion noise was much more significant.

For diffuse emission, the surface brightness sensitivity per pixel (in MJy/sr) was

$$\frac{0.03 f_p}{f_{\text{ex}} \sqrt{N_{\text{pix}}}} \times \text{the point source sensitivity [in } \mu\text{Jy}]. \quad (2.13)$$

The noise pixels, N_{pix} , are listed in Table 2.1 and defined in Section 2.2.2.

2.5.2 Saturation

The saturation limit for IRAC was calculated as follows. Using the same notation as earlier in this section,

$$F_{sat} = \frac{Wf_w - BT_F f_{ex}}{ST_F f_{cen} f_p}, \quad (2.14)$$

where W is the well depth (discussed in Section 2.3.2), $f_w = 0.9$ is the fraction of the well depth to which we can linearize the intensities, and f_{cen} is the fraction of the source flux falling onto the central pixel (Table 2.1). Table 2.11 shows the point source saturation limits of IRAC at each frame time. In an extremely bright area of the sky, such as an H II region, the saturation limit was lower. Note that the saturation value was conservatively computed from the worst case in which the PSF is directly centered on a pixel. To apply Table 2.11 for extended sources,

$$I_{sat} = 28.6 \times f_{cen} F_{sat} \quad \text{for compact (diameter } < 30'' \text{) sources} \quad (2.15)$$

$$I_{sat} = 28.6 \times \frac{f_{cen} f_p}{f_{ex}} F_{sat} \quad \text{for more extended sources,} \quad (2.16)$$

where I_{sat}^{ext} is the total surface brightness (in MJy/sr) at which a pixel saturates; f_p , f_{cen} , and f_{ex} are as defined above, and F_{sat} is the saturating point source flux density (in mJy) from Table 2.11, appropriate for the channel and integration time. For 8.0 μm observations at low ecliptic latitude, an estimate of the zodiacal light should be included in the surface brightness.

Table 2.11: Maximum unsaturated point source (in mJy), as a function of IRAC frame time. The second set of numbers in parentheses are for channels 1 and 2 are in the warm mission.

Frame Time (seconds)	3.6 μm	4.5 μm	5.8 μm	8.0 μm
200	1.9	1.9	14	28
100	3.8 (2.8)	3.9 (3.5)	27	28
30	13 (10)	13 (12)	92	48
12	32 (25)	33 (30)	230	120
6	(50)	(60)		
2	190 (160)	200 (200)	1400	740
0.6	630 (\approx 600)	650 (\approx 750)	4600	2500
0.4*	950 (\approx 1050)	980 (\approx 1350)	6950	3700
2**	(150)	(180)		
0.4**	1000 (700)	820 (900)	3100	2300
0.1**	4000 (3000)	3300 (3700)	13000	9000
0.02**	20000 (\approx 23000)	17000 (\approx 31500)	63000	45000

*stellar mode (cryogenic mission), full array (warm mission); **subarray mode

The zodiacal background only made a difference for long frames in channel 4 when observing near the ecliptic plane. If the bright extended source extended well beyond the 5.2 arcminutes \times 5.2 arcminutes FOV, then the saturation brightness was *lower* by the factor f_s ($= 1.2$; defined near the beginning of Section 2.5.1).

3 Operating Modes

The cryogenic and warm IRAC Astronomical Observation Templates (AOTs) consisted of a (optional) dither pattern superposed on a (optional) rectangular grid raster (mapping). An example of what the template looked like is given in Figure 3.1. More examples can be found in the Observation Planning Cookbooks at IRSA's Spitzer web pages:

<https://irsa.ipac.caltech.edu/data/SPITZER/docs/spitzermission/reportsandproceedings/historical/missiondocuments/>.

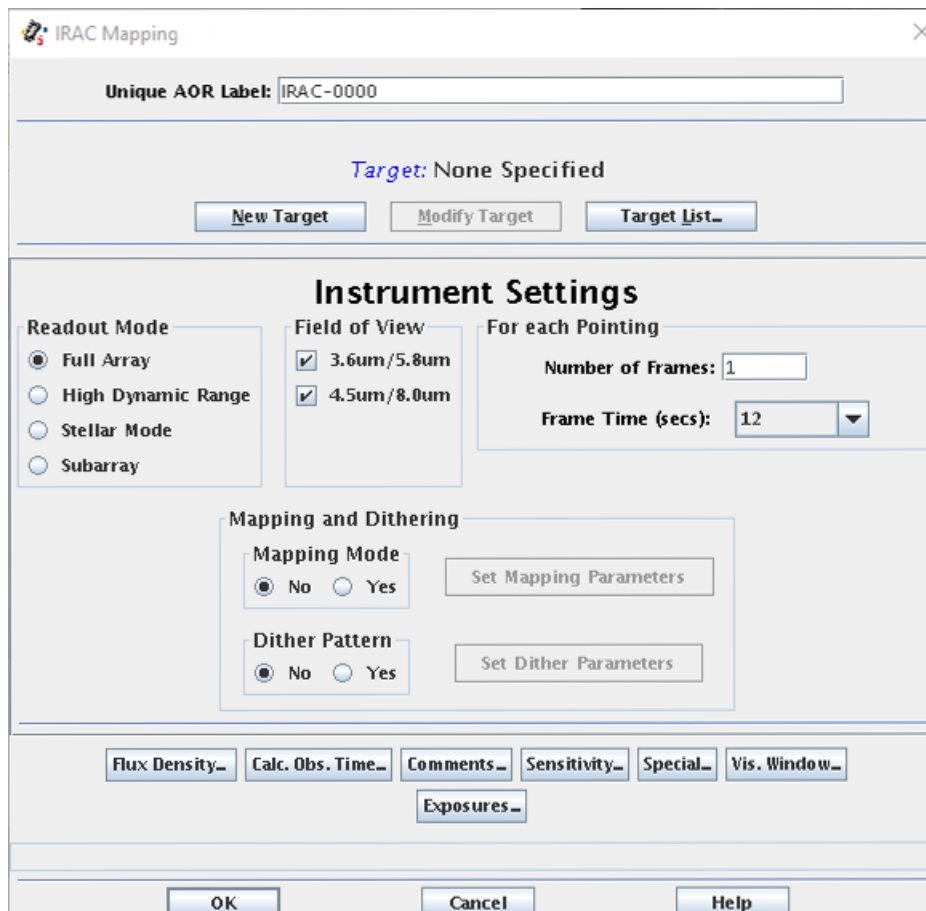


Figure 3.1: IRAC AOT template. The options for selecting observing mode, fields of view, frame repeats, dithering and mapping are shown.

3.1 Readout Modes and Frame Times

There were several possible observing modes, including full array, high dynamic range (HDR), subarray, stellar, and peak-up.

During the cryogenic mission, there were four selectable full array mode frame times: 2, 12, 30, and 100 seconds (and a fifth, 200 seconds, during the early mission; see Section 2.4.3 for more information about frame times and exposure times). The warm mission added the 0.4 and 6 second frame times. To allow sensitive observations without losing dynamic range, there was a high dynamic range option. When this option was selected, the IRAC AOT took extra frames, with frame times shorter than the selected frame time. Information about the HDR frame times is given in Table 2.7. No spacecraft repositioning was done between frames, and the frames were always taken from the shortest to the longest. If dithers were selected, then the entire frame set was repeated at each dither position. If mapping was selected, then the dithers and optional HDR frame sets were repeated at each map position.

A stellar photometry mode was available for observations of objects much brighter in channels 1 and 2 than in 3 and 4 (typically stars) in the cryogenic mission. This mode took short exposures in channels 1 and 2, and long exposures in channels 3 and 4. Originally developed as an engineering mode for taking observations of the calibration stars, this mode was made available for all the observers. Three framesets were available. The shortest set took a single 0.4 second frame in channels 1 and 2, and a 2 second frame in channels 3 and 4. The next set took two undithered 2 second frames in channels 1 and 2, and a 12 second frame in channels 3 and 4. The longest frame time combination took two undithered 12 second frames in channels 1 and 2, and a 30 second frame in channels 3 and 4. The sensitivities of each frame were identical to those in the full array mode. Dithering and mapping were also available in this mode.

In the subarray mode, only one corner, a 32×32 pixel square portion of the array (a field of view of $38 \text{ arcseconds} \times 38 \text{ arcseconds}$) offset by eight pixels from the edges was read out from one array. Pixels (9:40, 9:40) in raw frame coordinates of the array were read out (thus in [C]BCD data the location is 9:40, 217:248 in channels 1 and 2). The subarray pixel size was the same as the full array pixel size ($\approx 1.2 \text{ arcseconds}$). Fowler sampling was performed as in the full array mode, but 64 subarray images of the specified frame time were taken in succession (so the total time spent is $64 \times T_F$) and tiled into a single 256×256 pixel image before the data were sent from IRAC. In the subarray readout mode, there were three selectable frame times: 0.02, 0.1, and 0.4 seconds in the cryogenic mission. The warm mission added the 2 second subarray frame time. This means that the durations of a single frame set of 64 subarray images at each of the four subarray frame times were 1.28, 6.4, 25.6, and 128 seconds, respectively. In the subarray mode, Fowler sampling was performed at 0.01 second intervals. The IRAC AOT moved the telescope to point at the target in the subarray region of each requested channel, in turn. For the 0.02 second frame time, data rate limitations allowed only data in the channel actually pointing at the target to be taken. For the 0.1, 0.4, and 2 second (the last frame time in warm mission only) subarray frame times, data were taken in all four (two for the warm mission) channels at each pointing position, although only one channel at a time pointed at the target.

The subarray mode was useful for observing very bright sources, obtaining high temporal resolution, and for minimizing data volumes when observing single targets. No CBCDs were generated in the pipeline for subarray data, but the pipeline produced simple stacks of 64 frames median-averaged together (*sub2d.fits). Mapping was not allowed in the subarray mode. However, small maps could be made using a cluster target. To make a mosaic of subarray data, users can use the *sub2d.fits images with corresponding uncertainty and mask files that are available with the

BCD files. The *sub2d.fits images are median stacked two-dimensional combinations of the 64 plane BCD subarray cubes. These files can be used in the MOPEX mosaicking software (Makovoz & Khan 2005) in a similar way to the full array (C)BCD frames.

3.2 PCRS Peak-Up Observations

The PCRS peak-up option (see also Section 4.12.2) was designed to facilitate high precision (<1000 parts per million) relative photometry, and it introduced an overhead of 2 – 5 minutes into the observation. The PCRS peak-up option used the spacecraft's optical pointing system for peak-up. This option provided enhanced accuracy (down to about 0.1 pixels) in positioning a target on a science instrument default pixel (full array or subarray), and improved greatly the photometric precision in staring mode observations (e.g., exoplanet observations) by reducing the range of the pixel phase effect (see Section 4.6). The pixel phase effect is very well characterized and minimal in a sweet spot region, approximately 1/4 pixels on a side, near the center of the subarray in channels 1 and 2.

The PCRS was able to measure the centroids of stars to an accuracy of better than 0.14 arcseconds (1σ radial). For the PCRS peak-up to succeed, the peak-up target had to be in the Vega magnitude range $7.0 \text{ mag} < V < 12.5 \text{ mag}$, and there should not have been any stars brighter than $V = 13.0$ Vega mag within 40 arcseconds of the peak-up target. Peaking up could be done on either the science target itself or on an offset star. It was possible to select stars from the PCRS Guide Star Catalog, which contains a carefully selected subset of stars from the Tycho catalog, or specify your own offset star.

One important scientific benefit of the PCRS peak-up was the ability to reposition a target onto the same spot on a pixel during a long stare, thus enhancing the precision of time-domain measurements. Typically, the Spitzer pointing system drifted systematically by approximately 0.35 arcseconds per day (this is in addition to any potential short-term drift due to a change in the pitch angle; see Section 4.12.4 for more information). This meant that in about 12 hours, a target placed halfway between the center and the edge of the well-characterized 0.25-pixel radius sweet spot of the channel 1 or channel 2 subarray, had a good chance of drifting out of the region of minimal pixel response variation.

Although not a separate mode, exoplanet observations and some other observations were often taken in a so-called staring mode, combined with the PCRS peak-up. In this mode, the repeat option was used instead of dithering, resulting in hours of uninterrupted observation. The observers were encouraged to add a separate 30-minute AOR at the beginning of their observations, pointed off the target itself, to account for an initial drift in telescope pointing that usually stabilized after 30 minutes, and also a short 10-minute AOR, pointed off the target, at the end of the observation, to help form an additional skydark to be subtracted from their long-term staring observations.

3.3 Map Grid

If the mapping mode was used, a rectangular map grid needed to be specified in either array or celestial coordinates. First, in array coordinates, the map grid was aligned with the edges of the array, such that the map rows and columns corresponded to rows and columns of the array. Specifically, at the ecliptic, a column was along a line of constant solar elongation, and a row was along an ecliptic parallel (line of constant ecliptic latitude). It is worth noting that due to the instrument configuration, the two IRAC fields of view were at approximately constant solar elongation, so that a map with 1 column and several rows made a strip along the direction of the separation between the two fields of view, and yielded 4-array (2-array in the warm mission) coverage along part of the strip (if it was long enough). And, second, if the mapping was done in celestial coordinates, the rows and columns corresponded to J2000 right ascension (R.A.) and declination (Dec.). A position angle, degrees E of N, could be specified to orient the raster in equatorial coordinates. Specifically, if the position angle was zero, a column was along a line of constant R.A., and a row was along a parallel (a line of constant Dec.). The map could be offset from the specified coordinates by giving a map center offset.

If “No mapping” was selected in the AOT, the observation consisted of a single position at the coordinates specified in the Target section of the AOT. With “No mapping” selected, and selecting both fields of view, first the 4.8/8.0 μm field of view was pointed at the target, and then the telescope repositioned so that the 3.6/5.8 μm field of view pointed at the target. In both cases, data from all 4 (2) arrays were collected during the cryogenic (warm) mission, whether they were pointed at the target or not.

3.4 Dithering Patterns

All of the available dither patterns were chosen pre-flight to enable different types of observations. For the full array mode there were two types of dithering available, fixed and cycling. The five fixed patterns, described below in more detail, performed identically at each mapping position. The cycling pattern performed a different subset of dither points at each map position.

Two fixed patterns were available for the subarray mode, as the fields of view covered by the arrays in the subarray mode were much smaller than in the full array mode.

The characteristics of the available dither patterns are given in

Table 3.1.

- The Reuleaux Triangle patterns were designed with the idea of optimizing the Figure of Merit of Arendt et al. (2000), based on their usefulness for allowing calibration on all spatial scales. They thus sample a wide range of spatial frequencies in a fairly uniform manner, and were well suited to the Fixsen et al. (2000) least-squares flat-fielding technique.
- The 9-point and 16-point patterns were designed to have the optimum dither steps for 1/3 and 1/4 subpixel dithering, respectively.
- The random 9 pattern was based on a uniform random distribution.
- The spiral 16 pattern was designed by R. Arendt to provide a pattern which was both compact and had a good figure of merit for self-calibration.
- The cycling patterns were designed for observations (AORs) having many mapping/dithering pointings. The large and medium patterns were Gaussian distributions of offsets with dithers larger than 128 pixels removed. The small pattern was specifically designed for mapping, where only a few dithers were taken at each map position. It was also based on a Gaussian distribution, but the center was downweighted to decrease the fraction of small dithers in the pattern, and it was truncated at a maximum dither size of 11 pixels to ensure that maps with up to 280 arcsecond spacing have no holes, even if there was only one dither per map point.

All the patterns were constrained to have no pair of dithers closer than three pixels in any run of four consecutive points. The cycling dither table wraps around once the final (311th) element was reached. This pattern had a 1/2 sub-pixel sampling pattern superposed on it, starting with point 1 and repeating continuously every four points (at point 311, the final cycle was simply truncated early, thus patterns which wrapped around the table missed a sub-pixel dither point). The 5-point Gaussian pattern was a general use pattern suitable for shallow observations where the exact sub-pixel sampling was unimportant. It had a 1/2 sub-pixel pattern, with the fifth point at sub-pixel (1/4,1/4). Figure 3.2 shows the dither patterns at the default (large) scale. Figure 3.2 shows the cycling dither patterns and the distribution of both the dithers and of the separation between the dithers for each scale. The dither offsets are also available online at IRSA's Spitzer documentation website:

<https://irsa.ipac.caltech.edu/data/SPITZER/docs/irac/calibrationfiles/dither/> .

Table 3.1: Characteristics of the dither patterns.

Dither Pattern	Scale	Max dither (pixels from (0,0))	Median dither separation (pixels)	Sub-pixel dither pattern (pixels)
Cycling	Small	11	10.5	1/2
	Medium	119	53	1/2
	Large	161	97	1/2
5-point Gaussian	Small	26	23	1/2
	Medium	52	46	1/2
	Large	105	92	1/2
9-point random	Small	16	14	1/3
	Medium	34	28	1/3
	Large	69	59	1/3
12-point Reuleaux	Small	13	15	1/2
	Medium	27	30	1/2
	Large	55	59	1/2
16-point spiral	Small	16	12	1/4
	Medium	32	23	1/4
	Large	64	45	1/4
36-point Reuleaux	Small	17	19	1/4
	Medium	34	39	1/4
	Large	67	78	1/4

Each of the IRAC dither patterns was available in three sizes, large (default), medium, and small. For most of the patterns, the scaling of the large, medium, and small patterns was approximately in the ratio 4:2:1. Exceptions were the small cycling pattern, which was about 1/5 of the size of the large cycling pattern and had a lower-weighted inner region to reduce the numbers of small separation dithers, and the 4-point subarray pattern, where the scaling was 4:3:1.5. For all the patterns, the sub-pixel dithering was maintained, independent of scale.

Sub-pixel dithering, combined with the drizzle technique (Fruchter & Hook 2002) to reconstruct the images, could improve the sampling of the mosaics that are obtained from IRAC (or any other) observations. Such strategies have been used for the WFPC2, NICMOS, ACS, and WFC3 instruments on the HST for some time (for details, see the HST Multidrizzle Handbook). Dithering was also needed to calibrate the intrapixel sensitivity variations, and for programs requiring accurate photometry and astrometry (Anderson & King 2000). To be effective, however, accurate pointing and low image distortion were required. The offsetting accuracy of Spitzer was in the range 0.1 – 0.4 arcseconds. This, combined with the image distortion in the IRAC arrays, placed a limit of about 1/4 pixel on the sub-sampling that was likely to prove useful in practice. For example, the distortion of the IRAC camera was < 1% (see Figure 2.5). Thus, for the largest dither patterns, which typically offset up to ± 64 pixels from the starting point, the offsets were up to ± 0.6 pixels from the nominal values. Only in the small-scale patterns, where the offsets were less than ± 16 pixels, would the sub-pixel sampling work well, though even on the larger scales some improvement of the images would probably be noticeable.

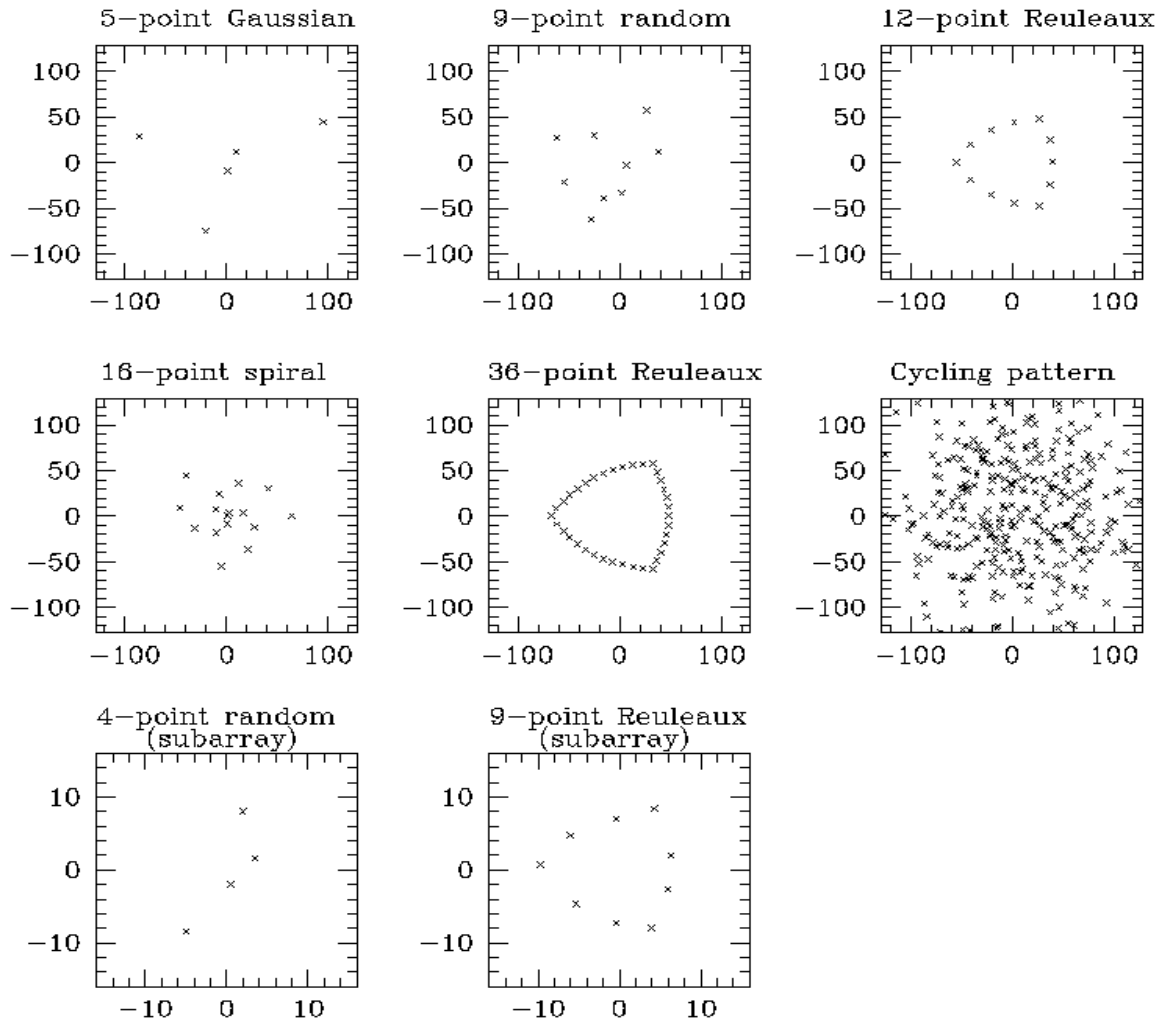


Figure 3.2: IRAC dither patterns for the “large” scale factor. The x - and y -axes are in pixels.

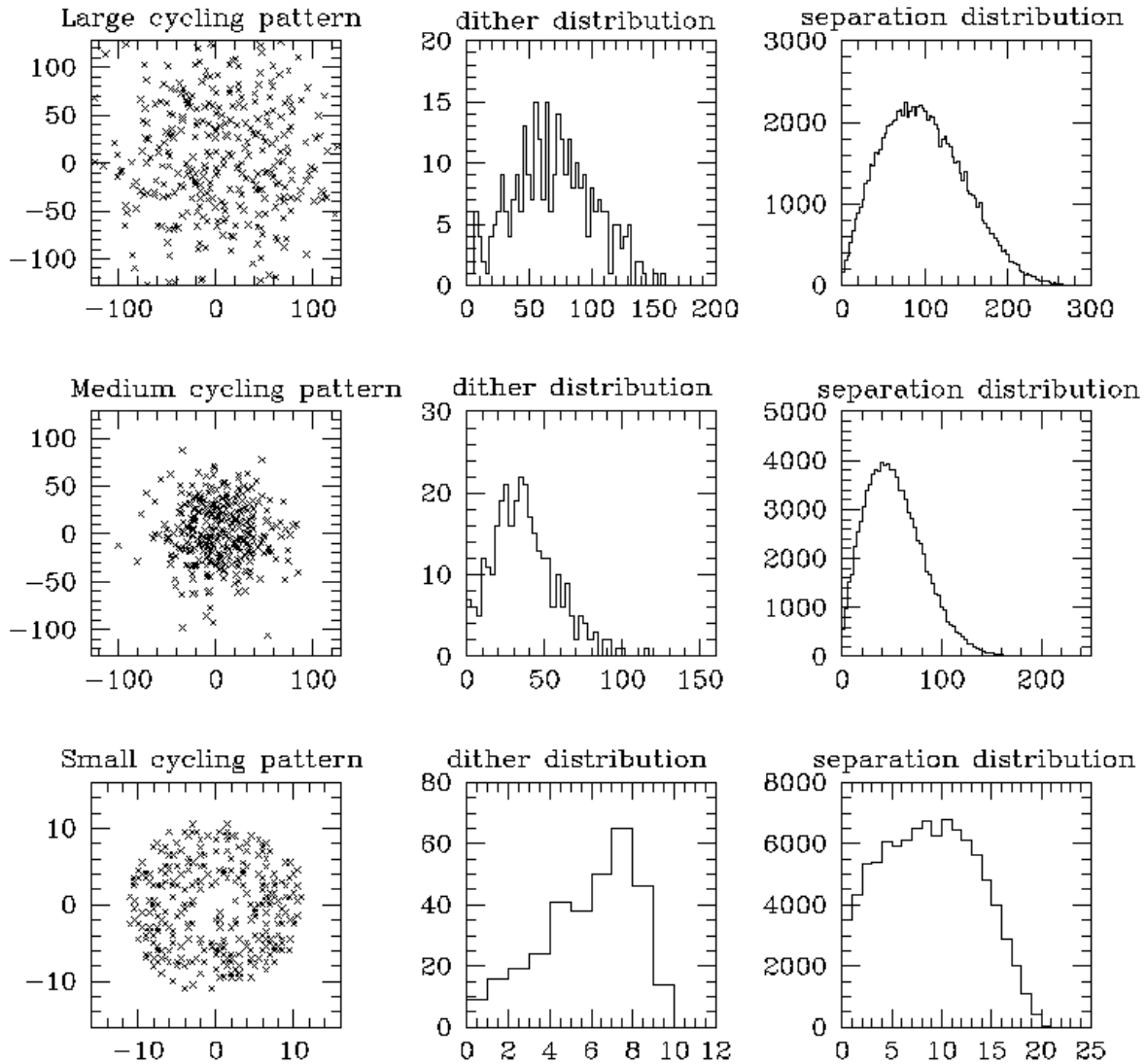


Figure 3.3: Characteristics of the cycling dither pattern. The x - and y -axes are in pixels in the left column plot. The histogram x -axis (separation) is in units of pixels (middle and right plots).

4 Calibration

The Spitzer Science Center (SSC) performed routine calibrations of IRAC using observations of standard stars and other astronomical objects. The data obtained in these observations were used to construct the necessary calibration inputs to the pipeline for the IRAC data processing of science observations. The calibration data files are available to the general user in the Spitzer Heritage Archive maintained by IRSA.

4.1 Darks

4.1.1 *Shutterless Skydarks*

Dark current and bias offsets were calibrated via the standard ground-based technique of dark subtraction. As part of routine operations (during both the cryogenic and warm missions), the SSC observed a “dark” region of the sky (skydark) with no sources brighter than Vega magnitude $V = 12$ near the north ecliptic pole at least twice per campaign (at the beginning and end). These data were reduced and combined in such a way as to reject stars and other astronomical objects with size-scales smaller than the IRAC array. The resulting image (Figure 4.1) of the minimal uniform sky background contained both the bias and the dark current. When subtracted from the routine science data, this eliminated both of these instrumental signatures. Naturally, this also subtracted a component of the true celestial background. The SSC included a COBE-based model estimate of the true celestial background in the (C)BCD headers. Note that the lack of an isolated measurement of the dark current and bias offset during shutterless operations limited the ability of IRAC to measure the true celestial background. The skydarks are available to download from the Spitzer Heritage Archive (SHA) at IRSA, at

<https://sha.ipac.caltech.edu/applications/Spitzer/SHA/>

together with science data.

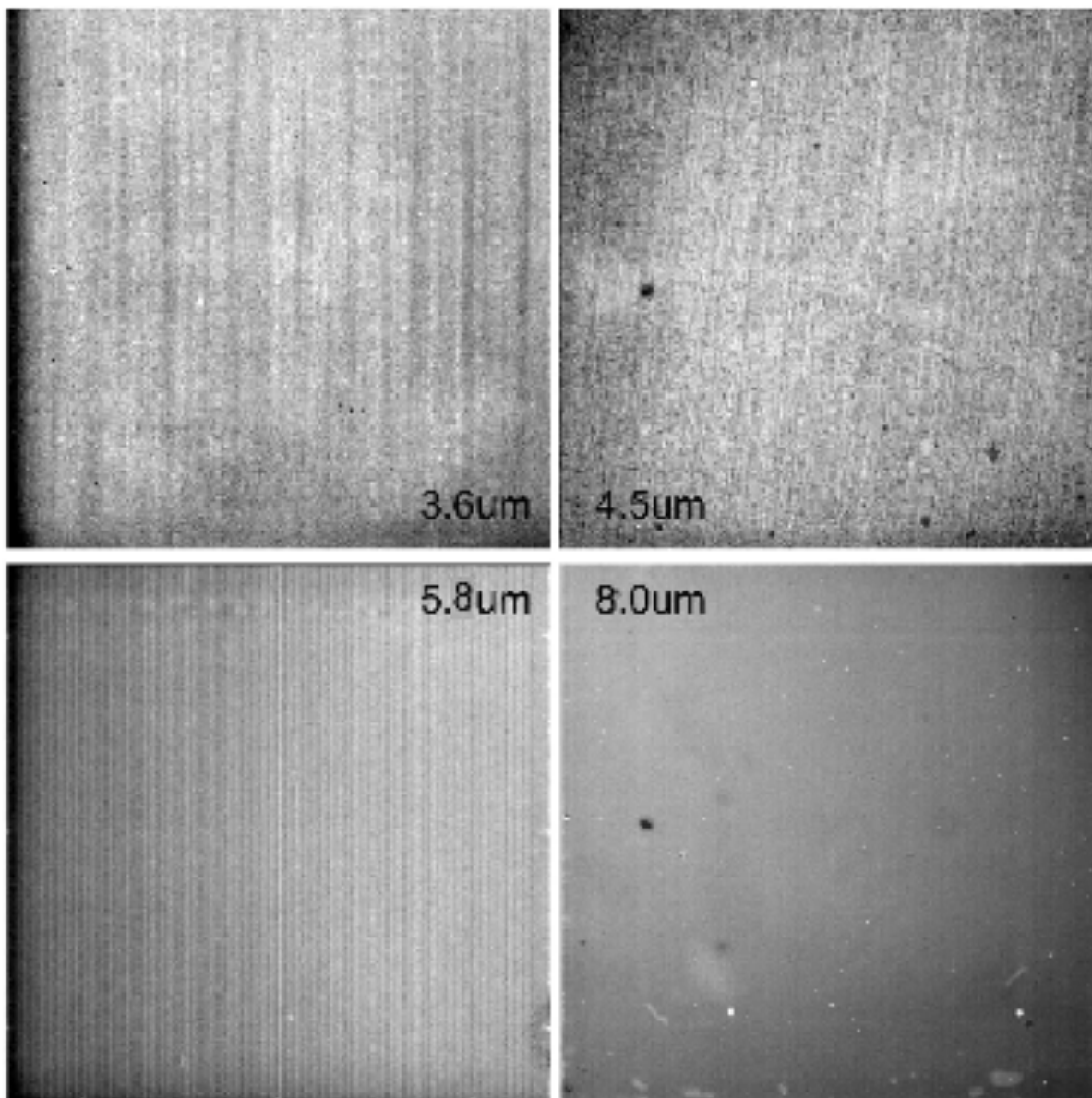


Figure 4.1: IRAC instrument skydark images. These images were taken during a normal campaign, and using 100 second frame time skydarks.

4.1.2 Closed Shutter Campaign

The shutter was allowed to be used on-board during the final science campaign to aid observations of the zodiacal background, and take a set of calibration observations. The obtained darks with the shutter closed were scientifically useful for zodiacal observations, however, two-thirds of the planned shutter-closed darks were lost due to an onboard command timing error.

Figure 4.2 shows the channel 2 skydark compared to the channel 2 dark taken with the shutter closed. Figure 4.3 demonstrates the visual difference between the shutter darks and regular

skydarks. The overall offset is 0.0746 MJy/sr at 3.6 μm and 0.251 MJy/sr at 4.5 μm for the 30 second frame times.

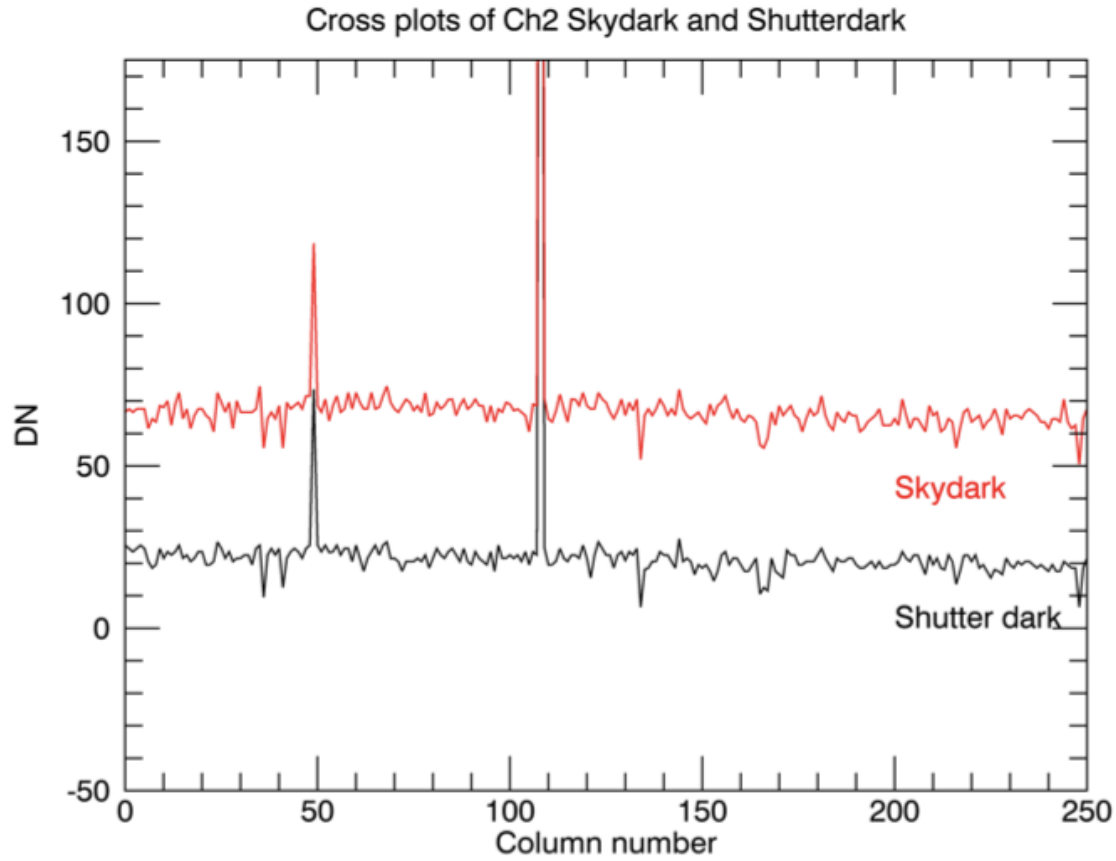


Figure 4.2: Row pixel values (in DN) of a shutter dark and a regular skydark. This plot shows the channel 2 skydark (red) pixel values along a row compared to the pixel values in a channel 2 shutter closed dark (black) in the same row. These observations used the 100 second frame times. The difference between the measurements is consistent with the astronomical background at the skydark position (1 DN = 3.7 electrons).

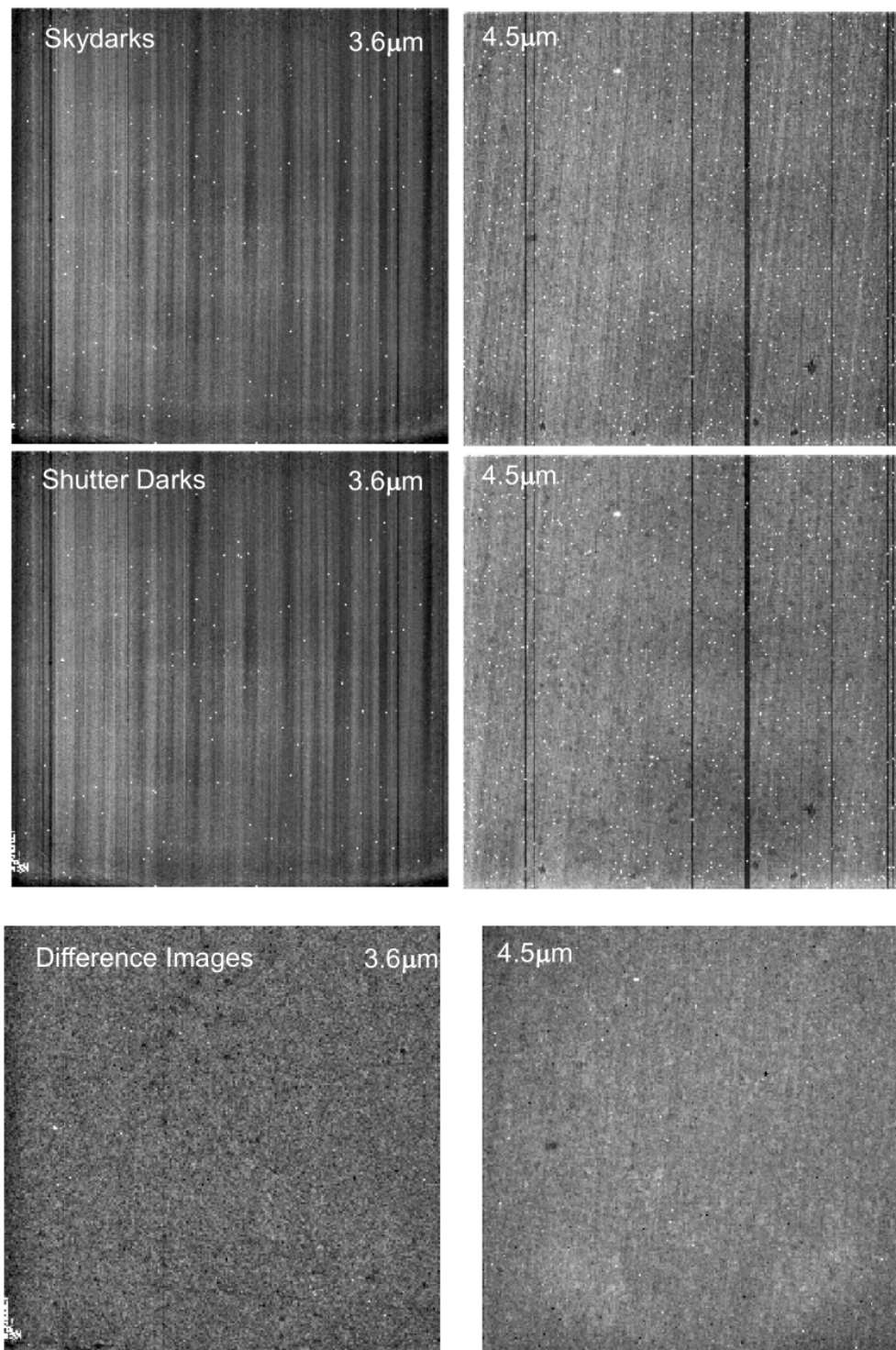


Figure 4.3: Nominal 30 second frame time skydarks (first row) and 30 second frame time shutter darks (second row) for channels 1 and 2 with relative scaling. The difference between the skydark and the shutter dark (last row) is also displayed.

4.2 Flat-Fields

Pixel-to-pixel relative gain variations are commonly known as the flat-field. To get the most accurate measurement of the flat-field, including the effects of the telescope and the IRAC pickoff mirrors, we had to use observations of the sky. Because the IRAC detectors were relatively large, there were few discrete astronomical objects large enough and bright enough to fill the detector field of view.

The flat-field was derived from many dithered observations of a network of 22 high zodiacal background regions of the sky in the ecliptic plane, which ensured a relatively uniform illumination with sufficient flux on all pixels such that the observations were relatively quick to perform. One such region was observed in every instrument campaign.

The data were combined with object identification and outlier rejection, creating an object-free image of the uniform celestial background, further smoothed by the dither pattern. An identical observation made at the north ecliptic pole (the “skydark”) was subtracted, and the result normalized to create the flat-field. The resulting flat-field was divided into the science data. Pixel-to-pixel accuracy of the flat-fielding derived from a single observing campaign was typically 2.4%, 1.2%, 1.0%, and 0.3%, 1σ , for channels 1 through 4, respectively.

Analysis of the flat-field response on a campaign-wide basis showed that there were no changes within the cryogenic or within the warm missions. Based on this, all of the flat-field data were combined into superskyflats. The 1σ pixel-to-pixel accuracy of the cryogenic (warm) superskyflat flat was 0.14% (0.17%), 0.09% (0.09%), 0.07%, and 0.01% in channels 1 – 4, respectively. This was the flat-field used for all pipeline-processed data. During warm operations the flat-field was remeasured to a similar accuracy as that of the cryogenic flat-field. While the warm flat-field was similar in overall appearance, details were sufficiently different so that the warm and cold flats cannot be interchanged. The superskyflats are available from the “IRAC calibration and analysis files” section of IRSA’s Spitzer/IRAC documentation website:

<https://irsa.ipac.caltech.edu/data/SPITZER/docs/irac/calibrationfiles/superflat/> .

Users should note that the flat-field data were generated from the zodiacal background, and are appropriate for objects with that color. There was a significant color term, of order 5% – 10%, for objects with a Rayleigh–Jeans spectrum in the mid-infrared (such as stars); see Section 4.5 for more information. Note that for deep survey observations and other data sets with a large number of frames and a good dithering strategy, the system gain could be determined by the actual survey frames themselves, rather than using the standard set of dedicated observations of some other part of the sky (see, e.g., Arendt et al. 2008).

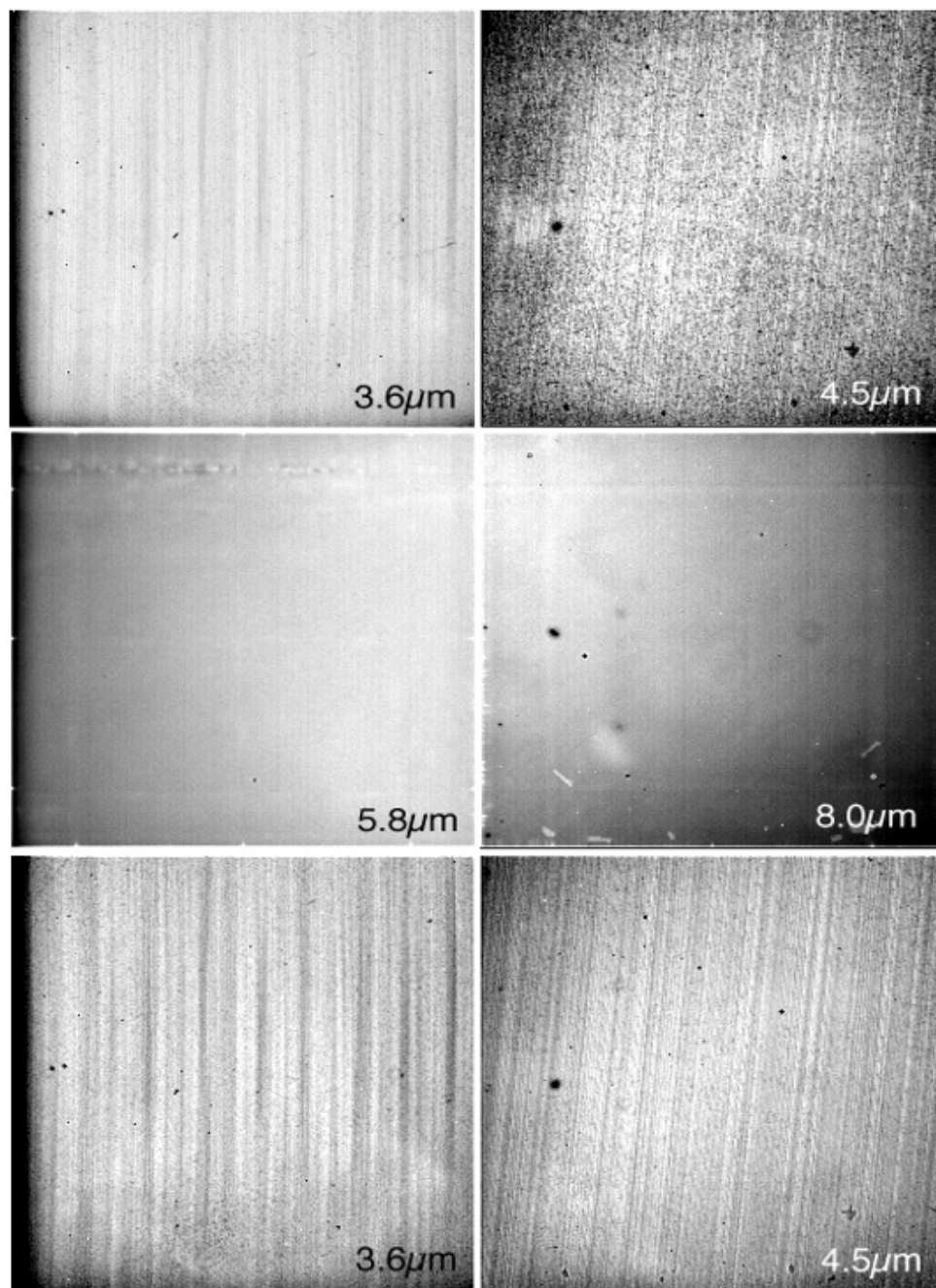


Figure 4.4: IRAC superskyflats. Shown are the cryogenic mission (top two rows, including channels 1 – 4) and the warm mission (bottom, including channels 1 and 2) superskyflats.

4.3 Photometric Calibration

A number of astronomical standard stars were observed to obtain a valid absolute flux calibration. Stars with a range of fluxes were observed at a number of positions across the array many times throughout the mission, to monitor any changes that may have occurred. Spectral types and accurate absolutely calibrated fluxes in the IRAC channels were determined for the calibration

stars. Their flux densities are given in Table 4.1. All of the calibration data taken with these stars are public, and are available in the Spitzer Heritage Archive.

The observational program to measure the flux calibration of IRAC and to ensure its constancy had two components. The primary calibrator stars in the continuous viewing zone (CVZ) were observed in every campaign, and used to derive the overall flux calibration. The secondary calibrator stars were used to monitor short-term variations in the absolute calibration. To avoid slew overheads, they were observed close to downlinks, and, therefore, had to be located near the ecliptic plane, within a tightly constrained window of about 20 degrees in width. Because of the motion of Earth about the Sun, this window constantly moved, and so any one secondary calibrator was visible and near the downlink pointing for only a campaign or two per year. Using the secondary standard stars, the IRAC calibration was measured to be stable over the mission.

The absolute calibration was derived by means of aperture photometry, using a 10 native pixel radius (≈ 12 arcseconds) aperture. The background was measured using a robust average in a 12 – 20 native pixel annulus around the centroid of the star. The steps to remove known systematics are described in detail by Reach et al. (2005), Hora et al. (2008) and Carey et al. (2012). To obtain photometry at the highest possible accuracy, photometric corrections for the location of the peak of the source within a single pixel, and the location of the source within the array, have to be made. If this methodology is not applied, then point source photometry from the Level 1 products (BCDs) can be in error by up to 10%.

Analysis of the flux calibrator data indicated that absolute flux calibration is accurate to 3%. Repeatability of the measurements of the individual stars is better than 1.5% (dispersion), and can be as good as 0.01% with very careful observation design (e.g., Charbonneau et al. 2005). Unfortunately, ground-based infrared calibrators were too bright to use as calibrators for IRAC. Therefore, we had to use models to predict the actual flux for each channel as a function of star spectral type. Uncertainty in those models, and, therefore, in the absolute flux densities of the calibration stars, are 2% – 3% (Cohen et al. 2003). Please note that if you measure aperture photometry on IRAC images, then in our nomenclature you will have measured F^*K^* (where F^* is the flux density of the calibration source at the nominal wavelength, and K^* is the color correction factor for the calibration source spectrum, see Section 4.4). If a comparison of values at the nominal IRAC channel wavelengths (listed in

Table 4.3) to measurements of the star at other wavelengths is desired (e.g., the spectral energy distribution), then the F^*K^* values should be divided by the corresponding K^* values in Table 4.1.

Table 4.1: IRAC primary calibrator quoted flux densities and color corrections.

Calibration Source Name(s)	Stellar Type	Ks mag	Quoted Flux Densities F^* (mJy) and Color Corrections K^*							
			3.6 μm		4.5 μm		5.8 μm		8.0 μm	
			F^*	K^*	F^*	K^*	F^*	K^*	F^*	K^*
NPM_67.0533 SAO17718 2MASS J17585466+6747368	K2III	6.4	804.4	1.0037	454.8	1.0614	318.8	1.0023	178.6	1.0554
HD 165459 2MASS J18023073+5837381	A1V	6.6	645.0	1.0055	422.6	0.9992	267.4	1.0114	145.4	1.0266
NPM1+68.0422 BD+68 1022 2MASS J18471980+6816448	K2III	6.8	554.6	1.0031	305.4	1.0711	218.5	1.0005	121.0	1.0684
KF09T1 GSC 04212-01074 2MASS J17592304+6602561	K0III	8.1	165.8	1.0050	97.65	1.0459	66.42	1.0054	37.26	1.043
NPM1+64.0581 HD 180609 2MASS J19124720+6410373	A0V	9.1	62.86	1.0060	41.09	1.0011	25.97	1.0142	14.16	1.0252
NPM1+60.0581 BD+60 1753 2MASS J17245227+6025508	A1V	9.6	38.10	1.0059	24.82	0.9994	15.67	1.0114	8.506	1.0304
KF06T1 2MASS J17575849+6652293	K1.5III	11.0	13.24	1.0040	7.567	1.0573	5.261	1.0022	2.955	1.051
KF08T3 2MASS J17551622+6610116	K0.5III	11.1	11.85	1.0047	6.922	1.0492	4.738	1.0047	2.662	1.0447
KF06T2 2MASS J17583798+6646522	K1.5III	11.3	10.22	1.0040	5.840	1.0573	4.061	1.0031	2.280	1.051
2MASS J18120957+6329423	A3V	11.3	8.663	1.0055	5.685	0.9986	3.611	1.0084	1.959	1.0252

Table 4.2 lists the calibration factors that were used in the final processing of all IRAC data.

Table 4.2: The photometric calibration and zero magnitude flux densities for IRAC. Warm mission corrections are given as the second set of values in channels 1 and 2. Note that at the beginning of the warm mission the calibration was changing frequently. Different FLUXCONV values for these first months can be found on IRSA’s IRAC web pages (under “Warm IRAC Characteristics”).

λ (μm)	FLUXCONV (MJy/sr)/(DN/second) Cryogenic/Warm		$F_{\nu 0}$ (Jy)
3.6	0.1069 \pm 0.0026	0.1257 \pm 0.0030	280.9 \pm 4.1
4.5	0.1382 \pm 0.0028	0.1447 \pm 0.0029	179.7 \pm 2.6
5.8	0.5858 \pm 0.0100		115.0 \pm 1.7
8.0	0.2026 \pm 0.0043		64.9 \pm 0.9

Table 4.2 lists the calibration factors derived from the primary calibration program that were used in the final processing of all IRAC data. These calibration factors can be used to convert native IRAC data units (DN/second) into units of surface brightness (MJy/sr). Note that the zero magnitude flux densities listed below are evaluated at exactly 3.6, 4.5, 5.8, and 8.0 μm and not at the nominal channel wavelengths given in

Table 4.3. To estimate the zero magnitude flux densities at the nominal channel wavelengths, scale the values in Table 4.2 by the square of the ratio of the wavelengths. For example, in channel 1 the zero-magnitude flux density at 3.544 μm would be $(3.544/3.6)^2 \times 280.9 \text{ Jy} = 272.2 \text{ Jy}$. The difference between the two is a few percent.

Note that IRAC was not an absolute background photometer, so the total brightness in IRAC images should be used with great caution. There was a cold shutter in the cold assembly, but it was not operated in flight, in order to minimize the mission risk. Therefore, in the cryogenic mission the offset level in IRAC images was referenced to laboratory measurements before the launch, where the offset level was observed to change very significantly from one laboratory experiment to another. In laboratory tests, the absolute offset of IRAC images was found to vary at levels that are comparable to the minimum celestial background in channels 1 and 2. Furthermore, the offset level changed depending on whether the detector was recently annealed (annealing means heating the detectors to 23 – 27 K for a short time with a small current flowing through the detectors. It restores the distribution of charges that are trapped to the same distribution each time, but does not restore most hot pixels; annealing was done only during the cryogenic mission). Thus, for diffuse surface brightness measurements, we recommend making differential measurements among at least two sky positions, preferably from the same campaign.

4.4 Color Correction

IRAC was a broad-band photometer. We provide here the prescription for how to interpret the data for sources with spectral shapes other than the nominal one assumed in the calibration process.

The conventions used by IRAC are the same as those used by IRAS (Beichman et al. 1988), COBE/DIRBE (Hauser et al. 1998), and ISO (Blommaert et al. 2003). The basic idea is to quote a flux density $F_{\nu_0}^{quot}$ at a nominal wavelength $\lambda_0 = c/\nu_0$ that would be accurate for a source with a nominal spectrum, $\nu F_{\nu}^{nom} = \text{constant}$. Using this F_{ν}^{nom} is merely a matter of convention; in fact a wide range of spectra are expected, both redder (e.g., interstellar medium, asteroids) and bluer (e.g., stars) than nominal. The color correction tables given below allow observers to convert the nominally-calibrated data, $F_{\nu_0}^{quot}$, into more accurate estimates of the flux density at the nominal wavelength.

The number of electrons at a frequency ν collected from the nominal source in a straight integration of duration t using a telescope with area A is

$$N_e^{nom} = tA \int \frac{F_{\nu}^{nom}}{h\nu} R d\nu; \quad (4.1)$$

where R is the system spectral response, h is the Planck constant, and ν is the frequency. The convention for R is that it is proportional to the number of electrons produced by a single photon with energy $h\nu$, where h is the Planck constant. If we define for convenience

$$\Delta\nu = \int (\nu/\nu_0)^{-2} R d\nu, \quad (4.2)$$

then the number of electrons collected from a source with the nominal spectrum is

$$N_e^{nom} = tA \frac{F_{\nu_0}^{nom}}{h\nu_0} \Delta\nu \quad (4.3)$$

The calibration factor, by which the number of electrons, N_e , from an arbitrary source must be divided in order to give the quoted flux density at the nominal wavelength, is

$$C = \frac{N_e^{nom}}{F_{\nu_0}^{nom}} = \frac{At\Delta\nu}{h\nu_0} \quad (4.4)$$

The calibration factor is measured using observations of a celestial calibrator source of known spectrum, F_{ν}^* . The number of electrons collected from the star is

$$N_e^* = tA \int \frac{F_\nu^*}{h\nu} R d\nu \quad (4.5)$$

Combining with equation (4.4), we can express the calibration factor in terms of the observed number of electrons from the calibration source:

$$C = \frac{N_e^* \Delta\nu}{h\nu_0 \int \frac{F_\nu^*}{h\nu} R d\nu} \quad (4.6)$$

We can now cast this in convenient terms as follows:

$$C = \frac{N_e^*}{F_{\nu_0}^* K^*}, \quad (4.7)$$

where $F_{\nu_0}^*$ is the flux density of the calibration source at the nominal wavelength, and K^* is the color correction factor for the calibration source spectrum.

The color correction factor for a source with spectrum F_ν is defined as

$$K = \frac{\int (F_\nu / F_{\nu_0}) (\nu / \nu_0)^{-1} R d\nu}{\int (\nu / \nu_0)^{-2} R d\nu}. \quad (4.8)$$

In this convention, the overall normalization of R is unimportant. Observers can correct the photometry to the spectrum of their source by either performing the integral in this equation, or looking up the color corrections for sources with similar spectra. Note that our definition of the color correction looks slightly different from that in the *IRAS Explanatory Supplement*, because we used the system spectral response R in electrons/photon, instead of ergs/photon.

We selected nominal wavelengths that minimize the need for color corrections, such that the quoted flux densities in IRAC data products are minimally sensitive to the true shape of the source spectrum. First, let us expand the source spectrum in a Taylor series about the nominal wavelength:

$$F_\nu = F_{\nu_0} \left[1 + \beta \left(\frac{\lambda - \lambda_0}{\lambda_0} \right) + \dots \right]. \quad (4.9)$$

Using equation 4.8, the color correction for a source with spectrum F_ν is

$$K = \frac{1}{\Delta\nu} \int \left[1 + \beta \left(\frac{\lambda - \lambda_0}{\lambda_0} \right) \right] (\nu / \nu_0)^{-1} R d\nu \quad (4.10)$$

The choice of λ_0 that makes K minimally sensitive to β is the one for which

$$\frac{dK}{d\beta} = 0.$$

Solving for λ_0 we get

$$\lambda_0 = \langle \lambda \rangle = \frac{\int \lambda (\nu / \nu_0)^{-1} R d\nu}{\int (\nu / \nu_0)^{-1} R d\nu} = C \frac{\int \nu^{-2} R d\nu}{\int \nu^{-1} R d\nu} \quad (4.11)$$

So the optimum choice of λ_0 for insensitivity to spectral slope is the weighted average wavelength.

Using the nominal wavelengths from

Table 4.3, the color corrections for a wide range of spectral shapes are less than 3%. Thus, when comparing IRAC fluxes to a theoretical model, placing the data points on the wavelength axis at λ_0 takes care of most of the potential color dependence. To place the data points more accurately on the flux density axis (F^* in Section 4.3), take the quoted flux densities ($F^* K^*$ in Section 4.3 but $F_{\nu_0}^{quot}$ here) derived from the images, and *divide* by the appropriate color correction factor in the tables below:

$$F_{\nu_0} = \frac{F_{\nu_0}^{quot}}{K}. \quad (4.12)$$

Or, calculate the color correction using equation 4.8 together with the spectral response tables, which are available in the IRAC section of IRSA's Spitzer documentation website:

<https://irsa.ipac.caltech.edu/data/SPITZER/docs/irac/calibrationfiles/spectralresponse/>.

Table 4.3: IRAC nominal wavelengths and bandwidths. R_{\max} is the maximum spectral response.

Channel	λ_0 (μm)	R_{\max}	Eff. Width $\Delta\nu$ (Eq. 4.2; 10^{12} Hz)	Width $\Delta\nu$ $/R_{\max}$ (10^{12} Hz)	$\frac{1}{2}$ -power wavelengths (μm)	
					red	blue
1	3.544	0.465	7.57	16.23	3.18	3.93
2	4.487	0.535	6.93	12.95	4.01	5.02
3	5.710	0.170	1.93	11.70	5.02	6.44
4	7.841	0.318	3.94	12.23	6.44	9.37

Table 4.4 shows the color corrections for sources with power-law spectra, $F_\nu \propto \nu^\alpha$, and Table 4.5 shows the color corrections for blackbody spectra with a range of temperatures. The nominal spectrum has $\alpha = -1$, so the color corrections are unity by definition in that column. These calculations are accurate to $\approx 1\%$. Note that the color corrections for a ν^{-1} and a ν^0 spectrum are always unity. This is in fact a theorem that is easily proven using equations 4.8 and 4.11.

Table 4.4: Color corrections for power-law spectra, $F_\nu \propto \nu^\alpha$.

Color correction for $\alpha =$					
Channel	-2	-1	0	1	2
1	1.0037	1	1	1.0037	1.0111
2	1.0040	1	1	1.0040	1.0121
3	1.0052	1	1	1.0052	1.0155
4	1.0111	1	1	1.0113	1.0337

Table 4.5: Color corrections for blackbody spectra.

Temperature (K)								
Channel	5000	2000	1500	1000	800	600	400	200
1	1.0063	0.9990	0.9959	0.9933	0.9953	1.0068	1.0614	1.5138
2	1.0080	1.0015	0.9983	0.9938	0.9927	0.9961	1.0240	1.2929
3	1.0114	1.0048	1.0012	0.9952	0.9921	0.9907	1.0042	1.1717
4	1.0269	1.0163	1.0112	1.0001	0.9928	0.9839	0.9818	1.1215

Table 4.6 gives the color corrections for the spectrum of the zodiacal light, which is the dominant diffuse background in the IRAC wavelength range. The first model is the COBE/DIRBE zodiacal light model as implemented in Spitzer Planning Observations Tool Spot. The zodiacal light is mostly due to thermal emission from grains at ≈ 260 K over the IRAC wavelength range, except in channel 1, where scattering contributes $\approx 50\%$ of the brightness. The second zodiacal light spectrum in Table 4.6 is the ISOCAM CVF spectrum (5.6 – 15.9 μm ; Reach et al. 2003) spliced with the COBE/DIRBE model at shorter wavelengths. The two backgrounds differ because of different pointings.

Table 4.6: Color corrections for zodiacal light spectrum.

Channel	COBE/DIRBE model			ISOCAM+COBE/DIRBE		
	I_{ν_0} (MJy / sr)	K	$I_{\nu_0}^{quot}$	I_{ν_0} (MJy / sr)	K	$I_{\nu_0}^{quot}$
1	0.067	1.0355	0.069	0.40	1.0355	0.42
2	0.24	1.0835	0.26	1.44	1.0835	1.56
3	1.11	1.0518	1.16	6.64	1.0588	7.00
4	5.05	1.0135	5.12	25.9	1.0931	28.4

For sources with a complicated spectral shape the color corrections can be significantly different from unity. The corrections are infinite in the case of a spectrum dominated by narrow lines, because there may be no flux precisely at the nominal wavelength, which only demonstrates that such sources should be treated differently than continuum-dominated sources. We calculated one illustrative example which may prove useful. The ISO SWS spectrum of NGC 7023 is dominated by PAH emission bands and a faint continuum over the IRAC wavelength range. Table 4.7 shows the color corrections using equation 4.8 and the ISO spectrum. The large value in channel 1 is due to the presence of the 3.28 μm PAH band, which dominates the in-band flux relative to the weak continuum at the nominal wavelength of 3.550 μm . Channel 2 is mostly continuum. Channel 3 is dominated by a PAH band at 6.2 μm . Channel 4 has significant PAH band emission throughout, with prominent peaks at 7.7 and 8.6 μm . The values in this table can be used for comparison to IRAC colors of other sources by anti-color-correction, which gives the predicted colors for NGC 7023 in the same units as the SSC calibrated data: $F_{\nu_0}^{quot} = F_{\nu_0} \times K$, which is shown in the last column of Table 4.7. Thus, PAH-dominated sources are expected to have

$$F_{\nu_0}^{quot}(8\mu\text{m}) / F_{\nu_0}^{quot}(5.8\mu\text{m}) = 599 / 237 = 2.5 \quad (4.13)$$

Table 4.7: Color corrections for NGC 7023 (PAH-dominated) spectrum.

Channel	F_{ν_0}	K	$F_{\nu_0}^{quot}$
1	17.3	2.21	38.3
2	30.3	1.21	36.6
3	169	1.40	237
4	1021	0.59	599

For observations of sources dominated by spectral lines, the quoted flux densities should be converted into fluxes using

$$F = \frac{F_{\nu_0}^{quot} \Delta \nu \lambda_0}{R_l \lambda}, \quad (4.14)$$

where λ is the wavelength of the spectral feature and R_l is the spectral response at that wavelength. Both λ_0 and effective width $\Delta\nu$ are in

Table 4.3. The formalism used for continuum sources is inappropriate for spectral-line sources, because it is likely that both F_{ν_0} and K can be infinity. It is important that the normalization of R used to determine $\Delta\nu$ and R_l is the same. In

Table 4.3, the column $\Delta\nu$ (effective width) was calculated with the same normalization of the response function as on the documentation website, so it is the appropriate one to use. The maximum response, R_{\max} is also given in that table, so the fluxes of lines near the center of the waveband can be estimated by simply multiplying the quoted flux densities by $\Delta\nu/R_{\max}$, which is listed in the table in the column “Width.”

4.5 Array Location-Dependent Photometric Corrections for Compact Sources with Stellar Spectral Slopes

Point source photometry requires an additional correction that arises from the way in which the data are flat-fielded. Flat-fielding is a way of removing pixel-to-pixel gain variations. The IRAC flat-field was derived by imaging the high surface brightness zodiacal background. The way the IRAC flat-field was derived has a few consequences on making photometric measurements using IRAC data.

First, the zodiacal background is extended and essentially uniform over the 5.2 arcminutes x 5.2 arcminutes IRAC field of view. The vast majority of objects seen by IRAC were not like this. Many were compact, being either stars or background galaxies. IRAC had significant scattering, as well as distortion. As a result, the extended source effective gain was slightly different from the point source effective gain. IRAC point source photometry then requires a correction for the effective gain change between extended and point sources.

Second, the spectrum of the zodiacal background peaks redward of the IRAC filters. The vast majority of the objects seen by IRAC were not like this. Many have spectral energy distributions in the IRAC filters more closely resembling stars. Stars (and many galaxies) have color temperatures that are fairly high, and peak blueward of the IRAC filters. Generally speaking, for these objects the IRAC filters were well on the Rayleigh–Jeans side of the blackbody spectrum. IRAC photometry of warmer sources then requires a correction for the spectral slope change between the zodiacal light and Rayleigh–Jeans spectra.

Lastly, there is a variation in the effective filter bandpass of IRAC as a function of the angle of incidence, which in turn depends on the exact position of an object on the array (Quijada et al. 2004). As a result of this, all objects in the IRAC field of view need to be corrected based on their location on the array.

All three of these effects can be directly measured and a correction derived. Stars (Rayleigh–Jeans, point sources) were sampled at many different locations on the array, and their flux was measured from the (C)BCD images (see Chapter 6 for the definition of the various types of data, including BCD and CBCD). The systematic variations in their measured fluxes were used to derive the corrections. The amplitude of this effect is sizeable. It may reach 10% peak-to-peak, depending on the detector array. This is larger than any other source of uncertainty in IRAC calibration. For well-dithered data, experiments showed that this effect tended to average out so that the amplitude of the effect is very small (less than 1%). However, depending on the exact details of mapping and dithering, it is not uncommon to have small areas of data where the mean correction approaches the full 10%.

Correction images may be downloaded from the IRAC web pages at IRSA. Note that the correction images for the cryogenic mission and the warm mission are different, and users should use the appropriate mission corrections. Note also the following:

- The correction images are oriented so that they apply multiplicatively to the (C)BCD images. Among other things, the channel 1 and 2 arrays were flipped around their vertical axis during the reduction by the BCD pipeline, hence the correction images cannot be directly applied to the raw data.
- The correction images are for compact, or point-like sources.
- The correction images are for a Rayleigh–Jeans (stellar, Vega-like) spectrum. Spectral indices differing from this will have different corrections. Generally, most IRAC objects had spectral slopes that are bracketed by the two extremes of the red zodiacal spectrum and the blue stellar spectrum, so the corrections will lie between zero and that in the correction image.
- The existing flat-field flattens the zodiacal background. After applying the correction, although the point sources may be correctly measured, the background will no longer be flat.

To apply the correction from these images to photometry on a single (C)BCD image, a) perform photometry on your (C)BCD image, b) measure the value from the correction images at the central pixel of your target for which you are performing photometry, c) multiply your photometric flux measurement by the measured correction value for the central pixel of your target to obtain a corrected flux density value. To apply the correction from these images to photometric measurements made on a mosaic image, you will need to first mosaic the correction images in the same way as the science images. Making the correction mosaic is possible using the MOPEX tool. MOPEX can be found at the IRSA website for Spitzer documentation.

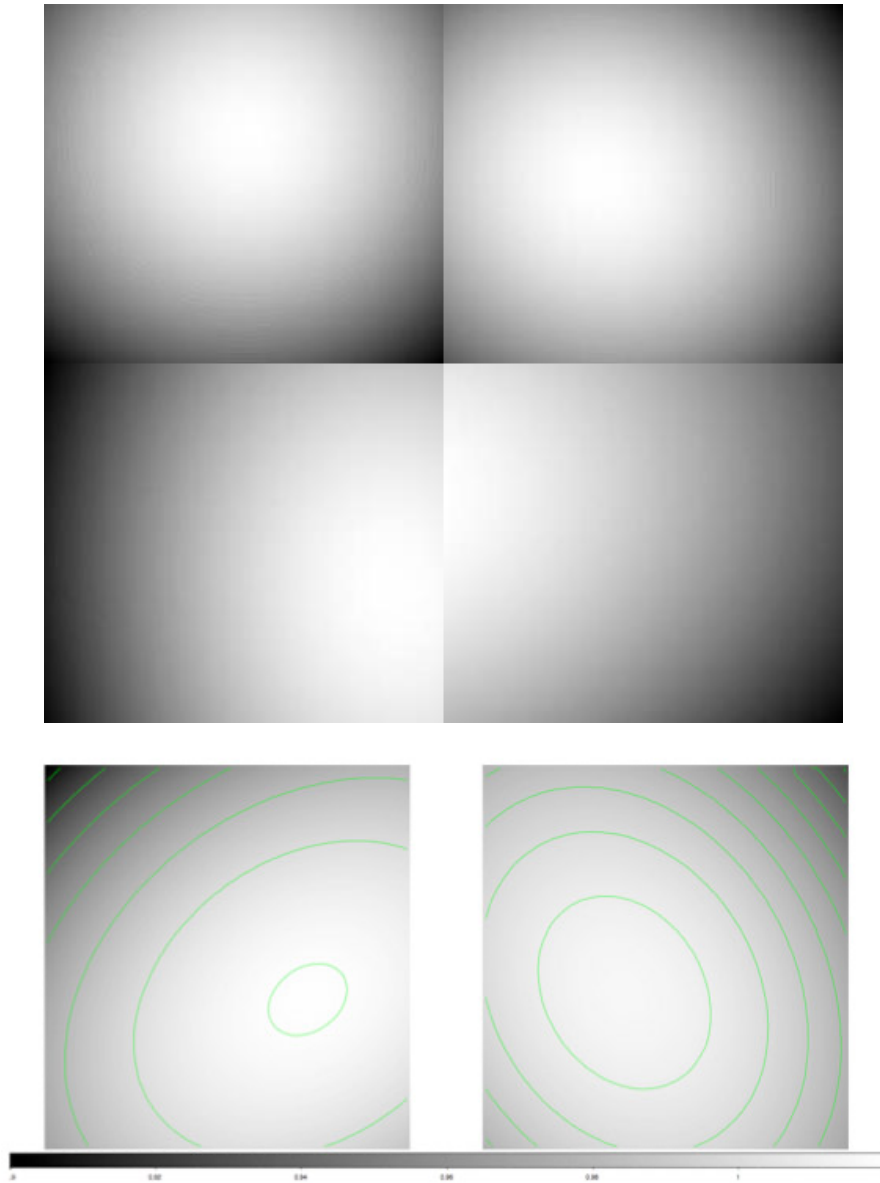


Figure 4.5: Array location-dependent photometric correction images. The cryogenic mission corrections are at the top, and the warm mission corrections at the bottom. For the cryogenic mission correction images, channel 1 is in the upper left, channel 2 in the upper right, channel 3 in the lower left, and channel 4 in the lower right. White is the largest value (about 1.046) and black is the smallest value (about 0.915). For the warm mission correction images, channel 1 is on the left, and channel 2 on the right. Again, white is the largest value (about 1.01757, 1.03167 in channels 1 and channel 2), and black is the smallest value (0.9476, 0.9223).

A note the on correction image filenames: The filenames for the cryogenic mission are in the pattern *ch[1-4]_photcorr_rj.fits* where “rj” means “Rayleigh–Jeans,” and for the warm mission in the pattern *ch[1-2]_photcorr_ap_5.fits*.

4.6 Pixel Phase-Dependent Photometric Correction for Point Sources

The flux density of a point source measured from an IRAC image depends on the exact location where the peak of the Point Spread Function (PSF) falls on a pixel. This effect is due to the variations in the quantum efficiency across a pixel, combined with the undersampling of the PSF. It is most severe in channel 1, partly due to the smallest PSF angular size. The correction for this effect can be as much as 4% peak to peak. Early in the cryogenic mission, the point source aperture flux was fit with a radial function in pixel phase (Reach et al. 2005). We define pixel phase as the offset between the centroid of a point source and the center of the pixel in which that centroid lies. Later, Mighell et al. (2008) found that the intrapixel sensitivity variation is better described by a two-dimensional function of (x,y) pixel phase, primarily because the peak of the response is not at the center of an IRAC channel 1 pixel. The effect is graphically shown in Figure 4.6. These images are subsampled in 0.01 pixel increments, starting at -0.5 and ending at $+0.5$ (in both x_{phase} and y_{phase}), and may be interpolated to the phase of a given stellar centroid and multiplied by the measured aperture flux. These correction images (the inverse of the response) that can be applied (multiplied) to the data can be downloaded in FITS format from IRSA's Spitzer documentation website at

<https://irsa.ipac.caltech.edu/data/SPITZER/docs/irac/> .

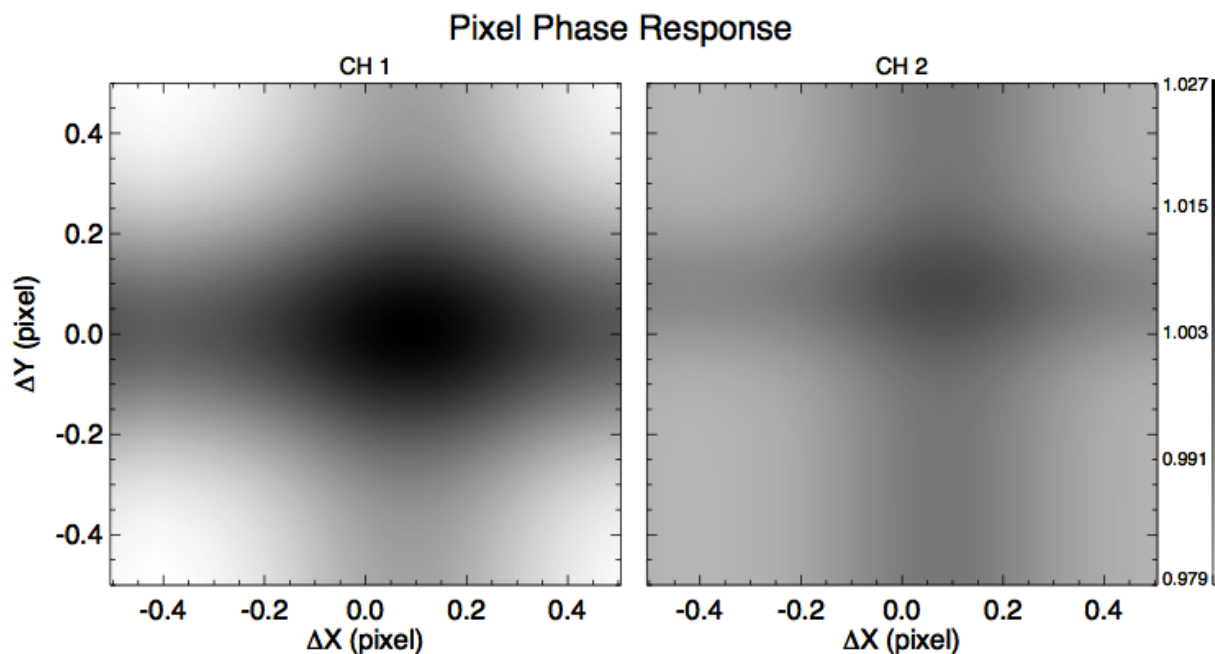


Figure 4.6: IRAC cryogenic pixel response model, showing intrapixel sensitivity variations as a function of pixel phase. Only channel 1 ($3.6\ \mu\text{m}$) and channel 2 ($4.5\ \mu\text{m}$) have significant variations.

At the beginning of the warm mission, we found that the pixel phase response peak-to-peak variation increased by a factor of about two in both channels 1 and 2. The larger dynamic range enabled us to model the intrapixel gain in terms of the sum of Gaussian functions in measured

($x_{\text{phase}}, y_{\text{phase}}$). See Section 8.3 and Appendix D for more details. See also the IDL code in the Contributed Spitzer software at IRSA about performing a simultaneous pixel phase and array location-dependent photometric correction to the observed fluxes.

4.7 IRAC Aperture Photometry Corrections

Because point source aperture photometry is often performed in apertures that have sizes that differ from the apertures used for the calibration stars (10 IRAC native BCD pixel radius aperture and a background measured between 12 and 20 IRAC native BCD pixel circular radii from the center of the source), an aperture correction is necessary. The native IRAC BCD pixel sizes are given in Table 2.1 (they are around 1.2 arcseconds).

The radius of the on-source aperture should be chosen in such a way that it includes as much of the flux from the star (thus, greater than 2 arcseconds) as possible, but it should be small enough that a nearby background annulus can be used to accurately subtract unrelated diffuse emission, and that other point sources are not contributing to the aperture. For calibration stars, an annulus of 12 arcseconds is used; such a wide aperture will often not be possible for crowded fields. The dominant background in regions of low interstellar medium (ISSA 100 μm brightness less than 10 MJy/sr) is zodiacal light, which is very smooth. In regions of significant interstellar emission, it is important to use a small aperture, especially in IRAC channels 3 and 4, where the interstellar PAH bands have highly-structured emission. For example, an aperture in a star-forming region might have a radius of 3 native pixels with a background annulus from 3 to 7 native pixels. The flux of a source can then be calculated in the standard way, taking the average over the background annulus, subtracting from the pixels in the on-source region, and then summing over the on-source region. Note that the calibration aperture did not capture all of the light from the calibration sources, so extended emission appears too bright in the delivered IRAC data products. See the more detailed discussion under Section 8.2.

Users should note that the spatial extent of the PSF in channels 3 and 4 was much larger than the subarray area. In other words, a large amount of the total power in the PSF is scattered onto arcminute size scales. As a result, special care needs to be taken when measuring fluxes in these channels, since accurate measurement of the “background” is difficult. Proper application of aperture corrections is very important.

For photometry using different aperture sizes, the aperture correction can be estimated with Table 4.8. All the radii in this table are in native pixels (≈ 1.2 arcseconds). Note that the post-BCD mosaics available at the Spitzer Heritage Archive use pixels that correspond to exactly 0.6 arcseconds \times 0.6 arcseconds. The aperture corrections as written will *increase* the flux measured by the listed method, i.e., your measured brightness should be *multiplied* by the aperture corrections in the table. The third decimal place in these numbers is included only to illustrate the trends; the accuracy of these corrections is $\approx 1\% - 2\%$. The aperture corrections in Table 4.8 are the modes of the distributions of aperture flux ratios measured using stars at several different positions covering the whole arrays. Standard deviations (including measurement errors and true

variations across the array) are less than 0.5% for all the entries except the smallest aperture, in which they are still less than 1%. The extended source (infinite) corrections in

Table 4.8 come from Reach et al. (2005). The measured flux densities can then be converted to magnitudes, if desired, using the zero-points in Table 4.2.

Table 4.8: Cryogenic and warm IRAC aperture corrections (warm corrections are given as the second set of values in channels 1 and 2). The radius is in native (≈ 1.2 arcsecond) pixels. To get arcseconds, multiply these numbers by the pixel size from Table 2.1.

Radius on source (native ≈ 1.2 arcsecond pixels)	Background annulus (native ≈ 1.2 arcsecond pixels)	Aperture correction			
		3.6 μm	4.5 μm	5.8 μm	8.0 μm
infinite	N/A	0.944	0.937	0.772	0.737
12	12-20	--/0.9931	--/0.9913	-	-
10	12-20	1.000/1.000	1.000/1.000	1.000/1.000	1.000/1.000
8	12-20	1.011/1.0112	1.013/1.0125	1.011	1.017
6	12-20	1.032/1.0315	1.036/1.0349	1.030	1.051
5	12-20	1.047/1.0482	1.048/1.0500	1.054	1.064
5	5-10	1.060/1.0588	1.063/1.0625	1.063	1.084
4	12-20	1.070/1.0736	1.080/1.0809	1.076	1.087
3	12-20	1.112/1.1132	1.112/1.1126	1.118	1.213
3	3-7	1.125/1.1233	1.120/1.1336	1.135	1.221
2	12-20	1.208/1.2026	1.220/1.2228	1.349	1.554
2	2-6	1.215/1.2132	1.233/1.2322	1.366	1.568

4.8 Photometric Variations in Data Taken with Full Array, Subarray, Dithering and Staring Modes

Differences in the photometric flux densities of the same targets in IRAC channel 1 and 2 images taken using various modes (full array, subarray, staring mode, dithering) were found. To investigate these differences, data from special calibration PIDs 1336 and 1367 were employed. A set of ten stars were observed using varying frame times, subarray and full array modes, staring (taking images successively at the same pointing position) and dithering. The stars used were IRAC calibration stars that are known to not have astrophysical variation in their flux densities. About 80000 photometry points in each of the channels 1 and 2 were measured and used in this study.

Staring mode data in the Spitzer Heritage Archive were processed through the pipeline in the same manner as dithered data, including the subtraction of a skydark image that was made by dithering. For this study, data from special calibration PID 1345 was used to make a staring mode skydark suite. Subtracting an appropriate staring mode skydark from the staring mode data, after having first undone the dithered dark subtraction, does have a measurable effect on staring mode

photometry. It is therefore recommended that anyone performing absolute photometry with staring mode data use a staring mode skydark instead of the pipeline-provided dithered dark. Instructions for how to make an appropriate skydark and subtract it are available in the Contributed Software section of IRSA's Spitzer web pages:

<https://irsa.ipac.caltech.edu/data/SPITZER/docs/dataanalysisistools/tools/contributed/irac/>.

For the comparison of the flux densities of the same star taken via various observing modes, all of the photometric corrections recommended in this chapter must be implemented first. To compare photometry on all the ten calibration stars on the same plots below, we used a normalization by dividing all the photometry points of a given star by the median flux of the same star in all of its measurements.

Figure 4.7 shows all the calibration star measurements divided into four subcategories: full array vs. subarray, and short frame times vs. long frame times. The division between short and long frame times is at 0.3 seconds (in terms of actual exposure time). There is no good way to compare flux density measurements of equal exposure times, because the exposure times are significantly different for the full array and the subarray. Longer frame times are in blue and green and shorter frame times in red and orange. There is an effect with both frame time and array read mode. The effect is stronger in channel 1 than in channel 2. For the stars which have full array observations with both short and long frame times, the median difference in flux density is 3.3% in channel 1 (for six stars) and 1.0% in channel 2 (for ten stars). For subarray, the median difference in flux density between short and long frame times is 2.9% in channel 1 and 1.7% in channel 2.

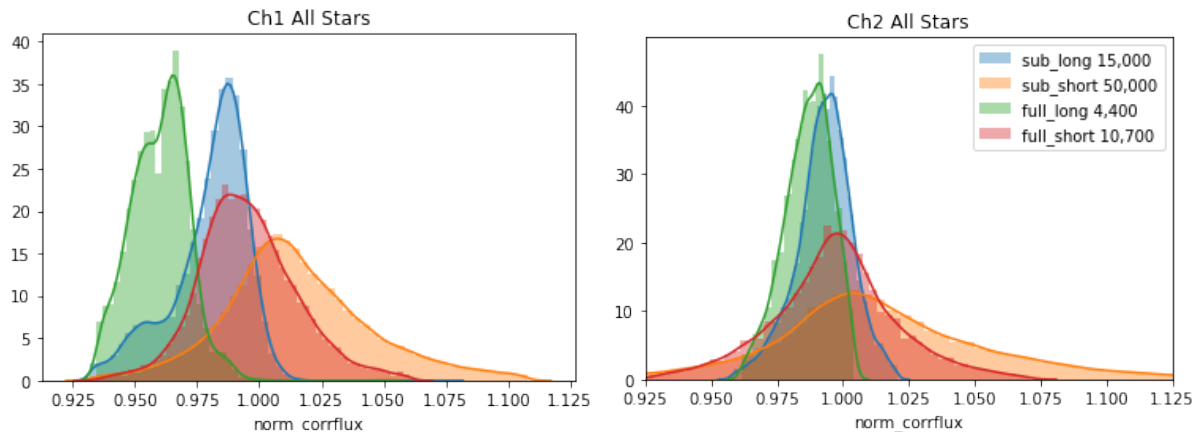


Figure 4.7: Distribution of normalized corrected calibration star flux densities. There is a difference in the absolute photometry of stars taken in different observing modes (shown here in the different colored distributions). The legend lists the different observing modes (full array vs. subarray, and long exposure times vs. short exposure times) as well as the number of photometry points per distribution. Channel 1 is on the left, channel 2 is on the right.

For three calibration stars observations exist in all the modes for the 2 second frame times (subarray staring, subarray dithering, full array staring, full array dithering). Remember that the 2 second subarray observations are really 1.92 second exposures and the 2 second full array observations

are really 1.2 second exposures, so these frame times are not equivalent, but they are the closest there are between the subarray and full array. Figure 4.8 shows the median and standard deviation of the corrected flux densities for observations in the different modes for each star. The legend also lists the number of the data points per mode. Again, one can see a difference in photometry between subarray and full array observations (blue points vs. red/orange points). The staring mode absolute photometry is within one sigma of the dithered data absolute photometry in both channels.

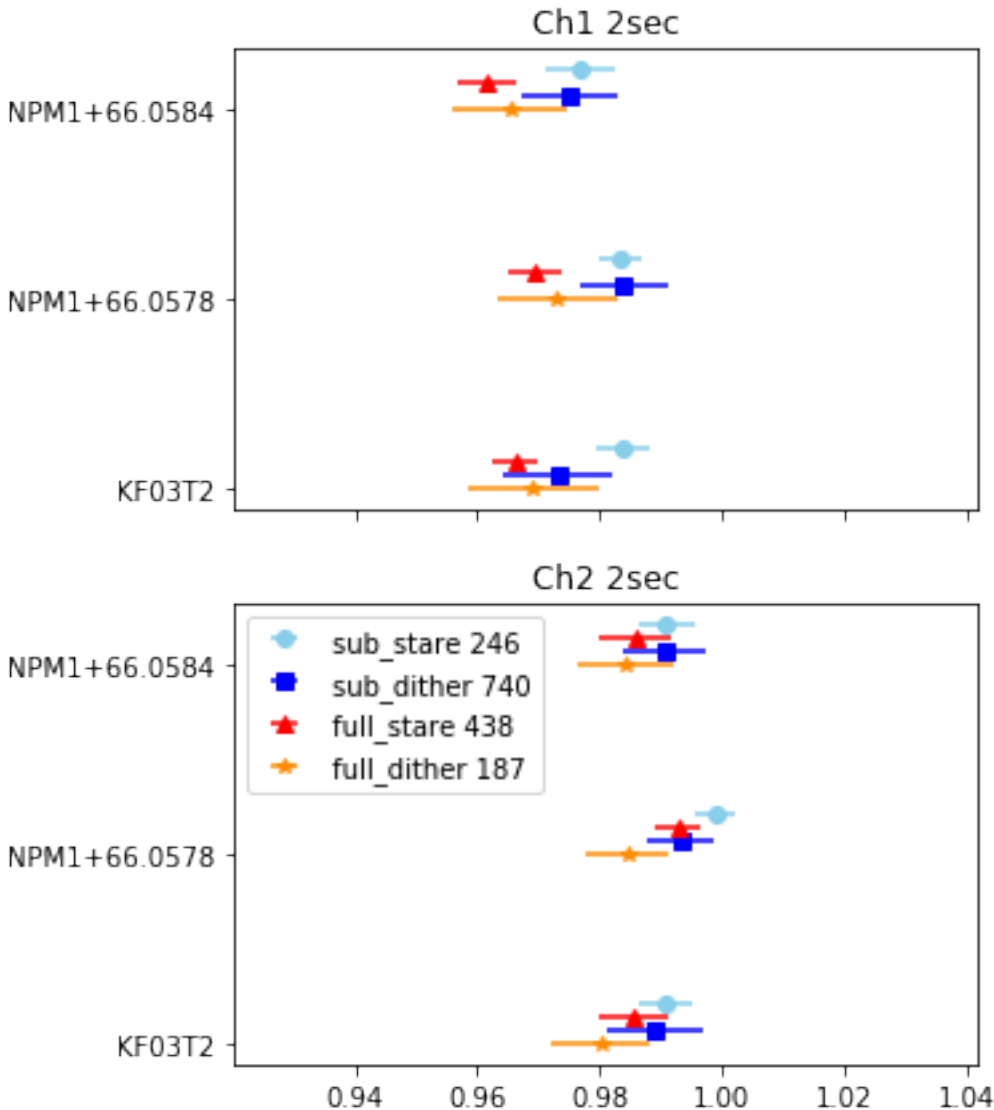


Figure 4.8: Cleveland dot plot showing medians and one sigma uncertainties of the distributions of photometry from four different modes shown in Figure 4.7 (subarray vs. full array and staring vs. dithering). The names of the three calibration stars considered here are shown on the y-axis, and the data points for different modes of photometry for each star are offset slightly in the y-direction for ease of viewing. Staring mode observations in the subarray and full array modes were taken at the same locations on the array (on the sweet spot pixel).

4.9 IRAC Point Spread and Point Response Functions

Because the point spread function (PSF) was grossly undersampled by the IRAC pixels, especially in channels 1 and 2, we use the concept of the point response function (PRF). In practice, the PRFs are stored in a table (not an image, though for convenience it is stored as a 2D FITS image file) that combines the information on the PSF, the detector sampling, and the intrapixel sensitivity

variation (see Section 4.6), and gives an appropriate PRF depending on where on the pixel the peak of a point source falls. By sampling this table at regular intervals corresponding to single detector pixel increments (for example, taking every fifth pixel for a five-times oversampled PRF), an estimate of the detector point response function (or PRF) can be obtained for a source centered at any given subpixel position. Such PRFs formed from the table are called “point source realizations” (PSRs) in Appendix C.

To build the PRFs, we sampled the PSF with much smaller “pixels.” In the case of IRAC, the oversampling is usually by either a factor of five or a factor of 100. See Appendix C for how to extract the correct PRF from the PRF table for a point source that peaks at a given location on a pixel. Figure 4.9 shows the $5 \times$ oversampled (in row and column direction) IRAC point response function tables.

FITS files of both the core and extended IRAC PRF tables are available in the IRAC section of IRSA’s Spitzer documentation website:

<https://irsa.ipac.caltech.edu/data/SPITZER/docs/irac/calibrationfiles/psfprf/> .

The appropriateness of a given PRF is dependent on the observation sampling and the photometric reduction package used.

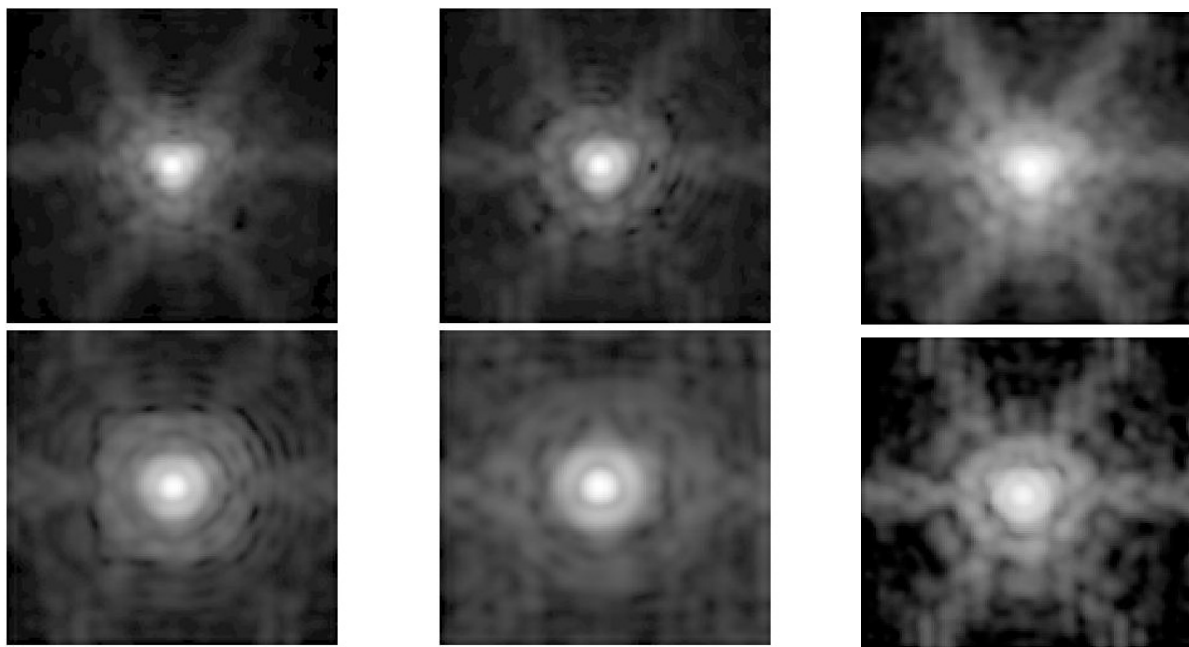


Figure 4.9: Images of the IRAC point response function (PRF) tables. These are shown at 3.6 (upper left), 4.5 (middle, top row), 5.8 (left, bottom row), and 8.0 μm (middle, bottom row) from the cryogenic mission and from the warm mission at 3.6 (right, upper row) and 4.5 μm (right, bottom row). The PRFs were generated from models refined with in-flight calibration test data involving a bright calibration star observed at several epochs. The PRFs are shown as they appear with 1/5 the native IRAC pixel sampling of 1.2 arcseconds to highlight the core structure. The PRFs were calculated using the Simfit routine in Hoffmann et al. (2004). The images are 128×128 1/5 native IRAC pixels in size (about 31 arcseconds \times 31 arcseconds).

The PRFs vary over the IRAC detectors' field of view due to the Spitzer/IRAC optics, including, but not limited to, the relative position of the optical ghosts (see Section 7.3.3). For this reason, the PRFs available at the Spitzer website at IRSA for use with MOPEX/APEX are given at 25 different positions. The PRF variation over the field of view in channel 1 (as an example) is demonstrated by Figure 4.10 that shows the “best” and “worst” case PRFs over the field of view and Figure 4.11 that shows the corresponding changes in the number of noise pixels. A step-by-step description of IRAC PRF-fitting photometry is given in Appendix C.

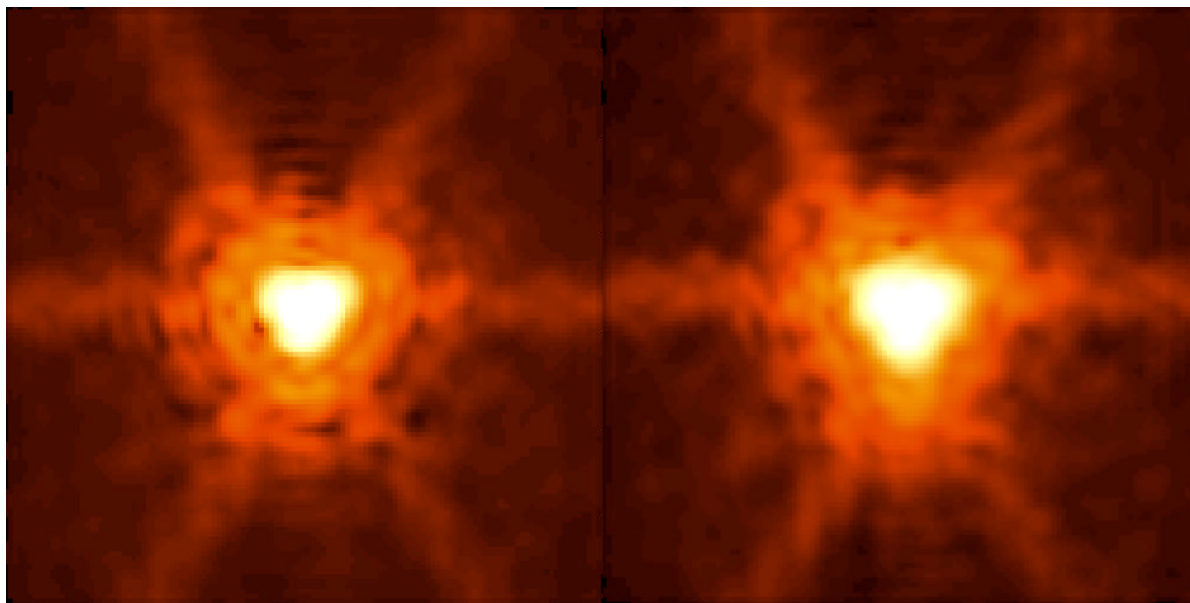


Figure 4.10: “Best” (left) and “worst” (right) channel 1 PRF images from the set of PRFs available for the cryogenic mission. A logarithmic stretch was used to highlight the low-level emission. The core of the “worst” image is a larger than the “best” image, and it has a $\approx 60\%$ higher noise pixel value.

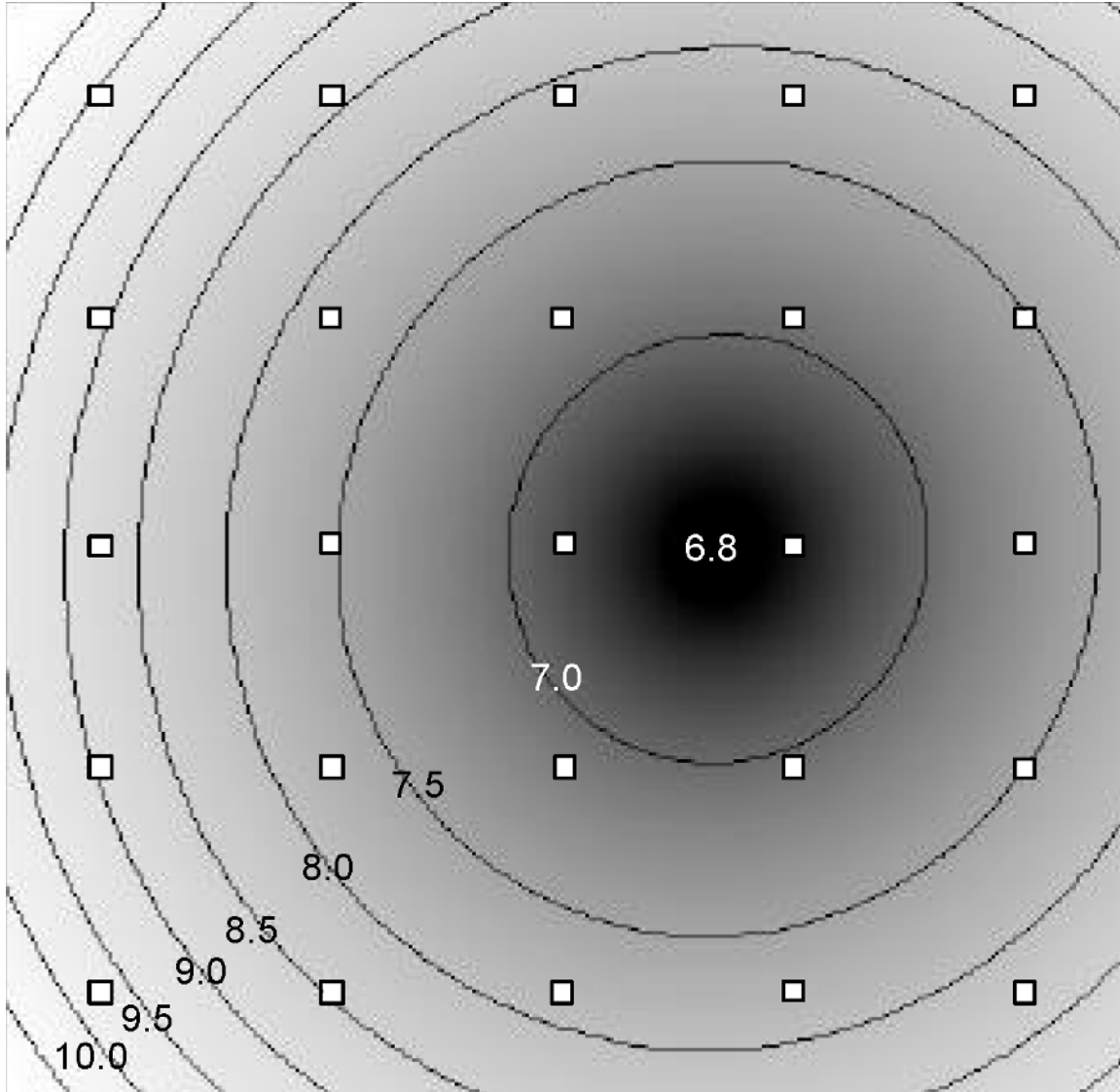


Figure 4.11: Distribution of noise pixel values over the channel 1 field of view in the cryogenic mission. The image matches the BCD orientation, with pixel (1,1) in the lower left corner. The mean point source noise pixel values (averaging over many different pixel phases) were measured at the 25 positions indicated by the small squares on the image, and a quadratic surface was fit to the data, plotted here as grayscale and contours. The lowest noise pixel value is 6.79 at (x,y) position (163,128). The highest noise pixel location, in the upper left corner, is 1.6 times this, requiring 1.6 times the integration time to achieve the same signal-to-noise as for the lowest noise pixel position.

4.9.1 Core PRFs

The FITS files of the core PRFs are linked off the IRAC web pages. These core PRFs can be used for PRF-fitting photometry and source extraction in (C)BCDs for all but the brightest sources. We recommend performing aperture photometry instead of PRF fitting in all instances except in crowded fields and regions with a strongly varying background, because aperture photometry is much simpler, more straightforward, and faster to do. In addition, especially in channels 1 and 2,

the PSF was undersampled by the native IRAC pixel size, causing further uncertainty to PRF fitting. PRF fitting does not work in image mosaics where the information from the PSFs has been blended together. Aperture photometry is the correct way to perform point source flux density measurements in image mosaics.

The PRFs are provided in two different samplings, 1/5 and 1/100 native pixels. The 1/100th native pixel sampling PRFs were created by interpolating the 1/5th sampled PRFs onto a finer grid. These PRFs were designed to work with the astronomical point source extractor for MOPEX, called APEX (Makovoz & Marleau 2005). The 1/5th pixel sampling versions are the originally derived versions and are appropriate for use with custom PRF-fitting software, but not APEX. For both versions of sampling, the PRFs are provided for 25 positions in a 5x5 grid upon the array for each channel. The PRFs are normalized such that the flux is unity within 12 arcsecond (10 native pixel) radius around each point source with the zero pixel phase instance (centered on a pixel).

4.9.2 Extended PSFs

The FITS files of the extended PSFs can be obtained using the links on IRSA's IRAC web pages. We will first address the cryogenic IRAC extended PSFs and then explain the procedure to generate the warm IRAC PSFs below. In order to gain high signal-to-noise out to the edge of the arrays, PSFs were generated from a combination of on-board calibration and science observations of stars with different brightness, joined together to produce extended high dynamic range (HDR) observational PSFs. These PSFs have two main components: a core HDR PSF created by the observations of a reference star, and the extended region from observations of a set of bright stars that saturated the IRAC array. They can be used to perform source extraction and PSF-fitting photometry of bright, highly saturated stars with extended wings. The core of the extended PSF was generated using the `prf_estimate` module of MOPEX, which has been shown to be inadequate for making high-quality PSFs for IRAC. As a result, the extended PSF should not be used for PSF-fitting photometry and source extraction of non-saturated point sources. Instead, the core PRF in Section 4.9.1 is more appropriate for PRF-fitting photometry. Also, note that the detailed structure of the center of saturated sources fitted using the extended PSF will not be correct.

Observations of the stars Vega, Epsilon Eridani, Fomalhaut, Epsilon Indi, and Sirius were used in the construction of the extended portion of the PSF. Each star was observed with a sequence of 12 second IRAC full frames, using a 12-point Reuleaux dither pattern (cf. Section 3.4) with repeats to obtain the required total integration time (the stars were typically observed for 20 – 60 minutes during each epoch). The images were aligned, rescaled to the observation of Vega, and then averaged together with a sigma-clipping algorithm to reject background stars.

These extended HDR PSFs have a pixel size of 0.2 IRAC pixels, or ≈ 0.24 arcseconds. The size of each PSF image is 1281x1281 pixels, covering an area of ≈ 5.1 arcminutes x 5.1 arcminutes. The PSFs are centered within each image. The PSFs are calibrated in MJy/sr. The PSFs represent an unsaturated, very high SNR image calibrated to Vega, and the flux density contained within a 10 native IRAC pixel aperture radius (50 HDR PSF pixels), with the sky level estimated in a radial annulus from 12 to 20 native IRAC pixels, is equal to the flux density of Vega. The pedestal level was set to zero in the corners of each PSF.

To produce the core portion of the HDR PSF, 300 HDR observations of a calibration star were obtained during three separate epochs, each observation consisting of short exposures (0.6 seconds/1.2 seconds) and long exposures (12 seconds/30 seconds). The HDR PSFs were generated by first combining short-exposure frames and long-exposure frames separately. The short frames enabled the cores to be constructed without a saturation problem, while the long exposures allowed the construction of a higher signal-to-noise PSF in the wings out to 15 arcseconds. The assembly required the replacement of any saturated areas in the long-exposure frames with unsaturated data from the same pixel area of the short-exposure frames. It also required the replacement of a few pixels in the long-exposure frames by the corresponding pixels in the short-exposure frames to mitigate the non-linear bandwidth effect in channels 3 and 4.

The core HDR PSFs were aligned and rescaled to the extended portion of the PSF by matching their overlapping areas. The alignment was done at best to an accuracy of ≈ 0.1 arcseconds. The rescaling was made by forcing the cores to have the same flux density, that of Vega, within a 10 native IRAC pixel radius aperture. The stitching was made using a mask with a smooth $1/r$ transition zone, 2.4 arcseconds wide, between the core (contributing where the extended portion PSF data were missing due to saturation cutoff), and the extended portion of the PSF. The merged PSFs were then cropped to a final 5.1 arcminutes \times 5.1 arcminutes size, and a pedestal level was removed in order to have a surface brightness as close as possible to zero in the corners of the images.

The warm mission extended PSFs were created in a similar way, except that 22 A–M V stars (PID 40976) were used, along with 122 observations of NPM1 +67.0536 from the IRAC calibration program. The original BCDs were corrected for pinstriping (see Section 7.2.2), and residual images were masked. Mosaics of each star were created with IRACproc (Schuster et al. 2006) on a 0.24 arcseconds/pix scale. All pixels above 50% of the saturation level were masked, and the mosaics aligned to a common center (with a typical accuracy ≈ 0.03 arcseconds) using the diffraction spikes of the images. The pedestal level and normalization levels were then fit by minimizing the chi-squared value of the difference in the binned radial profiles between the observation and the Vega calibration measurement. The aligned and normalized mosaics were averaged with sigma-clipping to remove outliers (background stars, other artifacts) to produce a normalized PSF image. This procedure was repeated for the observations that were not saturated in the core, and the core and extended PSFs were aligned and smoothly merged to produce the final PSF for each channel.

All of the extended PSFs are available at IRSA's Spitzer/IRAC documentation website at

<https://irsa.ipac.caltech.edu/data/SPITZER/docs/irac/calibrationfiles/psfprf/> .

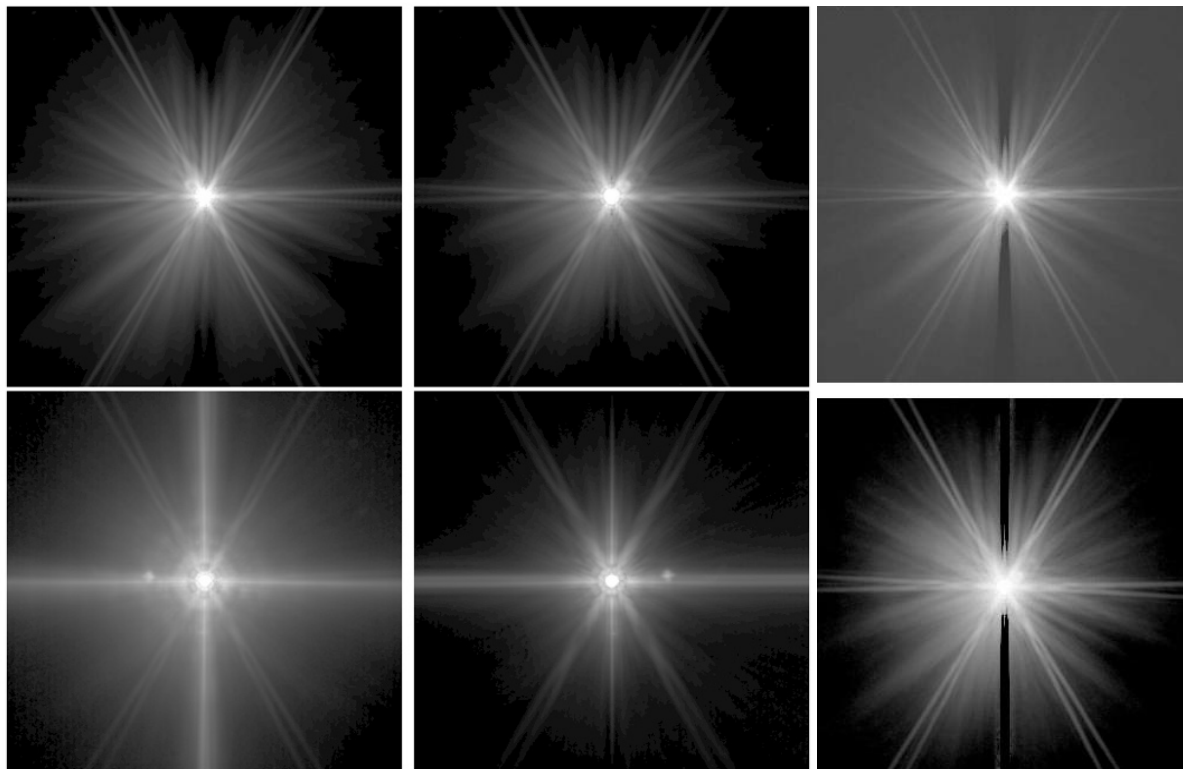


Figure 4.12: The IRAC extended PSFs. The cryogenic PSFs are shown on the left, with channel 1 PSF in upper left, channel 2 PSF in the middle (upper row), channel 3 in lower left, and channel 4 in the middle (lower row). The warm extended PSFs are shown on the right, with channel 1 on top and channel 2 at the bottom. See the text for how these were constructed.

4.10 Calculation of IRAC *zmag*s

Some software packages, such as IRAF's `phot` task, require specifying *zmag*. For IRAC data, you need to know the pixel size of the IRAC image being analyzed in order to convert surface brightness to flux density. The *zmag* can be evaluated from $2.5 \times \log_{10}(F_0/C)$, where F_0 is the zero magnitude flux density in Jy for the relevant channel, tabulated in Table 4.2, and C is the conversion factor from MJy/sr to $\mu\text{Jy}/\text{pixel}$, e.g., 8.461595 for 0.6 arcsecond \times 0.6 arcsecond pixels (the value of C will be different depending on the pixel size).

To understand where the IRAC *zmag* comes from, you can start with the fundamental equation between magnitudes and flux densities. In one incarnation, it becomes

$$m - M_0 = -2.5 \cdot \log_{10}(F/F_0). \quad (4.16)$$

Here m is the magnitude of the source you want to measure, M_0 is the zero magnitude ($= 0$), F is the flux density in Jy of the source you want to measure and F_0 is the flux density of a zero magnitude source. For IRAC channel 1, $F_0 = 280.9$ Jy. Expanded out,

$$m = -2.5 \cdot \log_{10}(F) + 2.5 \cdot \log_{10}(F_0). \quad (4.17)$$

Here $zmag = 2.5 \cdot \log_{10}(F_0)$. Now, because the IRAC images are in units of MJy/sr, we have to do some manipulation to get the equation to this form. Specifically, the measurable F that we have in IRAC images is the surface brightness, not the flux density. Therefore, the equation becomes

$$m = -2.5 \cdot \log_{10}(SB \times C) + 2.5 \cdot \log_{10}(F_0) \quad (4.18)$$

where SB is the measured surface brightness in the image in MJy/sr and C is a conversion factor from MJy/sr to Jy/pixel. For IRAC channel 1 mosaics with 0.6 arcsecond x 0.6 arcsecond pixels it equals $C = 8.461595 \times 10^{-6}$ Jy/pixel/(MJy/sr). Therefore, the equation becomes

$$m = -2.5 \cdot \log_{10}(SB) + 2.5 \cdot \log_{10}(F_0/C) \quad (4.19)$$

where $zmag$ now corresponds to the latter term, $+2.5 \cdot \log_{10}(F_0/C)$. Inserting the values of F_0 and C mentioned above, we get $zmag = 2.5 \cdot \log_{10}(280.9/8.461595E-06) = 18.80$ mag in channel 1.

Please remember that this is true only for the 0.6 arcseconds x 0.6 arcseconds pixel scale mosaics. For other pixel scales you will get a different value. Also, please remember the required corrections (e.g., aperture correction) that are needed for high accuracy photometry.

4.11 Astrometry and Pixel Scales

4.11.1 Optical Distortion

Optical distortion is a significant (measurable) effect in IRAC data. The $\approx 1\%$ distortion in all channels is due principally to IRAC being offset from the optical axis of Spitzer, with additional components from the telescope and camera optics. In addition to varying the effective pixel size, there are also higher-order terms such as skew (the two axes are not exactly perpendicular) and a difference in the pixel scales between the two axes. Failure to account for the distortion will lead

not only to errors in photometry (described below), but also shifts in astrometric position, approaching 1 arcsecond near the array corners.

Optical distortion corrections in each of the IRAC FOVs have been implemented in the (C)BCD FITS header keywords using a standard method described by Shupe et al. (2005). This method places the center of the distortion at the center of each detector array, in particular at CRPIX1 and CRPIX2. The linear terms and any skew are represented in the CD matrix header keywords (CD1_1, CD1_2, CD2_1, and CD2_2), while the distortion keywords provide the second and higher order terms. Importantly, these distortion corrections apply to the array coordinates, prior to the transformation to sky coordinates. This means that all IRAC data for a given detector share the same distortion keywords. In addition, we also provide a separate set of header keywords representing the “reverse” transformation from sky to array coordinates.

The form of the optical distortion that is encoded in the (C)BCDs is read properly by several standard tools available to the general astronomical community, e.g., the Spitzer mosaicker (MOPEX), WCSTools, and DS9 (except for grid overlays).

The optical distortion was fit independently for each IRAC detector. Originally a second-order fit was used, but an improved fit to third order was derived from the GOODS data by S. Casertano. The (C)BCD coefficients remove the distortion to 0.1 arcsecond accuracy.

4.11.2 Pixel Solid Angles

As a result of the optical distortion described above, the detector pixels did not all subtend the same projected solid angle on the sky. The variation in projected pixel solid angle was roughly 1.5%.

This size variation is accounted for in the flat-fielding process because the flats were derived from actual sky measurements. As a result, after flat-fielding, the (C)BCD images were calibrated in units of true surface brightness (MJy/sr). This poses a difficulty because virtually all software assumes that the pixels are in units of flux per pixel, and simply sum the pixel values. In order to properly measure fluxes from an image in surface brightness units, one must multiply the pixel value by the pixel size. Failure to do so could induce photometric errors at the 1% level, depending on the location on the array. Unfortunately, older photometry software cannot read the FITS-standard WCS distortion keywords written in the (C)BCD headers and properly account for the sizes of the pixels.

The simplest solution to this problem is to reproject the images onto an equal area (or nearly so) projection system (such as TAN – TAN) using suitable software that can understand the distortion keywords in the WCS header (e.g., MOPEX). MOPEX also has the significant advantage that it understands how to properly handle surface brightness images during coaddition. After processing, the pixels will all subtend the same solid angle, and hence any standard photometry software can produce the correct result.

However, some data users may prefer alternative approaches, in particular if they wish to measure photometry directly from the (C)BCD images. Therefore, we supply maps of the pixel size in the “Calibration and Analysis Files” section of IRSA’s IRAC documentation website that can be used

to correct the pixel solid angles in BCD images if any measurements are being directly made on them. Note that this correction is built into the “location-dependent photometric correction” image (see Section 4.5), also available on the website, so multiplying by this correction map (intended to provide correct photometry for point sources with stellar-like SEDs) will also produce the correct result.

4.12 Pointing Performance

Pointing was controlled by Spitzer's Pointing Control System (PCS). This used a combination of a star tracker and gyros to locate and control the attitude of the spacecraft. Absolute pointing was controlled by the star tracker through a filter known as the “Observer” that smooths the raw star tracker output. Slews under the control of the Observer took ≈ 10 seconds to settle, so only the initial slew and cluster slews in celestial coordinates were carried out using the Observer. Once the observatory had taken the initial frame at the starting position, attitude control was handed over to the gyros. Mapping and dithering slews were made under gyro control with a shorter (≈ 5 seconds) settle time. The price to be paid for the shorter settle time was that the spacecraft attitude slowly drifted with respect to the Observer attitude, at a rate of ≈ 1 milliarcseconds/second. For long integrations (100 second frame time), attitude control was returned to the Observer after 80 seconds to halt the drift.

In addition, attitude resets were performed regularly (about every 30 minutes) to return the spacecraft attitude to the Observer attitude. The system was designed to ensure that any motion to return the spacecraft attitude to that of the Observer did not take place during an IRAC integration, to avoid smearing the images. Throughout the first 18 months of the mission, the PCS system and the corresponding parts of the IRAC AOT were being adjusted for optimal performance. The sections below serve as a guide to the astrometric accuracy and image quality that can be expected from a typical observation.

4.12.1 Pointing Accuracy

Slews under the PCS Observer control settled to the accuracy to which the star tracker-to-IRAC pointing offset is known, or about 0.5 arcseconds. Offsets between dithering/mapping moves were accurate to 0.1 arcseconds, relative to the commanded move, for small moves (≈ 10 arcseconds), and for large moves (≈ 0.5 degrees) the accuracy was ≈ 0.5 arcseconds (though this was improved as of spring 2005, and should be ≈ 0.2 arcseconds thereafter). An additional pointing error comes from the gyro drift which can accumulate over the 30-minute period between attitude resets. This error was typically ≈ 2 arcseconds for a worst-case frame just before a reset. The pointing uncertainties due to various effects are summarized in Table 4.9.

Table 4.9: Pointing uncertainties.

Pointing Effect	Characteristic Amplitude [arcseconds]	Characteristic Timescale
Accuracy	0.07	N/A
Wobble	0.07	40 min. or greater
Initial drift	0.5	\approx 30 minutes
Long-term drift	0.3	\approx one day
Low frequency jitter	0.07	\approx 2 minutes
High frequency jitter	0.03	< 0.02 seconds

Settling is the drift motion that occurs after the telescope slews to a new position. This took place typically with every IRAC frame at some level, unless REPEATS > 1. The settling drift rate decreased with time after the slew. The magnitude of the settling depended on the length of the slew, and it was expected to be the largest for the initial slew to the object, smaller for mapping slews, and the least amount of settling was expected for dithering offsets. There was also a steady drift of the pointing, \approx 0.01 arcseconds/hour due to other changes in the star tracker to telescope alignment. The accumulated drift was removed using regular star tracker-to-telescope boresight calibrations every \approx 12 hours.

The pointing of each frame as reported in the header keywords CRVAL1 and CRVAL2 was an average of the Observer attitude during the frame, and was typically accurate to \approx 0.5 arcseconds (though it might be slightly worse for short frames where the Observer had not fully settled). Other header keywords related to pointing include RA_RQST and DEC_RQST, the requested R.A. and Dec. of the frame, and PTGDIFF, the difference between the requested and actual pointing. USEDBPHF should be T for all frames; if not, then pointing transfer had failed for the frame.

The Level 2 (post-BCD) pointing refinement module was run by default in the post-BCD pipeline to refine the pointing to 2MASS accuracy (\approx 0.15 arcseconds), and would be successful if there were a sufficient number of 2MASS stars in the data. The module operated by matching common stars between frames (“relative refinement”) and a fiducial set of stars from 2MASS (“absolute refinement”). The (R.A., Dec.) position and rotation of each frame was then adjusted until a global minimum in the residuals was found. Application of this to the Extragalactic IRAC First Look Survey (FLS) data resulted in a mean position error for high signal-to-noise stars with respect to 2MASS positions of 0.25 arcseconds.

The pointing refinement module wrote several new keywords to the header. The refined position is given by keywords RARFND and DECRFND, and rotation by CT2RFND. Note that the refined solution may be poor if the number of astrometry stars in the frame, NASTROM, was low (i.e., 0, or only a few stars). Pointing refinement works well for most channel 1 and 2 data, but short frames in fields near the Galactic poles in channels 3 and 4 frequently had too few stars for a good solution.

All the data had a superboresight pointing correction applied to the coordinates (see Section 5.3.2). Users wishing to make use of the superboresight solutions need to set

USE_REFINED_POINTING = 0 in MOPEX, as the superboresight pointing is contained in the standard CRVAL1, CRVAL2, and CD matrix keywords (this is the recommended pointing to be used when making mosaics etc.). Data which have had this correction applied will also have the ORIG_RA, ORIG_DEC, and ORIGCD* keywords present which contain the initial (uncorrected) pointing estimate.

4.12.2 Target Acquisition Accuracy

Under normal conditions, Spitzer had a target acquisition accuracy of about 1 arcsecond. An additional option in the warm mission allowed users to choose an adaptive positioning technique (“peak-up”) available from the Spitzer Pointing Calibration Reference Sensor (PCRS) to enhance the accuracy and repeatability of target acquisition. For staring mode observations used in high precision photometry, PCRS peak-up (see Section 3.2) was crucial for positioning a target on the same portion of a designated pixel every time we pointed to it. This was vital for lessening the impact of correlated noise due to the intrapixel sensitivity effect (see Section 8.3). The PCRS operated in the visual part of the spectrum (505–595 nm) and its main function on Spitzer was to calibrate and remove the optical offset between the star trackers and the telescope. It could measure the centroids of stars in the 7.0 mag < V < 11.8 mag range to within 0.14 arcseconds (1σ radial) and feed these data, in the form of a pointing correction, to the spacecraft pointing control system (PCS). The PCRS was used frequently in the Spitzer cryogenic mission with the Infrared Spectrograph (IRS).

With IRAC the PCRS peak-up allowed us to repeatedly place a target within a quarter-pixel sweet spot on a designated pixel. When the Peak-Up target was the science target, it was found that more than 90% of visits were placed somewhere inside the sweet spot; 68% of visits were within 0.1 pixels of the center of the sweet spot; and repeat visits to the same target resulted in a spread of initial positions less than 0.06 pixels 68% of the time. This gave two advantages: (1) it minimized the offset in intrapixel sensitivity caused by the initial target acquisition; and (2) it allowed us to calibrate a smaller fraction of the designated pixel, with better fidelity. Furthermore, reacquisition peak-ups spaced approximately 10 – 12 hours throughout long staring observations minimized the effects of the long-term pointing drift (see below) by restoring the initial pointing location.

Target acquisition was statistically less accurate when the peak-up target was a different star than the science target (“guide star peak-up”). Although PCRS peak-up with a guide star (1σ accuracy better than 0.4 pixels, or 0.5 arcseconds) was still *more accurate than blind pointing* (1 arcsecond), only 40% (channel 1) and 61% (channel 2) of visits were placed within the sweet spot after a guide star peak-up. The accuracy of the guide star peak-up depended on the relative astrometric accuracy between the science target and the guide star, which partially explains the poorer targeting for the guide star peak-up compared to the self-peak-up. Another reason for this discrepancy may be an on-average larger slew offset between the PCRS and the IRAC FOV when the peak-up star was not the science target. It was found that repeat visits to the same target using the same peak-up star resulted in an RMS spread in the acquisition location worse than about 0.1 pixels 32% of the time. Most observations that used the guide star peak-up did not re-acquire their targets more than once every 20 – 24 hours, because peaking up more frequently would likely have taken a target further from the center of the sweet spot than the long-term drift (approximately 0.2 pixels over that timespan).

4.12.3 Pointing Glitches

Instances of pointing glitches included cases in which a position jumps during an AOR, and then jumped back to the original position. These jumps were of order half a pixel in length (≈ 0.5 arcseconds), and are seconds in duration. They were not associated with a cosmic ray hit on the target because they lasted for more than a single frame. The jumps in position corresponded to reaction wheel speed shifts. Reaction wheel speed shifts were expected due to momentum rebalancing events in the wheel speed controller. The goal of this system was to avoid zero crossing disturbances (which would also induce position disturbances in the data) as long as possible. Autonomous momentum rebalancing only occurred when the system momentum grew above a certain threshold. Once this level was breached, the goal changed to balancing the reaction wheels so that it could stretch out the time until the next reaction wheel desaturation event. If the momentum fell back below that threshold, autonomous momentum rebalancing would once again be disabled. On average, only about one rebalancing per hour occurred. They mostly happened during slews, and therefore they were not expected to affect many IRAC images. They were most notable during staring mode observations (Figure 4.13).

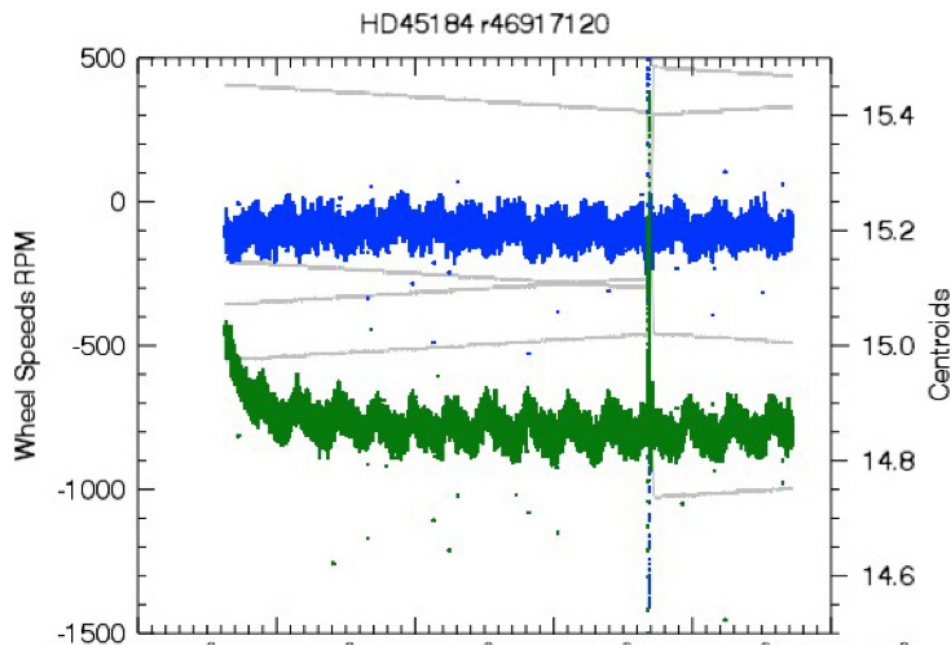


Figure 4.13: Reaction wheel speed and centroid position as a function of time. Wheel speed changes are a few seconds in duration and this entire AOR is 11.5 hours in duration. This particular AOR shows a reaction wheel speed shift with a return to the original position. Grey lines correspond to the wheel speeds in RPM (left y-axis). Spitzer had four reaction wheels, and they all changed speed simultaneously about 75% of the way through this observation. Blue and green data correspond to the X and Y centroids of the target in the observation (right y-axis).

4.12.4 Jitter, Drift, and Wobble

Pointing jitter, drift, and wobble can cause broadening of the effective PSF in an image and an offset in the centroid of an object during an AOR. In this section, we define jitter as pointing

motion on timescales of a few seconds or less, changing direction frequently, and typically affecting a single BCD image. We define drift as motion in a constant direction, and wobble as an oscillating motion, both of which occur on one minute or longer timescales, and therefore take place over many integrations in the AOR. Short-term drift usually dominates the first half hour of any given observation (although there is an underlying long-term drift during that time as well). We measure the magnitude of the long-term drift from the change in the position from 30 minutes after the beginning of the observation until the end of the observation. Long-term drift consists of a smooth change in the position of the target star over the entire duration of the observation, and is of order a few tenths of a pixel per day. See Section 4.12.4.2 for more details.

One manifestation of jitter and drift during integrations is that the measured target position in HDR short, medium (for 100 second HDR) and long frames is slightly different. These differences are usually ≈ 0.1 arcseconds, so they should not be a problem for most observers, but they are large enough to show up as residuals in difference images. Another manifestation of jitter and drift is the difference in positions between frames in staring mode observations (no dithering). This source of correlated noise is a significant source of error in high precision photometry.

4.12.4.1 Jitter

The jitter at short timescales was measured using the Galactic Center source at frame times of 0.02 seconds (50 Hz). The X and Y relative offsets of the source during these observations are shown in Figure 4.14. The jitter in these frames has a peak-to-peak amplitude of 0.04 pixel or less, and no discernable drift over periods of a couple of seconds. The jitter in the initial frames after the slew (left side of Figure 4.14) shows a higher variation, with a standard deviation of 0.01 pixels, and a peak-to-peak variation of ≈ 0.04 pixels. The frames at the end (right side of Figure 4.14) have a standard deviation of 0.004 pixels and a peak-to-peak variation of ≈ 0.02 pixels in each dimension. This could be due in part to settling motions after the slew (see Section 4.12.1).

We can also examine the jitter during a longer exposure with less frequent sampling. The jitter during a 100 second period at the beginning of a long monitoring observation is shown in Figure 4.15. This plot is based on the 2013 Galactic Center data referenced above, taken in the IRAC subarray mode with a 0.1 second frame time. At the beginning of the dataset after the initial slew, pointing seems to be oscillating back and forth with an amplitude of 0.05 pixels peak-to-peak and at a centroid slightly offset from the rest of the data. The later data sets during the 100 second period seem to walk randomly around the field with small steps between each position.

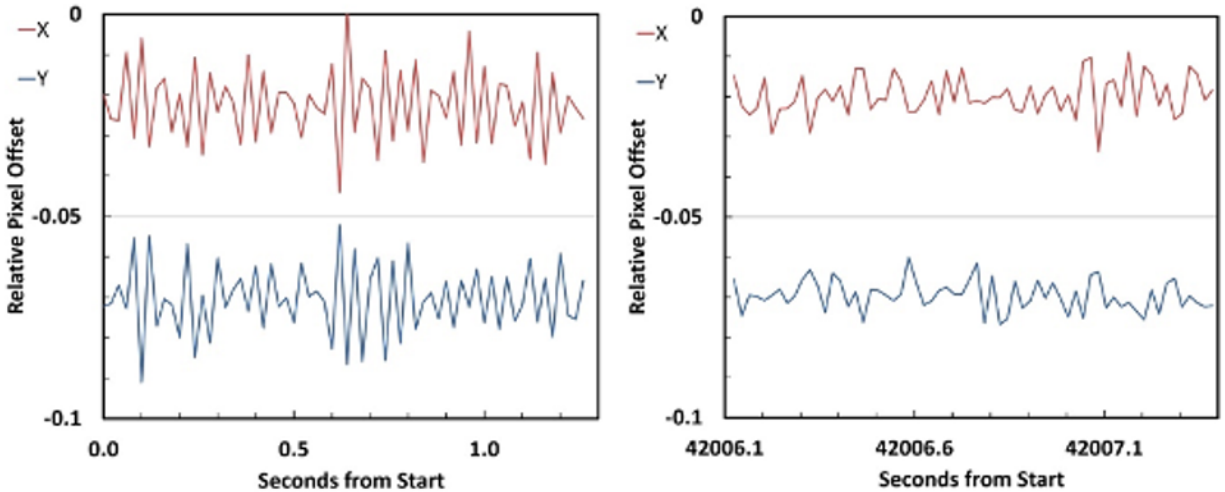


Figure 4.14: Two 0.02 second frame time samples taken during a long staring observation. The total monitoring period was 42,007.38 seconds or 11.67 hours. The left panel shows the data at the very start of the stare after the initial slew to the object, and the right panel shows the jitter at the very end of the monitoring period.

To illustrate the jitter behavior during a 100 second IRAC frame without an initial slew, Figure 4.16 shows two examples of the pointing motion during two 100 second periods of a long staring observation. These periods were during the middle of the observation, so they do not include any residual settling from the slew to this position. There was approximately a two second delay time between each set of the 64×0.1 second subarray frames, so that this dataset consists of a total of 770 frames of 0.1 second duration spread over the 100 second period. One can again see that the pointing seems to walk randomly over a region of ≈ 0.05 pixels in extent in both the X and Y directions. Sometimes it seems to dwell in one position for a longer time, and then at other times it moves at a more or less constant rate around the region near the pointing center.

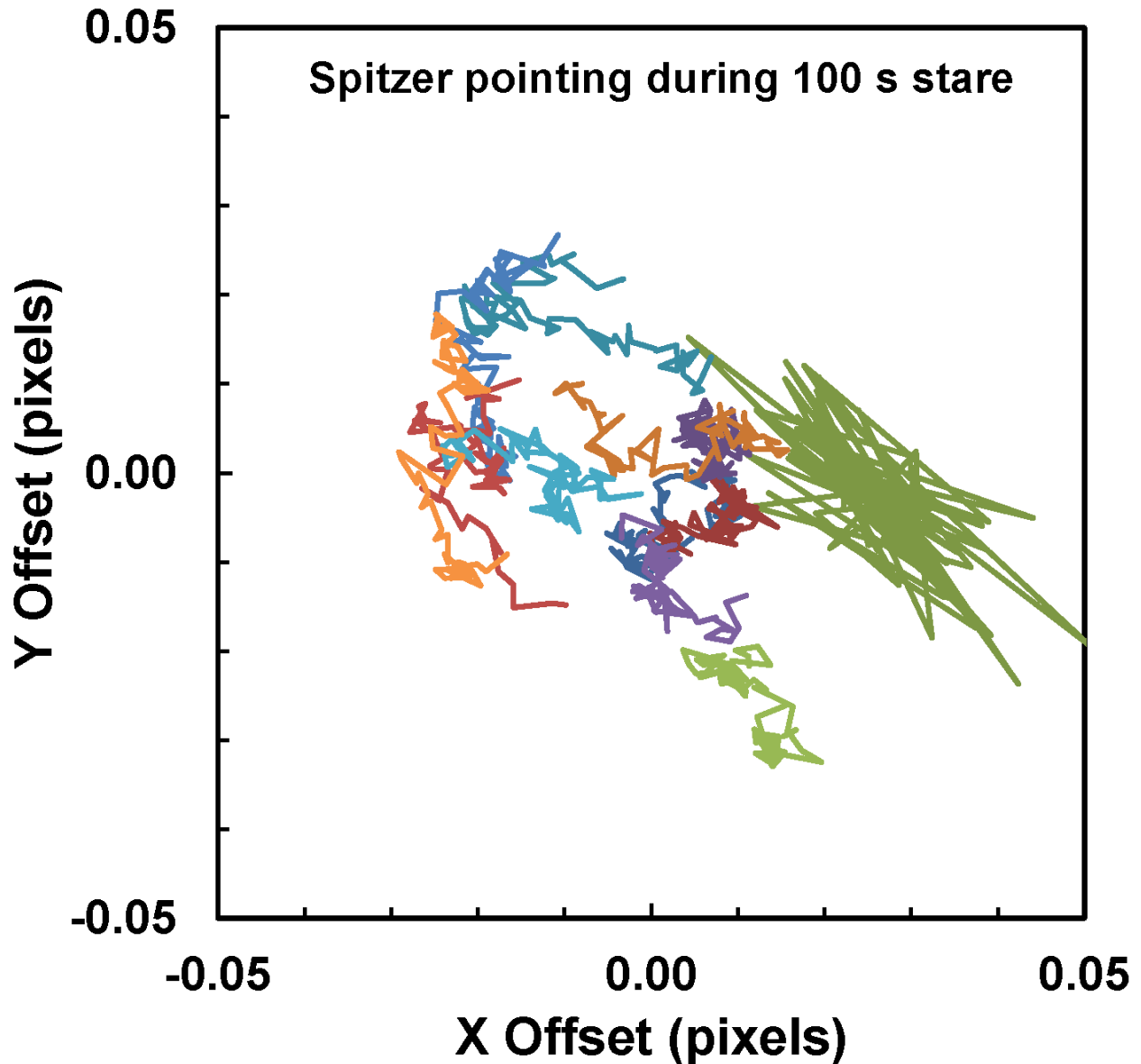


Figure 4.15: Spitzer pointing during the first 100 seconds after a PCS offset to the object position. The plot shows the pointing during the first 12 subarray data sets using 0.1 second frame time (6.4 seconds per subarray set). The first set, plotted in darker green, shows up on the right side of the plot, offset from the other data sets, and showing back-and-forth oscillations of about 0.05 pixels peak-to-peak. The following data sets show a much-reduced motion in successive frames, with a random walk around the reference position.

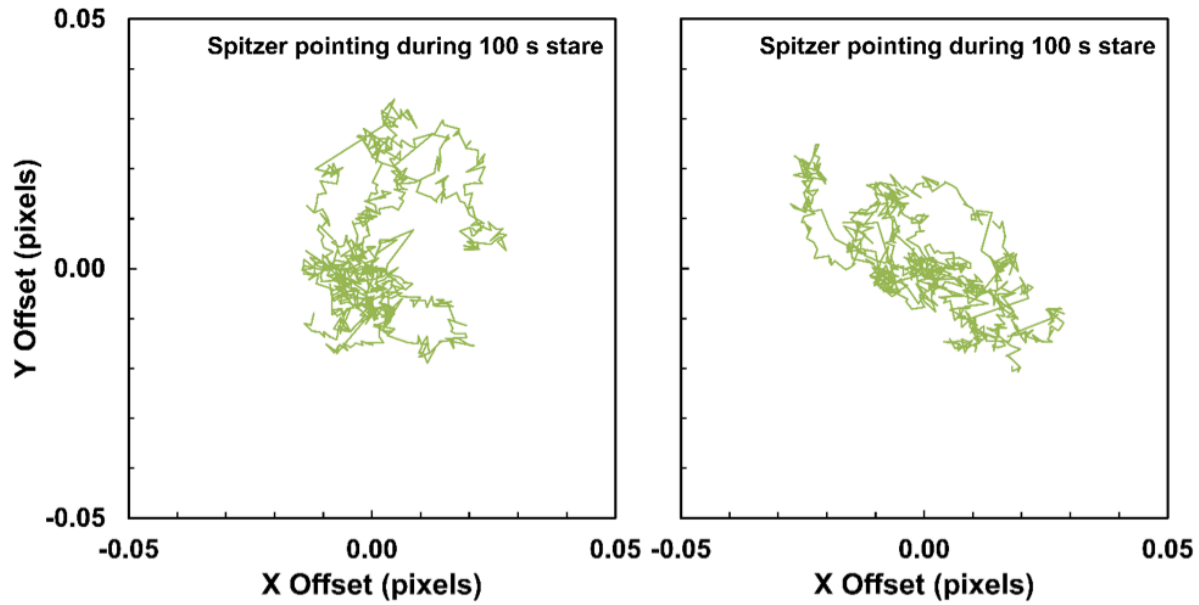


Figure 4.16: Two examples of the drift during 100-second periods of a long staring observation. The pointing seems to walk randomly over a region of ≈ 0.05 pixels in extent, sometimes dwelling at a position for some length of time, and then moving on a path around the pointing center.

4.12.4.2 Drift

Long- and short-term drifts have different causes, and are discussed here separately. See also Krick et al. (2018) and Grillmair et. al. (2014) for more details. Long-term drift is caused by the way that differential velocity aberration corrections are handled by the spacecraft's Command and Data Handling computer (C&DH) and by the star trackers. Figure 4.17 shows the measured drift in both X and Y positions (top and bottom rows, respectively) as a function of time on the left, and pitch to earth-point on the right. Spitzer was required to point at Earth to downlink data using its low gain antenna. Pitch to earth-point changes throughout the mission as Spitzer moves further away from Earth and around the Sun in its Earth-trailing orbit. Note: pitch to earth-point is different from the pitch angle of any given observation. Because pitch to earth-point and time are correlated, it is hard to disentangle trends seen in these plots. However, since pitch to earth-point is a more physical variable describing a change in the telescope, as opposed to time, the IRAC team thought this is the most likely origin of the trends.

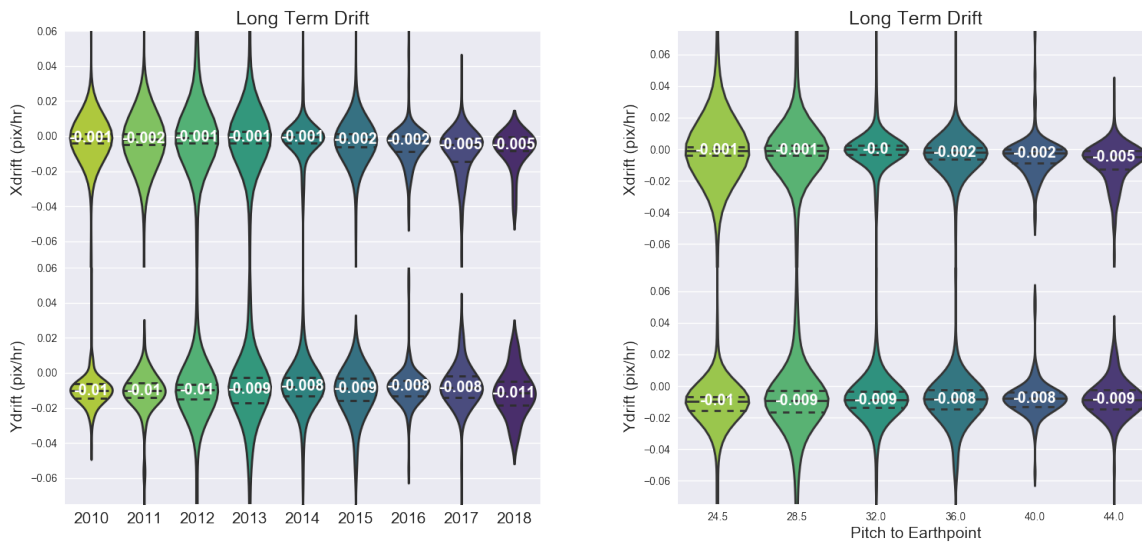


Figure 4.17: Distribution of long-term drift in both the X and Y directions as a function of time on the left and as a function of nearest in time downlink pitch angle on the right. These plots include all staring mode observations taken during the warm mission. Both plots are violin plots. Each violin-shaped object in the figure shows the median value and range for all the observations in that particular year (or at that particular pitch to earth point). Dashed lines show the median and inner quartiles of the distributions. The median values are printed at their locations. They can be thought of as smoothed histograms. Color variations between the violins have no meaning other than different years (itches) have different colors.

Short-term drift is the slow change in position over the first roughly half hour to two hours of a non-dithered observation. Figure 4.18 shows the Y centroid short-term drift as a function of pitch angle of the observation itself on the top and on the bottom as a function of change in pitch angle from the previous observation. Each plot has three panels: the top shows the duration of the short-term drift ranging from no drift to 2.4 hours with a median of around 0.5 hours. The middle panel is the total length of the drift in pixels, and the bottom panel shows the slope of the drift in pixels per hour. Points are color-coded by exposure time, for which we see no evidence of a correlation.

We do see evidence that both the scale and rate of the short-term drift are correlated with the pitch angle of the observation, and more strongly correlated with the change in the pitch angle from the previous observation. This implies that short-term drift is caused by a thermal settling of the telescope as it gets different illumination from the Sun through different pitch angles relative to the Sun, an idea first put forth by Grillmair et al. (2014). These correlations are likely not perfect because a) it is hard to measure the exact start and finish time of a drift superimposed on top of the other changes in the position of the centroids, and b) there is likely a correlation also with even earlier observations. The scale and rate of the short-term drift probably depend on the pitch angle and duration of several previous observations.

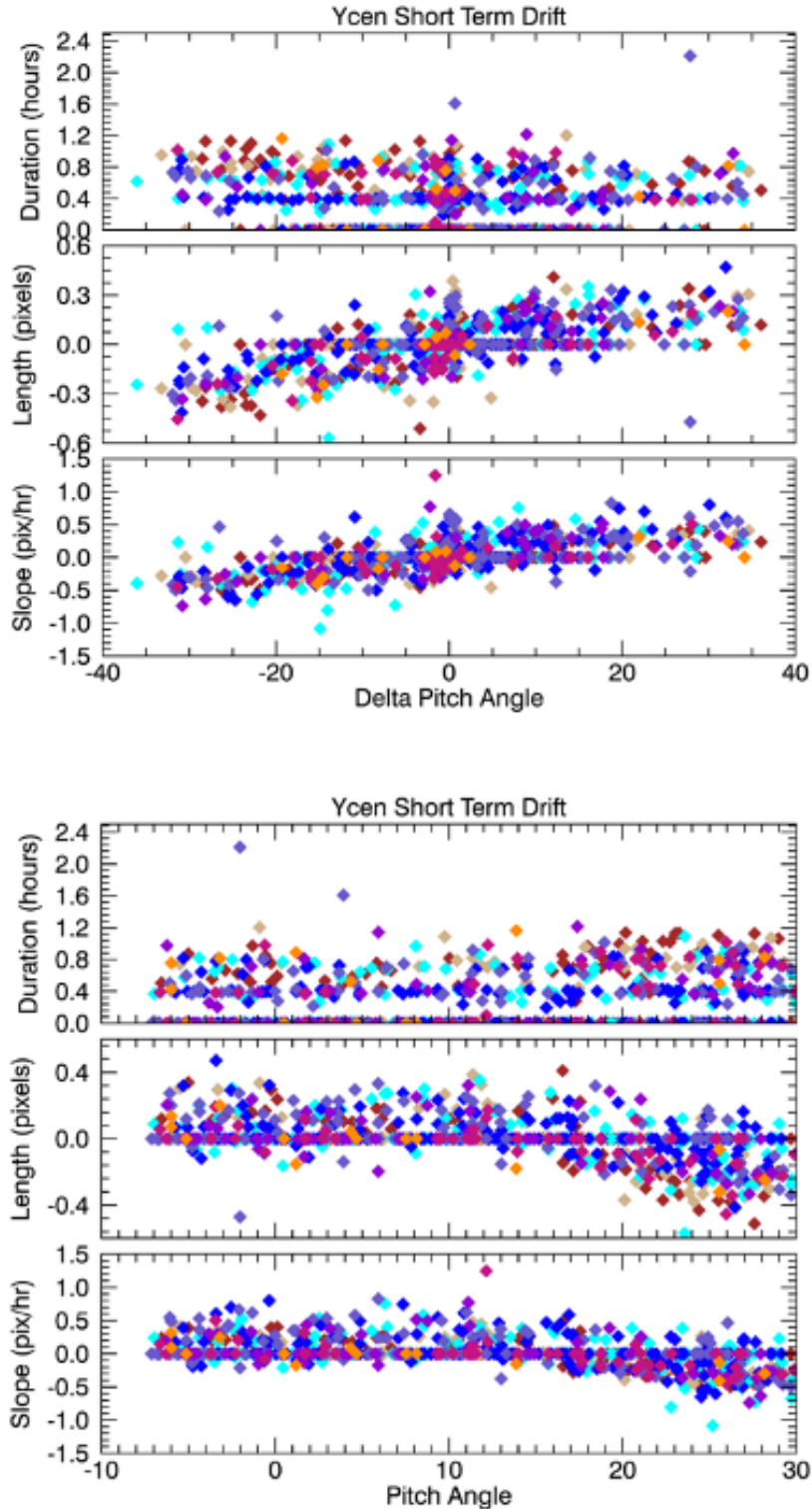


Figure 4.18: Short-term drift. Top: duration, length, and slope of the short-term drift as a function of the pitch angle of the observation itself. Bottom: same short-term drift parameters as a function of the change in the pitch angle from the previous to the current observation. Observations are color coded by exposure time, where shorter exposures are

red and longer exposures are blue. The scale and rate of the short-term drift correlate with the pitch angle and the duration of several previous observations.

4.12.4.3 Wobble

A slowly varying pointing oscillation is seen in many long staring observations. The oscillation is related to the spacecraft battery heating and cooling cycles that influence the mechanical link between the star tracker and the telescope, inducing a slight pointing wobble. The magnitude of the oscillation varies depending on the thermal state of the observatory and the recent pointing history. The characteristics of the oscillation have also changed over the warm mission. Prior to 2010 October 17, 07:25:00 UTC¹, the period was about one hour and the amplitude of the flux variation when staring at a star was $\approx 0.005\%$. The battery heater parameters were changed to reduce the temperature excursions from 1.0 K to 0.5 K. This reduced the period of the oscillation to ≈ 40 minutes, and the amplitude of the resulting relative flux variations to $\approx 0.002\%$. The offset variation of the short-term component after 2010 October 17 is ≈ 0.05 pixels (see Figure 4.19).

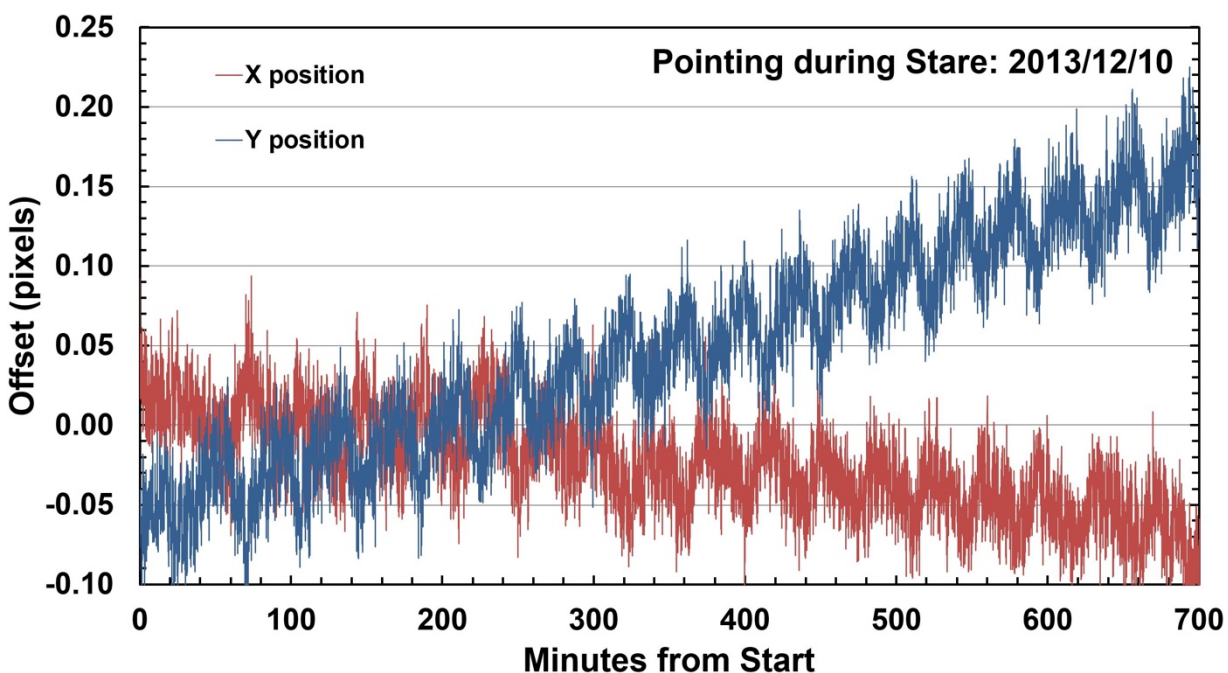


Figure 4.19: IRAC jitter observed during a long staring observation of the Galactic Center on 2013 December 10 (PID=10060). The X and Y offsets relative to the reference position are shown for both the X and Y directions on the IRAC array. Both directions show the oscillation (approximately 0.05 pixels) caused by the spacecraft heater, with about a 40-minute period. There is also an approximately linear drift in both dimensions over the length of the observation, larger in Y than in X .

In subsequent years of the warm mission, due to the increasing pitch angle necessary to perform downlinks, the spacecraft began to drain the battery more during downlinks, requiring the battery to be recharged during science observations and calibrations. This use of the battery results in a higher operating temperature, and therefore, the battery heater came on less frequently and often

¹ <https://irsa.ipac.caltech.edu/data/SPITZER/docs/files/spitzer/21oct2010memo.txt>

was not operating during science observations. Therefore, the pointing oscillation was not present in some staring observations later in the warm mission. The history of the amplitude and strength of the battery heater oscillation over the 2010 – 2017 period of the warm mission is shown in Figure 4.20. The upper bound is not visible for 2016 and 2017, but it is symmetric with the lower bound. The exact size of the distribution is unimportant, but the important point is that we did not find a strong oscillation peak, reflected in the range of peaks that is very large. This large range means that the oscillations are non-existent, as can also be seen by the dramatic decrease in the strength of the in 2016 and 2017.

An example of a long stare without the oscillation is shown in Figure 4.21. These are observations of the Galactic Center in 2016 July, performed in the same way as the dataset shown in Figure 4.19. However, the battery heater was apparently not operating during this period, so no periodic oscillation is seen in the pointing. These data also show much lower long-term drift.

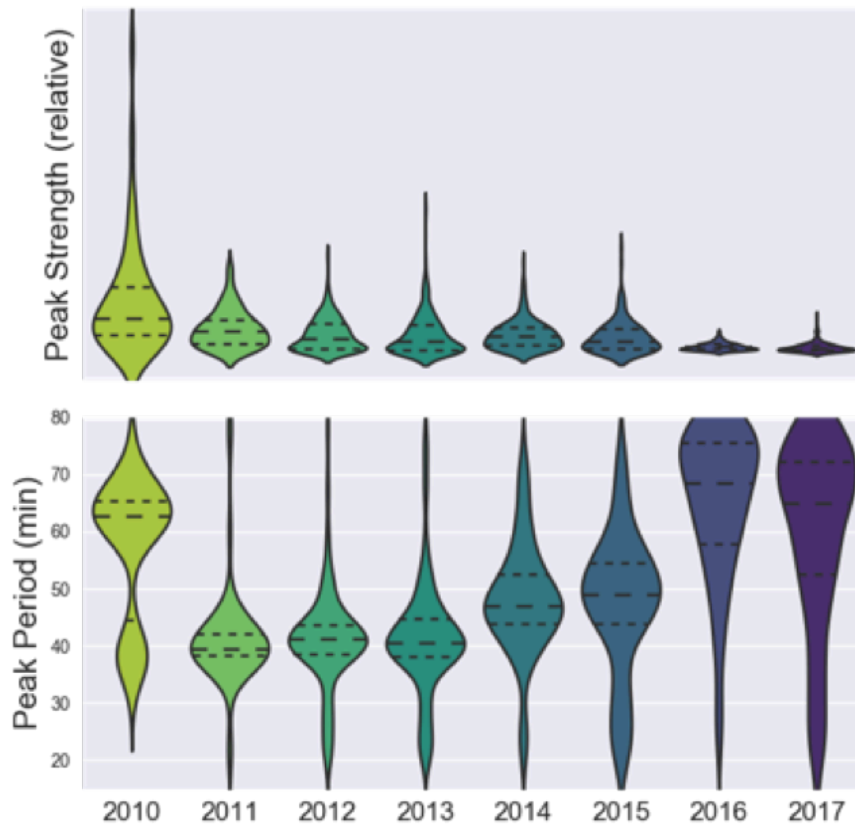


Figure 4.20: Amplitude and strength of the battery heater oscillation over the 2010 – 2017 period of the warm mission. Both plots are violin plots. Each violin shaped object in the figure shows the median value and range for all the observations in that particular year. Dashed lines show the median and inner quartiles of the distributions. Color variations between violins have no meaning other than different years have different colors.

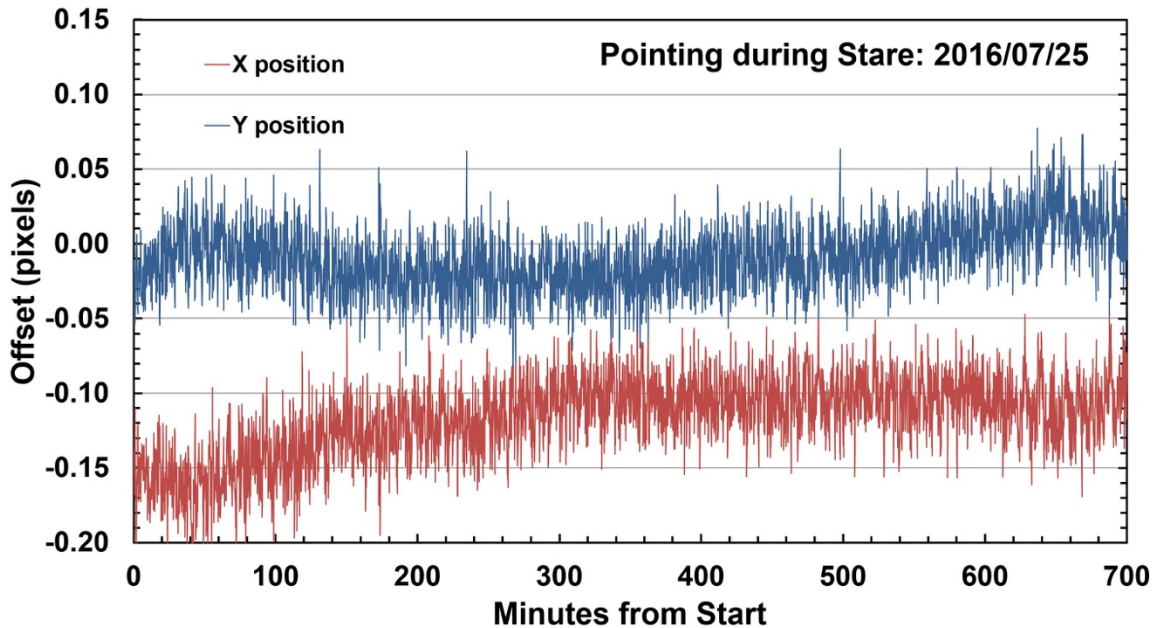


Figure 4.21: IRAC pointing variations observed during a long staring observation on 2016 July 25 (PID=12034). This observation was similar to that in Figure 4.19, but here we do not see the spacecraft heater oscillation.

4.13 Instrument Performance Trending

4.13.1 Photometric Stability

The 3.6 μm and 4.5 μm calibration star normalized flux densities were monitored and periodically checked to make sure that the aperture photometry of the calibration stars remained nominal throughout the mission (see also Section 8.3.7) for more details. In Figure 4.22, the primary calibrators are shown in blue, red, black, and green colors; the secondary calibrators are shown with a multitude of repeating colors as they cycle through the year. The primary calibrator data points are mostly not visible behind the more frequently observed secondary calibrator data points, but any deviations can be observed.

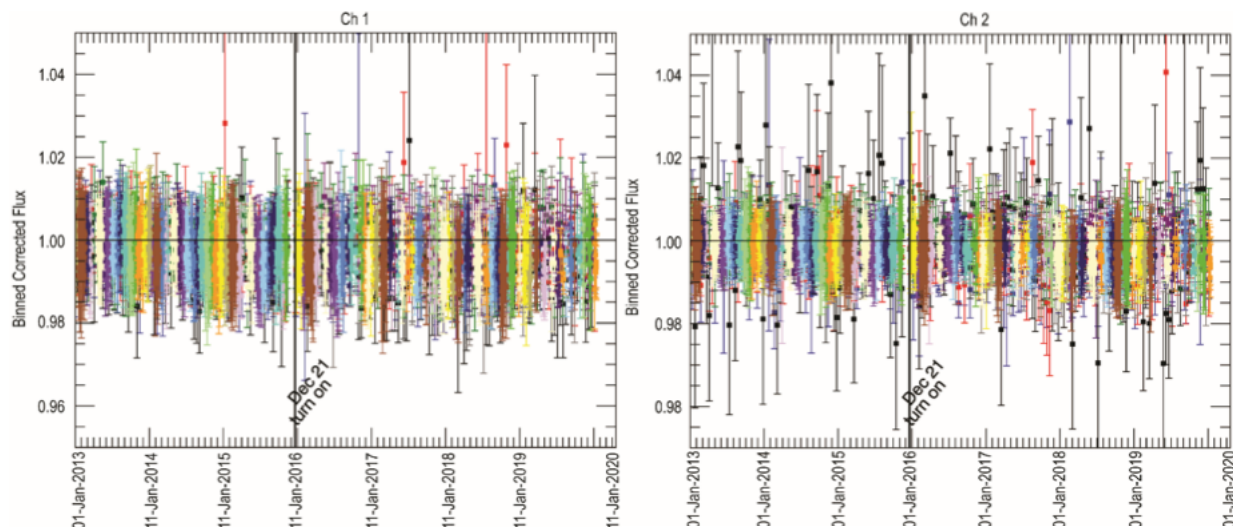


Figure 4.22: The 3.6 μm (left) and 4.5 μm (right) calibration star normalized flux densities as a function of time from 2013 to 2020. All flux densities are measured by aperture photometry and include 21 primary and secondary calibrators denoted with different colors. The line (and gap) in December 2015 denotes an anomaly in which IRAC was off and no observations were taken. There is no difference seen before or after this anomaly. See the text for the meaning of the various colors, and more information about the plots.

The flux densities have been measured using aperture photometry corrected for both the location of the center of the star with respect to the pixel (pixel phase effect) and the location on the array (array location dependence). The flux densities for each star measurement were normalized to the median value for that star. Error bars are calculated as the sigma clipped standard deviation in the bins, divided by the square root of the number of data points in each bin. The black line at normalized flux density = 1.0 is shown to aid the eye in determining what a flat line would look like. All the data have been processed with pipeline version S19.2. These 21 stars include full array and subarray observations, as well as many different exposure times and well depths.

Over the course of the entire mission, we do see a decrease in sensitivity of IRAC photometry of order 0.1% per year in channel 1 and 0.05% per year in channel 2. The suspected cause is radiation damage to the optics, which can be expected in space environment.

4.13.2 Skydark Bias Offsets

To monitor for any changes in the bias, the median value of the skydarks was checked after they had been pipeline processed. Only one frame time (12 seconds) was consistently used for monitoring, as similar trends in the background value as a function of time over the mission were seen in skydarks taken with all frame times. The 12 second frame time was chosen for its balance between read noise and background noise, so that changes in the bias level can be seen most clearly.

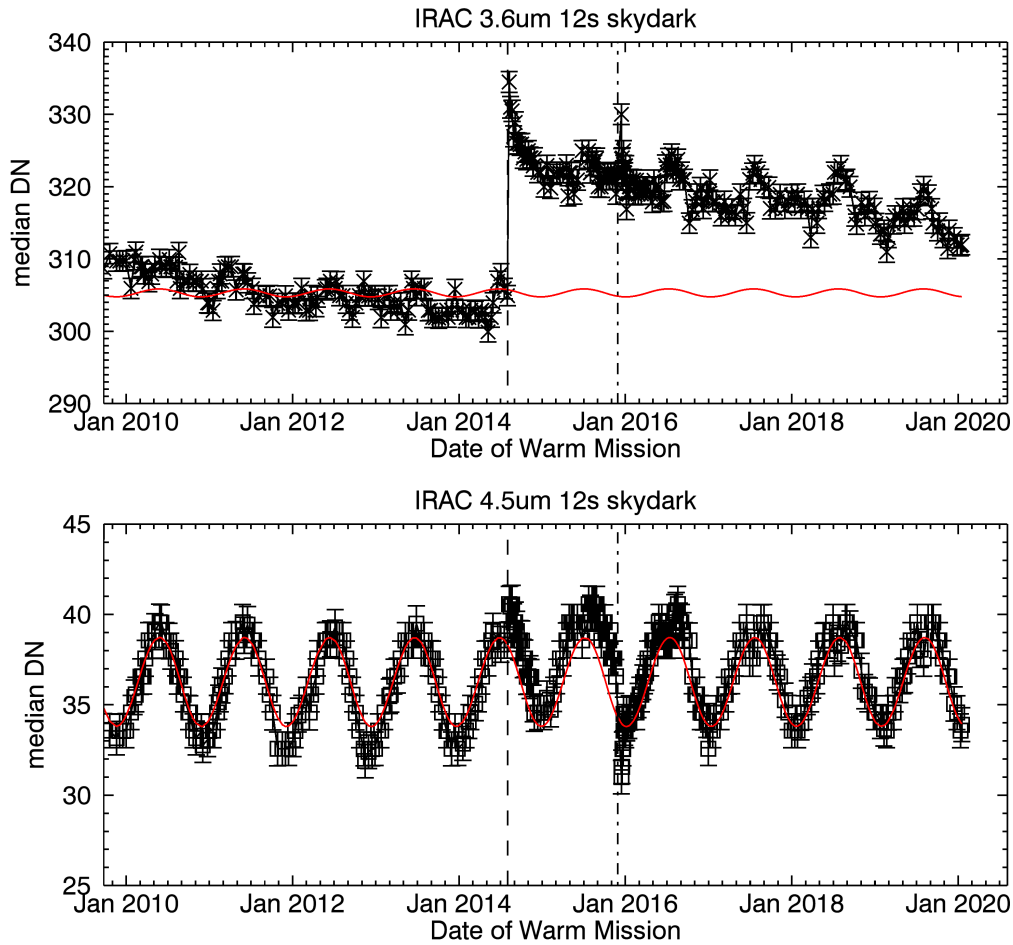


Figure 4.23: Median value of the 12 second skydarks plotted over time since the beginning of the warm mission. The vertical dotted lines denote two anomalies in which the array was reset. The median value was observed to settle to a new nominal level after the anomalies. The red lines give the shape of the predicted seasonal zodiacal variation normalized to the median value of the skydarks in January 2012, to help with the search for any trend changes in skydark values. See the text for more information.

For every combined 12 second skydark frame, a median value of the array is calculated and plotted with error bars over the course of the warm mission (Figure 4.23). Error bars were calculated from the Poisson electron noise and read noise error added in quadrature, as determined in the pipeline processing. There does appear to be a slight trend ($< 0.1\%$ per year) of decreasing bias in both channel 1 and 2. This could be due to a decrease in the zodiacal background as the distance of the spacecraft has increased from Earth, or it could be due in part to a decrease in the sensitivity of the optics. Any change in the bias in the skydark frames would also appear in the science frames, but because the darks were subtracted from the science frames, this does not cause any change in the overall calibration of the instrument.

The two vertical lines in the plot denote two anomalies, which occurred on 2014 August 2 and 2015 November 28. The first one caused the arrays to reset with less than the usual applied reverse voltage across the detectors. After normal operation was restored, the skydark bias levels settled

back to a level 3.2% higher in both channels. The second event caused IRAC to go to a safe mode. After recovery, the 3.6 μm array quickly settled back to the same higher bias, however, the temperature of the 4.5 μm array was below nominal for over a week while off. Once its normal temperature was restored, the skydark bias quickly settled to a level slightly lower than it was between the anomalies.

4.13.3 Radiation Hits

The number of radiation hit affected pixels (“bad pixels”) was tracked using the calibration observations taken with IRAC once a week. During the mission, the statistical baseline of the average number of affected pixels per second was established as approximately 4 – 6 saturated pixels per second (see Figure 4.24). The trend observed in the IRAC data follows the inverse of the solar cycle, as expected, with less cosmic rays during the peak of the solar activity.

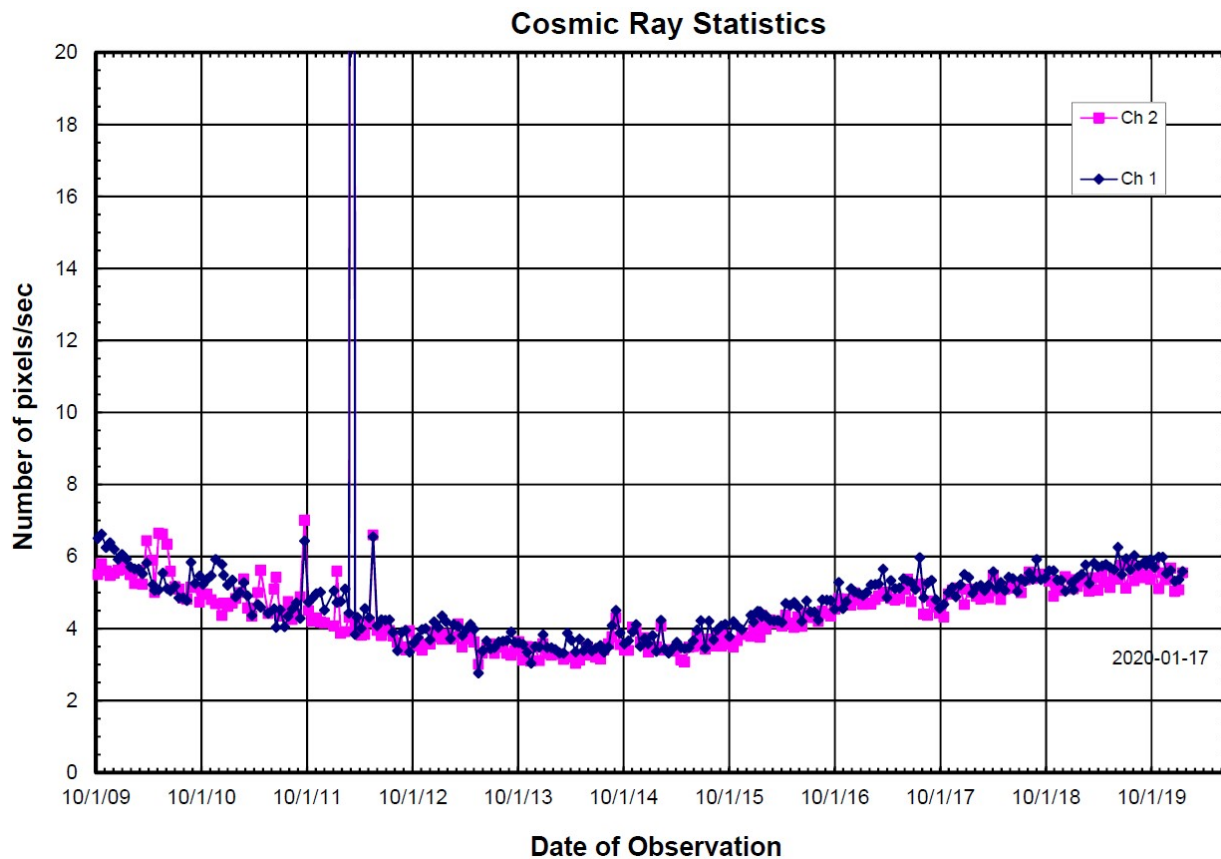


Figure 4.24: Average number of pixels per second affected by cosmic rays in the 100 second skydarks since the beginning of the warm mission. The spike in 2012 is due to a solar flare that occurred during the time the skydark calibration data were being taken.

The number of cosmic rays affecting an IRAC image was determined from the 100 second skydark measurements taken once a week. The dark frames consisted of 27 individual images taken in a 3×3 mapping pattern in the “Best NEP dark” region chosen at the beginning of the mission. This was within the continuous viewing zone and contained no bright sources that would saturate in 100 second images.

The individual images were registered and stacked to determine the affected pixels per second, using the number of pixels above a radiation cutoff level as a criterion (after masking bright stars in the image). These images were also used to count the number of bad, noisy, and dead pixels.

Hot and noisy pixels changed with time, as some pixels recovered and others became hot or noisy. Pixels were deemed to be noisy if the standard deviation was greater than 50 DN, and hot if the flux retained was $> 5\sigma$ of the flux of the surrounding pixels. Dead pixels, or non-responsive pixels, overall increased by 10 – 20 pixels during the mission (see Figure 4.25). These were trended since the beginning of the mission, with the result that more than 98% of pixels remained usable until the end of the mission.

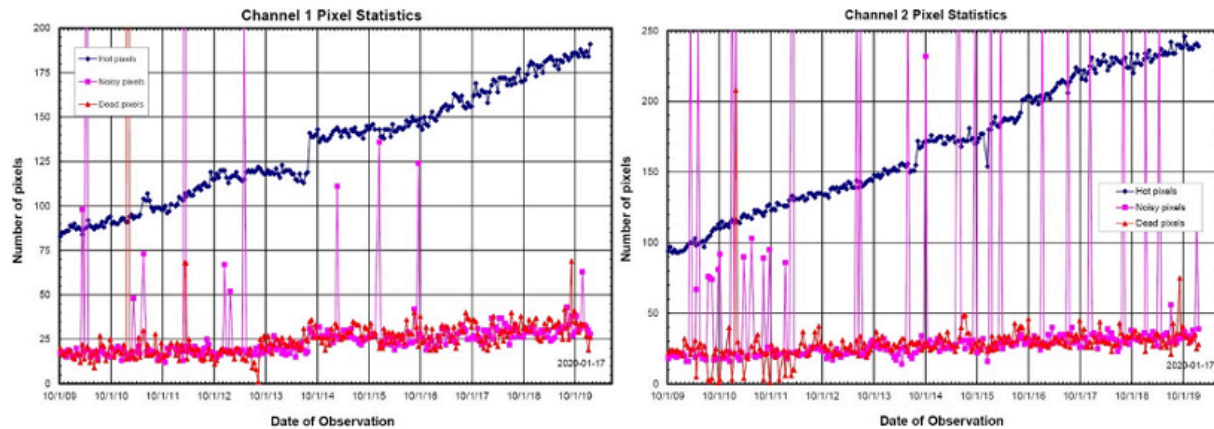


Figure 4.25: Number of pixels determined to be hot, noisy, or dead during each observing campaign in the 100 second skydarks since the beginning of the mission. Hot and noisy pixels changed over time as some pixels recovered and others became hot or noisy. Dead pixels only increased by 10 – 20 pixels over the entire mission.

5 Pipeline Processing

5.1 Level 1 (BCD) Pipeline

The IRAC Level 1 (BCD; basic calibrated data) pipeline is designed to take a single Level 0 (raw) image from a single IRAC detector and produce a flux-calibrated image which has had all well-understood instrumental signatures removed. The following describes the data reduction pipeline for science data. Similar pipelines are used for reducing calibration data. Note that the pipeline processing for moving targets is the same as for fixed targets. Chapter 7 on data features and artifacts provides more information on several image features addressed by the pipeline, and the appropriate sections of that chapter are cross-referenced from this chapter.

The IRAC pipeline consists of two principal parts: the data reduction software modules and the calibration server. The individual modules each correct a single instrumental signature. They are written as standalone code executable from the Unix command line. Each uses FITS files and text configuration files as input, and produces one or more FITS files and log files as output. These modules are strung together with a single Perl script. The actual calibration data needed to reduce a given DCE (data collection event) is produced via calibration pipelines. A raw IRAC DCE is thus passed between successive modules, and at each step becomes closer and closer to a finished, fully reduced image. The following sections describe the reduction steps used to produce the BCD data.

5.1.1 *SANITY DATATYPE (parameter checking)*

Before data proceeded through the pipeline, a check was made to make sure that the data were of the type that was expected. In particular, ancillary keywords were checked against their expected values to ensure that they were in range, and had the expected logical state. These included the shutter state (open/closed), transmission and flood calibrator lamp status (on/off), and read mode (full/subarray).

5.1.2 *SANITY CHECK (image contents checking)*

Before pipeline processing continued, the actual image contents were checked to ensure that they contained values expected for actual image data. These tests included checking to ensure that the image was not all zeros, that the pixels were not all identical, or that areas of the image did not have an abnormal data range.

5.1.3 *TRANHEAD (header processing)*

The FITS headers delivered by Jet Propulsion Laboratory (JPL)/Flight Operations System (FOS) were translated into a more readable format. For example, the FITS header keywords

```
A0612D00 = 14478455 / AINTBEG
A0612E00 = 1.4478455E5 / [Sec]
A0614D00 = 8 / AFOWLNUM
A0614E00 = / [NONE]
A0615D00 = 44 / AWAITPER
```

A0615E00 = / [NONE]
A0657D00 = 14479495 / ATIMEEND
A0657E00 = 1.4479495E5 / [Sec]

were translated to:

AINTBEG = 144784.55 / [Secs since IRAC turn-on] Time of integ. start
ATIMEEND = 144794.95 / [Secs since IRAC turn-on] Time of integ. end
AFOWLNUM = 8 / Fowler number
AWAITPER = 44 / [0.2 sec] Wait period

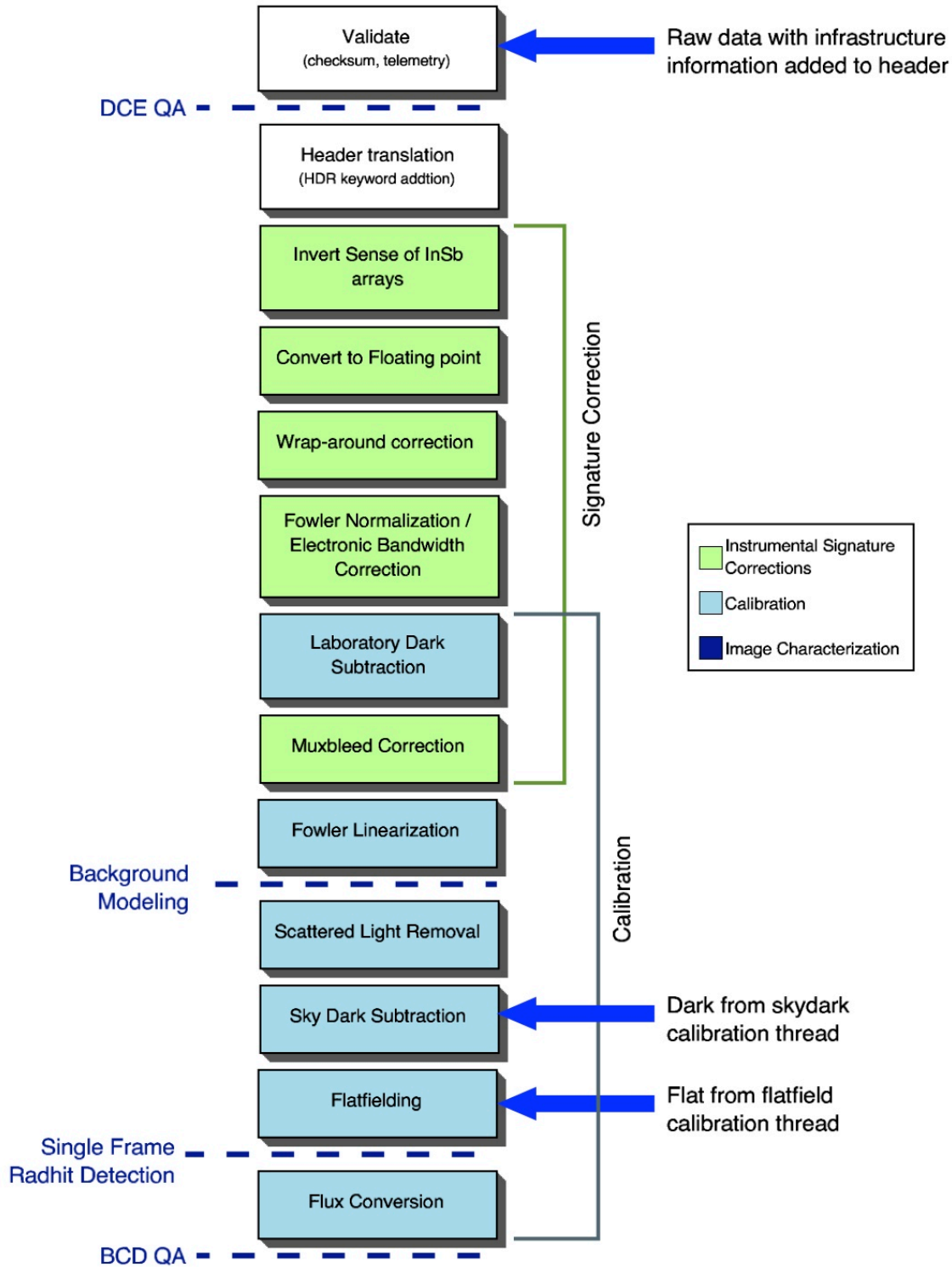


Figure 5.1: Data flow for processing a raw IRAC science DCE into a BCD.

It is also at this stage that derived parameters, most notably the integration time, were added to the headers. The integration time was related to the Fowler number (AFOWLNUM) and the number of wait periods (AWAITPER; see Sections 2.4.2 and 2.4.3 for the definition of these concepts) via

$$\text{EXPTIME} = \text{mode} \times (\text{AWAITPER} + \text{AFOWLNUM}) \quad (5.1)$$

The integration time was stored in the header in the keyword EXPTIME. Another timescale of importance is the frame time. This is the actual length of time that the observation was integrating on the sky, and is equal to

$$\text{FRAMTIME} = \text{mode} \times (\text{AWAITPER} + 2 * \text{AFOWLNUM}) \quad (5.2)$$

The factor *mode* is equal to 0.2 seconds for full array mode, and 0.01 seconds for subarray mode. The read mode was determined by the least significant bit of the ancillary keyword AREADMOD. If AREADMOD was 0 (or even), then the mode was full array. If it was 1 (or odd), then the read mode was subarray.

Note that because of TRANHEAD processing, the headers of the raw data and the final BCD data products are not identical. In general, users should only need to read the BCD headers. However, if it becomes somehow necessary to examine any of the camera telemetry (voltages, currents, etc.), then the desired telemetry values can be read from the complete raw data header.

5.1.4 INSBPOSDOM (*InSb array sign flipping*)

The IRAC InSb arrays (channels 1 and 2) were operated in such a way that flux appeared negative in the raw data (Figure 5.2). That is, data numbers start at 65,535 (16-bit max) for zero light levels and became increasingly close to 0 as light levels increased. The INSBPOSDOM module rectified this so that increasing DN (“data number,” denotes the pixel value, similar to analog-to-digital unit ADU often used in optical data) yielded increasing flux (0 to 65,535), as is more common. This was done by

$$A_{\text{out}} = (65,535 - A_{\text{in}}) \quad (5.3)$$

where A is the pixel intensity in DN for the two InSb arrays (ACHANID = 1 or 2). ACHANID was turned into CHNLNUM in the BCD header by the last step in the pipeline.

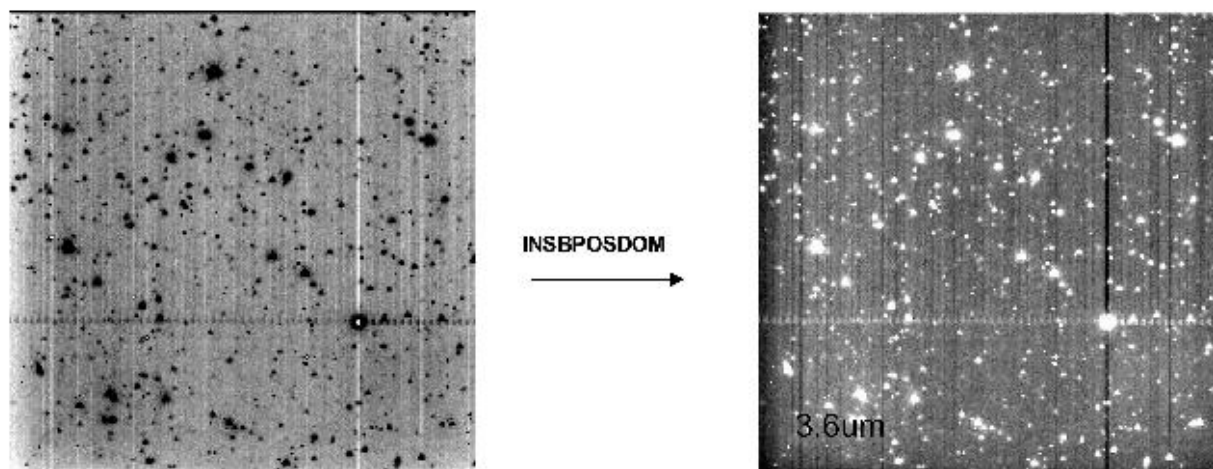


Figure 5.2: Effect of INSBPOSDOM . INSBPOSDOM worked only on the two InSb arrays (channels 1 & 2) and reversed the sense of intensities. Left is before INSBPOSDOM ran and right is after.

5.1.5 CVTI2R4 (byte type changing)

Data were converted from the native unsigned 16-bit format used by IRAC to the 32-bit floating point format used in astronomical calculations. At this point, the following DN was added to all the pixels in order to account for the bias introduced by the spacecraft on-board bit truncation.

$-0.5 \times (1 - 2^{-\text{ABARREL}})$ for channels 1 and 2

$+0.5 \times (1 - 2^{-\text{ABARREL}})$ for channels 3 and 4

Here, ABARREL is the barrel shift number keyword where the bit truncation occurred (see Section 5.1.7). Also, if the header indicated that any rows or columns were blank (usually due to data loss during transmission from Spitzer to the ground), then those pixels were set equal to NaN (Not a Number).

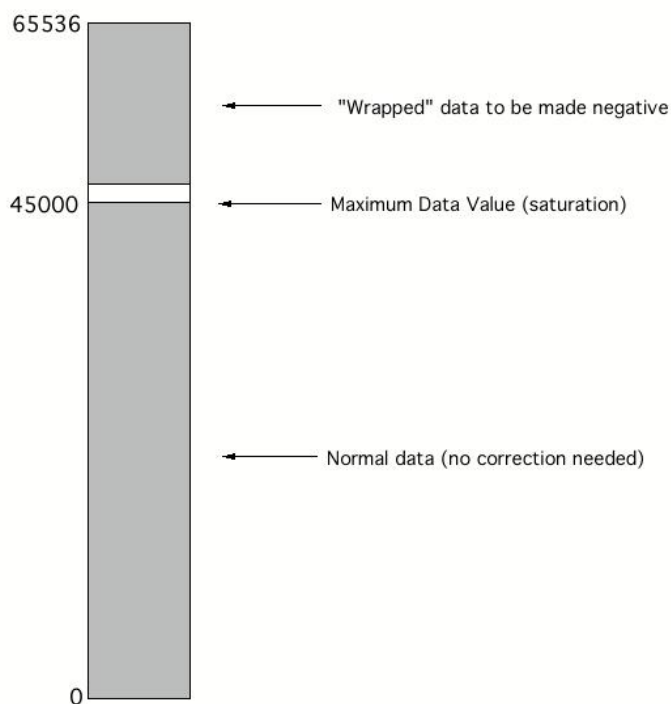


Figure 5.3: Diagram of the wrapping of negative values due to truncation of the sign bit.

5.1.6 Wraparound Correction: *IRACWRAPDET* and *IRACWRAPCORR*

IRAC raw data sometimes required correction for wraparound, wherein DN values were actually multi-valued. That is, a given DN actually corresponded to more than one possible flux level.

IRACWRAPDET (sign truncation wraparound)

As a means of data compression, IRAC discarded the sign bit of its data before transmission to the ground. IRAC used the 2s-complement storage system for negative numbers. In this system, negative numbers were coded without a negative sign, but with the bits flipped and 1 added. For example, with 16 bits, -1 is represented by 65535 in unsigned integer form. However, this created an ambiguity in that negative values appeared in the raw data as very large positive numbers. By design, the detector reached physical saturation before “electronic” (A/D) saturation (Figure 5.3). The maximum physical values the detectors reached were around 45,000 DN for the InSb arrays and 55,000 DN for the Si:As arrays, which were less than the maximum 16-bit value of 65,535. Values above these limits should be wrapped negative values. This module then flagged any pixels lying in the wraparound DN region. If any part of the image was near the saturation value (typically either 45,000 DN in channels 1 and 2 or 55,000 DN in channels 3 and 4, in cryogenic mission) then surrounding pixels may have been near saturation.

IRACWRAPCORR (wraparound correction)

This module used the flag bits set by the previous module and attempted to correct the wraparound problem (Figure 5.4). Note that both the sign truncation and the non-linearity wraparound, i.e., doughnuts (see discussion on saturation in Section 7.2.1), were corrected in the pipeline. The sign truncation correction was simply

$$A_{\text{corrected}} = A_{\text{uncorrected}} - 65535. \quad (5.4)$$

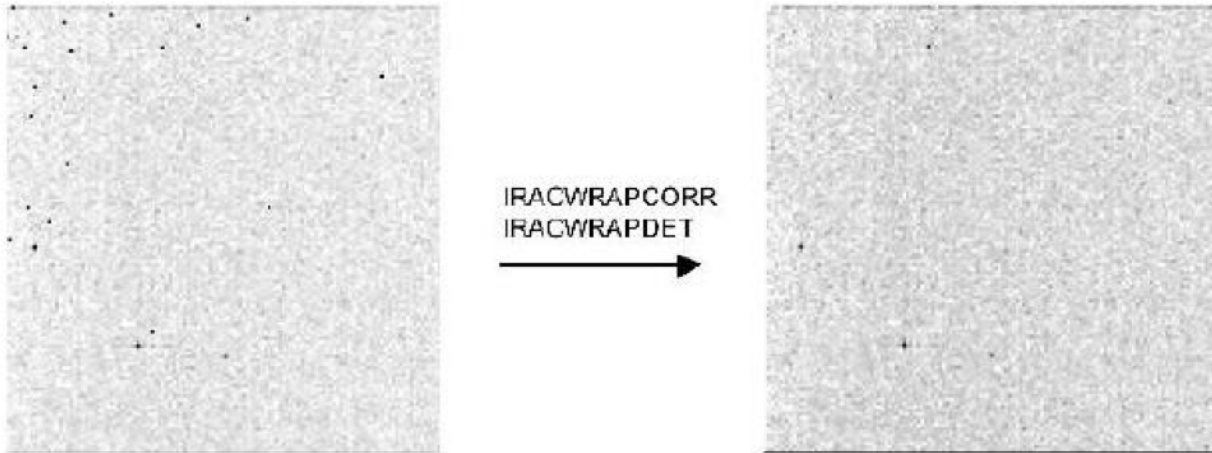


Figure 5.4: Application of IRACWRAPCORR to channel 1 data. The many apparently hot pixels were actually wrapped negative values, which were detected based on their data values vastly exceeding the physical saturation value for the detectors, and corrected by subtracting the appropriate value. Real hot pixels did not exceed the physical saturation value, and hence were not changed.

5.1.7 IRACNORM (Fowler sampling renormalization)

IRAC data were taken with Fowler (multi) sampling in order to reduce read noise. This was done by non-destructively reading the array multiple times (set by the Fowler number), and accumulating the sum into an internal register. Since these reads were summed, the result had to be divided by the number of reads in order to get the actual number of DN. Additionally, when data were transmitted to the ground, a variable number of least significant bits were discarded as a means of data compression (Figure 5.5).

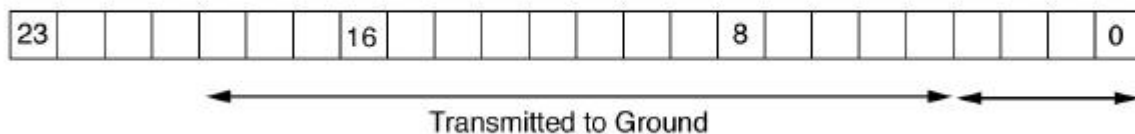


Figure 5.5: Illustration of bit truncation. Bit truncation was used by IRAC for ground transmission, necessitating IRACNORM. The internally stored 24-bit word was truncated to 16 bits, with a sliding window set by the barrel shift value. The figure illustrates the ABARREL=4 case.

In order to correct for the effects of bit-truncation and Fowler sampling the data were transformed by

$$A_{out} = \frac{A_{in} \times 2^{ABARREL}}{AFOWLNUM} . \quad (5.5)$$

Note that in normal usage the Fowler number and barrel shift actually used and commanded by the SSC were such that they canceled, i.e.,

$$\frac{2^{ABARREL}}{AFOWLNUM} = 1 \quad (5.6)$$

and hence observers should not be surprised if this module normally appeared to do nothing.

5.1.8 SNESTIMATOR (initial estimate of uncertainty)

The module SNESTIMATOR calculated the uncertainty of each pixel based on the input image (here, the input image was the output of IRACNORM). The uncertainty for each pixel was estimated as the Poisson noise in electrons, and the read noise was added in quadrature. The formula for the calculation was as follows:

$$\sigma^2 = \sigma_{readnoise}^2 + \sigma_{poisson}^2 \quad (5.7)$$

To obtain an expression in DN, σ was divided by gain. This uncertainty image was carried through the pipeline, and additional uncertainties (e.g., dark and flat uncertainties) were added in quadrature, when appropriate.

5.1.9 IRACEBWC (limited cable bandwidth correction)

The cables that connect the IRAC Cryogenic Assembly (the detectors) to the Warm Electronics Assembly (the readout electronics) had a characteristic time constant similar to the rate at which individual pixels were read. As a result, all pixels had an “echo” or ghost in the following readout pixel (Figure 5.6). Since the pixels were contained in four readout channels, the “next” pixel was actually four pixels to the right. The first pixel read out in an IRAC image was the first data byte in the image, and was situated in the lower left corner in most astronomical display software. This effect was corrected for by using the known readout order of the pixels. Starting at the first pixel, we corrected the following pixel, and so on.

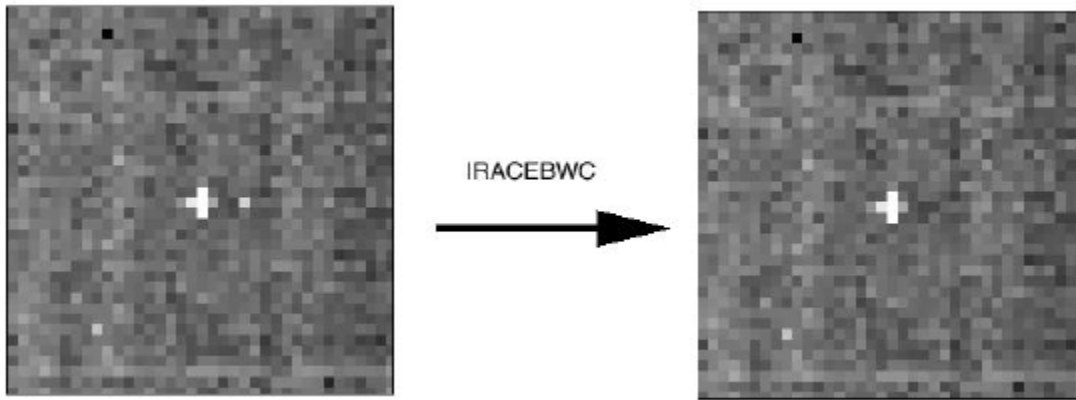


Figure 5.6: Correction of cable-induced bandwidth error by IRACEBWC. The illustrated data show a cosmic ray hit.

An additional wrinkle was that the time required to go from the end of one row to the beginning of the next was slightly longer (by 75%) than the time to go from one column to the next in the same row. As a result, a slightly different coefficient had to be applied. The task was simplified by two things. First, the effect was so small that it was only necessary to correct the following pixel, as the next echo was below 10^{-5} times the original in intensity. Second, the time of the effect was much faster than the echo decay time. Thus, the problem needed only to be solved in one direction. The current bandwidth coefficients are given in Table 5.1. They are applied using

$$A_{n+4} = A_{n+4} - \kappa A_n \quad (5.8)$$

where A is the pixel intensity in DN and κ is the correction coefficient for a given readout channel (of 4). A different value of κ was used for correcting the first four pixels in a row, based on the pixel values of the last four pixels of the previous row.

Table 5.1: Bandwidth correction coefficients.

Channel 1				
Readout	1	2	3	4
κ	1.58E-3	2.17E-3	2.33E-3	1.64E-3
κ (end of row)	1.2E-5	2.1E-5	2.4E-5	1.3E-5
Channel 2				
Readout	1	2	3	4
κ	1.71E-3	3.63E-3	1.06E-3	1.11E-3
κ (end of row)	1.4E-5	5.2E-5	6.0E-5	6.6E-5
Channel 3				
Readout	1	2	3	4
κ	3.19E-3	1.04E-2	3.3E-3	2.09E-3
κ (end of row)	4.2E-5	3.3E-4	4.4E-5	2.0E-5
Channel 4				
Readout	1	2	3	4
κ	3.74E-3	3.74E-3	3.74E-3	3.74E-3
κ (end of row)	5.5E-5	5.5E-5	5.5E-5	5.5E-5

5.1.10 Dark Subtraction I: FFCORR (“first frame effect” correction) and LABDARKSUB (labdark subtraction)

The true dark current in the IRAC detectors was actually very low – the most notable dark current features were the electronic glows seen in the Si:As arrays (channels 3 & 4). However, the IRAC arrays experienced considerable pedestal offsets which were commonly of the order of tens of DN. These offsets were dependent on the Fowler sampling, exposure time, and operation history of the arrays, and were thought to be due to very small thermal changes in the internal IRAC cold electronics. The most significant of these offsets was the first frame effect: the laboratory measurements showed that the dark patterns and DC levels changed as a function of the time elapsed between the end of the previous frame and the start of the current frame (called “delay time”). The first frame in a series of exposures was most affected, and therefore this effect is called the first frame effect. During cryogenic operations, channel 1 had very significant variations in offset, compared to the low background in that channel. Channel 2 had very small variations in offset. Channel 4 has significant variations, though they are very small compared to the background. The most significant first frame effect by far is in channel 3. Figure 5.7 shows how the DC levels of darks changed as a function of delay time.

In a sequence of images with the same frame time and Fowler number, the variation from one image to the next consists principally of a uniform change over the whole image. To a much smaller extent, there is also a change in the relative offsets on each of the four outputs of an array (pinstriping) and a small spatial gradient across the image. True dark current and multiplexer glow carry with them the usual shot noise in the number of charges collected at the integrating node, but the rest of the Fowler bias (effective bias due to read strategy) presumably is due to relaxation in the multiplexer and temperature changes. The noise in pixels with low dark current and low glow is the same as the read noise from the multiplexer, so the dark offset variations do not add to the

pixel noise. In general, the first frame of any sequence of images tends to have a different offset from the others, because it tends to have an interval, frame time, or Fowler number different from its preceding image. The largest dark offsets occur when a frame is taken with a very short interval from the preceding image, which occurs when multiple frames are commanded at once (using “repeats”).

In the warm mission, the “first-frame effect” is less pronounced in total offset in both arrays. At 3.6 μm , the average offset is 40 DN compared to 80 DN in the cryogenic mission for delay intervals of 7 to 40 seconds. For both arrays, a gradient in the “first-frame effect” has been noted. These residuals will mainly affect measurements of diffuse low surface brightness sources.

Due to the decision not to use the shutter on IRAC for dark and flat measurements, we had a somewhat sophisticated dark subtraction procedure. There were two steps for the dark subtraction, one using a dark from the ground-based laboratory measurements (called “labdarks”), and another using a delta dark which was the difference between the labdark and the skydark measured in a low zodiacal light region.

In the first step of dark subtraction, we subtracted a calibrated labdark from the data. This labdark subtraction occurred before the linearization of the array, so that we could linearize the data as well as possible. The labdark subtraction was handled by a combination of modules including LABDARKSUB and FFCORR, depending on which kind of labdark data were needed. In some observing modes (subarray mode, shortest frames within the HDR mode, and the first frame of an observation or AOR), not enough data were available to construct delay time dependent darks. In such cases, a single mean dark has been computed using 30 seconds as a delay time, and it was used as a labdark. The LABDARKSUB module subtracted this mean labdark. The correction of the first-frame effect for all other frames was handled by the FFCORR module, which interpolated the library of labdarks taken at different exposure times with different delay times, and created a labdark corresponding to the particular delay time of the frame being calibrated. These delay time dependent darks were then subtracted from the IRACEBWC-processed frame. Therefore, FFCORR required a number of different labdarks taken with different delay times to calibrate properly. These were taken pre-launch and were loaded into the calibration database. Note that as there were no prelaunch labdarks for warm mission operating temperatures, labdarks were not used in the warm mission pipeline. IRAC pipeline determined the delay time (header keyword INTRFRDLY), and the labdark file (header keyword LBDRKFLE) that was subtracted, and placed these within the header keywords of the BCD.

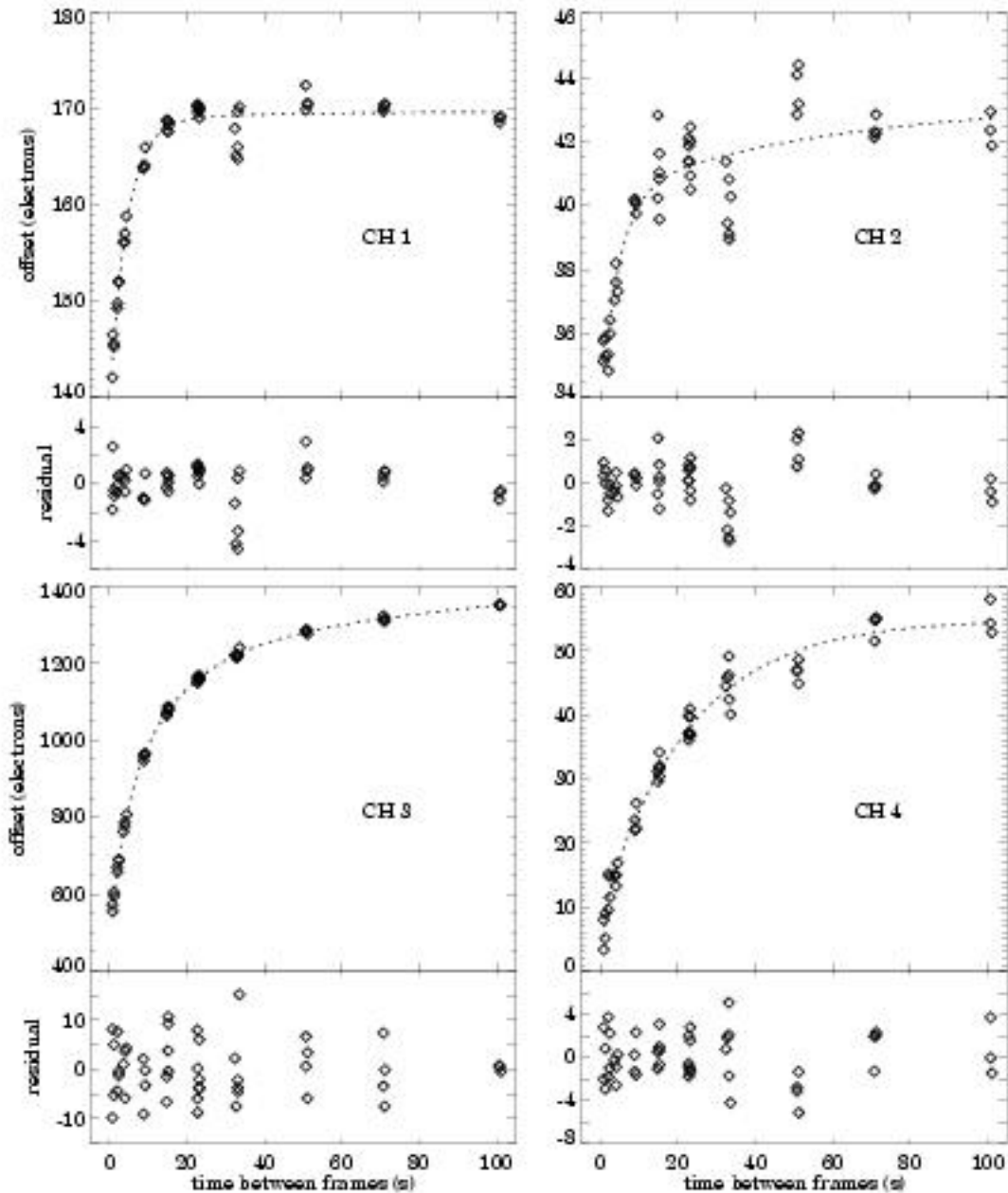


Figure 5.7: First frame effect: dark counts as a function of interval between frames. Each symbol is the mean dark signal in one output of each array, averaged over a box near the center of the array. The dashed curves are multiple exponential fits to the means in the set of 48 images, with the first image excluded. The lower portion of each panel shows the residuals, in electrons, between the data and the fitted curves. This figure is for a 30 second frame time.

The second step of the dark subtraction used a delta-dark found in the SKYDARKSUB module described below. This skydark, described in Section 4.1, was subtracted from the IRAC image

after the linearization, and should have removed any additional dark features that were not present in the labdarks, but existed in the flight data. Note that the delta-dark included the sky background around the low-zody region.

5.1.11 MUXBLEEDCORR (electronic ghosting correction)

The InSb arrays suffered from an effect known as “muxbleed” (for more information on this effect see Section 7.2.2). This was thought to be a result of operating the arrays at unusually cold temperatures. When a bright source was read out, the cold electronics did not return to their quiescent state for a considerable length of time. The result was ghosting along the pixel readout channels, sometimes referred to as “ant trails” (Figure 5.8). The effect was easily noticeable against a low background (such as a dark current measurement), and could extend the full length of the array. The muxbleed flux was not real, i.e., it was not “borrowed” from the actual source.

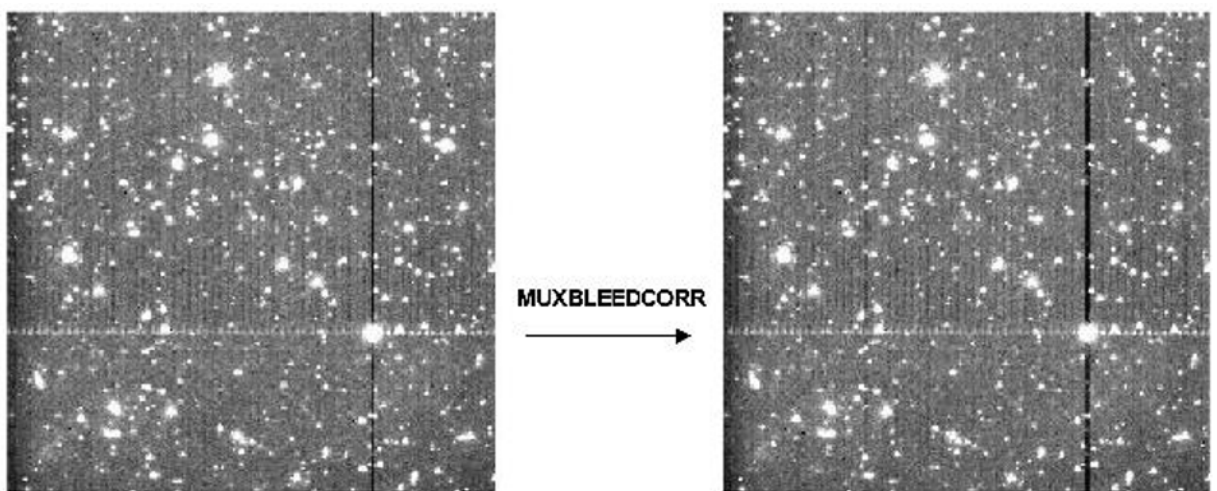


Figure 5.8: Before (left) and after (right) correction of pseudo-muxbled for channel 1. Shown is a bright source within a calibration AOR and a background of sources under the muxbled limit.

This effect was complicated. It appeared that a pixel bleeds only as a result of the light falling onto it, and not as the sum of the value of the pixel plus the bleeding from previous pixels. Since we knew the readout order of the pixels, we could start by correcting all the pixels downstream from the first pixel, and then move on to the next pixel. The exact shape of the muxbled pattern, obtained after examining hundreds of muxbled incidences, is summarized as a modified polynomial:

$$\begin{aligned} \text{Log}(\text{MuxbledIntensity [DN]}) = & 3.1880 - 2.4973x \\ & + 1.2010x^2 - 0.2444x^3 \end{aligned} \quad (5.9)$$

where

$$x = \log_{10}(\text{pixel number} + I). \quad (5.10)$$

Pixel numbers were counted along the detector readout direction, starting from the muxbleed causing pixel (pixel number zero). The muxbleed pattern appeared to be independent of readout channel, Fowler sampling, etc. Furthermore, the pattern seemed to be applicable to both the channel 1 and channel 2 muxbleed, with a slightly different scaling factor. The severity of muxbleed depended on the brightness of the bleeding pixel. Muxbleed scaling laws as a function of the bleeding pixel were obtained for channels 1 and 2. They are

$$\text{ScalingFactor} = A \cdot \exp\left(-\frac{1}{2}\left(\frac{x-B}{C}\right)^2\right) \quad (5.11)$$

where

$$x = \log_{10}(\text{bleeding pixel intensity in } DN). \quad (5.12)$$

For channel 1, $A = 0.6342$, $B = 5.1440$, and $C = 0.5164$. For channel 2, $A = 0.3070$, $B = 4.9320$, and $C = 0.4621$. Both the scale factors and the muxbleed pattern were fixed for all the pixels in a given array. Muxbleed from triggering pixels with brightnesses below 10,000 DN was not corrected, because the corrections in these cases would be just a few times the read noise. Muxbleed was also not corrected in the subarray observations.

Observers should note that calibration darks were not muxbleed corrected. Muxbleed occurred in these images due to the presence of hot pixels. However, this occurred equally both in the darks and in the science frames and was found to subtract noiselessly from the science data. Thus, any dark frame muxbleed was simply considered a feature of the darks.

Note that the muxbleed correction described here did not always correct 100% of the muxbleed effect. Muxbleed was not present in the warm mission data due to the higher operating temperature and voltages.

5.1.12 DARKDRIFT (“readout channel” bias offset correction)

Each IRAC array was read out through four separate channels. The pixels read out by these channels were arranged vertically, and repeated every four columns. Small drifts in the bias levels of these readouts, particularly relative to the calibration dark data, could produce a vertical striping called the “jailbar” effect. This was mostly noticeable in very low background conditions. This was corrected by adding to the individual readout channels a common mean offset. For any image, the flux in a pixel was assumed to be

$$A_{i,j} = S_{i,j} + B + D_{C_{i,j}} + D_{O_{i,j}} \quad (5.13)$$

where i is the readout channel number (1–4), j is the row number, A is the detected intensity in DN, S is the incident source flux (celestial background + objects), B is a constant offset in the frame, DC is the standard calibration dark, and DO is the dark offset. The first dark varied on a pixel by pixel basis, whereas the offsets were assumed to vary on a readout channel basis. The correction step determined a common background level, equal to the mean of the backgrounds in the four readout channels. These were determined by a robust mean estimator function M

$$M_i = \text{MeanEstimator}(S_{i,0} \dots S_{i,n}) \quad (5.14)$$

The corrected image (post dark-subtraction) was then

$$A'_{i,j} = A_{i,j} - \left(M_i - \frac{1}{4} \sum_{i=1}^4 M_i \right). \quad (5.15)$$

5.1.13 FOWLINEARIZE (detector linearization)

Like most detectors, the IRAC arrays were non-linear near full-well capacity. The number of readout DN was not proportional to the total number of incident photons; its rate of increase with fluence decreased as the fluence increased. In IRAC, if fluxes were at levels above half full-well (typically 20000–30000 DN in the raw data), they could be non-linear by several percent. During processing the raw data were linearized on a pixel-by-pixel basis using a model derived from ground-based test data and re-verified in flight. The software module that did this was called FOWLINEARIZE. FOWLINEARIZE worked by applying a correction to each pixel based on the number of DN, the frame time, and the linearity solution. For channels 1, 2, and 4, we used a quadratic solution, i.e., we modeled the detector response as

$$DN_{Obs} = kmt - Ak^2t^2 \quad (5.16)$$

where k is the source rate (linear DN/second), and m and A are linearity fit coefficients. The linearization solution to the above quadratic model is:

$$DN = \frac{-1 + \sqrt{1 - 4L\alpha DN_{obs}}}{2L\alpha} \quad (5.17)$$

where

$$L = \frac{\alpha}{n(w+n)^2} \left[\left(\sum_{i=n+w+1}^{2n+w} i^2 - \sum_{i=1}^n i^2 \right) - 2\left(1 - \frac{t_d}{t_c}\right)n(n+w) \right], \quad (5.18)$$

and $\alpha = \frac{A}{m^2}$, n is the Fowler number, w is the wait period, t_d is the delay from reset to first readout, and t_c is the clock readout time. The above expression for L is the correction required to account for multi-sampling. This was required because the multi-sampling resulted in the apparent time spent integrating not actually being equal to the real time spent collecting photons. Note that t_d is the time between the reset and the first readout of the pixel. For channel 3, we used a cubic linearization model:

$$DN_{obs} = Ckt^3 + Akt^2 + kmt \quad (5.19)$$

For the cubic model, the solution was derived via a numerical inversion.

5.1.14 *BGMODEL (zodiacal background estimation)*

For this module, a spacecraft-centric model of the celestial background was developed. For each image, the zodiacal background was estimated (a constant for the entire frame) based on the pointing and time that the data were taken. This value was written to the header keyword ZODY_EST in units of MJy/sr. The zodiacal background was also estimated for the subtracted skydark (see next module) and placed in the header keyword SKYDRKZB.

5.1.15 *Dark Subtraction II: SKYDARKSUB (sky “delta-dark” subtraction)*

This module, the second part of dark subtraction, strongly resembled traditional ground-based data reduction techniques for infrared data. Since IRAC did not use the shutter for its dark measurement, a pre-selected region of low zodiacal background in the north ecliptic cap was observed in order to create a skydark (see Section 4.1). At least twice during each campaign a library of skydarks of all Fowler numbers and frame times were observed, reduced, and created by the calibration pipeline. The skydarks had the appropriate labdark subtracted in their DARKCAL pipeline and were therefore a “delta-dark.” These skydarks were then subtracted from the data in the pipeline within this module, based on the exposure time, channel, and the time of the observation. Note that there was a problem with the skydark subtraction from the 58th frame in the subarray observations which left the background level in that frame different from the rest.

While this should not affect photometric measurements, users may want to choose to leave the 58th subarray frames out from their analysis.

5.1.16 FLATAP (flat-fielding)

Like all imaging detectors, each of the IRAC pixels had an individual response function (i.e., DN/incident photon conversion). To account for this pixel-to-pixel responsivity variation, each IRAC image was divided by a map of these variations, called a flat-field. See also Section 4.2 and 7.1.2.

Observations were taken of pre-selected regions of high-zodiacal background with relatively low stellar content located in the ecliptic plane. They were dithered frames of 100 seconds in each channel. These observations were processed in the same manner as science data and then averaged with outlier rejection. This outlier rejection included a sophisticated spatial filtering stage to reject the ever-present stars and galaxies that filled all IRAC frames of this depth. The result was a smoothed image of the already very uniform zodiacal background. This skyflat is similar to flat-fields taken during ground-based observations. The flat-fields were then normalized to one, using a median, and excluding a 3-pixel wide border at the edges of the image. A central area was used for calculating the normalizing median in the cryogenic mission, whereas the whole array was used in the warm mission (excluding the border mentioned above). The flat-field calibration pipeline produced a library of the flat-fields throughout each campaign as a flat-field was taken at the beginning and end of an observing campaign. We found that there was no difference in flat-fields from campaign to campaign, so a “superskyflat,” composed of five full years of data and therefore of very high SNR, was used for processing science data in the BCD pipeline. A separate superskyflat was created for cryogenic and warm data. It should be noted that this flat-field was generated from a very red target, i.e., the zodiacal background. There was considerable evidence for a spatially-dependent color term in the IRAC calibration (which was roughly a quadratic polynomial function across the array). Objects that have color temperatures radically different from the zodiacal background require an additional multiplicative correction of order 5% – 10%. This was not treated by the flat-fielding stage. See Section 4.5 for more details.

Software module FLATAP applied the flats generated by the calibration server. This operation was equivalent to division by the flat.

5.1.17 IMFLIPROT

IRAC utilized beamsplitters to redirect the incoming light for a given FOV through each of the two filters. As a result, although for a given FOV two filters such as for channel 1 and 3 viewed the same piece of sky, the detectors saw (and hence read out) mirror images of each other. An image transposition was applied to ensure that the two filters for each FOV were in the same orientation (Figure 5.9). Note that the *images were not de-rotated*, that is, each is now correct relative to the other filter for a given FOV, but all of the images still have the effects of spacecraft rotation, and are not in a north up, east left orientation.

$$A_{x,y}^{flipped} = A_{x,255-y}^{original} \quad (5.20)$$

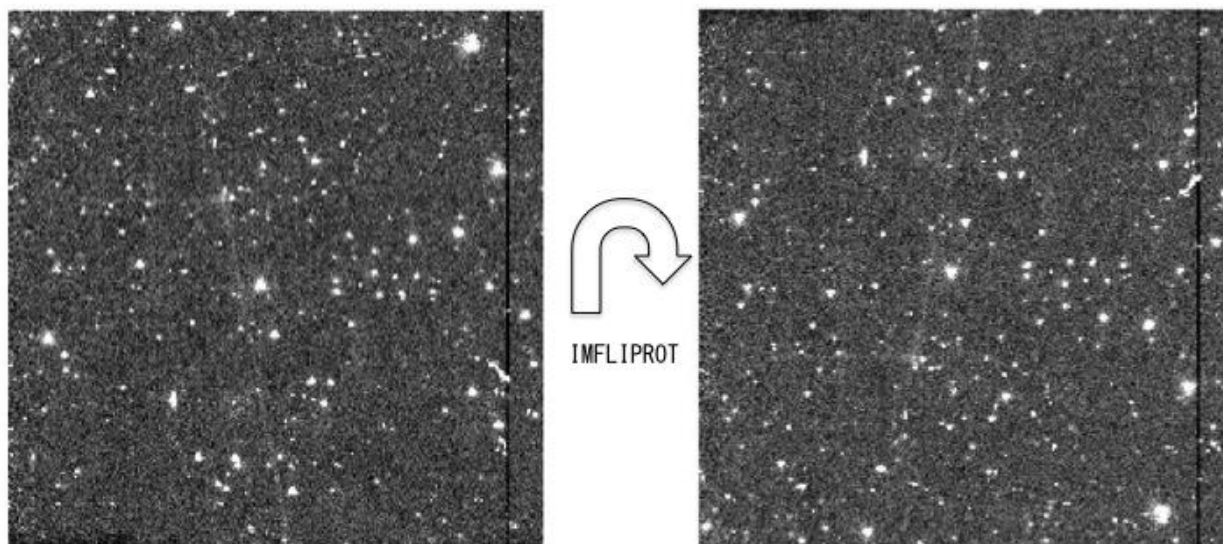


Figure 5.9: Transposition of an IRAC channel 1 dark image by the IMFLIPROT module.

Channels 1 and 2 were flipped about their vertical axis, which is illustrated by equation (5.20). The image flip of these two channels provided an array orientation with the E axis located to the left of N for all the channels. Since this image transposition was applied after skydark subtraction and flat-fielding, those calibration files were in the original (pre-flip/pre-transpose) orientation.

5.1.18 DETECT-RADHIT (cosmic ray detection)

Within this module, individual frames were analyzed for probable radiation hits (cosmic rays), and the results appeared as a flag in the imask file (see Section 7.1.1 for a definition of imask or BCD-specific bad pixel files). The flagging was computed by a median filtering technique. Input images were read in, and a median filter was applied. The difference between the input image and the median-filtered image was then computed. Pixels above a specified threshold (i.e., with more compact spatial distributions than possible for a true point source) were then flagged in a mask image (bit 9 of imask was set when a pixel was suspected to have been hit by a cosmic ray). See Section 7.1.1 for more information about the imask bits.

5.1.19 DNTOFLUX (flux calibration)

IRAC flux calibration is tied to a system of celestial standards measured at regular intervals during each campaign. The IRAC IST provided the calibration server with calibration files based upon these measurements. Because the flux calibration was determined with stellar point sources, the calibration for extended sources is somewhat different. For details of the photometric calibration and correction factors, see Chapter 4. The IRAC data were calibrated in units of MJy/sr in this module. This was accomplished by multiplying the data image by a conversion factor provided by the calibration server. This conversion factor was written to the data header as:

/ PHOTOMETRY

BUNIT = 'MJy/sr'
FLUXCONV = 0.2008

/ Units of image data
/ Flux Conv. factor (MJy/sr per DN/sec)

GAIN = 3.8 / e/DN conversion.

5.1.20 Pointing Transfer (calculation of pointing information)

The Pointing Transfer pipeline was a separate script from the actual data reduction pipeline script, designed to insert raw-pointing and distortion information into the FITS headers of BCDs. Like the reduction pipeline, it executed on a per-BCD basis. See Section 4.12 for more pointing related information. Pointing data was acquired by the spacecraft star tracker at a rate of 2 Hz, transferred to the boresight onboard, and down-linked every 12 hours as a Boresight Pointing History File (BPHF). The BPHF was received via a separate telemetry stream from the science data. The first step in pointing transfer was to acquire the portion of the BPHF which spanned the integration time of the BCD (GETPH module). The 2 Hz sampled data were then transferred to the specific channel-dependent science FOV using a set of Euler transformations handled by the BORESIGHTTRAN module. The Euler angles relating the boresight and the FOV positions were determined in-flight and were stored in a configuration file.

The pointing samples were then averaged and combined by the ANGLEAVG module to compute the raw pointing for the BCD: CRVAL1 (RA), CRVAL2 (Dec), and PA (position angle). These, along with uncertainties and reference pixel coordinates (CRPIX1, CRPIX2), were inserted as keywords into the FITS header of the BCD. The module also computed a CD matrix and transferred distortion coefficients (represented in the pixel coordinate frame) from a calibration file to the FITS header. The default projection type for the celestial reference system (CTYPE keyword) was “TAN–SIP.” This was a tangent (TAN) projection modified to make use of the Spitzer Imaging (distortion) Polynomials (SIP) in coordinate mappings (see Section 2.2.4 for more information on Spitzer image distortion).

The Final Product Generator (FPG) was executed at the end of the BCD pipeline. This reformatted the FITS header and added additional keywords, which were most useful to the user, from the database. Examples of BCD headers (also containing pointing and distortion information) are given in Appendix E.

5.1.21 PREDICTSAT (HDR saturation processing)

PREDICTSAT was used to process data taken in the High Dynamic Range (HDR) mode by identifying saturated pixels using the information obtained from the shorter exposure time frames. Specifically, if the shorter frame was frame 1 and the longer frame was frame 2, and they have Fowler numbers F , wait periods W , pixel values DN , and saturation values of DN_{sat} , then if

$$\frac{DN_1(2F_2 + W_2)}{F_1 + W_1} > DN_{sat} \quad (5.21)$$

for any pixel, then that pixel was masked as saturated in the longer frame 2. Optionally, surrounding pixels might also be masked. This information was used in the post-BCD pipeline by the mosaicker when coadding frames to reject saturated pixels before applying any other outlier rejection. High dynamic range data were received as separate DCEs by IRAC. No co-addition was

done of these frames at the BCD level, but they were received by the user as separate BCDs. See Section 7.2.1 for more information on saturation in IRAC data.

5.1.22 *LATIMFLAG (residual image flagging)*

The IRAC pipeline detected and flagged residual images left from imaging bright objects. A model of the charge decay was used to build a time history of the DCEs and set a mask bit (bit 10 in imask; see Section 7.1.1) to indicate that a given pixel in the DCE was contaminated by a residual. The algorithm worked in the following way: Starting with the first image in each observation or AOR, LATIMFLAG computed what is called a “latent-trap” image at the end of its exposure. This specified the amount of trapped charge in every pixel. The charge-trap decayed and appeared as a residual in subsequent images. The latent-trap image was effectively an image of the number of filled traps, which we label $N_F(t)_i$. The subscript i refers to the “trap-species” or type of latent trap distinguished by a characteristic decay time and trap filling efficiency. The latent-trap image was propagated forward in time, and updated with each consecutive image in the sequence. The images with pixels sustaining and exceeding a threshold above the background noise from image to image within the decay time were flagged in the imask (bit 10). Section 7.2.8 has more information on residual or persistent images.

5.2 The Artifact-Corrected BCD Pipeline

There are several artifacts commonly seen in IRAC images. For a complete description, see Chapter 7. To mitigate the commonly found artifacts of stray light, saturation, muxstripe (Section 7.2.2), column pull-down (Section 7.2.4), and banding (Section 7.3.2), an artifact correction pipeline was created. It performed the artifact correction on the BCD files. The pipeline then created a product called a corrected BCD, or CBCD. The CBCDs were used to create the pipeline mosaic. An archive user also has access to the BCD and CBCD files in case the artifact correction was not completely successful or it needs to be run again more conservatively.

At each step, an attempt was made to identify the artifacts in the BCDs, adjust the imask pixel values according to the identified artifact, and correct the artifact, with CBCD files being the corrected files. The history of these artifact changes was recorded within the imask file headers. The user can find all of the artifact correction modules on the contributed software section of IRSA’s Spitzer website, and replicate or improve the corrections using the BCD and imask files as input.

5.2.1 *Stray Light*

The IRAC stray light masker was designed to mask out stray or scattered light from stars outside the array location as well as filter ghosts from bright stars. The module would alter each imask, corresponding to each BCD file, with pixels likely to be affected by stray light, by turning bit 3 on for those pixels that are likely to be affected by scattered light. The program turned imask bit 2 on for those pixels likely to be affected by filter ghosts.

The module first queried the 2MASS database, producing a table of sources that were likely to produce scattered light within the field of view. Using the BCDs and the 2MASS table, including the flux of the bright sources, possible stray light affected areas were calculated. These pixel positions were then turned on within the imask. When the CBCDs were combined to a mosaic, the corresponding pixels in the CBCDs were not used to produce the mosaic, thereby masking out the input pixels possibly affected by scattered light.

IRAC data users are reminded that observations that were not adequately dithered (such as the ones made with the small-scale dither patterns) will have gaps if the stray light mask was used. In these cases, the stray light masking program can be downloaded from IRSA's Spitzer website

<https://irsa.ipac.caltech.edu/data/SPITZER/docs/dataanalysisistools/tools/contributed/irac/straylight/>

and run on the BCDs in an unaggressive mode by setting a keyword. This disables the production of the larger masks for very bright stars (which produce diffuse scattered light over a large fraction of the array), avoiding gaps in mosaics. More information about stray light can be found in Section 7.3.1.

5.2.2 Saturation

Many of the following artifact corrections need knowledge of the offending source's flux to work correctly. For observations of very bright sources, the signal (and even pedestal) reads can be saturated. Therefore, the next step in the artifact mitigation process was the saturation correction.

For a bright, strongly saturated point source, the DN will increase from some low number away from the source to the maximum value over 35,000 (InSb arrays) and 47,000 (Si:As) DN, and then decrease to a small, usually negative number, at the center. The image looks like a bright doughnut with a dark center. This inverted "crater" peak profile indicates that a significant fraction of the light from the bright star may have been lost due to saturation. Recovery, or flux rectification, was possible if the point spread function, or PSF, of the star was known. The PSF could then be scaled in flux until the non-saturated pixels in the "wings" of the stellar profile could be fit correctly.

There are several steps to rectify the inner region of the saturated star. First, the exact position of the saturated star was identified using the "craters". The program then created a sub-image around the saturated star, and that was resampled on a finer grid to match the 0.24 arcsecond resampled PSF. Remaining artifacts, such as banding and muxbleed, were masked out. The PSF was then matched pixel-by-pixel, the PSF flux wings were scaled to the target wings, mean flux ratios were computed, and the best fit outside the inner saturated region was determined. The "lost flux" was then calculated and the star was rectified by replacing the inner, saturated pixels with flux determined from the PSF profile.

The central portion of the IRAC PRF in channel 1 was found to be too narrow for stars due to undersampling, and so a "puffed up" version was empirically derived and found statistically to be more accurate by testing it on stars with known flux. Also, the program was not always successful in fitting a PSF to saturated stars that are closer than 20 pixels to the edge of the image. Such saturated stars were not corrected.

A star that was saturated, or predicted to be saturated, had bit 13 flipped on in the corresponding imask (see Section 7.1.1 for more information about the imask). After this module had corrected the saturation, it turned off bit 13 and turned on bit 4, meaning that the pixel was saturated, but had now been rectified. More information about saturation can be found in Section 7.2.1.

5.2.3 Sky Background Estimation

The remaining artifacts are caused by the flux in a pixel reaching a set threshold (documented in Chapter 7). Once the saturated stars had been corrected, all of the point sources that have fluxes over the respective artifact flux thresholds were detected and flagged. Each pixel that was potentially affected by the artifacts triggered by these high fluxes was flagged in the corresponding imask file (column pull-down has bit 7 set and banding has bit 6 set; see Section 7.1.1 for more information about the imask).

An estimated truth image of the sky background was created. To replace the masked pixels, a 5 pixel \times 5 pixel box around the corrupted pixel was used to create a weighted average for the pixel value to be replaced using a Gaussian-weighted interpolation from the pixels within the box. If there were not enough pixels in the 5 pixel \times 5 pixel area around the affected pixel due to masking, then an 11 pixel \times 11 pixel area was used in the calculation. Replacement of values of affected pixels was done in the CBCDs.

5.2.4 Column Pull-down

In all four arrays, a bright pixel triggered a bias shift within its respective column, creating a lower background value throughout the entire column than in the surrounding columns. The imask has bit 7 set (see Section 7.1.1 for more information about the imask), denoting the column pull-down artifact, as mentioned above.

In this module, the truth image of the sky background was used, and for each column, a robust weighted DC offset was determined. This was a simple offset between the affected column and the estimated background value. This offset was determined separately above and below the triggering source. The offset was then applied to the affected column and saved into the CBCD image, thereby removing the bias shift from all the pixels in the column. More information about column pull-down can be found in Section 7.2.4.

5.2.5 Banding Correction (Channels 3 and 4)

The banding effect manifests itself as the rows and columns that contain a bright source having an enhanced level of flux. This happened only in the Si:As arrays (channels 3 and 4) and has been shown to be due to internal optical scattering (inside the array). Both bright stellar sources and bright extended sources cause banding. It is clearly different from the optical diffraction patterns and the column pull-down effect.

Again, the truth image of the background was used to compute a robust weighted DC offset. The banding artifact was extra flux above the background and it was subtracted out and the image saved into the CBCD file. The IRAC pipeline did not model the flaring of banding towards the edges of

the array. Therefore, the pipeline correction was not always perfect. Pixels affected by the banding effect have bit 6 set in the imask. More information about banding can be found in Section 7.3.2.

5.2.6 Muxstripe Correction (Channels 1 and 2)

For a very bright source, muxbleed could be accompanied by another image artifact, a pinstripe pattern (“muxstripe;” every fourth column from the bright source was affected) that may extend over part of the image preceding or following the bright pixel (for example, see Figure 7.3 and Figure 7.4). Stars, hot pixels, and particle hits could generate muxbleed and muxstripe. In the artifact correction pipeline, a procedure was developed to mitigate the muxstripe in the image but there was no muxstripe bit in the imask.

The algorithm involved converting the BCD image into $256 \text{ pixel} \times 64 \text{ pixel}$ arrays (each of the four readout channels into a separate image; every fourth column was read out by the same channel). The muxstripe for one source contaminates only one readout channel, and therefore only one of these separate arrays. The median of the four arrays was created and subtracted from each array, which allowed deviation from the normal background to stand out.

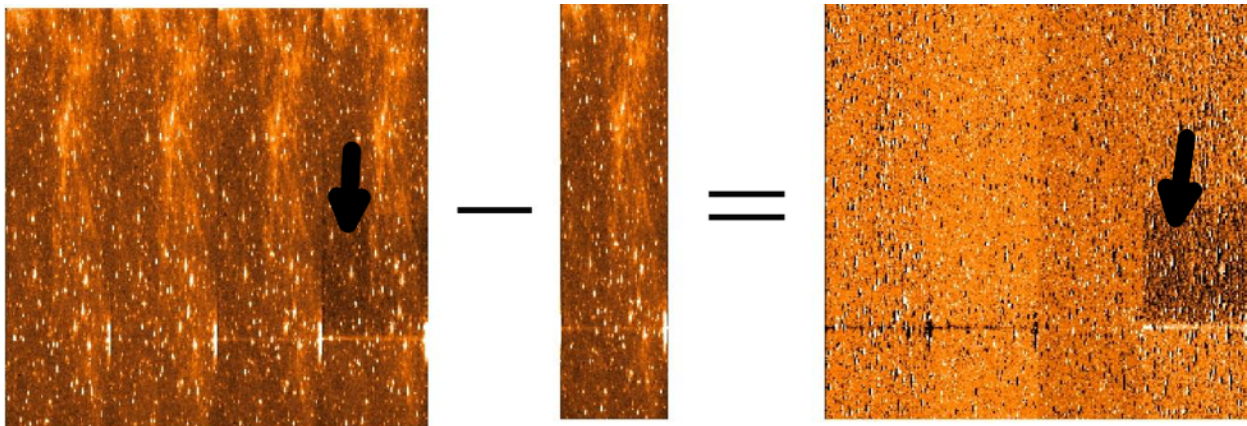


Figure 5.10: Subtraction of the median background from the readout channel images. The image on the left shows the original image divided into each of its four readout channels. The image in the middle is the median of the four readout channels. This makes the muxstripe much more apparent in the fourth readout channel image (on the right). The location of the muxstripe is shown with black arrows.

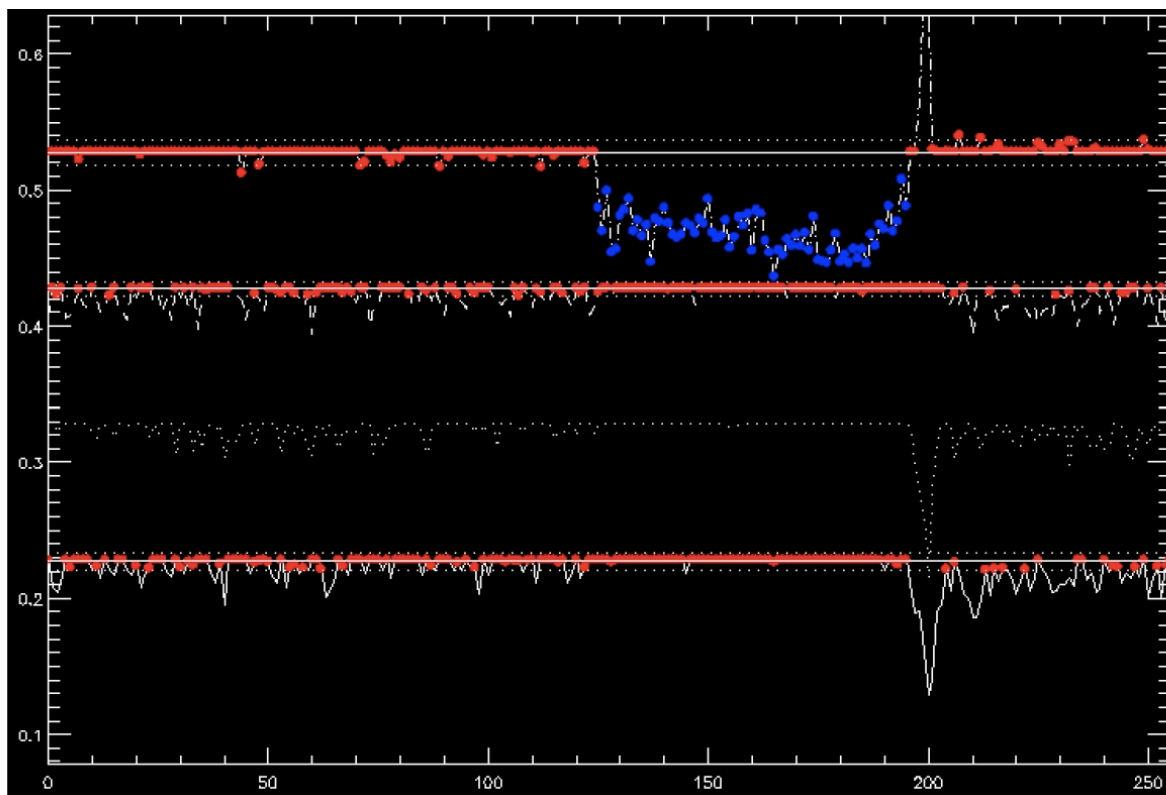


Figure 5.11: Profiles showing the column median versus row values for identifying muxstripe. The x -axis is in pixel units. The muxstripe is now identifiable between row pixels 125 and 200 (significantly lower values than the median background).

From each of these median-subtracted arrays, a one-dimensional array of the values along each row was then created, simply by combining the pixel values along the x -dimension. A profile that represented the median versus row was created. For each profile, statistics were calculated to identify any muxstripe. It was identified as a deviation larger than 3% of the median value for several rows. This missed the weakest muxstripe or a case where all readout channels have muxstripe in the same position (cluster of very bright stars), but this was rare. The subset of pixels that were affected by the muxstripe was identified and this column was corrected using the difference of the median of the “clean” pixels and the median of the affected pixels. The readout channel arrays were then reassembled to recreate the original image, and the corrected image was written to the CBCD file. More information about muxbleeding and muxstriping (“pinstriping”) can be found in Section 7.2.2.

5.3 Level 2 (Post-BCD) Pipeline

Pipeline processing of IRAC data also included more advanced processing of many individual IRAC frames together to form more advanced data products. Known by the generic title of “post-BCD” processing, this extended pipeline refined the telescope pointing, attempted to adjust background offsets of CBCDs and produced mosaicked images. We did not attempt to improve (relative to the BCD) the point source or extended emission flux calibration by automatically

comparing to a reference source catalog. The mosaic so created only included data from within a single AOR.

5.3.1 Pointing Refinement

All IRAC BCD images contain a pointing estimate based on the output of the Spitzer pointing control system (star tracker and gyros), i.e., the boresight pointing history file. This initial pointing estimate is accurate to about 0.5 arcseconds. To improve the ≈ 0.5 arcseconds blind pointing, a pointing refinement was run in which the point sources were identified in the IRAC frames and astrometrically correlated with stars near the source position in the 2MASS catalog. The pointing refinement typically improved the positional error to < 0.3 arcseconds and removed any systematic offsets.

First, point sources were extracted from the pipeline-processed mosaics and transformed to R.A. and Dec. using the transformations derived from the current pointing information. If there were fewer than five sources in an image, then there would be no refinement for that BCD. Second, a comparison was made of the coordinates of each point-source for which a match was found in the 2MASS point source catalog. Then a translational and rotational reference frame could be computed from the positional differences between the raw coordinates and the 2MASS point source catalog positions, and a refinement was made to the celestial coordinates and angles of each BCD in the observation or AOR used for the mosaic. These refined values were written to the FITS headers as RARFND, DECRFND, including many others with “RFND” as an indicator of refined pointing. More pointing related information can be found in Section 4.12.

5.3.2 Superboresight Pointing Refinement

Pointing refinement operated on each IRAC channel independently. This often resulted in poor pointing solutions for channels 3 and 4, in which stellar fluxes were lower and the background higher than in channels 1 and 2. We have therefore developed a technique which combined the results of pointing refinement in channels 1 and 2 and applied it to all four channels using the known offsets between the IRAC fields of view. This improved pointing solution was derived during campaign reprocessing. The results of the pointing refinement from the first run of the post-BCD pipelines were averaged, and the correction derived from this was applied to the boresight pointing history file (which contained the pointing estimate derived from the spacecraft telemetry and which provided our initial pointing estimate). This corrected pointing history file (the “superboresight” file) was then applied to the BCD at the pointing transfer stage of the BCD pipeline. The superboresight R.A. and Dec. estimates were recorded in the CRVAL1 and CRVAL2 FITS keywords, and the position angle estimate was recorded in the CD matrix keywords. The uncorrected R.A. and Dec. were retained, but called ORIG_RA, ORIG_DEC, as was the pointing refinement solution for each frame (as RARFND and DECRFND). Note that to use the superboresight solution, USE REFINED POINTING = 0 should be set in the MOPEX namelists.

Superboresight was implemented as a patch to the S13 software build (see Appendix A for more information on software builds), thus most (but not all) data processed with S13 or subsequent pipeline versions will have it. Users should check for the presence of the ORIG_RA, ORIG_DEC keywords to see if it has been applied to their data. From S14 onwards, the HDR data have the long frame R.A., Dec. solution copied to the short frames, as the short frame pointing solutions

are less accurate. If the BPHFNAME value in the (C)BCD FITS header does not start with “S,” then the superboresight did not run. Neither superboresight nor pointing refinement were run on the subarray data.

In a post-mission effort to improve Spitzer pointing refinement, proper motions of 2MASS stars were updated using the more recent and more accurate measurements made by the Gaia spacecraft. In the course of this effort an apparent bug was discovered in the superboresight code that reduced the magnitude of the correction applied to the original pointing solution to bring the (C)BCD FITS keyword CRVAL1 into agreement with the 2MASS pointing refinement. Comparing the differences between CRVAL1 and ORIG_RA, and RARFND and ORIG_RA (C)BCD header FITS keywords revealed that the CRVAL1 keyword values were underestimated by a factor of \cos^2 (declination) over much of the sky. This behavior was seen in both the cryogenic and warm mission data.

To correct for this error in the CRVAL1 keyword values, we performed a scaling by $1/\cos^2(\text{dec})$ to the superboresight-derived corrections for (C)BCDs with $|\text{Declination}| < 75^\circ$, and wrote the new, corrected (C)BCD CRVAL1 values to the FITS headers. For $|\text{Declination}| > 75^\circ$ CRVAL1 was instead replaced by the original pointing correction RARFND value in the (C)BCD FITS headers. After correcting for the superboresight CRVAL1 issue, pointing refinement improves the Spitzer IRAC (C)BCD positional information (CRVAL1 and CRVAL2) to better than ± 0.16 arcsec (one sigma).

5.3.3 *Mosaicking and Coaddition*

The post-BCD pipeline modules have been made available for general public use as part of the MOPEX tool. They consist of a number of C and C++ modules connected via Perl wrapper scripts. Namelists (plain text lists of parameters and values) are used for input. In most cases, the module operation simply consists of supplying the software with a list of input image files; by default it reads and understands the IRAC image headers.

Using the refined coordinates, individual IRAC (C)BCDs from a given observation (AOR) in a given channel are reconstructed onto a larger field (mosaicking), and overlapping frames are averaged together to achieve a higher SNR. The pipeline SSC mosaicker produces a single image, one per channel (and one per exposure time in case of the HDR observing mode) from many input (C)BCD images (the first long[er] frame[s] in non-HDR observations is [are] not included as it [they] is [are] taken in a different mode, the HDR-mode). First, the BCDs are corrected for overlap consistency. The images that overlap are forced to have the same background value via addition of an offset derived from a least-squares fit. Then a “fiducial frame” is derived. This is the definition for the output frame in terms of its physical size, projection, and orientation. Because IRAC has such a large field of view, projection effects are non-negligible, and the mosaicking and coadding process must reproject the data onto a common grid with a technique similar to “drizzle” (Fruchter & Hook 2002). The fiducial frame finder seeks to minimize the amount of “blank” area in the output mosaic by rotating the output projection such that it is aligned with the map axes. This is useful for long thin maps, where potentially the output mosaic could be very large, but with a great deal of empty space. The mosaicker then reprojects all of the input data onto the output projection. It reads the SSC WCS, which contains the field pointing center, rotation, scale, and

instrument distortion, and reprojects this onto a standard TAN FITS projection. In the process, the data are undistorted. The reprojected images are interpolated onto the fiducial image frame with outlier rejection, rejecting radiation hits in overlapping observations. Various masks (mostly the imask and pmask files, see Section 7.1, Table 7.1 and Table 7.2 for which mask bits are set in these masks) are used in the coaddition in such a way that the pixels previously flagged as bad (for example, hot or dead pixels) are rejected before the averaging process. The outlier rejection scheme is specifically designed to work well in the case of intermediate coverage and may not be adequate for all observations and science programs (it used the `radhit`, `dual outlier`, `multiframe`, and `box outlier` modules, see the MOPEX documentation for more details on these outlier methods) . The pixel size in the mosaics produced by the pipeline was exactly 0.6 arcseconds x 0.6 arcseconds in the final data processing. In addition to a sky map (in units of surface brightness), a noise image and coverage map were also produced.

6 Data Products

This section describes the basic data products the observer will receive from the Spitzer Heritage Archive. The available data products consist of Level 0 (raw) data, Level 1 (BCD) data, calibration files, log files, and Level 2 (post-BCD) data. IRAC data are supplied as standard FITS files.

6.1 File Characteristics

Each file consists of a single data collection event (i.e., a single exposure), and contains one image corresponding to one of the four IRAC arrays (the exception being post-BCD products, described below). The FITS headers are populated with keywords including (but not limited to) physical sky coordinates and dimensions, a photometric solution, details of the instrument and spacecraft, including telemetry when the data were taken, and the steps taken during pipeline processing.

Note that because of the “first-frame effect,” the first frame of every Astronomical Observation Request (AOR) has a different delay time and it cannot be calibrated perfectly. Therefore, the first frame of every AOR with a frame time greater than 2 seconds is taken in HDR mode which causes the first frame to be 0.6 seconds or 1.2 seconds in duration instead of the full frame time. This first frame usually has a name such as *SPITZER_I1_11111111_0000_0000_2_bcd.fits* (see Section 6.3 for explanation of the various parts of the file name) and has no associated cosmic ray mask (brmsk file). The observer is encouraged not to use this first short frame. The pipeline mosaicker does not use it either when building the mosaic.

6.2 File-Naming Conventions

Table 6.1 lists the IRAC data files produced by the IRAC data reduction pipelines, together with brief descriptions of these files. The Basic Calibrated Data (BCD) are the calibrated, individual images. These are in array orientation and have a size of 256 pixels \times 256 pixels for the full array images, and 64 planes times 32 pixels \times 32 pixels for the subarray images. These data are fully calibrated and have detailed file headers. The Post-BCD pipeline combines the BCD images into mosaics (per wavelength and per frame time). Calibration observations designated as darks or flats go through a similar but separate pipeline that generates the products listed in the last section of Table 6.1.

Please note that all of the calibration products (specifically: skydarks, skyflats, and linearity curves) are in the raw reference frame. In the raw images the subarrays are located at pixel range $(x1:x2,y1:y2)$ coordinates (9:40, 9:40). In the BCDs, the subarrays are located in $(x1:x2,y1:y2)$ coordinates (9:40, 9:40) in channels 3 and 4, and in $(x1:x2,y1:y2)$ coordinates (9:40, 217:248) in channels 1 and 2. Also note that those coordinates are for the case in which the first pixel is indexed as 1,1 (i.e., IRAF convention). By contrast, IDL pixel indices start from 0,0.

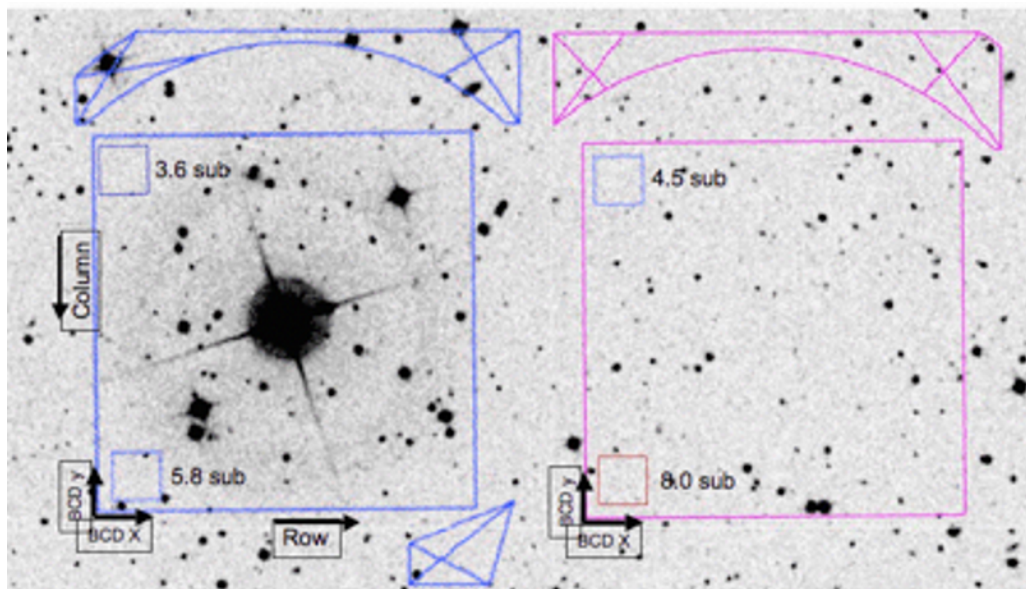


Figure 6.1: The orientation of the (C)BCDs on the sky.

Table 6.1: Sample IRAC file names.

Brief Description	
Basic Calibrated Data (BCD)	
<i>SPITZER II 0008845056 0031 0000 01 dce.fits</i>	Raw data (in units of DN)
<i>SPITZER II 8845056 0031 0000 1 bcd.fits</i>	BCD data (in units of MJy/sr)
<i>SPITZER II 8845056 0031 0000 1 bcd.log</i>	BCD pipeline log
<i>SPITZER II 8845056 0031 0000 1 bunc.fits</i>	BCD uncertainty file
<i>SPITZER II 8845056 0031 0000 1 bimsk.fits</i>	BCD imask file
<i>SPITZER II 8845056 0031 0000 1 brmsk.fits</i>	rmask image
<i>SPITZER II 8845056 0031 0000 1 ptn.log</i>	BCD Pointing log
<i>SPITZER II 8845056 0031 0000 1 sub2d.fits</i>	2D BCD image (subarray only)
<i>SPITZER II 8845056 0031 0000 1_unc2d.fits</i>	2D BCD uncertainty file (subarray only)
<i>SPITZER II 8845056 0031 0000 1_msk2d.fits</i>	2D BCD imask file (subarray only)
<i>SPITZER II 8845056 0031 0000 1_cov2d.fits</i>	2D BCD coverage file (subarray only)
Artifact-Corrected BCD Processing (CBCD)	
<i>SPITZER II 8845056 0031 0000 1 cbcd.fits</i>	Artifact-corrected BCD data
<i>SPITZER II 8845056 0031 0000 1_cbunc.fits</i>	Artifact-corrected BCD uncertainty file
Post-BCD Processing	
<i>SPITZER II 8845056 0000 1 E123458 maic.fits</i>	Mosaic
<i>SPITZER II 8845056 0000 1 A2987651 munc.fits</i>	Mosaic uncertainty file
<i>SPITZER II 8845056 0000 1 A2987653 mcov.fits</i>	Mosaic coverage file
<i>SPITZER II 8845056 0000 1 A2987653 mmsk.fits</i>	Mosaic mask file

<i>SPITZER_II_8845056_0000_1_A2987654_maicm.fits</i>	HDR intermediate frame time mosaic
<i>SPITZER_II_8845056_0000_1_A2987655_muncm.fits</i>	HDR intermediate frame time mosaic uncertainty file
<i>SPITZER_II_8845056_0000_1_A2987656_mcovm.fits</i>	HDR intermediate frame time mosaic coverage file
<i>SPITZER_II_8845056_0000_1_A2987657_mmskm.fits</i>	HDR intermediate frame time mosaic mask file
<i>SPITZER_II_8845056_0000_1_A2987658_maics.fits</i>	HDR short frame time mosaic
<i>SPITZER_II_8845056_0000_1_A2987659_muncs.fits</i>	HDR short frame time mosaic uncertainty file
<i>SPITZER_II_8845056_0000_1_A2987660_mcovs.fits</i>	HDR short frame time mosaic coverage file
<i>SPITZER_II_8845056_0000_1_A2987653_mmsks.fits</i>	HDR short frame time mosaic mask file
<i>SPITZER_II_8845056_0000_1_A26871875_irsa.tbl</i>	List of 2MASS stars for pointing refinement
<i>SPITZER_II_8845056_0000_1_A26871873_refptg.tbl</i>	Table of pointing refinement information
Calibration pipeline data files	
<i>SPITZER_II_13450853_0000_1_C92523_sdark.fits</i>	Skydark
<i>SPITZER_II_13450853_0000_1_A210654_scmsk.fits</i>	Skydark mask file
<i>FUL_2s_2sf4d1r1_ch[1-4]_v1.2.0_dark.fits</i>	IRAC labdark image (full array)
<i>FUL_2s_2sf4d1r1_ch[1-4]_v1.2.0_dark_noise.fits</i>	IRAC labdark noise image
<i>HDR_30s_1.2sf1d1r_ch[1-4]_v1.2.0_dark.fits</i>	IRAC labdark image (HDR short frame)
<i>HDR_30s_30sf16d1r_ch[1-4]_v1.2.0_dark.fits</i>	IRAC labdark image (HDR long frame)
<i>SUB_0.1s_0.1sf2d1r1_ch[1-4]_v1.2.0_dark.fits</i>	IRAC labdark image (subarray)
<i>irac_b[1-4]_[fa/sa]_superskyflat_finalcryo_091004.fits</i>	IRAC superskyflat image
<i>irac_b[1-4]_[fa/sa]_superskyflat_finalcryo_091004_cmask.fits</i>	IRAC superskyflat mask file
<i>irac_b[1-4]_[fa/sa]_20020921_lincal.fits</i>	linearization calibration image
<i>irac_b[1-4]_[fa/sa]_20020921_lincal_cmask.fits</i>	linearization calibration mask
<i>irac_b[1-4]_[fa/sa]_cdelt12_distort.tbl</i>	Array distortion table
<i>irac_b[1-4]_[fa/sa]_16_118_muxbleed_coeff_112003</i>	Muxbleed correction coefficients
<i>irac_b[1-4]_[fa/sa]_16_118_muxbleed_lut_100102</i>	Muxbleed correction look-up table
<i>[month][year]_ch[1-4]_pmask_[subarray].fits</i>	Pmask (nearest in time)
<i>[month][year]_ch[1-4]_fa_pmask[subarray]_flip.fits</i>	Flipped pmask (nearest in time; not in use)
<i>irac_b[1-4]_fa_slmodel_v1.0.1.fits</i>	Subtracted scattered light model
<i>irac_b[1-4]_fluxconv_10112010.tbl</i>	Flux conversion file used
<i>instrument_FOV.tbl</i>	IRAC array locations in Spitzer FOV

<i>irac_b[1-4]_mosaicPRF.fits</i>	PRF file used for pointing refinement
<i>irac_b[1-4]_PRF.tbl</i>	PRF table used for the four quadrants of the image
<i>SPITZER_II_21752576_0000_5_A41882936_avg.fits</i>	Average image of all BCDs in an AOR
<i>SPITZER_II_21752576_0000_5_A41882938_avmed.fits</i>	Average image of all HDR intermediate frames
<i>SPITZER_II_21752576_0000_5_A41882937_ashrt.fits</i>	Average image of all HDR short frames
<i>SPITZER_II_21752576_0000_5_C8232029_mdn.fits</i>	Median image of all BCDs in an AOR
<i>SPITZER_II_21752576_0000_5_A41882940_mdmed.fits</i>	Median image of all HDR intermediate frames
<i>SPITZER_II_21752576_0000_5_A41882939_mshrt.fits</i>	Median image of all HDR short frames

6.3 IRAC Specific Header Keywords

Here we describe some of the important header keywords (given in boldface in this section for clarity). Complete IRAC image headers are included in Appendix E.

AORLABEL is the name of the AOR as it was defined by the user in Spitzer Observation Planning Tool Spot when the observations were requested. The P.I. of a program under which the data were taken will be listed as the **OBSRVR** of each project. **AORKEY** is a unique identification number or digit sequence for each observation; it is also part of the filename for each BCD.

EXPID is an exposure counter incremented within a given AOR for each data-taking command. Most data-taking commands generate multiple files: one per array in full array mode. The **DCENUM** is a counter of individual frames (per wavelength) from an individual command; it can be used to separate frames generated with internal repeats. The only observations with non-zero **DCENUM** are channel 4 BCDs for 100/200 second frame time (taken as two/four 50 second frames). In high dynamic range mode, the long and short exposures are generated with independent commands and have different **EXPIDs**. Thus, for example, data from 12-second high dynamic range observations can be separated into long and short frames using the odd or even **EXPIDs**.

DATE_OBS is the time at the start of the AOR. Other times in the header include the time since IRAC was turned on (both for the beginning and end of the frame). **FRAMTIME** is the duration of the frame including Fowler sampling, and **EXPTIME** is the effective integration time (“exposure time”).

UTCS_OBS is the start of IRAC data taking sequence. **ET_OBS** is the beginning time of the observation (DCE) in barycentric dynamical time (TDB) seconds since J2000 or 2000 January 1,

12 hours (JD 2451545.0). **SCLK_OBS** is the Spitzer Spacecraft clock time at the beginning of the observation (DCE) since 1980, January 1, 00:00:00 UT. Modified Julian date is in keyword **MJD_OBS** and the corresponding heliocentric modified Julian date in **HMJD_OBS**. There is also a Solar System barycentric modified Julian date in **BMJD_OBS**. Note that $\text{BMJD_TDB} = \text{BMJD_OBS} + (\text{ET_OBS} - \text{UTCS_OBS})$ at the start of the DCE. In Instrument Engineering Request (IER; used by the IRAC team to perform non-standard IRAC observations) observations where several IERs are taken successively in the staring mode, only the first IER contains good requested pointing information that is used in calculations of HMJD and BMJD, and therefore these keywords are not reliable in the successive IERs. **ATIMEEND** is the correct time of an integration end. **HDRMODE** tells you if the frame was taken in the high dynamic range mode.

BUNIT gives the units (MJy/sr) of the images. For reference, $1 \text{ MJy/sr} = 10^{-17} \text{ erg s}^{-1} \text{ cm}^{-2} \text{ Hz}^{-1} \text{ sr}^{-1}$. **FLUXCONV** is the calibration factor derived from standard star observations; its units are (MJy/sr)/(DN/s). The raw files are in DN. To convert from MJy/sr back to DN, divide by **FLUXCONV** and multiply by **EXPTIME**. To convert DN to electrons, multiply by **GAIN**.

The predicted background (using the same model as what was implemented in Spitzer Planning Observations Tool Spot, evaluated for the wavelength, date, and coordinates of observation) is contained in three keywords: **ZODY_EST**, **ISM_EST**, **CIB_EST**. These are not based on the actual data from Spitzer. **SKYDRKZB** is the zodiacal background prediction for the skydark that was subtracted from the science image in the reduction pipeline. Thus, the predicted background in the BCD data is **ZODY_EST – SKYDRKZB**.

Absolute pointing information is contained in the following keywords. **ORIG_RA** and **ORIG_DEC** give the coordinates of the image center constructed from the telemetry using the Boresight Pointing History File, as indicated by the Boolean keyword **USEDBPHF**, and the file is listed in **BPHFNAME**. When pointing telemetry is not available, due to a telemetry outage, the commanded positions are inserted instead, **USEDBPHF** is false, and the coordinates will be less certain. **RARFND** and **DECRFND** are the refined positions derived by matching the brightest sources in the image with the 2MASS catalog. **PA** is the position angle of the +y axis of the BCD image, measured east from north. **CRVAL1** and **CRVAL2** give the coordinates of the image center (pixel coordinates **CRPIX1**, **CRPIX2**), derived from the refined positions in channels 1 and 2 (superboresight pointing refinement), and are usually the most accurate coordinates available.

Sometimes a bad pixel value (having the value of exactly zero) can be found among the array pixels in the FITS data field. These pixels are detected and shown in raw frame header where **ABADDATA** assumes the value of 1. In the BCD FITS header you will then find header keyword **BADTRIG** set to “T” (true) and the number of zero pixels in the frame listed in header keyword **ZEROPIX**. If there is only one bad pixel, the pipeline fixes the problem and gives the bad pixel position in header keyword **ZPIXPOS**.

The BCD +x-axis (bottom, or horizontal axis) is in the direction of the telescope +Y-axis, and the BCD –y-axis (left side or vertical axis) is in the direction of the telescope +Z-axis.

DS_IDENT is a journal identification number for the Astrophysics Data System (ADS) to keep track of papers published from these data.

Next, we give an example of how an AOR file translates into final data products. A Spitzer observation is specified by a small list of parameters that are listed in the “.aor” file. This file was generated when the observation was designed (using Spot). Here is an example AOR file:

```
# Please edit this file with care to maintain the
# correct format so that SPOT can still read it.
# Generated by SPOT on: 5/9/2003 12:10:9
HEADER: FILE_VERSION=7.0, STATUS = PROPOSAL
AOT_TYPE: IRAC Mapping
AOR_LABEL: IRAC-FLS-CVZ-a
AOR_STATUS: new
MOVING_TARGET: NO
TARGET_TYPE: FIXED SINGLE
TARGET_NAME: FLS-CVZ
COORD_SYSTEM: Equatorial J2000
POSITION: RA_LON=17h13m05.00s, DEC_LAT=+59d10m52.0s
OBJECT_AVOIDANCE: EARTH = YES, OTHERS = YES
READOUT_MODE: FULL_ARRAY
ARRAY: 3.6_5.8u=YES, 4.5_8.0u=YES
HI_DYNAMIC: NO
FRAME_TIME: 12.0
DITHER_PATTERN: TYPE=Cycling, N_POSITION=5, START_POINT=1
DITHER_SCALE: small
N_FRAMES_PER_POINTING: 1
MAP: TYPE=RECTANGULAR, ROWS=7, COLS=6, ROW_STEP=277.0, COL_STEP=280.0,
      ORIENT=ARRAY, ROW_OFFSET=0.0,COL_OFFSET=440.0,N_CYCLE=1
SPECIAL: IMPACT = none, LATE_EPHEMERIS = NO,SECOND_LOOK = NO
RESOURCE_EST: TOTAL_DURATION=5848.4, SLEW_TIME=1089.0,
SETTLE_TIME=1045.0, SLEW_OVERHEAD=180.0, SPECIAL_OVERHEAD=0.0,
UPLINK_VOLUME=9026, DOWNLINK_VOLUME=59065440, VERSION=S7.0.B2
INTEGRATION_TIME: IRAC_3_6=60.0,IRAC_4_5=60.0,IRAC_5_8=60.0,IRAC_8_0=60.0
```

For this AOR, there are 210 files (6 columns x 7 rows x 5 dither positions) of each type for each channel. The final data products from this AOR in channel 2, provided it got assigned the AORKEY 6213376, are as follows:

```
SPITZER_I2_0006213376_0000_0000_01_dce.fits
SPITZER_I2_6213376_0000_0000_1_bcd.fits
SPITZER_I2_6213376_0000_0000_1_cbcd.fits
SPITZER_I2_6213376_0000_0000_1_bcd.log
SPITZER_I2_6213376_0000_0000_1_bunc.fits
SPITZER_I2_6213376_0000_0000_1_cbunc.fits
SPITZER_I2_6213376_0000_0000_1_bimsk.fits
```

```

SPITZER_I2_6213376_0000_0000_1_brmsk.fits
SPITZER_I2_6213376_0000_0000_1_ptn.log
(SPITZER_I2_6213376_0000_0000_1_bdmsk.fits: historical; replaced by bimsk.fits)
....
SPITZER_I2_0006213376_0209_0000_01_dce.fits
SPITZER_I2_6213376_0209_0000_1_bcd.fits
SPITZER_I2_6213376_0209_0000_1_cbcd.fits
SPITZER_I2_6213376_0209_0000_1_bcd.log
SPITZER_I2_6213376_0209_0000_1_bunc.fits
SPITZER_I2_6213376_0209_0000_1_cbunc.fits
(SPITZER_I2_6213376_0209_0000_1_bdmsk.fits: historical; replaced by bimsk.fits)
SPITZER_I2_6213376_0209_0000_1_bimsk.fits
SPITZER_I2_6213376_0209_0000_1_brmsk.fits
SPITZER_I2_6213376_0209_0000_1_ptn.log

```

After the name of the telescope, the first partition gives the instrument (“I” = IRAC), and the number after the “I” gives the channel (in this case, 2). The next part gives the **AORKEY**, then we have the **EXPID**, **DCENUM**, and the version number (how many times these data have been processed through the pipeline). One should generally use only the data from the highest version number, in case multiple versions have been downloaded from the archive. To verify that the data are from the latest pipeline version, check the **CREATOR** keyword in the header. Finally, there is a group of letters that specify what kind of data are in the file (see Table 6.1 above), and the file type (usually “fits” or “log”). The post-BCD file names include telescope name (SPITZER), “I” (for “IRAC”), the channel number, the productid (not the same as the **AORKEY**), the **DCENUM**, the (pipeline) version, “ensemble product id,” the type of the data and the suffix. In the case of an ensemble product, “**DCENUM**” in the filename refers to the first DCE that was used in the ensemble creation, and “version” refers to the version of that first DCE. The letter “C” stands for “calibration” product: in the case of a calibration product, “**DCENUM**” refers to the first DCE that was used in the calibration creation, (pipeline) “version” refers to the version of that first DCE, and the number after the “C” letter is the “calibration number.” Note that for a given **AORKEY** of science data being retrieved, the **AORKEY** for the associated calibration products is different.

A list of 2MASS sources for the field of the IRAC observation is included in the data delivery as **irsa.tbl*. Note that the 2MASS magnitudes given in the **irsa.tbl* file are not meant for scientific use. For scientific use of the 2MASS data, query the 2MASS catalog directly from IRSA, and take into account the flux quality flags.

7 Data Features and Artifacts

The common artifacts in IRAC data are discussed in this chapter. Most of these have been mitigated by the pipeline processing (and we cross-reference the relevant section in Chapter 5 when one exists), which produces artifact-corrected images (CBCDs). Further mitigation is often possible by a judicious quality inspection of the data, and/or further processing of the BCDs. Note that many of these artifacts are quite commonly seen in IRAC images.

The most common artifacts are as follows. Persistent images usually come from a bright source observed as part of the observation. In some cases, however, persistent images from a preceding observation may be found. One way to check this is by inspecting a median of all the images in an observation (AOR). Another possible flaw in the observations would be an exceptionally high radiation dosage. The nominal rate is approximately 1.5 hits per array per second, and the radiation hits range from single pixels to connected streams (and occasionally small clouds of secondaries). High particle hit rates occurred following high intensity solar flares. There were four such events during IRAC operations. Typically, several hours of science data were rendered useless because of the large number of hits in the images. These science data were rescheduled for observation at a later time, so no science data were lost. Objects that are bright enough leave muxbleed trails and can generate pinstripe patterns over large parts of the image, and offsets along the columns and rows containing the bright source. Ghosts from internal reflections within the filters can be seen in almost every channel 1 or 2 BCD, and more ghosts in all channels are noticeable from bright objects.

We begin with a discussion of the basic characteristics of the dark frames and flat-fields that affect every image. We follow with a discussion of electronic artifacts. These effects arise from the inherent nonlinearity of the detector diodes and saturation of either the detector well, transistors in the mux (multiplexer; we use “mux” as a casual term for the ROIC, which selects four pixels at a time and puts their signals on the four outputs of the array), or the analog-to-digital converter (ADC) in the warm electronics; crosstalk within the mux or warm electronics; or from inductive coupling to currents in spacecraft cables. Most electronic effects have a short persistence, but image persistence, which is also nonlinear in photon fluence, can last seconds, minutes, hours, or even weeks. Next, we have a section on optical artifacts, which include stray light or ghosts from sources within or outside the FOV. Finally, we discuss the effects of cosmic rays and solar protons on IRAC observations. Please note that asteroids may be “contaminants” in the data as well, especially when the target is close to the ecliptic plane. Asteroids can most effectively be rejected from data sets that have been taken at least several hours apart, so that the asteroids have moved in the data and can be masked out by temporal outlier rejection routines.

7.1 Darks, Flats, Missing Data, and Bad Pixels

The true median dark currents, due to nonzero leakage resistance or recombination in reverse-biased detector diodes, are very small compared to the current from the background at the darkest part of the celestial sphere. Labdarks (addressed in Section 5.1.10) were only available in the

cryogenic data pipeline. They were measured with the cold IRAC shutter closed, and with zero incoming photon flux. Skydarks (addressed in Section 5.1.15) have pixel values that differ from zero, with significant pixel-dependent offsets. These offsets are usually positive and depend on the frame time and the Fowler number, as well as on the history of readouts and array idling over the previous several hours. Channel 3 is by far the most extreme case, in which, for example, a 100 second (Fowler-16) frame can be offset as much as 370 DN (median), or the equivalent of 1400 electrons at the integrating node, with no light incident on the array. The signal from the darkest background in a 100 second frame in channel 3 is only about 1000 electrons. Channel 1 has much smaller offsets, but the sky is so dark that the offsets are often larger than the background signal. Channel 2 has very small offsets, which are less than the background signal except in short frames or certain frames immediately following a change in integration time. The background in channel 4 is so large that the offsets are almost negligible except in very short integrations. There is no measurable excess noise from the offset itself: the noise is not the square root of the equivalent number of charge quanta on the integrating node. This is because the offset arises from the redistribution of charge within the mux in which the associated currents and capacitance are much greater than in the detector diodes. However, imperfect correction of this “first-frame” effect (see also Section 5.1.10) does increase the uncertainties in the BCD frames. The uncertainty scales with the size of the offset and its small-scale spatial nonuniformity. Only in channel 3 does it significantly increase the total pixel noise.

We can break down the offset into contributions beginning with the largest spatial scale down to the smallest. In this view, the largest part of the offset is uniform over the array, followed by the contribution of a few spatial gradients, and some pinstriping that repeats every four columns (due to the four array outputs), with a few columns with odd offsets (due to hot pixels or parts of the mux), and weakest of all, pixel-to-pixel dependent offsets.

There are some very obvious features imposed on the true offset, due to a relatively small number of hot pixels, and mux glow. Hot pixels usually appear bright, and in such cases one can see a trail of muxbleed (in raw images) or a pinstripe pattern in channel 1 and 2 arrays, or the bandwidth effect (in channel 3 and 4 arrays) following the hot pixel. These pixels have high dark currents and are usually isolated, but sometimes in a clump. “Dead” pixels are really just very hot pixels, so hot that they saturate before the first pedestal sample. In a BCD image, hot pixels do not appear bright because they have been canceled by the labdark (cryogenic data) or skydark (both cryogenic and warm missions) subtraction. Most hot pixels appeared after the launch and are the result of hits by energetic nuclei. By annealing the arrays during the cryogenic mission, we restored most pixels that got activated. Some of them could not be restored, and thus they became permanent hot pixels. Some pixels jumped randomly from normal to high dark current and back, dwelling in one state for anywhere from a few minutes to weeks, so they may not be canceled by a skydark subtraction. These are IRAC's “rogue pixels.” The IRAC “static” bad pixel masks were updated when significant changes in the permanent bad and/or hot pixels occurred.

Areas of mux glow are visible in the labdark and images. Electrons and holes recombine in diodes in the mux, allowing current to flow. Photons emitted in the recombination are detected in the InSb or Si:As detector above or near the source of the glow. Most prominent is the glow from the four output Field-Effect Transistors (FETs) visible only in Channels 3 and 4 (the Si:As arrays). These are semicircular areas about 17 pixels in radius located near column 256, row 30 at the right edge

of the images. The glow is most obvious in long frames. Another glow region is visible along the last few rows in all four channels; it comes from the unit cell FETs. Currents flow through all the unit cell FETs in the last row which is left selected during the integration, so the glow is particularly bright in the last row itself. The third and faintest glow region is along the left edge (column 1) of channel 3. Detected glows have shot noise, which can exceed the background noise along the last row and in the brightest parts of the semicircular areas. Pixels are masked in these areas where the noise significantly degrades sensitivity in 100 second frames.

Table 7.1: Definition of bits in the pmask. The pipeline used all the bits.

Bit	Condition
0	Not set
1	Not set
2	Not set
3	Not set
4	Not set
5	Not set
6	Not set
7	Dark current highly variable
8	Response to light highly variable
9	Pixel response to light is too high (unacceptably fast saturation)
10	Pixel dark current is too excessive
11	Not set
12	Not set
13	Not set
14	Pixel response to light is too low (pixel is dead)
15	[reserved: sign bit]

7.1.1 *Bad Pixels*

Included with the BCD data are three masks, a semi-static mask (the “pmask”; available in the cal/ directory after downloading all the data for an AOR) that contains permanent or semi-permanent bad pixels and regions, and which is the same for all the BCDs in a given AOR and channel, the “imask” that contains bad pixels specific to any one BCD, and the “rmask” that contains outliers masked by the post-BCD pipeline. All of the bits set in the imask indicate pixels that have been compromised in some fashion. Not all of the imask bits are set by the BCD pipeline, but some bits are placeholders for post-BCD processing of data artifacts. The higher the order of a bit set in the imask, the more severe the effect on data quality. Mask values are set as powers of two, and summed together for each pixel. Any pixel with a bit set in the pmask is suspect.

Several sets of pmaps have been produced. At the start of the mission, sets were produced at 3 – 6 month intervals. As the bad pixel behavior has been shown to vary little with time, these intervals were extended to 12 – 18 months. The masks are made from calibration data spanning (at least) three campaigns, allowing some short-term bad pixels to anneal out, while retaining the ones persistent on timescales of weeks or more. Pixels consistently noisy in the darks or flats in these three (or more) campaign sets are flagged. The regions of amplifier glow are also flagged (with bit 10). Combined masks are also available, with only bit 0 set to indicate a suspect pixel. The “OR” masks contain all the pixels that have been flagged in any pmap set during the mission, and the “AND” masks contain only those pixels set in every pmap set. Table 7.1 and Table 7.2 show the corresponding definitions for each bit value. The DCE Status Mask Fatal Bit Pattern = 32520 (bits 3, 8 – 14; to be used with the MOPEX software).

Table 7.2: Definition of bits in the “imask.” The pipeline used bits 3 and 8–14.

Bit	Condition
0	reserved for boolean mask (or if best practice bits set, data quality)
1	reserved for future use
2	optical ghost flag (set by post-BCD tool)
3	stray light flag (set by post-BCD tool)
4	saturation corrected in pipeline
5	muxbleed flag in channels 1,2; bandwidth effect in channels 3,4 (set by post-BCD tool)
6	banding flag (set by post-BCD tool)
7	column pull-down flag in channels 1,2; vertical banding flag in channels 3,4 (set by post-BCD tool)
8	crosstalk flag
9	radhit (single frame radhit detection)
10	residual image flag (not functional in IER observations)
11	not flat-field corrected
12	data not very linear
13	saturated (not corrected in pipeline), or predicted to be saturated in long HDR frames
14	data bad and/or missing
15	[reserved: sign bit]

7.1.2 Flat-field

IRAC superskyflats are shown in Figure 4.4 (see also Section 5.1.16). The y-axis in the 3.6 and 4.5 μm flat images is flipped with respect to (C)BCDs. For the cryogenic mission these were made by combining the flat-fields from the first five years of operations and for the warm mission the superskyflats were made by combining the flat-fields from the first five years of warm mission. The dark spot in channel 4, near the left side and about half way up, and the dark spot in about the same place in channel 2, are due to the same speck of contamination on the channel 2/4 pickoff mirror. The darkest pixels in the spot are 20% below the surrounding area in channel 2, and 32% in channel 4. Flat-fielding in the pipeline fully corrects for these dark spots in the data. These flats are extremely low-noise, with stochastic pixel-to-pixel uncertainties of 0.14% (0.17%), 0.09% (0.09%), 0.07%, and 0.01% in channels 1 through 4, respectively, where the values in parentheses refer to the warm mission. This is smaller in amplitude than the intrinsic pixel-to-pixel scatter in the gain. Furthermore, because the superskyflats are derived from data over many parts of the sky, with many dithers and rotations of the telescope, they are substantially free of errors arising from gradients in the zodiacal background, or from residual contamination by stars and galaxies. All the IRAC data were reduced with the same set of superskyflats (cryogenic or warm).

Large-scale gradients corrected by the flats are on the order of 10% – 15%. Systematic errors in the flats are due to the gradient in the zodiacal background and straylight removal errors. The former is expected to be very small based on results from other missions, e.g., ISOCAM 25 μm (Ábrahám et al. 1997). Diffuse stray light is a significant contaminant in the raw images at the \approx 5% – 10% level. This diffuse light looks like a “butterfly” across the top of the InSb detectors in channels 1 and 2, or a “tic-tac-toe” pattern in channels 3 and 4. It is always present, resulting from the scattering of the zodiacal background onto the detectors. In both the skyflats and the science data, a model of the stray light has been subtracted, but this leaves a residual pattern on the order of 1% that contaminates the flats. These errors are substantially ameliorated by dithering (errors will decrease as \sqrt{N} , where N is the number of dithers, and will quickly become very small relative to other uncertainties).

The left edges of channels 1 and 3 are vignetted due to a misalignment of the IRAC optics with the telescope. The darkest pixels have 50% of the mean throughput in channel 1, and 70% in channel 3. The vignetting only extends for 10 – 15 pixels. The vignetting is compensated for by the flat-fielding, and results primarily in an increase by at most $\sqrt{2}$ of the noise in the affected pixels.

Finally, one should note that the flat-fields are generated from a diffuse, extremely red emission source. While the resulting flats perfectly flatten the zodiacal background, they are not accurate for compact objects with different spectral slopes, the most obvious examples being stars. Please see the section on array location-dependent corrections (Section 4.5).

7.1.3 Missing Data

In some cases, there may be sections of data that are missing. These are usually marked in both the raw and the (C)BCD data headers in the header keywords `MISSDATA = T` (both full array and subarray data) and `MSLC1` (start of gap; raw only), `NMSD1` (number of missing lines, raw only), `MISS_LCT` (total missed line count in the current FITS file; raw only), and `MANCPKT = T` (if

ancillary data are missing; raw only). An example of missing full array data in a CBCD is shown in Figure 7.1. The subarray data are stored in blocks of four rows of 256 pixels, and missing frames may, for example, make an object completely disappear in a subframe. The corresponding mask image should show a flag revealing that the data are bad, and the header keywords should also indicate a missing line problem.

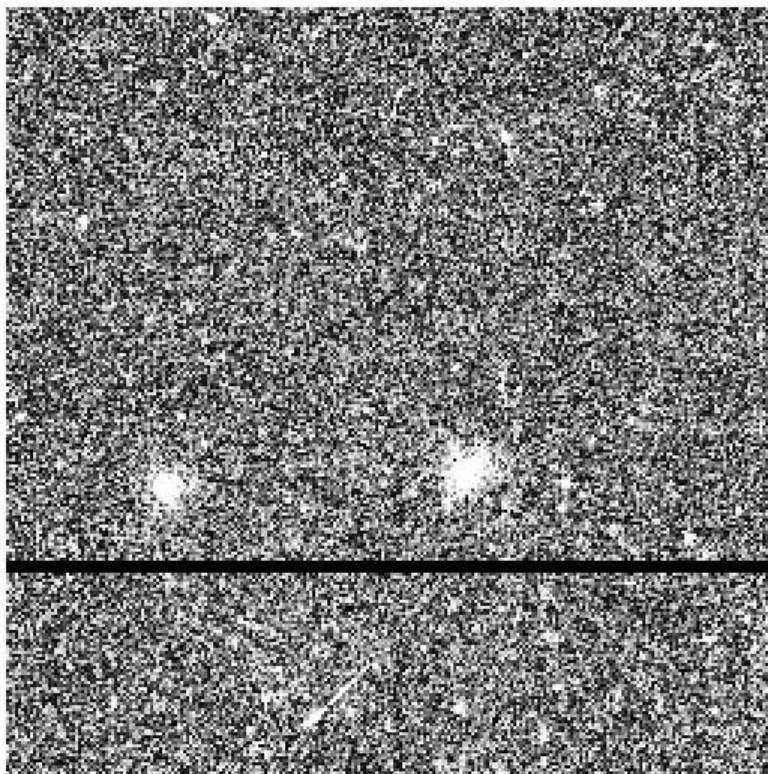


Figure 7.1: Full array CBCD image showing rows of missing data (dark band across the image). This observation is in channel 2, 12 second HDR frame, PID=80254, AORKEY 44050944.

7.2 Electronic Artifacts

7.2.1 Saturation and Nonlinearity

The IRAC detector pixels are limited in the number of photons (actually, electrons) they can accurately accumulate and detect. Once this maximum number is reached, the detector pixel is “saturated,” and additional photons will not result in an increase in read-out data numbers. Prior to this, the detector becomes effectively less sensitive as more photons are received, an effect referred to as “non-linearity.”

The saturation value varies slightly pixel-to-pixel, and substantially from detector to detector. The IRAC InSb (3.6 and 4.5 μm) detectors typically have saturation values of approximately 44000 DN in the raw data (30000 DN for warm mission data). The Si:As detectors (5.8 and 8.0 μm) have

saturation values closer to 55000 DN. The IRAC pipeline automatically detects pixels that exceed a pre-defined threshold, and marks them in the data mask. IRAC uses a Fowler-sampling scheme where the returned DN are the difference between a set of readouts at the end of the integration (signal reads) and a set at the beginning (pedestal reads). Thus, once a pixel has saturated the signal reads, the DN for that saturated pixel will actually start to decrease, and as a result of this double-valued nature the DN value alone is not a reliable saturation indicator. Examining the images containing very bright sources is necessary in order to evaluate saturation based on the observed spatial structure of the source. Very bright sources, for example, will appear to plateau or even develop a dark hole in the center. For point sources, a rough estimate of the flux in the saturated pixels can be made by fitting the wings of the PSF to the linearized pixels in the BCD image. If the data were taken in the high dynamic range mode, the IRAC pipeline will automatically identify pixels in the long frame times that are saturated based on the observed flux in the short frame times. The short frame time data can then be used to recover saturation in the long frame time data (this is not done automatically). This replacement is accurate to about 10% at the peak of bright sources as the ≈ 0.1 arcsecond jitter of the telescope coupled with pixel phasing in channels 1 and 2 and charge diffusion in all channels will cause the measured flux densities between short and long frames to vary.

The IRAC arrays are slightly nonlinear at all signal levels. At levels above 30000 DN (in the Level 0 raw data) the response is low by several percent. As part of pipeline processing, the data are linearized based on ground calibrations (which have been verified in flight) of this effect. The BCD data are linear to better than 1% up to about 90% of full well, which is defined to be the level where we no longer can fully linearize the data, and at which saturation, by definition, begins. Below 20% of full well the nonlinearity in the raw data is negligible.

In detail, there are four places in the electronics where a pixel may saturate: the detector diode, the unit cell source-follower in the Read-Out Integrated Circuit (ROIC), the output source-follower in the ROIC, and the analog-to-digital converter (ADC) in the warm electronics. In most cases, it is the ADC that saturates first, at 0 or 65535 units. ADC saturation produces a discontinuity in the second derivative of the measured Fowler DN versus the flux. The other saturations are smooth, with no discontinuity. In the other cases, depending on the channel, the detector diode may saturate before or after the source-followers.

In principle, for any source for which we already know the spatial variation of its intrinsic surface brightness, we can determine whether the pixel is above or below saturation, and therefore, its flux. In practice, we do not know the gains of the source-followers very well near saturation, nor do we know enough about the detector diode saturation, to make a good estimate of the flux. Therefore, we flag pixels which are above the range of our linearization correction (see Sections 5.1.13 and 5.1.21 for more information on how the pipeline handles linearity and saturation).

The users should note that the pipeline does a saturation correction for bright point sources (see Section 5.2.2). In some cases of a bright and variable background, such as the center of a globular cluster, the pipeline may be fooled to insert an artificial “star” into the CBCD image. Users are encouraged to carefully examine the CBCD images in such cases and use the BCD images if any new artificial-looking features are found in the CBCD images. An example of such an erroneous

saturation correction star substitution is shown in Figure 7.2. For point sources, the saturation corrected photometry should be good to roughly 10% accuracy.

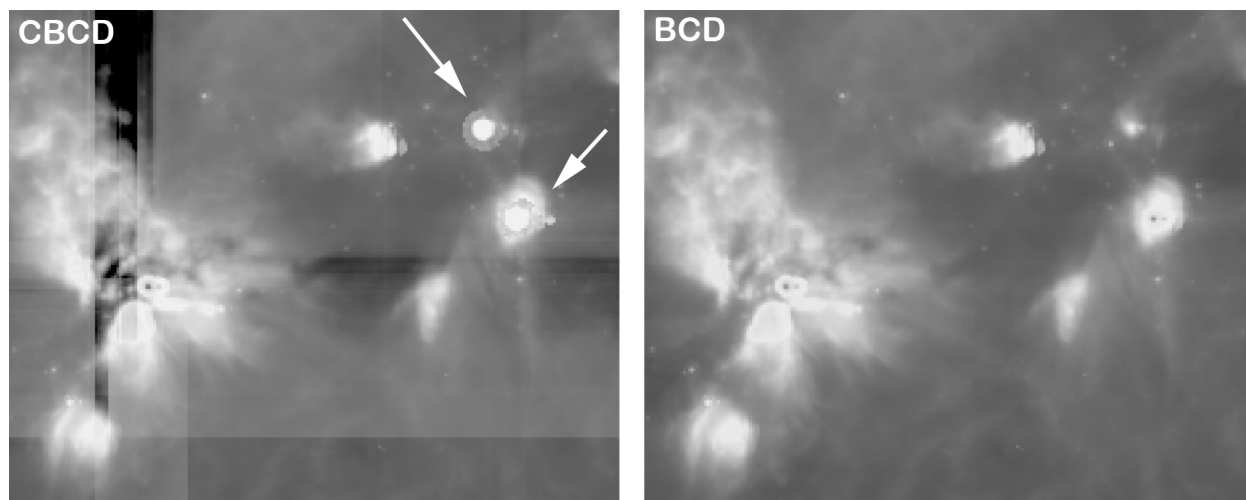


Figure 7.2: Erroneously inserted saturation correction stars in a CBCD image (left), compared to the original BCD image (right). These data are from PID=46, AORKEY 12484352. The arrows point to the sources erroneously inserted by the pipeline. There are column pull-down and banding correction artifacts in the CBCD image as well, inserted by overactive pipeline corrections.

7.2.2 Muxbleed (*InSb*)

Multiplexer bleed, or “muxbleed,” (see also Section 5.1.11) appears in IRAC channels 1 and 2 (3.6 and 4.5 μm). It looks like a decaying trail of pixels, repeating every fourth column, with an enhanced output level trailing a bright spot on the same array row. The effect can wrap around to subsequent rows, but it does not wrap from the last row to the first. Since columns are read simultaneously in groups of four, one for each mux output, the next pixel read out on any single output is four pixels to the right, in array coordinates. As the BCDs for channels 1 and 2 are flipped in the y-direction when compared to the raw images, the read direction is top to bottom for these BCDs, and muxbleed-triggering pixels will affect rows beneath the source. Muxbleed is usually accompanied by a pinstripe pattern (“muxstripe;” every fourth column) that may extend over part of the image preceding or following the pixel. It is caused by a slow relaxation of the mux following the momentary disequilibrium induced when a bright pixel's voltage is placed on an output FET during pedestal and signal reads. Although the pixel rise and fall times are fast (2.6 and 1.0 microseconds, respectively) compared to the 10 microsecond time to clock the next pixel onto an output, longer relaxation times are involved for an output FET to fully recover after the voltage from a bright pixel is briefly impressed on its gate. The decaying trail has a time constant of tens of microseconds, and the pinstripe, tens of seconds.

Stars, hot pixels, and particle hits can generate muxbleed, and the characteristics of the pinstripe depend on the frame time and the Fowler number. Hot pixels may show muxbleed in a raw image, but in the BCD the muxbleed induced by hot pixels may not be present because it was canceled in either the labdark subtraction or in the skydark subtraction. The pinstripe pattern is nearly constant

in areas of a single image that do not contain a saturating star, particle hit, or hot pixel. The characteristics of muxbleed from particle hits depend on when the hit occurs within the frame.

Muxbleed was characterized long before the launch of Spitzer, and it is reasonably well understood, and it is fully corrected in the final IRAC pipeline. The pinstripe is strongest in channel 2, particularly in 12 second frames. In channel 2 mosaics, even with overlap correction, there may appear to be bright and dark patches everywhere, about the size of one frame or part of a frame. Upon close inspection, though, individual patches are revealed as areas of a nearly constant pinstripe pattern that runs between the edges of the array, bright stars, hot pixels, and particle hits. A systematic and automated pinstripe correction scheme has been implemented in the pipeline.

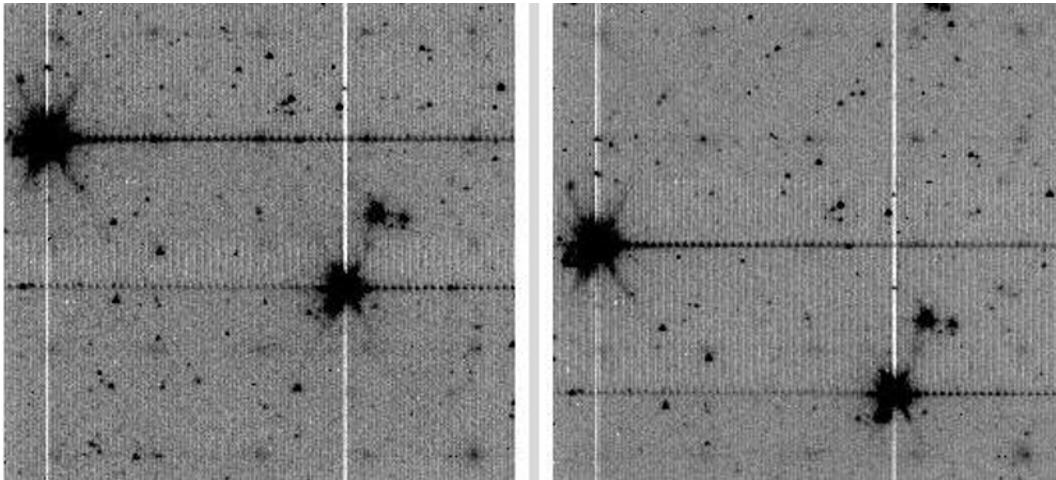


Figure 7.3: Images showing the muxbleed effect (the horizontal line on both sides of a bright stellar image). The pixels on the left side of the bright source are pixels on rows following the row in which the bright source was located (and have wrapped around in the readout order of the array). The vertical (white) lines are due to the so-called “column pull-down” effect. These are 12-second BCD frames in IRAC channel 1, taken from IRAC PID=618, AORKEY 6880000. Pinstriping is also seen in these images.

The amplitude of the effect decays as one moves away from the bright spot, and this decrease can be nicely described by a simple function. In general, muxbleed decays rapidly within 5 – 10 reads and plateaus at a roughly constant value. The functional form of muxbleed is frame time independent. However, the amplitude does not scale linearly with the flux at the brightest pixel or the integrated flux of the triggering source, and this often leaves over/undercorrected muxbleed in BCD frames. For this reason, an additional muxbleed correction by fitting the functional form of the muxbleed pattern to the actual muxbleed incidence is performed after the BCD frame creation (i.e., CBCD frames), and this corrected muxbleed below the rms noise level of the image.

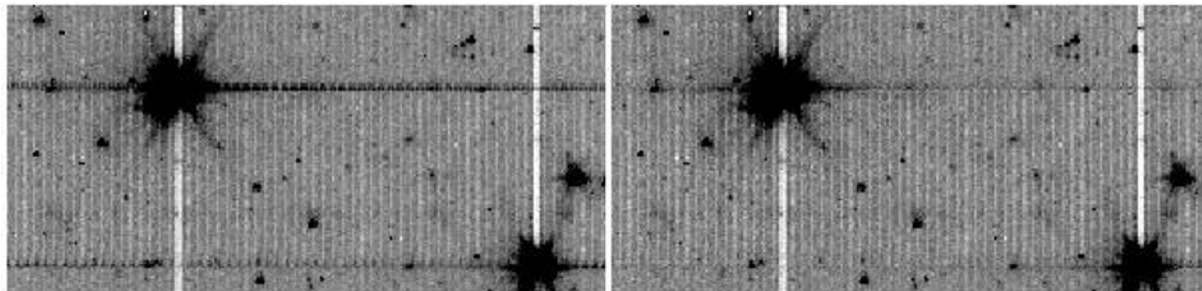


Figure 7.4: Demonstration of the S18 pipeline muxbleed removal. The image on the left is before and the one on the right is after the correction. These are First Look Survey channel 1 data, taken from AORKEY 4958976. Note that the brightest star in the upper-left corner is heavily saturated and the current muxbleed scheme can correct muxbleed from a saturated source also.

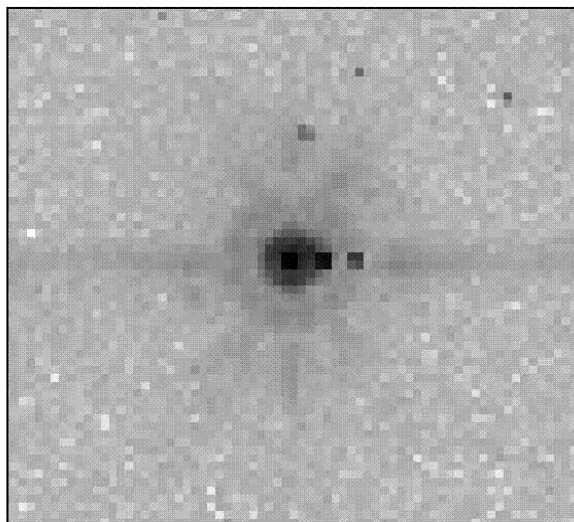


Figure 7.5: A typical bandwidth effect trail in channel 4, in a 30 second frame. These data were taken from PID=1154, AORKEY 13078016.

An example of muxbleed correction is shown in Figure 7.4 (see also Figure 5.8, and see Section 5.1.11 for information on muxbleed correction in the pipeline). It can be seen that at least cosmetically the effect can be greatly reduced without introducing new artifacts. With an additional correction to residual muxbleed during the CBCD pipeline, resultant images should be nearly muxbleed-free.

7.2.3 Bandwidth Effect (Si:As)

The bandwidth effect appears in IRAC channels 3 and 4 (5.8 and 8.0 μm). It looks like a decaying trail of pixels 4, 8, and 12 columns to the right of a bright or saturated spot. Only in the most highly saturated cases is the effect visible 12 columns to the right. It is not corrected in the pipeline. A typical case for a star is shown in Figure 7.5. The principal cause is that the IRAC impurity band conduction (IBC) arrays were operated with insufficient current to raise the voltage on the output bus in the ROIC from a very bright pixel and settle on a dark pixel within 10 or even 20 microseconds. The small signal delays from driving the signal cable and from the lowpass filters

in the preamps also come into play. And the slew rate is different in each of the four outputs of each array. The bandwidth effect is nonlinear. A rare case which gives rise to a bizarre image is shown in Figure 7.6. Here, an extremely bright star saturates an area in the last four columns. The bandwidth effect appears in the first 12 columns of the succeeding rows, making it appear as if the right edge of the image was cut and pasted onto the left side of the image.

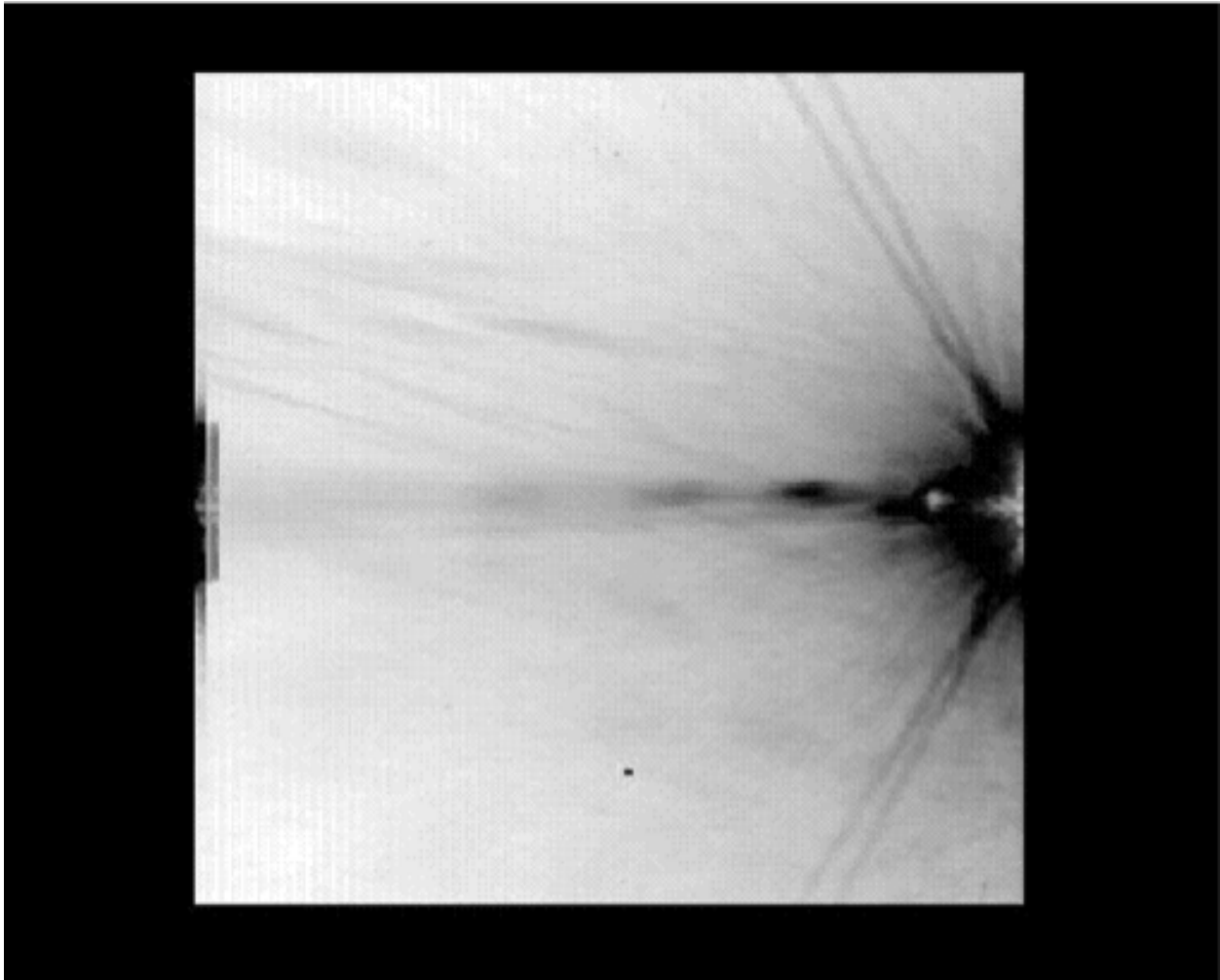


Figure 7.6: The bandwidth effect when a bright object is in the last four columns. IRC+10216, strongly saturated, is just off the right side of the channel 3 array. Even the filter ghost is saturated. The bandwidth effect appears on the left side of the array. These data were taken from PID = 124, AORKEY 5033216.

7.2.4 Column Pull-Down/Pull-Up

When a bright star or cosmic ray on the array reaches a level of approximately 35000 DN, there is a change in the intensity of the column in which the signal is found. In channels 1 and 2, the intensity is often reduced throughout the column (thus the term “column pull-down”); see Figure 7.7. Column pull-up is caused in a similar manner, but the bias difference between the pulled-up

column and its surrounding columns is positive rather than negative. When the effect occurs, it shifts the intensities of the pixels above and below the position of the responsible source, within the same column. This effect is limited to the brightest sources. The amplitude of the column pull-down does not scale linearly with the flux of the source or the brightest pixel. The effect appears to be constant on either side of the source and algorithms which fit separate DC offsets above and below the source should be effective. Cosmetic corrections are partially successful. One, provided by the GOODS Legacy team and available at the Spitzer Contributed Software web pages at IRSA, takes the median of each column, identifies columns that deviate from the local average by more than some threshold, and then adds back in a constant to the apparently affected columns. The code does not work in fields with extended emission. A more general algorithm which estimates the “true” sky value for the affected pixels and fits DC offsets is also available for observations of more structured emission. This algorithm is implemented in the BCD pipeline (see Section 5.2.4).

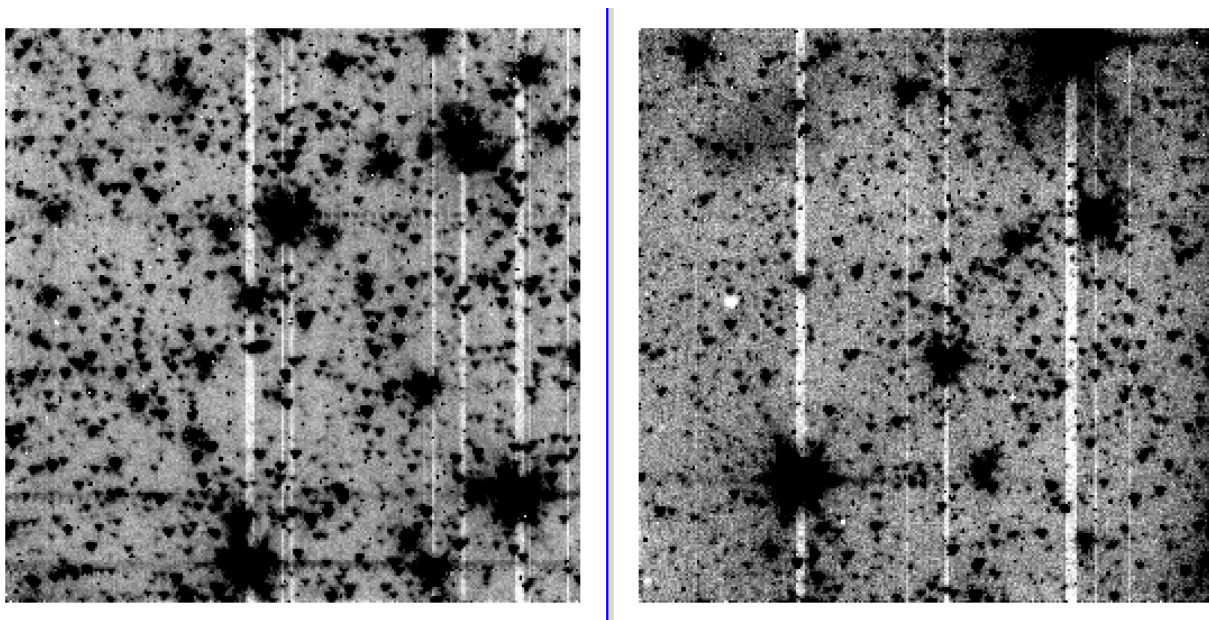


Figure 7.7: IRAC channel 1 (left) and channel 2 (right) observations of a crowded field with column pull-down apparent from the brightest sources. Note that the brighter sources affect a larger number of columns. These data were taken from PID=613, AORKEY 6801408.

7.2.5 Row Pull-Up

In addition to muxbleed in channels 1 and 2, there may be electronic banding, which is manifest as a positive offset for rows that contain bright pixels. This effect is at least an order of magnitude smaller than muxbleed. Electronic banding is more significant in channels 3 and 4 but it is not as significant as the optical banding in those channels (see Section 7.3.2). The BCD pipeline mitigates against these effects. The algorithm finds instances of pull-up and banding and fits the DC offsets on either side of the triggering source to them.

7.2.6 *Full-Array Pull-Up*

In all four arrays, there is also an effect where an entire image is uniformly offset by some amount of DN's that is approximately proportional to the total flux or fluence integrated over the array. It is easily noticed in a mosaic when overlap correction is turned off, and when the mosaic contains areas with and without strongly saturated stars. We call this effect “full-array pull-up,” but it is also known as “droop” to the community of users of doped silicon IBC arrays. The effect can go unnoticed when overlap correction is done in the mosaic. It has no significant effect on aperture photometry of point sources or extended sources when a good background mean can be obtained within the same 5 arcminutes x 5 arcminutes image as the source. The effect is largest in channels 3 and 4, and if uncorrected, can lead to significant errors in the derived flux of extended objects, and especially in the brightness of the background itself. It is hard to distinguish the effect from the internal scattering in channels 3 and 4. The IRAC pipeline does not correct this effect.

7.2.7 *Inter-Channel Crosstalk*

We have detected electronic crosstalk between channels only in the brightest sources that have been observed. All four channels are read out simultaneously, except for the 100/200-second frames in channel 4, for which two/four 50-second frames are taken instead of the long integrations in the other channels, because IRAC is background-limited in channel 4. When a source falls on a pixel of one array, crosstalk may occur in the same pixel location in the other arrays, or in the next pixel read out. Crosstalk appears as a combination of either a positive or a negative offset in the same pixel and the derivative of the signal in the same or previous pixel. As the source is dithered, the crosstalk follows it, and therefore crosstalk appears in the mosaics. It is so weak that we have detected it so far only in channel 3, when the source is in channels 2 and 4, and in channel 4, when the source is in channels 1 and 3. Figure 7.8 shows parts of the mosaics from the off-beams in a dithered observation of a very bright star. The star was observed in channel 1 and 3 FOVs first, so there are residual images in channels 1 and 3 from the bright star. The residual images appear as a diffuse glow near the center. This glow is a combination of the residual images of a very strongly saturated star observed with a Reuleaux dither pattern (cf. Section 3.4), thus effectively smoothed by outlier rejection. The crosstalk appears in channels 3 and 4 as a partial dark ring with a bright core. Crosstalk is not corrected in the pipeline.

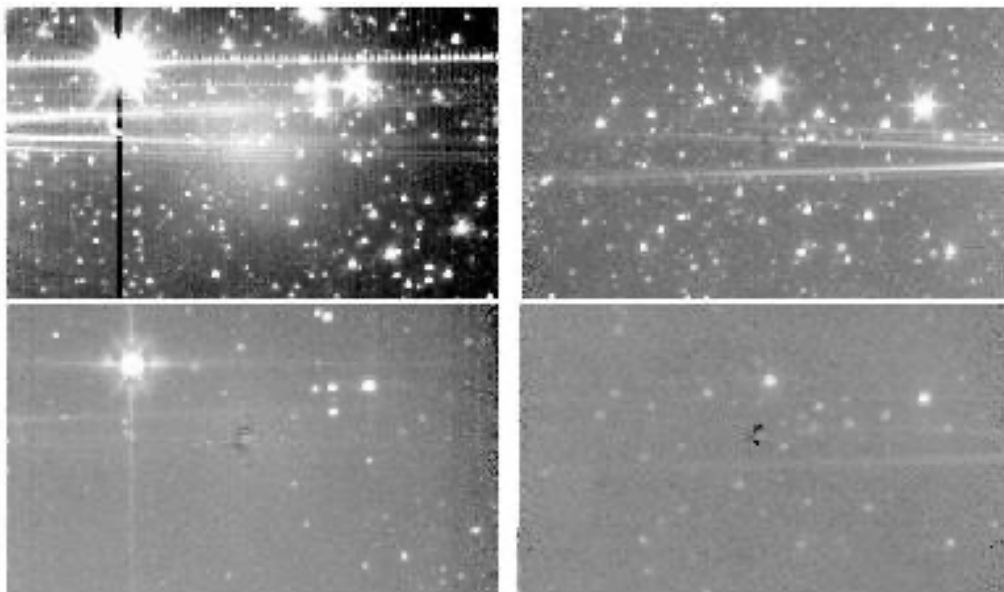


Figure 7.8: Channels 1 and 2 (top) and 3 and 4 (bottom) showing inter-channel crosstalk (dark spots near the center of the lower panels).

7.2.8 *Persistent Images*

The terms “persistent image,” “residual image,” and “latent image” are used interchangeably to describe the contamination of an IRAC image by a bright source from a previous exposure. When a pixel is illuminated, a small fraction of the photoelectrons become trapped. The traps have characteristic decay rates, and can release a hole or electron that accumulates on the integrating node long after the illumination has ceased. The warm mission short-term residual images are different in character than the cryogenic residuals, as the behavior of the trap populations is a function of the impurity type and array temperature. During the cryogenic mission, in all arrays, the longest e-folding decay time is about 1000 seconds. For the warm mission, residuals in channel 1 are $< 0.01\%$ of the fluence of the illuminating source after 60 seconds.

For extremely bright sources, residuals are produced even when the source is not imaged on the array. Residuals at 3.6 and 4.5 μm can be produced during slews from one science target to another and from one dither position to the next. These slew residuals appear as linear features streaking across IRAC images. Note that while the pipeline flags persistent images (Section 5.1.22), the pipeline cannot flag slew residuals, as there is no reasonable way of tracking the appearance of bright sources relative to the moving telescope pointing.

Observations contaminated by residual images can often be corrected with the data themselves. If the observations were well dithered, it is likely that the persistent image artifacts will be rejected as outliers when building the mosaic. Examining the median stack images that can be downloaded from the Spitzer Heritage Archive together with the data can often be used to identify pixels that are affected by residual images. Residual images can often be at least partially mitigated by subtracting the normalized median stack image (made with object and outlier rejection).

7.2.8.1 *Cryogenic Mission Persistent Images*

Tests performed during the In-Orbit Checkout (IOC) revealed that there are both short-term persistent images, with time scales of order minutes and which are present in all four arrays, and longer-term persistent images in channels 1 and 4. The short-term persistent images were known before the launch, and extensive calibrations and data analysis were performed to characterize them. The pipeline produces a mask (bit 10 of the imask) for each image that indicates whether a bright source seen by a previous exposure would have left a persistent image above three times the predicted noise in the present frame. To identify persistent images in your own data, we recommend doing a visual search on a median combined stack.

The longer-term persistent images were discovered in flight. In channel 1, the persistent images are generated by stars as faint as Vega K mag = 13 (in very long stares). They can be generated by any long dwell time with a bright star on the array, whether or not the array is being read out. They were first noticed during a high-gain antenna downlink, when IRAC was left at a fixed position viewing the Galactic plane (by chance) for 45 minutes. The persistent images do not have the same size as a direct point source; they are significantly more diffuse (looking more like the logarithm of the point spread function). The channel 1 long-term persistent images have time scales of order six hours, and they decay gradually. The cause of these persistent images has been identified as a known feature of the flight array (broken clamp) that cannot be fixed. The longer-term persistent images in channel 4 are induced by bright mid-infrared sources or bright stars. The channel 4 persistent images have very unusual properties: they have lasted for as long as two weeks, they can survive instrument power cycles, they do not decay gradually, and they can switch sign, as they decay, from positive to negative. The amplitude and decay rate of long-term persistent images is variable and no secure model exists to remove these artifacts from the data.

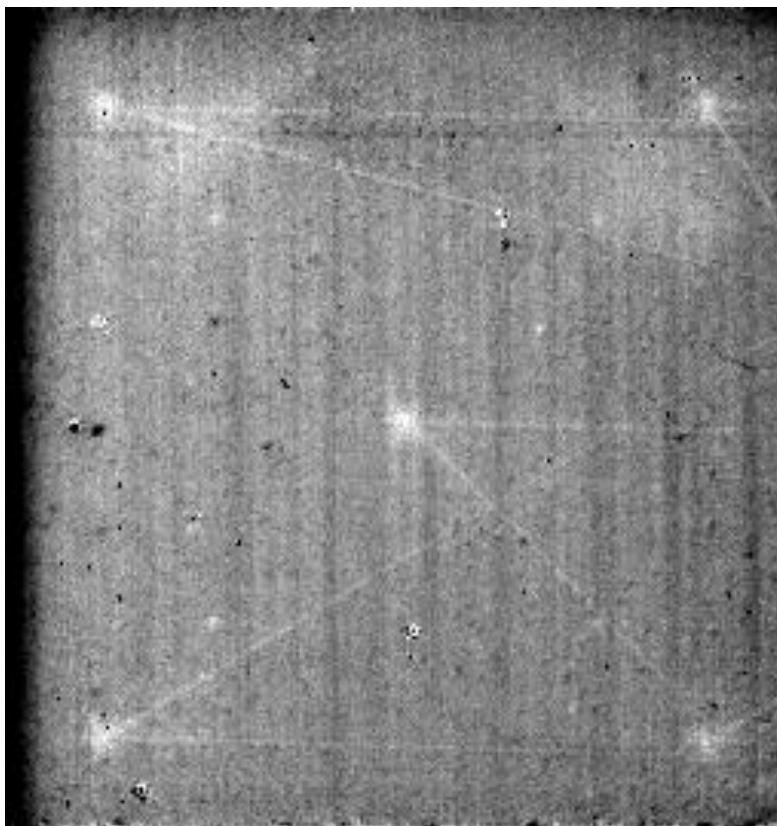


Figure 7.9: Median of channel 1 images from a calibration observation performed after observing Polaris. The five bright spots are persistent images from staring at the star while observing, while the set of criss-crossing lines were generated by slews between the various pointings. These observations were taken from PID=19, AORKEY 3835904.

We instituted a proactive and highly successful method of eliminating persistent images in the cryogenic mission. Channels 1 and 4 were temporarily heated, or “annealed” briefly, with a small current running through the detector. The arrays were annealed after every telemetry downlink, which erased any persistent images built up during the downlink or during the previous 12-hour period of autonomous operations (PAO). This strategy, combined with scheduling known bright object observations immediately before downlinks, greatly decreased the possibility that preceding observations produced persistent images.

We have found that stars brighter than about magnitude -1 at $3.6\ \mu\text{m}$, when observed for more than about six seconds, left a residual image that persisted through an anneal, and even through multiple anneals. These latents from extremely bright objects are seldom visible in a mosaic of a science observation, but they appear in skydarks and other median-filtered stacked images of longer science observations. In channels 2, 3, and 4, all residual images are completely removed by a single anneal, and since January 2006 until the end of the cryogenic mission, we annealed all four arrays every 12 to 24 hours.

Finally, we show an example of persistent images. Note that not all cases will be this obvious. In Figure 7.9 we see not only residual images of the star Polaris, but also residual streaks left by Polaris as the telescope moved between dither positions.

7.2.8.2 Warm Mission Persistent Images

Channel 1 and channel 2 have different persistent image responses in the warm mission data. There are no long-term residual images that last for weeks, such as those seen in channel 4 data during the cryogenic mission. Channel 1 residual images last for minutes to hours, depending on the brightness of the original source and the background levels in the subsequent images. The residual images in channel 1 in warm mission never exceed 1% of the illuminating source in exposures beginning immediately after the illumination of the bright source ends. Figure 7.10 shows this persistent image behavior for a first magnitude star (data taken from PID 1318). The residual image decay in channel 1 is exponential in character, as expected for trapped electron decay rates. The decay rate is constant for all sources, so that while residual images from brighter sources take longer to decay below the background level, all the persistent images decay at the same rate. These rates have been implemented for residual image flagging in the warm mission IRAC pipeline.

A consequence of the intermediate-term (hours) residual images is that it is possible for observations from a previous AOR to produce residual images. The residual image flagging module correspondingly tracks residuals from one AOR to the next. Given the original brightness of the saturation-corrected source, and the decay time calculated with the exponential decay rate, the pipeline flags all residual images until their aperture fluxes are less than three times the background noise in each image. For channel 1, each image in each AOR observed is checked for residual images from all previous observations within the observing campaign, and the residual images are followed across PAOs (downlinks). Using calibration data from bright stars in channel 1 we have empirically modeled the residual flux density (in electrons) decreasing as

$$A \times e^{\frac{-ltime}{4.4}} \quad (7.1)$$

where A is $-5614.36 + 880.12 \cdot \log_{10} F$ (residual causing source flux in electrons) and $ltime$ is the time in hours since the residual causing source was observed. An example of this function is shown in Figure 7.10. We determine the background in each image by randomly selecting 100 regions in the frame, fitting a Gaussian to the electron number distribution and taking the mean from that fit as the background. If the predicted residual flux in electrons is more than 2σ above the background, the pixel is flagged as containing a residual image. To remove a saturated star from a possible residual image causing source list, its predicted flux in electrons needs to be below the 2σ background level in four consecutive images (which allows two HDR mode long exposure images to not contain a residual).

Residual images in channel 2 decay much faster than those in channel 1. In channel 2 the residual images last less than 10 minutes for even the brightest stars. Therefore, the pipeline flagging for channel 2 does not cross AORs. Channel 2 residuals start out as positive, but then become negative. The timing of the switch from positive to negative depends on the exposure time and brightness

of the source. In channel 2 the decay times are much faster (minutes) and a linear function of the flux of the culprit source. The duration of channel 2 pixel flagging after a culprit bright source in warm mission is given in Table 7.3.

Table 7.3: Fluence thresholds required for warm mission channel 2 residual image flagging.

Fluence (electrons)	Duration of residual image flagging after bright source(seconds)
$< 1.96 \times 10^7$	220
$< 1.31 \times 10^8$	320
$< 3.74 \times 10^8$	360
$> 3.74 \times 10^8$	440

Table 7.4: Warm mission residual image durations.

Star K-magnitude	Channel 1 residual duration (hours)	Channel 2 residual duration (minutes!)
1	10	6
2	7	< 6
3	3.5	< 6
4	1.5	< 6

The arrays were not annealed during the warm mission as there was no evidence that annealing removed residual images (the arrays operated at nearly the old annealing temperature), and all residual images decayed in a reasonably short time scale compared to those mitigated by annealing in the cryogenic mission.

Table 7.4 gives a rough idea of warm mission latent durations. Durations should not be taken as exact because they also depend on the background levels in the images that will change from one AOR to the next. This example comes from bright star observations in PID 1318 and starts with 12 second observations of the bright stars.

Residual image flagging is only done for full array frames, because subarray frames do not have saturated stars tracked in the saturated star module of the pipeline, which is a necessary input to the residual image flagging routine. Residual images from non-saturated stars have not been studied.

Examples of residual images are given in Figure 7.11 and Figure 7.12.

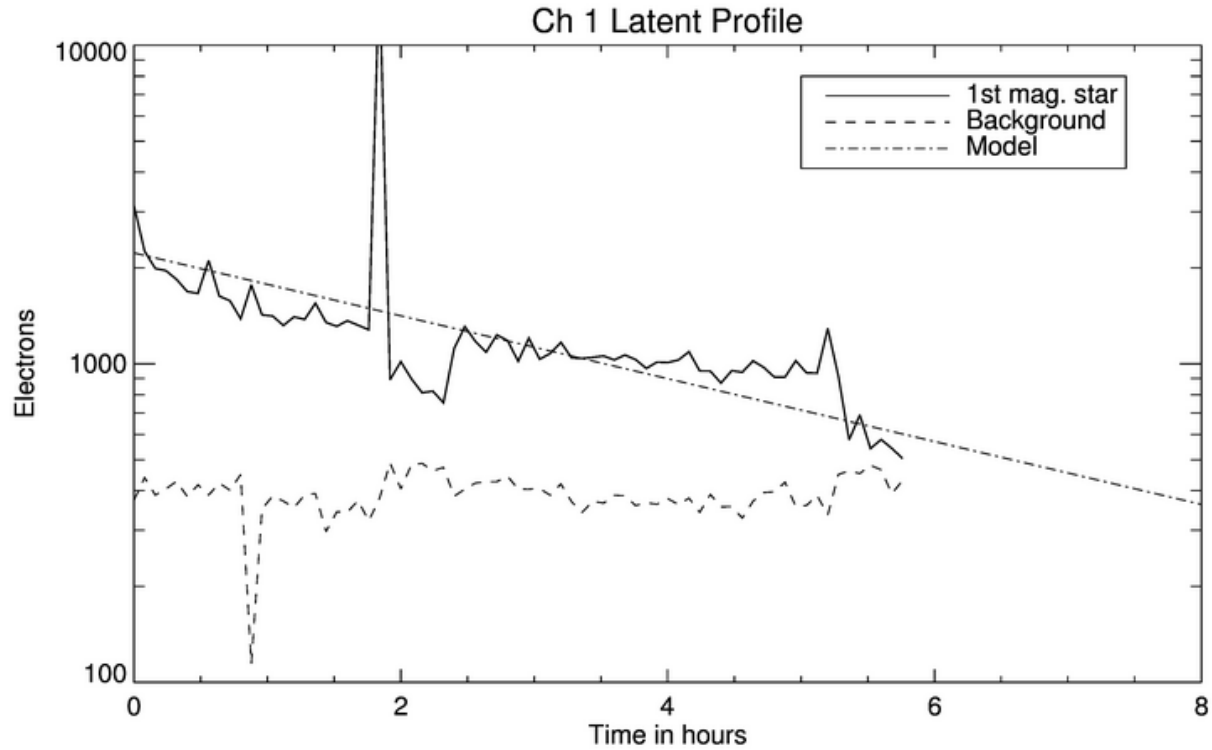


Figure 7.10: Residual image brightness decay as a function of time interval since exposure to a first magnitude source at $3.6\ \mu\text{m}$. The residual is compared to three times the noise in the sky background as measured in an equivalent aperture. The fitted exponential decay function is plotted as the dot-dashed line. These curves have been smoothed to mitigate flux jumps due to sources at the position of the original source in subsequent images.

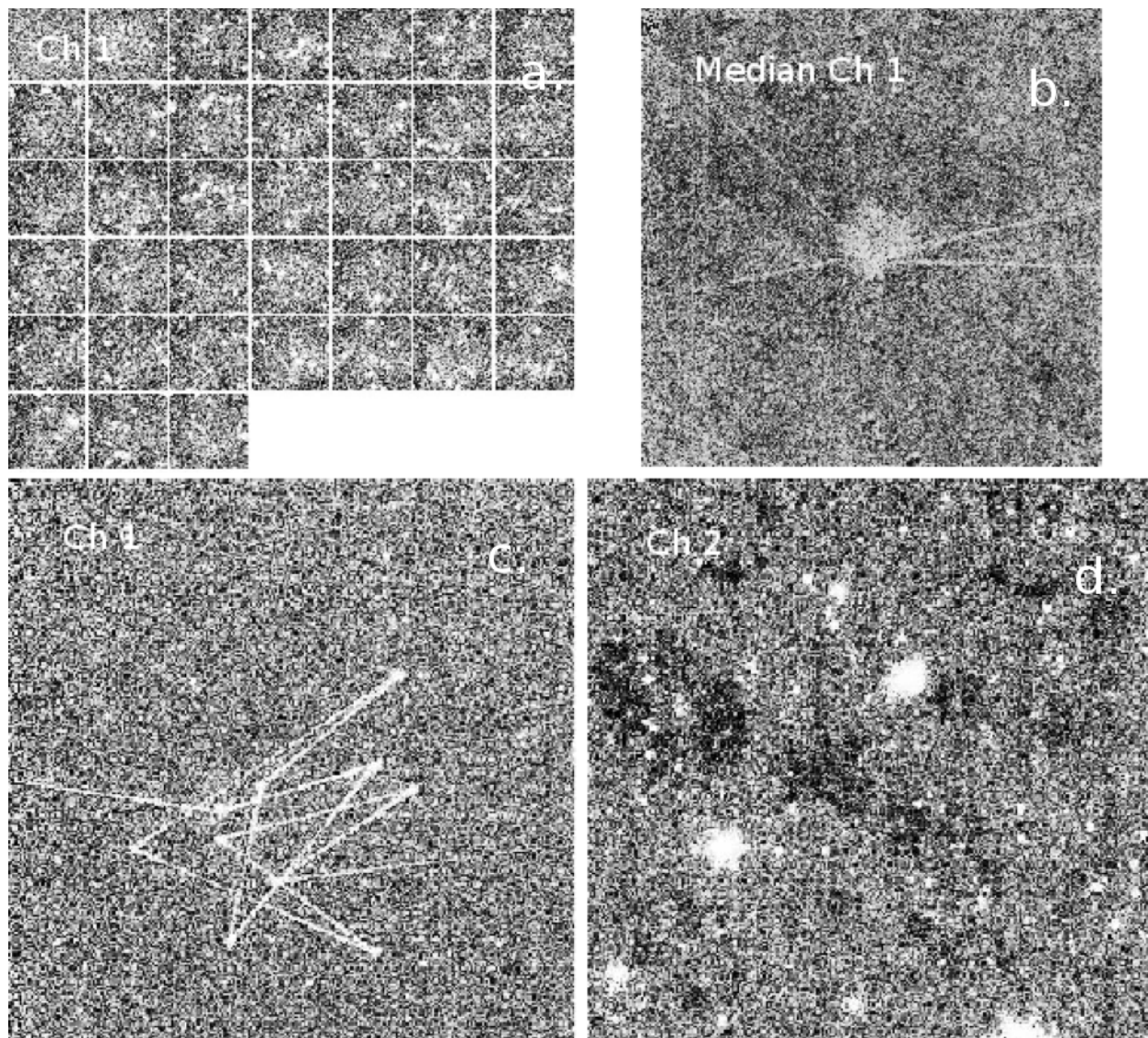


Figure 7.11: Residual image examples: a. channel 1 positive residual images near the center of the array, PID=90175, AORKEY 47943424; b. same as previous but showing the median image of the observation that has also positive slew residuals; c. channel 1 positive slew residuals, PID=80096, AORKEY 45585920; d. channel 2 negative residual images, PID=90109, AORKEY 47828736.

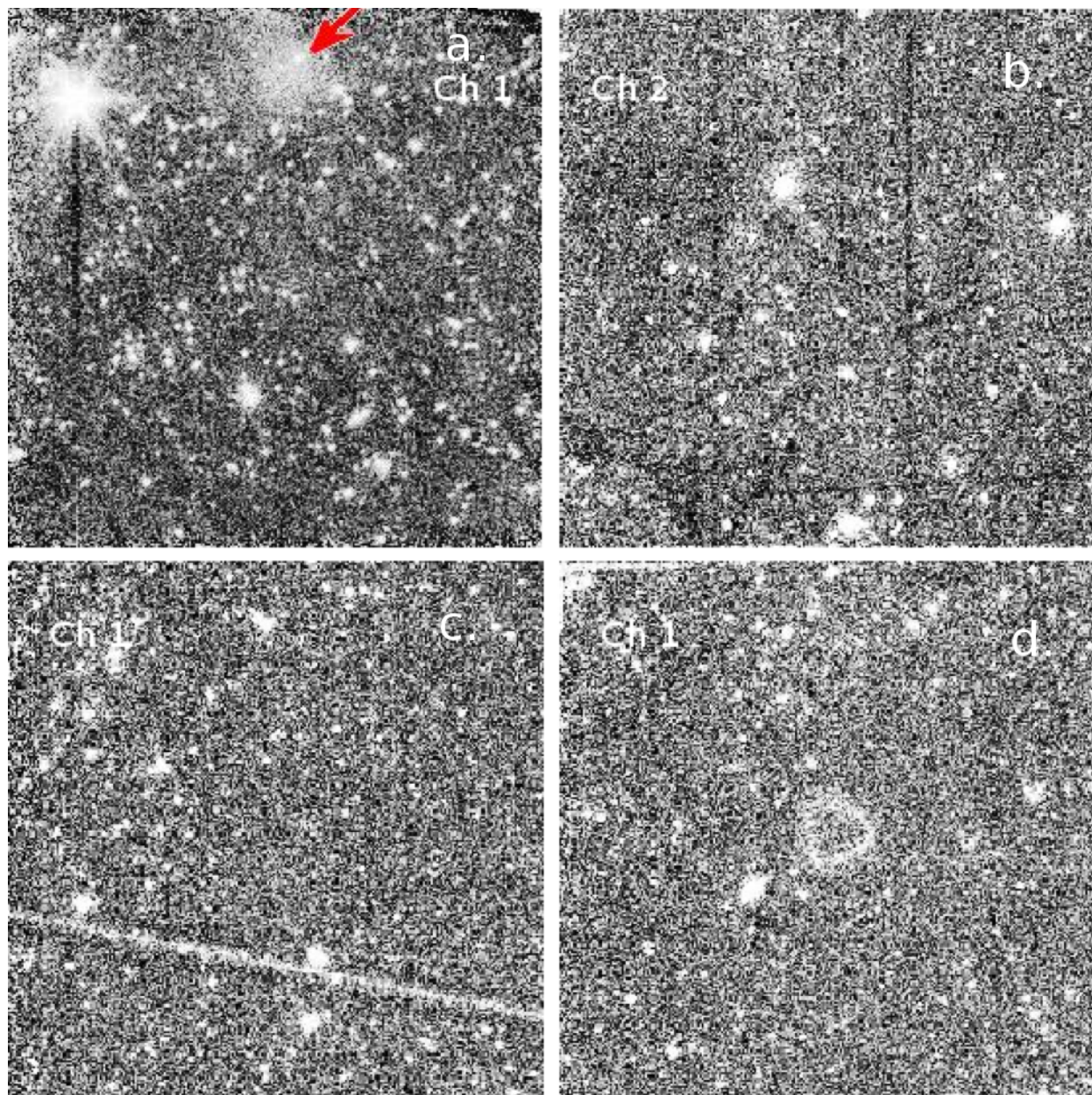


Figure 7.12: More residual image examples; a. channel 1, PID=90124, AORKEY 48337408 (the red arrow is pointing to an image residual); b. channel 2, negative slew residuals and column pull-down residuals PID=70044, AORKEY 40840192; c. channel 1 bright slew residual, PID=61009, AORKEY 35354880; d. channel 1 bright residual image from Reuleaux pattern dithering in center, PID=80015, AORKEY 42191104.

7.3 Optical Artifacts²

7.3.1 Stray Light from Array Covers

Stray or scattered light on the arrays can be produced by illuminating regions off the edges of the arrays. Stray light from outside the IRAC fields of view is scattered into the active region of the IRAC detectors in all four channels. The problem is significantly worse in channels 1 and 2 than in channels 3 and 4. Stray light has two implications for observers. First, patches of stray light can show up as spurious sources in the images. Second, background light, when scattered into the arrays, is manifest as additions to the flat-fields when they are derived from observations of the sky. The scattered light is an additive, not a multiplicative term, so this will result in incorrect photometry when the flat-field is divided into the data unless the scattered light is removed from the flat. Stars which fall into those regions which scatter light into the detectors produce distinctive patterns of scattered light on the array. We identified scattered light avoidance zones in each channel in which observers were told to avoid placing bright stars if their observations were sensitive to scattered light.

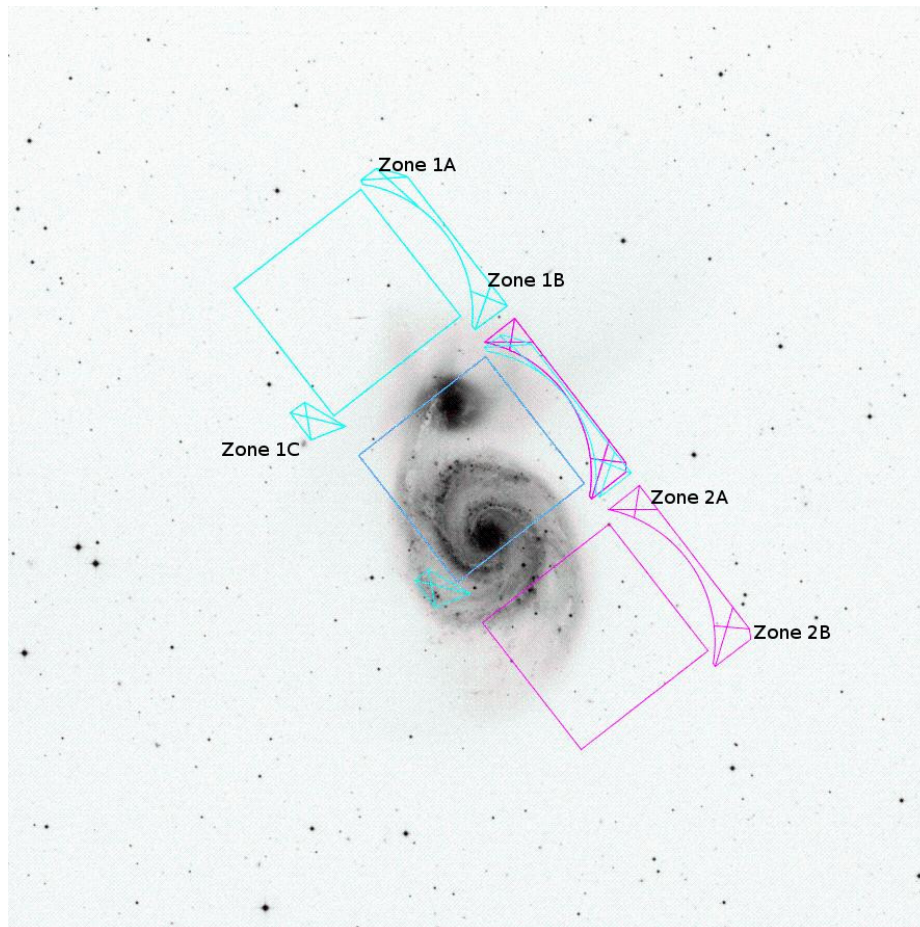


Figure 7.13: An image of the M51 system, showing an overlay of the IRAC fields of view, with the scattered light origin zones for channels 1 and 2 overlaid.

² We thank R. Arendt for providing us with most of the information that was presented in this section.

Figure 7.13 shows the zones for channels 1 and 2 as overlays. Zones 1A, 1B, 2A, and 2B (that produce the strongest scattered light) typically scatter about 2% of the light from a star into a scattered light “splatter pattern” which has a peak value of about 0.2% of the peak value of the star. Figure 7.14 to Figure 7.17 show examples of stray light in channels 1 – 4. Both point sources and the diffuse background generate stray or scattered light. Stray light due to the diffuse background is removed in the pipeline by assuming the source of illumination is uniform and has a brightness equal to the COBE/DIRBE zodiacal light model. This assumption is not true at low Galactic latitudes or through interstellar clouds, but in the 3.6 – 8.0 μm wavelength range it is nearly correct. A scaled stray light template is subtracted from each image, in both the science and calibration pipelines. Before this correction was implemented, diffuse stray light from scattered zodiacal background contaminated the flats, which are derived from observations of high zodiacal background fields, and led to false photometric variations of 5% – 10% in the portions of the array affected by stray light; this photometric error is now estimated to be less than 2%.

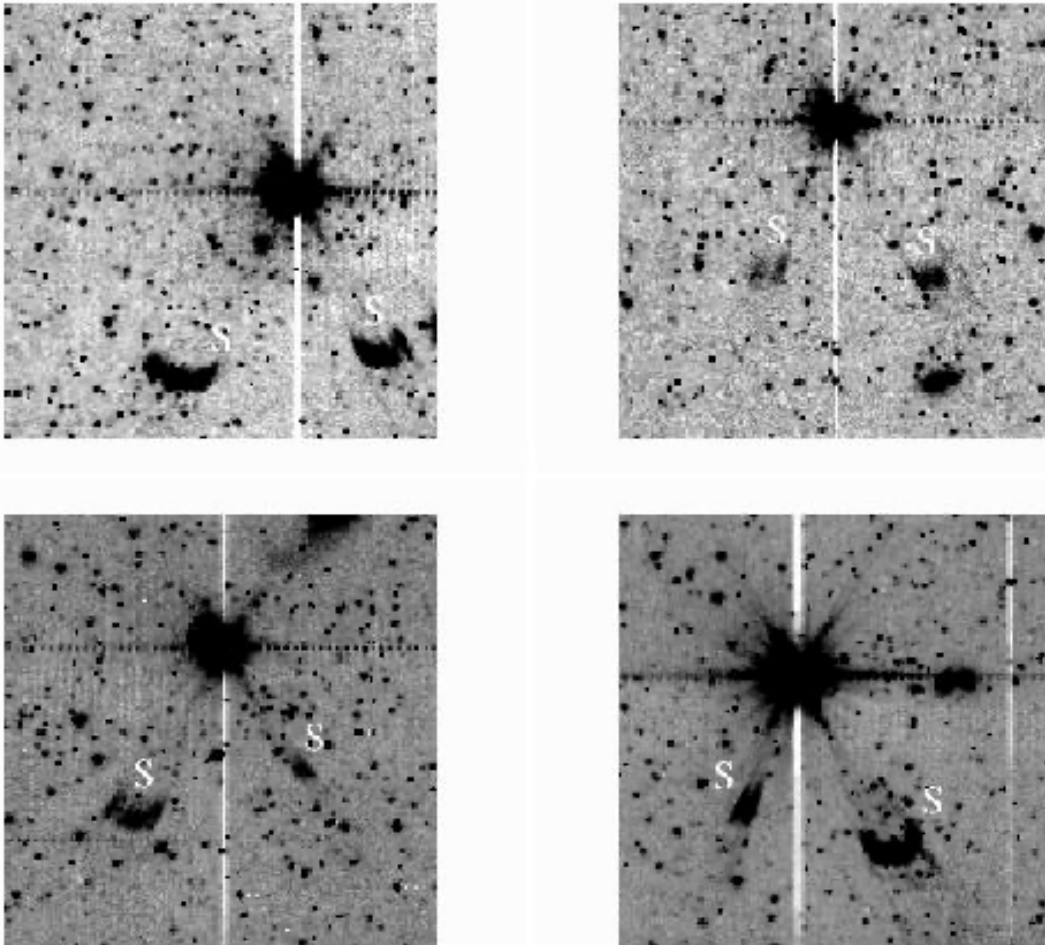


Figure 7.14: Channel 1 image showing scattered light on both sides of a bright star. The scattered light patches are marked with white “S” letters. The images were taken from PID=30 data.

Example images of scattered light are shown here to alert you in case you see something similar in your IRAC images. The scattered light pattern from point sources is difficult to predict, and very difficult to model for removal. To first order, you should not use data in which scattered light from point sources is expected to cover or appears to cover your scientific target. Stray light masking was done in the pipeline. This procedure incorporates our best understanding of the stray light producing regions. The procedure updated the corresponding imask for a BCD by determining whether a sufficiently bright star was in a stray light-producing region. The 2MASS point source list was used to determine the bright star positions.

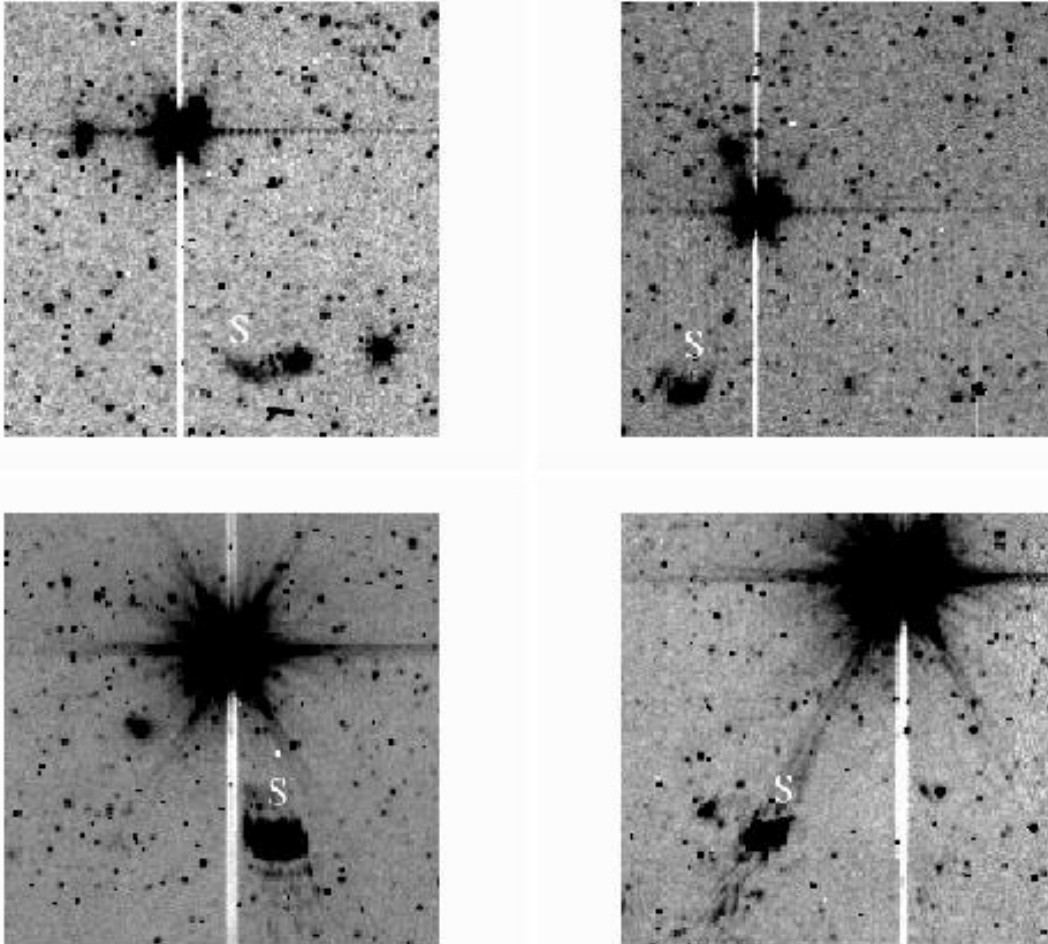


Figure 7.15: Similar to Figure 7.14 but for channel 2.

Figure 7.14 to Figure 7.17 are 201 pixels (4.1 arcminutes) square, and have been extracted from larger mosaics produced from the IRAC GTO shallow survey (from PID 30). This survey covered 9 square degrees with three 30-second images at each position. Because the mosaics cover large areas, the star causing the scattered light appears in many of the images. All of the sample images have the same array orientation as the BCD images. The sample images are mosaics of a BCD that contains the stray light and the BCD that contains the star that produces the stray light. Figure 7.14 and Figure 7.15 show scattered light in channels 1 and 2, from zones 1A, 1B, 2A, and 2B as identified in Figure 7.13. Figure 7.16 and Figure 7.17 show scattered light in channels 3 and 4.

Because stars are much fainter in these channels, and the scattering geometry is much less favorable, these scattered light spots are much less obvious than in the short-wavelength channels. Dithering by more than a few pixels would take the bright star off the channel 3 and 4 “scattering strip,” so the scattered light spots should be removed from mosaics made with adequately dithered data.

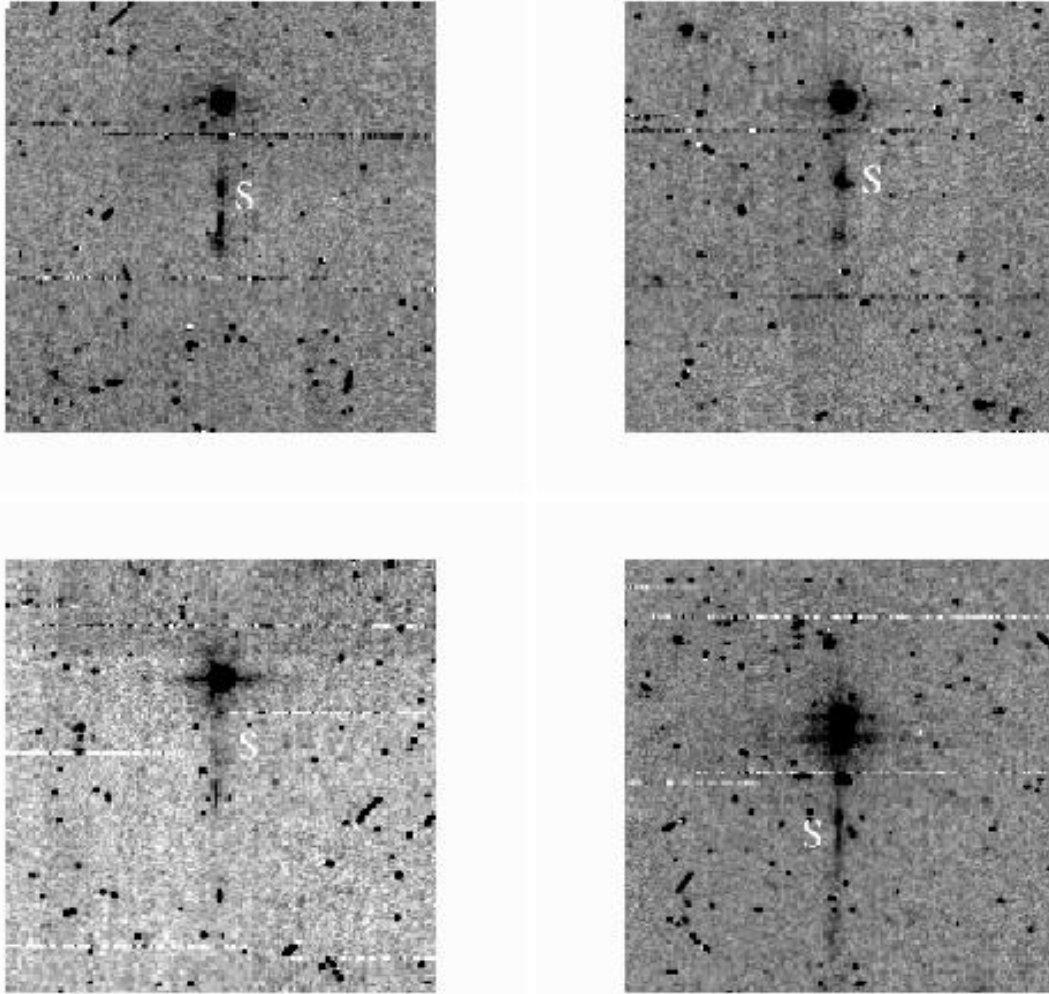


Figure 7.16: Similar to Figure 7.14 but for channel 3.

Please note that Figure 7.14 – Figure 7.17 were made with no outlier rejection. A dithered observation, combined with outlier rejection, will have much reduced stray light. Further, a diligent data analyst, who recognizes and masks stray light in the individual BCDs, will be able to eliminate stray light from well-planned mosaics. Observations made with little or no redundancy, or with dithers on scales smaller than the size of the stray light patches, will contain stray light and should be used with caution. Information on how the pipeline masks suspected stray light areas is given in Section 5.2.1.

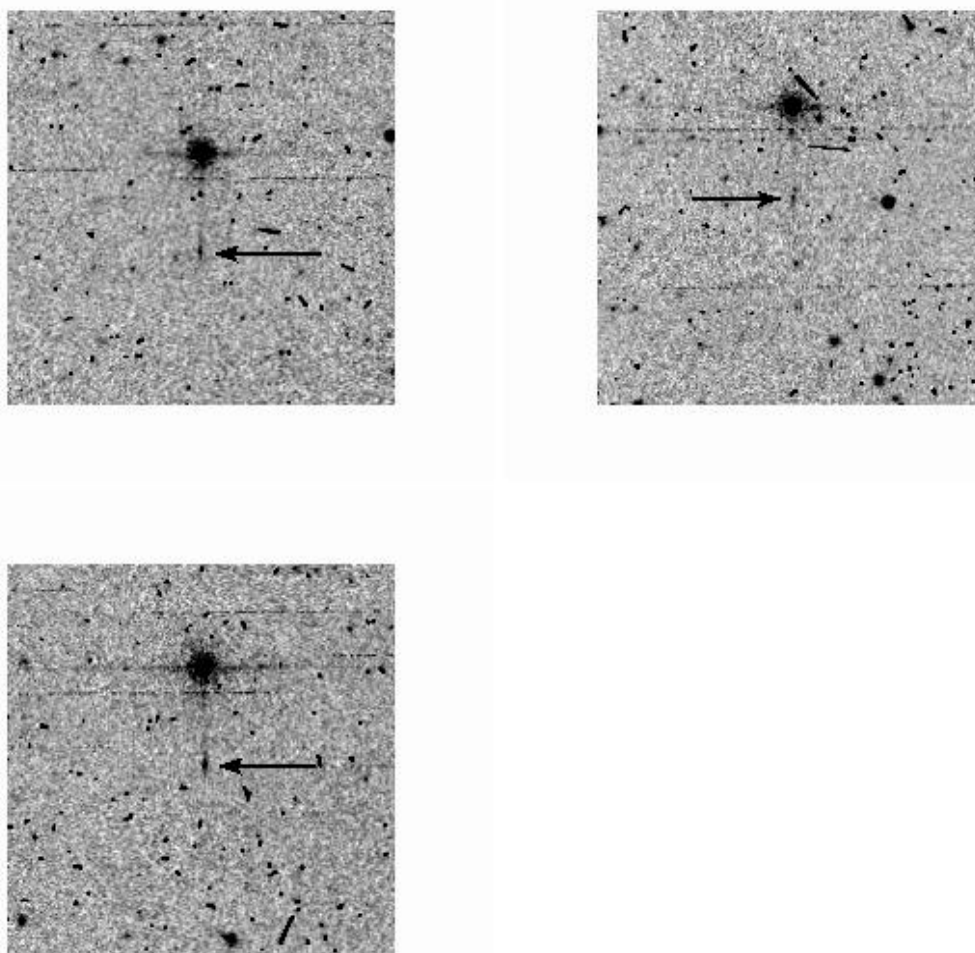


Figure 7.17: Similar to Figure 7.14 but for channel 4. The scattered light patches are pointed to by black arrows.

7.3.2 Optical Banding and Internal Scattering

The banding effect manifests itself as the rows and columns that contain a bright source having an enhanced level of brightness. This happens only in the Si:As arrays and has been shown to be due to internal optical scattering (inside the array). Both bright stellar sources and bright extended sources cause banding. It is clearly different from the optical diffraction patterns and the column pull-down effect. The SSC pipeline corrects for banding, but it does not model the flaring of banding towards the edges of the array. Therefore, the pipeline correction is not always perfect.

Banding only appears in IRAC channels 3 and 4 (5.8 and 8.0 μm channels), and it is stronger in channel 3. Banding probably occurs at all intensity levels, but only appears obvious around bright sources that are at or near saturation levels. Banding is seen both in row and column directions, though their relative intensities are somewhat different. In addition, there is an electronic effect. Channel 4 has a strong row pull-up, and channel 3 has a weak column pull-up. The column pull-

up is uniform across the row where the source is bright. The optical banding intensity falls off with distance from the bright spot. Cosmic ray hits cause electronic banding, but not optical banding.

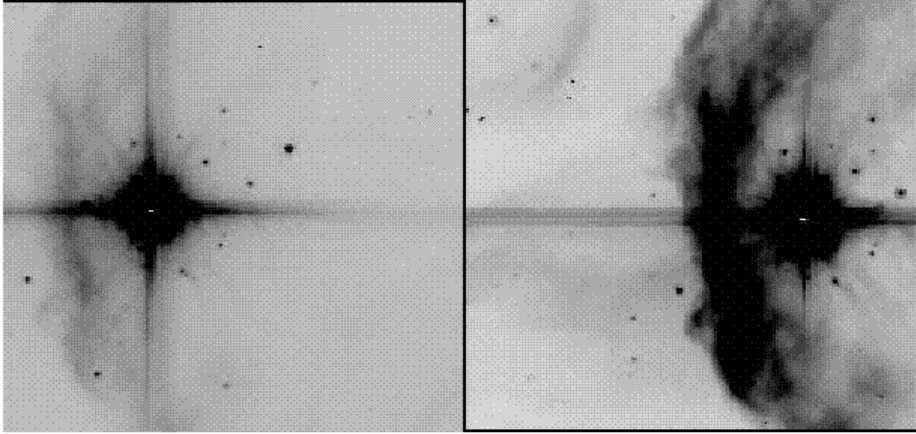


Figure 7.18: Typical image sections showing the banding effect. These are channel 3 (left) and channel 4 (right) images of the same object (S140), adopted from a report by R. Gutermuth. These data were taken from PID=1046, AORKEY 6624768.

The optical banding is only an enhancement of the optical scattering in channels 3 and 4 near the row and column where the source is. Approximately 25% of the light incident from a point source is scattered throughout the channel 3 array. The detected scattered light falls with distance from the source. Channel 4 has the same problem to a smaller degree. Laboratory tests have confirmed the large amount of optical scattering within the Si:As arrays. At wavelengths shorter than about 10 μm , the Si:As in the channel 3 and 4 arrays is not opaque, and most of the incident photons, especially in channel 3, reach the front surface of the detector chip, where they are diffracted by the rectilinear grid of conductive pads. Many are diffracted into high angles and are multiply-reflected within the detector chip, and some can travel fully across the array before being absorbed (and detected). Other photons can pass through the detector chip and be scattered back into the detector chip where they are detected. The interference pattern tends to concentrate the scattered light along the rows and columns, causing the optical banding. The pattern is due to interference that depends on wavelength and the spatial extent of the source at each wavelength. The banding/scattering pattern does not vary much for point sources with a continuous spectrum, but a narrow-band source has a complex banding/scattering pattern.

Users should be aware of the uncertainties resulting from banding, specifically when attempting measurements of faint sources near the affected rows or columns. For bright sources with significant banding, aperture photometry may not be successful, and it would be better to measure these sources using frames of shorter exposure times. Users are encouraged to experiment with image restoration techniques of their choice. Algorithms similar to the pull-down corrector may have some effectiveness in mitigating banding. The pipeline-performed banding correction is discussed in Section 5.2.5.

7.3.3 Optical Ghosts

There are three types of known or potential optical ghosts visible in IRAC images. The brightest and most common ghosts are produced by internal reflections within the filters. The first-order filter ghosts (one pair of internal reflections) in channels 1 and 2 are triangular, and in the BCD images they appear above and/or to the left of the star in channel 1, and above and/or to the right of the star in channel 2. The channel 1 first order filter ghost contains $\approx 0.5\%$ of the flux of the main PSF in channel 1, and the channel 2 ghost $\approx 0.8\%$ of the flux of the channel 2 PSF. Because of the increase in the optical path length, ghost images are not in focus. The separation between the main image and its ghost is roughly proportional to the distance of the main image from the Spitzer optical axis in both Y and Z directions, i.e., $(\Delta Y, \Delta Z) = (A_y y + B_y, A_z z + B_z)$ where (y, z) are normalized coordinates in which the Focal Plane Arrays (FPAs) span the range $[0, 1]$ with the axes increasing away from the Spitzer optical axis, and the coefficients are as listed in Table 7.5 below. The $+Y$ direction is in the IRAC (C)BCD $+x$ direction and the $+Z$ direction is in the IRAC (C)BCD $-y$ direction. The peak intensity of the ghost is roughly 0.05% of the (unsaturated) peak intensity of the star. The second-order filter ghosts (two pairs of internal reflections) are much fainter ($\approx 25\%$ of the flux and $\approx 6\%$ of the surface brightness of the first order ghosts), rounder, larger, and about twice as far away from the star. The separation between the star and its ghosts increases with distance from the optical axis of the telescope. The channel 3 and 4 filter ghosts appear as small crosses at a larger distance, mostly to the left or right of the star, respectively. They are offset from the primary image by approximately $(+36 \text{ pix}, +2 \text{ pix})$ and $(-36 \text{ pix}, +2 \text{ pix})$ in the Spitzer (Y, Z) directions for channels 3 and 4, respectively. The Z -offset varies slightly with position on the array. The channel 3 and 4 filter ghosts contain $< 0.2\%$ of the flux of the main PSF in these channels. The separation and orientation are different from channels 1 and 2 because of the different orientations of the filters. Examples of filter ghosts are shown in Figure 7.19.

Table 7.5: Coefficients for channel 1 and 2 ghost locations.

Channel	A_y	B_y	A_z	B_z
1	0.04351	0.00288	0.04761	0.00211
2	0.04956	0.00105	0.04964	0.00387

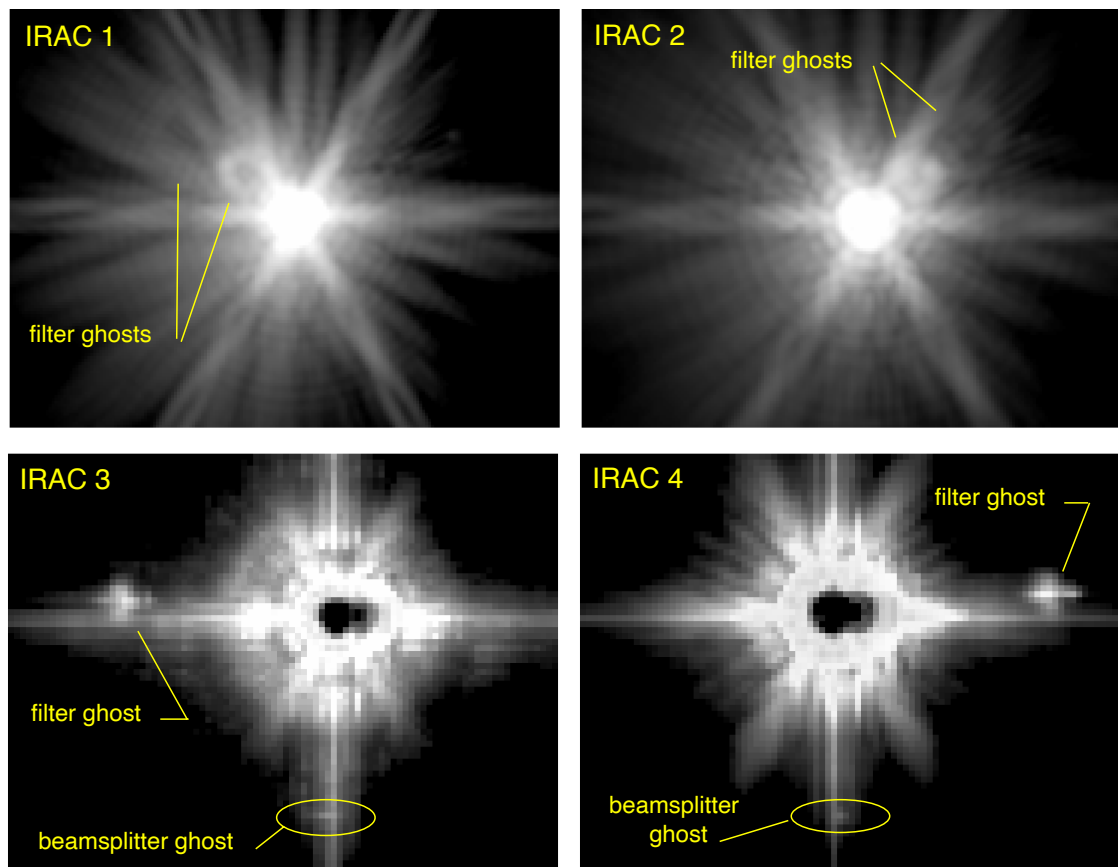


Figure 7.19: Filter and beamsplitter ghosts in IRAC. Top: Channel 1 and 2 mosaics of saturated images of Fomalhaut near the center of each array from PID=90, AORKEY 4875776. The panels are 180 pixels \times 140 pixels of 0.6 arcseconds; the greyscale is logarithmic. Bottom: channel 3 and 4 single, highly saturated images of Sirius near the center of each array from PID=1156, AORKEY 16412416. The panels are 90 raw pixels \times 70 raw pixels; the greyscale stretch is square-root. The channel 3 and 4 filter ghosts are nearly saturated and the bandwidth effect is saturated. Even the optical banding (light diffracted and internally reflected within the arrays) in the column containing the star center suffers the bandwidth effect, which appears as bright vertical spikes 4 and 8 pixels to the right of the center of the star.

Similar ghosts are created by internal reflections within the beamsplitters. These only affect channels 3 and 4 which are transmitted through the beamsplitters. They appear as a very faint, short, horizontal bar at $\Delta y \approx -36$ pixels relative to a bright star (below the bright star in Figure 7.19), but are often obscured by brighter “banding” artifacts. They are slightly fainter than the filter ghosts.

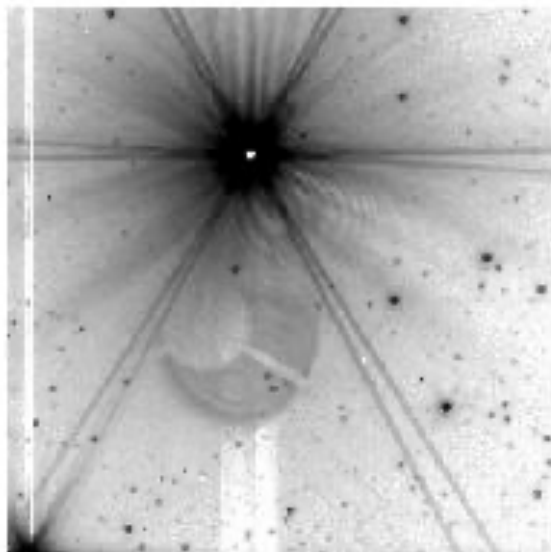


Figure 7.20: Pupil ghost in channel 2 from V416 Lac.

The faintest identified ghosts appear as images of the Spitzer entrance pupil, i.e., the primary mirror shadowed by the secondary and supports. These pupil ghosts are only found in channels 2 and 4, and require an extremely bright source (e.g., a first magnitude star in a 12-second frame) to be seen due to their low surface brightness. The pupil image is at a fixed location on the array (but in different locations in different channels). However, the pupil image is only partially illuminated by a single source, and the portion of the image that is illuminated depends on the source position on the array. An example of a pupil ghost is shown in Figure 7.20. This figure also shows some fringes in between the pupil ghost and the star. It is not clear if the fringes are directly related to the ghost. The total flux in these ghosts is $\approx 0.05\% - 0.5\%$ of the total flux in the PSF.

We flag the ghosts in the pipeline with imask bit 2 (see Section 7.1.1). However, because the relative locations of the ghosts do vary with position on the array, sufficiently large dithering can help reduce or eliminate their effects. The stray light masking software also will flag the filter ghosts. The PRFs that we provide on our web pages include all the ghosts, and the apertures used in calibrating channels 1 and 2 include the filter ghosts. In performing photometry for channels 1 and 2, the filter ghosts should be included.

7.3.4 Large Stray Light Ring and Splotches

There is a faint ring of scattered light with a mean radius of about 23.7 arcminutes in channel 1 that is visible around bright objects. There is also a slightly larger, fainter ring in channel 2. They were first noticed in mosaics of a SWIRE field that was adjacent to the bright star Mira in PID 181 (see Figure 7.21). The ring was visible in channel 1 and 2 mosaics. We verified that the ring was an artifact by observing the field near Beta Gru where we observed pieces of the ring in the same places relative to the star. Starlight that is specularly reflected off the telescope mirrors cannot enter the Multiple Instrument Chamber (MIC) directly when the star is more than 16 arcminutes off the telescope boresight. IRAC's pupil stop is a little oversized, so the ring is probably light that is once or twice diffusely scattered at areas outside the secondary and/or near the top of the primary

conical baffle. The mean surface brightness of the ring in channel 1 is 4.5×10^{-10} ($\pm 30\%$) times the peak surface brightness of a pixel-centered point source. Presumably there are stray light rings in channels 3 and 4, but they are too faint to see.

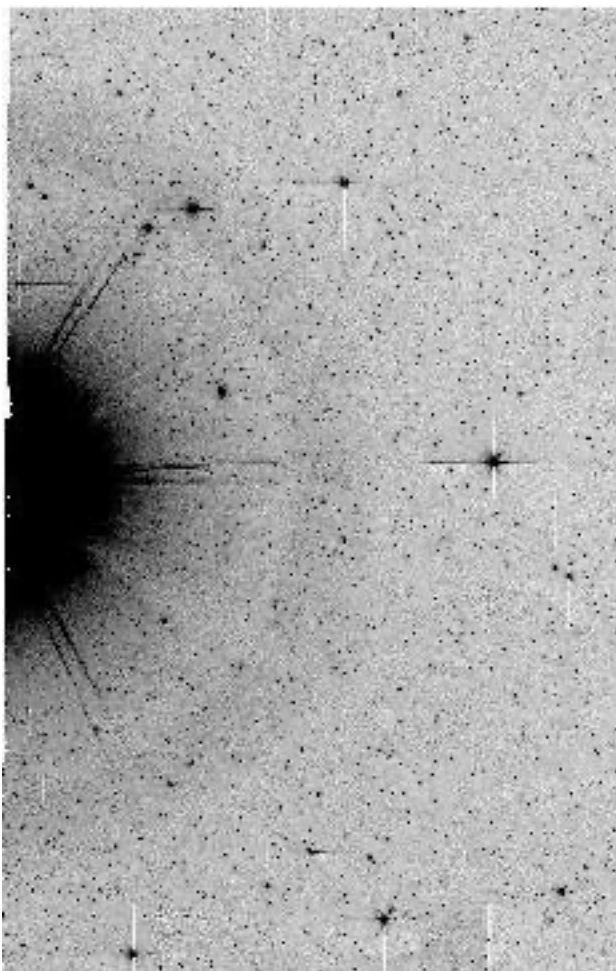


Figure 7.21: Part of the channel 1 mosaic (from observations in PID=181; AORKEYs 5838336, 5838592, 5839872, and 5840128) of the SWIRE field near Mira showing the 24 arcminute radius ring of stray light from the telescope. The dimensions of the image are about 0.7 degrees (x-axis) by 1.1 degrees (y-axis).

The “plotches” (see Figure 7.22) are areas of more concentrated stray light that appear when a bright source is about 20 – 32 arcminutes off the center of the FOV, to the left or right in array coordinates. The plotches were seen in the SWIRE field near Mira and in the Beta Gru tests in channels 1, 2, and 4. The presence or absence of a plotch is very sensitive to the position relative to the bright object – a bright plotch can be present in one image and absent in an image with the telescope pointed a few pixels away. Even fainter plotches appeared in channel 2 about 1 degree away from Beta Gru, along the same directions. The rings and plotches are not corrected in the pipeline.

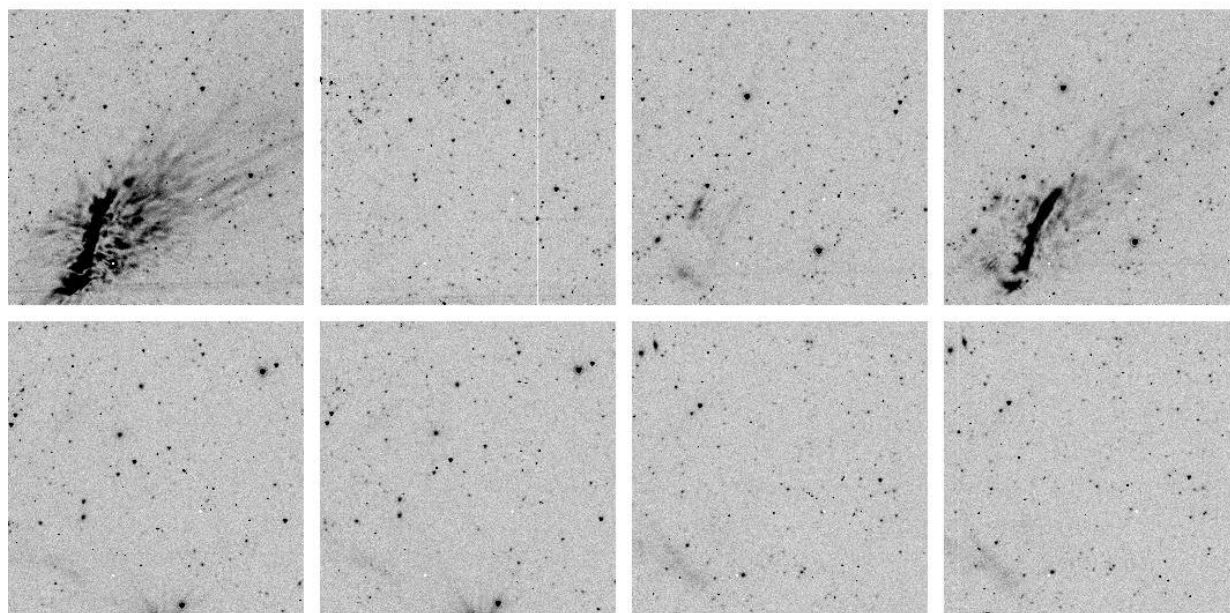


Figure 7.22: Channel 2 images from the SWIRE map showing stray light splashes from Mira, which was about 30 arcminutes away. Successive pairs of images were slightly dithered. The last pair is about 5 arcminutes from the first pair, but has a similar splotch. Note the absence of any stray light in the second image, though it was centered only a few pixels away from the first image. The images are from PID=181, AORKEY 5838336; EXPID 187 – 192, 199, and 200.

7.4 Cosmic Rays and Solar Protons

The SSC mosaicker, MOPEX, identifies energetic particle hits as follows. All pixels in BCDs that contribute to a given pixel in the final mosaic are identified, and significant outliers (a user-specified number of sigmas above or below the filtered mean of all overlapping pixels of overlapping BCDs) are rejected. This method is very similar to the outlier rejection performed by shifting and adding ground-based images. The rejected pixels can be inspected in the “rmask” output files (one per input image). Outlier rejection in MOPEX can be adjusted. The parameters used in the online pipeline-generated mosaics rely on three or more sightings of each sky pixel. In general, a coverage of at least five is necessary to produce optimal results with the multi-frame (standard) outlier rejection.

A special outlier rejection scheme can be used for sparse (2 – 4x) coverage; this “dual outlier” mode can be turned on using the namelist parameter file. Dual outlier rejection identifies pixels with flux values greater than a specified threshold above the background, groups these pixels and adjacent pixels above a threshold into objects, and compares the object to objects in overlapping frames. If the object overlaps with objects in other frames (in celestial coordinates), then it is not a cosmic ray. If the object is not detected in a user-specified fraction of overlapping images, it is

flagged as a cosmic ray. This information is written into the rmask files used for mosaicking and source extraction.

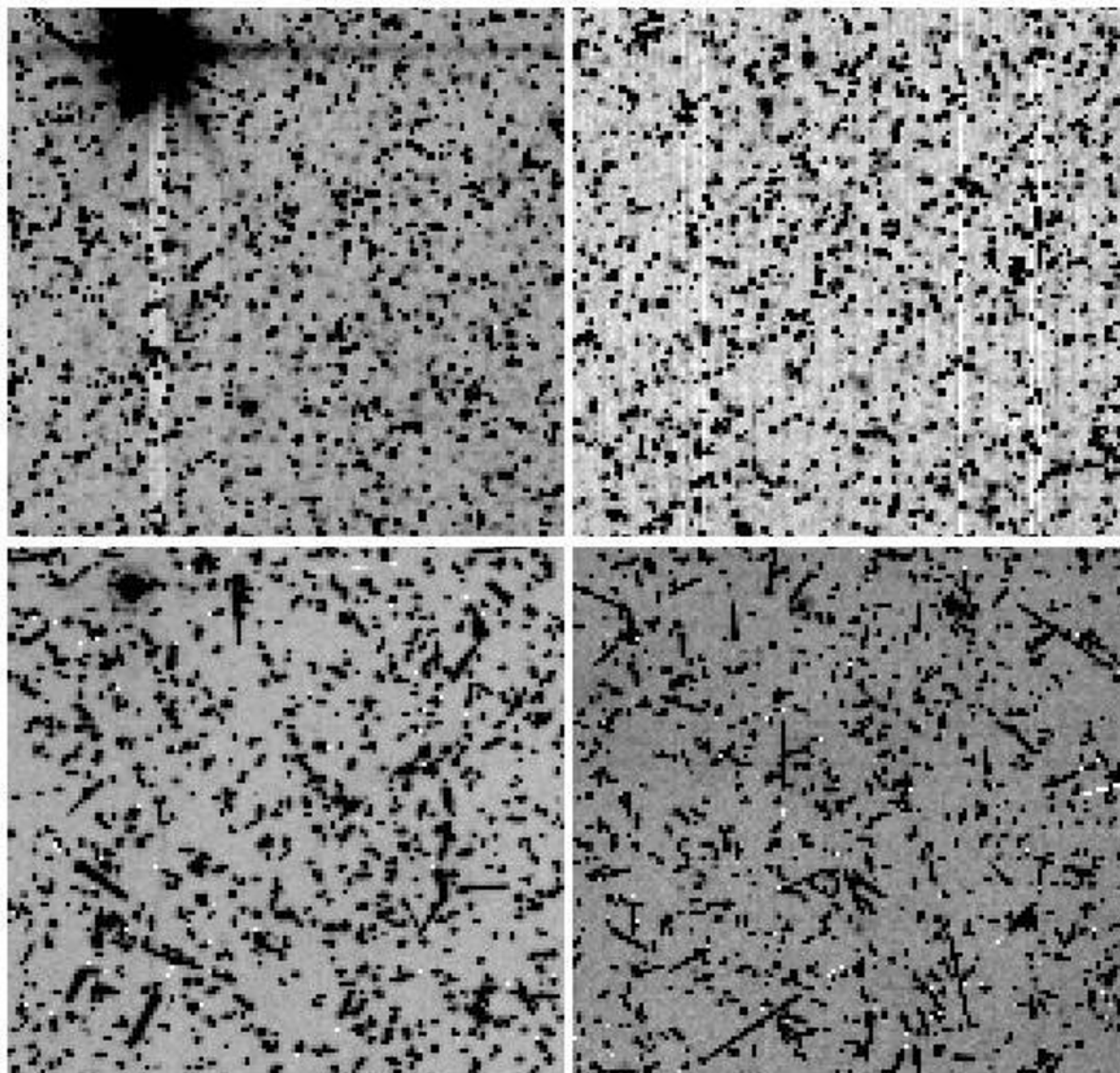


Figure 7.23: The central 128 pixels \times 128 pixels of IRAC 12-second images taken on January 20, 2005 during a major solar proton event. Channels 1 and 2 are top left and top right; channels 3 and 4 are bottom left and bottom right. Except for the bright star in channels 1 and 3, almost every other source in these images is a cosmic ray. These data are from observations in PID=3126.

The dual outlier method should also be used in conjunction with the multi-frame outlier rejection method. Multi-frame rejection may throw out data around bright sources depending on the thresholding, due to pixel phase effects between BCDs. Using the dual outlier rejection and the `REFINE_OUTLIER = 1` option in MOPEX will prevent this.

Additionally, a single-frame radiation hit detector is run and produces bit 9 in the imask, but this bit is not used by the SSC post-BCD software and is not recommended because radiation hits cannot be uniquely separated from real sources in single images.

Cosmic rays for channels 3 and 4 are larger and affect more pixels than the channel 1 and 2 cosmic rays due to the larger width of the active layer of the Si:As detectors. Some tuning of cosmic ray detection parameters may be necessary when working with deep integrations, especially for channels 3 and 4.

Each IRAC array receives approximately 1.5 cosmic ray hits per second, with ≈ 2 pixels per hit affected in channels 1 and 2, and ≈ 6 pixels per hit affected in channels 3 and 4. The cosmic ray flux varies randomly by up to a factor of a few over time scales of minutes but does not undergo increases larger than that. Also, the cosmic ray flux is normally about a factor of two higher on average around solar minimum compared with solar maximum. Radiation hits do increase suddenly and dramatically during some major solar proton events. Historically, several such events have occurred over the course of the active part of a solar cycle.

Two major solar proton events occurred during IOC, so we gained experience in identifying them and their effects. Because of shielding around the instruments, only extremely energetic protons (> 100 MeV) of any origin appeared as cosmic ray hits in the data. Thus, many solar weather phenomena (“storms,” etc.) which do occasionally affect other spacecraft, or ground systems, were not of concern to Spitzer.

Radiation had very little effect on the IRAC arrays beyond elevating the counts in a given pixel. Some high energy cosmic rays caused persistent images, column pull-down, and muxbleed effects.

8 Introduction to Data Analysis

8.1 Point Source Photometry

Please refer to Appendix B for a detailed description of how to achieve the highest possible accuracy when performing point source photometry. Appendix C summarizes the proper use of PRF fitting to obtain high accuracy point source photometry in a crowded field or in a field with highly varying background. Photometry using IRAC data is no different from that with any other high-quality astronomical data. Both aperture photometry and PRF-fitting work successfully. Aperture photometry is most commonly used, so we will discuss it briefly.

Aperture photometry measurements should be corrected by multiplying by the aperture correction, the array location-dependent correction, and the pixel phase correction. It is customary to perform the latter two corrections first. IDL functions to perform the correction for the cryogenic and warm mission data can be found at

<https://irsa.ipac.caltech.edu/data/SPITZER/docs/dataanalysis/tools/contributed/irac/iracaphotcorr/>

on IRSA's Spitzer/IRAC documentation website to apply the latter two (position dependent) corrections. You will need to measure the centroid location in addition to the aperture flux. The corrections in the IDL functions have been derived assuming first moment centroids. The link to the IDL function contains a link to a code to derive first moment centroids as well.

The improvement in data quality after applying these corrections can be significant. We show in Figure 8.1 the cumulative distribution of the flux percent difference from the mean (absolute value), for the original (BCD) and corrected data for calibration star NPM1+67.0536 (approximately 3000 data points). The corrected data have a factor of two smaller dispersion than the original data. The 68% confidence interval (1σ for a Gaussian distribution) for the original data is about 2.5% in channel 1. In comparison, the array location-dependent photometric and intrapixel sensitivity corrected data have a 68% confidence interval of about 1.4%. The corrections available earlier (now obsolete), including the radial pixel phase correction, were only about half as good at reducing the scatter in the data, with a 68% confidence interval of about 1.9%.

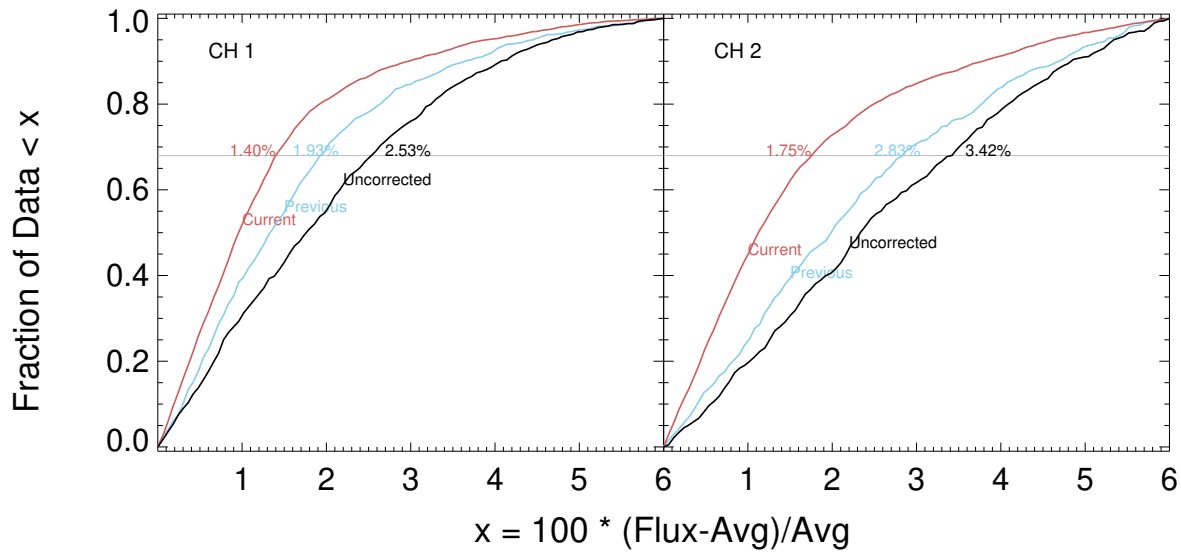


Figure 8.1: Correcting photometric measurements of calibration star NPM1+67.0536 using the pixel phase and array location-dependent corrections. Black curves show the cumulative distribution of aperture photometry measurements throughout the cryogenic mission, for which a value is within a given per cent of the mean. Blue curves show the distribution after correction using an earlier (now obsolete) set of location-dependent functions. Red curves are the result of the improved (now final) correction. A gray horizontal line at 68% (1σ for a Gaussian distribution) is labeled with the corresponding spread in values for each of the three distributions.

8.2 Extended Source Photometry

The photometric calibration of IRAC is tied to point sources (calibration stars) measured within a standard aperture with a radius of 12 arcseconds. This point source calibration is applied to all IRAC data products during pipeline processing to put them into units of MJy/sr ($1 \text{ MJy/sr} = 10^{-17} \text{ erg s}^{-1} \text{ cm}^{-2} \text{ Hz}^{-1} \text{ sr}^{-1}$). This method results in a highly accurate calibration for point sources. However, transferring this calibration to extended sources is not straightforward. The discrepancy between the (standard) point source calibration and the extended source calibration arises from the complex scattering of incident light in the array focal planes. Our best understanding is that there is a truly diffuse scattering that distributes a portion of the incident flux on a pixel throughout the entire array.

The surface brightness of extended emission in IRAC images will tend to appear BRIGHTER than it actually is. The reason for this is two-fold. First, photons that would normally scatter out of the PSF aperture used to measure a point source are instead captured by an extended source. The scattering depends on the convolution between the IRAC PSF and how the light is distributed across the focal plane, which is usually quite complex for extended sources (galaxies, ISM, and nebulae). Second, photons are scattered into the aperture from the emission regions outside the

aperture. As a thought experiment, one can imagine a single point source inside an aperture, which is easy to measure. But if four point sources are placed around it just outside the measurement aperture, each of them scatters light into the aperture, which leads to an overestimate of the real flux. For the extended source case, we can imagine the same experiment taken to the limit where all the regions have emitters in them.

For photometry of extended sources (over 1 arcminute in size), the calculated flux inside an aperture must be scaled by the ratio of the extended and point source throughputs. The scaling factors (f_p/f_{ex}) to be used are given in Table 4.8 (the infinite aperture case). Note that these are not really throughputs, in the sense that they have anything to do with the number of photons reaching the detector. It is more accurate to think of them as a special type of an aperture correction. The values in Table 4.8 are for a very extended, red source like the Zodiacal light.

The more challenging case is correcting aperture photometry of extended objects with spatial scales between a point source and the very extended case, e.g., a relatively nearby galaxy. Here the underlying surface brightness distribution of the object is important. One technique is to determine aperture corrections via a curve-of-growth from actual data. Below, a detailed analysis of early-type spheroidal galaxies (chosen because of the relatively simple light profile of these stellar-dominated sources), ranging in size from 20 arcseconds to several arcminutes, is presented. The aperture corrections may, within limits, be applied to other galaxy types. Note that the large-aperture corrections derived here are fairly close to the infinite aperture corrections of Table 4.8.

A commonly encountered problem is that of measuring the total flux of extended objects that are still smaller than the standard aperture size used for the photometric calibration. For example, the background galaxies seen in all IRAC images are often slightly extended on size-scales of a few arcseconds. PRF-fitting photometry of such objects will obviously underestimate their fluxes. One methodology for handling such sources was developed by the SWIRE project; readers are referred to the data release document for SWIRE, especially section 8.4.2, at

https://irsa.ipac.caltech.edu/data/SPITZER/SWIRE/docs/delivery_doc_r2_v2.pdf.

Detailed analysis by SWIRE has indicated that Kron fluxes, with no aperture corrections applied, provide measurements of small extended sources that agree closely with hand-measured fluxes. Kron fluxes are provided as one of several flux measures in the popular SExtractor software (Bertin & Arnouts 1996). Note that it is important to determine that an object actually is extended before using the Kron flux, as it is ill-defined otherwise. This may be determined by using the stellarity and isophotal area as defined by the SExtractor software. Selecting limits on these parameters based on their breakdown as a function of signal-to-noise ratio generally will mimic SExtractor's own auto function.

To measure *absolute* flux on large scales (sizes of order the field of view), consider all the sources of flux that go into each pixel. The IRAC images are in surface brightness units. The flux of an extended object is the integral of the surface brightness over the solid angle of the object. The value of a pixel in an IRAC BCD is the real sky value plus a contribution from the zodiacal light minus the dark current value at that pixel. The dark current value is made from observations of a low background region at the north ecliptic pole and so it contains some small amount of flux of

astrophysical origin. The darks have also had an estimate of zodiacal light subtracted from them before use. The (theoretically) estimated zodiacal light brightness during an observation is in the BCD header keyword ZODY_EST, and that for the sky dark observation is listed as SKYDRKZB. While it is possible using the above keywords to recover something similar to the absolute sky surface brightness, this brightness estimate is still limited by the accuracy of the underlying model of the zodiacal emission.

In practice, most extended source photometry will usually be performed with respect to a background region within the image (for example, large aperture photometry of galaxies, nebulae, etc.) and one does not attempt to measure the absolute sky brightness on large scales (like the zodiacal cloud). The median value of the pixels located in user-selected background regions is generally a reasonable estimator of the background.

8.2.1 *Best Practices for Extended Sources*

Resolved galaxies with apertures centered on the nucleus:

- For sources $< 8 - 9$ arcseconds in size, treat as point source (small aperture photometry, with local annular background subtraction)
- For sources $> 8 - 9$ arcseconds in size, apply extended source aperture corrections (see below).

Emission knots, embedded resolved sources

- If the source is small (compact, $r < 7 - 8$ arcseconds in size), treat as point source (small aperture photometry, with local annular background subtraction)
- If the source is large and fuzzy, use the extended source aperture corrections (see below). Beware that background structure will introduce large uncertainties ($\approx 10\%$)

Surface Brightness (pixel-to-pixel measurements)

- For very extended sources (> 300 arcseconds) or flat, low surface brightness sources (e.g., Magellanic-type galaxies), use the *maximum scaling factors* given below.

Cross-comparing IRAC images (e.g., channel 1 versus channel 4), we recommend that you first cross-convolve the images. For the example above, convolve the channel 4 image with the channel 1 PSF, and convolve the channel 1 image with the channel 4 PSF. This operation will reduce the deleterious effects of the light scattering, but will not completely eliminate them. Be very conservative in interpreting colors as surface brightness measurements can be off by 5% – 10% in the short-wavelength channels and 30% in the long-wavelength channels.

8.2.2 *Extended Source Aperture Correction*

The following aperture corrections are intended to correct the photometry of extended sources (e.g., galaxies) whose absolute calibration is tied to point sources. These corrections not only account for the extended emission from the IRAC PSF itself, but also from the diffuse scattering of the emission across the IRAC focal plane. The curves were derived from a detailed analysis of elliptical galaxies (see related notes in Section 8.2.4). The curves may be applied to all types of galaxies, but beware that significant departures can be expected for sources that are

morphologically different from elliptical galaxies (e.g., late-type LSB galaxies; see surface brightness recommendations above).

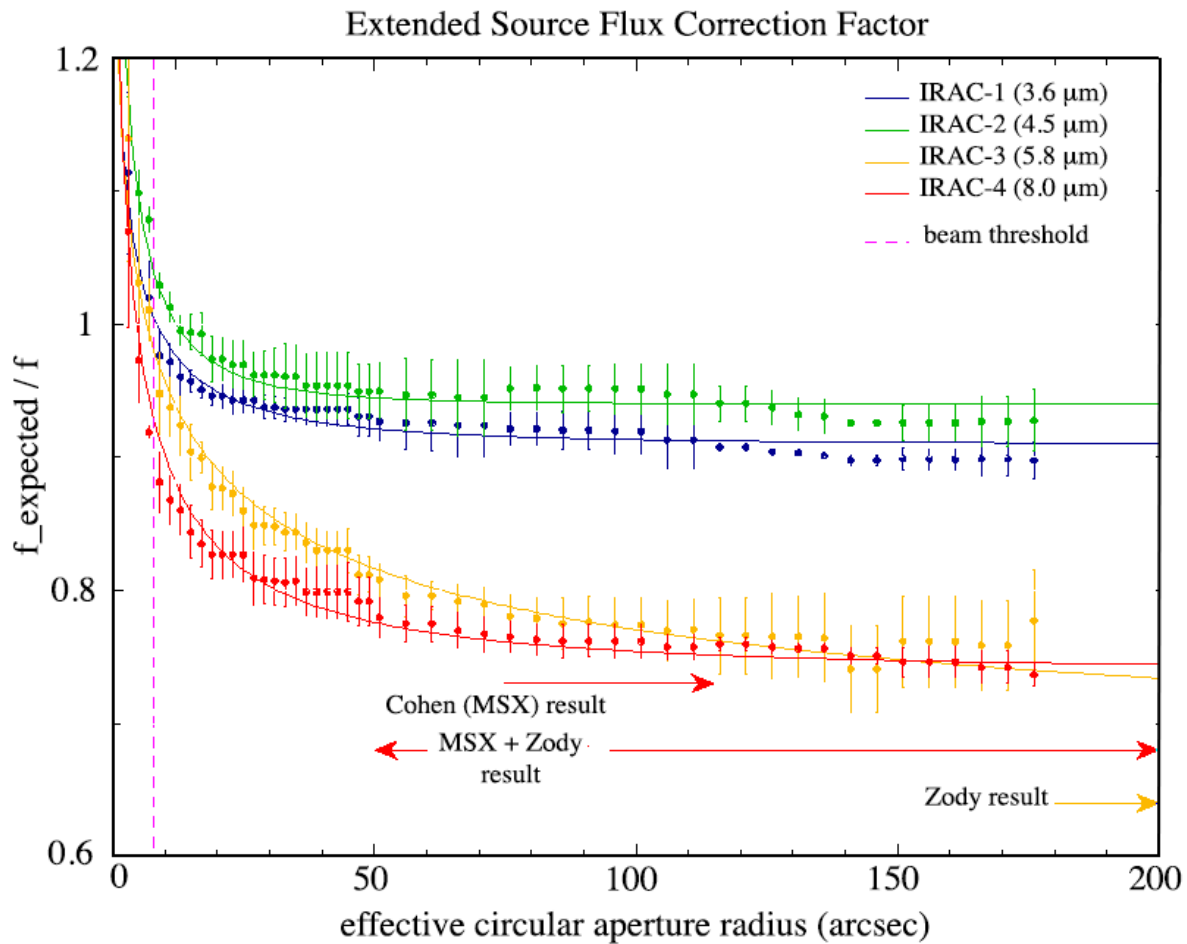


Figure 8.2: Extended source flux aperture correction factors; solid lines represent exponential function fits to the data. Also indicated are correction factors derived from zodiacal light tests, and Galactic HII region tests (e.g., GLIMPSE vs. MSX).

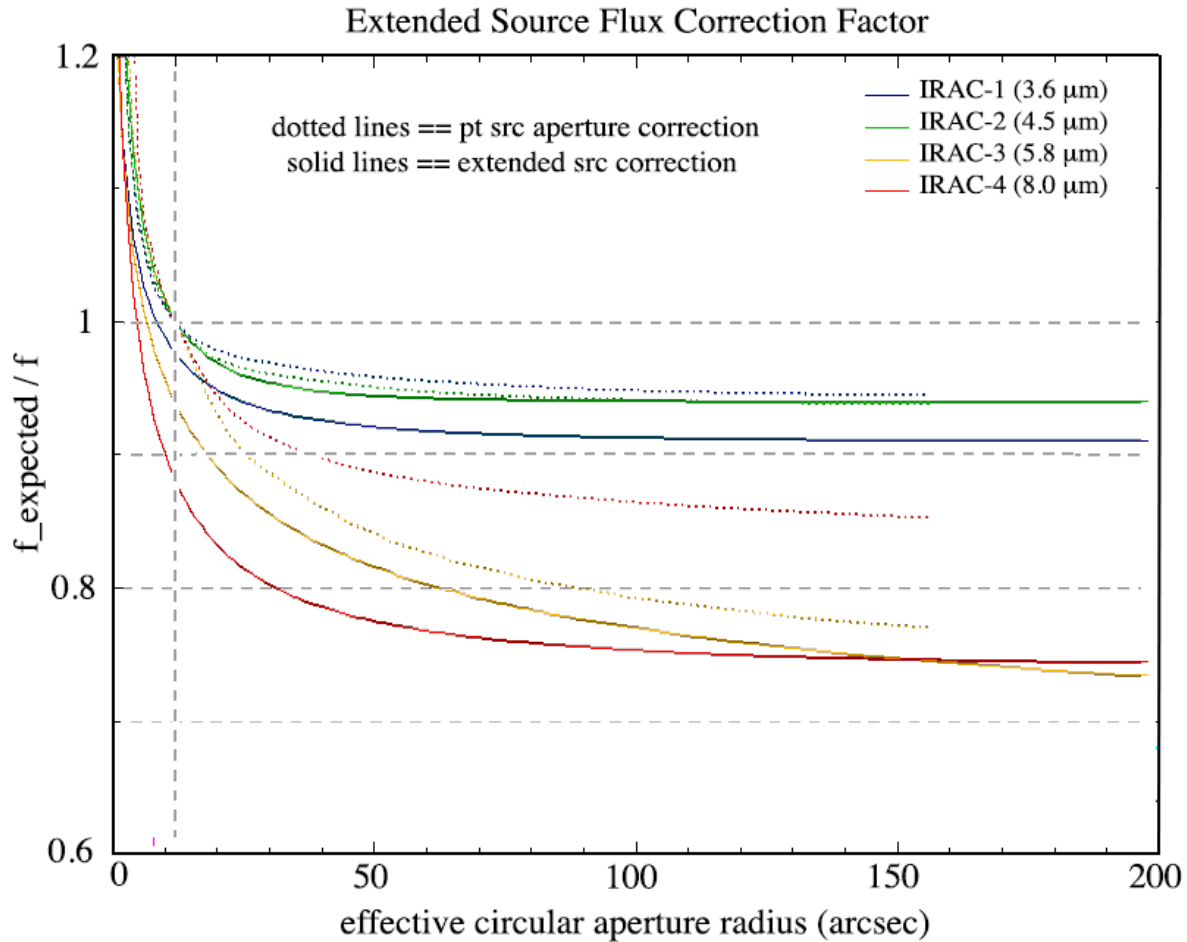


Figure 8.3: Extended source flux correction factors for galaxies (solid lines) versus the PSF aperture correction factors (dotted lines). The main difference between the two is the truly diffuse scattering internal to the array.

Aperture photometry should also include a background subtraction; we recommend that you use an annulus that is located just outside the boundary of your galaxy. Circular or elliptical apertures may be used.

The procedure for correcting extended source photometry is to apply the correction factor to the integrated flux measured from the IRAC image (subject to the standard or point source calibration). The correction factor is a function of the circular aperture radius or the effective circular aperture radius (if using ellipses). These corrections should be good to 10%. For convenience, we have converted the empirical curves into a functional form:

$$\begin{aligned}
 \text{integrated flux } (r) & \\
 &= \text{measured flux } (r) \\
 &\times \text{correction_factor } (r)
 \end{aligned}
 \tag{8.1}$$

$$\text{correction_factor}(r) = \frac{\text{true flux}}{\text{flux}} = A \times e^{-\text{radius}^B} + C \quad (8.2)$$

where radius is in arcseconds, and A, B, and C are the best fit coefficients tabulated below:

Table 8.1: IRAC extended source photometric correction coefficients.

Channel	A	B	C
3.6 μm	0.82	0.370	0.910
4.5 μm	1.16	0.433	0.94
5.8 μm	1.49	0.207	0.66
8.0 μm	1.37	0.330	0.740

The coefficient C represents the infinite, asymptotic value.

8.2.3 Low Surface Brightness Measurements and the Maximum Scaling Factors

Photometry of diffuse emission or low surface brightness objects is also subject to a large calibration correction in the IRAC 5.8 and 8.0 μm channels. The way to think about flat extended objects is that any aperture you use to measure the integrated flux (or surface brightness) is equivalent to an infinitely large aperture applied to a point source (or galaxy). Hence, the appropriate aperture correction (or equivalently, surface brightness factor) is the large radius case of the above aperture corrections:

Table 8.2: IRAC surface brightness correction factors.

Channel	Surface Brightness Correction Factor
3.6 μm	0.91
4.5 μm	0.94
5.8 μm	0.66–0.73
8.0 μm	0.74

Surface Brightness = measured surface brightness * correction_factor, where the correction factors represent the infinite aperture value. Note that for IRAC channel 3 the recommended correction is somewhere between 0.66 and 0.73, depending on the downward curvature of the aperture corrections (which is highly uncertain). These aperture corrections should be good to 10%. Low surface brightness objects include large, late-type galaxies such as NGC 300, Magellanic-type galaxies such as NGC 6822, diffuse dwarf galaxies, such as M81 DwA, and HII regions that are larger than ≈ 100 arcseconds but not very centrally condensed.

8.2.4 Caveats & Cautionary Notes

At small radii, $r < 7 - 8$ arcseconds, the extended source aperture corrections should not be used. Instead, we recommend using the point source aperture corrections for small radii.

It remains uncertain how much the spectral shape of the extended object determines the flux corrections; the aperture corrections presented here were derived using relatively old spheroidal galaxies. To first order, the extended source aperture corrections apply to most types of galaxies.

Likewise, with the spectral color caveat, it remains uncertain how much the spatial distribution of the light determines the flux corrections; these corrections were derived using relatively high surface brightness spheroidal galaxies; it is unknown whether these corrections apply to lower surface brightness galaxies (e.g., late-type spirals, irregulars, Magellanic-types).

8.2.5 Faint Surface Brightness Behavior

Note that the discussion in this section applies only to warm mission IRAC data. For more detailed information, please see Krick et al. (2011).

8.2.5.1 Binning

Binning data by essentially making larger “pixels” should reduce the noise in the image linearly with binning length. Figure 8.4 and Figure 8.5 show a plot of noise versus binning length for a set of deep mapping data in the Virgo cluster (PID 60173). These data have been carefully corrected for the first-frame effect (See Section 7.1) using the data themselves. The measured noise does not achieve the expected linear relation with binning length, as elaborated in the following subsections.

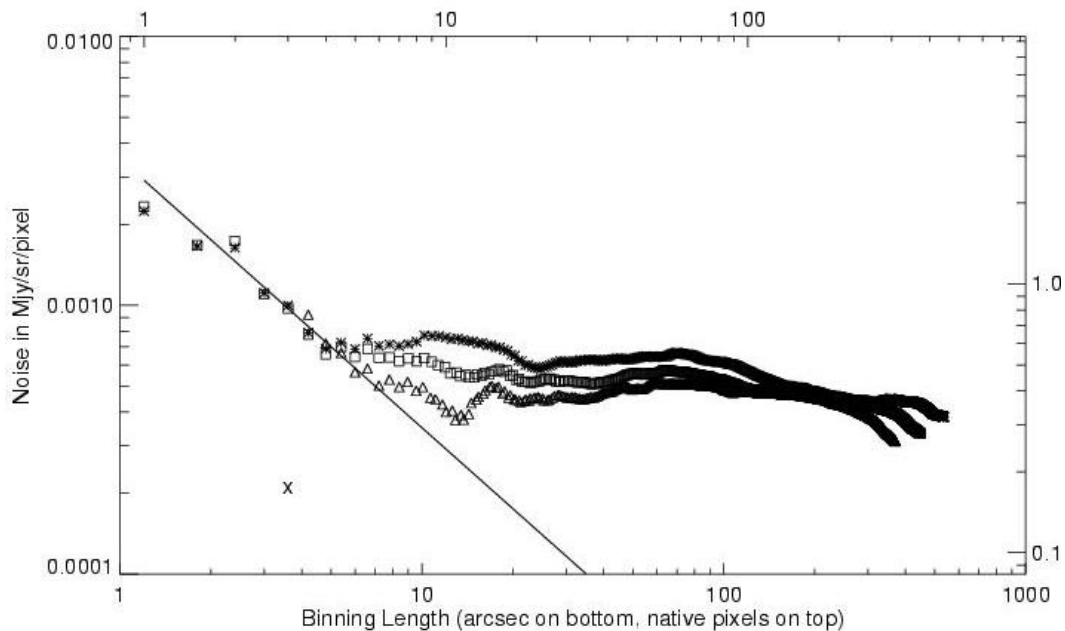


Figure 8.4: Noise versus binning length in channel 1. To make this plot, the surface brightness was measured in nine regions across an object-masked mosaic. These regions are not near bright galaxies, stars, or diffuse plumes. The noise is defined as the standard deviation of those nine regions. The box size is incrementally increased until the box length is many hundreds of pixels. For reference the solid line shows the expected linear relation.

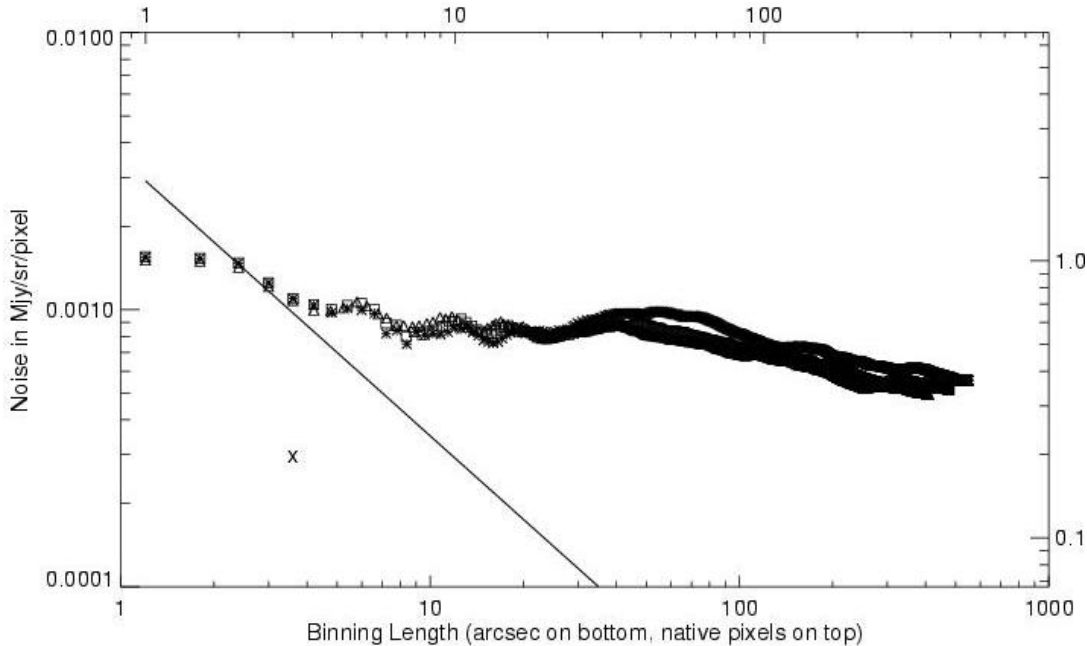


Figure 8.5: Similar to Figure 8.4 but for channel 2.

8.2.5.2 *Small Scales*

There is a discrepancy between the expected linear behavior and the data at short binning length scales of just a few pixels or a few arcseconds (mosaics only). This discrepancy occurs because we have correlated noise on a mosaicked image on small pixel scales (a few pixels), so the noise does not bin down appropriately.

8.2.5.3 *Medium Scales*

On 5 – 30 arcsecond scales much of the extra noise is due to sources in the image. The first level of masking used the SExtractor segmentation map as a mask. The resulting noise properties are shown with asterisks. Increasing the size of the masks to 1.5 (2.0) times the SExtractor-determined object radii produced noise properties shown with a square (triangle) symbol. Further increases in mask size are inconsequential. The discrepancy between the observed and expected behaviors in this binning length regime is dominated by noise from the wings of galaxies that are improperly masked. Even after increasing the mask sizes, extra sources of noise remain which prevent detection of ultra-low surface brightness. There appears to be a floor to the noise at roughly 0.0005 MJy/sr at 3.6 μm and 0.0008 MJy/sr at 4.5 μm .

8.2.5.4 *Large Scales*

Some of the large-scale (a few arcminutes) noise is caused by the mapping pattern used for the observations. On scales of roughly half a field of view there are differences in the total exposure time and hence the total number of electrons detected (not a dominant source of noise). There are remaining sources of noise on the large scales, both instrumental and astronomical, which are very hard to disentangle. Uncertainties in the flat-fielding and removal of the first frame effect are two instrumental effects that are contributing to the noise on large scales. The first-frame effect has a

column-wise dependence that requires special calibration data to measure. Astrophysically, there is real structure in the zodiacal light and Galactic cirrus. There is also documented diffuse intracluster light in the Virgo cluster itself, and a small signal from the extragalactic background light that are both adding to the noise at low levels. There is potentially also noise due to the blue infrared color of intracluster light, while the zodiacal light from which the flats are made is red in near-IR (see Section 4.2). Differentiating between all of these sources of noise is difficult.

8.2.5.5 Increasing exposure time

The IRAC dark field was used to study whether the noise decreases with the square root of exposure time, as expected. The dark field has extremely low zodiacal light and low Galactic diffuse emission. Using all the warm mission dark calibration data through 2010, a mosaic was made from 300 dark frames (each with a 100 second frame time). Object masking was made with the SExtractor segmentation image. The noise on the distribution of pixel values is the standard deviation of the Gaussian fit to that distribution. Each distribution has > 750 pixels in it. For comparison the same analysis was performed on the dark field mosaics from the first year of the cryogenic mission. The results from both are in Figure 8.6 and Figure 8.7.

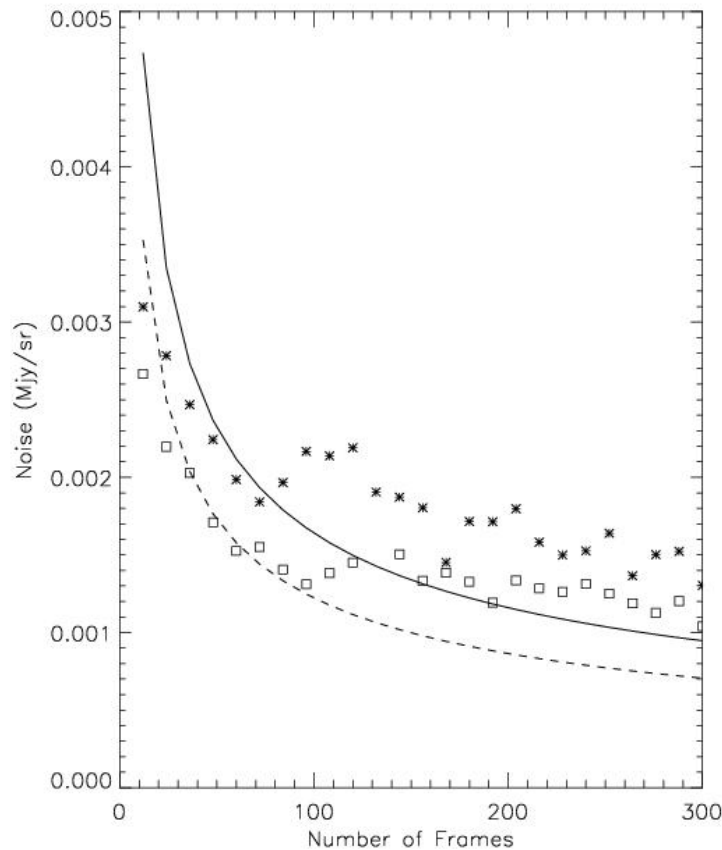


Figure 8.6: Noise as a function of exposure time (number of frames) in channel 1. The results from the warm mission data are shown with crosses and the expected behavior with the solid

line. The results from the cryogenic mission are shown with open squares and the expected behavior with the dashed line.

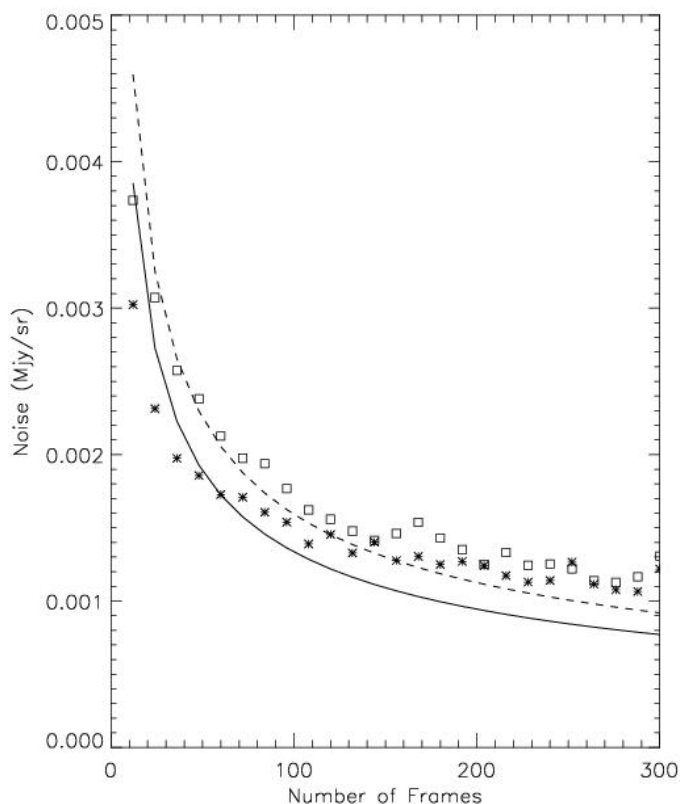


Figure 8.7: Similar to Figure 8.6 but for channel 2.

These plots show that background noise in IRAC channels 1 and 2 does decrease roughly as expected with exposure time. The slight deviation at larger exposure times is likely caused by the first-frame effect (Section 7.1) and by residual source wings.

8.3 IRAC High Precision Time Series Photometry

The goal of time series photometry is to produce a light curve of an astronomical source. The main challenge in producing light curves for systems whose intrinsic variations represent a small fraction (<1%) of the source average flux is to reduce or remove time-correlated noise and achieve photon-noise limited precision over all temporal binning scales. This section presents our best understanding of the sources of correlated noise and their mitigation, and recommendations for reducing time series data.

8.3.1 *Time-Correlated Noise*

Data reduction for time series is challenging due to both instrumental and astrophysical effects. This subsection focuses on the known instrumental effects which prevent observers from achieving Poisson noise limited light curves from IRAC data.

The relative strengths of instrumental systematics are shown in Figure 8.8 (Krick et al. 2016), and discussed in this section. We plot all known noise sources in units of electrons as a function of binned number of frames on the bottom and averaged minutes on the top, assuming 2 second frame times. This figure includes the Poisson contribution from an assumed source at half-full well as the solid diagonal black line, and the background noise, along with the readout noise, as the solid diagonal gray lines. The level of the intrapixel gain effect for both channel 1 and channel 2 are shown as the top horizontal gray lines (intrapixel gain effect is sometimes referred to as the “pixel phase” effect in literature and the effects for channels 1 and 2 are labeled “Pixphase” in the diagram). An estimate of the level of uncertainty caused by bias pattern effects and persistent images (latents) is indicated with dashed gray lines. We show the rough levels expected for a hot Jupiter transit, eclipse, and a 70 ppm super-Earth transit event.

The strongest instrumental effect in the warm mission IRAC is the under-sampled PSF coupled with gain variations within a single pixel, also known as the intrapixel gain (sensitivity) effect. When combined with random pointing fluctuations and systematic drifts, this becomes the largest source of noise in time-series measurements. In subsection 8.3.2 we discuss the ability of the Spitzer spacecraft to hold its position. A separate concern is pointing repeatability (subsection 8.3.3), where we have deliberately localized the pointing fluctuations to a single pixel. Once the spacecraft is able to repeatedly point to a single position, it was possible to map out intrapixel gain variations (subsection 8.3.4) for one particular pixel on each IRAC array. We review a number of additional potential sources of noise in time-series data, such as residual non-linearity (subsection 8.3.5), time-varying detector bias (subsection 8.3.6), pointing drifts (subsection 8.3.7), and persistent images (subsection 8.3.8). Techniques for removing correlated noise (subsection 8.3.9) are then discussed. We also address methods for measuring the improvement in photometry (subsection 8.3.10) achieved by removing correlated noise.

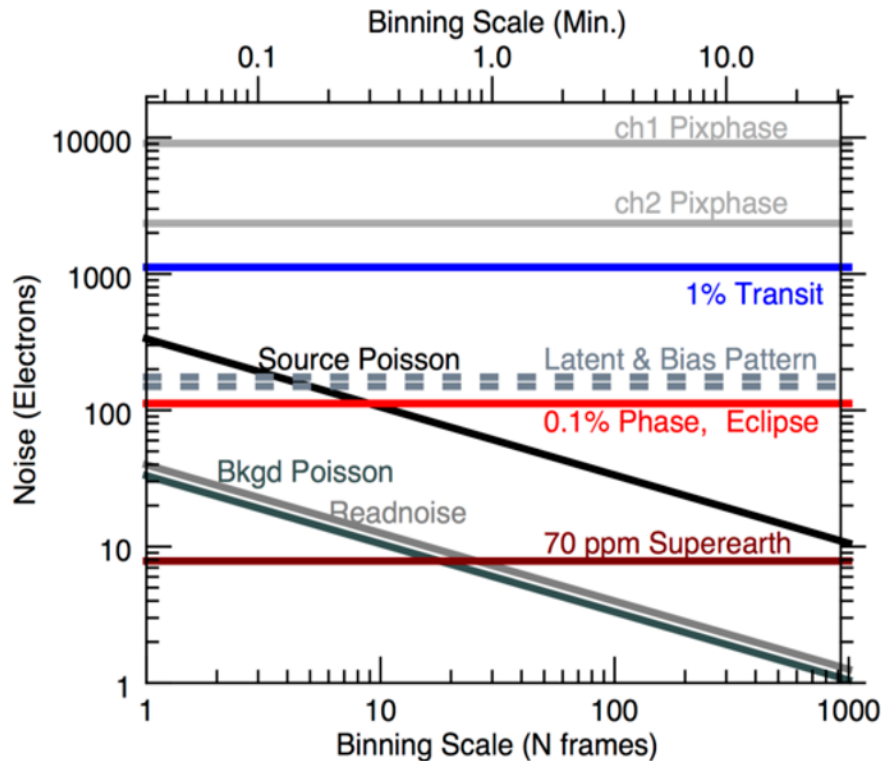


Figure 8.8: Noise in electrons as a function of binning scale showing the relative strength of instrument systematics. Noise contributions from the source and background are shown as diagonal lines. Known instrumental systematics are shown as horizontal lines. For reference, also shown are the strengths of a hot Jupiter (1%) transit, 0.1% eclipse, and a 70 ppm super-Earth transit.

8.3.2 Spacecraft Motion

Motion of a target across the detector array can be caused by spacecraft-induced motions including drifts, wobble, and jitter. Section 4.12 describes these effects in detail. Here we give a basic summary.

Settling drifts on the order of 0.5 arcseconds over the course of half an hour after slewing are thought to be due to variable heating and cooling within the spacecraft bus. The resulting small temperature changes cause very slight changes in the alignment between the star trackers and the boresight of the telescope. The temperature changes themselves are thought to be caused by heating of the spacecraft bus when the telescope is observing (or communicating with Earth) at relatively large pitch angles, and radiative cooling when the pitch angle returns to less than ± 10 degrees. Depending on the amount of time spent at such high pitch angles, the spacecraft may require anywhere from hours to days to reach a temperature equilibrium.

On top of the initial settling drifts, there is a roughly constant, long-term drift (see Section 4.12.4.2) of 0.34 arcseconds per day in the y -pixel direction. This drift is thought to be due to an inconsistency in the way that velocity aberration corrections are handled by the spacecraft's Command and Data Handling computer (C&DH) and the star trackers. Whereas the C&DH assumes that velocity aberration is constant over the course of each AOR, the star trackers update the velocity aberration corrections continuously. The result is a constant error signal sent by the star trackers, for which the spacecraft constantly attempts to correct.

A second thermally-induced pointing drift is an oscillating “sawtooth” motion in both x - and y -pixel directions (also known as “wobble”; see Section 4.12.4.3). This is thought to be due to thermo-mechanical expansions and contractions of many of the same spacecraft components as above, motivated here by the periodic, on-off cycling of a battery heater within the spacecraft bus. The amplitude of the sawtooth was ≈ 0.15 arcseconds, with a period of about an hour. To reduce the amplitude of the oscillation and move the period away from the typical durations of exoplanet transits, the cycling range was reduced to 1 K on 17 October 2010. Data taken since that time show a sawtooth amplitude reduced by a factor of two, with a period of 39 ± 2 minutes.

Jitter (see Section 4.12.4.1) has both high frequency (> 50 Hz) and low frequency (≈ 0.01 Hz) components, with peak-to-peak amplitudes ranging from 0.03 to 0.1 arcseconds. Possible causes are many, and may include noise in the star tracker solutions, momentum variations in the reaction wheel assembly, harmonically coupled to the spacecraft structure, and even micrometeoroid impacts. High frequency jitter will presumably continue to set a noise floor for bright targets.

8.3.3 Repeatability Pointing

8.3.3.1 “Sweet Spot”

The first step towards reducing correlated noise is to localize the sub-pixel position of a point source on an area of minimal sensitivity (gain) variation. We have defined the “sweet spot” region of each array to be the 0.5-pixel square surrounding the point of maximum response in the subarray field of view center pixel (pixel [15,15] in [0,0]-based coordinates). Specifically, the sweet spot peak is at [15.198, 15.020] in channel 1 and [15.120, 15.085] in channel 2. To place the target on the sweet spot we used the PCRS function on Spitzer (see Section 3.2 for more information about the PCRS Peak-Up).

8.3.3.2 Why This Sweet Spot?

As shown in Figure 8.9, the peak pixel response in channel 2 is not at the center of the pixel. Also, note the 0.2% variation in gain around this peak for a typical pointing wobble, plus a drift of about 0.2 pixels, whereas the same motion would result in 1% gain variations closer to the corner of the pixel. Keeping a target within the sweet spot minimizes correlated noise.

Furthermore, the sweet spot of each array has been targeted by the IRAC team as a region for special calibration. Many thousands of photometric measurements of non-variable stars have been made in an effort to build a high spatial resolution, low noise map of intrapixel gain. Kernel

regression techniques can be used to reduce correlated noise and provide an independent check on other noise reduction techniques.

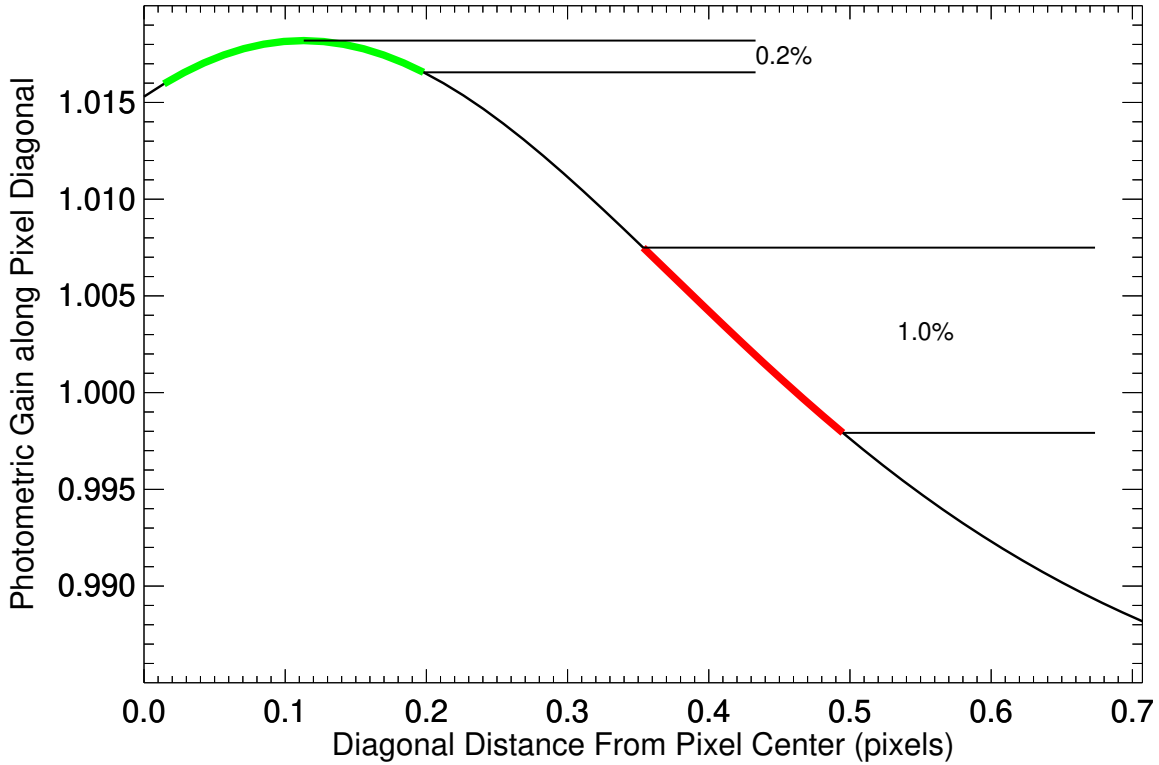


Figure 8.9: Channel 2 photometric gain versus diagonal sub-pixel position, based on a crude Gaussian model of the pixel. The vertical ranges show the amount of gain variation over about 0.2 pixels at the peak of gain (green) and near the corner of the pixel (red).

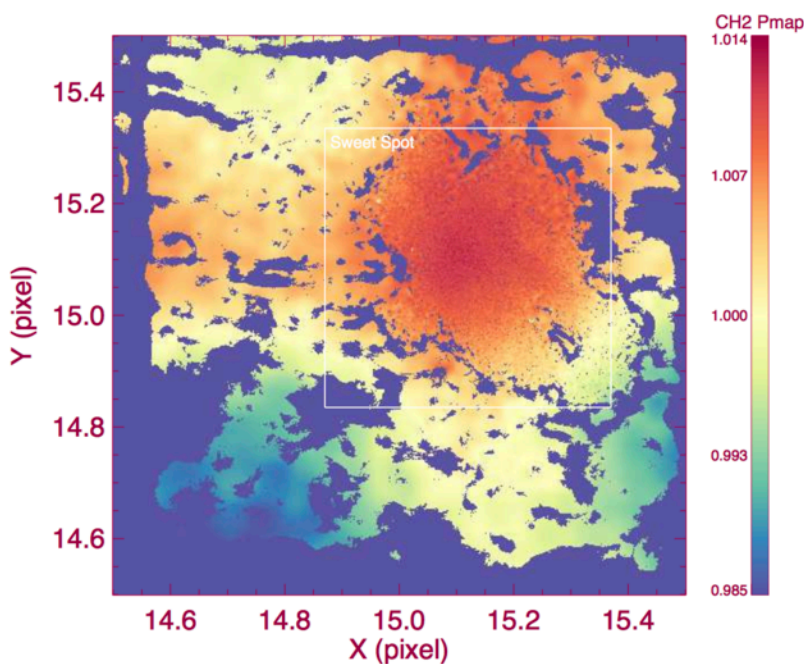


Figure 8.10: The map of intrapixel photometric gain, or “pmap” for channel 2 post-cryogenic data. This is the pmap built from data collected as of 2014/09/04. Note that gain is not symmetric around the center of the sweet spot and that the peak is not at the nominal center of the pixel.

8.3.4 Mapping Intrapixel Gain

Due to the undersampled nature of the PSF, the warm IRAC arrays show variations of as much as 8% in sensitivity as the center of the PSF moves across a pixel due to normal spacecraft motions. These intrapixel gain variations are the largest source of correlated noise in IRAC photometry. Many data reduction techniques rely on the science data themselves to remove the gain variations as a function of position. The IRAC team has generated a high-resolution gain map (called the “pmap”; see Figure 8.10) from standard star data, which can be used as an alternative when reducing data.

8.3.4.1 Centroiding

Finding accurate centroids for photometry is critical because it determines how much flux gets into the aperture. Systematic offsets from the measured centroid to the real centroid cause biases in photometry. Centroiding accuracy appears to be dependent on both the measurement technique and the geometric effects due to the location on the pixel. Measurement techniques include center of light, Gaussian fitting, and least asymmetry. The geometric effect of shifting flux into neighboring pixels generates the dependence on pixel location. If you are using the gain map provided by the IRAC team, it is important to use the same centroiding method (`box_centroider.pro` on IRSA’s Spitzer Contributed Software website, linked from `irac_aphot_corr.pro`) as was used for the gain map for consistency.

8.3.4.2 Noise Pixels

The number of noise pixels (see Section 2.2.2 for definition) is a measure of the apparent size of the image. Specifically, it is the equivalent number of pixels whose noise contributes to the flux of a point source. This quantity is useful as a parameter in removing the systematics of motion across a pixel over the course of a staring mode observation.

Summing over all pixels i , the intensity of each pixel is $I(i)$, so that the noise pixel is the sum of the intensity squared divided by the sum of the squares of the intensity. The same measure can be split into its directional components, $XFWHM$ and $YFWHM$.

$$\text{Noise pixels} = \frac{\sum I(i)^2}{(\sum I(i))^2} \quad (8.3)$$

$$XFWHM = 2 \times \sqrt{2 \times \log_2 2} \times \sqrt{\left[\frac{\sum (x(i) - x_0)^2 \times I(i)}{\sum I(i)} \right]} \quad (8.4)$$

$$YFWHM = 2 \times \sqrt{2 \times \log_2 2} \times \sqrt{\left[\frac{\sum (y(i) - y_0)^2 \times I(i)}{\sum I(i)} \right]} \quad (8.5)$$

These values do vary with the size of the regions used to do aperture photometry. If you are using these values with the gain map dataset, it is imperative that you calculate noise pixels and $XFWHM$ and $YFWHM$ in the same way as `box_centroider.pro` (available on IRSA's Spitzer/IRAC web pages in the Calibration and Analysis Files section, warm mission intrapixel sensitivity corrections). That code uses an aperture radius of 3 pixels and a background of 3 – 7 pixels. Preliminary indications are that using the `pmap` with x , y , $xyFWHM$ is not more effective than x , y , noise pixels.

Noise pixel values have a range 4 – 8 depending on the location on the pixel, and which pixel the target falls on. There is no evidence that the PSF itself changed during the Spitzer mission.

We do see evidence for the number of noise pixels being correlated with exposure time (see Figure 8.11). Using all of the staring mode AORs in the warm mission archive through June 2017 (\approx 1300 AORs), we see a statistically significant change in noise pixels with exposure time.

A few times over the course of the mission, the number of noise pixels has been seen to sharply increase in value for a short duration (\approx 30 minutes) before returning to normal (see Figure 8.12, at 16 and 30 hours). Figure 8.12 shows simulated data instead of archival data to demonstrate that we can successfully replicate noise pixel spikes, and therefore have a better understanding of their cause. See Appendix Section D.1.4 for a discussion of noise pixel spikes.

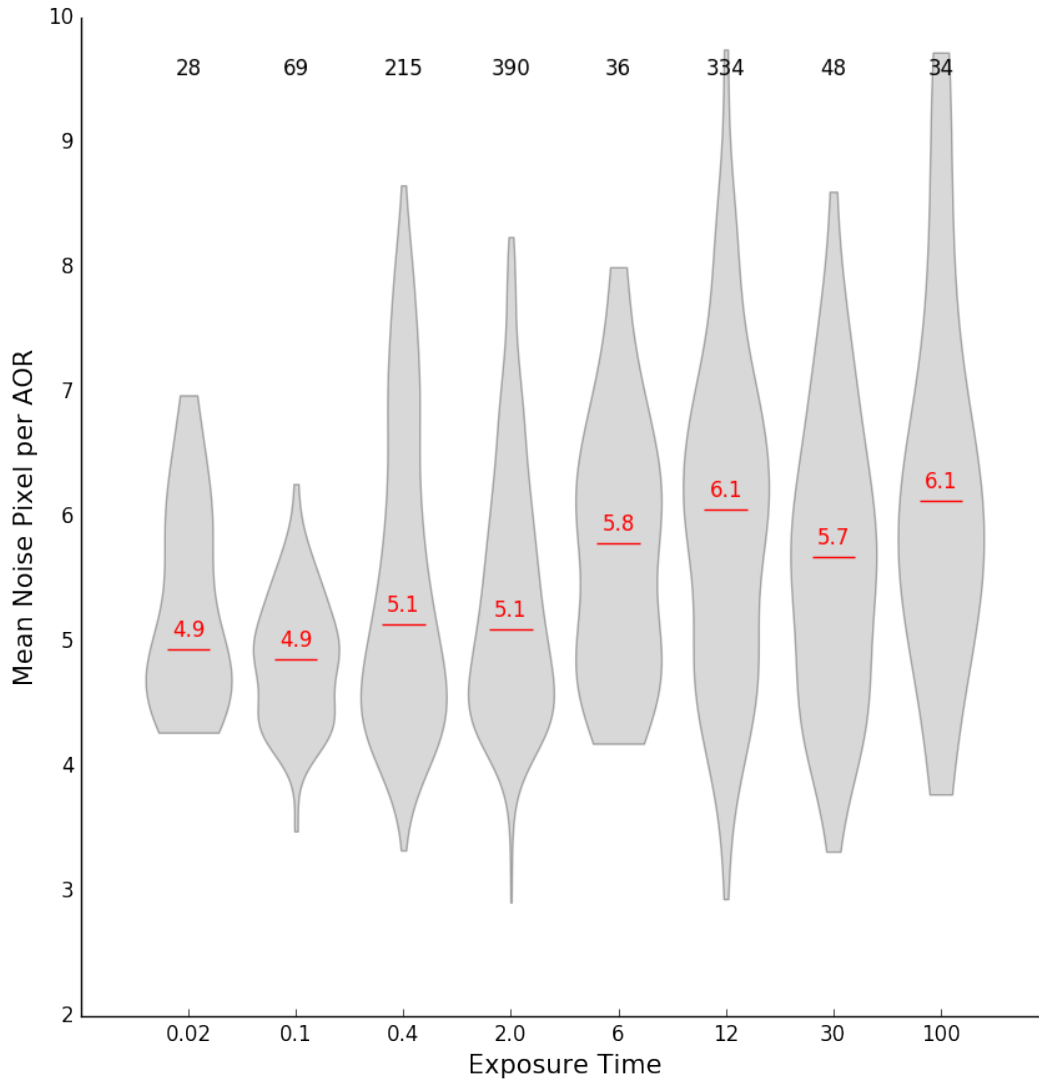


Figure 8.11: Distribution of average noise pixels per AOR vs. exposure time. All ≈ 1300 staring mode AORs from the warm mission through June 2017 were used. Each of the gray shapes represents the distribution for the corresponding exposure time. Red lines show the median value per exposure time and are marked with that median noise pixel value. The total number of AORs per exposure time bin is printed at the top of the plot. We use 3σ clipping to remove outliers, such as those that fell far away from the sweet spot.

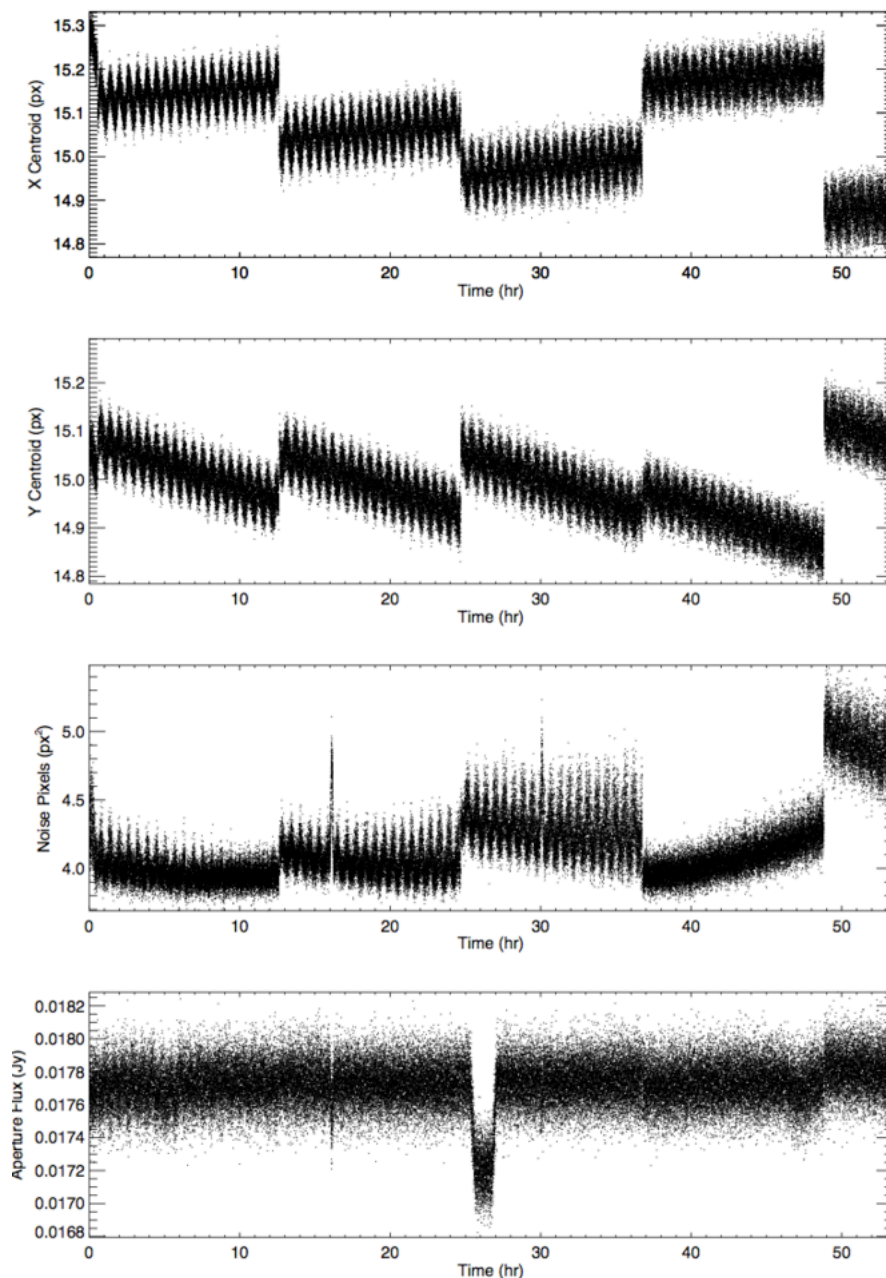


Figure 8.12: x , y , noise pixels, and flux values as a function of time over five simulated AORs. Note the noise pixel spikes at 16 and 30 hours which are seen in the noise pixel and flux plots, but not in the x and y position plots. This simulated dataset is of WASP 52.

8.3.4.3 *Optimal Aperture Size*

There is an optimal aperture size to use which is bound on the small side by wanting to include enough target flux and on the large size by the exclusion of too much background noise. The optimal size varies from observation to observation and must be tested for each dataset.

One way to determine the optimal aperture size is to look at a plot of signal-to-noise ratio (SNR) versus aperture size radius for a range of aperture sizes around the known FWHM of the IRAC PSF (≈ 1.7 pixels). It is also informative to look at a plot of just the noise as a function of aperture

size. Figure 8.13 shows this for one example data set from the archive. A plot of sigma vs. aperture size is the inverse of Figure 8.13 where the noise decreases from aperture sizes 1.5 pixels until about 2 pixels, where it holds roughly steady until 2.75 pixel radius and then starts slowly increasing. We use gain map corrected SNRs, otherwise the uncertainties are dominated by the gain variations and not by the aperture size. In this case the signal is the mean corrected flux over the whole staring mode AOR, and the noise is the standard deviation of those corrected fluxes over the whole stare. The optimal aperture size for this target would be 2.25 pixels because that is where the SNR is highest and the uncertainties the lowest. Smaller aperture sizes do not include enough of the target star flux and larger aperture sizes include too much of the background and its associated uncertainty.

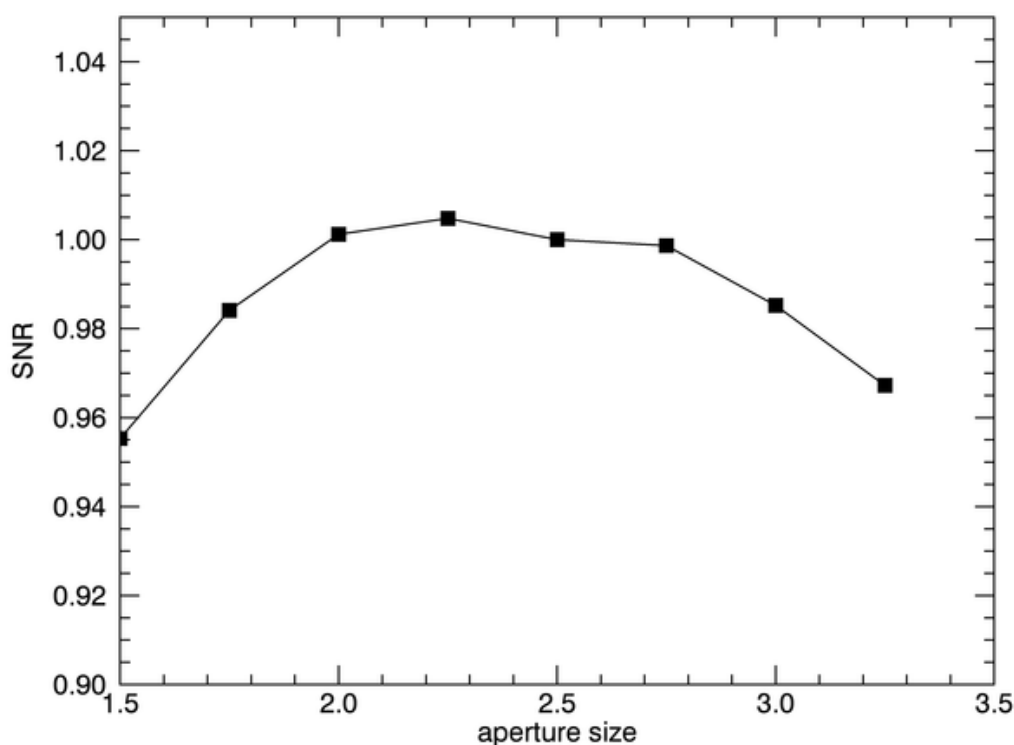


Figure 8.13: Signal-to-noise ratio versus aperture size for the WASP-14b exoplanet, normalized to an aperture size of 2.5 pixels in radius.

8.3.5 Residual Nonlinearity

In certain regimes, the IRAC detectors are nonlinear such that a given increase in the flux of incoming photons does not lead to a linear increase in the electron count rate measured by the detectors and electronics (see Section 2.3.2 for a discussion of IRAC detector linearity). The pipeline corrects for the effects of this nonlinearity on BCD pixel values, however, this correction is only good to 1%, depending on well depth. High precision photometry studies that want to use the gain map taken at one fluence (accumulated electron counts or well depth, often measured using analog-to-digital data number or DN at the pixel of peak response to a star; fluence in DN is

proportional to the total electron counts) to correct science data taken potentially at another fluence level may be sensitive to variations in the uncorrected “residual nonlinearity.” We document the existence of this residual nonlinearity, and show that as long as the observations stay between 1000 and 15000 DN (in channel 2), it does not seriously affect flux as a function of position on the pixel.

On both panels of Figure 8.14 we see a nonlinear relation between the amount of input counts (DN) and the measured flux. These are two different data sets that were designed to look at this relation by changing either the exposure time on the same star using IERs (a) or changing the exposure times on a set of stars using AORs (b). Both datasets have already been corrected by the pipeline nonlinearity. Anything that is not a flat line in these plots is a residual nonlinearity.

However, the existence of residual nonlinearity does not appear to affect the shape of the gain map (pmap) as a function of gain. We show this as a plot of peak pixels in DN vs. distance from the center of the sweet spot (D_{sweet} ; Figure 8.15). The DN in the peak pixel decreases, as expected, with larger distance from the center of the sweet spot. The shape of this falloff is not symmetric around the center, and therefore leads to an envelope of points in Figure 8.15. Each color in this plot represents a different star with a different peak pixel DN level, where each star has been normalized to the center of the sweet spot. The fact that these envelopes are all of the same shape and overlap on the normalized plot indicates that the pmap does not have a different shape depending on DN. Therefore, residual nonlinearity does exist, but is not changing the shape of the pmap.

This probably works because most of the stars tested in Figure 8.15 have DN's in the range of 10000 to 25000 where the Fowler-sampled count rates have been sufficiently linearized. As seen in Figure 8.14, the slope of residual nonlinearity does not change for this range of DN's. That slope is already incorporated into the pmap because the pmap star has a source DN which varies significantly as a function of position, so the pmap is made with some degree of residual nonlinearity built into it. This makes the shape of the gain map the same for all the DN's in the “good” range.

Proof that this is a good plot to use to understand the effect of the residual nonlinearity comes in the second part of Figure 8.15. To see this best, we have plotted only the pmap 3000 DN observations and HD 158460 28000 DN observations. The observations at 28000 DN have a different slope to the top envelope that we do not see in any of the other observations in the more linear regime.

These results imply several things. First, the gain map can be used to correct photometry in the good DN range. Second, pixel level decorrelation (PLD) can be used with the gain map dataset coefficients to correct other photometry in the good DN range. Third, it should be ok to add other datasets to the gain map data set to fill in coverage, although this has not been tested. And fourth, distance from the sweet spot should be used carefully in all analysis tasks.

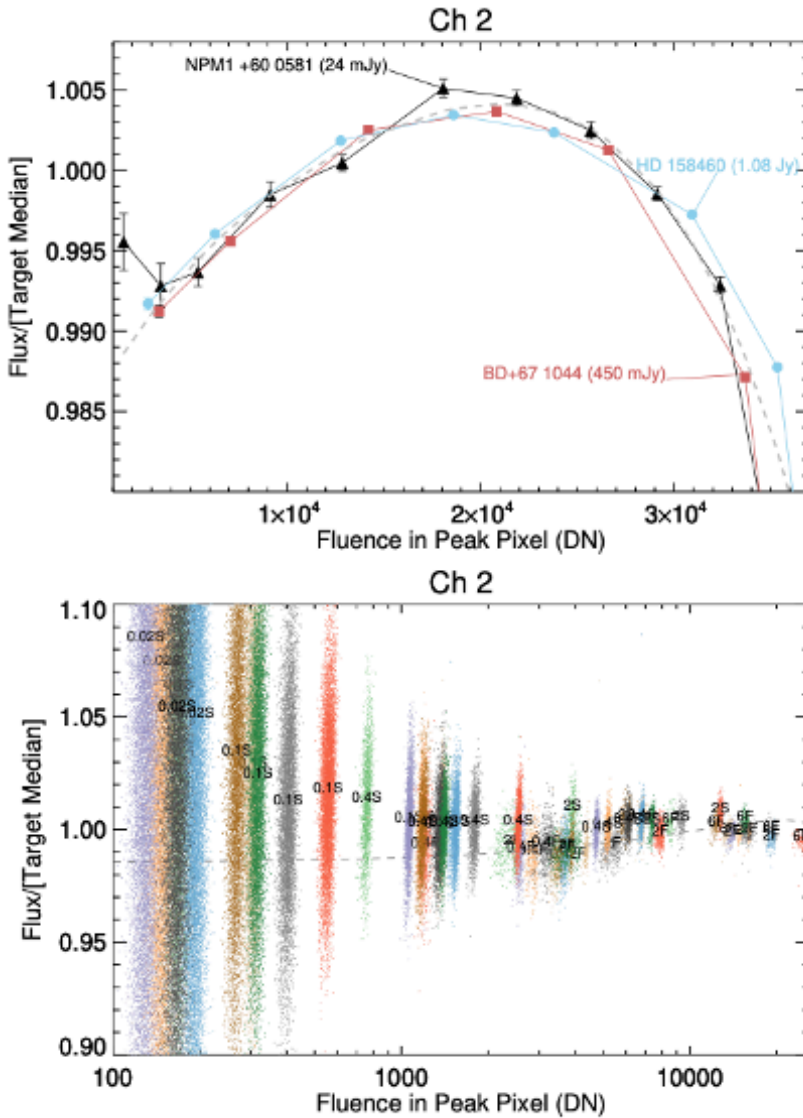


Figure 8.14: Residual nonlinearity in warm mission channel 2 data. These plots show linearity-corrected aperture flux as a function of well depth (fluence) for a set of targets, measured on the “sweet spot” of Channel 2. Top: binned aperture flux measurements of three targets, normalized to the median of each target. Well depth was varied using instrument engineering requests (IERs) to vary the frame time and corrected with special dark frames obtained the same way. Data were binned by frame time. A 4th order polynomial fit to the data is overlaid as a dashed curve. Names of the stars are labeled, along with average flux densities. Bottom: Unbinned aperture flux vs. fluence data for 15 additional stars measured using AORs, color-coded by star. Frame times are labeled (in seconds) at the location of the median flux and fluence for a given frame time and star, with the qualifier “S” or “F” to denote full or sub-array readout mode. For comparison, we have overlaid the fit from the top plot. Measurements with perfectly corrected nonlinearity should lie on a straight horizontal line.

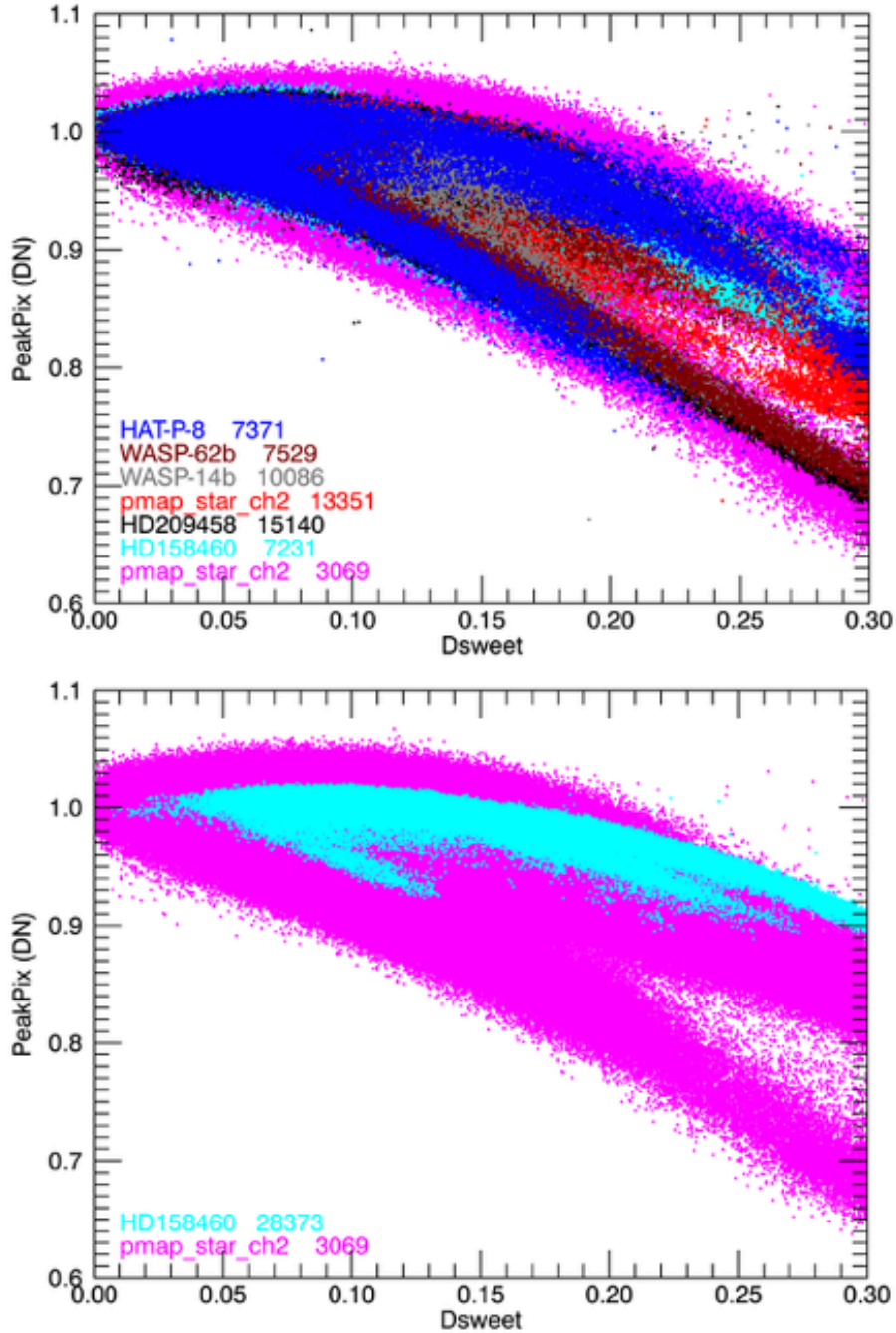


Figure 8.15: Peak pixel value in DN vs. distance from the sweet spot in channel 2. Sweet spot is defined here to be [15.12, 15.1] (when [0,0] is defined as the bottom left corner). These stars are all observed with multiple snapshots, and include the gain map calibration star itself taken with two different frame times. The second plot shows the different slope when using a 28 K source.

8.3.6 *Time-varying Bias in Point Source Data*

8.3.6.1 *Staring Mode Darks*

Observations taken with a dither pattern will have a different bias level and pattern than observations taken in staring mode. This is because the bias is sensitively dependent on both the time between observations, and all previous observations. The dither pattern is important because the frame delay times are determined by the slew times inside of that pattern. The delay time is at least seven seconds between pointings for dithered observations (includes slewing), but only about two seconds between successive staring frames, and within a 64-frame subarray, there will be 0 seconds frame delay.

This is relevant to light curve staring mode photometry because the IRAC pipeline uses an image of the dark current which is made from dithered observations to remove the bias pattern from all observations, regardless of dithering or staring. Because IRAC did not use a shutter, an image of the dark current was generated by making weekly observations of a relatively blank region of the sky at the north ecliptic pole (NEP). When this dithered dark observation was used to correct a staring mode observation, there was the potential for a low-level bias pattern residual in the dataset. This residual pattern could affect the photometry of staring mode observations. The inaccuracy in the bias level (as opposed to pattern) does not matter for aperture photometry.

IRAC data do have a change in inter-frame delay times over the 64 subframes of a single BCD, since the first sub-frame will have a longer delay time than the subsequent sub-frames. We have also seen evidence in archival data of a bias level change over the course of long (5 – 10 hour) stares (see Figure 8.16), which leaves open the possibility that there is also a bias pattern change on those timescales.

To explore these bias patterns, the IRAC team designed and executed test observations of the NEP field with the staring mode. Our goal with these observations was to measure the difference between dithered and staring mode darks at the frame times which are useful for high precision staring mode photometry, and to determine the necessity and feasibility of using staring mode darks on staring mode observations. Please see Section 4.8 for more information on the recommended staring mode skydarks.

8.3.6.2 *Superdarks*

IRAC dark taking procedure is summarized in Section 4.1 and Section 5.1.15. Note specifically that for each science frame, the nearest-in-time skydark was used to correct that frame. The advantage of this weekly dark is that it removes any low-level persistent images which may be present in the science frames.

This means that a) different darks are used for different observations of the gain map since that dataset was observed over many years, and b) for datasets that use the gain map, different dark frames are subtracted from the gain map than are subtracted from target observations.

We tested the use of different darks in the gain map data set by first generating a superdark frame and then applying it to all the data frames of the same frame time. The superdark was generated

by median-combining all dark images taken during the warm mission of a single frame time. The median-combine will reject all sources since these data were taken on-sky. The background level of the dark frames taken at the north ecliptic pole will vary as a function of time, but since most users are doing aperture photometry, and not absolute photometry, we do not care that the mean level of the dark is incorrect by the amount that the zodiacal light fluctuates over a year. The superdark is applied to each data frame by first backing out the calibrations already applied to the BCD, including the weekly dark, and then calibrating those images with our superdark.

We tested the superdark versus weekly dark in the gain map calibration star data set by testing both versions in a set of ≈ 30 different AORs taken on a different calibration star. We saw lower scatter in the observations taken with the weekly dark. Therefore, we did not use the superdarks in our current gain map dataset. The cause for this difference in scatter is likely to be local in time persistent images in the science frames which the local darks were able to partially mitigate, whereas the superdarks did not.

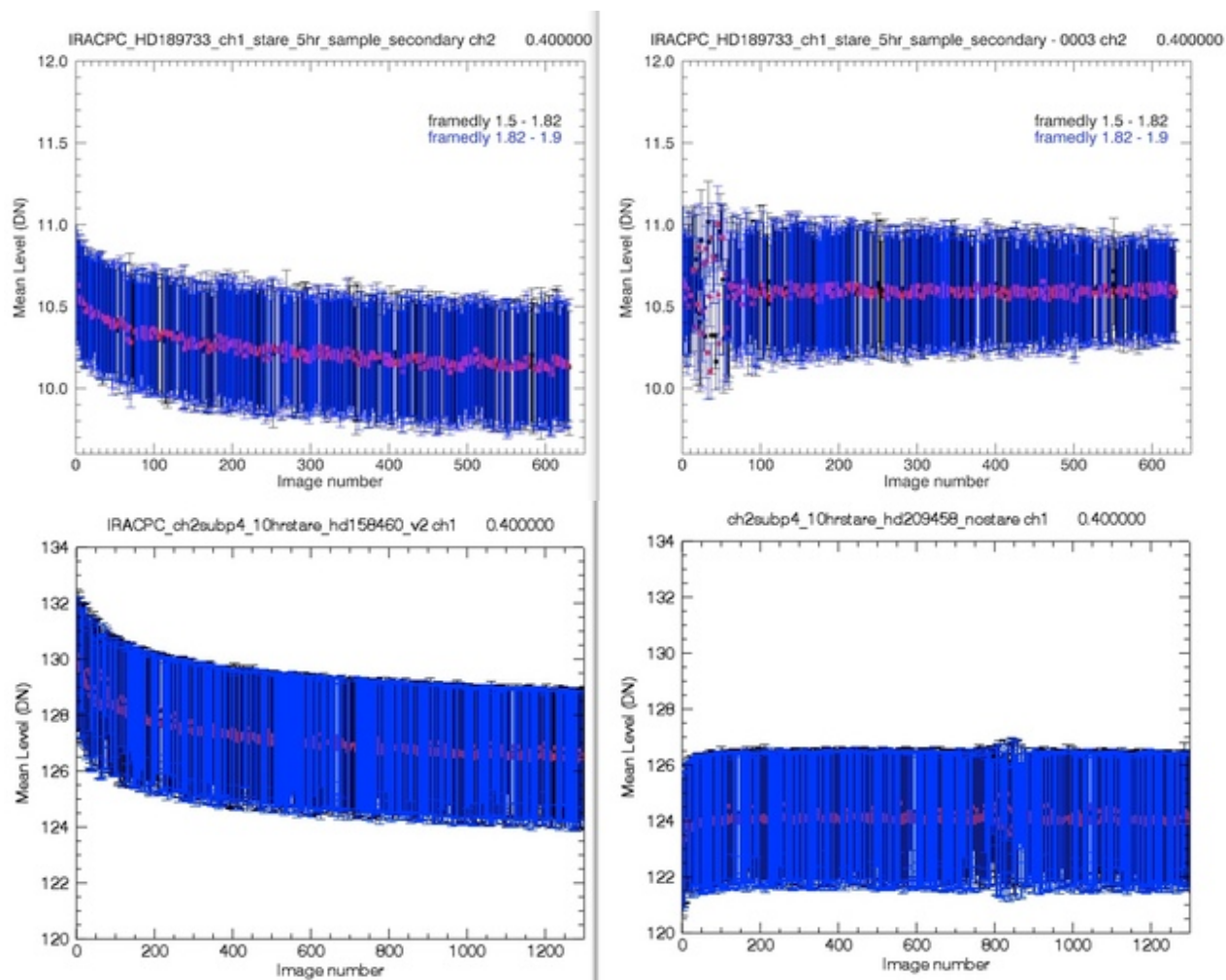


Figure 8.16: Bias Level in DN as a function of time. Bias level changes on long time scales (≈ 10 hours). Bias level as a function of time appears to not be repeatable from AOR to AOR. The data set used to make these plots consists of ten serendipitous staring mode AORs (five in each channel, 0.4 second frame time) in the off-field position, so theoretically empty of stars, although there are some stars in these observations. This bias change is not dependent on the frame delay (all frame delays show the change as a function of time). From these five AORs per channel, the maximum deviation is ≈ 2 DN in channel 1 and ≈ 0.5 DN in channel 2. These are binned over the whole BCD, so each point includes the mean from all 64 subframes. Only one amplifier is shown. Blue and black points show the different frame delays, for which there is no correlation with the shape of the long time scale change. Here we show two plots for each channel to demonstrate the range of level changes.

8.3.7 IRAC's Photometric Stability

We examined the photometric stability of the IRAC detectors as a function of time over the course of the first 11 years. This is relevant to high-precision time-series photometry in considering the use of the pixel phase gain map to correct data sets which were not taken contemporaneously with the gain map dataset. The data for the gain map itself were taken over the course of more than one

year, and will consequently also be affected by instabilities in photometry over year-long timescales.

We used the primary calibrators to examine photometric stability. The data set consists of A and K stars, known to be stable at these wavelengths, observed roughly every two weeks throughout the mission. Figure 8.17 shows aperture photometry of seven calibration stars observed with a dither pattern in full array, binned together on two-week timescales. Photometry is corrected for both the array location dependence and pixel phase effect using a double Gaussian approximation to the pixel phase effect. Dithering to many positions and binning over all stars will reduce systematics from each of these effects. Each individual star is normalized to its median cryogenic mission level before being binned together with the other calibration stars. Error bars show the 1σ standard deviation on the mean divided by the square root of the number of data points in the bin. The cryogenic mission has more data points per bin, but a lower frequency of observations since the instrument was not always in use, accounting for the smaller cryogenic mission error bars.

Data from the end of the cryogenic mission to about nine months into warm mission was processed with a different flux conversion value, and the fluxes are therefore offset for that time period. In channel 1 they are not even within the axis range plotted, which causes the gap in the plot at about six years. The offset in normalized flux from the cryogenic to warm mission is likely caused by the fact that flux conversions are determined from the entire dataset without regard to this measured slope. Taken as an ensemble, the cryogenic and warm mission flux conversions are designed to be consistent. The channel 2 data set is noisier because the stars have a lower signal-to-noise ratio (the same star is fainter in channel 2 than in channel 1).

Individual light curves for each of the calibration stars used in this analysis were checked to rule out the hypothesis that one or two of the stars varied in a way as to be the sole cause of the measured decrease in binned flux as a function of time. This is shown in Figure 8.18 for the channel 1 warm dataset, with each star represented by a different color. Slopes and their chi-squared fits as well as the star names are printed on the plot. While the slope for each individual star is not as well measured as for the ensemble of stars, it is apparent that the decreasing trend is seen in all or most stars, and is not caused by outliers.

There is a statistically significant decrease in the sensitivity of both channel 1 and channel 2 over the course of the mission. The deviation from zero change, a flat line fit to the data as a function of time, is tested using a Monte Carlo techniques. We ran 1000 instances, randomly shuffling the order of the times associated with each flux bin. The resulting distribution of the measured slope is consistent with a Gaussian distribution around a zero slope, and is not consistent with the slopes measured here in the sense that $> 95\%$ of the instances have slopes closer to zero than what the calibration star data show. This is shown in the blue histogram in Figure 8.19 for the channel 2 warm data sets. The dashed line shows the measured slope.

One hypothesis as to the cause of the decrease in flux over time is the decrease in cosmic rays (CR) hits over time due to the solar cycle. Green points show the CR counts taken from the 100 second north ecliptic pole fields. Solar minimum occurs around the changeover between the cryogenic and warm missions. Solar maximum was around 2014, 11 years into the mission. CR counts should decrease as the solar activity increases because the solar activity pushes the volume

of solar influence further out, which decreases the number of CRs that reach Spitzer. Since we see both CR counts increasing and decreasing over the mission, whereas the fluxes always decrease, the solar cycle cannot be the cause of the flux decrease.

The decrease in sensitivity is potentially caused by radiation damage to the optics. The decrease in sensitivity is different for the two channels, with the slope of the change being steeper for channel 1.

What are the implications of this for science? The degradation is of the order of 0.1% per year in channel 1 and 0.05% per year in channel 2. These levels are only relevant to high precision studies. Relative photometry studies will be immune to such changes since all the photometry will change equally. Similarly, measurements of transit and eclipse depths will not change as a function of time due to this effect because they are measured relative to the rest of the light curve.

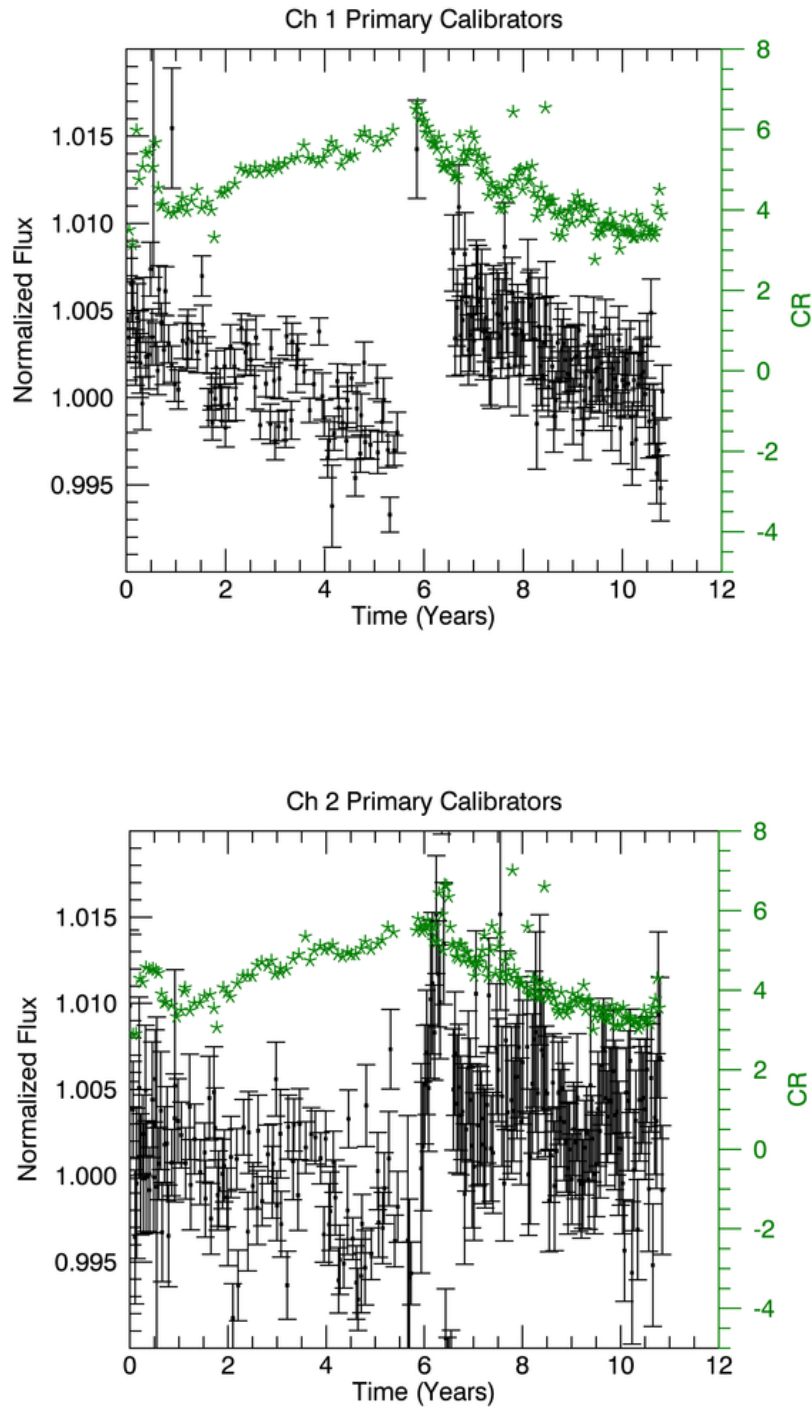


Figure 8.17: Channel 1 and 2 ensembles of primary calibrator fluxes as a function of time since the start of the mission. Black points show the ensemble of primary calibrators while green stars show the cosmic ray counts.

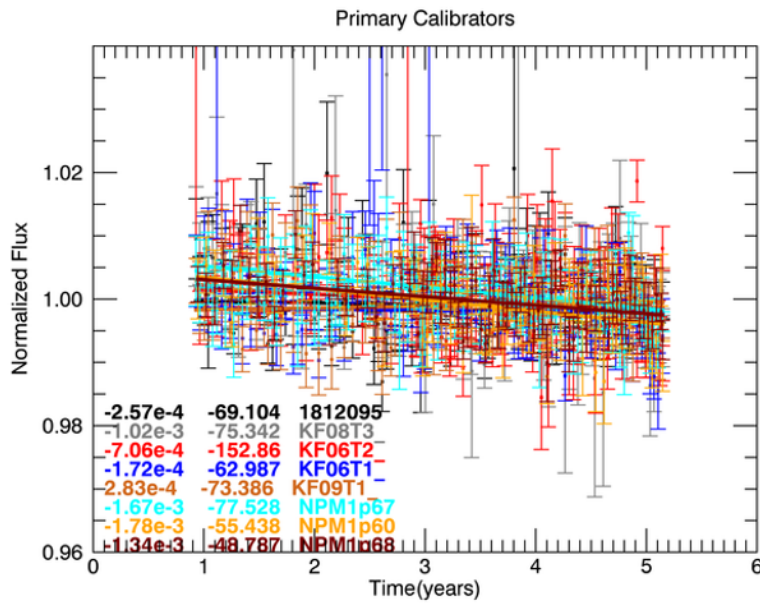


Figure 8.18: Individual calibration stars as a function of time. There is no evidence for a single outlier star as the source of the flux degradation trend.

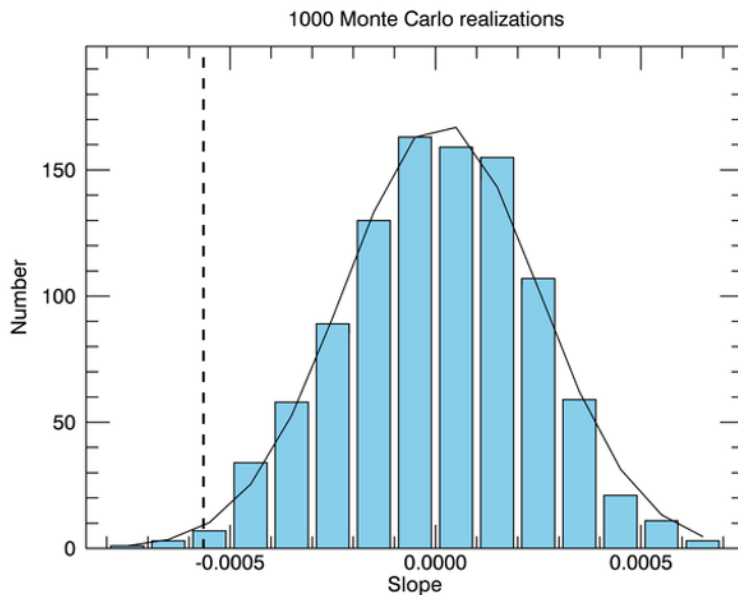


Figure 8.19: A Monte Carlo simulation of calibration flux vs. time stamp slopes. This figure shows what the slopes would be if the time stamps for each data point were shuffled using a Fisher – Yates shuffle. The actual measured slope for channel 2 is shown with the dashed line. Because this measured slope is outside of 1σ , we take the slope to be significant.

8.3.8 *Persistent Images*

Persistent or residual images are discussed in Section 7.2.8. Both IRAC channels 1 and 2 sometimes show residual images of a source after it has been moved off a pixel. Beyond intrapixel gain effects, we expect these persistent images to be the next largest source of noise in multi-epoch high precision photometry observations. When a pixel is illuminated, a small fraction of the photoelectrons are trapped. The traps have characteristic decay rates, and can release a hole or electron that accumulates on the integrating node long after the illumination has ceased. Persistent images on the IRAC array start out as positive flux remaining after a bright source has been observed. At some later point in time the residual images turn from positive to negative, so that they are actually below the background level (trapping a hole instead of trapping an electron). Positive and negative persistent images in either the aperture or background annulus in either the dark frame or the science frames can lead to artificial increases or decreases in aperture photometry fluxes. Persistent images are pervasive. We will use the terms persistent images and residual images interchangeably throughout this discussion.

Short-term persistent images start at about 1% of the source flux and can be seen to decay over the course of minutes to hours. While some patterns change weekly, some persist over multiple weeks. We show a plot in Figure 8.20 of the change in photometry on a blank region in difference images for the channel 112-second frame time. Using the size of the fluctuations in the blank sky photometry, we then calculate the percentage effect that the residual images have on photometry which is shown for all frame times and both channels in Table 8.3 below. The apparent ping-pong back and forth from week to week at the level of 10 – 15 μ Jy is likely due to the “first-frame effect” because of the way that the skydarks are observed. Residual images have a much stronger effect in channel 1 than in channel 2, and are strongest at 0.4 and 2 second subarray frame times.

Beyond knowing of their existence, it is very difficult to quantify these low-level latent images, especially since we know that the residual images are both growing with new observations dependent on the specific observing history, and shrinking over time as they dissipate. Our superdark analysis shows that persistent images can affect photometry at the 0.1% level (see Figure 8.20).

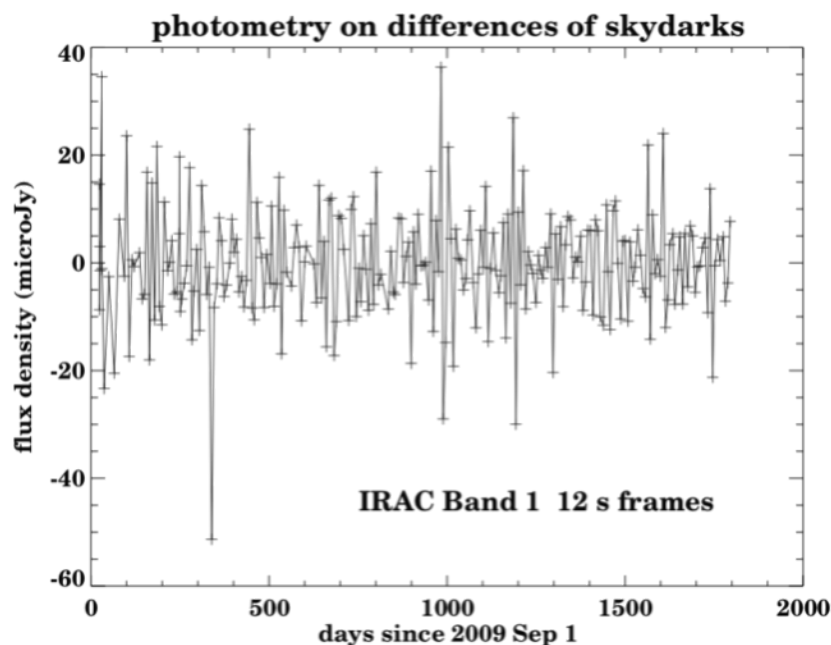


Figure 8.20: Skydark variations in channel 1 over the course of the warm mission. The y-axis is a difference of the flux density present in the darks after an average dark frame has been removed.

Table 8.3: Approximate levels of the residual fluxes as a function of channel and frame time.

Frame time (seconds)	Channel 1 sigma (%)	Channel 2 sigma (%)
0.02 sub	0.03	0.01
0.1 sub	0.07	0.01
0.4 sub	0.1	0.02
2 sub	0.11	0.03
0.4 full	0.06	0.05
2 full	0.06	0.04
6 full	0.07	0.03
12 full	0.07	0.04

8.3.9 Removing Correlated Noise – Repeatability and Accuracy

There are several techniques in the literature for removing correlated noise from IRAC high precision photometry data sets. Please refer to the following papers as starting points for a discussion of those techniques.

- BiLinearly Interpolated Subpixel Sensitivity (BLISS; Stevenson et al. 2012)*
- Kernel Regression Mapping, using the data to be corrected (KR/Data; Ballard et al. 2010, Knutson et al. 2012)*
- Gaussian Process Models (GP; Evans et al. 2015)*
- Independent Component Analysis (ICA; Morello et al. 2015)*
- MCMC Evaluation (Gillon et al. 2010)

- Pixel Level Decorrelation (PLD; Deming et al., 2015)*
- Kernel Regression using a calibration pixel mapping dataset (KR/Pmap; Krick et al. 2016)*
- Polynomial fitting (Charbonneau et al. 2008)
- Segmented Polynomial for the K2 Pipeline [SP(K2)] ((Buzasi, D. L. et al, 2015))*

*Methods compared in FiguresFigure **8.21** and Figure 8.22.

Ingalls et al. (2016) examined the repeatability, reliability, and accuracy of differential exoplanet eclipse depth measurements made using IRAC during the warm mission. The authors re-analyzed an existing 4.5 μm data set, consisting of ten observations of the XO-3b system during the secondary eclipse, using seven different techniques for removing correlated noise. They found that, on average, for a given technique the eclipse depth estimate is repeatable from epoch to epoch to within 150 parts per million (ppm; see Figure 8.21). Most techniques derive eclipse depths that do not vary by more than a factor of three of the photon noise limit. All methods but one accurately assess their own errors: for these methods the individual measurement uncertainties are comparable to the scatter in eclipse depths over the ten-epoch sample. To assess the accuracy of the techniques as well as to clarify the difference between instrumental and other sources of measurement error, the authors also analyzed a simulated data set of ten visits to XO-3b, for which the eclipse depth is known (Figure 8.22). They found that three of the methods (BLISS mapping, Pixel Level Decorrelation, and Independent Component Analysis) obtain results that are within three times the photon limit of the true eclipse depth. When averaged over the ten-epoch ensemble, five out of seven techniques come within 100 ppm of the true value. Spitzer exoplanet data, if measured following best practices and reduced using methods such as those described, can measure repeatable and accurate single eclipse depths, with close to photon-limited results.

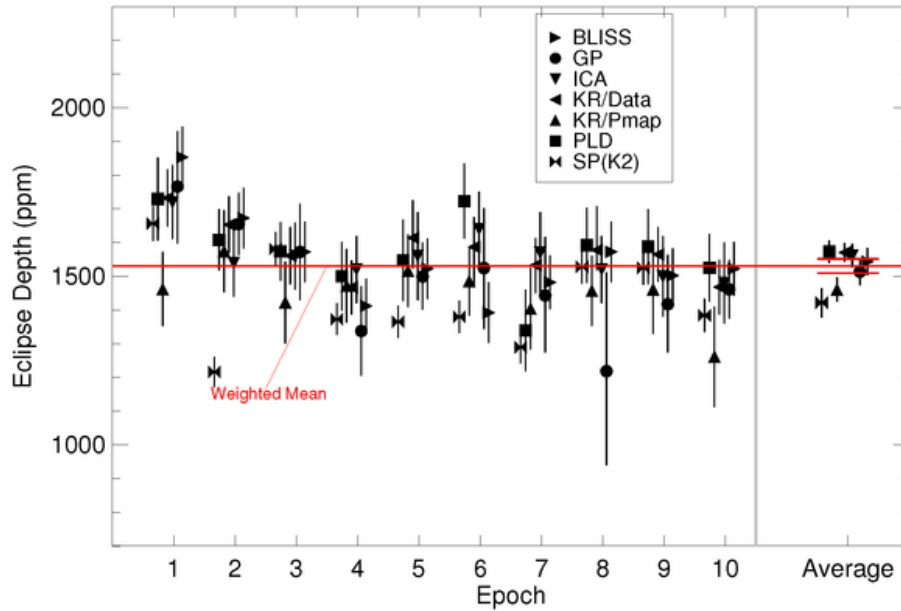


Figure 8.21: Eclipse depths for ten visits to XO-3b, as computed via various methods. The group of points for each epoch is separated to minimize confusion. Error bars in this plot are symmetric; in cases where the technique returned asymmetric uncertainties, we used the largest of the two values. We show the results for the separate visits to the left of the gray vertical line, and the average results to the right. Error bars on the separate visits are the uncertainties reported by the technique. Error bars on the averages are the uncertainties in the weighted mean, adjusted for “underdispersion” using the scatter in the group of measurements. The horizontal red lines display the grand mean for all the results, and its uncertainty.

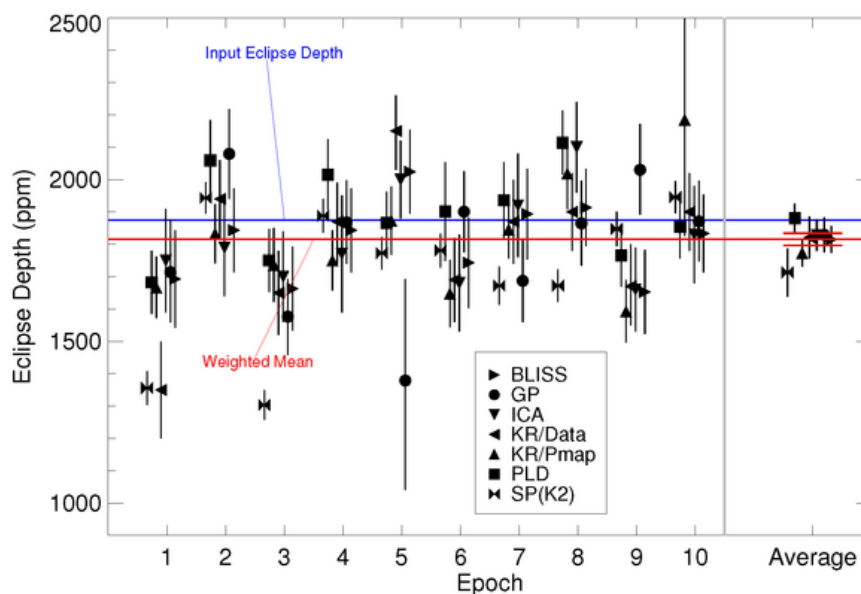
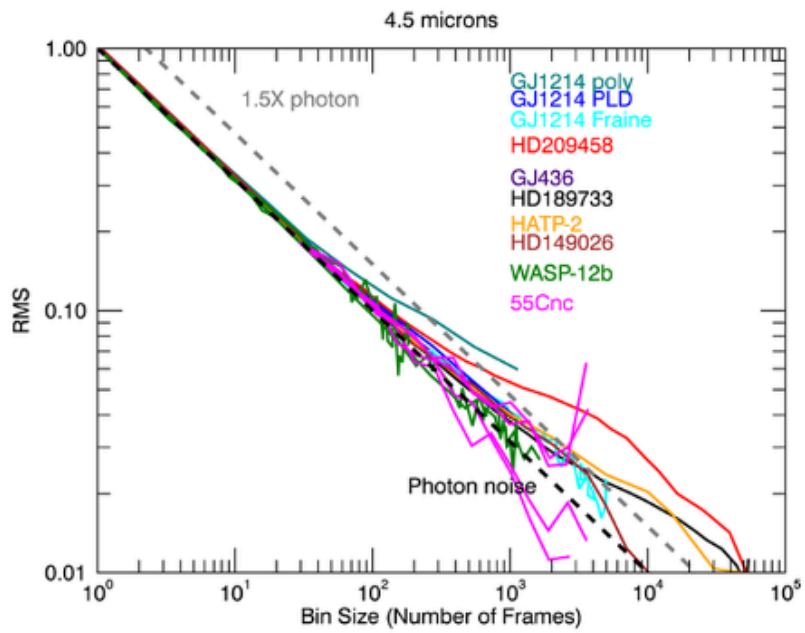
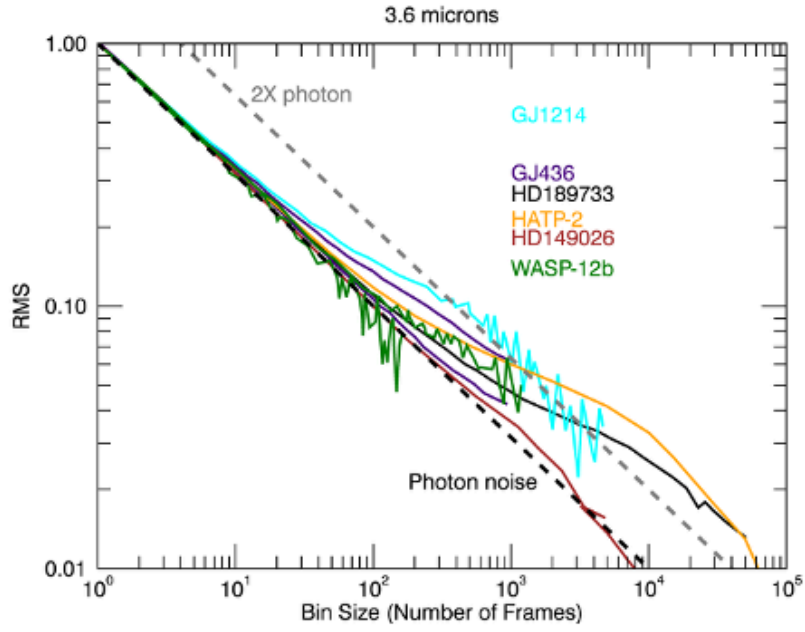


Figure 8.22: Similar to Figure 8.21. A blue horizontal line indicates the eclipse depth input to the simulations, 1875 ppm.

8.3.10 Measuring Noise Reduction

We explore how well any given IRAC data reduction has removed the above sources of correlated noise. It is challenging to remove systematics without removing time-varying astrophysical signal. One possible metric of the final achieved precision is to examine the RMS as a function of binning scale and compare that to the photon noise limit. References to the data presented in Figure 8.23 are HD 189733 (Knutson et al., 2012); GJ 436 (Knutson et al. 2011); GJ 1214 (Fraine et al. 2013); HD 209458 (Zellem et al. 2014); HD 149026 (Stevenson et al. 2012); HAT-P-2 (Lewis et al. 2013); WASP-12 (Stevenson et al. 2014); and 55 Cnc (Demory et al. 2016).



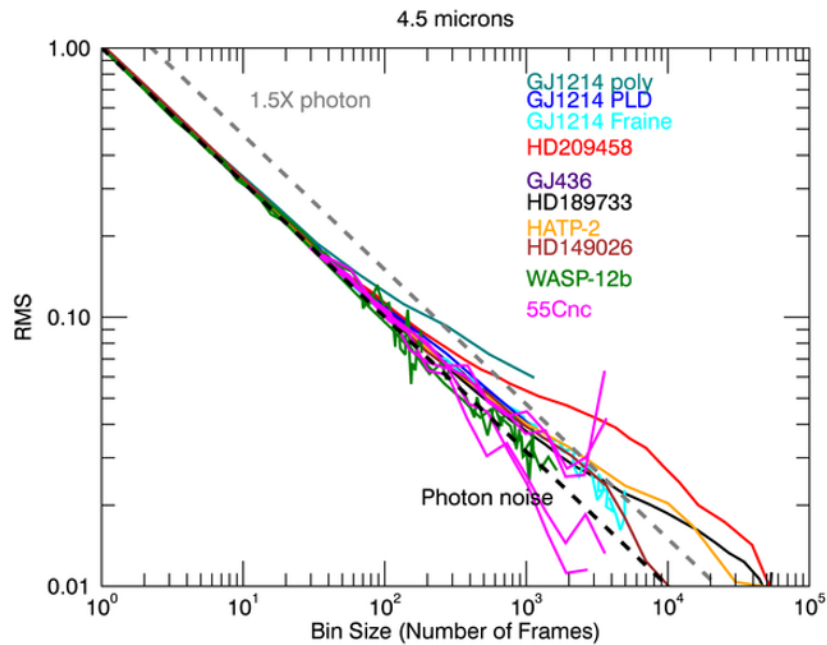


Figure 8.23: Actual precision reached for published, single epoch, IRAC observations. Plots are normalized at a binning size of one. The dashed black line is photon noise limited. The dashed grey line is two (1.5) times the photon noise limit for channel 1 (2). The third plot is a zoom-in on channel 2.

8.4 Post-BCD Data Processing

All processing of IRAC data beyond the individual, calibrated, 256 x 256 pixel square images produced by the BCD science pipeline was called “post-BCD.” This included combining all the images from an observation (AOR) into a mosaic, detecting sources, and flagging outliers, e.g., cosmic ray hits, in the images that are not based on understood instrumental artifacts or detector physics. Two important post-BCD processes were performed routinely by the pipeline and generated results that were placed in the science archive. These included pointing refinement, wherein a set of point sources were identified in the images and were astrometrically matched to the 2MASS catalog, and mosaicking, wherein the individual images in an AOR were robustly combined into celestial coordinate mosaics for each IRAC waveband. The post-BCD mosaic generation could (and should) be performed in different ways for different observing strategies and scientific goals. The post-BCD pipeline processing was performed with a specific, conservative, set of parameters. Observers and archival researchers will very likely need to do post-BCD processing on their own. Most common will be generating mosaics from data in multiple AORs.

The following subsections deal with each part of the post-BCD pipeline in turn, starting with the pointing refinement, then overlap correction, then mosaicking. Point source extraction is discussed

briefly, though it is not done in the pipeline. The post-BCD software is available in the MOPEX package at

<https://irsa.ipac.caltech.edu/data/SPITZER/docs/dataanalysisistools/tools/mopex/>.

This consists of a series of modules linked by Perl wrapper scripts and controlled by namelists. Namelists are placed in a subdirectory called `cdf` and have filenames ending in `.nl`. The namelist controls which modules are called, along with the parameters each uses. Input file lists can also be provided in the namelists. The file lists should not have any blank lines, otherwise the programs will look for non-existent files.

While the discussion of overlap correction and mosaicking here is tied to the MOPEX package, other software can be used as long as it understands the -SIP distortion of the (C)BCDs. Also note that the discussion of the tools here is far from a complete description, but just touches on some issues relevant to IRAC.

8.4.1 Pointing Refinement

Pointing refinement corrects the pointing of each frame to the 2MASS sky. In the pipeline, the pointing refinement solutions for channels 1 and 2 were combined and applied to all four (two) channels to produce the default pointing via the “superboresight” in the cryogenic and warm mission data, respectively. However, if they wish to try to improve on the supplied pointing, users may rerun the pointing refinement themselves using scripts that come with the MOPEX software package. Pointing refinement may not always be successful in channels 3 and 4, in which there are few 2MASS stars per image. Note that each run of pointing refinement overwrites any previous solutions (in the header keywords `RARFND`, `DECRFND`, etc.), so users should make copies of the BCDs before rerunning the pointing refinement, if they wish to retain the old corrections.

8.4.2 Overlap Correction

The post-BCD software contains an overlap correction module that matches the background levels of overlapping frames in a mosaic. Generating new mosaics by running MOPEX with overlap correction turned on can remove the “patchiness” often seen in mosaics due to bias fluctuations in the array (due both to the first-frame effect and bright source effects). Note that background matching does not always work well, especially between areas of unequal depth.

8.4.3 Mosaicking of IRAC Data

8.4.3.1 Creating a Common Fiducial Frame

Note that in the following we name the settings needed for the command line version of MOPEX. Corresponding values need to be set if using the MOPEX GUI.

As a first step in creating a mosaic, run the mosaicker with all the modules turned off except for the fiducial frame module (i.e., `run_fiducial_image_frame = 1` in the namelist), and include all the files you wish to mosaic from all the four channels in the input list. This will generate the boundaries of the mosaic and will allow all the channels to be mosaicked onto the exact same grid.

Rename this file to, e.g., *FIF_all.tbl*, to prevent it from being accidentally overwritten. Then, when running the mosaicker, set the fiducial frame to the file created by the fiducial frame module in this initial run using `FIF_FILE_NAME = (path)/FIF_all.tbl`, and turn off the fiducial frame module (i.e., set `run_fiducial_image_frame = 0` in the namelist). The use of the common fiducial frame will ensure that the mosaics from all the four channels will be accurately co-aligned. The pixel scale is controlled by the `MOSAIC_PIXEL_RATIO X/Y` parameters. Set `Edge Padding = 100` to get a good border around the image. You can also specify `CROTA2` for the output mosaic if you wish, or set `CROTA2 = "A"` to get the smallest possible mosaic. The pixel size in the mosaic produced by the final pipeline is exactly 0.6 arcseconds x 0.6 arcseconds.

8.4.3.2 *Outlier Rejection*

The mosaicker has four outlier rejection strategies: single-frame outlier rejection, dual-outlier rejection, multi-frame outlier rejection and box outlier rejection. For IRAC, the most useful are the dual outlier and multi-frame rejections. Be sure to set `THRESH_OPTION = 1` in the namelist in the multi-frame `&MOSAICOUTLIERIN` section. Setting the thresholds too low in the outlier modules can result in unwanted rejection of pixels in the cores of real objects. Users of these modules should carefully check the coverage maps produced by the mosaicker to ensure that the centers of real objects are not being masked out. The outlier rejection modules set bits in the `rmasks`. Bit 0 is set by the single-frame outlier rejection, bit 1 by the temporal (multi-frame) rejection, bit 2 by the dual outlier rejection, and bit 3 by the box outlier detection. Which `rmask` bits are used by the mosaicker is controlled by the `RMask_Fatal_BitPattern`. The mosaicker takes the `rmasks` and makes an `rmask` mosaic. The switches `USE_OUTLIER_FOR_RMASK`, `USE_DUAL_OUTLIER_FOR_RMASK`, and `USE_BOX_OUTLIER_FOR_RMASK` control which of the outlier detection modules are used. An important parameter is `RM_THRESH` in `&MOSAICRMASKIN`. When the `rmask` is made it is projected back onto the input images to determine which pixels will be masked in the final mosaic. An `rmask` pixel is divided amongst the overlapping pixels in the input image. Input image pixels with projected values of the `rmask` mosaic above `RM_THRESH` have the multi-frame outlier bit (1) set in their `rmask`. For channels 1 and 2 a fairly high value (e.g., 0.5) can be used. The more diffuse radhits in channels 3 and 4 can be more effectively rejected by setting `RM_THRESH` to a lower value, e.g., 0.05, which has the effect of growing the `rmask`, and thus it rejects the more diffuse edges of a radhit.

All the outlier rejection modules require uncertainty images. The BCD uncertainty images are adequate for this purpose, and the list of them should be specified with the `SIGMALIST_FILE_NAME` keyword in the namelist. To use them set `have_uncertainties = 1` and `compute_uncertainties_internally = 0`. To compute your own uncertainty images, set `compute_uncertainties_internally = 1`, `have_uncertainties = 0`, and set the appropriate values in the `&SNESTIMATORIN` section of the namelist (see the MOPEX documentation for more details). Outlier rejection creates another set of masks, the `rmasks`. These indicate the pixels flagged by outlier rejection, and which are used by the mosaicker. A mosaic of the `rmasks` can be provided by setting `run_mosaic_rmask = 1`. As a check on the outlier rejection, it is often helpful to examine the coverage maps output by the mosaicker. If the outlier rejection has been over-zealous, then there will be reductions in coverage at the positions of real sources in the mosaic. Blinking the mosaics and coverage maps in, e.g., DS9 can thus be very helpful for determining whether the outlier rejection is set up correctly to reject only genuine outliers.

8.4.3.3 *Mosaicker Output Files*

The output directory structure after running the mosaicker looks like: BoxOutlier, Coadd, DualOutlier, Interp, ReInterp, Combine, Medfilter, Rmask, Detect, Sigma, Dmask, Outlier with “-mosaic” appended to these names, and the files in the output directory are *FIF.tbl*, *header_list.tbl*, and a namelist file with a date stamp. The directory Combine contains the mosaic, *mosaic.fits*, a coverage map, *mosaic_cov.fits*, and an uncertainty map *mosaic_unc.fits*.

8.4.3.4 *To Drizzle or Not to Drizzle?*

The mosaicker has three interpolation options, set by the INTERP_METHOD keyword. The default is a linear interpolation. Drizzling is available as an option, as is a grid interpolation (useful for creating quick mosaics if the PSF quality is not important). Our experience with the drizzle option suggests that it is effective when used on data sets with many dithers per sky position, and it can reduce the point response function (PRF) width by 10% – 20%, though at the expense of an unevenly-weighted image. The coverage map produced by the mosaicker can be used to investigate the pixel-to-pixel variation in the coverage of the drizzled image.

8.4.3.5 *Mosaicking Moving Targets*

Although Spitzer does track moving targets to a sub-pixel accuracy, the BCD pipeline only produces mosaics of IRAC data in fixed celestial coordinates. The user may opt to generate his or her own mosaic in a moving coordinate reference frame by setting the appropriate flags in MOPEX. The individual BCDs or CBCDs should be overlap-corrected first and then the mosaicker should be run with the flag MOVING_OBJECT_MOSAIC = 1 set, using outlier rejection. Stars in the frames may be removed by outlier rejection, and the resultant composite of a moving target will be produced.

8.4.4 *Source Extraction*

The Spitzer source extractor, APEX, may be used to fit point sources in IRAC data. This software can be run in two modes, in a single frame mode (*apex_1frame*) which can be run on an individual BCD, CBCD or a mosaic, and in a multi-frame mode which uses the mosaic to detect sources, but the individual BCDs or CBCDs to measure their fluxes. Note that PRF fitting is not recommended to be performed on IRAC mosaics, but on (C)BCDs only.

8.4.4.1 *Noise Estimation*

The BCD uncertainty files are rough uncertainty estimations and do not include all of the systematic effects associated with IRAC detectors, nor do they include the absolute flux uncertainty. These uncertainty images are generated as follows. They begin as an estimate of the read noise (one number in electrons for the whole image) and the shot-noise due to the sky (proportional to the square-root of the number of electrons in the image as calculated in Section 2.5.1). Then each module propagates the uncertainty image forward, including the uncertainties in dark and flat calibration files. The pipeline modules used the uncertainty image as a way to quantitatively estimate the quality of the sky estimate given by the value of a pixel. In the end, the uncertainty images overestimate the formal uncertainty of the image, because the net propagated uncertainty is much higher than the observed pixel-to-pixel fluctuations in the images. We therefore recommend that the uncertainty images only be used for relative weights between pixels, for example when performing outlier rejection or making a weighted mosaic that combines multiple input frames that view the same sky mosaic pixel.

The accuracy of the fluxes from APEX is very sensitive to the noise estimates, as these affect the fitted background value. For crowded fields, it is essential to include an estimate of the confusion noise (not included in the BCD uncertainty image). This can be estimated by measuring the difference between the actual image RMS and the estimated RMS in the uncertainty image, and then either adding it to the uncertainty image, or using it as the confusion noise value when generating uncertainty images with the post-BCD software (see Section 8.4.3.2).

8.4.4.2 *PRF Estimation*

The PRFs released with MOPEX should be fairly good matches to the data and a significant improvement on the previous versions. We do not recommend using the `prf_estimate.pl` script to generate PRFs from the mosaics.

8.4.4.3 *Background Estimation*

For point source fitting the parameter `use_background_subtracted_image_for_fitting = 1` is the default and self-explanatory. An additional option `Background_Fit` is available in the Source Estimate block. This lets a background level to be one of the point source fit parameters. The default is off – the background subtracted image is assumed to have had a robust measure of the background removed. But `Background_Fit` may be useful in crowded regions or with structured backgrounds. Aperture photometry (done on the mosaics in multi-frame APEX) by default uses a background annulus on non-background subtracted data.

8.4.4.4 *Source Extraction*

Source detection and extraction are controlled by the parameters `Detection max/min area` and `detection threshold`. APEX will frequently try to split bright sources into several components. This tendency can be controlled by setting the `Max_Number_PS` parameter in `&SOURCEESTIMATE` to a low number (2 – 3). Two files are output: `extract_raw.tbl` contains all detections, and `extract.tbl`, which is a subset of `extract_raw.tbl`, contains the objects and fields which are selected by select conditions and select columns. Source extraction from the BCDs or CBCDs (multiframe mode) is recommended for IRAC data.

8.4.4.5 *Outlier Rejection*

By default, APEX will not perform outlier rejection. This can be gotten around by running the `mosaicker` with outlier rejection turned on and keeping the intermediate products (`delete_intermediate files = 0`).

8.5 Things to Check and Important Notes for Data Analysis

When working on and analyzing Spitzer/IRAC data, there are several important things to keep in mind. We have collected the most important things to keep in mind here so that the user can go through this list before starting to work on IRAC data, and come back to it during data reduction and analysis.

- Before you start using IRAC data, we recommend that you familiarize yourself very carefully with this document, and specifically Chapter 7, which discusses the various artifacts in IRAC data.

- In general, we caution the user to be extremely careful when using data from PC1 – PC4 campaigns as the calibration was constantly changing during this time period (2009 July 28 – September 23).
- The CBCD frames contain the artifact-corrected observations, and should usually be a starting point for your further data reduction and analysis. However, you always have the option of going back to the BCD frames if you are not happy with how artifacts were corrected in the CBCDs, and perform your own corrections.
- Point source photometry should be performed with aperture photometry, unless the targets lie in an area of sky that has an extremely high surface density or a strongly spatially variable background.
- The user should read the caveats in Section 8 and think carefully before publishing any results about extended emission flux densities and surface brightnesses.
- For diffuse surface brightness measurements, we recommend making differential measurements among at least two sky positions, preferably from the same campaign.
- The saturation estimates were conservatively computed from the worst case in which the PSF is directly centered on a pixel.
- The lack of an isolated measurement of the dark current and bias offset during shutterless operations limited the ability of IRAC to measure the true celestial background.
- The flat-field data were generated from the zodiacal background, and are appropriate for objects with that color. There was a significant color term, of order 5%–10%, for objects with a Rayleigh–Jeans spectrum in the mid-infrared (such as stars); see Section 4.5 for more information.
- For deep survey observations and other data sets with a large number of frames and a good dithering strategy, the system gain could be determined by the actual survey frames themselves, rather than using the standard set of dedicated observations of some other part of the sky.
- Our definition of the color correction looks slightly different from that in the *IRAS Explanatory Supplement*, because we used the system spectral response R in electrons/photon, instead of ergs/photon.
- The array location-dependent photometric correction images for the cryogenic mission and the warm mission are different, and users should use the appropriate mission corrections. See Section 4.5 for more notes about these corrections.

- It is important to apply an aperture correction to flux densities measured through aperture photometry or PRF fitting, unless the exact same aperture and background radii and annuli were used as for the calibration stars.
- The spatial extent of the PSF in channels 3 and 4 was much larger than the subarray area. In other words, a large amount of the total power in the PSF is scattered onto arcminute size scales. As a result, special care needs to be taken when measuring fluxes in these channels, since accurate measurement of the background is difficult. Proper application of aperture corrections is very important.
- The post-BCD mosaics available from the Spitzer Heritage Archive use pixels that correspond to exactly 0.6 arcseconds * 0.6 arcseconds.
- PRF fitting does not work in image mosaics where the information from the PSFs has been blended together. Aperture photometry is the correct way to perform point source flux density measurements in image mosaics.
- The extended PSF should not be used for PSF-fitting photometry and source extraction of non-saturated point sources.
- There is a problem with the skydark subtraction from the 58th frame in the subarray observations which leaves the background level in that frame different from the rest.
- Because of the “first-frame effect,” the first frame of every Astronomical Observation Request (AOR) has a different delay time and it cannot be calibrated perfectly.
- The pipeline cannot flag slew residuals, as there is no reasonable way of tracking the appearance of bright sources relative to the moving telescope pointing.
- Users should be aware of the uncertainties resulting from banding, specifically when attempting measurements of faint sources near the affected rows or columns.
- The aperture fluxes reported by APEX are always made using the median background, and hence may be inaccurate for faint sources.

Appendix A. Pipeline History Log

S19.2 (Warm Mission Only; processing started on 2015 June 15)

1. Recalibration of IRAC Flux Densities in Channels 1 and 2.

The absolute photometric calibration was updated using the same method that was used for the final cryogenic IRAC calibration. The uncertainty in the absolute photometric calibration is dominated by the uncertainty in the flux density of the fundamental calibrators, Vega and Sirius, and is $\approx 2\%$ in both channels.

2. Linearity Solution Improved in Channel 1.

The linearity solution was adjusted in channel 1 only. The change in flux from the old to new linearity solution is $< 1\%$. The solution in channel 2 did not need to be changed.

3. Pmasks Updated

The quasi-static bad pixel masks were updated.

4. New Flat-fields Derived

Newly derived flat-fields are now in use with final precisions of 0.17% and 0.09% in channel 1 (3.6 μm) and channel 2 (4.5 μm), respectively.

5. Header Information Updated

Keywords for PCRS peak-up observations were added to FITS headers, including the R.A., Dec., and Proper Motion of the star used for the peak-up.

6. Pointing Refinement Catalog Updated

Pointing refinement in the IRAC pipeline utilizes the 2MASS catalog. The positional information of stars in the 2MASS catalog has now been improved with US Naval Observatory's astrometric catalog UCAC4 proper motions, as 22% of 2MASS sources have non-zero proper motions.

7. Read Noise Values Updated to Observed Warm Campaign Values

Previously, the cryogenic read noise values were used in the (C)BCD pixel value uncertainty calculations. The read noises have now been updated to measured warm mission read noise values.

8. Distortion Correction Updated

The distortion correction has now been updated from a third order polynomial solution to a fifth order polynomial solution, allowing an improvement of relative astrometric accuracy from 125 milliarcseconds to 30 milliarcseconds in both channels.

S19.1 (Warm Mission Only; 2015 August 29)

1. Imask Updates

Turning on the residual image ("latent") bit (10) in the imask now uses both residual images created within the current AOR and residual images left by preceding observations. The latter are found with algorithms that track the time decay of residual images.

2. Saturation Correction and Column Pull-down Updates

Updated saturation and column pull-down thresholds for artifact correction.

S18.25 (Cryogenic Mission Final Processing; 2012 March 15)

1. Recalibration of IRAC Fluxes in Channels 3 and 4.

While checking the calibration of Spitzer instruments by comparing the IRAC calibration to the HST calibration database, an error was identified in the S18.18 IRAC processing. In updating the flux conversions (FLUXCONV), erroneous color corrections were used for the calibration stars. The color corrections used were incorrect for the 5.8 and 8.0 μm channels. The S18.18 flux values were multiplied by 1.000, 1.000, 0.968, and 0.973 for the 3.6, 4.5, 5.8, and 8.0 μm channels, respectively. The headers were also updated to indicate pipeline version S18.24 and revised flux conversion values.

S18.18 (Warm Mission Only; 2010 May 27)

1. Recalibration of IRAC Flux Densities in Channels 1 and 2.

The absolute photometric calibration has been updated using the first year of warm campaign calibration stars.

2. Added Header Keywords

BMJD_OBS (barycentric modified Julian Date) and AORHDR (AOR requested to be observed in HDR mode) were added to (C)BCD FITS header.

3. New Pmasks and Flat-fields Created Using only Warm Mission Data.

S18.18 (2010 May 27)

1. Saturation Correction in Pipeline

Saturation is now corrected before artifacts. Artifact correction for saturated sources is now possible. The criteria for selecting sources for correction were changed. The source selection is now frame time dependent. Bit 13 in imask is changed to bit 4 after correction has been performed.

2. Imask Updates

Imask header is now formatted in a way similar to the BCD header and includes information about the various bits that may have been set.

3. ABADDATA Now Often Corrected

Frames with ABADDATA set in raw file headers are now corrected. This problem is due to shifting the data by one pixel after an extra word was read into the data. If only one such instance occurs in a frame it is now corrected. Frames with multiple instances are not corrected. The BCDs will include a header keyword BADPIX. If BADPIX = T, then another header keyword ZEROPIX gives the number of bad pixels. If ZEROPIX = 1, then header keyword ZPIXPOS gives the position of the pixel that was fixed and header keyword BADFILL gives the value (in DN) of the fixed pixel.

4. New Added Header Keywords

Barycentric Julian Date calculated with SCLK precision is now included in header keyword BMJD_OBS. Also, a new header keyword AORHDR has been added. This keyword is true if the entire AOR in which the frame was taken (not just the frame itself, such as the first frame in every AOR) was taken in the high dynamic range (HDR) mode.

S18.14 (2010 December 10)

1. Saturation Correction Update

Only sources in the 2MASS Point Source Catalog are now corrected (extended sources, such as the nuclei of bright galaxies are not corrected). Bit 13 in imasks is now flipped to zero after the saturation has been corrected.

2. Mosaic of Imasks

Mosaics of all the imasks for a given frame time in a given AOR are now produced by the pipeline and placed in the PBCD directory (mmsk files).

3. Dmasks No Longer Archived

We no longer provide dmasks as they contain misleading and incomplete information. The imasks are more robust, include flagging of various artifacts that are not present in dmasks, and make full use of the saturation correction made by the pipeline.

4. Higher Accuracy Pointing Refinement

Pointing refinement is now done with the help of the 100x sampled PRFs, leading to a more accurate pointing solution.

S18.5 (2008 December 1)

1. A New Saturated Source Fitter

The pipeline now attempts to systematically find all saturated point sources in the images and fit them using an appropriate PSF that is matched to the unsaturated wings of the source. The new module replaces the saturated point source with an unsaturated point source that has the correct flux density of the point source. Please note that the new module does not successfully fit super-saturated point sources or point sources that are too close to the edge of the field of view for proper fitting. Only the CBCD files are saturation corrected (not the BCD files). The saturated pixels that have been replaced are identified within the bimsk (imask) files (bit 13).

2. A New Muxstripe Remover

Muxstripping is now fit and corrected in a new pipeline module. The noise of the affected pixel area is compared to the unaffected pixels in the frame and a deviation is removed, without changing the background level or the flux in the pixels. Occasionally this correction fails and the muxstripping is unchanged. Only the CBCD files include this correction, not the BCD files.

3. Pmask Bits Now Included As Part of Imasks

See the imask bit definition in Section 7.1 of the IRAC Instrument Handbook for the definition of the various bits.

4. Mosaic Mask Files Now Available

The PBCD mosaics created in the pipeline now have associated mask files. The imasks associated with the CBCDs that were used for the creation of the mosaic have been combined to create the mask file, so the bit values can be deduced from the imask bit definition table.

5. Improved First-Frame Correction

More appropriate skydarks are now used in the pipeline, producing an improved first-frame effect correction.

S18.0 (2008 June 12)

1. Muxbleed Correction Update

The correction of the muxbleed effect in the BCD frames was updated. After extensive testing a new functional form and scaling law was developed for muxbleed correction in channels 1 and 2. The new functional form and scaling law correct muxbleed better than before.

2. MOPEX Now Using the *bimsk.fits* Files

In creating the final mosaic image, **maic.fits*, the MOPEX pipeline now uses the **bimsk.fits* files as input, instead of the **dmsk.fits* files. The **bimsk.fits* files have more relevant information useful for flagging when building mosaics and analyzing the images.

3. Header Information Updated

WCS CD matrix keywords were added to the Post-BCD file headers. The CDELTA1, CDELTA2, and CROTA2 keywords have been preserved but were placed in comments to avoid any confusion when handled by astronomical software. The following keywords were added to the BCD, CBCD, and Post-BCD image files: PXSCAL1, and PXSCAL2, and PA. The keywords are the pixel scale along axis 1 and axis 2 in arcseconds/pixel and the position angle of axis 2 (East of North) in degrees. Keywords containing additional information on the AOR mapping parameters have been added in a separate section of the header.

S17.0 (2007 December 5)

1. Artifact Mitigation Within the Pipeline

Artifact-mitigated images from the BCD pipeline and their associated uncertainty images (**bcd.fits* and **cbunc.fits*) are now available in the archive. These images include corrections for column pull-down and banding, induced by bright sources in the images. The corrections are empirical fits to the BCDs and may not always improve the data quality. The standard BCD files (**bcd.fits*) remain available in the archive. The mosaics (post-BCD products) are now created from the **bcd.fits* images.

2. Muxbleed Correction Updated Again

The muxbleed correction has been revised to include a better empirical fit.

3. Two-Dimensional Subarray Images

A two-dimensional image is now generated for each subarray BCD cube. Each pixel in the 2D image (**sub2d.fits*) is a robust (outlier-rejected) mean of the 64 samples of the **bcd.fits* cube. Two-dimensional masks, uncertainty images, and coverage maps are now also provided.

4. Artifacts Now Flagged In Subarray Images

The subarray imasks (**_bimsk.fits*) now include masking for muxbleed, column pull-down and banding, induced by bright sources. The updated masks can be used to mitigate bright source artifacts the same way as with the full array data.

5. Darkdrift Values Written Out in the Subarray Header

The pipeline darkdrift module reduces a “jailbar” bias effect in the IRAC images. The values used for the reduction within the pipeline are included in the header of the full array data, and now in the header of the subarray data for all the planes. This allows the user to remove the correction, if desired.

6. Mosaic Header Updated

We have added more information to the mosaic header.

S16.0 (2007 April 9)

1. Labdark Change for 100 Second HDR Data

Within 100 second AORs, the channel 4 observations are split into two 50s frames. The second 50 second frame received an incorrect non-HDR 50 second labdark instead of an HDR labdark. This was a minor problem, and has now been corrected.

2. Muxbleed Correction Updated

The module that detects and corrects the muxbleed caused by bright sources has been updated. It now performs a more consistent and better correction than previously.

3. Artifacts Flagged Within the Pipeline

The imasks (**_bimask.fits*) now include masking for muxbleed, column pull-down, and banding induced by bright sources on images. The updated masks can be used with existing contributed software to mitigate bright source artifacts, and will be used in future versions of the IRAC pipeline after mitigation algorithms have been implemented. In general, observers should not flag artifacts in mosaicking unless they have observations at various roll angles.

4. Pixel Linearization

The handling of bad and saturated pixels has been changed – they are in most cases now left with their original values, as opposed to being set equal to NaN. The method of flagging saturation in BCD mask files was changed, and now more accurately reflects the presence of saturation.

S15.0 (2006 November 28)

1. Ghost Images And Scattered Light Flagged Within Pipeline

Pipeline versions of the ghost image and scattered light detection algorithms have been integrated into the IRAC pipeline. The modules use the location of bright sources upon the array (ghost image) or just outside the array, as found in 2MASS catalogs (scattered light) to predict possible optical ghosts and scattered light locations, and flag these pixels within the imask. The imask is an ancillary data product now available through the archive. IRAC observers should use the imask instead of the dmask when making mosaics etc.

2. Incorrect Group Ids in Header to Be Fixed

A bug that caused a small percentage of BCDs (< 0.1%) to have an unreadable header and which were therefore not pipeline-processed, has been fixed. This should significantly decrease the number of missed BCDs in large mapping programs.

S14.0 (2006 May 3)

1. Darkdrift Module Changes

As mentioned below, in S13 the darkdrift module was applied only to channel 3 data. This module is used to adjust the bias level in the four readouts in an array, thereby removing vertical striping in the data, the so-called "jailbar effect." After S13 reprocessing of IRAC data it was found that the jailbar effect can be triggered in channels 1, 2 and 4 as well. Therefore, the darkdrift module will again be applied to all four channels, and all the IRAC data will be reprocessed with pipeline

version S14. We have released a "jailbar corrector," which may be used to correct for the jailbar effect. It produces similar results to the darkdrift corrector module in the IRAC pipeline.

2. Added Keywords

Individual array readout noise (RONOISE) keywords.

S13.0 (2005 October 27)

1. "Superboresight" Pointing Refinement (S13.2 And Thereafter)

Previous versions of the pipeline performed pointing refinement on each IRAC channel separately. The refinement was performed by matching detected point sources to 2MASS stars and registering the astrometry to minimize the positional offset between matches. In most cases, the refinement of channels 3 and 4 is less accurate as the number of stars detected in an individual frame is less than in channels 1 and 2. Superboresight refinement corrects the astrometry for all the four channels by simultaneously using appropriately weighted matches from all the four channels and the known orientations of the FPAs. This method can dramatically improve the pointing accuracy for channels 3 and 4, and it removes any positional offsets between channels. The superboresight pointing is inserted into the CRVAL1 and CRVAL2 keywords in the header, while the basic (less accurate) pointing refinement remains in RARFND and DECFND header keywords, and the original boresight pointing solution is placed in new header keywords ORIG_RA and ORIG_DEC.

2. First-Frame Effect

The interval between frames (INTRFDLY) is now maintained in a database, instead of the pipeline reading the previous image in an AOR to process the current image. This streamlines operations and handling of missing images. It is also placed in the header as a keyword.

3. Linearity Correction

New linearity corrections have been calculated from on-orbit tests and small changes were made to channel 3 full array and all channel subarray data. The effect is roughly 2% at half-well, and 8% at 90% full-well in channel 3. The other channels are within specifications and the linearity corrections were not changed for them.

4. Darkdrift Module Changes

The darkdrift or jailbar effect (see Section 5.1.12) is corrected in the pipeline software by applying a constant offset per readout channel (arranged in columns), derived from the median of those columns such that their arithmetic mean is zero. In other words, all readout channels are adjusted to a common additive bias level. In in-orbit tests, the mean offset and correction was found to be negligible, except in channel 3 data. Therefore, in S13 reprocessing, the darkdrift correction was only applied to channel 3 data. The derived correction values for each channel are located in the header in the keywords DRICORR1, DRICORR2, DRICORR3, and DRICORR4. The overall background term determined is DRIBKGND.

5. Distortion Files

The subarray distortion files were found to be derived from an incorrect place on the full array and have now been updated with correct ones. This should only make a small, but noticeable difference in pixel sizes when measuring relative separations in the subarray.

6. Superskyflat

A new superskyflat has been derived from the first two years of flat-field data on IRAC and will be used as the flat-field for all reprocessing and in future campaigns. Uncertainties in the pixel-to-pixel responsivity calibration are only 0.5%, 0.2%, 0.2%, and 0.05% for channels 1 – 4, respectively.

7. Flux Conversion

The flux conversion has been updated to reflect the derivation described in the IRAC calibration paper by Reach et al. (2005). The previously used numbers were from a nearly complete phase of this derivation, but different by 3% in channel 4.

8. Added Keywords

1. Median brightness of calibration skydark (SKYDKMED)
2. More precise start time of observation (SCLK_OBS).

S12.0 (2005 May 9)

1. New Stellar Mode

New observing mode, “Stellar Mode” has multiple full array short time exposures within channel 1 and 2 and at the same time has a longer integration in channels 3 and 4. This allows for brighter objects to be observed in the longer wavelength channels to higher signal-to-noise without saturating in the shorter wavelength observations. Available frame times are 0.4/2 seconds, 2x2/12 seconds, and 2x12 seconds/30 seconds. The first number(s) refer to channels 1 and 2, the last number to channels 3 and 4.

2. Median Subtracted Skydark Value

The median value of the frames used to create the skydark subtracted from the data was placed in the header of the BCD: keyword SKYDKMED.

3. Labdark Name to Headers

The name of the labdark subtracted from the data was placed in the header: keyword LBDRKFLE.

4. Exact Time of Observation to Headers

The time of the observation (SCLK_OBS) is now computed using telemetry only to allow for more exact timing. This keyword will be placed in the database and header. Further S13 changes will include calculating the first-frame correction from this more exact timing.

5. Pointing Keyword Additions

Keywords PTGDIFFX, PTGDIFFY were inserted to refer to the pointing differences in actual pixels along the X and Y axis.

S11.0 (2004 November 30)

1. Fix to EQUINOX Keyword

The EQUINOX header keyword for BCDs has been fixed.

2. New Delay Header Keywords

Other changes to the header include the addition of the First Frame Delay and Immediate Delay (FFDLAY & IMMDELAY) times, calculated from the first-frame correction.

3. CHECKSUM Changes

Previously, a DCE with a non-zero CHECKSUM from MIPL was not allowed to process through the pipeline. In S11, the CHECKSUM will now be reported within the header and the DCE processed.

4. First Frame Correction for HDR Observations

The first-frame effect correction has been fixed for the high dynamic-range observations. The only remaining bug is for the intermediate frame times (12 seconds) when used as part of an HDR

frameset. This effect will not be noticeable except as a slight background DC-level offset from frame to frame in the 12 second data as part of 100 second or 200 second HDR framesets.

5. Super Skyflat Creation

After studying last year's flat-fields and finding no noticeable change from campaign to campaign, a superskyflat has been made from last year's flat observations. A subarray flat has been extracted from this superskyflat, and both have been loaded into the pipeline.

6. Overlap Correction Added to Pipeline

Overlap correction is now applied in the post-BCD pipeline.

7. Mosaic Image Keyword Additions

The mosaic image headers have been populated with more keywords.

S10.5 (2004 June 2)

1. FFCORR Delay Time Update

Updated the FFCORR module to use the correct delay time between frames for full array non-HDR frames. The HDR frames will be fixed in S11.

S10.0 (2004 May 7)

1. New Linearity Mode

New linearity model in channel 4 (full and sub). Change from quadratic to cubic (actually updated in S9.5.2).

2. FFCORR Output Changes

Module FFCORR set to output only one plane for interpolated correction image rather than all planes.

3. New FITS Keyword

Create and populate new FITS header keyword (DS_IDENT).

4. Readnoise Update

Update to read noise in initial noise image.

5. NaN-Value Consequences in Uncertainty Images

If BCD pixel = NaN, uncertainty pixel = 0.

6. New Skydark Keyword

Keyword from dark ensemble placed in BCD header (SKYDRKZB; skydark zodiacal background estimate added into header of science BCD).

S9.5 (2004 March 1)

1. New Fields in Caldata Tables

Addition of two fields, hdrmode and numrepeats, to caldata tables. Requires a backfill script to transform and migrate current fallbacks and metadata to new tables. The HDRMODE field is in current use. The NUMREPEATS field is to facilitate use of the external repeat number in future calibration activities.

2. Flux Conversion

In S9.5 the flux conversion will be delivered in an IPAC table, for example:

```
\char Comment Calibration data file for dntoflux module.
\char INSTRUME = 'IRAC'
\int CHNLNUM = 4
\char fluxconv = 'Conversion factor in MJy/sr per DN/s'
\char fluxconvunc = 'Uncertainty in fluxconv'
|fluxconv |fluxconvunc |
|float |float |
0.195 0.020
```

3. HDR Skydark Change

HDR skydarks are now different from non-HDR skydarks. The skydark processing branch of the pipeline is now aware of channel 4 repeats and the pipelines fetch skydarks for the correct repeat. This is possible due to new fields in the caldata tables.

4. Scattered Light Removal Added

Scattered light removal module (“SLREMOVE”) added to science pipeline and calibration preprocessing.

5. FPGEN Used in Product Header

Calibration ensemble pipelines now use “FPGEN” to clean up the product header.

6. Subarray Flat Creation

New pipeline to create subarray flat-fields from full array flat-fields.

7. Latent Ensemble Additions

Latent ensemble creates new request median and request average images.

8. New Keywords to Mosaic Headers

New keywords to be added to the mosaic header: AOT_TYPE, AORLABEL, FOVID, FOVNAME, PRIMEARR, OBJECT, PAONUM, CAMPAIGN.

S9.1 (2004 January 22)

1. Pointing Reconstruction

Less than 0.1% of the DCEs may not have pointing reconstruction applied to the data. BCDs with USEDDBPHF=F indicate that the Boresight Pointing History File was not used, and the R.A. and Dec. in the headers for these cases are based on pre-observation predictions which can be off by 5 – 50 arcseconds. Do not use such data if pointing is important.

S9.0 (2004 January 14)

1. Annealing in Channel 1 and 4

Anneals: Both channels 1 and 4 will continue to be annealed simultaneously, every 12 hours (after each downlink) to reduce persistent images.

S8.9 (2003 December 8)

1. Impact of Long Term Residual Images

Some AORs have been affected by long term residual images from previous observations. For the most part, observers have sufficiently dithered so that the impact is minimal, on processed and co-added data.

2. Noise in Data vs. Predictions

Note that the noise in the images and the sensitivity to point sources are not equal to our pre-launch predictions (e.g., as available from our website until December 19, or in the Observer's Manual versions before 4.0), although they are close. New sensitivity numbers are available in the revised Observer's Manual (version 4.0), which was available at our website starting \approx December 19, 2003. For reference, the ratio of the new point source detection threshold to the pre-launch advertised value, for low background observations in 30 second frames, is 0.69, 0.75, 1.60, and 1.31 in channels 1, 2, 3, and 4, respectively. The apparent modest decrease in sensitivity in channels 3 and 4 is under investigation.

3. Persistent Images in Channel 1

When a bright source ($K=13$ mag or brighter) is stared at for a long time, for example, during a downlink, it will leave a persistent image in channel 1 that decays very slowly (persists for several hours or more). A persistent image mitigation strategy involving annealing the array after downlinks has been put in place for nominal operations. These anneals will erase the persistent images from the array, but do not protect against persistent images from bright object observations that can accumulate on the array before the next downlink. Science impact: left unmitigated, you will have extra, spurious sources in your image. These sources have a PSF that is wider than the actual true source PSF. Dithering helps to get rid of these spurious sources.

4. Persistent Images in Channel 4

These are different in nature from the channel 1 persistent images. A bright source leaves a persistent image that can last for more than a week and even through IRAC power cycles. These images keep building up on the array. However, the amplitude of the persistent images is rather low. Annealing has been found to erase also the channel 4 persistent images. Therefore, we will anneal both channels 1 and 4 simultaneously, every 12 hours (after each downlink), to erase persistent images. Again, dithering helps to get rid of these spurious images.

5. Diffuse Stray Light

All IRAC images contain a stray light pattern, resembling a “butterfly” in channels 1 and 2, and a “tic-tac-toe” board in channels 3 and 4. These artifacts are due to zodiacal light scattered onto the arrays, possibly reflected from a hole in the FPA covers above the channel 1 and 2 arrays, and from reflective surfaces outside the edges of channel 3 and 4 arrays. The stray light scales with zodiacal light, which is the light source for our flat-fields, so the stray pattern contaminates the flats. As a result, the flat-fields will aesthetically remove the stray light rather well from images but will induce systematic errors of approximately 5% in flux calibration for point sources that fall in the peak stray light location. Dithering will mitigate this effect, because it is unlikely that a dithered observation will keep a source within the stray light lobes. Diffuse stray light will be removed from both the flat-fields and the science frames in a future version of the pipeline.

6. Stray Light from Point Source

Spot allows you to overlay stray light boxes on any image; if a bright star is placed in those boxes during an observation, a scattered light patch will appear on the array. We have found three more such boxes during testing, in channels 1 and 2. The new stray light boxes are included in Spot now and are also shown in the new Observer's Manual. Channels 3 and 4 have less stray light, and the stray light inducing regions are not the same as the ones we guessed (by analogy to channels 1 and 2) from the lab tests, so the channel 3 and 4 boxes were removed from Spot. In channels 3 and 4

the stray light arises when a star lands on a thin region just outside the array (the same region that causes the “tic-tac-toe” pattern from diffuse stray light in flat-fields). A redundant observing strategy will help eliminate stray light problems. Observers covering fields with bright sources should inspect the individual images; this is required if the depth of coverage is less than three, to identify spurious spots and rays that could be mistaken for real astronomical objects.

7. Dark Spots on Pick-Up Mirror

Dark spots on pick-up mirror. There is contamination on the mirror, which causes a dark spot about 10 pixels wide in channels 2 and 4. This is a 15% effect. Flat-fields completely correct for this feature in the data.

8. Muxbleed

We have a correction algorithm, but the coefficients need fine-tuning. Furthermore, for bright sources, muxbleed does not scale linearly with source brightness, so even a sophisticated algorithm cannot accurately remove it. Some experiments at fitting the muxbleed for bright sources indicate that the decay pattern is always the same, and only the amplitude appears to be variable.

9. Banding and Column Pull-down

Banding and column pull-down. A bright source on the array will cause its column to be pulled down by a small amount. An algorithm to cosmetically correct the images for column pull-down has been developed and is being tested. This appears to be an additive effect. An analogous effect for an extremely bright source is that the entire image appears to have a different DC level from the preceding and following images. The physical origin of these effects and the probably related (and already known) banding effect is not yet understood. This work is in progress.

10. Mosaics

Mosaics produced by the online pipeline for HDR mode data incorrectly weight the short and long frame times. For long exposures (> 12 seconds), data are effectively taken in HDR mode, and hence the pipeline produced mosaics will not be very useful.

11. Cosmic Ray Rejection in Pipeline

Cosmic ray rejection is not functioning well.

Appendix B. Performing Photometry on IRAC Images

This is a quick guide for performing point source photometry on IRAC images.

A. Point Source Photometry on a Mosaic

1. If you are only interested in photometry down to about 10% accuracy and have bright point sources, you can usually perform photometry on the pipeline mosaic. Set the aperture size to 10 native (≈ 1.2 arcseconds) or 20 mosaic (≈ 0.6 arcseconds) pixels and the sky annulus to between 12 and 20 native (≈ 1.2 arcseconds) pixels (or between ≈ 24 and 40 0.6 arcseconds mosaic pixels). The IRAC calibration is based on an aperture of this size (see Section 4.3), so for this aperture no aperture correction is necessary. For fainter stars, it is better to use a smaller aperture and then apply an aperture correction (see Section 4.7). Remember that the units of the images are in MJy/sr, so you need to convert your measured values into flux density units in micro-Jy, by accounting for the pixel size in steradians. Conversion into magnitudes is $\text{magnitudes} = -2.5 \cdot \log_{10}(f/f(0))$, where f is your measured flux density and $f(0)$ is the zero magnitude flux density. If using software such as “phot” or “qphot” in IRAF/DAOPHOT that requires a magnitude zeropoint, the “zmag” keyword in `photpars` should be set to 18.80 (channel 1), 18.32 (channel 2), 17.83 (channel 3) and 17.20 (channel 4) if using a mosaic pixel scale of 0.6 arcseconds/pixel. Other zmag values will be needed for other pixel sizes. Note that if you require photometry to a higher accuracy than 10% – 20%, you should follow the steps listed below.

2. Examine your data (CBCDs) and identify artifacts that could affect your photometry and that need to be corrected. See the Contributed Software page for useful tools at

<https://irsa.ipac.caltech.edu/data/SPITZER/docs/dataanalysis/tools/contributed/> .

3. First perform artifact mitigation on the pipeline-produced CBCDs. While the pipeline-reduced CBCD files are mostly artifact-free, some residual artifacts remain. For example, the pipeline and contributed software have difficulty recognizing very saturated pixels that produce artifacts. As a result, they will not usually correct artifacts from very saturated point sources or from extended saturated regions. Data at 5.8 and 8.0 μm exhibiting the bandwidth effect (see Section 7.2.3) should be masked before performing photometry.
4. Make a mosaic of artifact-corrected images (see Section 8.4.3), for example with the MOPEX package. When creating the mosaic, the overlap correction option should be used in MOPEX, most importantly in channels 3 and 4, to match the backgrounds. Inspect the mosaic to confirm that outlier rejection is acceptable. If not, then re-mosaic with more appropriate MOPEX parameters. Comparing mosaics of adjacent channels on a per-pixel basis will readily identify if outliers remain in a mosaic. The mosaic coverage maps should be inspected to verify that the outlier rejection has not preferentially removed data from

actual sources. If the coverage map systematically shows lower weights on actual sources, then the rejection is too aggressive and should be redone.

5. If you are interested in blue point sources (sources with spectral energy distributions, SEDs, that decline toward the longer wavelength IRAC passbands) you should create an array location-dependent photometric correction image mosaic (see Section 4.5). If you are interested in only red sources (with SEDs that rise toward the longer wavelength IRAC passbands), you do not need to apply the photometric correction images and make a mosaic out of them. We recommend making a correction mosaic, instead of multiplying the correction images with the CBCDs and then mosaicking these CBCDs together, since you may need to iterate this a few times or you may have both red and blue sources in the field, and thus the correction only applies to a subset of sources. This location-dependent effect is as large as 10%. *It is the dominant source of uncertainty in the photometry of IRAC images.* For observations that well sample the array for each sky position the effect will average out. MOPEX software now is capable of creating these correction mosaics for you. If you want to make the BCD-matched photometric correction images yourself, first copy the FITS header keywords CTYPE1, CTYPE2, CRPIX1, CRPIX2, CRVAL1, CRVAL2, CD1_1, CD1_2, CD2_1, CD2_2 from the headers of the BCDs to the headers of the photometric correction images in each channel using your favorite FITS manipulation software. Thus, you make the same number of photometric correction images (otherwise identical except for the keyword information) as there are CBCDs in each channel. The correction images must be divided by the pixel solid angle correction images before mosaicking them together, because the pixel solid angle effect is essentially corrected for already in the photometric correction images and thus needs to be “canceled out” before running the images through MOPEX (which corrects for this effect). Then, copy the namelist you used to make the CBCD mosaic images into some other name, and edit the namelist to disable all the outlier rejection modules. Do not run the fiducial image frame module but instead point MOPEX to the existing “*FIF.tbl*” file used for generating the corresponding CBCD mosaic. Next, specify the RMASK_LIST file (generate a file listing the rmask and their path, as created by the mosaicker run for the corresponding CBCDs). Finally, make the correction image mosaic with MOPEX.

6. Perform photometry with your favorite software. Aperture photometry is preferred over PRF-fitting photometry due to the undersampled nature of the data. To properly estimate the uncertainties in your photometry, the uncertainty images provided with the CBCDs can be used and mosaicked into an uncertainty mosaic. The CBCD uncertainties are slightly conservative as they take the uncertainties into account in each pipeline calibration step. For packages that estimate noise directly from the data assuming Poisson noise, in low background cases you can convert the mosaic into electron units, so as to calculate the uncertainty due to source shot noise and background correctly. The conversion from MJy/sr is $*GAIN * EXPTIME / FLUXCONV$ where GAIN, EXPTIME, and FLUXCONV are the keywords from the CBCD header. In determining the noise, the coverage of the observation at the position of your target should also be taken into account (e.g., by entering the correct number of frames in DAOPHOT or by dividing the noise by the square root of coverage, from the coverage mosaic at the position of each target). Your aperture photometry

software should of course subtract the appropriate background (usually in an annulus around the source).

7. Apply aperture correction, found in Chapter 4 of this Handbook, if you perform aperture photometry in an aperture different from the 10 pixel radius aperture used for IRAC calibration or determine the background by other means than an annulus. Observers can determine their own aperture corrections by downloading IRAC calibration star observations from the Spitzer Heritage Archive, and comparing the photometry to that published in the IRAC Calibration Paper (Reach et al. 2005).
8. Observers should apply the array location-dependent photometric correction for blue sources and the appropriate color correction (see Section 4.4) for all sources (based on the spectral energy distribution of the source). Determine the array location-dependent photometric correction (for blue compact sources) from the correction mosaic, constructed in step 5 above, by looking at the values of the pixels at the positions of the peaks of your point sources. Apply a color correction from Chapter 4 of this Handbook using the tabulated values, if appropriate, or calculate the color correction for a source spectral energy distribution as done in that chapter. To calculate a color correction, you will need the IRAC spectral response curves a

<https://irsa.ipac.caltech.edu/data/SPITZER/docs/irac/calibrationfiles/spectralresponse/>.

9. Color corrections are typically a few percent for stellar and blackbody sources, but can be more significant for sources with ISM-like source functions (50% – 250% depending on spectrum and passband). Measured flux density is the flux density at the effective wavelength of the array: 3.550, 4.493, 5.731, and 7.872 μm , for channels 1 – 4, respectively.
10. A pixel phase correction (see Section 4.6) to the measured channel 1 flux densities should then be considered. More information on the pixel phase correction can be found in Chapter 4 of this Handbook. This effect is as large as 4% peak-to-peak at 3.6 μm and < 1% at 4.5 μm . To apply a correction for mosaicked data is difficult, as the pixel phase correction depends on the placement of the source centroid on each CBCD. For well-sampled data the pixel phase should average out for the mosaic. For precise photometry in low coverage data, the source centroids on the CBCDs should be measured and the phase corrections averaged together and applied to the final source photometry.

B. Point Source Photometry on a Mosaic

Although most of the time it is a good idea to use the mosaic for performing photometry, performing photometry on the (C)BCD stack is important for variability studies and can be useful for faint sources as one can measure N out of M statistics (how many times you found the source). Using (C)BCDs is also required when performing absolute photometry (as indicated below). For

absolute photometry, you can also refer to the IRAC calibration papers by Reach et al. (2005) and Carey et al. (2012). When performing source profile fitting, performing photometry on the (C)BCD stack is better as the phase information of the PRF is preserved.

1. Examine your data (CBCDs) and identify artifacts that could affect your photometry and that need to be corrected.
2. First perform artifact mitigation, for example by using the Contributed Software at

<https://irsa.ipac.caltech.edu/data/SPITZER/docs/dataanalysisistools/tools/contributed/>

on the pipeline-produced CBCDs. While the pipeline-reduced CBCD files are mostly artifact-free, some residual artifacts remain. The pipeline and contributed software have difficulty recognizing very saturated pixels that produce artifacts. As a result, they will not usually correct artifacts from very saturated point sources and extended saturated regions. Data at 5.8 and 8.0 μm exhibiting the bandwidth effect should be masked. If performing aperture photometry on the CBCDs, a particular CBCD should not be used for a source when there are masked (bad) data in the source aperture.

3. Make a mosaic of artifact-corrected images, for example with the MOPEX package (see Section 8.4.3). This needs to be done to create the proper rmask files to be applied to the CBCDs when performing APEX-based photometry on them, and also to get a nice comparison of CBCD-revealed and mosaic-revealed image features. When creating the mosaic, the overlap correction option should be used in MOPEX, most importantly in channels 3 and 4, to match the backgrounds. Inspect the mosaic to confirm that outlier rejection is acceptable, and if not, then remosaic with more appropriate parameters. Comparing mosaics of adjacent channels on a per-pixel basis will readily identify if outliers remain in a mosaic. The mosaic coverage maps should be inspected to verify that the outlier rejection has not preferentially removed data from actual sources. If the coverage map systematically shows lower weights on actual sources, then the rejection is too aggressive and should be redone. One result of making the mosaic is the production of rmask files which identify bad pixels in the CBCDs. One should apply the rmask when performing the photometry in the next step so that bad pixels are not included within the apertures.
4. Perform photometry with your favorite software. The PRFs supplied can be used with APEX in multiframe mode for point source fitting. A “How To” guide and details of the validation are presented in Appendix C. The CBCD uncertainties are slightly conservative as they take into account the uncertainties in each pipeline calibration step. For packages that estimate noise directly from the data assuming Poisson noise, you can convert the CBCDs into electron units, so as to calculate the uncertainty due to source shot noise and background correctly. The conversion from MJy/sr is $*\text{GAIN} * \text{EXPTIME} / \text{FLUXCONV}$ where GAIN, EXPTIME, and FLUXCONV are the keywords from the CBCD header. For accurate photometry, a good background estimate is required. When performing point source fitting with APEX, the parameters of the `medfilter` module should be tuned to ensure good background subtraction. For aperture photometry, the background estimate

can be obtained from an annulus around the source (but note that the radii of the background annulus will affect the aperture correction). Also for aperture photometry, the centroids of the point sources can be estimated with the contributed box centroid code:

https://irsa.ipac.caltech.edu/data/SPITZER/docs/irac/calibrationfiles/pixelphase/box_centroider.pro

5. Observers should apply the array location-dependent photometric correction (see Section 4.5 and Figure 4.5) for blue sources and the appropriate color correction for all sources (based on the spectral energy distribution of the source). The photometric array location-dependent correction images are linked from the IRAC web pages at

<https://irsa.ipac.caltech.edu/data/SPITZER/docs/irac/calibrationfiles/locationcolor/> .

6. Apply a color correction from Chapter 4 of this Handbook, using the tabulated values, if appropriate, or calculate the color correction for a source spectral energy distribution as done in that chapter. To calculate a color correction, you will need the IRAC spectral response curves, which are also available on IRSA's IRAC web pages. Color corrections are typically a few percent for stellar and blackbody sources, but can be more significant for sources with ISM-like source functions (50% – 250% depending on the spectrum and passband). The measured flux density is the flux density at the effective wavelength of the array: 3.550, 4.493, 5.731, and 7.872 μm , for channels 1 – 4, respectively.
7. Pixel phase corrections (see Section 4.6) need to be applied in channels 1 and 2. The PRFs include the pixel phase effect, so the single mean correction given in Appendix C is adequate. In the case of aperture fluxes, all the fluxes need correction. More information on the pixel phase correction can be found in Chapter 4 of this Handbook. You can use the contributed code at

<https://irsa.ipac.caltech.edu/data/SPITZER/docs/irac/calibrationfiles/pixelphasecryo/>

for cryogenic data or the contributed code at

https://irsa.ipac.caltech.edu/data/SPITZER/docs/irac/calibrationfiles/pixelphase/pixel_phase_correct_gauss.pro

for warm data. Note that this effect is as large as 4% peak-to-peak at 3.6 μm and < 1% at 4.5 μm (channels 3 and 4 do not have a pixel phase correction). Steps 5 and 6 may be conveniently performed using the contributed code at

<https://irsa.ipac.caltech.edu/data/SPITZER/docs/dataanalysisistools/tools/contributed/irac/iracaphotcorr/>

but this assumes that you will use the 3 pixel radius for aperture photometry, with the 3 – 7 pixel radius annulus for background determination (and requires a corresponding aperture correction in the next step).

8. Apply aperture correction, found in Chapter 4 of this Handbook, if you perform aperture photometry in an aperture different from the 10 pixel radius aperture used for IRAC calibration. The 10 pixel radius with 12 – 20 pixel background annulus is ideal for measuring calibration star photometry as those values were used in IRAC flux density calibration. Observers can determine their own aperture corrections by downloading IRAC calibration star observations (c.f. Table 4.1 and Table 4.8) from the Spitzer Heritage Archive and comparing the photometry to that published in the IRAC Calibration Paper (Reach et al. 2005). Aperture corrections for fitted fluxes are given in Appendix C.
9. Combine photometry from CBCDs, taking uncertainties into account, to generate a robust, weighted mean value. Verify that the dispersion in these measurements is comparable to the uncertainty of the individual measurements (if not, use the dispersion until you track down the source of extra error, e.g., bad pixels/cosmic rays in source). Note that what you have actually measured is F^*K^* in terms of Table 4.1. If you have tried to measure calibration stars, your results may slightly differ from those in Table 4.1, as the Table values are based on the average results for all the calibration stars, and therefore differ from the values measured for each individual star.
10. Apply a color correction. If you want a flux density that can be compared to any instrument's absolute flux density measurement, then calculate a color correction as explained in Section 4.4, and divide F^*K^* by the color correction to arrive at F^* .

Appendix C. Point Source Fitting IRAC Images with a PRF

This Appendix discusses the use of point source response functions (PRFs) for fitting sources in IRAC data. For true point sources, it is possible to obtain agreement between PRF-fitted and aperture photometry flux measurements at better than the 1% level. In this Appendix, we describe validation tests on point sources in IRAC data using the PRFs in combination with the MOPEX/APEX software. The procedure for using the PRFs in conjunction with MOPEX/APEX is given in the form of a “How To” description, and the necessary corrections to the resulting flux densities are detailed.

Point source fitting is a valuable tool for characterizing images. If the image consists of true point sources, PRF fitting can make optimal use of the information in the image, thus improving astrometric and photometric results beyond what is achievable using other techniques. PRF fitting also allows point sources to be subtracted from an image (for example, using the `apex_qa` task in MOPEX/APEX), enabling any diffuse background emission to be more easily characterized. Point source fitting is less useful in fields containing large numbers of partially-resolved objects (as typically seen in IRAC extragalactic survey fields), and aperture photometry is recommended in such fields. (In principle, model fitting could be used for extended sources by convolving a source model with the appropriate point source realizations, but such techniques lie outside the scope of this Appendix.) For isolated point sources on featureless backgrounds aperture photometry and point source fitting should give almost identical results.

Point source fitting to IRAC data has proven problematic as the PSF is undersampled, and, in channels 1 and 2, there is a significant variation in sensitivity within pixels. Techniques for dealing with these problems were developed for the WFPC2 and NICMOS instruments on HST (Lauer 1999; (Anderson, J. & King, I. R., 2000) (Franceschini, A. et al., 1991), see also Mighell et al. 2008). These techniques involve building a “point response function” (PRF; Anderson & King use the alternative terminology “effective PSF”), and users interested in the detailed theory of the PRF should refer to these papers. In summary, the PRF is a table (not an image, though for convenience it is stored as a 2D FITS image file) which combines the information on the PSF, the detector sampling and the intrapixel sensitivity variation. By sampling this table at regular intervals corresponding to the grid of pixel phases sampled, an estimate of the detector point source response can be obtained for a source at any given pixel phase.

PRFs for IRAC have been created by William Hoffmann of the University of Arizona, a member of the IRAC instrument team. The starting point for these PRFs was the Code V optical models for Spitzer/IRAC, made at the Goddard Space Flight Center [see also the technical memo “25 Position Model Pixel Response Functions (PRF) Description and Quality” by Hoffmann in the IRAC Papers section at

<https://irsa.ipac.caltech.edu/data/SPITZER/docs/irac/iracpapers/>].

These were constructed on a 5×5 grid of sub-pixels covering each of the IRAC arrays. Observations of a calibration star made during the in-orbit checkout at each of these 25 positions

per array were then deconvolved by their respective optical models. The results were averaged into a single convolution kernel per array which represents additional PRF scatter from unmodeled optical effects and spacecraft jitter. A paper by Hoffmann et al. “Simfit and Focus Diversity: Methods for determining the focus of the SIRTf telescope in space without a focus slew” gives more details and is included in the IRAC Papers section of IRSA’s Spitzer website. The intrapixel sensitivity function was estimated using a polynomial fit as a function of pixel phase. The PRFs were then transposed, and flipped in x and y to align them with the BCD coordinate system.

C.1 Use of the Five Times Oversampled PRFs Outside of APEX

As supplied in the documentation website, the PRFs are oversampled by a factor of five in Δ_x and Δ_y . This allows for $5*5=25$ independent realizations of a point source, corresponding to 25 different pixel phase combinations (five each in x and y ; see also Figure C.5). An IRAC pixel image (point source realization) can be obtained by overlaying the IRAC pixel pattern on the higher resolution PRF grid. The value on the PRF grid at the center of a given IRAC pixel is taken for the pixel value. If the IRAC pattern is not registered exactly with the PRF grid, the values must be interpolated between grid points. Thus, lower numbered PSRs result from overlaying the IRAC pixel pattern lower and to the left on the PRF grid, so the source appears on the top right; and vice-versa. To obtain any given point source realization (PSR), the PRF needs to be sampled every fifth pixel in x and y at the appropriate phase, i.e.,

$$\text{PSR1}(i,j) = \text{PRF}(5i-4,5j-4)$$

$$\text{PSR2}(i,j) = \text{PRF}(5i-4,5j-3)$$

$$\text{PSR3}(i,j) = \text{PRF}(5i-4,5j-2)$$

$$\text{PSR4}(i,j) = \text{PRF}(5i-4,5j-1)$$

$$\text{PSR5}(i,j) = \text{PRF}(5i,5j)$$

$$\text{PSR6}(i,j) = \text{PRF}(5i-3,5j-4)$$

.....

$$\text{PSR13}(i,j) = \text{PRF}(5i-2,5j-2)$$

$$\text{PSR25}(i,j) = \text{PRF}(5i,5j)$$

where i,j are integers running from 1 to n in the case of a PRF table which is $5n * 5n$ in size. The current PRF table available on IRAC web pages at IRSA has a size of 128,128. You may copy this

to, e.g., a 125,125 array so that the peak pixel is in the center pixel of this new array. In this case, *PSR13* corresponds to the source landing in the center of a pixel. Note that the PRF should not be block averaged, as this will result in the loss of the pixel phase information.

These PRFs may be implemented directly by those willing to write their own code. In IDL, for example, a point source realization may be generated using the `/SAMPLE` switch in `rebin`, e.g,

```
psr = rebin(phasedPRF,n,n,/SAMPLE)
```

where `phasedPRF` is the $5n \times 5n$ PRF shifted to the appropriate pixel phase in both dimensions. In IRAF, use:

```
imcopy PRF.fits[1:5n-4:5,1:5n-4:5] PSR1.fits
```

Note that the PSRs are normalized to unity at infinity, not to the IRAC 10 pixel calibration aperture. Fluxes obtained with these thus need to be multiplied by the appropriate infinite aperture correction. These have been determined to be 0.943 in channel 1 and 0.929 in channel 2, based on measurements of the PRF, and can be compared to direct measurements of 0.944 and 0.937. Estimates from the PRF are unavailable in channels 3 and 4, but the corrections given in this Handbook are 0.772 and 0.737, respectively (Table 4.8).

C.2 Modifications to the IRAC PRFs for Use with APEX

The IRAC PRFs are centered relative to the optical axis, so they are slightly off center in array coordinates due to array distortion. APEX assumes that the PRF is centered on its array, so to use the PRFs with APEX requires them to be re-centered. APEX also requires odd-valued axes.

APEX performs PRF fitting by varying the position and flux of a source using a modified simplex technique (see the APEX manual). However, for IRAC data, particularly in channels 1 and 2, where the PRF is undersampled, the default 5x sampling of the PRF is insufficient to obtain a sufficiently accurate position for fitting.

Therefore, the following transformations were applied to the PRFs:

- i) The PRFs were magnified (using linear interpolation) by a factor of 20 (so the resultant PRF sampling is $\times 100$).
- ii) The last row and column were removed to give odd-valued axes.
- iii) In the cryogenic mission, the PRF was re-centered on a first-moment centroid measured using the array values within a 250 (resampled) pixel border. In the warm mission, the PRF was recentered to ensure that the point source realization centered on entry [1279, 1279] of the 2559 x 2559 PRF array will appear to be perfectly centered on a pixel. In other words, its first moment centroid will be measured to have a phase of [0, 0] (in zero-based indexing).

- iv) The PRF was zeroed out in a 50 (resampled) pixel border (to avoid wrapping problems).
- v) Information describing the PRFs and their modifications was added to the headers.

C.3 Results of Tests with PRF fitting

C.3.1 Test on Calibration Stars

One sample observation (AOR) was selected for each of the nine brightest IRAC calibration stars (Reach et al. 2005). The selected AORs were from 2005 June 05 to 2006 September. Photometry was performed on the five BCDs in each AOR and the results averaged. (C)BCD uncertainties and imasks were used. The pipeline versions were S14.0 – S14.4. The central PRF, modified for APEX use as described above, was used as the stars were close to the center of the array in each of the images.

APEX_1frame was used with current default parameters in the namelists provided in the `cdf/` sub-directory of the MOPEX distribution, e.g., `apex_1frame_11.nl` etc, with one change. A Normalization Radius for the PRF is needed to correspond to the IRAC calibration radius of 10 pixels. This was placed in the parameter block for `sourceestimate`: `Normalization_Radius = 1000` (since it is in units of PRF pixels, and the sampling is 100x).

We performed aperture photometry using a 10 pixel (calibration) radius for IRAC channels 1 and 2, and a 3 pixel radius for IRAC channels 3 and 4, and a 12–20 pixel background annulus for all. Aperture corrections from Table 4.8 were applied to IRAC channels 3 and 4. The use of smaller apertures at longer wavelengths is not critical but reduces the effect of background noise. No aperture corrections were needed for IRAC channels 1 and 2 for this aperture/annulus combination as it is used to define the flux calibration. The IRAC channel 1 aperture photometry was divided by the empirical pixel-phase flux correction:

$$Corr = 1 + 0.0535 \times \left[\frac{1}{\sqrt{2\pi}} - p \right] \quad (C.1)$$

where p is the radial pixel phase, defined as the distance of the centroid of the stellar image from the center of its peak pixel. This corrects to an average pixel phase of $p = \frac{1}{\sqrt{2\pi}} \approx 0.4$ pix.

The average PRF-fitted fluxes compared to aperture photometry are shown in Figure C.1. The weighted average differences between PRF fluxes and (corrected) aperture fluxes are shown as long blue dashes.

There are offsets in all four channels between the aperture and fitted fluxes. In IRAC channels 3 and 4, the offset is due to the fact that in these channels, the PSFs are wide and there is significant flux in the 12 – 20 pixel background annulus subtracted out in the IRAC calibration. APEX does not know about this in its PRF normalization, so the PRF fluxes are too high. We examined the core PRFs and estimated this factor. The estimated effect of the annulus on the PRF fluxes is shown in Fig. C.1 as black, short dashes. These are within 1% of the IRAC channel 3 and 4 estimates from the calibration stars. For IRAC channels 1 and 2, these annulus terms appear to be small, so we assume zero correction. The annulus correction factors (divide PRF fluxes by these) are 1.022 for IRAC channel 3, and 1.014 for IRAC channel 4 (Table C.1).

C.3.2 Subpixel Response in Channels 1 and 2

The offset for IRAC channel 1 in Figure C.1 is due to a completely different effect, namely the pixel phase effect described above. Aperture sums on the channel 1 IRAC PRFs match reasonably well the pixel phase relation in Eqn. C.1 if we sum a 10-pixel radius aperture.

APEX performs normalization on the “center-of-pixel” (pixel phase [0,0]) PRF, and applies this normalization factor to all sub-pixel positions. This results in an offset of the photometry relative

to the mean pixel phase of $p = \frac{1}{\sqrt{2\pi}}$. We need to “back out” APEX's center normalization. Setting $p=0$ in Eqn. C.1 gives us the required factor: divide the PRF fluxes by 1.021. Similarly, using the pixel phase slope of 0.0301 in IRAC channel 2 leads to a correction factor of 1.012.

With these corrections, the PRF fitting on single CBCDs matches aperture results with any systematics less than a percent in all IRAC channels (Fig. C.2). The remaining scatter is most likely due to residual pixel phase effect not removed by the one-dimensional correction applied to the aperture photometry. The true pixel phase effect has two-dimensional structure which is included in the PRF (see also Mighell et al. 2008).

Table C.1: Correction factors for PRF flux densities

Channel	PRF aperture corrections			Correction to mean	Total
	From Core PRFs	From Cal Stars	Adopted	pixel phase	correction
3.6 μm	1.004		1.000	1.021	1.021
4.5 μm	1.004		1.000	1.012	1.012
5.8 μm	1.021	1.023 \pm 0.002	1.022	1.000	1.022
8.0 μm	1.014	1.014 \pm 0.002	1.014	1.000	1.014

Note for use: divide PRF fluxes by the last column.

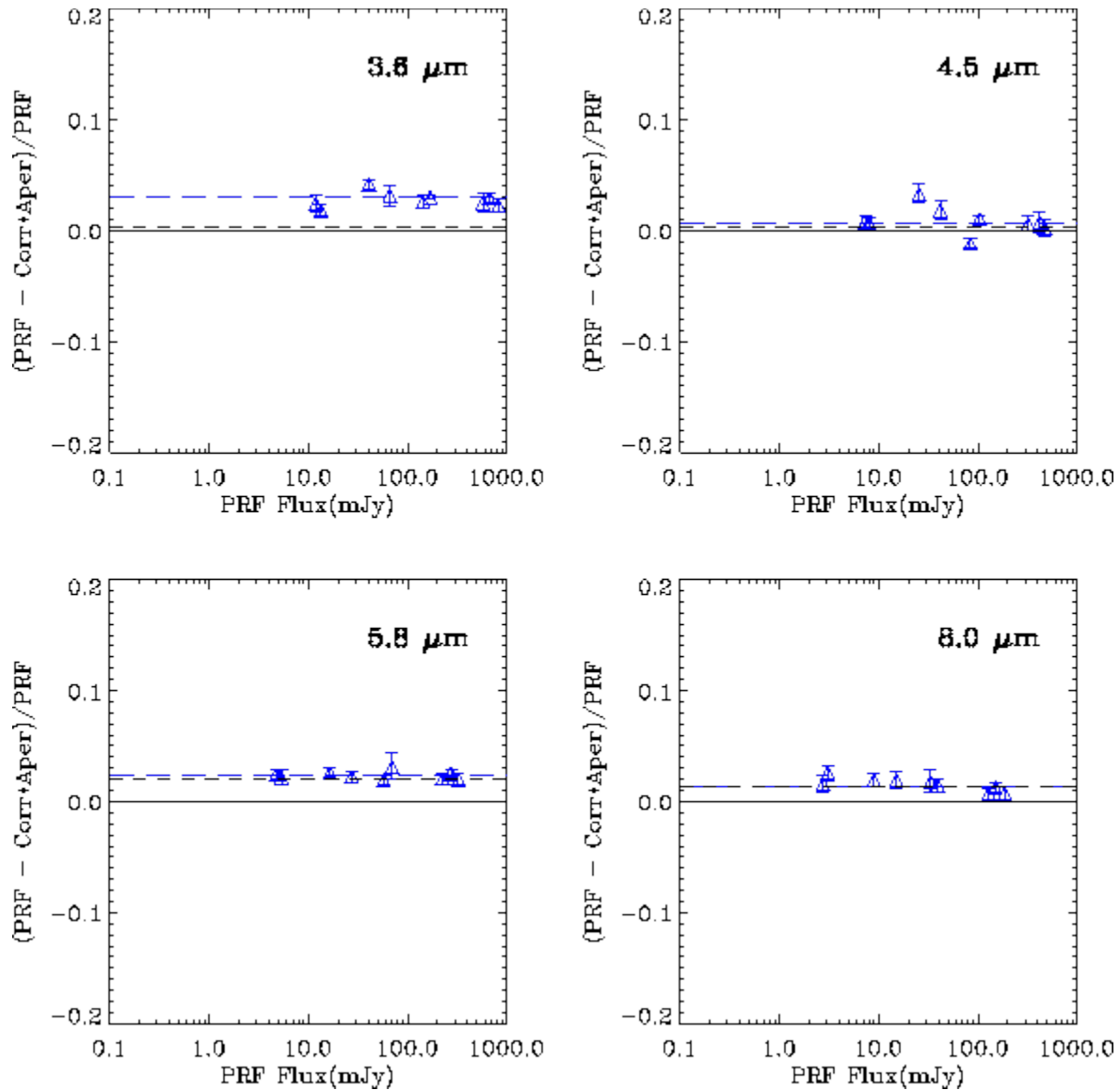


Figure C.1: PRF fits vs. aperture photometry for selected IRAC calibration star CBCDs. The vertical axis is the fractional difference between the PRF fit and corrected aperture photometry. The aperture photometry for IRAC channels 3 and 4 is in a 3-pixel radius with a 12 – 20 pixel background annulus and an aperture correction factor from this Handbook. For IRAC channels 1 and 2, it is in a 10-pixel radius with the same annulus. Short black dashed lines are the expected annulus correction needed. Long blue dashed line is the offset estimated from a weighted average of the data. Note this is essentially the expected value for IRAC channels 3 and 4. But IRAC channel 1 (and IRAC channel 2 to a lesser extent) requires a pixel phase correction (see text).

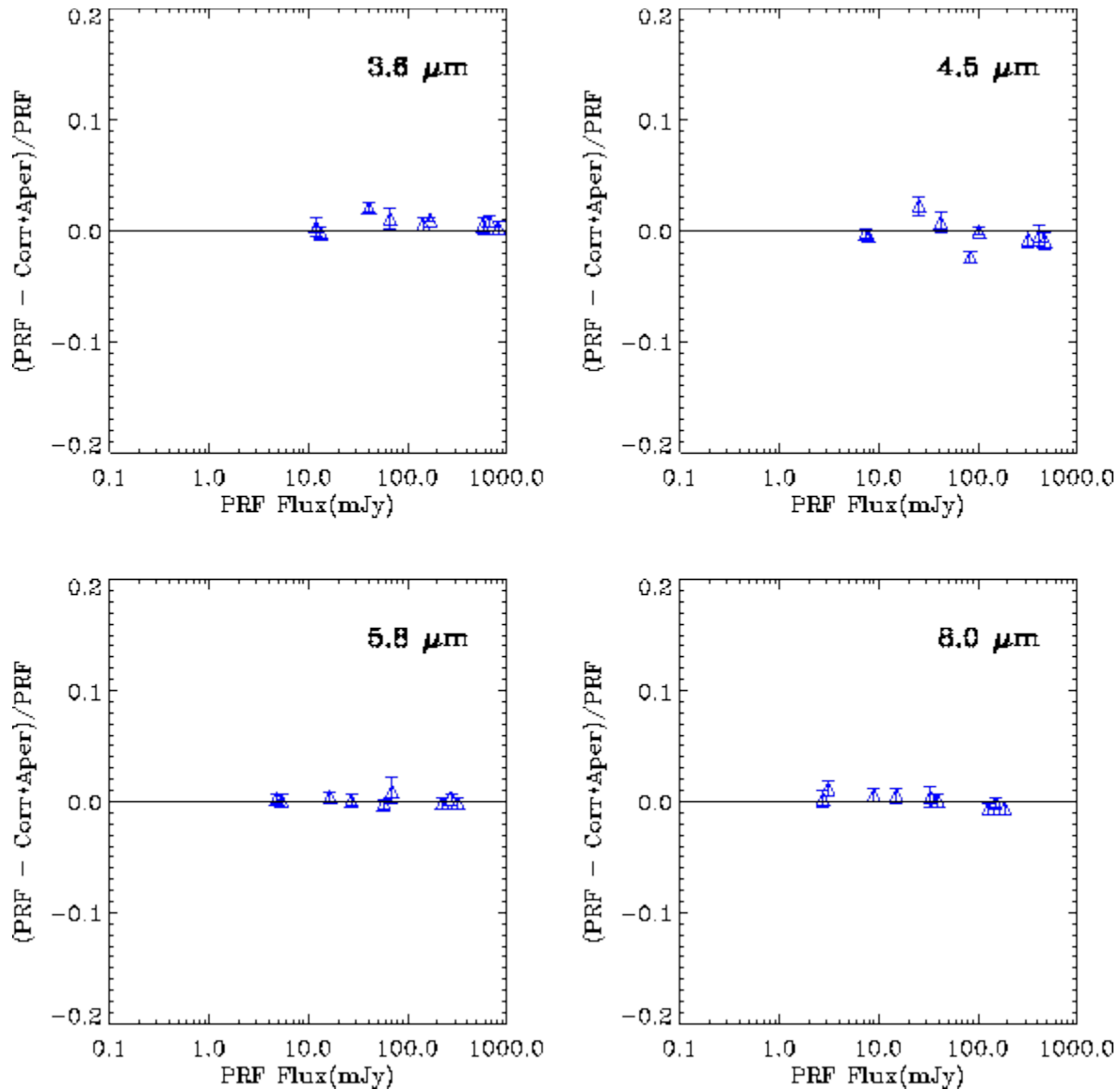


Figure C.2: Data from Fig. C.1, with IRAC channels 3 and 4 corrected for the annulus contribution, and IRAC channels 1 and 2 corrected for the pixel phase effect.

C.3.3 The Serpens Test Field

Data for this test is a C2D off-cloud field (OC3) near Serpens, AORKEY 5714944 (S14.0). The observation is HDR mode data (0.6 and 12 seconds) from all four IRAC channels. The observation used two repeats of two dithers, so the typical coverage is four frames. The observation consisted of a 3x4 map. The field was chosen to be a crowded, predominantly stellar, field. The BCD data were run through artifact mitigation to correct muxbleed, column pull-down/pull-up, electronic banding, and the first-frame effect. No pixel replacement was done. Long and short HDR data were handled separately. The tests here are with the long frames.

APEX multiframe was used with the Hoffmann PRFs, using a complete set of 25 array location-dependent PRFs. Note that APEX does aperture photometry on the mosaic, but PRF fits on the stack (individual images). Final extracted sources shown are those with $\text{SNR} > \approx 8$.

Figure C.3 shows the comparison of PRF-fitted fluxes to aperture-corrected aperture photometry in a 3-pixel radius aperture. For IRAC channels 1 and 2, this is without pixel-phase corrections; for IRAC channels 3 and 4 it is *with* correction for the PRF aperture (Table C.1), but *without* correction for mosaic smear. Mosaicking involves an interpolation process which smears out point sources. Aperture corrections for aperture photometry off the mosaics need therefore to be made either based on point sources in the mosaic itself, or using values for CBCDs with a correction for mosaic smear. The amount of smearing depends on the pixel sampling in the final mosaic.

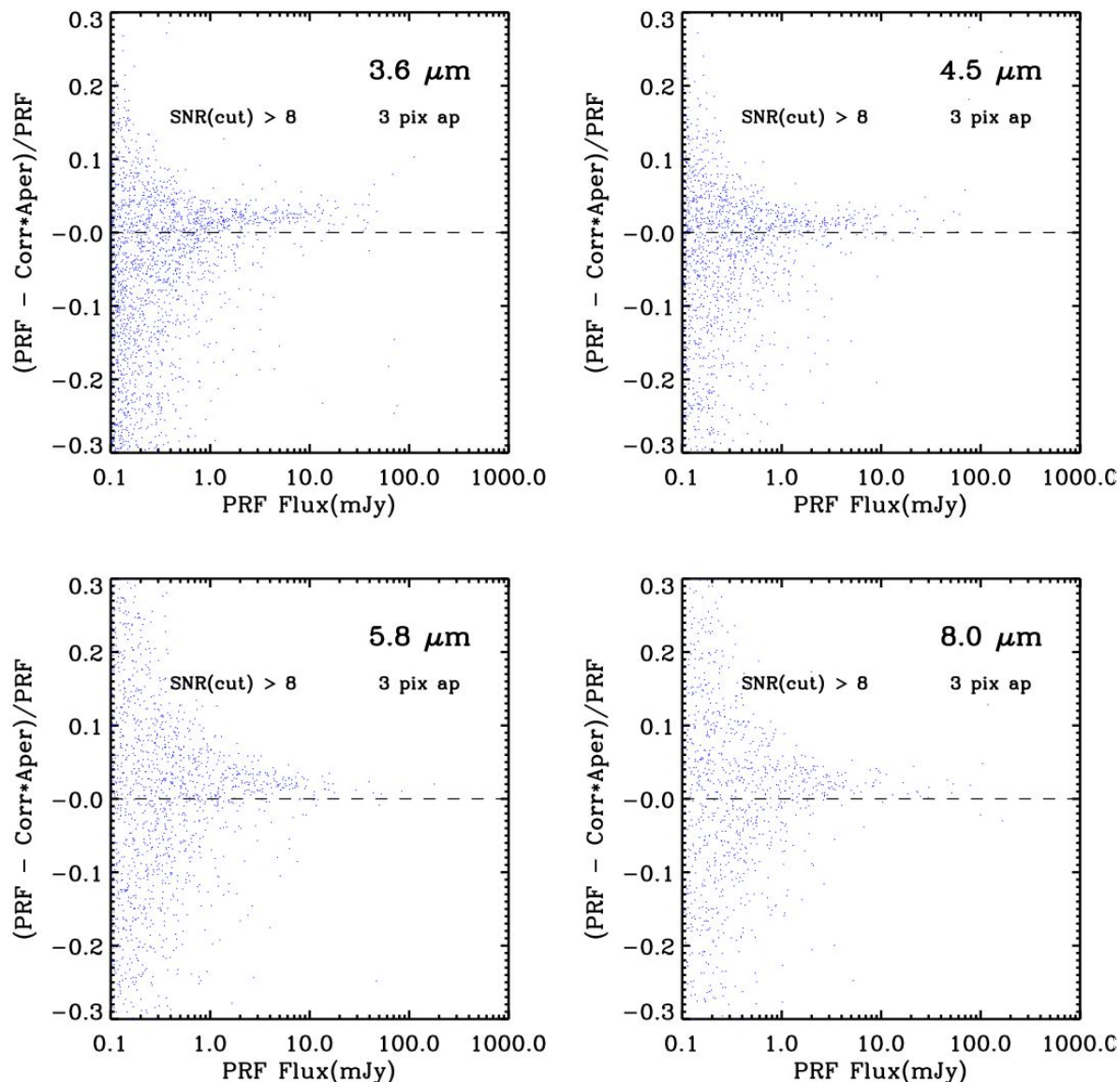


Figure C.3: APEX PRF-fitted photometry in the Serpens test field, with array location-dependent PRFs vs. aperture photometry. The aperture has a 3 pixel radius, the background annulus is 12 – 20 pixels. The aperture fluxes have been corrected using the aperture corrections in Table 4.8. The IRAC channel 3 and 4 PRF fluxes have been corrected for annulus contribution.

Figure C.4 shows the data with the remaining corrections discussed above applied. PRF fluxes for IRAC channels 1 and 2 were corrected for the pixel phase effect (Table C.1). Mosaic smear corrections for the aperture fluxes were determined empirically by comparing BCD and mosaic aperture fluxes. In IRAC channels 1 and 2 they were negligible, but IRAC channel 3 and 4 fluxes were corrected by 2.8% and 1.5%, respectively. The results (Fig. C.4) show generally good agreement with aperture photometry, with any systematic offset < 1%.

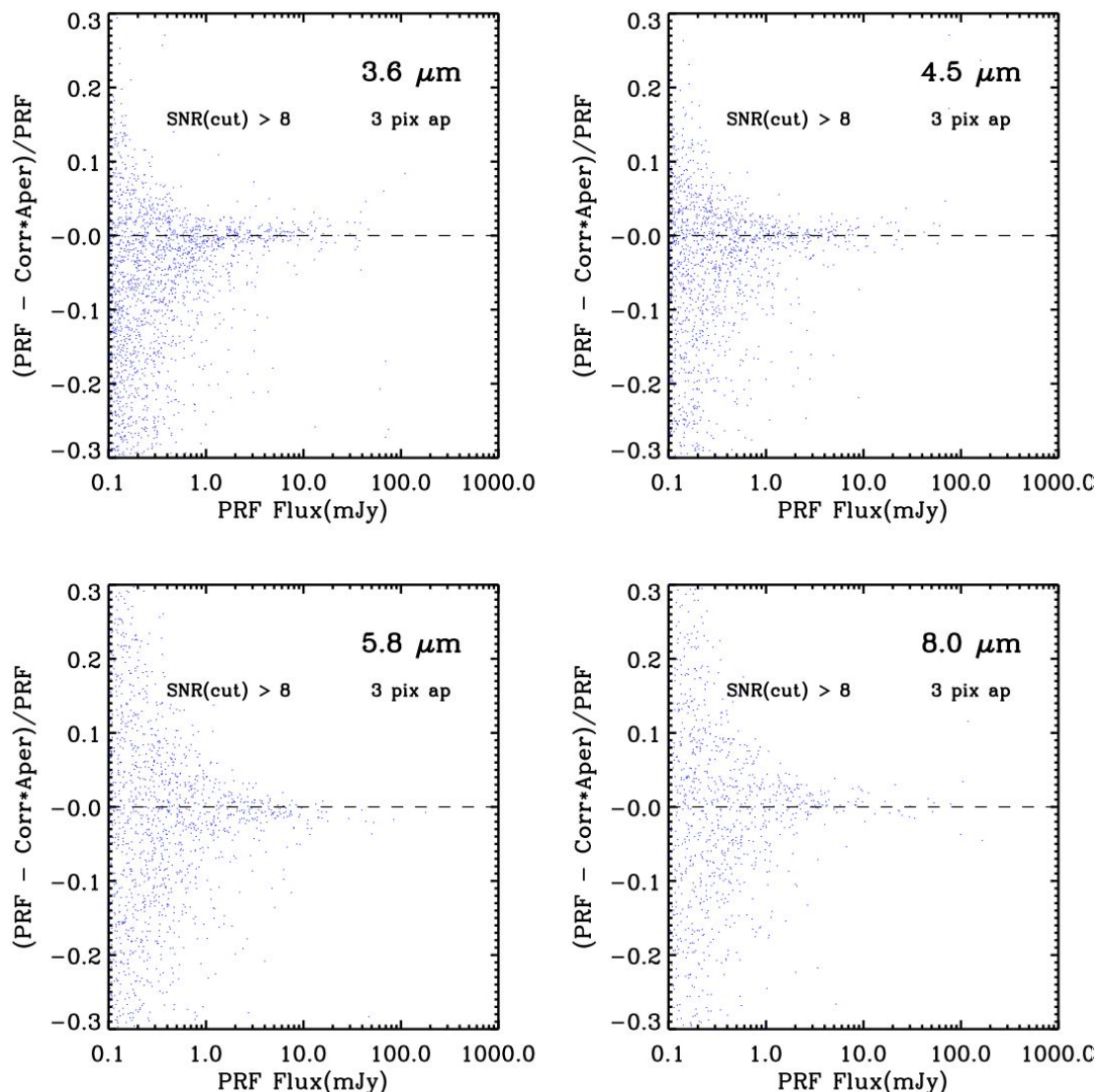


Figure C.4: APEX PRF-fitted photometry with a PRF Map vs. aperture photometry in the Serpens test field. PRF and aperture fluxes have been corrected as described in the text.

C.3.4 The GLIMPSE Test Field

We also analyzed the GLIMPSE AORKEY 9225728 in a similar manner. This produced similarly good agreement between the aperture and fitted fluxes. In addition, we stacked the residuals of the brighter sources in an attempt to determine the size of any systematics, and plotted out the ratio of the residuals to the uncertainties for the inner four pixels closest to the source position. No significant residual could be found in a stack of 111 sources with channel 1 fluxes between 50 and 100 mJy, corresponding to a limit of $\approx 0.1\%$ on the size of any systematic residual. Similarly, no significant difference could be found for the distribution of the ratio of residual to uncertainty between the pixels near to the peak star position and pixels in the remainder of the image.

C.3.5 Photometry of Moderately-Resolved Sources

Point source fitting is most appropriate for true point sources. The flux of astronomical objects that are extended will be underestimated by such a procedure. Nearly all fields observed by IRAC have a substantial population of faint (tens of micro-Jy) background sources, which are in fact galaxies, and in a typical 100-second exposure these can approach 100 galaxies per IRAC frame at 3.6 μm . Although a casual visual inspection of the IRAC data would seem to indicate that the majority of these sources are compact and point-like, in fact treating them as such will lead to substantial errors in photometry, as these objects are typically resolved on a scale of ≈ 1 arcsecond (e.g., Lacy et al. 2005).

This issue has been studied in substantial detail in the IRAC Dark Field, which is the dark calibration field for IRAC. This is an extremely deep IRAC pointing of approximately 200 square arcminutes near the north ecliptic pole, and which reaches the confusion limit in all IRAC channels. More importantly, there is also deep high spatial resolution HST optical imaging over the same field, which can provide prior information on true source sizes and shapes.

Point source fitting was used to extract photometry for the IRAC Dark Field. An examination of the point-source subtracted residual images shows clearly that the residuals mimic the HST source morphology, conclusively demonstrating that IRAC does in fact resolve the majority of the faint galaxies. This result is strongest at the shorter IRAC wavelengths, where the spatial resolution is higher and the galaxies may be slightly more extended. This result was hardly unexpected - calculations of expected galaxy angular sizes assuming a modern cosmology indicated that most galaxies would be marginally resolved by IRAC almost regardless of distance, modulo changes in galaxy morphology with redshift and the ability to detect faint extended emission.

Curves of growth were generated for the galaxies, and when used in conjunction with the optical priors, the amount of error associated with point source fitting was quantified. Sources below a few micro-Jy start to be affected by confusion issues, so we describe here results for galaxies brighter than this. At 3.6 μm , roughly 50% of all galaxies are demonstrably resolved by IRAC. In 20% of the objects, the use of point source fitting will underestimate the true flux by a factor of two or more.

A much more effective solution is to use aperture photometry for such sources. The SWIRE survey performed detailed analyses to determine an ideal extraction aperture such that it minimized noise. This aperture was 1.9 arcseconds in radius, or roughly twice the FWHM. Most other survey groups have found similar results, and this mirrors well-known ideas about aperture photometry of small sources. When such an aperture is used, even though some objects may be larger than this the number where the flux differs by a factor of two falls to only 3%. This improvement over the PSF-fitting reflects the fact that the summation over an aperture larger than the PSF FWHM will always capture a better representation of the true flux of an extended object, even if that is more extended than the aperture itself. A more ideal solution is to use Kron-like apertures (which are dynamically sized based on moments derived from the image) which are either derived from the data themselves or from image priors in some other band.

We may thus conclude that for the extragalactic background, which is present in nearly all IRAC data, at least half the objects are resolved by IRAC in a meaningful fashion. Ideally, measurements should dynamically use shape information determined from the data themselves, or from priors derived from other, higher resolution datasets. Barring the use of shape parameters, use of aperture photometry in circular apertures somewhat larger than the PSF provides a more accurate result than PRF fitting.

C.3.6 Positional Accuracy

Tests were performed on GLIMPSE AORKEY 9225728, which contained approximately 10000 point sources in channels 1 and 2. Comparisons were made with respect to SExtractor Gaussian-windowed centroids XWIN_WORLD, YWIN_WORLD using both the pipeline mosaics, and mosaics made with the original pointing. Using the 100x oversampled PRFs recentered as previously described we found that the source positions agreed with SExtractor to within ≈ 0.1 arcseconds. Systematic shifts with respect to 2MASS are ≈ 0.2 arcseconds in the pipeline (superboresight) pointing, and ≈ 0.4 arcseconds in the original pointing. Recentering the PRF has no effect on photometry but is required for use in APEX. The shifted and unshifted PRFs gave nearly identical photometric results in channels 1 – 4.

C.3.7 A How-To-Guide for IRAC Point Source Photometry with APEX

It is recommended that APEX in point source fitting mode should be used only directly on the BCD data using the Hoffmann PRFs modified for use with APEX as described above. Trying to fit point sources on the mosaic is not recommended as the mosaicking process both blurs the undersampled point sources, and loses the pixel phase information. Therefore, the fitting should be done to individual (C)BCD frames whereas a mosaic should only be used to find the point sources. We also do not recommend using the `prf_estimate` tool to derive a PRF from IRAC data, as it does not deal correctly with the undersampling of the PRF.

We list below the steps towards producing a point source list using APEX in multiframe mode (i.e., on the stack of individual [C]BCDs).

1. Source fitting versus aperture fluxes: ask yourself if point source photometry is appropriate for your sources of interest. If in doubt after reading about photometry of moderately resolved sources above, use aperture photometry with APEX or SExtractor.
2. Artifact correction: use CBCDs or preprocess your IRAC BCD data to remove or mask artifacts as necessary.
3. Rmasks: assuming the data were taken with overlapping (C)BCDs, make a mosaic with MOPEX, doing outlier rejection, and creating rmasks. Then include the appropriate rmasks with your input data to APEX.

4. PRF: put the center Hoffmann 100x PRF (the one with ...col129_row129...) in your MOPEX cal/ subdirectory for command-line (this will be PRF_FILE_NAME in the namelist file), or type it into the GUI. Although you can run APEX with just the center PRF, we recommend using the whole PRF Map set, as it noticeably improves the quality of the fits for sources outside of the central region of the arrays. To do this, create a table like the one linked from the PSF/PRF section of IRSA's IRAC web pages (substituting appropriate filenames and paths). PRF position refers to the bottom-left corner of the region of size NAXIS1, NAXIS2 over which the PRF is valid (in native pixels). This will be PRFMAP_FILE_NAME in a namelist, or you can type it into the GUI. Figure C.5 shows how the PRFs are distributed over the arrays.
5. Normalization Radius: the Hoffmann PRFs require a normalization that matches the IRAC calibration radius. In the `Sourceestimate` block, set `Normalization_Radius = 1000` (since it is in PRF pixels and the sampling is 100x).
6. Run APEX. If doing command-line for IRAC1, edit the default namelist for your data and run: `apex.pl -n apex_11_yourdata.nl`
7. PRF Flux: The PRF flux column is called "flux" in the `extract.tbl` output file, and the units are micro-Jy. These need to be divided by the appropriate photometric correction factors from Table C.1: 1.021 (IRAC 1), 1.012 (IRAC2), 1.022 (IRAC3), and 1.014 (IRAC4).
8. PRF Flux Uncertainty: The column labelled "delta_flux" is the formal uncertainty from the least-squares fit. It will in general underestimate the flux uncertainty. Do not use the column labelled "SNR" for IRAC, as it only takes into account the background noise, and ignores the Poisson (shot) noise term which typically dominates the error. The best estimate is the aperture uncertainty (calculated from the data uncertainties) in a 3 pixel radius. This covers the majority of the PSF without going too far out. (For the default namelist, the relevant uncertainty is in column "ap_unc2" [microJy].)
9. Array Location-Dependent Photometric Corrections: Use MOPEX to make an array location-dependent photometric correction mosaic and correct APEX-produced fluxes by the values at the locations of source centroids in the correction mosaic. The fluxes will be correct for blue sources that have colors of an early-type stellar photosphere. For red sources with colors close to that of the zodiacal light, use fluxes derived from running APEX on unmodified CBCDs.
10. Color Correction: This is the correction needed to get the right monochromatic flux if your source spectrum is different from the reference spectrum used to calibrate the IRAC filters ($\sqrt{F_\nu} = \text{constant}$). There is a good discussion of this in Chapter 4 of this Handbook.

If all these steps are followed, then the systematic error in the flux measurement for bright, isolated point sources should be $\approx 1\%$. A comparable systematic error exists in the flux density scale.

Background estimation errors will contribute significantly to the error budget for fainter sources and in confused fields.

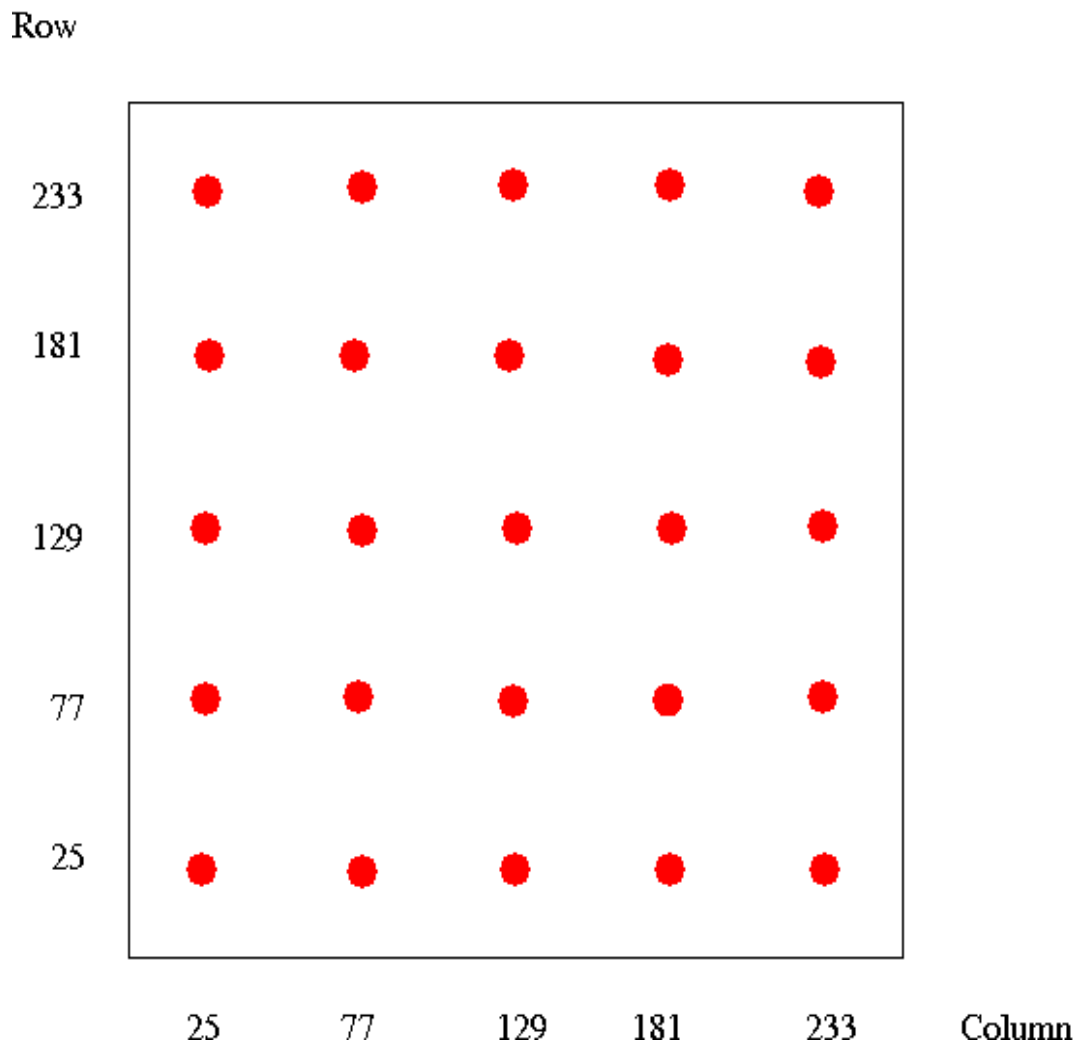


Figure C.5: The 25 PRF positions on an IRAC BCD.

C.3.8 Pixel Phase

As in 4.6, we define pixel phase as the offset between the centroid of a stellar image and the center of the pixel in which that centroid lies. For example, an object whose centroid has pixel coordinates 128.23, 127.85 has a pixel phase of $Dx, Dy = (-0.27, 0.35)$. The pixel phase effect is here characterized in terms of the radial pixel phase $p = \sqrt{D_x^2 + D_y^2}$. To shift a 5×5 oversampled PRF to a given pixel phase we have adopted the following technique:

- i) Magnify the PRFs by a large factor, e.g. 20, using linear interpolation (so the resultant PRF sampling is x100).

ii) Re-center the PRF by shifting it to its centroid. (Note that the estimate of the centroid of a source is itself a function of the method used to determine the centroid, so ideally you would use equivalent algorithms to find centroids in the (C)BCDs as you do to centroid the PRF. Note also that some of the IDL centroiding functions perform poorly with the very undersampled IRAC data at 3.6 and 4.5 μm).

ii) Shift the PRF array (in the example above a shift by 27, -35 resampled pixels would move the desired PRF to the center of the array).

iii) Extract the point source realization by sampling the PRF at intervals corresponding to native pixel increments (every 100 oversampled pixels in this example), making sure to pick up the center of the central pixel.

In IDL the commands would be:

i) Use `rebin` on the 128^2 , 5x oversampled PRF to produce the magnified PRF: `magPRF = rebin(PRF,2560,2560)`.

ii) Re-center the PRF. We find that calculating the first moments is usually a robust way to find the centroids. Set `xmin`, `xmax`, and `ymin` and `ymax` to approximately the same values in native pixels as you use to estimate the centroids in your data:

```
xx=float(lindgen(2560,2560)mod2560)
yy=float(lindgen(2560,2560)/2560)
```

```
xcen=total(xx[xmin:xmax,ymin:ymax]*magPRF[xmin:xmax,ymin:ymax])/total(magPRF[xmin:
xmax,ymin:ymax])
```

```
ycen=total(yy[xmin:xmax,ymin:ymax]*magPRF[xmin:xmax,ymin:ymax])/total(magPRF[xmin:
xmax,ymin:ymax])
```

```
xcensh=nx/2-round(xcen)
ycensh=ny/2-round(ycen)
cenPRF = shift(magPRF,xcensh,ycensh)
```

ii) Shift the re-centered PRF to the center of the central PRF pixel and trim to an integer multiple of the 100x oversampling factor such that the central pixel (1280,1280) is moved to (1200,1200), the center of the trimmed array:

```
shiftedPRF=shift(cenPRF,27,-35)
phasedPRF=fltarr(2500,2500)
trimmedPRF=shiftedPRF[80:2559,80:2559]
phasedPRF[0:2479,0:2479]=trimmedPRF
```

iii) Sample the trimmed PRF to produce the point source realization:

```
PSR = rebin(trimmedPRF,25,25,/SAMPLE)
```

The center of the zero phase PSR in this example should be IDL pixel (12,12).

Appendix D. Time Series Photometry Supplement

D.1 Data Features

Occasionally there are features in the data which are not regularly seen and are likely not of astrophysical origin. These include rare events on the spacecraft or detectors. In this section, we discuss known data features and our understanding of their causes.

D.1.1 Header Keywords

There are a couple of header keywords that should be consulted for issues before performing high precision photometry. These include `MISS_DATA` and `MISS_LCT`. These have been found in the 55 Cnc dataset AORKEY 48070144, EXPIDs 353 and 6399. The symptom is a position problem in the frames. If `MISS_DATA = T` and/or `MISS_LCT` is greater than 0, there is likely a problem with missing data. Images with these header issues should not be included in the data analysis.

Another header keyword that may indicate a problem is `BADTRIG`. Such a problem can be found in the 55 Cnc dataset AORKEY 48072960, EXPIDs 7950, 5259, and 9256 among others. This problem manifests itself as centroids of whole images being off in x-direction (in BCD coordinates). In the headers of these images `BADTRIG=T`, and `ZEROPIX` is greater than 1 (often ≈ 4800). An occasional problem was observed during the warm mission wherein an extra byte appeared in the science packet (image data). As a result, all pixels after this byte are shifted by one pixel. Such images are identified by having the `ABADDATA` header keyword set in the raw data (`BADTRIG` in the BCD images); the images themselves usually become stripy as a result of the mismatch between the science and calibration data. The SSC pipeline corrects this by locating the first pixel in the image with a value of exactly 0, and then shifts all later pixels.

In the case of these images, there is more than one `ZEROPIX`, so the pipeline cannot correct the images for the shift in pixels. Images with these header issues should not be included in the data analysis.

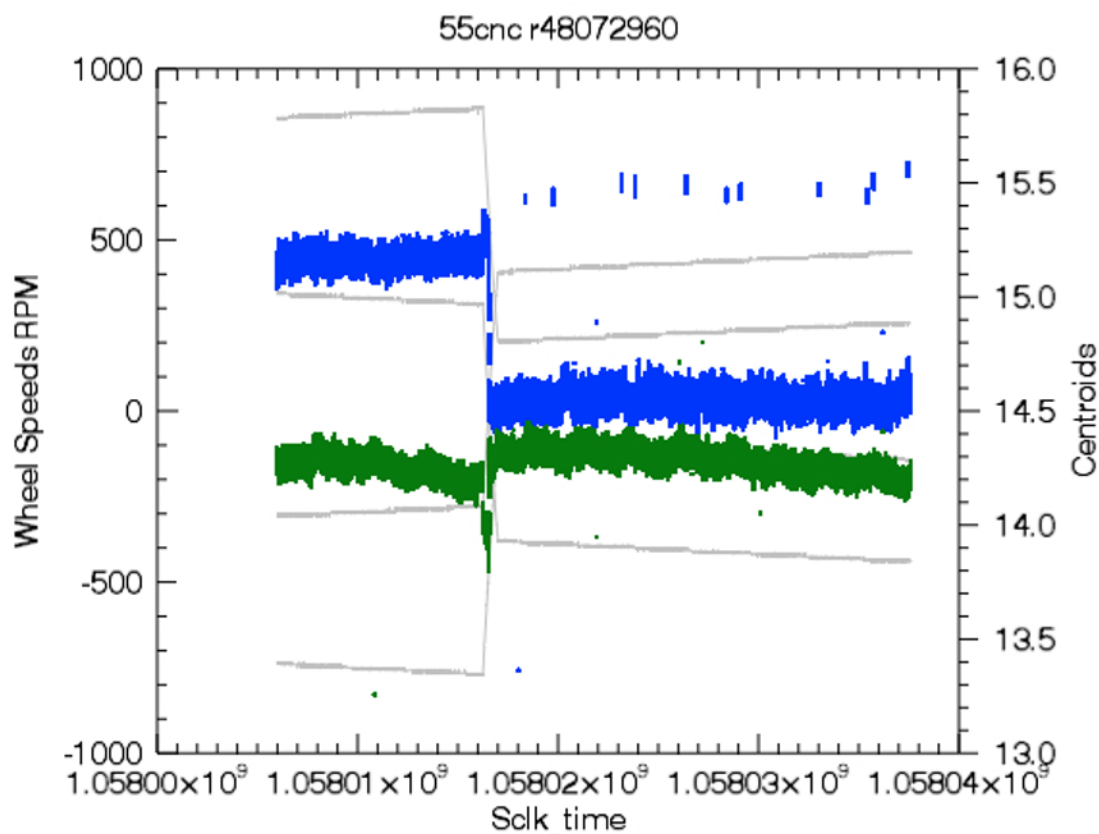


Figure D.1: A BADTRIG problem in staring mode data. Left side vertical axis is for the grey lines and wheel speed RPM. The right-side vertical axis corresponds to x (blue) and y (green) centroids of the AOR as a function of sclk time. BADTRIG is set for the x-positions which have centroids of 14.5 after sclk time of 1.058017×10^9 .

D.1.2 Skydark Change in the Middle of an Observation

Observers that use long staring mode observations, including exoplanet observations and brown dwarf monitoring observations, should be aware that the applied skydark may have changed in the middle of the observation. This change is possible due to the dynamic nature of the skydark determination, which chooses the best dark that is nearest in time to a given BCD (single image). For observations that do not require high relative precision, the current calibration assures the best absolute photometric calibration.

The change in skydark will cause a small jump in the stellar flux and background levels, when inspected as a function of time. To check whether this happened, one can check the FITS header of a BCD file taken near the beginning of the continuous observation, and look for a header keyword SDRKEPID, which is found under the “DATA FLOW KEYWORDS” section of the

header. Compare the value of this keyword to the same keyword value in a BCD taken near the end of the continuous observation. If the SDRKEPID is different, the applied skydark has changed during the observation. The pipeline has been configured so as to prevent this from happening in high relative precision observations, but it is possible that this problem could have slipped through for some datasets.

D.1.3 Background modulation

This has been seen in a number of AORs, although it is not very common. The modulation is of order one electron for roughly two hours, although the duration varies (see Figure D.2). We do see that the signal is correlated. Over the same period that the background levels modulate, we see a similarly shaped decrease in the background uncertainty values.

Despite intensive checks, nothing in the telemetry appears to change during the time of the modulation nor are there changes in the telemetry that correlate with frequencies seen in the modulation. The signal does appear to be correlated, in that if one connects the dots (Figure D.3) there is coherent structure in the background modulated by an expanding and contracting envelope. There is similar coherent structure in the background sigma. The noise in the background only goes down during that time. There are what look like gaps in the waveform, corresponding to regions where the background is extremely correlated over timescales of about five minutes. These gaps seem to be synchronized with extrema in the position sawtooth. This is somewhat similar to frequency modulation (FM) and amplitude modulation (AM) signals.

There is no evidence of the background modulation affecting photometry.

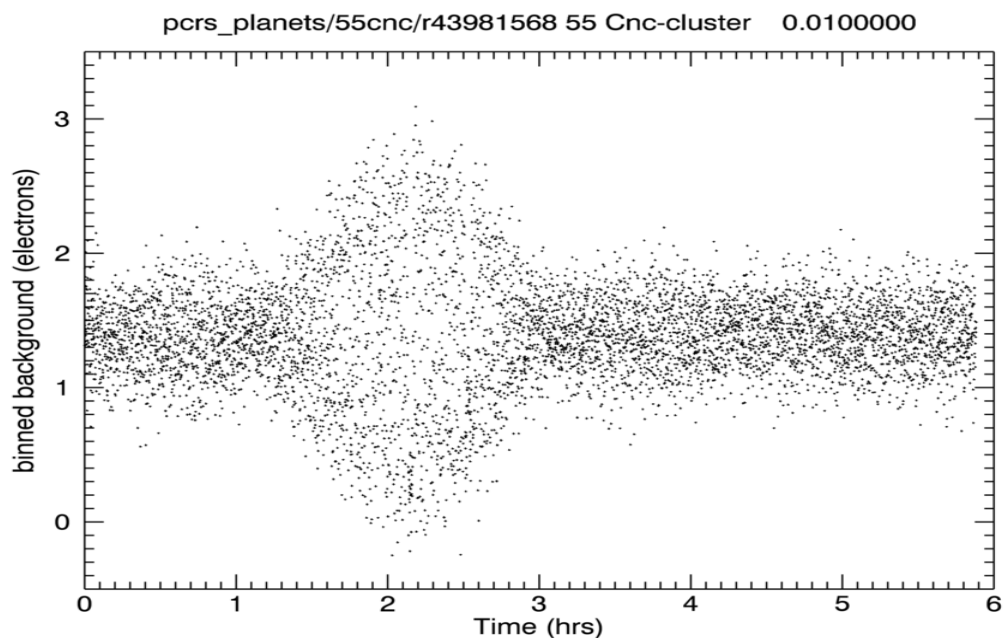


Figure D.2: Background measured in electrons as a function of time for 0.02 second subarray data.

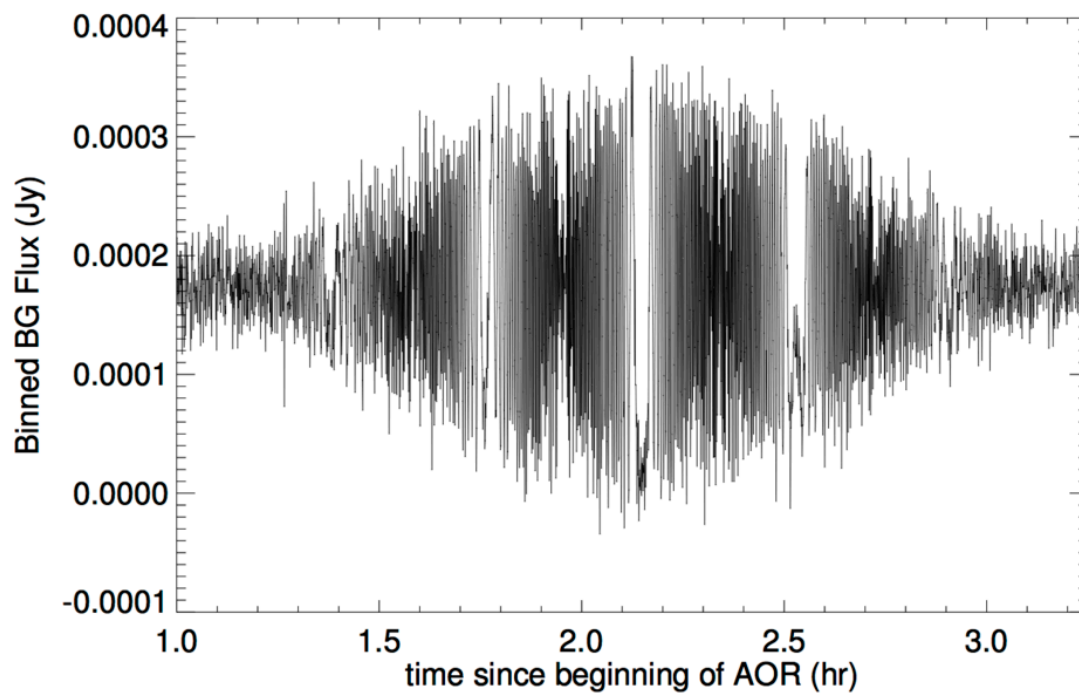


Figure D.3: Same as Figure D.2, only now with each data point connected by a line, and zoomed in on the background modulation portion of the light curve.

D.1.4 Noise Pixel Spikes

A few times over the course of the mission the number of noise pixels has been seen to sharply increase in value for a short duration (≈ 30 min) before returning to normal (see Figure 8.12, at 16 and 30 hours). These noise pixel spikes are alarming because as the number of noise pixels goes up, the measured aperture flux will decrease, which mimics the signal of a transit. During the spikes, positions do not show out of the ordinary trends. There is also no apparent correlation with any particular spot on the pixel, so these are not related to a single position.

Using the IRAC data simulator we have successfully replicated the noise pixel spikes seen in these datasets using a high frequency position oscillation. At frequencies higher than the observation rate, oscillations of the instrument will have the effect of smearing out the image, and thereby increasing the number of noise pixels, without changing the object centroids. Although we have looked for correlations with telemetry values, there is no known cause for the suggested oscillations onboard Spitzer.

Table D.1: Examples of datasets with known noise pixel spikes.

Planet host star name	AORKEY	start_sclk	stop_sclk
HD 7924	46981888	1041429073.301	1041455525.016
HD 7924	44605184	1004594183.339	1004622735.006
XO-3	46482944	1050530251.708	1050573212.475
HD 20003	48408064	1062587169.546	1062628187.337

D.1.5 Timing

Both UTCS_OBS and ET_OBS use the standard convention of offset from J2000 which is defined as 2451545.0 TT (Terrestrial Time) and January 1, 2000, 11:58:55.816 UTC. ET_OBS and UTCS_OBS are both ephemeris times in the sense that they refer to a clock in the Spitzer reference frame that differs from Earth-based clocks by the light travel time difference of the observed event and GR effects. UTCS_OBS uses the UTC time system and includes leap seconds and the offset from the International Atomic Time (TAI). ET_OBS is in the TDB (Barycentric Dynamical Time) system as defined by the JPL CSPICE routines used to calculate ET_OBS from the internal spacecraft time and standard timing kernels.

The difference between UTCS_OBS and ET_OBS is in the time system used. UTCS_OBS differs from ET_OBS by the addition of leap seconds, the offset in the definition of TAI to UTC and GR effects (accounted for in ET_OBS) which are lost in the precision that the time is reported. ET_OBS is counted from Julian date 2451545.0 which is 64.186 seconds earlier than the epoch UTCS_OBS is counted from. As of 2009, $ET_OBS - UTCS_OBS = 66.186$ seconds, two of those seconds are for leap seconds, the remaining offset is the difference between the zero point of the clocks, 64.186 seconds. That is, the reference time for ET_OBS is 64.186 seconds earlier than for UTCS_OBS. The reference point for ET_OBS is J2000 or 2000 January 1 12:00:00 TT or 2000 January 1 11:58:55.816 UTC.

MJD_OBS is the modified Julian date using the UTC time system in the Spitzer reference frame. That is, it is UTCS_OBS converted directly to Julian day. HJD_OBS is the heliocentric Julian date as calculated using the observed position. It correctly accounts for the difference in light travel time between a heliocentric observer and Spitzer for the specified observation.

UTCS_OBS is the start of IRAC data taking sequence, that is the initial reset modulo timing uncertainties between the spacecraft and the IRAC instrument (less than 70 milliseconds worst case, 20 milliseconds is probably a decent estimate of the uncertainty). It is approximately 8.221 milliseconds before the first pedestal read of an integration.

The midpoint time of an individual subframe j (where j runs from 1 to 64) of a subarray DCE is given by

$$t_{mid}(j) = UTCS_OBS + (j - 0.5) * FRAMTIME + 3.231 \text{ milliseconds} \quad (D.1)$$

where the 3.231 milliseconds is the result of the difference of the initial reset times and one half of an IRAC clock tick (clock ticks are 10 milliseconds in subarray mode). The above quantity is the exact midpoint time for the central pixel of the subarray (pixel 16,16 when counting from 1,1 to 32,32).

As each subarray row is read out in ten microseconds, to find the time of the midpoint for an integration for a particular pixel, in row r , column c :

$$t_{mid}(c,r,j) = t_{mid}(j) + \text{int}((c-1)/4 - 3) * 10 \text{ microseconds} + (r - 16) * 108 \text{ microseconds}. \quad (D.2)$$

The equation takes into account the fact that the actual readout size of the subarray is 40 pixels \times 40 pixels and it takes 8 microseconds for each row reset.

Each successive DCE in a subarray AOR is the result of a new commanded integration. There is an inherent latency in the sequencing of commands. The rule is that a data taking command will take the integration time rounded to the next nearest second plus one second for commanding overhead. As a result, a 0.4 second subarray frame which takes approx (64*0.4 seconds = 25.6 seconds) actually takes 27 seconds. In addition, you need to factor in the amount of time it may take for the next command to be issued by the spacecraft and received by IRAC. This is of order 0.4 seconds, but can vary. Therefore, in this case a total latency of about 1.8 seconds is expected.

Finally, AINTBEG is unfortunately not a good indicator of exactly when an integration starts due to the design of the IRAC firmware. However, ATIMEEND is the correct time of the end of an integration.

D.1.6 58th Frame in Subarray Datasets

The 58th subarray frame in both IRAC channels 1 and 2 exhibits a general variation in the background level of the subframe compared to other frames. This background variation does not appear to have a significant effect on the results of aperture photometry performed using annular

background subtraction. While the exact cause of the background variation in this frame is unknown, it has been traced to a problem in the pipeline applying the skydark, being due to some periodic variation (or a slight timing difference) when subtracting the detector bias level. It does not appear to have a gain component. To be sure that there is no detrimental effect on the reduced data due to this feature many researchers omit this subframe in their analysis.

D.1.7 Corrupted Header

In AORKEY 42615040, WASP-434.5 micron, 2 second subarray observations at time 2011-07-29T23:08:34.966 all 64 frames in one BCD, about 2.7 hours into the observation, have elevated flux across the whole frame (multiplied by $\approx 10^5$). It looks like a normal image when displaying with DS9, only the photometry indicates something is wrong. The flux levels in the BCDs before and after are fine. The imask implies the whole image is non-linear. The uncertainties (*_bunc.fits) image is all NaN's.

The source of this problem is a corrupted header. The barrel shift and some other header keywords were corrupted in transmission, causing the pipeline to not be able to correctly process the image.

D.1.8 Position Jumps Due to Reaction Wheel Speed Change

In the 55 Cnc datasets AORKEYs 48072704 and 48072960, there are several times when one can see jumps in position within AORs which do return to their original positions. Such times include 2013-07-08T12:55:21.630, 2013-07-11T13:26:19.537 and sclk times 1062887000.00, 1062602000.00, 1062610000.00, 1041435000.00, 1043545000.00, 1047548000.00, 1058016500.00, and 1057755000.00. During the summer 2013 anomaly, these jumps in position did not return to their original position. This behavior of not returning to its original position is confined to that anomaly.

The jumps in position correspond to wheel speed shifts. Wheel speed shifts are expected due to momentum rebalancing events in the wheel speed controller. The goal of this system is to avoid zero crossing disturbances (which would also induce position disturbances in the data) as long as possible. Autonomous momentum rebalancing only occurs when the system momentum grows above a certain threshold. Once this level is breached, the goal changes to balancing the wheels so that it can stretch out the time until the next desat. If the momentum falls back below that threshold, autonomous momentum rebalancing will once again be disabled.

We see different behavior during the PCS anomaly during the summer of 2013 because that anomaly was not allowing the momentum error integrator to compensate for the bearing drag in the wheels. A shift in wheel speed would introduce a different bearing drag torque, and without the integrator to compensate for this, the shift would not be removed.

These images can be used in analysis as long as the gain associated with the different centroids can be appropriately corrected for.

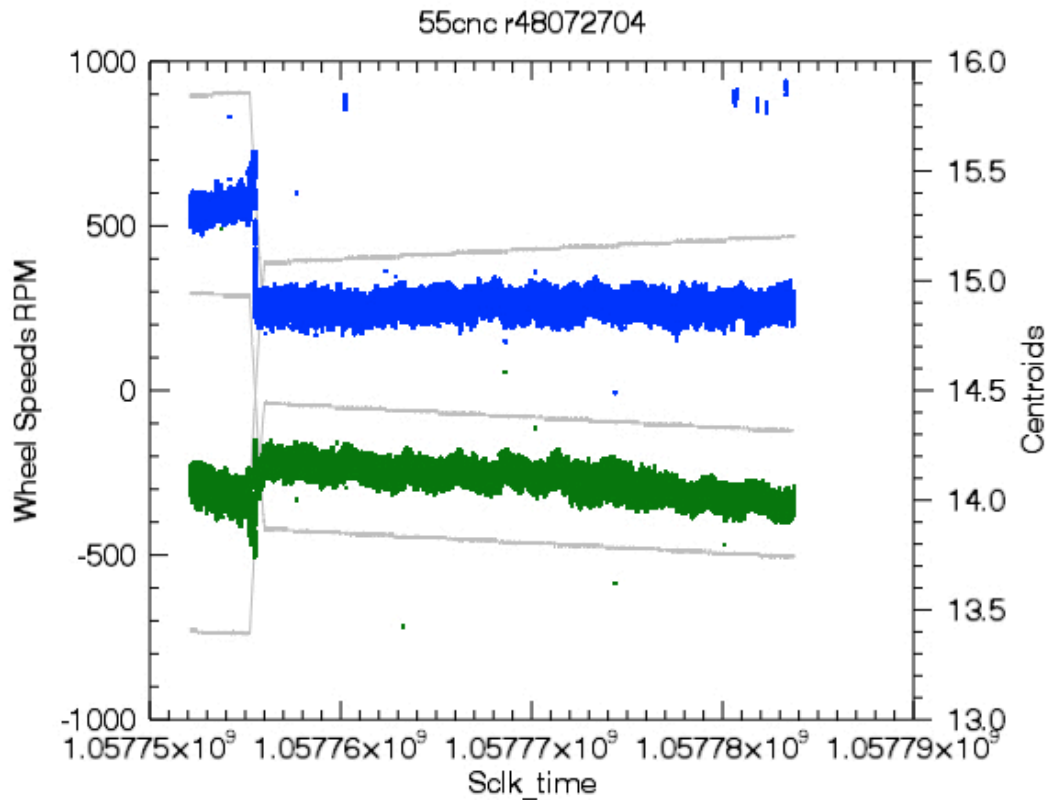


Figure D.4: Same as Figure 4.13, except this AOR was during the 2013 anomaly. A wheel speed shift occurs at time 1.057755, but the centroids never return to their pre-wheel-shift positions.

D.1.9 Pointing History File Change

In dataset AORKEY 48014336 (target HD 209458) centroids of the target change unpredictably near the end of a staring mode AOR. When examining the images by eye, the star is not actually moving around the detector. However, FITS header values CRVAL 1 and 2 change at the boundary from normal centroids to random centroids.

Often a photometry code takes R.A. and Dec. as input and converts those to x - and y -positions using the FITS header astrometric information, and then uses those initial values of x and y to refine an actual centroid. Pointing history files are what the SSC used to generate the astrometry in the header given the telemetry from the telescope. In this particular AOR, the pointing history file which was used to reconstruct the astrometry changed at an sclk time of $\approx 1.06246 \times 10^9$. This caused a change in the value of the CRVAL keywords in the FITS headers. When the value of the CRVAL keyword changes, then it appears as though the image shifted, when in fact it did not. In

this case it shifted by enough distance that the centroiding routine lost the star and is attempting to centroid on noise, which explains the large scatter in positions after the shift (see Figure D.5).

We have since re-run the pipeline on this AOR, and it now has correct astrometry in the headers. We have seen this problem only once in the warm mission.

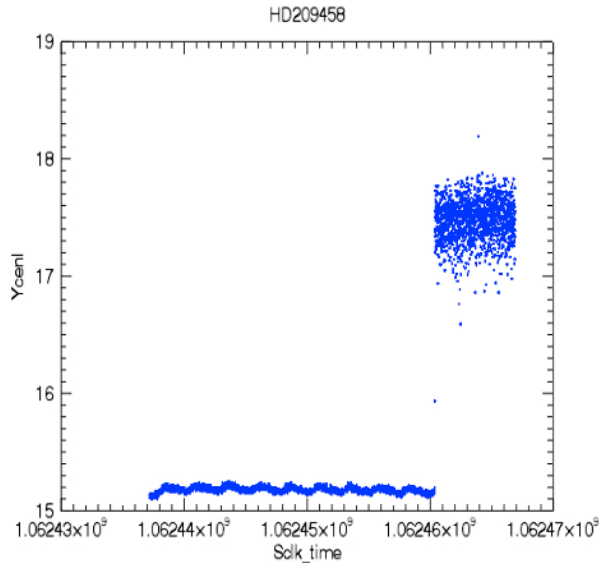


Figure D.5: x- and y-centroids as a function of time. The pointing history file changes just beyond sclk time 1.06246×10^9 , which changes the expected position of the star in the image, and therefore makes the centroiding algorithm essentially fail to find the target. This AOR has been re-processed and now no longer shows this problem.

D.1.10 Effects of Cosmic Rays on Centroiding Algorithm

We concentrate on the effects of cosmic rays on the supplied `box_centroider.pro` centroiding algorithm. In all datasets, a few measured positions are just slightly different from the mean levels (usually less than one pixel).

For completeness, we looked at five of these for a WASP-15b AOR, and all five are caused by cosmic rays (CR). The CRs will change the center of light calculation in the centroiding routine. Not surprisingly, although we have not quantified it, the brightness of the CR seems to be correlated with the difference in position from the mean. The rate at which we see the centroid deviations is consistent with the known CR rate.

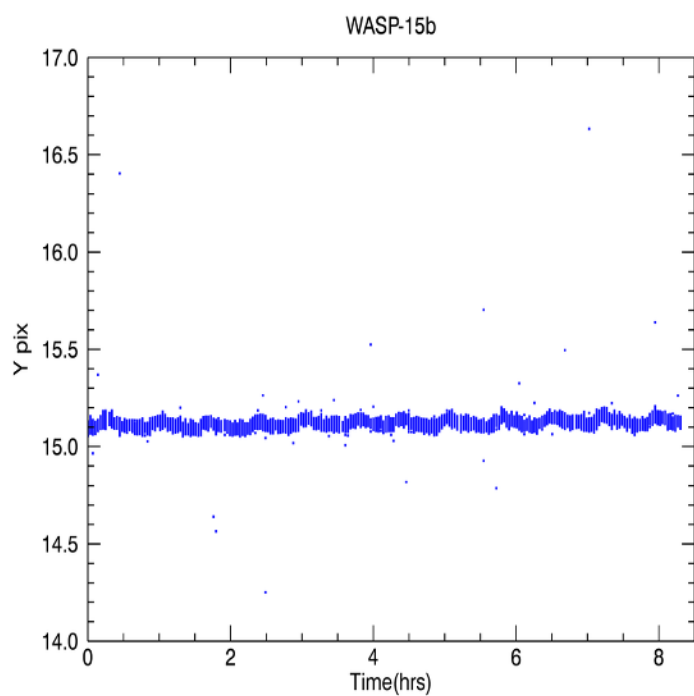
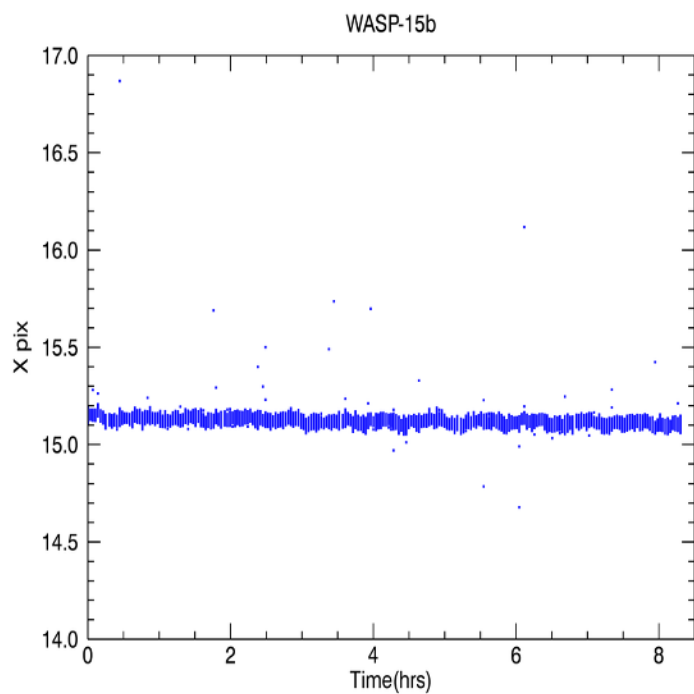


Figure D.6: x - and y -positions as a function of time for a WASP-15 AOR. The position points which do not follow the sawtooth pattern are caused by CRs.

D.1.11 Pattern noise (horizontal striping)

Pattern noise or horizontal striping (see example in Figure D.7) appears to randomly affect an indeterminate number of successive frames in an AOR. It was first noticed to affect the data more continuously on July 25, 2014. The pattern noise disappeared around 2014 December 9 but it reappeared briefly in some of the skydarks taken on 2015 March 13.

After 2014 July 25, short frame time (less than 12 seconds) images began to indiscriminately contain a low-level interference modulation of the signal across the array, or horizontal striping. A more careful investigation of images from all the AORs in one full campaign revealed that horizontal striping affected all frame times, but it is most prominent in the shortest frame times because of their lower backgrounds and fewer Fowler samples. The horizontal striping is stronger in channel 2 than in channel 1 (again presumably due to the lower background in channel 2). Its intensity can vary from barely detectable to easily seen, when looked at with the histogram equalization scaling. Subarray frames were found to be affected as well, although the noise is much higher in them and the effect is harder to see.

There is no detailed understanding of the origin of this effect, although it is thought to be related to electronic interference, probably from current running in some nearby part of the spacecraft, such as the battery charging currents. Tests were made to perform aperture photometry on data with pattern noise. No statistically significant difference in the derived flux densities were found when comparing point source photometry of the same source in observations with and without the pattern noise.

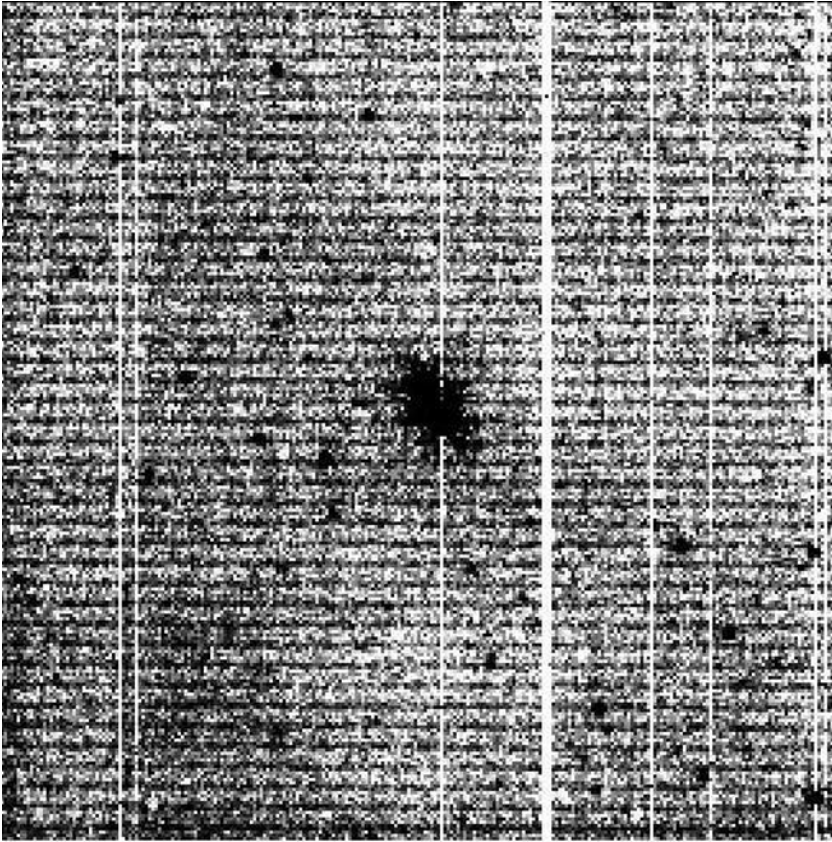


Figure D.7: Strong horizontal dark stripes in a 6-second frame time raw image in channel 2.

D.2 Time Series Photometry Tools

There are several tools available in the Contributed Software page

<https://irsa.ipac.caltech.edu/data/SPITZER/docs/dataanalysisistools/tools/contributed/>

that can be used when analyzing high precision photometry. These include

- `box_centroider.pro` that calculates centroids for a source using a simple first moment box centroider.
- `pmap_correct.pro` that corrects for intrapixel gain variations in warm IRAC photometry. It performs a kernel regression on measured centroids and aperture photometry using a pixel mapping dataset taken on a calibration star. Because of the nearest neighbor calculation, it can be slow for large datasets, but it is much more accurate than `iracpc_pmap_corr.pro` (see below).
- `iracpc_pmap_corr.pro` that corrects IRAC aperture photometry-derived fluxes from the post-cryogenic, or warm mission (IRACPC) for the intrapixel response, using the (pre-

gridded) pixel maps of the 3.6 μm and 4.5 μm subarray sweet spots. Note that this uses a pre-gridded pmap. It is faster, but less accurate than, pmap_correct.pro (above).

- `irac_aphot_corr.pro` that corrects IRAC aperture photometry-derived fluxes for the pixel phase and array location-dependent response functions. Built-in corrections are available for data from both the cryogenic (S18.24 processing; keyword /CRYO) and warm (S19.2 processing; keyword /WARM) missions. Note that this parametrized function for the intra-pixel response is a rough approximation and does not replicate the structure of the gain on less than 0.1-pixel scales. It may be useful as a first pass in correcting photometry.

Appendix E. IRAC BCD File Headers

E.1 Cryogenic Mission Channel 1

```

SIMPLE = T / Fits standard
BITPIX = -32 / FOUR-BYTE SINGLE PRECISION FLOATING POINT
NAXIS = 2 / STANDARD FITS FORMAT
NAXIS1 = 256 / STANDARD FITS FORMAT
NAXIS2 = 256 / STANDARD FITS FORMAT
ORIGIN = 'Spitzer Science Center' / Organization generating this FITS file
CREATOR = 'S18.25.0' / SW version used to create this FITS file
TELESCOP= 'Spitzer ' / SPITZER Space Telescope
INSTRUME= 'IRAC ' / SPITZER Space Telescope instrument ID
CHNLNUM = 1 / 1 digit instrument channel number
EXPTYPE = 'sci ' / Exposure Type
REQTYPE = 'AOR ' / Request type (AOR, IER, or SER)
AOT_TYPE= 'IracMap ' / Observation template type
AORLABEL= 'IRAC_calstar_NPM1p67.0536_spt4l2 - copy' / AOR Label
FOVID = 74 / Field of View ID
FOVNAME = 'IRAC_Center_of_4.5&8.0umArray' / Field of View Name

/ PROPOSAL INFORMATION

OBSRVR = 'Sean Carey' / Observer Name (Last, First)
OBSRVRID= 137 / Observer ID of Principal Investigator
PROCYCL = 3 / Proposal Cycle
PROGID = 1182 / Program ID
PROTITLE= 'SIRTF IRAC Calibration Program' / Program Title
PROGCAT = 32 / Program Category

/ TIME AND EXPOSURE INFORMATION

DATE_OBS= '2009-04-26T04:19:10.088' / Date & time (UTC) at DCE start
UTCS_OBS= 293991550.088 / [sec] DCE start time from noon, Jan 1, 2000 UTC
MJD_OBS = 54947.1799779 / [days] MJD in UTC at DCE start (,JD-2400000.5)
HMJD_OBS= 54947.179932 / [days] Corresponding Helioc. Mod. Julian Date
BMJD_OBS= 54947.1799324 / [days] Solar System Barycenter Mod. Julian Date
ET_OBS = 293991616.273 / [sec] DCE start time (TDB seconds past J2000)
SCLK_OBS= 925186991.09 / [sec] SCLK time (since 1/1/1980) at DCE start
SPTZR_X = -149438962.941318 / [km] Heliocentric J2000 x position
SPTZR_Y = 14190531.939344 / [km] Heliocentric J2000 y position
SPTZR_Z = 4150999.902977 / [km] Heliocentric J2000 z position
SPTZR_VX= -3.040365 / [km/s] Heliocentric J2000 x velocity
SPTZR_VY= -27.085559 / [km/s] Heliocentric J2000 y velocity
SPTZR_VZ= -12.252653 / [km/s] Heliocentric J2000 z velocity
SPTZR_LT= 500.908501 / [sec] One-way light time to Sun's center
AORTIME = 2. / [sec] Frameset selected in IRAC AOT
SAMPTIME= 0.2 / [sec] Sample integration time
FRAMTIME= 0.4 / [sec] Time spent integrating (whole array)
COMMENT Photons in Well = Flux[photons/sec/pixel] * FRAMTIME
EXPTIME = 0.2 / [sec] Effective integration time per pixel
COMMENT DN per pixel = Flux[photons/sec/pixel] / GAIN * EXPTIME
FRAMEDLY= 16.8 / [sec] Frame Delay Time
FRDLYDET= 'T ' / Frame Delay Time Determinable (T or F)
INTRFDLY= 16.8 / [sec] Inter Frame Delay Time
IMDLYDET= 'T ' / Immediate Delay Time Determinable (T or F)
AINTBEG = 422410.45 / [Secs since IRAC turn-on] Time of integ. start
ATIMEEND= 422410.82 / [Secs since IRAC turn-on] Time of integ. end
AFOWLNUM= 1 / Fowler number

```

```

AWAITPER=          0 / [0.2 sec] Wait period
ANUMREPS=          1 / Number of repeat integrations
AREADMOD=          0 / Full (0) or subarray (1)
AORHDR =           F / Requested AOT is HDR mode
HDRMODE =          F / DCE taken in High Dynamic Range mode
ABARREL =           0 / Barrel shift
APEDSIG =           0 / 0=Normal, 1=Pedestal, 2=Signal

```

/ TARGET AND POINTING INFORMATION

```

OBJECT = 'NPM1p67.0536' / Target Name
OBJTYPE = 'TargetFixedCluster' / Object Type
CRPIX1 =          128. / Reference pixel along axis 1
CRPIX2 =          128. / Reference pixel along axis 2
CRVAL1 =          269.68752396109 / [deg] RA at CRPIX1,CRPIX2 (using Ptg. Recon.)
CRVAL2 =          67.8873279620983 / [deg] DEC at CRPIX1,CRPIX2 (using Ptg. Recon.)
CRDER1 = 0.000301832469270907 / [deg] Uncertainty in CRVAL1
CRDER2 = 0.000301933698571944 / [deg] Uncertainty in CRVAL2
RA_HMS = '17h58m45.0s' / [hh:mm:ss.s] CRVAL1 as sexagesimal
DEC_DMS = '+67d53m14s' / [dd:mm:ss] CRVAL2 as sexagesimal
RADESYS = 'ICRS' / International Celestial Reference System
EQUINOX =          2000. / Equinox for ICRS celestial coord. system
CD1_1 = -3.41120758089606E-05 / Corrected CD matrix element with Ptg. Recon.
CD1_2 = -0.000338051716176839 / Corrected CD matrix element with Ptg. Recon.
CD2_1 = -0.000338100825225606 / Corrected CD matrix element with Ptg. Recon.
CD2_2 = 3.44346881534758E-05 / Corrected CD matrix element with Ptg. Recon.
CTYPE1 = 'RA---TAN-SIP' / RA---TAN with distortion in pixel space
CTYPE2 = 'DEC--TAN-SIP' / DEC--TAN with distortion in pixel space
PXSCAL1 = -1.22334117768332 / [arcsec/pix] Scale for axis 1 at CRPIX1,CRPIX2
PXSCAL2 = 1.22328355209902 / [arcsec/pix] Scale for axis 2 at CRPIX1,CRPIX2
PA = -84.1837897266392 / [deg] Position angle of axis 2 (E of N)
UNCRTPA = 0.00171832722634256 / [deg] Uncertainty in position angle
CSDRADEC= 5.63708025523962E-06 / [deg] Costandard deviation in RA and Dec
SIGRA = 0.0139972443264757 / [arcsec] RMS dispersion of RA over DCE
SIGDEC = 0.0912513013597778 / [arcsec] RMS dispersion of DEC over DCE
SIGPA = 0.0779422863269417 / [arcsec] RMS dispersion of PA over DCE
RA_RQST = 269.687600971031 / [deg] Requested RA at CRPIX1, CRPIX2
DEC_RQST = 67.8873605827309 / [deg] Requested Dec at CRPIX1, CRPIX2
PM_RA = 0. / [arcsec/yr] Proper Motion in RA (J2000)
PM_DEC = 0. / [arcsec/yr] Proper Motion in Dec (J2000)
RMS_JIT = 0.00403435731250964 / [arcsec] RMS jitter during DCE
RMS_JITY= 0.00355000676759918 / [arcsec] RMS jitter during DCE along Y
RMS_JITZ= 0.00191663530046798 / [arcsec] RMS jitter during DCE along Z
SIG_JTYZ= 0.00248656703609615 / [arcsec] Costandard deviation of jitter in YZ
PTGDIFF = 0.15708395676444 / [arcsec] Offset btwn actual and rqsted pntng
PTGDIFFX= 0.127405302856778 / [pixels] rqsted - actual pntng along axis 1
PTGDIFFY= -0.0920439160135617 / [pixels] rqsted - actual pntng along axis 2
RA_REF = 269.727166666667 / [deg] Commanded RA (J2000) of ref. position
DEC_REF = 67.79369444444462 / [deg] Commanded Dec (J2000) of ref. position
USEDBPHF= T / T if Boresight Pointing History File was used
BPHFNAME= 'BPHF.0925171200.03.pntg' / Boresight Pointing History Filename
FOVVERSN= 'BodyFrames_FTU_14a.xls' / FOV/BodyFrames file version used
RECONFOV= 'IRAC_Center_of_3.6umArray' / Reconstructed Field of View
RARFND = 269.687530517578 / [deg] Refined RA
DECRFND = 67.887329101562 / [deg] Refined DEC
CT2RFND = -84.183746337891 / [deg] Refined CROT2
ERARFND = 0.000000000000 / [deg] Error in RARFND value
EDECRFND= 0.000000000000 / [deg] Error in DECRFND value
ECT2RFND= 0.000000000000 / [deg] Error in CT2RFND value
NASTROM = 0 / Astrometric sources for absolute refinement

```

/ DISTORTION KEYWORDS

```

A_ORDER =          3 / polynomial order, axis 1, detector to sky

```

```

A_0_2 = 2.9656E-06 / distortion coefficient
A_0_3 = 3.7746E-09 / distortion coefficient
A_1_1 = 2.1886E-05 / distortion coefficient
A_1_2 = -1.6847E-07 / distortion coefficient
A_2_0 = -2.3863E-05 / distortion coefficient
A_2_1 = -8.561E-09 / distortion coefficient
A_3_0 = -1.4172E-07 / distortion coefficient
A_DMAX = 1.394 / [pixel] maximum correction
B_ORDER = 3 / polynomial order, axis 2, detector to sky
B_0_2 = 2.31E-05 / distortion coefficient
B_0_3 = -1.6168E-07 / distortion coefficient
B_1_1 = -2.4386E-05 / distortion coefficient
B_1_2 = -5.7813E-09 / distortion coefficient
B_2_0 = 2.1197E-06 / distortion coefficient
B_2_1 = -1.6583E-07 / distortion coefficient
B_3_0 = -2.0249E-08 / distortion coefficient
B_DMAX = 1.501 / [pixel] maximum correction
AP_ORDER = 3 / polynomial order, axis 1, sky to detector
AP_0_1 = -6.4275E-07 / distortion coefficient
AP_0_2 = -2.9425E-06 / distortion coefficient
AP_0_3 = -3.582E-09 / distortion coefficient
AP_1_0 = -1.4897E-05 / distortion coefficient
AP_1_1 = -2.225E-05 / distortion coefficient
AP_1_2 = 1.7195E-07 / distortion coefficient
AP_2_0 = 2.4146E-05 / distortion coefficient
AP_2_1 = 6.709E-09 / distortion coefficient
AP_3_0 = 1.4492E-07 / distortion coefficient
BP_ORDER = 3 / polynomial order, axis 2, sky to detector
BP_0_1 = -1.6588E-05 / distortion coefficient
BP_0_2 = -2.3424E-05 / distortion coefficient
BP_0_3 = 1.651E-07 / distortion coefficient
BP_1_0 = -2.6783E-06 / distortion coefficient
BP_1_1 = 2.4753E-05 / distortion coefficient
BP_1_2 = 3.8917E-09 / distortion coefficient
BP_2_0 = -2.151E-06 / distortion coefficient
BP_2_1 = 1.7E-07 / distortion coefficient
BP_3_0 = 2.0482E-08 / distortion coefficient

```

/ PHOTOMETRY

```

BUNIT = 'MJy/sr ' / Units of image data
FLUXCONV= 0.1069 / Flux Conv. factor (MJy/sr per DN/sec)
GAIN = 3.3 / e/DN conversion
RONOISE = 22.4 / [Electrons] Readout Noise from Array
ZODY_EST= 0.04681149 / [MJy/sr] Zodiacal Background Estimate
ISM_EST = 0.005453848 / [MJy/sr] Interstellar Medium Estimate
CIB_EST = 0. / [MJy/sr] Cosmic Infrared Background Estimate
SKYDRKZB= 0.046132 / [MJy/sr] Zodiacal Background Est of Subtracted
SKYDKMED= 0.326073 / [MJy/sr] Median of Subtracted Skydark
SKDKRKEY= 33270016 / Skydark AOR Reqkey
SKDKTIME= 2. / [sec] Skydark AOR Duration Time
SKDKFDLY= 13.58 / [sec] Average Frame Delay Time of Skydark
SKDKIDLY= 13.58 / [sec] Average Immediate Delay Time of Skydark

```

/ IRAC MAPPING KEYWORDS

```

READMODE= 'FULL ' / Readout mode (full or sub)

```

/ INSTRUMENT TELEMETRY DATA

```

ASHTCON = 2 / Shutter condition (1:closed, 2: open)
AWEASIDE= 0 / WEA side in use (0:B, 1:A)
ACTXSTAT= 0 / Cmded transcal status
ATXSTAT = 0 / transcal status
ACFLSTAT= 0 / Cmded floodcal status

```

```

AFLSTAT = 0 / floodcal status
AVRSTUCC= -3.5 / [Volts] Cmded VRSTUC Bias
AVRSTBEG= -3.5120896 / [Volts] VRSTUC Bias at start integration
AVDETC = -2.75 / [Volts] Cmded VDET Bias
AVDETBEG= -2.7585216 / [Volts] VDET Bias at start of integration
AVGG1C = -3.65 / [Volts] Cmded VGG1 Bias
AVGG1BEG= -3.6628801 / [Volts] VGG1 Bias at start of integration
AVDDUCC = -3.5 / [Volts] Cmded VDDUC Bias
AVDDUBEG= -3.5003509 / [Volts] VDDUC Bias at start integration
AVGGCLC = 1. / [Volts] Cmded VGGCL clock rail voltage
AVGGCBEG= 1. / [Volts] VGGCL clock rail voltage
AHTRIBEG= 204.90478 / [uAmps] Heater current at start of integ
AHTRVBEG= 2.3924802 / [Volts] Heater Voltage at start integ.
AFPAT2B = 15.02195 / [Deg_K] FPA Temp sensor #2 at start integ.
AFPAT2BT= 422402.6 / [Sec] FPA Temp sensor #2 time tag
AFPAT2E = 15.02195 / [Deg_K] FPA temp sensor #2, end integ.
AFPAT2ET= 422402.6 / [Sec] FPA temp sensor #2 time tag
ACTENDT = 20.285331 / [Deg_C] C&T board thermistor
AFPECTE = 18.21777 / [Deg_C] FPE control board thermistor
AFPEATE = 21.683101 / [Deg_C] FPE analog board thermistor
ASHTEMPE= 21.443602 / [Deg_C] Shutter board thermistor
ATCTEMPE= 22.601873 / [Deg_C] Temp. controller board thermistor
ACETEMPE= 20.193888 / [Deg_C] Calib. electronics board thermistor
APDTEMPE= 20.407254 / [Deg_C] PDU board thermistor
ACATMP1E= 1.2900473 / [Deg_K] CA Temp, Foot 2
ACATMP2E= 1.2724768 / [Deg_K] CA Temp, Foot 1
ACATMP3E= 1.3060768 / [Deg_K] CA Temp, Shutter
ACATMP4E= 1.3026365 / [Deg_K] CA Temp, Top OMH
ACATMP5E= 1.3005989 / [Deg_K] CA Temp, Bottom OMH
ACATMP6E= 1.2987331 / [Deg_K] CA Temp, Top TxCal Sphere
ACATMP7E= 1.2974439 / [Deg_K] CA Temp, Bottom TxCal Sphere
ACATMP8E= 1.2902828 / [Deg_K] CA Temp, Foot 3

```

/ DATA FLOW KEYWORDS

```

ORIGIN0 = 'JPL_FOS ' / Site where RAW FITS file was written
CREATOR0= 'J5.3 ' / SW system that created RAW FITS
DATE = '2010-11-04T16:17:27' / [YYYY-MM-DDThh:mm:ss UTC] file creation date
AORKEY = 33258752 / AOR or EIR key. Astrnmy Obs Req/Instr Eng Req
DS_IDENT= 'ads/sa.spitzer#0033258752' / Data Set Identification for ADS/journals
EXPID = 8 / Exposure ID (0-9999)
DCENUM = 0 / DCE number (0-9999)
TLMGRPS = 1 / expected number of groups
FILE_VER= 1 / Version of the raw file made by SIS
RAWFILE = 'IRAC.1.0033258752.0008.0000.01.mipl.fits' / Raw data file name
CPT_VER = '3.1.11 ' / Channel Param Table FOS version
CTD_VER = '3.0.94S ' / Cmded telemetry data version
EXPDFLAG= T / (T/F) expedited DCE
MISS_LCT= 0 / Total Missed Line Cnt in this FITS
MANCPKT = F / T if this FITS is Missing Ancillary Data
MISSDATA= F / T if this FITS is Missing Image Data
BADTRIG = F / Bad data (zero pixel) was located in raw frame
CHECKSUM= 0 / MIPL computed checksum
PAONUM = 3443 / PAO Number
CAMPAIGN= 'IRAC013900' / Campaign
DCEID = 119198499 / Data-Collection-Event ID
DCEINSID= 24670147 / DCE Instance ID
DPID = 331591638 / Data Product Instance ID
PIPENUM = 107 / Pipeline Script Number
SOS_VER = 1 / Data-Product Version
PLVID = 4 / Pipeline Version ID
CALID = 6 / CalTrans Version ID
SDRKEPID= 7915958 / Sky Dark ensemble product ID
PMSKFBID= 1975 / Pixel mask ID
LDRKFBID= 856 / Fall-back lab dark ID

```

```

LINCFBID=          357 / Fall-back Linearity correction ID
FLATFBID=          1589 / Fall-back flat ID
FLXCFBID=          1898 / Flux conversion ID
MBLTFBID=          1153 / Muxbleed Lookup Table ID
MBCFFBID=          1154 / Muxbleed Coefficients ID
LBDRKFLE= 'FUL_0.4s_0.4sf1dlr1_ch1_v1.2.0_dark.txt' / Labdark File Used
LBDRKTD = 'F'      / Labdark Time Dependent (T or F)
DDCORR1 =          -0.1561639 / Darkdrift Correction for Readout Channel 1
DDCORR2 =           0.2232306 / Darkdrift Correction for Readout Channel 2
DDCORR3 =           0.03184047 / Darkdrift Correction for Readout Channel 3
DDCORR4 =          -0.0989072 / Darkdrift Correction for Readout Channel 4
DDBKGND =           0.06926759 / Darkdrift 'Background' Term

```

/ PROCESSING HISTORY

```

HISTORY job.c ver: 1.50
HISTORY TRANHEAD          v.          13.1, ran Thu Nov  4 09:17:06 2010
HISTORY CALTRANS          v.           4.0, ran Thu Nov  4 09:17:12 2010
HISTORY INSBPOSDOM        v.           1.1, ran Thu Nov  4 09:17:12 2010
HISTORY cvti2r4           v.  1.31 A61025, generated 11/04/10 at  9:17:12
HISTORY hdrupd8           v.  1.6 A70821, updated 11/04/10 at  9:17:15
HISTORY hdrupd8           v.  1.6 A70821, updated 11/04/10 at  9:17:15
HISTORY hdrupd8           v.  1.6 A70821, updated 11/04/10 at  9:17:16
HISTORY hdrupd8           v.  1.6 A70821, updated 11/04/10 at  9:17:16
HISTORY hdrupd8           v.  1.6 A70821, updated 11/04/10 at  9:17:17
HISTORY hdrupd8           v.  1.6 A70821, updated 11/04/10 at  9:17:17
HISTORY hdrupd8           v.  1.6 A70821, updated 11/04/10 at  9:17:18
HISTORY FFC               v.           1.0, ran Thu Nov  4 09:17:18 2010
HISTORY MUXBLEEDCORR      v.          1.600, ran Thu Nov  4 09:17:19 2010
HISTORY FOWLINEARIZE      v.          4.900000, ran Thu Nov  4 09:17:19 2010
HISTORY hdrupd8           v.  1.6 A70821, updated 11/04/10 at  9:17:20
HISTORY BGMODEL           v.           1.0, ran Thu Nov  4 09:17:20 2010
HISTORY SLREMOVE          v.           1.0, ran Thu Nov  4 09:17:20 2010
HISTORY hdrupd8           v.  1.6 A70821, updated 11/04/10 at  9:17:20
HISTORY hdrupd8           v.  1.6 A70821, updated 11/04/10 at  9:17:21
HISTORY hdrupd8           v.  1.6 A70821, updated 11/04/10 at  9:17:22
HISTORY hdrupd8           v.  1.6 A70821, updated 11/04/10 at  9:17:22
HISTORY hdrupd8           v.  1.6 A70821, updated 11/04/10 at  9:17:23
HISTORY hdrupd8           v.  1.6 A70821, updated 11/04/10 at  9:17:23
HISTORY DARKSUBNG         v.  1.000, ran Thu Nov  4 09:17:23 2010
HISTORY DARKDRIFT         v.           4.1, ran Thu Nov  4 09:17:24 2010
HISTORY FLATAP            v.  1.500  Thu Nov  4 09:17:24 2010
HISTORY DNTOFUX           v.           4.2, ran Thu Nov  4 09:17:27 2010
HISTORY CALTRANS          v.           4.0, ran Thu Nov  4 09:20:19 2010
HISTORY PTNTRAN           v.           1.4, ran Thu Nov  4 09:20:23 2010
HISTORY FPGen             v.           1.26, ran Thu Nov  4 09:20:25 2010
HISTORY PTGADJUST         v.           1.0, ran Thu Nov  4 09:21:24 2010
HISTORY Data rescaled using correct flux conversion : 25 Jun 2012 14:17:25 PDT
HISTORY FLUXCONV rescaled from 0.1069 to 0.1069 : 25 Jun 2012 14:17:25 PDT
HISTORY FLUXCONV updated in header : 25 Jun 2012 14:17:25 PDT
HISTORY CREATOR keyword updated : 25 Jun 2012 14:17:25 PDT
END

```

E.2 Cryogenic Mission Channel 2

```

SIMPLE =              T / Fits standard
BITPIX =             -32 / FOUR-BYTE SINGLE PRECISION FLOATING POINT
NAXIS  =              2 / STANDARD FITS FORMAT
NAXIS1 =             256 / STANDARD FITS FORMAT

```

```

NAXIS2 = 256 / STANDARD FITS FORMAT
ORIGIN = 'Spitzer Science Center' / Organization generating this FITS file
CREATOR = 'S18.25.0' / SW version used to create this FITS file
TELESCOP= 'Spitzer' / SPITZER Space Telescope
INSTRUME= 'IRAC' / SPITZER Space Telescope instrument ID
CHNLNUM = 2 / 1 digit instrument channel number
EXPTYPE = 'sci' / Exposure Type
REQTYPE = 'AOR' / Request type (AOR, IER, or SER)
AOT_TYPE= 'IracMap' / Observation template type
AORLABEL= 'IRAC_calstar_NPM1p67.0536_spt4l2 - copy' / AOR Label
FOVID = 74 / Field of View ID
FOVNAME = 'IRAC_Center_of_4.5&8.0umArray' / Field of View Name

/ PROPOSAL INFORMATION

OBSRVR = 'Sean Carey' / Observer Name (Last, First)
OBSRVRID= 137 / Observer ID of Principal Investigator
PROCYCL = 3 / Proposal Cycle
PROGID = 1182 / Program ID
PROTITLE= 'SIRTF IRAC Calibration Program' / Program Title
PROGCAT = 32 / Program Category

/ TIME AND EXPOSURE INFORMATION

DATE_OBS= '2009-04-26T04:19:10.088' / Date & time (UTC) at DCE start
UTCS_OBS= 293991550.088 / [sec] DCE start time from noon, Jan 1, 2000
UTCMJD_OBS = 54947.1799779 / [days] MJD in UTC at DCE start (,JD-2400000.5)
HMJD_OBS= 54947.1799317 / [days] Corresponding Helioc. Mod. Julian Date
BMJD_OBS= 54947.1799321 / [days] Solar System Barycenter Mod. Julian Date
ET_OBS = 293991616.273 / [sec] DCE start time (TDB seconds past J2000)
SCLK_OBS= 925186991.09 / [sec] SCLK time (since 1/1/1980) at DCE start
SPTZR_X = -149438962.941318 / [km] Heliocentric J2000 x position
SPTZR_Y = 14190531.939344 / [km] Heliocentric J2000 y position
SPTZR_Z = 4150999.902977 / [km] Heliocentric J2000 z position
SPTZR_VX= -3.040365 / [km/s] Heliocentric J2000 x velocity
SPTZR_VY= -27.085559 / [km/s] Heliocentric J2000 y velocity
SPTZR_VZ= -12.252653 / [km/s] Heliocentric J2000 z velocity
SPTZR_LT= 500.908501 / [sec] One-way light time to Sun's center
AORTIME = 2. / [sec] Frameset selected in IRAC AOT
SAMPIME= 0.2 / [sec] Sample integration time
FRAMTIME= 0.4 / [sec] Time spent integrating (whole array)
COMMENT Photons in Well = Flux[photons/sec/pixel] * FRAMTIME
EXPTIME = 0.2 / [sec] Effective integration time per pixel
COMMENT DN per pixel = Flux[photons/sec/pixel] / GAIN * EXPTIME
FRAMEDLY= 16.8 / [sec] Frame Delay Time
FRDLYDET= 'T' / Frame Delay Time Determinable (T or F)
INTRFDLY= 16.8 / [sec] Inter Frame Delay Time
IMDLYDET= 'T' / Immediate Delay Time Determinable (T or F)
AINTBEG = 422410.45 / [Secs since IRAC turn-on] Time of integ. start
ATIMEEND= 422410.82 / [Secs since IRAC turn-on] Time of integ. end
AOWLNUM= 1 / Fowler number
AWAITPER= 0 / [0.2 sec] Wait period
ANUMREPS= 1 / Number of repeat integrations
AREAMOD= 0 / Full (0) or subarray (1)
AORHDR = F / Requested AOT is HDR mode
HDRMODE = F / DCE taken in High Dynamic Range mode
ABARREL = 0 / Barrel shift
APEDSIG = 0 / 0=Normal, 1=Pedestal, 2=Signal

/ TARGET AND POINTING INFORMATION

OBJECT = 'NPM1p67.0536' / Target Name
OBJTYPE = 'TargetFixedCluster' / Object Type
CRPIX1 = 128. / Reference pixel along axis 1
CRPIX2 = 128. / Reference pixel along axis 2

```

```

CRVAL1 = 269.666277461727 / [deg] RA at CRPIX1,CRPIX2 (using Ptg. Recon.)
CRVAL2 = 67.7744849654857 / [deg] DEC at CRPIX1,CRPIX2 (using Ptg. Recon.)
CRDER1 = 0.000301832149720566 / [deg] Uncertainty in CRVAL1
CRDER2 = 0.000301931756352039 / [deg] Uncertainty in CRVAL2
RA_HMS = '17h58m39.9s' / [hh:mm:ss.s] CRVAL1 as sexagesimal
DEC_DMS = '+67d46m28s' / [dd:mm:ss] CRVAL2 as sexagesimal
RADESYS = 'ICRS' / International Celestial Reference System
EQUINOX = 2000. / Equinox for ICRS celestial coord. system
CD1_1 = -3.50053520800047E-05 / Corrected CD matrix element with Ptg. Recon.
CD1_2 = -0.000335925118777663 / Corrected CD matrix element with Ptg. Recon.
CD2_1 = -0.000336075848067756 / Corrected CD matrix element with Ptg. Recon.
CD2_2 = 3.49466019474603E-05 / Corrected CD matrix element with Ptg. Recon.
CTYPE1 = 'RA---TAN-SIP' / RA---TAN with distortion in pixel space
CTYPE2 = 'DEC--TAN-SIP' / DEC--TAN with distortion in pixel space
PXSCAL1 = -1.21641835430637 / [arcsec/pix] Scale for axis 1 at CRPIX1,CRPIX2
PXSCAL2 = 1.21585676679388 / [arcsec/pix] Scale for axis 2 at CRPIX1,CRPIX2
PA = -84.0608333104913 / [deg] Position angle of axis 2 (E of N)
UNCRTPA = 0.00171832722634256 / [deg] Uncertainty in position angle
CSDRADEC= 6.04296117996226E-06 / [deg] Costandard deviation in RA and Dec
SIGRA = 0.0133896774557494 / [arcsec] RMS dispersion of RA over DCE
SIGDEC = 0.0912513013542275 / [arcsec] RMS dispersion of DEC over DCE
SIGPA = 0.0779422863328491 / [arcsec] RMS dispersion of PA over DCE
RA_RQST = 269.666387352644 / [deg] Requested RA at CRPIX1, CRPIX2
DEC_RQST= 67.7745168483211 / [deg] Requested Dec at CRPIX1, CRPIX2
PM_RA = 0. / [arcsec/yr] Proper Motion in RA (J2000)
PM_DEC = 0. / [arcsec/yr] Proper Motion in Dec (J200)
RMS_JIT = 0.00403435731250964 / [arcsec] RMS jitter during DCE
RMS_JITY= 0.00355000676759918 / [arcsec] RMS jitter during DCE along Y
RMS_JITZ= 0.00191663530046798 / [arcsec] RMS jitter during DCE along Z
SIG_JTYZ= 0.00248656703609615 / [arcsec] Costadard deviation of jitter in YZ
PTGDIFF = 0.18856889371851 / [arcsec] Offset btwn actual and rqsted pntng
PTGDIFFX= 0.129645818168439 / [pixels] rqsted - actual pntng along axis 1
PTGDIFFY= -0.136943408923376 / [pixels] rqsted - actual pntng along axis 2
RA_REF = 269.727166666667 / [deg] Commanded RA (J2000) of ref. position
DEC_REF = 67.79369444444462 / [deg] Commanded Dec (J2000) of ref. position
USEDBPHF= T / T if Boresight Pointing History File was used
BPHFNAME= 'BPHF.0925171200.03.pntg' / Boresight Pointing History Filename
FOVVERS= 'BodyFrames_FTU_14a.xls' / FOV/BodyFrames file version used
RECONFOV= 'IRAC_Center_of_4.5umArray' / Reconstructed Field of View

```

/ DISTORTION KEYWORDS

```

A_ORDER = 3 / polynomial order, axis 1, detector to sky
A_0_2 = 1.0582E-08 / distortion coefficient
A_0_3 = -3.0831E-09 / distortion coefficient
A_1_1 = 3.0188E-05 / distortion coefficient
A_1_2 = -1.8817E-07 / distortion coefficient
A_2_0 = 1.9063E-05 / distortion coefficient
A_2_1 = 6.5975E-09 / distortion coefficient
A_3_0 = -1.8531E-07 / distortion coefficient
A_DMAX = 1.645 / [pixel] maximum correction
B_ORDER = 3 / polynomial order, axis 2, detector to sky
B_0_2 = 3.4386E-05 / distortion coefficient
B_0_3 = -1.7897E-07 / distortion coefficient
B_1_1 = 1.8781E-05 / distortion coefficient
B_1_2 = 3.7246E-09 / distortion coefficient
B_2_0 = 3.7734E-06 / distortion coefficient
B_2_1 = -1.7747E-07 / distortion coefficient
B_3_0 = -5.2103E-10 / distortion coefficient
B_DMAX = 1.738 / [pixel] maximum correction
AP_ORDER= 3 / polynomial order, axis 1, sky to detector
AP_0_1 = 5.0237E-07 / distortion coefficient
AP_0_2 = -5.1645E-08 / distortion coefficient
AP_0_3 = 3.0939E-09 / distortion coefficient
AP_1_0 = -2.1471E-05 / distortion coefficient

```

```

AP_1_1 = -3.0796E-05 / distortion coefficient
AP_1_2 = 1.9379E-07 / distortion coefficient
AP_2_0 = -1.9359E-05 / distortion coefficient
AP_2_1 = -4.4162E-09 / distortion coefficient
AP_3_0 = 1.8929E-07 / distortion coefficient
BP_ORDER= 3 / polynomial order, axis 2, sky to detector
BP_0_1 = -1.997E-05 / distortion coefficient
BP_0_2 = -3.491E-05 / distortion coefficient
BP_0_3 = 1.8428E-07 / distortion coefficient
BP_1_0 = 5.83E-07 / distortion coefficient
BP_1_1 = -1.9129E-05 / distortion coefficient
BP_1_2 = -1.2856E-09 / distortion coefficient
BP_2_0 = -3.8713E-06 / distortion coefficient
BP_2_1 = 1.821E-07 / distortion coefficient
BP_3_0 = 7.0846E-10 / distortion coefficient

/ PHOTOMETRY

BUNIT = 'MJy/sr ' / Units of image data
FLUXCONV= 0.1382 / Flux Conv. factor (MJy/sr per DN/sec)
GAIN = 3.71 / e/DN conversion
RONOISE = 23.7 / [Electrons] Readout Noise from Array
ZODY_EST= 0.2400851 / [MJy/sr] Zodiacal Background Estimate
ISM_EST = 0.007908594 / [MJy/sr] Interstellar Medium Estimate
CIB_EST = 0. / [MJy/sr] Cosmic Infrared Background Estimate
SKYDRKZB= 0.234029 / [MJy/sr] Zodiacal Background Est of Subtracted
SKYDKMED= -0.019194 / [MJy/sr] Median of Subtracted Skydark
SKDKRKEY= 33270016 / Skydark AOR Reqkey
SKDKTIME= 2. / [sec] Skydark AOR Duration Time
SKDKFDLY= 13.58 / [sec] Average Frame Delay Time of Skydark
SKDKIDLY= 13.58 / [sec] Average Immediate Delay Time of Skydark

/ IRAC MAPPING KEYWORDS

READMODE= 'FULL ' / Readout mode (full or sub)

/ INSTRUMENT TELEMETRY DATA

ASHTCON = 2 / Shutter condition (1:closed, 2: open)
AWEASIDE= 0 / WEA side in use (0:B, 1:A)
ACTXSTAT= 0 / Cmded transcal status
ATXSTAT = 0 / transcal status
ACFLSTAT= 0 / Cmded floodcal status
AFLSTAT = 0 / floodcal status
AVRSTUCC= -3.5 / [Volts] Cmded VRSTUC Bias
AVRSTBEG= -3.5082063 / [Volts] VRSTUC Bias at start integration
AVDETC = -3. / [Volts] Cmded VDET Bias
AVDETBEG= -3.0065797 / [Volts] VDET Bias at start of integration
AVGG1C = -3.65 / [Volts] Cmded VGG1 Bias
AVGG1BEG= -3.658379 / [Volts] VGG1 Bias at start of integration
AVDDUCC = -3.5 / [Volts] Cmded VDDUC Bias
AVDDUBEG= -3.4964314 / [Volts] VDDUC Bias at start integration
AVGGCLC = 0. / [Volts] Cmdded VGGCL clock rail voltage
AVGGCBEG= 0. / [Volts] VGGCL clock rail voltage
AHTRIBEG= 241.19451 / [uAmps] Heater current at start of integ
AHTRVBEG= 2.8425994 / [Volts] Heater Voltage at start integ.
AFPAT2B = 15.081714 / [Deg_K] FPA Temp sensor #2 at start integ.
AFPAT2BT= 422402.7 / [Sec] FPA Temp sensor #2 time tag
AFPAT2E = 15.081714 / [Deg_K] FPA temp sensor #2, end integ.
AFPAT2ET= 422402.7 / [Sec] FPA temp sensor #2 time tag
ACTENDT = 20.285331 / [Deg_C] C&T board thermistor
AFPECTE = 18.349365 / [Deg_C] FPE control board thermistor
AFPEATE = 21.332181 / [Deg_C] FPE analog board thermistor
ASHTEMPE= 21.443602 / [Deg_C] Shutter board thermistor
ATCTEMPE= 22.601873 / [Deg_C] Temp. controller board thermistor

```



```

ACETEMPE=          20.193888 / [Deg_C] Calib. electronics board thermistor
APDTEMPE=          20.407254 / [Deg_C] PDU board thermistor
ACATMP1E=          1.2900473 / [Deg_K] CA Temp, Foot 2
ACATMP2E=          1.2724768 / [Deg_K] CA Temp, Foot 1
ACATMP3E=          1.3060768 / [Deg_K] CA Temp, Shutter
ACATMP4E=          1.3026365 / [Deg_K] CA Temp, Top OMH
ACATMP5E=          1.3005989 / [Deg_K] CA Temp, Bottom OMH
ACATMP6E=          1.2987331 / [Deg_K] CA Temp, Top TxCal Sphere
ACATMP7E=          1.2974439 / [Deg_K] CA Temp, Bottom TxCal Sphere
ACATMP8E=          1.2902828 / [Deg_K] CA Temp, Foot 3

```

/ DATA FLOW KEYWORDS

```

ORIGIN0 = 'JPL_FOS ' / Site where RAW FITS file was written
CREATOR0 = 'J5.3 ' / SW system that created RAW FITS
DATE = '2010-11-04T16:19:28' / [YYYY-MM-DDThh:mm:ss UTC] file creation date
AORKEY = 33258752 / AOR or EIR key. Astrnmy Obs Req/Instr Eng Req
DS_IDENT= 'ads/sa.spitzer#0033258752' / Data Set Identification for ADS/journals
EXPID = 8 / Exposure ID (0-9999)
DCENUM = 0 / DCE number (0-9999)
TLMGRPS = 1 / expected number of groups
FILE_VER= 1 / Version of the raw file made by SIS
RAWFILE = 'IRAC.2.0033258752.0008.0000.01.mipl.fits' / Raw data file name
CPT_VER = '3.1.11 ' / Channel Param Table FOS version
CTD_VER = '3.0.94S ' / Cmded telemetry data version
EXPDFLAG= T / (T/F) expedited DCE
MISS_LCT= 0 / Total Missed Line Cnt in this FITS
MANCPKT = F / T if this FITS is Missing Ancillary Data
MISSDATA= F / T if this FITS is Missing Image Data
BADTRIG = F / Bad data (zero pixel) was located in raw frame
CHECKSUM= 0 / MIPL computed checksum
PAONUM = 3443 / PAO Number
CAMPAIGN= 'IRAC013900' / Campaign
DCEID = 119198498 / Data-Collection-Event ID
DCEINSID= 24670148 / DCE Instance ID
DPID = 331591686 / Data Product Instance ID
PIPENUM = 107 / Pipeline Script Number
SOS_VER = 1 / Data-Product Version
PLVID = 5 / Pipeline Version ID
CALID = 7 / CalTrans Version ID
SDRKEPID= 7915980 / Sky Dark ensemble product ID
PMSKFBID= 1977 / Pixel mask ID
LDRKFBID= 858 / Fall-back lab dark ID
LINCFBID= 359 / Fall-back Linearity correction ID
FLATFBID= 1591 / Fall-back flat ID
FLXCFBID= 1900 / Flux conversion ID
MBLTFBID= 1155 / Muxbleed Lookup Table ID
MBCFFBID= 1156 / Muxbleed Coefficients ID
LBDRKFLE= 'FUL_0.4s_0.4sfdlrl1_ch2_v1.2.0_dark.txt' / Labdark File Used
LBDRKTD = 'F' / Labdark Time Dependent (T or F)
DDCORR1 = 0.00405313 / Darkdrift Correction for Readout Channel 1
DDCORR2 = -0.0897068 / Darkdrift Correction for Readout Channel 2
DDCORR3 = 0.02722468 / Darkdrift Correction for Readout Channel 3
DDCORR4 = 0.05842899 / Darkdrift Correction for Readout Channel 4
DDBKGNL = -0.1313909 / Darkdrift 'Background' Term

```

/ PROCESSING HISTORY

```

HISTORY job.c ver: 1.50
HISTORY TRANHEAD v. 13.1, ran Thu Nov 4 09:18:50 2010
HISTORY CALTRANS v. 4.0, ran Thu Nov 4 09:19:01 2010
HISTORY INSBPOSDOM v. 1.1, ran Thu Nov 4 09:19:01 2010
HISTORY cvti2r4 v. 1.31 A61025, generated 11/04/10 at 9:19:02
HISTORY hdrupd8 v. 1.6 A70821, updated 11/04/10 at 9:19:05
HISTORY hdrupd8 v. 1.6 A70821, updated 11/04/10 at 9:19:06

```

```

HISTORY hdrupd8          v. 1.6 A70821, updated 11/04/10 at 9:19:07
HISTORY hdrupd8          v. 1.6 A70821, updated 11/04/10 at 9:19:08
HISTORY hdrupd8          v. 1.6 A70821, updated 11/04/10 at 9:19:10
HISTORY hdrupd8          v. 1.6 A70821, updated 11/04/10 at 9:19:11
HISTORY hdrupd8          v. 1.6 A70821, updated 11/04/10 at 9:19:12
HISTORY FFC              v.          1.0, ran Thu Nov 4 09:19:13 2010
HISTORY MUXBLEEDCORR    v.          1.600, ran Thu Nov 4 09:19:14 2010
HISTORY FOWLINEARIZE    v.          4.900000, ran Thu Nov 4 09:19:14 2010
HISTORY hdrupd8          v. 1.6 A70821, updated 11/04/10 at 9:19:16
HISTORY BGMODEL         v.          1.0, ran Thu Nov 4 09:19:16 2010
HISTORY SLREMOVE        v.          1.0, ran Thu Nov 4 09:19:16 2010
HISTORY hdrupd8          v. 1.6 A70821, updated 11/04/10 at 9:19:17
HISTORY hdrupd8          v. 1.6 A70821, updated 11/04/10 at 9:19:18
HISTORY hdrupd8          v. 1.6 A70821, updated 11/04/10 at 9:19:19
HISTORY hdrupd8          v. 1.6 A70821, updated 11/04/10 at 9:19:20
HISTORY hdrupd8          v. 1.6 A70821, updated 11/04/10 at 9:19:21
HISTORY hdrupd8          v. 1.6 A70821, updated 11/04/10 at 9:19:22
HISTORY DARKSUBNG       v. 1.000, ran Thu Nov 4 09:19:22 2010
HISTORY DARKDRIFT       v.          4.1, ran Thu Nov 4 09:19:22 2010
HISTORY FLATAP          v. 1.500   Thu Nov 4 09:19:23 2010
HISTORY DNTOFLUX       v.          4.2, ran Thu Nov 4 09:19:28 2010
HISTORY CALTRANS        v.          4.0, ran Thu Nov 4 09:21:55 2010
HISTORY PTNTRAN         v.          1.4, ran Thu Nov 4 09:21:59 2010
HISTORY FPGen           v.          1.26, ran Thu Nov 4 09:22:00 2010
HISTORY PTGADJUST       v.          1.0, ran Thu Nov 4 09:23:06 2010
HISTORY Data rescaled using correct flux conversion : 25 Jun 2012 14:17:30 PDT
HISTORY FLUXCONV rescaled from 0.1382 to 0.1382 : 25 Jun 2012 14:17:30 PDT
HISTORY FLUXCONV updated in header : 25 Jun 2012 14:17:30 PDT
HISTORY CREATOR keyword updated : 25 Jun 2012 14:17:30 PDT
END

```

E.3 Cryogenic Mission Channel 3

```

SIMPLE = T / Fits standard
BITPIX = -32 / FOUR-BYTE SINGLE PRECISION FLOATING POINT
NAXIS = 2 / STANDARD FITS FORMAT
NAXIS1 = 256 / STANDARD FITS FORMAT
NAXIS2 = 256 / STANDARD FITS FORMAT
ORIGIN = 'Spitzer Science Center' / Organization generating this FITS file
CREATOR = 'S18.25.0' / SW version used to create this FITS file
TELESCOP= 'Spitzer ' / SPITZER Space Telescope
INSTRUME= 'IRAC ' / SPITZER Space Telescope instrument ID
CHNLNUM = 3 / 1 digit instrument channel number
EXPTYPE = 'sci ' / Exposure Type
REQTYPE = 'AOR ' / Request type (AOR, IER, or SER)
AOT_TYPE= 'IracMap ' / Observation template type
AORLABEL= 'IRAC_calstar_NPM1p67.0536_spt4l2 - copy' / AOR Label
FOVID = 74 / Field of View ID
FOVNAME = 'IRAC_Center_of_4.5&8.0umArray' / Field of View Name

/ PROPOSAL INFORMATION

OBSRVR = 'Sean Carey' / Observer Name (Last, First)
OBSRVRID= 137 / Observer ID of Principal Investigator
PROCYCL = 3 / Proposal Cycle
PROGID = 1182 / Program ID
PROTITLE= 'SIRTF IRAC Calibration Program' / Program Title
PROGCAT = 32 / Program Category

```

/ TIME AND EXPOSURE INFORMATION

```

DATE_OBS= '2009-04-26T04:19:10.088' / Date & time (UTC) at DCE start
UTCS_OBS= 293991550.088 / [sec] DCE start time from noon, Jan 1, 2000
UTCMJD_OBS = 54947.1799779 / [days] MJD in UTC at DCE start (,JD-2400000.5)
HMJD_OBS= 54947.1799319 / [days] Corresponding Helioc. Mod. Julian Date
BMJD_OBS= 54947.1799324 / [days] Solar System Barycenter Mod. Julian Date
ET_OBS = 293991616.273 / [sec] DCE start time (TDB seconds past J2000)
SCLK_OBS= 925186991.09 / [sec] SCLK time (since 1/1/1980) at DCE start
SPTZR_X = -149438962.941318 / [km] Heliocentric J2000 x position
SPTZR_Y = 14190531.939344 / [km] Heliocentric J2000 y position
SPTZR_Z = 4150999.902977 / [km] Heliocentric J2000 z position
SPTZR_VX= -3.040365 / [km/s] Heliocentric J2000 x velocity
SPTZR_VY= -27.085559 / [km/s] Heliocentric J2000 y velocity
SPTZR_VZ= -12.252653 / [km/s] Heliocentric J2000 z velocity
SPTZR_LT= 500.908501 / [sec] One-way light time to Sun's center
AORTIME = 2. / [sec] Frameset selected in IRAC AOT
SAMPTIME= 0.2 / [sec] Sample integration time
FRAMTIME= 2. / [sec] Time spent integrating (whole array)
COMMENT Photons in Well = Flux[photons/sec/pixel] * FRAMTIME
EXPTIME = 1.2 / [sec] Effective integration time per pixel
COMMENT DN per pixel = Flux[photons/sec/pixel] / GAIN * EXPTIME
FRAMEDLY= 15.2 / [sec] Frame Delay Time
FRDLYDET= 'T' / Frame Delay Time Determinable (T or F)
INTRFDLY= 15.2 / [sec] Inter Frame Delay Time
IMDLYDET= 'T' / Immediate Delay Time Determinable (T or F)
AINTBEG = 422410.45 / [Secs since IRAC turn-on] Time of integ. start
ATIMEEND= 422412.42 / [Secs since IRAC turn-on] Time of integ. end
AFOWLNUM= 4 / Fowler number
AWAITPER= 2 / [0.2 sec] Wait period
ANUMREPS= 1 / Number of repeat integrations
AREADMOD= 0 / Full (0) or subarray (1)
AORHDR = F / Requested AOT is HDR mode
HDRMODE = F / DCE taken in High Dynamic Range mode
ABARREL = 2 / Barrel shift
APEDSIG = 0 / 0=Normal, 1=Pedestal, 2=Signal

```

/ TARGET AND POINTING INFORMATION

```

OBJECT = 'NPM1p67.0536' / Target Name
OBJTYPE = 'TargetFixedCluster' / Object Type
CRPIX1 = 128. / Reference pixel along axis 1
CRPIX2 = 128. / Reference pixel along axis 2
CRVAL1 = 269.687752461083 / [deg] RA at CRPIX1,CRPIX2 (using Ptg. Recon.)
CRVAL2 = 67.8851329621642 / [deg] DEC at CRPIX1,CRPIX2 (using Ptg. Recon.)
CRDER1 = 0.000301832149720566 / [deg] Uncertainty in CRVAL1
CRDER2 = 0.000301933570794702 / [deg] Uncertainty in CRVAL2
RA_HMS = '17h58m45.1s' / [hh:mm:ss.s] CRVAL1 as sexagesimal
DEC_DMS = '+67d53m07s' / [dd:mm:ss] CRVAL2 as sexagesimal
RADESYS = 'ICRS' / International Celestial Reference System
EQUINOX = 2000. / Equinox for ICRS celestial coord. system
CD1_1 = -3.24254394094693E-05 / Corrected CD matrix element with Ptg. Recon.
CD1_2 = -0.000338061133513596 / Corrected CD matrix element with Ptg. Recon.
CD2_1 = -0.000339218895493648 / Corrected CD matrix element with Ptg. Recon.
CD2_2 = 3.3500826367185E-05 / Corrected CD matrix element with Ptg. Recon.
CTYPE1 = 'RA---TAN-SIP' / RA---TAN with distortion in pixel space
CTYPE2 = 'DEC--TAN-SIP' / DEC--TAN with distortion in pixel space
PXSCAL1 = -1.22673962032422 / [arcsec/pix] Scale for axis 1 at CRPIX1,CRPIX2
PXSCAL2 = 1.22298117494211 / [arcsec/pix] Scale for axis 2 at CRPIX1,CRPIX2
PA = -84.3406427565143 / [deg] Position angle of axis 2 (E of N)
UNCRTPA = 0.00171832722634256 / [deg] Uncertainty in position angle
CSDRADEC= 5.64852488118211E-06 / [deg] Costandard deviation in RA and Dec
SIGRA = 0.0133263705660201 / [arcsec] RMS dispersion of RA over DCE
SIGDEC = 0.0912513013597778 / [arcsec] RMS dispersion of DEC over DCE
SIGPA = 0.0779422863653394 / [arcsec] RMS dispersion of PA over DCE

```

```

RA_RQST =      269.687830215568 / [deg] Requested RA at CRPIX1, CRPIX2
DEC_RQST=      67.8851650499982 / [deg] Requested Dec at CRPIX1, CRPIX2
PM_RA   =           0. / [arcsec/yr] Proper Motion in RA (J2000)
PM_DEC  =           0. / [arcsec/yr] Proper Motion in Dec (J2000)
RMS_JIT = 0.00403435731250964 / [arcsec] RMS jitter during DCE
RMS_JITY= 0.00355000676759918 / [arcsec] RMS jitter during DCE along Y
RMS_JITZ= 0.00191663530046798 / [arcsec] RMS jitter during DCE along Z
SIG_JTYZ= 0.00248656703609615 / [arcsec] Costadard deviation of jitter in YZ
PTGDIFF = 0.156360619275311 / [arcsec] Offset btwn actual and rqsted pntng
PTGDIFFX= 0.125344235665602 / [pixels] rqsted - actual pntng along axis 1
PTGDIFFY= -0.0939088764668035 / [pixels] rqsted - actual pntng along axis 2
RA_REF  =      269.727166666667 / [deg] Commanded RA (J2000) of ref. position
DEC_REF =      67.7936944444462 / [deg] Commanded Dec (J2000) of ref. position
USEDBPHF=           T / T if Boresight Pointing History File was used
BPHFNAME= 'BPHF.0925171200.03.pntg' / Boresight Pointing History Filename
FOVVERSN= 'BodyFrames_FTV_14a.xls' / FOV/BodyFrames file version used
RECONFOV= 'IRAC_Center_of_5.8umArray' / Reconstructed Field of View

```

/ DISTORTION KEYWORDS

```

A_ORDER =           3 / polynomial order, axis 1, detector to sky
A_0_2   =      -4.3447E-06 / distortion coefficient
A_0_3   =      -1.016E-09 / distortion coefficient
A_1_1   =       3.5897E-05 / distortion coefficient
A_1_2   =      -1.5883E-07 / distortion coefficient
A_2_0   =      -1.6032E-05 / distortion coefficient
A_2_1   =      -1.0378E-09 / distortion coefficient
A_3_0   =      -1.5738E-07 / distortion coefficient
A_DMAX  =       1.641 / [pixel] maximum correction
B_ORDER =           3 / polynomial order, axis 2, detector to sky
B_0_2   =       2.5424E-05 / distortion coefficient
B_0_3   =      -1.6169E-07 / distortion coefficient
B_1_1   =      -9.977E-06 / distortion coefficient
B_1_2   =       7.6924E-09 / distortion coefficient
B_2_0   =      -7.8167E-06 / distortion coefficient
B_2_1   =      -1.6873E-07 / distortion coefficient
B_3_0   =      -1.1593E-08 / distortion coefficient
B_DMAX  =       1.184 / [pixel] maximum correction
AP_ORDER=           3 / polynomial order, axis 1, sky to detector
AP_0_1  =      -2.3883E-07 / distortion coefficient
AP_0_2  =       4.406E-06 / distortion coefficient
AP_0_3  =       6.4348E-10 / distortion coefficient
AP_1_0  =      -1.5761E-05 / distortion coefficient
AP_1_1  =      -3.6428E-05 / distortion coefficient
AP_1_2  =       1.64E-07 / distortion coefficient
AP_2_0  =       1.6243E-05 / distortion coefficient
AP_2_1  =      -9.3393E-10 / distortion coefficient
AP_3_0  =       1.5989E-07 / distortion coefficient
BP_ORDER=           3 / polynomial order, axis 2, sky to detector
BP_0_1  =      -1.6807E-05 / distortion coefficient
BP_0_2  =      -2.5772E-05 / distortion coefficient
BP_0_3  =       1.6546E-07 / distortion coefficient
BP_1_0  =      -8.8532E-07 / distortion coefficient
BP_1_1  =       1.0173E-05 / distortion coefficient
BP_1_2  =      -8.7895E-09 / distortion coefficient
BP_2_0  =       7.8383E-06 / distortion coefficient
BP_2_1  =       1.7089E-07 / distortion coefficient
BP_3_0  =       1.2114E-08 / distortion coefficient

```

/ PHOTOMETRY

```

BUNIT   = 'MJy/sr' / Units of image data
FLUXCONV= 0.5858 / Flux Conv. factor (MJy/sr per DN/sec)
GAIN    = 3.8 / e/DN conversion
RONOISE = 9.1 / [Electrons] Readout Noise from Array

```

```

ZODY_EST=          2.070159 / [MJy/sr] Zodiacal Background Estimate
ISM_EST =          0.1687349 / [MJy/sr] Interstellar Medium Estimate
CIB_EST =           0. / [MJy/sr] Cosmic Infrared Background Estimate
SKYDRKZB=          2.031035 / [MJy/sr] Zodiacal Background Est of Subtracted
SKYDKMED=         -1.052963 / [MJy/sr] Median of Subtracted Skydark
SKDKRKEY=          33267456 / Skydark AOR Reqkey
SKDKTIME=          2. / [sec] Skydark AOR Duration Time
SKDKFDLY=          11.97 / [sec] Average Frame Delay Time of Skydark
SKDKIDL=           11.97 / [sec] Average Immediate Delay Time of Skydark

```

/ IRAC MAPPING KEYWORDS

```

READMODE= 'FULL' / Readout mode (full or sub)

```

/ INSTRUMENT TELEMETRY DATA

```

ASHTCON =          2 / Shutter condition (1:closed, 2: open)
AWEASIDE=          0 / WEA side in use (0:B, 1:A)
ACTXSTAT=          0 / Cmded transcal status
ATXSTAT =          0 / transcal status
ACFLSTAT=          0 / Cmded floodcal status
AFLSTAT =          0 / floodcal status
AVRSTUCC=         -3.4 / [Volts] Cmded VRSTUC Bias
AVRSTBEG=        -3.3878126 / [Volts] VRSTUC Bias at start integration
AVDETC =          -4. / [Volts] Cmded VDET Bias
AVDETBEG=        -3.9877046 / [Volts] VDET Bias at start of integration
AVGG1C =          -3.45 / [Volts] Cmded VGG1 Bias
AVGG1BEG=        -3.4382206 / [Volts] VGG1 Bias at start of integration
AVDDUCC =          -3. / [Volts] Cmded VDDUC Bias
AVDDUBEG=        -2.9821749 / [Volts] VDDUC Bias at start integration
AVGGCLC =          0. / [Volts] Cmded VGGCL clock rail voltage
AVGGCBEG=          0. / [Volts] VGGCL clock rail voltage
AHTRIBEG=         149.63724 / [uAmps] Heater current at start of integ
AHTRVBEG=         1.9369638 / [Volts] Heater Voltage at start integ.
AFPAT2B =          6.0631644 / [Deg_K] FPA Temp sensor #2 at start integ.
AFPAT2BT=         422402.8 / [Sec] FPA Temp sensor #2 time tag
AFPAT2E =          6.0631644 / [Deg_K] FPA temp sensor #2, end integ.
AFPAT2ET=         422402.8 / [Sec] FPA temp sensor #2 time tag
ACTENDT =         20.285331 / [Deg_C] C&T board thermistor
AFPECTE =         17.340471 / [Deg_C] FPE control board thermistor
AFPEATE =         20.411017 / [Deg_C] FPE analog board thermistor
ASHTEMPE=         21.443602 / [Deg_C] Shutter board thermistor
ATCTEMPE=         22.601873 / [Deg_C] Temp. controller board thermistor
ACETEMPE=         20.193888 / [Deg_C] Calib. electronics board thermistor
APDTEMPE=         20.407254 / [Deg_C] PDU board thermistor
ACATMP1E=         1.2900473 / [Deg_K] CA Temp, Foot 2
ACATMP2E=         1.2724768 / [Deg_K] CA Temp, Foot 1
ACATMP3E=         1.3060768 / [Deg_K] CA Temp, Shutter
ACATMP4E=         1.3026365 / [Deg_K] CA Temp, Top OMH
ACATMP5E=         1.3005989 / [Deg_K] CA Temp, Bottom OMH
ACATMP6E=         1.2987331 / [Deg_K] CA Temp, Top TxCal Sphere
ACATMP7E=         1.2974439 / [Deg_K] CA Temp, Bottom TxCal Sphere
ACATMP8E=         1.2902828 / [Deg_K] CA Temp, Foot 3

```

/ DATA FLOW KEYWORDS

```

ORIGIN0 = 'JPL_FOS' / Site where RAW FITS file was written
CREATOR0= 'J5.3' / SW system that created RAW FITS
DATE = '2010-11-04T16:19:37' / [YYYY-MM-DDThh:mm:ss UTC] file creation date
AORKEY = 33258752 / AOR or EIR key. Astrnmy Obs Req/Instr Eng Req
DS_IDENT= 'ads/sa.spitzer#0033258752' / Data Set Identification for ADS/journals
EXPID = 8 / Exposure ID (0-9999)
DCENUM = 0 / DCE number (0-9999)
TLMGRPS = 1 / expected number of groups
FILE_VER= 1 / Version of the raw file made by SIS

```

```

RAWFILE = 'IRAC.3.0033258752.0008.0000.01.mipl.fits' / Raw data file name
CPT_VER = '3.1.11' / Channel Param Table FOS version
CTD_VER = '3.0.94S' / Cmded telemetry data version
EXPFLAG= T / (T/F) expedited DCE
MISS_LCT= 0 / Total Missed Line Cnt in this FITS
MANCPKT = F / T if this FITS is Missing Ancillary Data
MISSDATA= F / T if this FITS is Missing Image Data
BADTRIG = F / Bad data (zero pixel) was located in raw frame
CHECKSUM= 0 / MIPL computed checksum
PAONUM = 3443 / PAO Number
CAMPAIGN= 'IRAC013900' / Campaign
DCEID = 119198497 / Data-Collection-Event ID
DCEINSID= 24670149 / DCE Instance ID
DPID = 331591688 / Data Product Instance ID
PIPENUM = 107 / Pipeline Script Number
SOS_VER = 1 / Data-Product Version
PLVID = 6 / Pipeline Version ID
CALID = 8 / CalTrans Version ID
SDRKEPID= 7916044 / Sky Dark ensemble product ID
PMSKFBID= 1979 / Pixel mask ID
LDRKFBID= 852 / Fall-back lab dark ID
LINCFBID= 1021 / Fall-back Linearity correction ID
FLATFBID= 1593 / Fall-back flat ID
FLXCFBID= 1902 / Flux conversion ID
LBDRKFLE= 'FUL_2s_2sf4dlr1_ch3_v1.2.0_dark.txt' / Labdark File Used
LBDRKTD = 'T' / Labdark Time Dependent (T or F)
DDCORR1 = -0.04849106 / Darkdrift Correction for Readout Channel 1
DDCORR2 = -0.1956504 / Darkdrift Correction for Readout Channel 2
DDCORR3 = 0.1452298 / Darkdrift Correction for Readout Channel 3
DDCORR4 = 0.09891168 / Darkdrift Correction for Readout Channel 4
DDBKGND = 14.38143 / Darkdrift 'Background' Term

```

/ PROCESSING HISTORY

```

HISTORY job.c ver: 1.50
HISTORY TRANHEAD v. 13.1, ran Thu Nov 4 09:19:08 2010
HISTORY CALTRANS v. 4.0, ran Thu Nov 4 09:19:18 2010
HISTORY cvti2r4 v. 1.31 A61025, generated 11/04/10 at 9:19:19
HISTORY hdrupd8 v. 1.6 A70821, updated 11/04/10 at 9:19:21
HISTORY hdrupd8 v. 1.6 A70821, updated 11/04/10 at 9:19:22
HISTORY hdrupd8 v. 1.6 A70821, updated 11/04/10 at 9:19:23
HISTORY hdrupd8 v. 1.6 A70821, updated 11/04/10 at 9:19:24
HISTORY hdrupd8 v. 1.6 A70821, updated 11/04/10 at 9:19:25
HISTORY hdrupd8 v. 1.6 A70821, updated 11/04/10 at 9:19:25
HISTORY hdrupd8 v. 1.6 A70821, updated 11/04/10 at 9:19:26
HISTORY FFC v. 1.0, ran Thu Nov 4 09:19:27 2010
HISTORY FOWLINEARIZE v. 4.900000, ran Thu Nov 4 09:19:28 2010
HISTORY hdrupd8 v. 1.6 A70821, updated 11/04/10 at 9:19:28
HISTORY BGMODEL v. 1.0, ran Thu Nov 4 09:19:29 2010
HISTORY SLREMOVE v. 1.0, ran Thu Nov 4 09:19:29 2010
HISTORY hdrupd8 v. 1.6 A70821, updated 11/04/10 at 9:19:30
HISTORY hdrupd8 v. 1.6 A70821, updated 11/04/10 at 9:19:30
HISTORY hdrupd8 v. 1.6 A70821, updated 11/04/10 at 9:19:31
HISTORY hdrupd8 v. 1.6 A70821, updated 11/04/10 at 9:19:32
HISTORY hdrupd8 v. 1.6 A70821, updated 11/04/10 at 9:19:33
HISTORY hdrupd8 v. 1.6 A70821, updated 11/04/10 at 9:19:34
HISTORY DARKSUBNG v. 1.000, ran Thu Nov 4 09:19:34 2010
HISTORY DARKDRIFT v. 4.1, ran Thu Nov 4 09:19:35 2010
HISTORY FLATAP v. 1.500 Thu Nov 4 09:19:35 2010
HISTORY DNTOFUX v. 4.2, ran Thu Nov 4 09:19:37 2010
HISTORY CALTRANS v. 4.0, ran Thu Nov 4 09:22:01 2010
HISTORY PTNTRAN v. 1.4, ran Thu Nov 4 09:22:04 2010
HISTORY FPGen v. 1.26, ran Thu Nov 4 09:22:05 2010
HISTORY PTGADJUST v. 1.0, ran Thu Nov 4 09:22:58 2010
HISTORY Data rescaled using correct flux conversion : 25 Jun 2012 14:17:35 PDT

```

```

HISTORY FLUXCONV rescaled from 0.6054 to 0.5858 : 25 Jun 2012 14:17:35 PDT
HISTORY FLUXCONV updated in header : 25 Jun 2012 14:17:35 PDT
HISTORY CREATOR keyword updated : 25 Jun 2012 14:17:35 PDT
END

```

E.4 Cryogenic Mission Channel 4

```

SIMPLE = T / Fits standard
BITPIX = -32 / FOUR-BYTE SINGLE PRECISION FLOATING POINT
NAXIS = 2 / STANDARD FITS FORMAT
NAXIS1 = 256 / STANDARD FITS FORMAT
NAXIS2 = 256 / STANDARD FITS FORMAT
ORIGIN = 'Spitzer Science Center' / Organization generating this FITS file
CREATOR = 'S18.25.0' / SW version used to create this FITS file
TELESCOP= 'Spitzer' / SPITZER Space Telescope
INSTRUME= 'IRAC' / SPITZER Space Telescope instrument ID
CHNLNUM = 4 / 1 digit instrument channel number
EXPTYPE = 'sci' / Exposure Type
REQTYPE = 'AOR' / Request type (AOR, IER, or SER)
AOT_TYPE= 'IracMap' / Observation template type
AORLABEL= 'IRAC_calstar_NPM1p67.0536_spt4l2 - copy' / AOR Label
FOVID = 74 / Field of View ID
FOVNAME = 'IRAC_Center_of_4.5&8.0umArray' / Field of View Name

/ PROPOSAL INFORMATION

OBSRVR = 'Sean Carey' / Observer Name (Last, First)
OBSRVRID= 137 / Observer ID of Principal Investigator
PROCYCL = 3 / Proposal Cycle
PROGID = 1182 / Program ID
PROTITLE= 'SIRTF IRAC Calibration Program' / Program Title
PROGCAT = 32 / Program Category

/ TIME AND EXPOSURE INFORMATION

DATE_OBS= '2009-04-26T04:19:10.088' / Date & time (UTC) at DCE start
UTCS_OBS= 293991550.088 / [sec] DCE start time from noon, Jan 1, 2000
UTCMJD_OBS = 54947.1799779 / [days] MJD in UTC at DCE start (,JD-2400000.5)
HMJD_OBS= 54947.1799318 / [days] Corresponding Helioc. Mod. Julian Date
BMJD_OBS= 54947.1799322 / [days] Solar System Barycenter Mod. Julian Date
ET_OBS = 293991616.273 / [sec] DCE start time (TDB seconds past J2000)
SCLK_OBS= 925186991.09 / [sec] SCLK time (since 1/1/1980) at DCE start
SPTZR_X = -149438962.941318 / [km] Heliocentric J2000 x position
SPTZR_Y = 14190531.939344 / [km] Heliocentric J2000 y position
SPTZR_Z = 4150999.902977 / [km] Heliocentric J2000 z position
SPTZR_VX= -3.040365 / [km/s] Heliocentric J2000 x velocity
SPTZR_VY= -27.085559 / [km/s] Heliocentric J2000 y velocity
SPTZR_VZ= -12.252653 / [km/s] Heliocentric J2000 z velocity
SPTZR_LT= 500.908501 / [sec] One-way light time to Sun's center
AORTIME = 2. / [sec] Frameset selected in IRAC AOT
SAMPTIME= 0.2 / [sec] Sample integration time
FRAMTIME= 2. / [sec] Time spent integrating (whole array)
COMMENT Photons in Well = Flux[photons/sec/pixel] * FRAMTIME
EXPTIME = 1.2 / [sec] Effective integration time per pixel
COMMENT DN per pixel = Flux[photons/sec/pixel] / GAIN * EXPTIME
FRAMEDLY= 15.2 / [sec] Frame Delay Time
FRDLYDET= 'T' / Frame Delay Time Determinable (T or F)
INTRFDLY= 15.2 / [sec] Inter Frame Delay Time
IMDLYDET= 'T' / Immediate Delay Time Determinable (T or F)

```

```

AINTBEG =          422410.45 / [Secs since IRAC turn-on] Time of integ. start
ATIMEEND=          422412.42 / [Secs since IRAC turn-on] Time of integ. end
AFOWLNUM=           4 / Fowler number
AWAITPER=           2 / [0.2 sec] Wait period
ANUMREPS=           1 / Number of repeat integrations
AREADMOD=           0 / Full (0) or subarray (1)
AORHDR =            F / Requested AOT is HDR mode
HDRMODE =           F / DCE taken in High Dynamic Range mode
ABARREL =           2 / Barrel shift
APEDSIG =           0 / 0=Normal, 1=Pedestal, 2=Signal

```

/ TARGET AND POINTING INFORMATION

```

OBJECT = 'NPM1p67.0536' / Target Name
OBJTYPE = 'TargetFixedCluster' / Object Type
CRPIX1 =           128. / Reference pixel along axis 1
CRPIX2 =           128. / Reference pixel along axis 2
CRVAL1 =          269.664834461771 / [deg] RA at CRPIX1,CRPIX2 (using Ptg. Recon.)
CRVAL2 =           67.7742149654938 / [deg] DEC at CRPIX1,CRPIX2 (using Ptg. Recon.)
CRDR1 = 0.000301832124156524 / [deg] Uncertainty in CRVAL1
CRDR2 = 0.000301931896907846 / [deg] Uncertainty in CRVAL2
RA_HMS = '17h58m39.6s' / [hh:mm:ss.s] CRVAL1 as sexagesimal
DEC_DMS = '+67d46m27s' / [dd:mm:ss] CRVAL2 as sexagesimal
RADESYS = 'ICRS' / International Celestial Reference System
EQUINOX =           2000. / Equinox for ICRS celestial coord. system
CD1_1 = -3.11952075052725E-05 / Corrected CD matrix element with Ptg. Recon.
CD1_2 = -0.000337287558240409 / Corrected CD matrix element with Ptg. Recon.
CD2_1 = -0.000338707421730689 / Corrected CD matrix element with Ptg. Recon.
CD2_2 = 3.00663549690224E-05 / Corrected CD matrix element with Ptg. Recon.
CTYPE1 = 'RA---TAN-SIP' / RA---TAN with distortion in pixel space
CTYPE2 = 'DEC--TAN-SIP' / DEC--TAN with distortion in pixel space
PXSCAL1 =          -1.2244968325831 / [arcsec/pix] Scale for axis 1 at CRPIX1,CRPIX2
PXSCAL2 =           1.21904995758086 / [arcsec/pix] Scale for axis 2 at CRPIX1,CRPIX2
PA =             -84.9060288181049 / [deg] Position angle of axis 2 (E of N)
UNCRTPA = 0.00171832722634256 / [deg] Uncertainty in position angle
CSDRADEC= 6.047410711134816E-06 / [deg] Costandard deviation in RA and Dec
SIGRA = 0.0133898318703144 / [arcsec] RMS dispersion of RA over DCE
SIGDEC = 0.0912513013542275 / [arcsec] RMS dispersion of DEC over DCE
SIGPA = 0.0779422863269417 / [arcsec] RMS dispersion of PA over DCE
RA_RQST =          269.664944519428 / [deg] Requested RA at CRPIX1, CRPIX2
DEC_RQST=           67.7742465481562 / [deg] Requested Dec at CRPIX1, CRPIX2
PM_RA =            0. / [arcsec/yr] Proper Motion in RA (J2000)
PM_DEC =            0. / [arcsec/yr] Proper Motion in Dec (J200)
RMS_JIT = 0.00403435731250964 / [arcsec] RMS jitter during DCE
RMS_JITY= 0.00355000676759918 / [arcsec] RMS jitter during DCE along Y
RMS_JITZ= 0.00191663530046798 / [arcsec] RMS jitter during DCE along Z
SIG_JTYZ= 0.00248656703609615 / [arcsec] Costadard deviation of jitter in YZ
PTGDIFF = 0.188117471327791 / [arcsec] Offset btwn actual and rqsted pntng
PTGDIFFX= 0.126554845531278 / [pixels] rqsted - actual pntng along axis 1
PTGDIFFY= -0.138809718941152 / [pixels] rqsted - actual pntng along axis 2
RA_REF =           269.7271666666667 / [deg] Commanded RA (J2000) of ref. position
DEC_REF =           67.79369444444462 / [deg] Commanded Dec (J2000) of ref. position
USEDBPHF=          T / T if Boresight Pointing History File was used
BPHFNAME= 'BPHF.0925171200.03.pntg' / Boresight Pointing History Filename
FOVERSN= 'BodyFrames_FTU_14a.xls' / FOV/BodyFrames file version used
RECONFOV= 'IRAC_Center_of_8.0umArray' / Reconstructed Field of View

```

/ DISTORTION KEYWORDS

```

A_ORDER =           3 / polynomial order, axis 1, detector to sky
A_0_2 =           9.0886E-06 / distortion coefficient
A_0_3 =           4.8066E-09 / distortion coefficient
A_1_1 =           4.8146E-05 / distortion coefficient
A_1_2 =          -1.7096E-07 / distortion coefficient
A_2_0 =           2.82E-05 / distortion coefficient

```



```

A_2_1 = 3.3336E-08 / distortion coefficient
A_3_0 = -1.8684E-07 / distortion coefficient
A_DMAX = 2.146 / [pixel] maximum correction
B_ORDER = 3 / polynomial order, axis 2, detector to sky
B_0_2 = 4.1248E-05 / distortion coefficient
B_0_3 = -1.9016E-07 / distortion coefficient
B_1_1 = 1.4761E-05 / distortion coefficient
B_1_2 = 2.1973E-08 / distortion coefficient
B_2_0 = -6.4708E-06 / distortion coefficient
B_2_1 = -1.8188E-07 / distortion coefficient
B_3_0 = 1.0084E-10 / distortion coefficient
B_DMAX = 1.606 / [pixel] maximum correction
AP_ORDER= 3 / polynomial order, axis 1, sky to detector
AP_0_1 = 3.6698E-06 / distortion coefficient
AP_0_2 = -9.1825E-06 / distortion coefficient
AP_0_3 = -3.8909E-09 / distortion coefficient
AP_1_0 = -2.0239E-05 / distortion coefficient
AP_1_1 = -4.8946E-05 / distortion coefficient
AP_1_2 = 1.7951E-07 / distortion coefficient
AP_2_0 = -2.8622E-05 / distortion coefficient
AP_2_1 = -2.9553E-08 / distortion coefficient
AP_3_0 = 1.9119E-07 / distortion coefficient
BP_ORDER= 3 / polynomial order, axis 2, sky to detector
BP_0_1 = -2.1339E-05 / distortion coefficient
BP_0_2 = -4.189E-05 / distortion coefficient
BP_0_3 = 1.9696E-07 / distortion coefficient
BP_1_0 = 2.8502E-06 / distortion coefficient
BP_1_1 = -1.5089E-05 / distortion coefficient
BP_1_2 = -2.0219E-08 / distortion coefficient
BP_2_0 = 6.4625E-06 / distortion coefficient
BP_2_1 = 1.849E-07 / distortion coefficient
BP_3_0 = -7.6669E-10 / distortion coefficient

/ PHOTOMETRY

BUNIT = 'MJy/sr ' / Units of image data
FLUXCONV= 0.2026 / Flux Conv. factor (MJy/sr per DN/sec)
GAIN = 3.8 / e/DN conversion
RONOISE = 7.1 / [Electrons] Readout Noise from Array
ZODY_EST= 5.686473 / [MJy/sr] Zodiacal Background Estimate
ISM_EST = 0.1868807 / [MJy/sr] Interstellar Medium Estimate
CIB_EST = 0. / [MJy/sr] Cosmic Infrared Background Estimate
ISM_EST = 0.1868807 / [MJy/sr] Interstellar Medium Estimate
CIB_EST = 0. / [MJy/sr] Cosmic Infrared Background Estimate
SKYDRKZB= 5.601609 / [MJy/sr] Zodiacal Background Est of Subtracted
SKYDKMED= 8.815732 / [MJy/sr] Median of Subtracted Skydark
SKDKRKEY= 33267456 / Skydark AOR Reqkey
SKDKTIME= 2. / [sec] Skydark AOR Duration Time
SKDKFDLY= 11.97 / [sec] Average Frame Delay Time of Skydark
SKDKIDLY= 11.97 / [sec] Average Immediate Delay Time of Skydark

/ IRAC MAPPING KEYWORDS

READMODE= 'FULL ' / Readout mode (full or sub)

/ INSTRUMENT TELEMETRY DATA

ASHTCON = 2 / Shutter condition (1:closed, 2: open)
AWEASIDE= 0 / WEA side in use (0:B, 1:A)
ACTXSTAT= 0 / Cmded transcal status
ATXSTAT = 0 / transcal status
ACFLSTAT= 0 / Cmded floodcal status
AFLSTAT = 0 / floodcal status
AVRSTUCC= -3.2 / [Volts] Cmded VRSTUC Bias
AVRSTBEG= -3.2100936 / [Volts] VRSTUC Bias at start integration

```

```

AVDETC = -4.4 / [Volts] Cmded VDET Bias
AVDETBEG= -4.4160263 / [Volts] VDET Bias at start of integration
AVGG1C = -3.45 / [Volts] Cmded VGG1 Bias
AVGG1BEG= -3.4608823 / [Volts] VGG1 Bias at start of integration
AVDDUCC = -3. / [Volts] Cmded VDDUC Bias
AVDDUBEG= -3.0015937 / [Volts] VDDUC Bias at start integration
AVGGCLC = 0. / [Volts] Cmdded VGGCL clock rail voltage
AVGGCBEG= 0. / [Volts] VGGCL clock rail voltage
AHTRIBEG= 162.34725 / [uAmps] Heater current at start of integ
AHTRVBEG= 1.7389799 / [Volts] Heater Voltage at start integ.
AFPAT2B = 6.03335 / [Deg_K] FPA Temp sensor #2 at start integ.
AFPAT2BT= 422402.9 / [Sec] FPA Temp sensor #2 time tag
AFPAT2E = 6.03335 / [Deg_K] FPA temp sensor #2, end integ.
AFPAT2ET= 422402.9 / [Sec] FPA temp sensor #2 time tag
ACTENDT = 20.285331 / [Deg_C] C&T board thermistor
AFPECTE = 19.182799 / [Deg_C] FPE control board thermistor
AFPEATE = 21.726966 / [Deg_C] FPE analog board thermistor
ASHTEMPE= 21.443602 / [Deg_C] Shutter board thermistor
ATCTEMPE= 22.601873 / [Deg_C] Temp. controller board thermistor
ACETEMPE= 20.193888 / [Deg_C] Calib. electronics board thermistor
APDTEMPE= 20.407254 / [Deg_C] PDU board thermistor
ACATMP1E= 1.2900473 / [Deg_K] CA Temp, Foot 2
ACATMP2E= 1.2724768 / [Deg_K] CA Temp, Foot 1
ACATMP3E= 1.3060768 / [Deg_K] CA Temp, Shutter
ACATMP4E= 1.3026365 / [Deg_K] CA Temp, Top OMH
ACATMP5E= 1.3005989 / [Deg_K] CA Temp, Bottom OMH
ACATMP6E= 1.2987331 / [Deg_K] CA Temp, Top TxCal Sphere
ACATMP7E= 1.2974439 / [Deg_K] CA Temp, Bottom TxCal Sphere
ACATMP8E= 1.2902828 / [Deg_K] CA Temp, Foot 3

```

/ DATA FLOW KEYWORDS

```

ORIGIN0 = 'JPL_FOS ' / Site where RAW FITS file was written
CREATOR0= 'J5.3 ' / SW system that created RAW FITS
DATE = '2010-11-04T16:20:08' / [YYYY-MM-DDThh:mm:ss UTC] file creation date
AORKEY = 33258752 / AOR or EIR key. Astrnmy Obs Req/Instr Eng Req
DS_IDENT= 'ads/sa.spitzer#0033258752' / Data Set Identification for ADS/journals
EXPID = 8 / Exposure ID (0-9999)
DCENUM = 0 / DCE number (0-9999)
TLMGRPS = 1 / expected number of groups
FILE_VER= 1 / Version of the raw file made by SIS
RAWFILE = 'IRAC.4.0033258752.0008.0000.01.mipl.fits' / Raw data file name
CPT_VER = '3.1.11 ' / Channel Param Table FOS version
CTD_VER = '3.0.94S ' / Cmded telemetry data version
EXPFLAG= T / (T/F) expedited DCE
MISS_LCT= 0 / Total Missed Line Cnt in this FITS
MANCPKT = F / T if this FITS is Missing Ancillary Data
MISSDATA= F / T if this FITS is Missing Image Data
BADTRIG = F / Bad data (zero pixel) was located in raw frame
CHECKSUM= 0 / MIPL computed checksum
PAONUM = 3443 / PAO Number
CAMPAIGN= 'IRAC013900' / Campaign
DCEID = 119198496 / Data-Collection-Event ID
DCEINSID= 24670150 / DCE Instance ID
DPID = 331591758 / Data Product Instance ID
PIPENUM = 107 / Pipeline Script Number
SOS_VER = 1 / Data-Product Version
PLVID = 7 / Pipeline Version ID
CALID = 9 / CalTrans Version ID
SDRKEPID= 7916003 / Sky Dark ensemble product ID
PMSKFBID= 1981 / Pixel mask ID
LDRKFBID= 854 / Fall-back lab dark ID
LINCFBID= 1023 / Fall-back Linearity correction ID
FLATFBID= 1595 / Fall-back flat ID
FLXCFBID= 1904 / Flux conversion ID

```

```

LBDRKFLE= 'FUL_2s_2sf4dlr1_ch4_v1.2.0_dark.txt' / Labdark File Used
LBDRKTD = 'T' / Labdark Time Dependent (T or F)
DDCORR1 = 0.02211534 / Darkdrift Correction for Readout Channel 1
DDCORR2 = -0.3486368 / Darkdrift Correction for Readout Channel 2
DDCORR3 = 0.02940748 / Darkdrift Correction for Readout Channel 3
DDCORR4 = 0.297114 / Darkdrift Correction for Readout Channel 4
DDBKGND = -0.08159822 / Darkdrift 'Background' Term

```

/ PROCESSING HISTORY

```

HISTORY job.c ver: 1.50
HISTORY TRANHEAD v. 13.1, ran Thu Nov 4 09:19:43 2010
HISTORY CALTRANS v. 4.0, ran Thu Nov 4 09:19:51 2010
HISTORY cvti2r4 v. 1.31 A61025, generated 11/04/10 at 9:19:52
HISTORY hdrupd8 v. 1.6 A70821, updated 11/04/10 at 9:19:54
HISTORY hdrupd8 v. 1.6 A70821, updated 11/04/10 at 9:19:54
HISTORY hdrupd8 v. 1.6 A70821, updated 11/04/10 at 9:19:55
HISTORY hdrupd8 v. 1.6 A70821, updated 11/04/10 at 9:19:56
HISTORY hdrupd8 v. 1.6 A70821, updated 11/04/10 at 9:19:57
HISTORY hdrupd8 v. 1.6 A70821, updated 11/04/10 at 9:19:57
HISTORY hdrupd8 v. 1.6 A70821, updated 11/04/10 at 9:19:58
HISTORY FFC v. 1.0, ran Thu Nov 4 09:19:59 2010
HISTORY FOWLINEARIZE v. 4.900000, ran Thu Nov 4 09:19:59 2010
HISTORY hdrupd8 v. 1.6 A70821, updated 11/04/10 at 9:20:00
HISTORY BGMODEL v. 1.0, ran Thu Nov 4 09:20:00 2010
HISTORY SLREMOVE v. 1.0, ran Thu Nov 4 09:20:01 2010
HISTORY hdrupd8 v. 1.6 A70821, updated 11/04/10 at 9:20:01
HISTORY hdrupd8 v. 1.6 A70821, updated 11/04/10 at 9:20:02
HISTORY hdrupd8 v. 1.6 A70821, updated 11/04/10 at 9:20:03
HISTORY hdrupd8 v. 1.6 A70821, updated 11/04/10 at 9:20:03
HISTORY hdrupd8 v. 1.6 A70821, updated 11/04/10 at 9:20:04
HISTORY hdrupd8 v. 1.6 A70821, updated 11/04/10 at 9:20:04
HISTORY DARKSUBNG v. 1.000, ran Thu Nov 4 09:20:05 2010
HISTORY DARKDRIFT v. 4.1, ran Thu Nov 4 09:20:05 2010
HISTORY FLATAP v. 1.500 Thu Nov 4 09:20:06 2010
HISTORY DNTOFUX v. 4.2, ran Thu Nov 4 09:20:08 2010
HISTORY CALTRANS v. 4.0, ran Thu Nov 4 09:23:37 2010
HISTORY PTNTRAN v. 1.4, ran Thu Nov 4 09:23:40 2010
HISTORY FPGen v. 1.26, ran Thu Nov 4 09:23:42 2010
HISTORY PTGADJUST v. 1.0, ran Thu Nov 4 09:24:25 2010
HISTORY Data rescaled using correct flux conversion : 25 Jun 2012 14:17:40 PDT
HISTORY FLUXCONV rescaled from 0.2083 to 0.2026 : 25 Jun 2012 14:17:40 PDT
HISTORY FLUXCONV updated in header : 25 Jun 2012 14:17:40 PDT
HISTORY CREATOR keyword updated : 25 Jun 2012 14:17:40 PDT
END

```

E.5 Warm Mission Channel 1

```

SIMPLE = T / Fits standard
BITPIX = -32 / FOUR-BYTE SINGLE PRECISION FLOATING POINT
NAXIS = 2 / STANDARD FITS FORMAT
NAXIS1 = 256 / STANDARD FITS FORMAT
NAXIS2 = 256 / STANDARD FITS FORMAT
ORIGIN = 'Spitzer Science Center' / Organization generating this FITS file
CREATOR = 'S19.2.0' / SW version used to create this FITS file
TELESCOP= 'Spitzer' / SPITZER Space Telescope
INSTRUME= 'IRAC' / SPITZER Space Telescope instrument ID
CHNLNUM = 1 / 1 digit instrument channel number

```

```

EXPTYPE = 'sci      ' / Exposure Type
REQTYPE = 'AOR      ' / Request type (AOR, IER, or SER)
AOT_TYPE= 'IracMapPC' / Observation template type
AORLABEL= 'IRAC_calstar_NPM1p67.0536_p4' / AOR Label
FOVID    =          74 / Field of View ID
FOVNAME  = 'IRAC_Center_of_4.5&8.0umArray' / Field of View Name

/ PROPOSAL INFORMATION

OBSRVR   = 'IRAC Calibration' / Observer Name (Last, First)
OBSRVRID=          58326 / Observer ID of Principal Investigator
PROCYCL  =          16 / Proposal Cycle
PROGID   =          2017 / Program ID
PROTITLE = 'Spitzer IRAC Calibration Program' / Program Title
PROGCAT  =          32 / Program Category

/ TIME AND EXPOSURE INFORMATION

DATE_OBS= '2018-01-07T09:46:06.321' / Date & time (UTC) at DCE start
UTCS_OBS=          568590366.321 / [sec] DCE start time from noon, Jan 1, 2000
UTCMJD_OBS =          58125.4070176 / [days] MJD in UTC at DCE start (,JD-2400000.5)
HMJD_OBS=          58125.407087 / [days] Corresponding Helioc. Mod. Julian Date
BMJD_OBS=          58125.407087 / [days] Solar System Barycenter Mod. Julian Date
ET_OBS   =          568590435.505 / [sec] DCE start time (TDB seconds past J2000)
SCLK_OBS=          1199786144.66 / [sec] SCLK time (since 1/1/1980) at DCE start
SPTZR_X  =          153233610.767491 / [km] Heliocentric J2000 x position
SPTZR_Y  =          -3061072.710861 / [km] Heliocentric J2000 y position
SPTZR_Z  =          922272.505034 / [km] Heliocentric J2000 z position
SPTZR_VX=           0.308888 / [km/s] Heliocentric J2000 x velocity
SPTZR_VY=           26.68973 / [km/s] Heliocentric J2000 y velocity
SPTZR_VZ=           12.032747 / [km/s] Heliocentric J2000 z velocity
SPTZR_LT=           511.24354 / [sec] One-way light time to Sun's center
AORTIME  =           0.4 / [sec] Frameset selected in IRAC AOT
SAMPTIME =           0.2 / [sec] Sample integration time
FRAMTIME =           0.4 / [sec] Time spent integrating (whole array)
COMMENT  Photons in Well = Flux[photons/sec/pixel] * FRAMTIME
EXPTIME  =           0.2 / [sec] Effective integration time per pixel
COMMENT  DN per pixel = Flux[photons/sec/pixel] / GAIN * EXPTIME
FRAMEDLY=           15.6 / [sec] Frame Delay Time
FRDLYDET= 'T      ' / Frame Delay Time Determinable (T or F)
INTRFDLY=           15.6 / [sec] Inter Frame Delay Time
IMDLYDET= 'T      ' / Immediate Delay Time Determinable (T or F)
AINTBEG  =           22241724.7 / [Secs since IRAC turn-on] Time of integ. start
ATIMEEND =           22241725.07 / [Secs since IRAC turn-on] Time of integ. end
AFOWLNUM =           1 / Fowler number
AWAITPER =           0 / [0.2 sec] Wait period
ANUMREPS =           1 / Number of repeat integrations
AREADMOD =           0 / Full (0) or subarray (1)
AORHDR   =           F / Requested AOT is HDR mode
HDRMODE  =           F / DCE taken in High Dynamic Range mode
ABARREL  =           0 / Barrel shift
APEDSIG  =           0 / 0=Normal, 1=Pedestal, 2=Signal

/ TARGET AND POINTING INFORMATION

OBJECT   = 'NPM1p67.0536_cal' / Target Name
OBJTYPE  = 'TargetFixedCluster' / Object Type
CRPIX1   =           128. / Reference pixel along axis 1
CRPIX2   =           128. / Reference pixel along axis 2
CRVAL1   =           269.78620195812 / [deg] RA at CRPIX1,CRPIX2 (using Ptg. Recon.)
CRVAL2   =           67.7016229676727 / [deg] DEC at CRPIX1,CRPIX2 (using Ptg. Recon.)
CRDER1   = 6.41172824333331E-05 / [deg] Uncertainty in CRVAL1
CRDER2   = 7.28849973554652E-05 / [deg] Uncertainty in CRVAL2
RA_HMS   = '17h59m08.7s' / [hh:mm:ss.s] CRVAL1 as sexagesimal

```

```

DEC_DMS = '+67d42m06s' / [dd:mm:ss] CRVAL2 as sexagesimal
RADESYS = 'ICRS' / International Celestial Reference System
EQUINOX = 2000. / Equinox for ICRS celestial coord. system
CD1_1 = 6.77319036231518E-06 / Corrected CD matrix element with Ptg. Recon.
CD1_2 = 0.000339658951438648 / Corrected CD matrix element with Ptg. Recon.
CD2_1 = 0.000339825923706216 / Corrected CD matrix element with Ptg. Recon.
CD2_2 = -7.14005945938052E-06 / Corrected CD matrix element with Ptg. Recon.
CTYPE1 = 'RA---TAN-SIP' / RA---TAN with distortion in pixel space
CTYPE2 = 'DEC--TAN-SIP' / DEC--TAN with distortion in pixel space
PXSCAL1 = -1.22361484682187 / [arcsec/pix] Scale for axis 1 at CRPIX1,CRPIX2
PXSCAL2 = 1.22304236283526 / [arcsec/pix] Scale for axis 2 at CRPIX1,CRPIX2
PA = 91.2042548879129 / [deg] Position angle of axis 2 (E of N)
UNCRTPA = 0.000864692681616987 / [deg] Uncertainty in position angle
CSDRADEC= 4.90267693475138E-06 / [deg] Costandard deviation in RA and Dec
SIGRA = 0.00532325482935507 / [arcsec] RMS dispersion of RA over DCE
SIGDEC = 0.0738219479553574 / [arcsec] RMS dispersion of DEC over DCE
SIGPA = 0.310443699243675 / [arcsec] RMS dispersion of PA over DCE
RA_RQST = 269.786490249328 / [deg] Requested RA at CRPIX1, CRPIX2
DEC_RQST= 67.7015457522802 / [deg] Requested Dec at CRPIX1, CRPIX2
PM_RA = 0. / [arcsec/yr] Proper Motion in RA (J2000)
PM_DEC = 0. / [arcsec/yr] Proper Motion in Dec (J200)
RMS_JIT = 0.00468277796825773 / [arcsec] RMS jitter during DCE
RMS_JITY= 0.00431458650394218 / [arcsec] RMS jitter during DCE along Y
RMS_JITZ= 0.00182009692049627 / [arcsec] RMS jitter during DCE along Z
SIG_JTYZ= -0.00256228659599195 / [arcsec] Costadard deviation of jitter in YZ
PTGDIFF = 0.482014197276189 / [arcsec] Offset btwn actual and rqsted pntng
PTGDIFFX= 0.269636762216625 / [pixels] rqsted - actual pntng along axis 1
PTGDIFYF= 0.399253391973825 / [pixels] rqsted - actual pntng along axis 2
RA_REF = 269.7271666666667 / [deg] Commanded RA (J2000) of ref. position
DEC_REF = 67.7936944444453 / [deg] Commanded Dec (J2000) of ref. position
USEDBPHF= T / T if Boresight Pointing History File was used
BPHFNAME= 'SBPHF.1199750400.031.pntg' / Boresight Pointing History Filename
FOVERSN= 'BodyFrames_FTU_14a.xls' / FOV/BodyFrames file version used
RECONFOV= 'IRAC_Center_of_3.6umArray' / Reconstructed Field of View
RARFND = 269.786224365234 / [deg] Refined RA
DECRFND = 67.701522827148 / [deg] Refined DEC
CT2RFND = 91.204467773438 / [deg] Refined CROT2
ERARFND = 0.000000000000 / [deg] Error in RARFND value
EDECRFND= 0.000000000000 / [deg] Error in DECRFND value
ECT2RFND= 0.000000000000 / [deg] Error in CT2RFND value
NASTROM = 0 / Astrometric sources for absolute refinement
ORIG_RA = 269.786224365234 / [deg] Original RA from raw BPHF
ORIG_DEC= 67.7015228271484 / [deg] Original Dec from raw BPHF
ORIGCD11= 6.77249E-06 / [deg/pix] Original CD1_1 element
ORIGCD12= 0.00033965896 / [deg/pix] Original CD1_2 element
ORIGCD21= 0.0003398259287 / [deg/pix] Original CD2_1 element
ORIGCD22= -7.1393597E-06 / [deg/pix] Original CD2_2 element

```

/ DISTORTION KEYWORDS

```

A_ORDER = 5 / polynomial order, axis 1, detector to sky
A_0_2 = 3.0882E-06 / distortion coefficient
A_0_3 = 6.54E-09 / distortion coefficient
A_0_4 = 3.4787E-11 / distortion coefficient
A_0_5 = -1.1354E-13 / distortion coefficient
A_1_1 = 2.0844E-05 / distortion coefficient
A_1_2 = -2.1434E-07 / distortion coefficient
A_1_3 = -3.1804E-11 / distortion coefficient
A_1_4 = 1.535E-12 / distortion coefficient
A_2_0 = -1.8056E-05 / distortion coefficient
A_2_1 = 1.3568E-08 / distortion coefficient
A_2_2 = -4.4371E-11 / distortion coefficient
A_2_3 = -3.5879E-13 / distortion coefficient
A_3_0 = -2.0787E-07 / distortion coefficient
A_3_1 = 8.3137E-11 / distortion coefficient

```

```

A_3_2 = 1.7807E-12 / distortion coefficient
A_4_0 = -3.594E-10 / distortion coefficient
A_4_1 = -1.1255E-12 / distortion coefficient
A_5_0 = 3.5288E-12 / distortion coefficient
A_DMAX = 1.32 / [pixel] maximum correction
B_ORDER = 5 / polynomial order, axis 2, detector to sky
B_0_2 = 2.4494E-05 / distortion coefficient
B_0_3 = -1.6723E-07 / distortion coefficient
B_0_4 = -7.9325E-11 / distortion coefficient
B_0_5 = -3.9338E-13 / distortion coefficient
B_1_1 = -2.306E-05 / distortion coefficient
B_1_2 = -6.8347E-10 / distortion coefficient
B_1_3 = -5.5814E-11 / distortion coefficient
B_1_4 = -9.3255E-14 / distortion coefficient
B_2_0 = -1.9548E-06 / distortion coefficient
B_2_1 = -1.8908E-07 / distortion coefficient
B_2_2 = -3.5398E-11 / distortion coefficient
B_2_3 = 2.2959E-12 / distortion coefficient
B_3_0 = 2.9749E-08 / distortion coefficient
B_3_1 = -3.9458E-11 / distortion coefficient
B_3_2 = -2.3376E-13 / distortion coefficient
B_4_0 = 2.2713E-10 / distortion coefficient
B_4_1 = -3.0168E-13 / distortion coefficient
B_5_0 = -2.7808E-12 / distortion coefficient
B_DMAX = 1.442 / [pixel] maximum correction
AP_ORDER = 5 / polynomial order, axis 1, sky to detector
AP_0_1 = 6.6096E-07 / distortion coefficient
AP_0_2 = -3.0748E-06 / distortion coefficient
AP_0_3 = -6.4289E-09 / distortion coefficient
AP_0_4 = -3.7802E-11 / distortion coefficient
AP_0_5 = 1.184E-13 / distortion coefficient
AP_1_0 = -4.0087E-06 / distortion coefficient
AP_1_1 = -2.0916E-05 / distortion coefficient
AP_1_2 = 2.1616E-07 / distortion coefficient
AP_1_3 = 1.5615E-11 / distortion coefficient
AP_1_4 = -1.5028E-12 / distortion coefficient
AP_2_0 = 1.8081E-05 / distortion coefficient
AP_2_1 = -1.5661E-08 / distortion coefficient
AP_2_2 = 6.203E-11 / distortion coefficient
AP_2_3 = 3.7178E-13 / distortion coefficient
AP_3_0 = 2.0979E-07 / distortion coefficient
AP_3_1 = -9.4784E-11 / distortion coefficient
AP_3_2 = -1.6838E-12 / distortion coefficient
AP_4_0 = 3.7551E-10 / distortion coefficient
AP_4_1 = 1.1137E-12 / distortion coefficient
AP_5_0 = -3.488E-12 / distortion coefficient
BP_ORDER = 5 / polynomial order, axis 2, sky to detector
BP_0_1 = -1.3737E-06 / distortion coefficient
BP_0_2 = -2.4517E-05 / distortion coefficient
BP_0_3 = 1.686E-07 / distortion coefficient
BP_0_4 = 6.1176E-11 / distortion coefficient
BP_0_5 = 4.6583E-13 / distortion coefficient
BP_1_0 = 2.1186E-06 / distortion coefficient
BP_1_1 = 2.31E-05 / distortion coefficient
BP_1_2 = -1.8514E-09 / distortion coefficient
BP_1_3 = 7.4183E-11 / distortion coefficient
BP_1_4 = 9.777E-14 / distortion coefficient
BP_2_0 = 1.9457E-06 / distortion coefficient
BP_2_1 = 1.9043E-07 / distortion coefficient
BP_2_2 = 1.7116E-11 / distortion coefficient
BP_2_3 = -2.1729E-12 / distortion coefficient
BP_3_0 = -3.0437E-08 / distortion coefficient
BP_3_1 = 5.5266E-11 / distortion coefficient
BP_3_2 = 2.8199E-13 / distortion coefficient
BP_4_0 = -2.2607E-10 / distortion coefficient

```

```

BP_4_1 =          4.21E-13 / distortion coefficient
BP_5_0 =          2.8215E-12 / distortion coefficient

  / PHOTOMETRY

BUNIT = 'MJy/sr ' / Units of image data
FLUXCONV=          0.1257 / Flux Conv. factor (MJy/sr per DN/sec)
GAIN =            3.7 / e/DN conversion
RONOISE =          22.4 / [Electrons] Readout Noise from Array
ZODY_EST=          0.03293199 / [MJy/sr] Zodiacal Background Estimate
ISM_EST =          0.005258262 / [MJy/sr] Interstellar Medium Estimate
CIB_EST =           0. / [MJy/sr] Cosmic Infrared Background Estimate
SKYDRKZB=          0.033397 / [MJy/sr] Zodiacal Background Est of Subtracted
SKYDKMED=          41.49778 / [MJy/sr] Median of Subtracted Skydark
SKDKRKEY=          65218816 / Skydark AOR Reqkey
SKDKTIME=           0.4 / [sec] Skydark AOR Duration Time
SKDKFDLY=          12.59 / [sec] Average Frame Delay Time of Skydark
SKDKIDLY=          12.59 / [sec] Average Immediate Delay Time of Skydark

  / GENERAL MAPPING KEYWORDS

CLUSTPOS= '5 ' / Current cluster position

  / IRAC MAPPING KEYWORDS

READMODE= 'FULL ' / Readout mode (full or sub)

  / PEAKUP STAR KEYWORDS

COMMENT Either offsets OR absolute positions will be listed for the peakup tar

  / INSTRUMENT TELEMETRY DATA

ASHTCON =          2 / Shutter condition (1:closed, 2: open)
AWEASIDE=          0 / WEA side in use (0:B, 1:A)
ACTXSTAT=          0 / Cmded transcal status
ATXSTAT =          0 / transcal status
ACFLSTAT=          0 / Cmded floodcal status
AFLSTAT =          0 / floodcal status
AVRSTUCC=          -3.6 / [Volts] Cmded VRSTUC Bias
AVRSTBEG=          -3.613939 / [Volts] VRSTUC Bias at start integration
AVDETC =           -3.1 / [Volts] Cmded VDET Bias
AVDETBEG=          -3.1110762 / [Volts] VDET Bias at start of integration
AVGG1C =           -3.684 / [Volts] Cmded VGG1 Bias
AVGG1BEG=          -3.6981353 / [Volts] VGG1 Bias at start of integration
AVDDUCC =           -3.6 / [Volts] Cmded VDDUC Bias
AVDDUBEG=          -3.6061158 / [Volts] VDDUC Bias at start integration
AVGGCLC =           1. / [Volts] Cmded VGGCL clock rail voltage
AVGGCBEG=          1. / [Volts] VGGCL clock rail voltage
AHTRIBEG=          86.098712 / [uAmps] Heater current at start of integ
AHTRVBEG=          0.95335756 / [Volts] Heater Voltage at start integ.
AFPAT2B =          28.706814 / [Deg_K] FPA Temp sensor #2 at start integ.
AFPAT2BT=          22241717. / [Sec] FPA Temp sensor #2 time tag
AFPAT2E =          28.706814 / [Deg_K] FPA temp sensor #2, end integ.
AFPAT2ET=          22241717. / [Sec] FPA temp sensor #2 time tag
ACTENDT =          22.083699 / [Deg_C] C&T board thermistor
AFPECTE =          20.147828 / [Deg_C] FPE control board thermistor
AFPEATE =          24.007943 / [Deg_C] FPE analog board thermistor
ASHTEMPE=          23.363894 / [Deg_C] Shutter board thermistor
ATCTEMPE=          24.583127 / [Deg_C] Temp. controller board thermistor
ACETEMPE=          22.083699 / [Deg_C] Calib. electronics board thermistor
APDTEMPE=          22.114418 / [Deg_C] PDU board thermistor
ACATMP1E=          27.500894 / [Deg_K] CA Temp, Foot 2
ACATMP2E=          27.502644 / [Deg_K] CA Temp, Foot 1

```

```

ACATMP3E=          27.531015 / [Deg_K] CA Temp, Shutter
ACATMP4E=          27.588415 / [Deg_K] CA Temp, Top OMH
ACATMP5E=          27.675731 / [Deg_K] CA Temp, Bottom OMH
ACATMP6E=          27.589667 / [Deg_K] CA Temp, Top TxCal Sphere
ACATMP7E=          27.634638 / [Deg_K] CA Temp, Bottom TxCal Sphere
ACATMP8E=          27.657626 / [Deg_K] CA Temp, Foot 3

```

/ DATA FLOW KEYWORDS

```

ORIGIN0 = 'JPL_FOS ' / Site where RAW FITS file was written
CREATOR0= 'J5.3 ' / SW system that created RAW FITS
DATE = '2018-01-22T16:12:36' / [YYYY-MM-DDThh:mm:ss UTC] file creation date
AORKEY = 65216512 / AOR or EIR key. Astrnmy Obs Req/Instr Eng Req
DS_IDENT= 'ads/sa.spitzer#0065216512' / Data Set Identification for ADS/journals
EXPID = 8 / Exposure ID (0-9999)
DCENUM = 0 / DCE number (0-9999)
TLMGRPS = 1 / expected number of groups
FILE_VER= 1 / Version of the raw file made by SIS
RAWFILE = 'IRAC.1.0065216512.0008.0000.01.mipl.fits' / Raw data file name
CPT_VER = '3.1.11 ' / Channel Param Table FOS version
CTD_VER = '3.0.94S ' / Cmded telemetry data version
EXPFLAG= T / (T/F) expedited DCE
MISS_LCT= 0 / Total Missed Line Cnt in this FITS
MANCPKT = F / T if this FITS is Missing Ancillary Data
MISSDATA= F / T if this FITS is Missing Image Data
BADTRIG = F / Bad data (zero pixel) was located in raw frame
CHECKSUM= 0 / MIPL computed checksum
PAONUM = 5805 / PAO Number
CAMPAIGN= 'IRAC046900' / Campaign
DCEID = 181088957 / Data-Collection-Event ID
DCEINSID= 35961748 / DCE Instance ID
DPID = 419066836 / Data Product Instance ID
PIPENUM = 107 / Pipeline Script Number
SOS_VER = 2 / Data-Product Version
PLVID = 21 / Pipeline Version ID
CALID = 6 / CalTrans Version ID
SDRKEPID= 12399705 / Sky Dark ensemble product ID
PMSKFBID= 2167 / Pixel mask ID
LDRKFBID= 1308 / Fall-back lab dark ID
LINCFBID= 2028 / Fall-back Linearity correction ID
FLATFBID= 2026 / Fall-back flat ID
FLXCFBID= 2180 / Flux conversion ID
MBLTFBID= 1153 / Muxbleed Lookup Table ID
MBCFFBID= 1412 / Muxbleed Coefficients ID
LBDRKFLE= 'FUL_0.4s_0.4sfdlrl_ch1_v1.2.0_dark.txt' / Labdark File Used
LBDRKTD = 'F' / Labdark Time Dependent (T or F)
DDCORR1 = 0.04800264 / Darkdrift Correction for Readout Channel 1
DDCORR2 = -0.01963533 / Darkdrift Correction for Readout Channel 2
DDCORR3 = 0.06960913 / Darkdrift Correction for Readout Channel 3
DDCORR4 = -0.09797645 / Darkdrift Correction for Readout Channel 4
DBBKND = -0.6289024 / Darkdrift 'Background' Term

```

/ PROCESSING HISTORY

```

HISTORY job.c ver: 1.50
HISTORY TRANHEAD v. 13.2, ran Mon Jan 22 08:11:57 2018
HISTORY CALTRANS v. 4.0, ran Mon Jan 22 08:12:07 2018
HISTORY INSBPOSDOM v. 1.1, ran Mon Jan 22 08:12:07 2018
HISTORY cvti2r4 v. 1.31 A61025, generated 1/22/18 at 8:12:08
HISTORY hdrupd8 v. 1.6 A70821, updated 1/22/18 at 8:12:11
HISTORY hdrupd8 v. 1.6 A70821, updated 1/22/18 at 8:12:12
HISTORY hdrupd8 v. 1.6 A70821, updated 1/22/18 at 8:12:13
HISTORY hdrupd8 v. 1.6 A70821, updated 1/22/18 at 8:12:15
HISTORY hdrupd8 v. 1.6 A70821, updated 1/22/18 at 8:12:16
HISTORY hdrupd8 v. 1.6 A70821, updated 1/22/18 at 8:12:17

```



```

HISTORY hdrupd8          v. 1.6 A70821, updated 1/22/18 at 8:12:19
HISTORY FFC              v.          1.0, ran Mon Jan 22 08:12:20 2018
HISTORY FOWLINEARIZE    v.          4.900000, ran Mon Jan 22 08:12:20 2018
HISTORY hdrupd8          v. 1.6 A70821, updated 1/22/18 at 8:12:22
HISTORY BGMODEL         v.          1.0, ran Mon Jan 22 08:12:22 2018
HISTORY SLREMOVE        v.          1.0, ran Mon Jan 22 08:12:22 2018
HISTORY hdrupd8          v. 1.6 A70821, updated 1/22/18 at 8:12:23
HISTORY hdrupd8          v. 1.6 A70821, updated 1/22/18 at 8:12:25
HISTORY hdrupd8          v. 1.6 A70821, updated 1/22/18 at 8:12:26
HISTORY hdrupd8          v. 1.6 A70821, updated 1/22/18 at 8:12:27
HISTORY hdrupd8          v. 1.6 A70821, updated 1/22/18 at 8:12:28
HISTORY hdrupd8          v. 1.6 A70821, updated 1/22/18 at 8:12:30
HISTORY DARKSUBNG       v. 1.000, ran Mon Jan 22 08:12:30 2018
HISTORY DARKDRIFT       v.          4.1, ran Mon Jan 22 08:12:31 2018
HISTORY FLATAP          v. 1.500 Mon Jan 22 08:12:32 2018
HISTORY DNTOFLUX        v.          4.2, ran Mon Jan 22 08:12:36 2018
HISTORY CALTRANS        v.          4.0, ran Mon Jan 22 08:35:15 2018
HISTORY PTNTRAN         v.          1.4, ran Mon Jan 22 08:35:24 2018
HISTORY FPGen           v.          1.26, ran Mon Jan 22 08:35:31 2018
HISTORY PTGADJUST       v.          1.0, ran Mon Jan 22 08:48:19 2018
END

```

E.6 Warm Mission Channel 2

```

SIMPLE = T / Fits standard
BITPIX = -32 / FOUR-BYTE SINGLE PRECISION FLOATING POINT
NAXIS = 2 / STANDARD FITS FORMAT
NAXIS1 = 256 / STANDARD FITS FORMAT
NAXIS2 = 256 / STANDARD FITS FORMAT
ORIGIN = 'Spitzer Science Center' / Organization generating this FITS file
CREATOR = 'S19.2.0 ' / SW version used to create this FITS file
TELESCOP= 'Spitzer ' / SPITZER Space Telescope
INSTRUME= 'IRAC ' / SPITZER Space Telescope instrument ID
CHNLNUM = 2 / 1 digit instrument channel number
EXPTYPE = 'sci ' / Exposure Type
REQTYPE = 'AOR ' / Request type (AOR, IER, or SER)
AOT_TYPE= 'IracMapPC' / Observation template type
AORLABEL= 'IRAC_calstar_NPM1p67.0536_p4' / AOR Label
FOVID = 74 / Field of View ID
FOVNAME = 'IRAC_Center_of_4.5&8.0umArray' / Field of View Name

/ PROPOSAL INFORMATION

OBSRVR = 'IRAC Calibration' / Observer Name (Last, First)
OBSRVRID= 58326 / Observer ID of Principal Investigator
PROCYCL = 16 / Proposal Cycle
PROGID = 2017 / Program ID
PROTITLE= 'Spitzer IRAC Calibration Program' / Program Title
PROGCAT = 32 / Program Category

/ TIME AND EXPOSURE INFORMATION

DATE_OBS= '2018-01-07T09:46:06.321' / Date & time (UTC) at DCE start
UTCS_OBS= 568590366.321 / [sec] DCE start time from noon, Jan 1, 2000
UTCMJD_OBS = 58125.4070176 / [days] MJD in UTC at DCE start (,JD-2400000.5)
HMJD_OBS= 58125.4070868 / [days] Corresponding Helioc. Mod. Julian Date
BMJD_OBS= 58125.4070868 / [days] Solar System Barycenter Mod. Julian Date
ET_OBS = 568590435.505 / [sec] DCE start time (TDB seconds past J2000)

```

```

SCLK_OBS=      1199786144.66 / [sec] SCLK time (since 1/1/1980) at DCE start
SPTZR_X =     153233610.767491 / [km] Heliocentric J2000 x position
SPTZR_Y =     -3061072.710861 / [km] Heliocentric J2000 y position
SPTZR_Z =      922272.505034 / [km] Heliocentric J2000 z position
SPTZR_VX=      0.308888 / [km/s] Heliocentric J2000 x velocity
SPTZR_VY=      26.68973 / [km/s] Heliocentric J2000 y velocity
SPTZR_VZ=      12.032747 / [km/s] Heliocentric J2000 z velocity
SPTZR_LT=      511.24354 / [sec] One-way light time to Sun's center
AORTIME=       0.4 / [sec] Frameset selected in IRAC AOT
SAMPTIME=      0.2 / [sec] Sample integration time
FRAMTIME=      0.4 / [sec] Time spent integrating (whole array)
COMMENT Photons in Well = Flux[photons/sec/pixel] * FRAMTIME
EXPTIME =      0.2 / [sec] Effective integration time per pixel
COMMENT DN per pixel = Flux[photons/sec/pixel] / GAIN * EXPTIME
FRAMEDLY=      15.6 / [sec] Frame Delay Time
FRDLYDET= 'T'   ' / Frame Delay Time Determinable (T or F)
INTRFDLY=      15.6 / [sec] Inter Frame Delay Time
IMDLYDET= 'T'   ' / Immediate Delay Time Determinable (T or F)
AINTBEG =      22241724.7 / [Secs since IRAC turn-on] Time of integ. start
ATIMEEND=      22241725.07 / [Secs since IRAC turn-on] Time of integ. end
AFOWLNUM=      1 / Fowler number
AWAITPER=      0 / [0.2 sec] Wait period
ANUMREPS=      1 / Number of repeat integrations
AREADMOD=      0 / Full (0) or subarray (1)
AORHDR =       F / Requested AOT is HDR mode
HDRMODE =      F / DCE taken in High Dynamic Range mode
ABARREL =      0 / Barrel shift
APEDSIG =      0 / 0=Normal, 1=Pedestal, 2=Signal

```

/ TARGET AND POINTING INFORMATION

```

OBJECT = 'NPM1p67.0536_cal' / Target Name
OBJTYPE = 'TargetFixedCluster' / Object Type
CRPIX1 =      128. / Reference pixel along axis 1
CRPIX2 =      128. / Reference pixel along axis 2
CRVAL1 =      269.783436208203 / [deg] RA at CRPIX1,CRPIX2 (using Ptg. Recon.)
CRVAL2 =      67.8147452142769 / [deg] DEC at CRPIX1,CRPIX2 (using Ptg. Recon.)
CRDER1 = 6.41153925731943E-05 / [deg] Uncertainty in CRVAL1
CRDER2 = 7.28842924162574E-05 / [deg] Uncertainty in CRVAL2
RA_HMS = '17h59m08.0s' / [hh:mm:ss.s] CRVAL1 as sexagesimal
DEC_DMS = '+67d48m53s' / [dd:mm:ss] CRVAL2 as sexagesimal
RADESYS = 'ICRS' / International Celestial Reference System
EQUINOX =      2000. / Equinox for ICRS celestial coord. system
CD1_1 = 8.20084505255358E-06 / Corrected CD matrix element with Ptg. Recon.
CD1_2 = 0.00033753777196295 / Corrected CD matrix element with Ptg. Recon.
CD2_1 = 0.000337583565863835 / Corrected CD matrix element with Ptg. Recon.
CD2_2 = -7.97598226661874E-06 / Corrected CD matrix element with Ptg. Recon.
CTYPE1 = 'RA---TAN-SIP' / RA---TAN with distortion in pixel space
CTYPE2 = 'DEC--TAN-SIP' / DEC--TAN with distortion in pixel space
PXSCAL1 = -1.21565884910524 / [arcsec/pix] Scale for axis 1 at CRPIX1,CRPIX2
PXSCAL2 = 1.21547518065199 / [arcsec/pix] Scale for axis 2 at CRPIX1,CRPIX2
PA =      91.3536440942703 / [deg] Position angle of axis 2 (E of N)
UNCRTPA = 0.000864692681616987 / [deg] Uncertainty in position angle
CSDRADEC= 5.02403912562417E-06 / [deg] Costandard deviation in RA and Dec
SIGRA = 0.00485391820345622 / [arcsec] RMS dispersion of RA over DCE
SIGDEC = 0.0726885823245135 / [arcsec] RMS dispersion of DEC over DCE
SIGPA = 0.311905981987993 / [arcsec] RMS dispersion of PA over DCE
RA_RQST =      269.783692468039 / [deg] Requested RA at CRPIX1, CRPIX2
DEC_RQST=      67.8146680875655 / [deg] Requested Dec at CRPIX1, CRPIX2
PM_RA =      0. / [arcsec/yr] Proper Motion in RA (J2000)
PM_DEC =      0. / [arcsec/yr] Proper Motion in Dec (J200)
RMS_JIT = 0.00468277796825773 / [arcsec] RMS jitter during DCE
RMS_JITY= 0.00431458650394218 / [arcsec] RMS jitter during DCE along Y
RMS_JITZ= 0.00182009692049627 / [arcsec] RMS jitter during DCE along Z
SIG_JTYZ= -0.00256228659599195 / [arcsec] Costadard deviation of jitter in YZ

```

```

PTGDIFF =      0.44546842490805 / [arcsec] Offset btwn actual and rqsted pntng
PTGDIFFX=     0.269348651692721 / [pixels] rqsted - actual pntng along axis 1
PTGDIFFY=     0.354993196055767 / [pixels] rqsted - actual pntng along axis 2
RA_REF =      269.7271666666667 / [deg] Commanded RA (J2000) of ref. position
DEC_REF =      67.79369444444453 / [deg] Commanded Dec (J2000) of ref. position
USED_BPHF=      T / T if Boresight Pointing History File was used
BPHFNAME= 'SBPHF.1199750400.031.pntg' / Boresight Pointing History Filename
FOVVERSN= 'BodyFrames_FTU_14a.xls' / FOV/BodyFrames file version used
RECONFOV= 'IRAC_Center_of_4.5umArray' / Reconstructed Field of View
RARFND =      269.783386230469 / [deg] Refined RA
DECRFND =      67.814704895020 / [deg] Refined DEC
CT2RFND =      91.353340148926 / [deg] Refined CROT2
ERARFND =      0.000091113936 / [deg] Error in RARFND value
EDECRFND=      0.000132534260 / [deg] Error in DECRFND value
ECT2RFND=      0.001532432972 / [deg] Error in CT2RFND value
NASTROM =      2 / Astrometric sources for absolute refinement
ORIG_RA =      269.783447265625 / [deg] Original RA from raw BPHF
ORIG_DEC=      67.8146438598633 / [deg] Original Dec from raw BPHF
ORIGCD11=      8.2001461E-06 / [deg/pix] Original CD1_1 element
ORIGCD12=      0.0003375377855 / [deg/pix] Original CD1_2 element
ORIGCD21=      0.000337583595 / [deg/pix] Original CD2_1 element
ORIGCD22=      -7.9752836E-06 / [deg/pix] Original CD2_2 element

```

/ DISTORTION KEYWORDS

```

A_ORDER =      5 / polynomial order, axis 1, detector to sky
A_0_2 =      6.3419E-07 / distortion coefficient
A_0_3 =      -2.4851E-09 / distortion coefficient
A_0_4 =      7.4353E-13 / distortion coefficient
A_0_5 =      -7.7919E-14 / distortion coefficient
A_1_1 =      3.04E-05 / distortion coefficient
A_1_2 =      -1.9759E-07 / distortion coefficient
A_1_3 =      -4.1504E-11 / distortion coefficient
A_1_4 =      4.2184E-13 / distortion coefficient
A_2_0 =      2.1231E-05 / distortion coefficient
A_2_1 =      6.9765E-09 / distortion coefficient
A_2_2 =      -3.1891E-11 / distortion coefficient
A_2_3 =      -1.0864E-13 / distortion coefficient
A_3_0 =      -1.6079E-07 / distortion coefficient
A_3_1 =      2.1279E-11 / distortion coefficient
A_3_2 =      1.2951E-13 / distortion coefficient
A_4_0 =      -1.2411E-10 / distortion coefficient
A_4_1 =      2.167E-14 / distortion coefficient
A_5_0 =      -4.0834E-13 / distortion coefficient
A_DMAX =      1.552 / [pixel] maximum correction
B_ORDER =      5 / polynomial order, axis 2, detector to sky
B_0_2 =      3.5372E-05 / distortion coefficient
B_0_3 =      -1.6567E-07 / distortion coefficient
B_0_4 =      -2.5109E-11 / distortion coefficient
B_0_5 =      -8.132E-13 / distortion coefficient
B_1_1 =      1.8711E-05 / distortion coefficient
B_1_2 =      -1.7651E-10 / distortion coefficient
B_1_3 =      -8.6718E-12 / distortion coefficient
B_1_4 =      3.4181E-13 / distortion coefficient
B_2_0 =      3.8984E-06 / distortion coefficient
B_2_1 =      -2.057E-07 / distortion coefficient
B_2_2 =      -2.5154E-11 / distortion coefficient
B_2_3 =      6.99E-13 / distortion coefficient
B_3_0 =      -2.9019E-09 / distortion coefficient
B_3_1 =      8.8986E-13 / distortion coefficient
B_3_2 =      -5.0511E-14 / distortion coefficient
B_4_0 =      1.81E-11 / distortion coefficient
B_4_1 =      9.3724E-13 / distortion coefficient
B_5_0 =      1.5535E-13 / distortion coefficient
B_DMAX =      1.681 / [pixel] maximum correction

```

```

AP_ORDER=                5 / polynomial order, axis 1, sky to detector
AP_0_1 =                 9.2542E-08 / distortion coefficient
AP_0_2 =                -6.3441E-07 / distortion coefficient
AP_0_3 =                 2.5166E-09 / distortion coefficient
AP_0_4 =                -1.7427E-12 / distortion coefficient
AP_0_5 =                 8.2936E-14 / distortion coefficient
AP_1_0 =                 7.5978E-08 / distortion coefficient
AP_1_1 =                 -3.04E-05 / distortion coefficient
AP_1_2 =                 1.9975E-07 / distortion coefficient
AP_1_3 =                 1.1478E-11 / distortion coefficient
AP_1_4 =                -3.3048E-13 / distortion coefficient
AP_2_0 =                -2.1248E-05 / distortion coefficient
AP_2_1 =                -4.4764E-09 / distortion coefficient
AP_2_2 =                 1.454E-11 / distortion coefficient
AP_2_3 =                 1.0456E-13 / distortion coefficient
AP_3_0 =                 1.6169E-07 / distortion coefficient
AP_3_1 =                -4.9803E-11 / distortion coefficient
AP_3_2 =                 7.3712E-14 / distortion coefficient
AP_4_0 =                 1.0922E-10 / distortion coefficient
AP_4_1 =                -4.1098E-14 / distortion coefficient
AP_5_0 =                 4.8996E-13 / distortion coefficient
BP_ORDER=                5 / polynomial order, axis 2, sky to detector
BP_0_1 =                -8.569E-08 / distortion coefficient
BP_0_2 =                -3.5361E-05 / distortion coefficient
BP_0_3 =                 1.6798E-07 / distortion coefficient
BP_0_4 =                -8.1491E-12 / distortion coefficient
BP_0_5 =                 9.2745E-13 / distortion coefficient
BP_1_0 =                -2.2769E-07 / distortion coefficient
BP_1_1 =                -1.8727E-05 / distortion coefficient
BP_1_2 =                 2.8463E-09 / distortion coefficient
BP_1_3 =                -7.5609E-12 / distortion coefficient
BP_1_4 =                -3.5417E-13 / distortion coefficient
BP_2_0 =                -3.912E-06 / distortion coefficient
BP_2_1 =                 2.0734E-07 / distortion coefficient
BP_2_2 =                -7.7834E-12 / distortion coefficient
BP_2_3 =                -5.1008E-13 / distortion coefficient
BP_3_0 =                 3.1962E-09 / distortion coefficient
BP_3_1 =                -1.7172E-11 / distortion coefficient
BP_3_2 =                 4.6967E-14 / distortion coefficient
BP_4_0 =                -1.9585E-11 / distortion coefficient
BP_4_1 =                -8.6274E-13 / distortion coefficient
BP_5_0 =                -1.5746E-13 / distortion coefficient

/ PHOTOMETRY

BUNIT = 'MJy/sr ' / Units of image data
FLUXCONV=          0.1447 / Flux Conv. factor (MJy/sr per DN/sec)
GAIN =              3.71 / e/DN conversion
RONOISE =           23.7 / [Electrons] Readout Noise from Array
ZODY_EST=          0.1634331 / [MJy/sr] Zodiacal Background Estimate
ISM_EST =          0.007788374 / [MJy/sr] Interstellar Medium Estimate
CIB_EST =           0. / [MJy/sr] Cosmic Infrared Background Estimate
SKYDRKZB=          0.167733 / [MJy/sr] Zodiacal Background Est of Subtracted
SKYDKMED=          2.887192 / [MJy/sr] Median of Subtracted Skydark
SKDKRKEY=          65218816 / Skydark AOR Reqkey
SKDKTIME=           0.4 / [sec] Skydark AOR Duration Time
SKDKFDLY=           12.59 / [sec] Average Frame Delay Time of Skydark
SKDKIDLY=           12.59 / [sec] Average Immediate Delay Time of Skydark

/ GENERAL MAPPING KEYWORDS

CLUSTPOS= '5 ' / Current cluster position

/ IRAC MAPPING KEYWORDS

READMODE= 'FULL ' / Readout mode (full or sub)

```

/ PEAKUP STAR KEYWORDS

COMMENT Either offsets OR absolute positions will be listed for the peakup tar

/ INSTRUMENT TELEMETRY DATA

```

ASHTCON =                2 / Shutter condition (1:closed, 2: open)
AWEASIDE=                0 / WEA side in use (0:B, 1:A)
ACTXSTAT=                0 / Cmded transcal status
ATXSTAT =                0 / transcal status
ACFLSTAT=                0 / Cmded floodcal status
AFLSTAT =                0 / floodcal status
AVRSTUCC=               -3.55 / [Volts] Cmded VRSTUC Bias
AVRSTBEG=             -3.5591532 / [Volts] VRSTUC Bias at start integration
AVDETC =               -3.05 / [Volts] Cmded VDET Bias
AVDETBEG=             -3.056874 / [Volts] VDET Bias at start of integration
AVGG1C =               -3.61 / [Volts] Cmded VGG1 Bias
AVGG1BEG=             -3.6191892 / [Volts] VGG1 Bias at start of integration
AVDDUCC =               -3.55 / [Volts] Cmded VDDUC Bias
AVDDUBEG=             -3.5512971 / [Volts] VDDUC Bias at start integration
AVGGCLC =                0. / [Volts] Cmded VGGCL clock rail voltage
AVGGCBEG=                0. / [Volts] VGGCL clock rail voltage
AHTRIBEG=               79.793616 / [uAmps] Heater current at start of integ
AHTRVBEG=              0.88265303 / [Volts] Heater Voltage at start integ.

AFPAT2B =               28.686249 / [Deg_K] FPA Temp sensor #2 at start integ.
AFPAT2BT=              22241717. / [Sec] FPA Temp sensor #2 time tag
AFPAT2E =               28.686249 / [Deg_K] FPA temp sensor #2, end integ.
AFPAT2ET=              22241717. / [Sec] FPA temp sensor #2 time tag
AFENDT =                22.083699 / [Deg_C] C&T board thermistor
AFPECTE =               20.323288 / [Deg_C] FPE control board thermistor
AFPEATE =               23.613159 / [Deg_C] FPE analog board thermistor
ASHTEMPE=               23.363894 / [Deg_C] Shutter board thermistor
ATCTEMPE=               24.583127 / [Deg_C] Temp. controller board thermistor
ACETEMPE=               22.083699 / [Deg_C] Calib. electronics board thermistor
APDTEMPE=               22.11418 / [Deg_C] PDU board thermistor
ACATMP1E=               27.500894 / [Deg_K] CA Temp, Foot 2
ACATMP2E=               27.502644 / [Deg_K] CA Temp, Foot 1
ACATMP3E=               27.531015 / [Deg_K] CA Temp, Shutter
ACATMP4E=               27.588415 / [Deg_K] CA Temp, Top OMH
ACATMP5E=               27.675731 / [Deg_K] CA Temp, Bottom OMH
ACATMP6E=               27.589667 / [Deg_K] CA Temp, Top TxCal Sphere
ACATMP7E=               27.634638 / [Deg_K] CA Temp, Bottom TxCal Sphere
ACATMP8E=               27.657626 / [Deg_K] CA Temp, Foot 3

```

/ DATA FLOW KEYWORDS

```

ORIGIN0 = 'JPL_FOS ' / Site where RAW FITS file was written
CREATOR0= 'J5.3 ' / SW system that created RAW FITS
DATE = '2018-01-22T16:10:04' / [YYYY-MM-DDThh:mm:ss UTC] file creation date
AORKEY = 65216512 / AOR or EIR key. Astrnmy Obs Req/Instr Eng Req
DS_IDENT= 'ads/sa.spitzer#0065216512' / Data Set Identification for ADS/journals
EXPID = 8 / Exposure ID (0-9999)
DCENUM = 0 / DCE number (0-9999)
TLMGRPS = 1 / expected number of groups
FILE_VER= 1 / Version of the raw file made by SIS
RAWFILE = 'IRAC.2.0065216512.0008.0000.01.mipl.fits' / Raw data file name
CPT_VER = '3.1.11 ' / Channel Param Table FOS version
CTD_VER = '3.0.94S ' / Cmded telemetry data version
EXPFLAG= T / (T/F) expedited DCE
MISS_LCT= 0 / Total Missed Line Cnt in this FITS
MANCPKT = F / T if this FITS is Missing Ancillary Data

```

```

MISSDATA=          F / T if this FITS is Missing Image Data
BADTRIG =          F / Bad data (zero pixel) was located in raw frame
CHECKSUM=          0 / MIPL computed checksum
PAONUM =           5805 / PAO Number
CAMPAIGN= 'IRAC046900' / Campaign
DCEID =            181088956 / Data-Collection-Event ID
DCEINSID=          35961749 / DCE Instance ID
DPID =             419066253 / Data Product Instance ID
PIPENUM =          107 / Pipeline Script Number
SOS_VER =           2 / Data-Product Version
PLVID =            22 / Pipeline Version ID
CALID =            7 / CalTrans Version ID
SDRKEPID=          12399707 / Sky Dark ensemble product ID
PMSKFBID=          2171 / Pixel mask ID
LDRKFBID=          1309 / Fall-back lab dark ID
LINCFBID=          1578 / Fall-back Linearity correction ID
FLATFBID=          2027 / Fall-back flat ID
FLXCFBID=          2182 / Flux conversion ID
MBLTFBID=          1155 / Muxbleed Lookup Table ID
MBCFFBID=          1411 / Muxbleed Coefficients ID
LBDRKFILE= 'FUL_0.4s_0.4sfdlrl_ch2_v1.2.0_dark.txt' / Labdark File Used
LBDRKTD = 'F' / Labdark Time Dependent (T or F)
DDCORR1 =          -0.05274831 / Darkdrift Correction for Readout Channel 1
DDCORR2 =          -0.03699508 / Darkdrift Correction for Readout Channel 2
DDCORR3 =           0.07617409 / Darkdrift Correction for Readout Channel 3
DDCORR4 =           0.0135693 / Darkdrift Correction for Readout Channel 4
DDBKGND =          0.1220955 / Darkdrift 'Background' Term

```

/ PROCESSING HISTORY

```

HISTORY job.c ver: 1.50
HISTORY TRANHEAD          v.          13.2, ran Mon Jan 22 08:09:27 2018
HISTORY CALTRANS          v.           4.0, ran Mon Jan 22 08:09:38 2018
HISTORY INSBPOSDOM        v.           1.1, ran Mon Jan 22 08:09:39 2018
HISTORY cvti2r4           v.  1.31 A61025, generated 1/22/18 at 8:09:40
HISTORY hdrupd8           v.  1.6 A70821, updated 1/22/18 at 8:09:42
HISTORY hdrupd8           v.  1.6 A70821, updated 1/22/18 at 8:09:43
HISTORY hdrupd8           v.  1.6 A70821, updated 1/22/18 at 8:09:44
HISTORY hdrupd8           v.  1.6 A70821, updated 1/22/18 at 8:09:45
HISTORY hdrupd8           v.  1.6 A70821, updated 1/22/18 at 8:09:46
HISTORY hdrupd8           v.  1.6 A70821, updated 1/22/18 at 8:09:47
HISTORY hdrupd8           v.  1.6 A70821, updated 1/22/18 at 8:09:48
HISTORY FFC                v.           1.0, ran Mon Jan 22 08:09:49 2018
HISTORY FOWLINEARIZE      v.           4.900000, ran Mon Jan 22 08:09:49 2018
HISTORY hdrupd8           v.  1.6 A70821, updated 1/22/18 at 8:09:51
HISTORY BGMODEL           v.           1.0, ran Mon Jan 22 08:09:51 2018
HISTORY SLREMOVE          v.           1.0, ran Mon Jan 22 08:09:51 2018
HISTORY hdrupd8           v.  1.6 A70821, updated 1/22/18 at 8:09:52
HISTORY hdrupd8           v.  1.6 A70821, updated 1/22/18 at 8:09:53
HISTORY hdrupd8           v.  1.6 A70821, updated 1/22/18 at 8:09:54
HISTORY hdrupd8           v.  1.6 A70821, updated 1/22/18 at 8:09:56
HISTORY hdrupd8           v.  1.6 A70821, updated 1/22/18 at 8:09:57
HISTORY hdrupd8           v.  1.6 A70821, updated 1/22/18 at 8:09:58
HISTORY DARKSUBNG         v.  1.000, ran Mon Jan 22 08:09:59 2018
HISTORY DARKDRIFT         v.           4.1, ran Mon Jan 22 08:09:59 2018
HISTORY FLATAP            v.  1.500 Mon Jan 22 08:10:00 2018
HISTORY DNTOFLUX          v.           4.2, ran Mon Jan 22 08:10:04 2018
HISTORY CALTRANS          v.           4.0, ran Mon Jan 22 08:33:04 2018
HISTORY PTNTRAN           v.           1.4, ran Mon Jan 22 08:33:15 2018
HISTORY FPGen             v.           1.26, ran Mon Jan 22 08:33:26 2018
HISTORY PTGADJUST         v.           1.0, ran Mon Jan 22 08:36:37 2018
END

```

Appendix F. Acronyms

2MASS	The Two Micron All Sky Survey.
A/D	Analog-to-Digital.
ACS	The Advanced Camera for Surveys.
ADC	Analog-to-Digital Converter.
ADS	Astrophysics Data System.
AM	Amplitude Modulation.
AOR	Astronomical Observation Request - an individual observation.
AORKEY	Astronomical Observation Request Key - a unique numerical identification of an observation.
AOT	Astronomical Observation Template - the IRAC observing mode.
APEX	Astronomical Point source Extractor.
BCD	Basic Calibrated Data, the Level 1 data product from each DCE that has been pipeline-processed and is fully calibrated.
BLISS	BiLinearly Interpolated Subpixel Sensitivity.
BPHF	Boresight Pointing History File.
C&DH	Command and Data Handling.
CA	Cryogenic Assembly.
CBCD	Corrected Basic Calibrated Data. This should be the starting point for further scientific analysis in most cases.
CMOS	Complementary Metal Oxide Semiconductor.
COBE	Cosmic Background Explorer.
CR	Cosmic Ray.
CTA	Cryogenic Telescope Assembly.
CTE	Charge Transfer Efficiency.
CVF	Circular Variable Filter.
CVZ	Continuous Viewing Zone.
DAOPHOT	Dominion Astrophysical Observatory Photometry stellar photometry package.
DC	Direct Current.
DCE	Data Collection Event, for IRAC a single 256 pixel by 256 pixel image from a single detector.
DIRBE	Diffuse InfraRed Background Experiment.
DN	Data Number (similar to ADU, Analog to Digital Unit).
FET	Field Effect Transistor.
FITS	Flexible Image Transportation System.
FLS	First Look Survey.
FM	Frequency Modulation.
FOS	Flight Operations System.

FOV	Field Of View.
FPA	Focal Plane Assembly, housing one IRAC detector.
FPG	Final Product Generator.
FWHM	Full Width Half Maximum.
GOODS	The Great Observatories Origins Deep Survey.
GP	Gaussian Process.
GSFC	Goddard Space Flight Center.
GTO	Guaranteed Time Observer.
HDR	High Dynamic Range.
HST	The Hubble Space Telescope.
I&T	Integration and Test.
IDL	Interactive Data Language.
IER	Instrument Engineering Request - like an AOR, but for specific engineering tasks that cannot be accomplished with an AOR.
InSb	Indium Antimonide, the detector material used in the short wavelength channels of IRAC (1 and 2).
IOC	In-Orbit Checkout, the two-month long testing period of the telescope following its launch.
IRAC	InfraRed Array Camera.
IRAF	Image Reduction and Analysis Facility.
IRAS	InfraRed Astronomical Satellite.
IRS	InfraRed Spectrograph.
IRSA	InfraRed Science Archive.
ISO	Infrared Space Observatory.
ISOCAM	Infrared Space Observatory Camera.
ISSA	IRAS Sky Survey Atlas.
IST	Instrument Support Team
IT	Instrument Team.
IWIC	IRAC Warm Instrument Characterization, the two-month long testing period of the telescope at the beginning of the warm mission and immediately following the end of the cryogenic mission.
JPL	Jet Propulsion Laboratory.
K2	Kepler 2 Mission (“Second Light”).
KR	Kernel Regression.
LSB	Low Surface Brightness.
MCMC	Markov Chain Monte Carlo.
MIC	Multiple Instrument Chamber.
MIPS	Multiband Imaging Photometer for Spitzer.
MOPEX	MOsaicker and Point source EXtractor
NaN	Not a Number.

NASA	National Aeronautics and Space Administration.
NEP	North Ecliptic Pole.
NICMOS	The Near Infrared Camera and Multi-Object Spectrometer.
NOAO	National Optical Astronomy Observatory.
P.I.	Principal Investigator.
PAH	Polycyclic Aromatic Hydrocarbon.
PAO	Period of Autonomous Operation, the interval between ground contacts for uplinking commands and downlinking data, normally 12-24 hours.
PBCD	Post Basic Calibrated Data.
PC	Post Cryogenic.
PCRS	Pointing Calibration and Reference Sensor.
PCS	Pointing Control System.
PID	Program Identification (Number). This number uniquely identifies the program to which any given observations belong.
PLD	Pixel Level Decorrelation.
PRF	Point Response Function. The PRF is essentially the convolution of a box the size of the image pixel with the PSF.
PSF	Point-Spread Function.
PSR	Point Source Realization.
QA	Quality Analysis.
QE	Quantum Efficiency.
RMS	Root Mean Square.
RPM	Revolutions Per Minute.
ROIC	Read-Out Integrated Circuit. It is the chip that contains the multiplexer (column and row scanners and the buses), the unit cell amplifiers, and the output amplifiers. The chip containing the detector diodes is bonded to it. It is often called simply the “mux.”
S/C	SpaceCraft.
SAO	Smithsonian Astrophysical Observatory, Cambridge, MA.
SSC	Spitzer Science Center.
SED	Spectral Energy Distribution.
SERVS	The Spitzer Extragalactic Representative Volume Survey.
SHA	Spitzer Heritage Archive.
Si:As	Arsenic-doped Silicon, the detector material in the IRAC long-wavelength channels (3 & 4).
SIP	Simple Imaging Polynomial.
SIRTF	Space InfraRed Telescope Facility.
SNR	Signal-to-Noise Ratio.
SOM	Spitzer Observer’s Manual.
SP	Segmented Polynomial.

SV	Science Validation, a 35-day period after the IOC during which the science instruments and their observational modes were commissioned.
SWIRE	Spitzer Wide Area Infrared Survey.
TDB	Barycentric Dynamical Time.
UCAC4	USNO CCD Astrograph Catalog 4.
UT	Universal Time.
UTC	Coordinated Universal Time.
WCS	World Coordinate System.
WEA	Warm Electronics Assembly.
WFC3	The Wide Field Camera 3.
WFPC2	The Wide-Field and Planetary Camera 2.

Appendix G. Acknowledgments

IRAC would not have been the successful instrument it was without the enthusiastic and capable contribution of many colleagues (see the lists of collaborators and laboratories below). Support for the IRAC instrument was provided by NASA through contract 960541 issued by JPL.

Principal Investigator

Dr. Giovanni Fazio (SAO, Harvard)
Dr. Gary J. Melnick, Deputy Principal Investigator (SAO, Harvard)
Dr. Joseph L. Hora, Project Scientist (SAO, Harvard)
Richard S. Taylor, Project Manager (SAO, Harvard)

Co-Investigators

The co-investigators played a central role in defining the technical characteristics of IRAC in order to carry out the science programs agreed upon by all of them. Lynne Deutsch, a co-investigator of IRAC, died on 2004 April 2, after a long illness. Lynne was a dear friend and a close colleague. The IRAC team deeply misses her presence.

Dr. William F. Hoffmann (University of Arizona)
Dr. Craig R. McCreight (Ames Research Center)
Dr. S. Harvey Moseley (Goddard Space Flight Center)
Dr. Judith L. Pipher (University of Rochester)
Dr. Lori E. Allen (SAO, Harvard)
Dr. Matthew L. N. Ashby (SAO, Harvard)
Dr. Pauline Barmby (SAO, Harvard)
Dr. Lynne K. Deutsch (SAO, Harvard)
Dr. Peter Eisenhardt (JPL, Caltech)
Dr. Jiasheng Huang (SAO, Harvard)
Dr. David I. Koch (SAO, Harvard)
Dr. Massimo Marengo (SAO, Harvard)
Dr. S. Thomas Megeath (SAO, Harvard; University of Toledo)
Dr. Michael Pahre (SAO, Harvard)
Dr. Brian Patten (SAO, Harvard)
Dr. Howard Smith (SAO, Harvard)
Dr. John R. Stauffer (SAO, Harvard; SSC, Caltech)
Dr. Eric V. Tollestrup (SAO, Harvard)
Dr. Zhong Wang (SAO, Harvard)
Dr. Steven P. Willner (SAO, Harvard)
Dr. Edward L. Wright (UCLA)
Dr. William F. Hoffmann (U. Arizona)
Dr. William J. Forrest (University of Rochester)
Dr. Daniel Gezari (GSFC)

Collaborators

Construction and ground calibration phase

People listed here include those that participated in the mechanical, optical, and cryo-mechanical studies that led to the definition of IRAC, as well as those who designed and built the on-board electronic subsystems, developed the on-board software and worked on the Ground Support Equipment. Others participated in the development of the extensive software systems and procedures later used for the in-flight calibration, system tests and uplink subsystems or in the Off-Line pipeline.

Dr. Jon Chappell, Data Systems Analyst (SAO, Harvard)

Dr. Martin Cohen, Calibration Scientist (SAO, Harvard)

Dr. Steven Kleiner, IT Specialist (SAO, Harvard)

Dr. John Spitzak, Data Systems Analyst (SAO, Harvard)

SAO IRAC PROJECT OFFICE

Christina M. Arabadjis, Project Administrator

Jo-Ann Campbell-Cameron, Group Secretary

Mary L. Horan, Project Administrator

Ralph Paganetti, Management Support

S. Douglas Smith, Project Administrator

Jane I. Wamback, Group Administrator

SAO CENTRAL ENGINEERING

John P. Polizotti, IRAC Systems Engineer

Vaman S. Bawdekar, Quality Assurance Engineer

David A. Boyd, Thermal Engineer

John Boczenowski, Quality Assurance Manager

Kathy Daigle, Documentation Control Engineer

Leslie Frazier, Quality Assurance Engineer

Thomas Gauron, Mechanical Engineer

Joaquim J. Gomes, Electrical Engineer

Everett Johnston, Electrical Engineer

Maggie Kanouse, Documentation Specialist

Warren Martell, Quality Assurance Engineer

Paul Okun, Electrical Engineer

Joel Rosenberg, Electrical Engineer

AMES RESEARCH CENTER

Dr. Craig R. McCreight, Lead Si:As Scientist

Roy R. Johnson, Detector Test Engineer

Roderick N. McHugh, Electronic Technician

Mark E. McKelvey, Detector Test Lead

Robert E. McMurray, Jr., Detector Scientist

Nicolas N. Moss, Programmer

William I. Ogilvie, Programmer

Nicholas N. Scott, Mechanical and Electrical Tech

Steven I. Zins, Programmer

UNIVERSITY OF ARIZONA

Dr. William F. Hoffmann

Thomas J. Tysenn, Research Specialist

Patrick M. Woida, Staff Technician, Sr.

UNIVERSITY OF ROCHESTER

Dr. Judith L. Pipher, Lead InSb Scientist

Dr. William J. Forrest

InSb ARRAY DEVELOPMENT

Hao Chen, Senior Engineer

Dr. James D. Garnett, Research Associate

Dr. William J. Glaccum, Research Associate

Brad Marazus, Engineer

Dr. Zoran Ninkov, Research Associate

Jian Wu, Senior Engineer

InSb ARRAY TESTING

Candice Bacon, Graduate Student

Bob Benson, Graduate Student

Nathaniel Cowen, Programmer/Analyst

Chad Engelbracht, Undergraduate Student

Brian Goss, Graduate Student

Andrea La Barbera, Undergraduate Student

Scott Libonate, Graduate Student

Kevin McFadden, Programmer/Analyst

Craig McMurtry, Undergraduate Student

D. Michael Myers, Programmer/Analyst

Ryan Overbeck, Programmer/Analyst

Bruce Pirger, Undergraduate Student

Pratap Ranade, Undergraduate Student

Aaron Reichman, Undergraduate Student

Richard Sarkis, Programmer/Analyst

Justin Schoenwald, Programmer/Analyst

Steve Solomon, Graduate Student

Brendan White, Programmer/Analyst

OBSERVATIONAL PLANNING AND DATA ANALYSIS

Jessica Benjou, Undergraduate Student

Justin Comparetta, Graduate Student

Margaret Drennan, Graduate Student

Mike Dunham, Undergraduate Student

Kevin Flaherty, Undergraduate Student

Rob Gutermuth, Graduate Student

Alaina Henry, Undergraduate Student
Osa Igbinosun, Undergraduate Student
Angela Lowell, Undergraduate Student
Rebecca Madson, Undergraduate Student
Dawn Peterson, Graduate Student

**RAYTHEON VISION SYSTEMS
 SANTA BARBARA RESEARCH CENTER
 InSb AND Si:As DETECTOR DEVELOPMENT, FABRICATION, AND TEST**

Dr. Alan Hoffman, Project Manager
Dr. George Domingo, Si:As Development Lead, Project Manager
Conrad Anderson, IBC Detector & Test
Jim Asbrock, Readout Design
Virginia Bowman, Si:As Processing
George Chapman, Detector Test
Elizabeth Corrales, Business Manager
Arnold Estrada, Array Test
Bruce Fletcher, Hybridization Engineer
Peter Love, System Engineer
Dr. Larry Lum, Readout Engineer
Dr. Nancy Lum, Multiplexer Designer
Susan Morales, Production Control
Olivia Moreno, Quality Assurance
Heidi Mosel-Riedo, Business Manager
Joseph Rosbeck, InSb Detector Engineer
Kiomi Schartz, IBC Processing
Michael S. Smith, Detector Test Engineer
Steve Solomon, Array Test Engineer
Kevin Sparkman, Test Engineer
Andrew S. Toth, IBC Detector Engineer
Peter S. Villa, Hybridization Engineer
Sharon E. Woolaway, Hybridization Engineer

GODDARD SPACE FLIGHT CENTER

INSTRUMENT MANAGEMENT
Lois Workman, Instrument Manager
Felicia Jones-Selden, Instrument Engineer/Manager
Juan Rivera, Instrument Engineer/Manager
Rich Barney, Instrument Manager, Branch Head

SCIENCE TEAM
Dr. S. Harvey Moseley, Instrument Scientist
Dr. Richard Arendt, Science Support
Dr. Sean Casey, Science Support

Dr. Dale Fixsen, Science Support
Dr. Daniel Gezari, Instrument Scientist
Dr. Alexander Kutyrev, Science Support
Tim Powers, Electronics Technician

REVIEW TEAM

William T. Tallant, Review Team Chairman
Steve Bartel, Review Team
James Caldwell, Review Team
Robert Coladonato, Review Team
Michael Dipirro, Review Team
Pam Davila, Review Team,
Gene Gochar, Review Team
Frank Kirchman, Review Team
Robert Martineau, Review Team
Ian Mclean, Review Team
Vern Weyers, Review Team

INSTRUMENT SYSTEM ENGINEERS

Gabe Karpati, Instrument System Engineer
Neil Martin, Instrument System Engineer
Robert Maichle, Instrument System Engineer
Kevin Brenneman, System Engineer
Robert Kichak, Chief Engineer, Electrical
John Wolfgang, Verification Lead

MECHANICAL SYSTEMS

Claef Hakun, Mechanical System Lead
Willie Blanco, Mechanical Branch Head
Willie Barber, Mechanical Technician
Carlos Bernabe, Mechanical Engineer
Ken Blumenstock, Mechanical Engineer
Gary Brown, Mechanical Engineer
Dr. Philip Chen, Contamination Engineer
Rainer Fettig, Mechanical Engineer
Bryan Grammer, Designer
Paul Haney, Mechanical Technician
Tom Hanyok, Designer
Darron Harris, Mechanical Technician
Mike Hersh, Mechanical Engineer
Sid Johnson, Mechanical Technician
Ben Lewit, Mechanisms Engineer
Carlos Lugo, Mechanical Engineer
Dave Pfenning, Electro/Mechanical Tech
George Reinhardt, Mechanical Engineer
Scott Schwinger, Mechanical Engineer

Ryan Simmons, Systems Analyst
Dr. Michael G. Ryschkewitsch, Designer, 1988-1989
Charles Tomasevich, Mechanical Engineer, 1997-2000
George Voellmer, Mechanical Engineer, 1995-1996
Steve Wood, Mechanical Technician, 1997-2000

ELECTRICAL SYSTEMS

Jose Florez, Electrical System Lead
Harlan Bowers, OSC Task Manager
Vicky Brocius, Parts Procurement
Robert Clark, Parts Procurement
Tracy Clay, WEA Enclosure Supervisor
Jim Cook, PWA Assembly
Glenn Davis, Polymerics
Mitch Davis, ESE Engineer
Bob Demme, PWA Assembly Manager
Melissa Eberhardinger, Parts Procurement
Majed El Alami, Parts Procurement
Patricia Gilbertson, Parts Procurement
Steve Graham, Electrical Engineer
David Hessler, Electrical Engineer
Gina Kanares, Parts Stock
Richard Katz, Electrical Engineer
Igor Kleiner, BTE S/W
Tracie Lampke, PWA Assembly
David Liu, Electrical Engineer
Jim Lohr, Parts Engineer
Bill Long, WEA Enclosure Supervisor
Jack Lorenz, WEA Enclosure Designer
John McCloskey, Electrical Engineer
Charlie McClunin, WEA Enclosure Designer
Margaret McVicker, PWA Assembly
Tim Miralles, WEA Test Engineer
Keyvan Mortazavi, J&T Task Manager
Kim Moats, PWA Assembly
Trang Nguyen, Electrical Engineer
J. R. Norris, Litton Task Manager
Larry Pack, Packaging Lead
Laddawan Ruamsuwan, Electrical Engineer
Allen Rucker, WEA Test Engineer
Kamdin Shakoorzadeh, Electrical Engineer
Narenda Shukla, DC-DC Converter
Kevin Smith, WEA PWA Designer
Steve Smith, WEA Test Engineer
John Stewart, Electronics Technician
Victor Torres, Electrical Engineer

Yen Tran, WEA PWA Designer
Steven Van Nostrand, WEA PWA Designer
Sherry Wagner, PWA Assembly
Banks Walker, WEA PWA Designer
Mark Walter, DC-DC Converter
Richard Williams, Parts Engineer

SOFTWARE SYSTEMS

Raymond Whitley, Software Manager
Louise Bashar, Software Engineer
Craig Bearer, Ground Software Engineer
Glenn Cammarata, Software Engineer
Jenny Geiger, Software Engineer
Bob Koehler, Software Engineer
Steve Mann, Software Engineer
Dave McComas, Software Engineer
Janet McDonnell, Software Engineer
Ken Rehm, Software Engineer
Jann Smith, Software Engineer
Carlos Trujillo, Software Engineer
David Vavra, Software Engineer

CRYOGENICS

Dan McHugh, Cryogenics Technician,
John Bichell, Cryogenics Technician
Rob Boyle, Cryogenics Engineer
Susan Breon, Cryogenics Engineer
Michael Dipirro, Cryogenics Engineer
Darrell Gretz, Cryogenics Technician
Ed Quinn, Cryogenics Technician
Peter Shirron, Cryogenics Engineer

FLIGHT ASSURANCE

Ted Ackerson, Systems Assurance Manager
Dick Bolt, Flight Assurance
Jerry Bushman, Flight Assurance
Jack Galleher, System Reliability
Steve Hull, Parts Assurance
Ron Kolecki, Flight Assurance Manager
Norman Lee, Flight Assurance
Shirley Paul, Flight Assurance

OPTICAL SYSTEMS

Peter Maymon, Lead Optics, Optics Consultant, Branch Head
Catherine Marx, Optical Designer, Optics Lead

Pat Losch, Lead Optics, Optics I&T
Bill Eichorn, Lead Optics, Optical I&T
Julie Crooke, Optical Engineer
Andy Dantzler, Optical Designer
Dr. Bruce Dean, Optical Analyst
Dennis Evans, Optical Design
Thomas French, Optical Technician
Dr. David Glenar, Calibration Optics
Dr. Qian Gong, Optical Engineer
Paul Hannan, Optical Designer
Dr. Donald Jennings, Optics Engineer
Jay Jett, Optical Technician
Linette Kolos, Plating Technician
Dr. Ritva Keski-Kuha, Optics Engineer
James Lyons, Optical Technician
Eric Mentzell, Optical Analyst
Joseph McMann, Optics Engineer
Dr. Ray Ohl, Optical Engineer
Dean Osgood, Optical Technician
Grant Piegari, Optical Technician
Dr. Manuel Quijada, Optics Engineer
Steve Rice, Thin Films Technician
Kevin Redman, Optical Technician
Vicki Roberts, Optical Technician
Dr. Frederick Robinson, Optics Engineer
Dr. Kenneth Stewart, Optics Engineer
Carl Strojny, Optical Technician
Felix Threat, Thin Films Technician
Larry White, Mechanical Technician
Mark Wilson, Optical Designer
Lou Worrel, Optics Technician

THERMAL SYSTEMS

Rick Stavely, Lead Thermal Engineer
Carol Mosier, Lead Thermal Engineer
Mike Choi, Thermal Engineer
Raymond Trunzo, Thermal Engineer

FOCAL PLANE ASSEMBLIES

Dr. Danny Krebs, FPA Lead
Dr. Murzy D. Jhabvala, FPA Lead
Christine Allen, FPA Engineer
Sachi Babu, Detector Assembly Technician
Mark Cushman, Detector Assembly Tech
John Godfrey
Steve Graham, Electronics Engineer

Anh La, Test Engineer
Gerald Lamb, FPA Engineer
Kim Moats, Electronics Technician
Trang Nguyen, Electronics Engineer
Frank Peters, Detector Technician
David Rapchun, Detector Technician
Peter Shu, Science Team
Robert Stanley, Electronics Technician
Jeff Travis, Electronics Engineer

INTEGRATION AND TEST

Ray Jungo, Integration and Test Manager
Michael Alexander, Test Conductor
Maureen Armbruster, Test Conductor
Craig Bearer, S/C Simulator Programmer
Marty Brown, Test Conductor
Jamie Britt, Environmental Test Engineer
Frank Carroll, Test Conductor
James E. Golden, Programmer
Peter Gorog, Programmer
Shirley M. Jones, Harness Technician
Don Kirkpatrick, Harness Technician
Juli Lander, Test Conductor
Matthew E. (Ed) Lander, Test Conductor
Jim MacLeod, Test Conductor
Rudy Manriquez, Harness Technician
Ayman Mekhail, Test Conductor
James Mills, Harness Fabrication Supervisor
Brian Ottens, Environmental Test Engineer
Ramjit Ramrattan, Harness Technician
Marco Rosales, Harness Technician
Charles Stone, Harness Technician

INSTRUMENT TEAM SUPPORT

John Anders, Configuration Manager
Kim Brecker, Web Page Manager
Walt Carel, Transportation
Ron Colvin, Web Server
John Davis, Scheduler
Robert Dipalo, Transportation
Cristina Doria-Warner, Resource Analyst
Steve Ford, Program Analyst
Toni Hegarty, Configuration Manager
Ken Lathan, Web Page Support
Lois Pettit, Configuration Manager
Bob Read, Support Team Supervisor

Chris Romano, Program Analyst
Sharmaine Stewart, Resource Analyst
Lynette Sullivan, Configuration Manager
Catherine Traffanstedt, Transportation
Debra A. Yoder, Configuration Manager

Operations phase

The following are the people who participated in the operational phase of IRAC. The list includes those actively involved with the day-to-day operations within the IRAC Instrument Support Team (IST) at SSC, and those on the “home team” within the IRAC Instrument Team (IT) at SAO, Harvard, and anyone that contributed to a better understanding of IRAC by producing software code used in the online and offline pipelines.

IRAC INSTRUMENT SUPPORT TEAM (IST) AT SPITZER SCIENCE CENTER, CALTECH

Dr. William Reach, Team Lead
Dr. Sean Carey, Team Lead
Dr. Patrick Lowrance, Team Lead
Dr. Jason Surace, Deputy Lead
Dr. Bidushi Bhattacharya
Heidi Brandenburg
Dr. Peter Capak
Dr. David Cole
Dr. William Glaccum
Dr. Carl Grillmair
Dr. Myungshin Im
Dr. James Ingalls
Dr. Thomas Jarrett
Iffat Khan
Dr. Jessica Krick
Dr. Mark Lacy
Dr. Seppo Laine
Wen-Piao Lee
Dr. Brant Nelson
Dr. JoAnn O’Linger-Luscusk
Dr. Roberta Paladini
Dr. Bernhard Schulz
Dr. Inseok Song
Dr. Gillian Wilson

IRAC INSTRUMENT TEAM AT SAO/HARVARD

Dr. Giovanni Fazio, IRAC Principal Investigator
Dr. Joseph L. Hora, Instrument Scientist
Dr. Lori E. Allen

Dr. Matthew L. N. Ashby
Dr. Pauline Barmby
Dr. Jiasheng Huang
Dr. Massimo Marengo
Dr. S. Thomas Megeath
Dr. Michael Pahre
Dr. Brian Patten
Dr. Howard Smith
Dr. Zhong Wang
Dr. Steven P. Willner

SPITZER SCIENCE CENTER OBSERVER SUPPORT/SCIENCE USER SUPPORT

Dr. Seppo Laine
Dr. Solange Ramirez

IRAC IOC/SV

Dr. Peter Eisenhardt (JPL)
Dr. Daniel Stern (JPL)

IRAC CALIBRATION/SOFTWARE CONTRIBUTORS

Dr. Stefano Casertano (STScI)
Dr. Mark Dickinson (STScI; NOAO)
Dr. David Elliott (JPL)
Dr. Robert Gehrz (U. Minnesota)
Dr. William Hoffmann (U. Arizona)
Dr. Leonidas Moustakas (JPL)
Edward Romana (JPL)

List of Laboratories

Caltech (California Institute of Technology, Pasadena, CA)
 SAO (Smithsonian Astrophysical Observatory, Harvard, MA)
 SBRC (RaytheonVision Systems/Santa Barbara Research Center, Santa Barbara, CA)
 GSFC (Goddard Space Flight Center, Greenbelt, MD)
 JPL (Jet Propulsion Center, Pasadena, CA)
 Steward Observatory, University of Arizona, Tucson, AZ
 NASA Ames Research Center, Moffett Field, CA
 University of Rochester, Rochester, NY

Appendix H. List of Figures

Figure 2.1: IRAC Cryogenic Assembly model, with the top cover removed to show the inner components.	4
Figure 2.2: IRAC optical layout, top view. The layout was similar for both pairs of channels; the light entered the doublet and the long wavelength passes through the beamsplitter to the Si:As detector (channels 3 and 4), and the short wavelength light was reflected to the InSb detector (channels 1 and 2).	6
Figure 2.3: IRAC optics, side view. The Si:As detectors are shown at the far right of the figure. The InSb arrays are behind the beamsplitters.	7
Figure 2.4: Spectral response curves for all four IRAC channels. The full array average curve is displayed in black. The subarray average curve is in green. The extrema of the full array per-pixel transmission curves are also shown for reference. The red curves are for the pixel in the array with the highest nominal wavelength bandpass and the blue curves for the pixel in the array with the lowest nominal wavelength bandpass. For definition of the “nominal wavelength” see Hora et al. (2008). The spectral response curve data are available at	11
Figure 2.5: Optical image distortion in IRAC channels in the cryogenic mission (above) and warm mission (below). The panels show the image distortions as calculated from a quadratic polynomial model (above) and a fifth-order polynomial (below) that was fit to in-flight data. The magnitude of the distortion and the direction to which objects have moved from their ideal tangential plane projected positions is shown with arrows. The length of the arrows has been increased by a factor of ten for clarity. The maximum positional deviations across the arrays for this quadratic distortion model are less than 1.3, 1.6, 1.4, and 2.2 pixels for channels 1 – 4, respectively. The derivation of the pixel scales that are listed in Table 2.1 fully accounted for the quadratic (cryogenic data) and fifth order (warm data) distortion effects shown here.	12
Figure 2.6: Cryogenic linearity curves for the IRAC detectors. As noted in text, the warm detectors were roughly linear to 30000 DN.	16
Figure 2.7: Fowler sampling times for one pixel (Fowler N=4). The P_n (n=1,2,3,4) show the “Pedestal” readouts, and the S_n show the “Signal” readouts. T_{ex} is the effective exposure time, and $T_f - T_i$ is the “frame time,” or total time to obtain one IRAC image. The reset part of the sketch is not at the same time and voltage scale as the rest of the figure.	17
Figure 2.8: IRAC point source sensitivity as a function of frame time, for low background. The cryogenic values are on the left, and the warm mission values are on the right. To convert to MJy/sr, see equation (2.13). Subarrays are plotted in blue.	27
Figure 2.9: Similar to Figure 2.8, but for medium background.	28
Figure 2.10: Similar to Figure 2.8, but for high background.	29
Figure 3.1: IRAC AOT template. The options for selecting observing mode, fields of view, frame repeats, dithering and mapping are shown.	32
Figure 3.2: IRAC dither patterns for the “large” scale factor. The x- and y-axes are in pixels.	38
Figure 3.3: Characteristics of the cycling dither pattern. The x- and y-axes are in pixels in the left column plot. The histogram x-axis (separation) is in units of pixels (middle and right plots).	39
Figure 4.1: IRAC instrument skydark images. These images were taken during a normal campaign, and using 100 second frame time skydarks.	41
Figure 4.2: Row pixel values (in DN) of a shutter dark and a regular skydark. This plot shows the channel 2 skydark (red) pixel values along a row compared to the pixel values in a channel 2 shutter closed dark (black) in the same row. These observations used the 100 second frame times. The difference between the measurements is consistent with the astronomical background at the skydark position (1 DN = 3.7 electrons).	42
Figure 4.3: Nominal 30 second frame time skydarks (first row) and 30 second frame time shutter darks (second row) for channels 1 and 2 with relative scaling. The difference between the skydark and the shutter dark (last row) is also displayed.	43
Figure 4.4: IRAC superskyflats. Shown are the cryogenic mission (top two rows, including channels 1 – 4) and the warm mission (bottom, including channels 1 and 2) superskyflats.	45

Figure 4.5: Array location-dependent photometric correction images. The cryogenic mission corrections are at the top, and the warm mission corrections at the bottom. For the cryogenic mission correction images, channel 1 is in the upper left, channel 2 in the upper right, channel 3 in the lower left, and channel 4 in the lower right. White is the largest value (about 1.046) and black is the smallest value (about 0.915). For the warm mission correction images, channel 1 is on the left, and channel 2 on the right. Again, white is the largest value (about 1.01757, 1.03167 in channels 1 and channel 2), and black is the smallest value (0.9476, 0.9223). 56

Figure 4.6: IRAC cryogenic pixel response model, showing intrapixel sensitivity variations as a function of pixel phase. Only channel 1 (3.6 μm) and channel 2 (4.5 μm) have significant variations. 57

Figure 4.7: Distribution of normalized corrected calibration star flux densities. There is a difference in the absolute photometry of stars taken in different observing modes (shown here in the different colored distributions). The legend lists the different observing modes (full array vs. subarray, and long exposure times vs. short exposure times) as well as the number of photometry points per distribution. Channel 1 is on the left, channel 2 is on the right. 60

Figure 4.8: Cleveland dot plot showing medians and one sigma uncertainties of the distributions of photometry from four different modes shown in Figure 4.7 (subarray vs. full array and staring vs. dithering). The names of the three calibration stars considered here are shown on the y-axis, and the data points for different modes of photometry for each star are offset slightly in the y-direction for ease of viewing. Staring mode observations in the subarray and full array modes were taken at the same locations on the array (on the sweet spot pixel). 62

Figure 4.9: Images of the IRAC point response function (PRF) tables. These are shown at 3.6 (upper left), 4.5 (middle, top row), 5.8 (left, bottom row), and 8.0 μm (middle, bottom row) from the cryogenic mission and from the warm mission at 3.6 (right, upper row) and 4.5 μm (right, bottom row). The PRFs were generated from models refined with in-flight calibration test data involving a bright calibration star observed at several epochs. The PRFs are shown as they appear with 1/5 the native IRAC pixel sampling of 1.2 arcseconds to highlight the core structure. The PRFs were calculated using the Simfit routine in Hoffmann et al. (2004). The images are 128 \times 128 1/5 native IRAC pixels in size (about 31 arcseconds \times 31 arcseconds). 64

Figure 4.10: “Best” (left) and “worst” (right) channel 1 PRF images from the set of PRFs available for the cryogenic mission. A logarithmic stretch was used to highlight the low-level emission. The core of the “worst” image is a larger than the “best” image, and it has a \approx 60% higher noise pixel value. 65

Figure 4.11: Distribution of noise pixel values over the channel 1 field of view in the cryogenic mission. The image matches the BCD orientation, with pixel (1,1) in the lower left corner. The mean point source noise pixel values (averaging over many different pixel phases) were measured at the 25 positions indicated by the small squares on the image, and a quadratic surface was fit to the data, plotted here as grayscale and contours. The lowest noise pixel value is 6.79 at (x,y) position (163,128). The highest noise pixel location, in the upper left corner, is 1.6 times this, requiring 1.6 times the integration time to achieve the same signal-to-noise as for the lowest noise pixel position. 66

Figure 4.12: The IRAC extended PSFs. The cryogenic PSFs are shown on the left, with channel 1 PSF in upper left, channel 2 PSF in the middle (upper row), channel 3 in lower left, and channel 4 in the middle (lower row). The warm extended PSFs are shown on the right, with channel 1 on top and channel 2 at the bottom. See the text for how these were constructed. 69

Figure 4.13: Reaction wheel speed and centroid position as a function of time. Wheel speed changes are a few seconds in duration and this entire AOR is 11.5 hours in duration. This particular AOR shows a reaction wheel speed shift with a return to the original position. Grey lines correspond to the wheel speeds in RPM (left y-axis). Spitzer had four reaction wheels, and they all changed speed simultaneously about 75% of the way through this observation. Blue and green data correspond to the X and Y centroids of the target in the observation (right y-axis). 75

Figure 4.14: Two 0.02 second frame time samples taken during a long staring observation. The total monitoring period was 42,007.38 seconds or 11.67 hours. The left panel shows the data at the very start of the stare after the initial slew to the object, and the right panel shows the jitter at the very end of the monitoring period. 77

Figure 4.15: Spitzer pointing during the first 100 seconds after a PCS offset to the object position. The plot shows the pointing during the first 12 subarray data sets using 0.1 second frame time (6.4 seconds per subarray set). The first set, plotted in darker green, shows up on the right side of the plot, offset from the other data sets, and showing back-and-forth oscillations of about 0.05 pixels peak-to-peak. The following data sets show a much-reduced motion in successive frames, with a random walk around the reference position. 78

Figure 4.16: Two examples of the drift during 100-second periods of a long staring observation. The pointing seems to walk randomly over a region of ≈ 0.05 pixels in extent, sometimes dwelling at a position for some length of time, and then moving on a path around the pointing center..... 79

Figure 4.17: Distribution of long-term drift in both the *X* and *Y* directions as a function of time on the left and as a function of nearest in time downlink pitch angle on the right. These plots include all staring mode observations taken during the warm mission. Both plots are violin plots. Each violin-shaped object in the figure shows the median value and range for all the observations in that particular year (or at that particular pitch to earth point). Dashed lines show the median and inner quartiles of the distributions. The median values are printed at their locations. They can be thought of as smoothed histograms. Color variations between the violins have no meaning other than different years (itches) have different colors..... 80

Figure 4.18: Short-term drift. Top: duration, length, and slope of the short-term drift as a function of the pitch angle of the observation itself. Bottom: same short-term drift parameters as a function of the change in the pitch angle from the previous to the current observation. Observations are color coded by exposure time, where shorter exposures are red and longer exposures are blue. The scale and rate of the short-term drift correlate with the pitch angle and the duration of several previous observations. 81

Figure 4.19: IRAC jitter observed during a long staring observation of the Galactic Center on 2013 December 10 (PID=10060). The *X* and *Y* offsets relative to the reference position are shown for both the *X* and *Y* directions on the IRAC array. Both directions show the oscillation (approximately 0.05 pixels) caused by the spacecraft heater, with about a 40-minute period. There is also an approximately linear drift in both dimensions over the length of the observation, larger in *Y* than in *X*. 82

Figure 4.20: Amplitude and strength of the battery heater oscillation over the 2010 – 2017 period of the warm mission. Both plots are violin plots. Each violin shaped object in the figure shows the median value and range for all the observations in that particular year. Dashed lines show the median and inner quartiles of the distributions. Color variations between violins have no meaning other than different years have different colors. 83

Figure 4.21: IRAC pointing variations observed during a long staring observation on 2016 July 25 (PID=12034). This observation was similar to that in Figure 4.19, but here we do not see the spacecraft heater oscillation. 84

Figure 4.22: The 3.6 μm (left) and 4.5 μm (right) calibration star normalized flux densities as a function of time from 2013 to 2020. All flux densities are measured by aperture photometry and include 21 primary and secondary calibrators denoted with different colors. The line (and gap) in December 2015 denotes an anomaly in which IRAC was off and no observations were taken. There is no difference seen before or after this anomaly. See the text for the meaning of the various colors, and more information about the plots. 85

Figure 4.23: Median value of the 12 second skydarks plotted over time since the beginning of the warm mission. The vertical dotted lines denote two anomalies in which the array was reset. The median value was observed to settle to a new nominal level after the anomalies. The red lines give the shape of the predicted seasonal zodiacal variation normalized to the median value of the skydarks in January 2012, to help with the search for any trend changes in skydark values. See the text for more information. 86

Figure 4.24: Average number of pixels per second affected by cosmic rays in the 100 second skydarks since the beginning of the warm mission. The spike in 2012 is due to a solar flare that occurred during the time the skydark calibration data were being taken..... 87

Figure 4.25: Number of pixels determined to be hot, noisy, or dead during each observing campaign in the 100 second skydarks since the beginning of the mission. Hot and noisy pixels changed over time as some pixels recovered and others became hot or noisy. Dead pixels only increased by 10 – 20 pixels over the entire mission. 88

Figure 5.1: Data flow for processing a raw IRAC science DCE into a BCD. 91

Figure 5.2: Effect of INSBPOSDOM . INSBPOSDOM worked only on the two InSb arrays (channels 1 & 2) and reversed the sense of intensities. Left is before INSBPOSDOM ran and right is after.	93
Figure 5.3: Diagram of the wrapping of negative values due to truncation of the sign bit.	94
Figure 5.4: Application of IRACWRAPCORR to channel 1 data. The many apparently hot pixels were actually wrapped negative values, which were detected based on their data values vastly exceeding the physical saturation value for the detectors, and corrected by subtracting the appropriate value. Real hot pixels did not exceed the physical saturation value, and hence were not changed.....	95
Figure 5.5: Illustration of bit truncation. Bit truncation was used by IRAC for ground transmission, necessitating IRACNORM. The internally stored 24-bit word was truncated to 16 bits, with a sliding window set by the barrel shift value. The figure illustrates the ABARREL=4 case.	95
Figure 5.6: Correction of cable-induced bandwidth error by IRACEBWC. The illustrated data show a cosmic ray hit.	97
Figure 5.7: First-frame effect: dark counts as a function of interval between frames. This figure is for a 30 second exposure frame.....	100
Figure 5.8: Before (left) and after (right) correction of pseudo-muxbleed for channel 1. Shown is a bright source within a calibration AOR and a background of sources under the muxbleed limit.	101
Figure 5.9: Transposition of an IRAC channel 1 dark image by the IMFLIPROT module.	106
Figure 5.10: Subtraction of the median background from the readout channel images. The image on the left shows the original image divided into each of its four readout channels. The image in the middle is the median of the four readout channels. This makes the muxstripe much more apparent in the fourth readout channel image (on the right). The location of the muxstripe is shown with black arrows.	111
Figure 5.11: Profiles showing the column median versus row values for identifying muxstripe. The x-axis is in pixel units. The muxstripe is now identifiable between row pixels 125 and 200 (significantly lower values than the median background).	112
Figure 6.1: The orientation of the (C)BCDs on the sky.	117
Figure 7.1: Full array CBCD image showing rows of missing data (dark band across the image). This observation is in channel 2, 12 second HDR frame, PID=80254, AORKEY 44050944.	128
Figure 7.2: Erroneously inserted saturation correction stars in a CBCD image (left), compared to the original BCD image (right). These data are from PID=46, AORKEY 12484352. The arrows point to the sources erroneously inserted by the pipeline. There are column pull-down and banding correction artifacts in the CBCD image as well, inserted by overactive pipeline corrections.	130
Figure 7.3: Images showing the muxbleed effect (the horizontal line on both sides of a bright stellar image). The pixels on the left side of the bright source are pixels on rows following the row in which the bright source was located (and have wrapped around in the readout order of the array). The vertical (white) lines are due to the so-called "column pull-down" effect. These are 12-second BCD frames in IRAC channel 1, taken from IRAC PID=618, AORKEY 6880000. Pinstriping is also seen in these images.	131
Figure 7.4: Demonstration of the S18 pipeline muxbleed removal. The image on the left is before and the one on the right is after the correction. These are First Look Survey channel 1 data, taken from AORKEY 4958976. Note that the brightest star in the upper-left corner is heavily saturated and the current muxbleed scheme can correct muxbleed from a saturated source also.	132
Figure 7.5: A typical bandwidth effect trail in channel 4, in a 30 second frame. These data were taken from PID=1154, AORKEY 13078016.....	132
Figure 7.6: The bandwidth effect when a bright object is in the last four columns. IRC+10216, strongly saturated, is just off the right side of the channel 3 array. Even the filter ghost is saturated. The bandwidth effect appears on the left side of the array. These data were taken from PID = 124, AORKEY 5033216.....	133
Figure 7.7: IRAC channel 1 (left) and channel 2 (right) observations of a crowded field with column pull-down apparent from the brightest sources. Note that the brighter sources affect a larger number of columns. These data were taken from PID=613, AORKEY 6801408.	134
Figure 7.8: Channels 1 and 2 (top) and 3 and 4 (bottom) showing inter-channel crosstalk (dark spots near the center of the lower panels).	136
Figure 7.9: Median of channel 1 images from a calibration observation performed after observing Polaris. The five bright spots are persistent images from staring at the star while observing, while the set of criss-	

- crossing lines were generated by slews between the various pointings. These observations were taken from PID=19, AORKEY 3835904. 138
- Figure 7.10: Residual image brightness decay as a function of time interval since exposure to a first magnitude source at 3.6 μm . The residual is compared to three times the noise in the sky background as measured in an equivalent aperture. The fitted exponential decay function is plotted as the dot-dashed line. These curves have been smoothed to mitigate flux jumps due to sources at the position of the original source in subsequent images. 141
- Figure 7.11: Residual image examples: a. channel 1 positive residual images near the center of the array, PID=90175, AORKEY 47943424; b. same as previous but showing the median image of the observation that has also positive slew residuals; c. channel 1 positive slew residuals, PID=80096, AORKEY 45585920; d. channel 2 negative residual images, PID=90109, AORKEY 47828736. 142
- Figure 7.12: More residual image examples; a. channel 1, PID=90124, AORKEY 48337408 (the red arrow is pointing to an image residual); b. channel 2, negative slew residuals and column pull-down residuals PID=70044, AORKEY 40840192; c. channel 1 bright slew residual, PID=61009, AORKEY 35354880; d. channel 1 bright residual image from Reuleaux pattern dithering in center, PID=80015, AORKEY 42191104. 143
- Figure 7.13: An image of the M51 system, showing an overlay of the IRAC fields of view, with the scattered light origin zones for channels 1 and 2 overlaid. 144
- Figure 7.14: Channel 1 image showing scattered light on both sides of a bright star. The scattered light patches are marked with white "S" letters. The images were taken from PID=30 data. 145
- Figure 7.15: Similar to Figure 7.13 but for channel 2. 146
- Figure 7.16: Similar to Figure 7.13 but for channel 3. 147
- Figure 7.17: Similar to Figure 7.13 but for channel 4. The scattered light patches are pointed to by black arrows. 148
- Figure 7.18: Typical image sections showing the banding effect. These are channel 3 (left) and channel 4 (right) images of the same object (S140), adopted from a report by R. Gutermuth. These data were taken from PID=1046, AORKEY 6624768. 149
- Figure 7.19: Filter and beamsplitter ghosts in IRAC. Top: Channel 1 and 2 mosaics of saturated images of Fomalhaut near the center of each array from PID=90, AORKEY 4875776. The panels are 180 pixels \times 140 pixels of 0.6 arcseconds; the greyscale is logarithmic. Bottom: channel 3 and 4 single, highly saturated images of Sirius near the center of each array from PID=1156, AORKEY 16412416. The panels are 90 raw pixels \times 70 raw pixels; the greyscale stretch is square-root. The channel 3 and 4 filter ghosts are nearly saturated and the bandwidth effect is saturated. Even the optical banding (light diffracted and internally reflected within the arrays) in the column containing the star center suffers the bandwidth effect, which appears as bright vertical spikes 4 and 8 pixels to the right of the center of the star. 151
- Figure 7.20: Pupil ghost in channel 2 from V416 Lac. 152
- Figure 7.21: Part of the channel 1 mosaic (from observations in PID=181; AORKEYs 5838336, 5838592, 5839872, and 5840128) of the SWIRE field near Mira showing the 24 arcminute radius ring of stray light from the telescope. The dimensions of the image are. 153
- Figure 7.22: Channel 2 images from the SWIRE map showing stray light splotches from Mira, which was about 30 arcminutes away. Successive pairs of images were slightly dithered. The last pair is about 5 arcminutes from the first pair, but has a similar splotch. Note the absence of any stray light in the second image, though it was centered only a few pixels away from the first image. The images are from PID=181, AORKEY 5838336; EXPID 187 – 192, 199, and 200. 154
- Figure 7.23: The central 128 pixels \times 128 pixels of IRAC 12-second images taken on January 20, 2005 during a major solar proton event. Channels 1 and 2 are top left and top right; channels 3 and 4 are bottom left and bottom right. Except for the bright star in channels 1 and 3, almost every other source in these images is a cosmic ray. These data are from observations in PID=3126. 155
- Figure 8.1: Correcting photometric measurements of calibration star NPM1+67.0536 using the pixel phase and array location-dependent corrections. Black curves show the cumulative distribution of aperture photometry measurements throughout the cryogenic mission, for which a value is within a given per cent of the mean. Blue curves show the distribution after correction using an earlier (now obsolete) set of location-dependent functions. Red curves are the result of the improved (now final) correction. A gray

horizontal line at 68% (1σ for a Gaussian distribution) is labeled with the corresponding spread in values for each of the three distributions.	158
Figure 8.2: Extended source flux aperture correction factors; solid lines represent exponential function fits to the data. Also indicated are correction factors derived from zodiacal light tests, and Galactic HII region tests (e.g., GLIMPSE vs. MSX).	161
Figure 8.3: Extended source flux correction factors for galaxies (solid lines) versus the PSF aperture correction factors (dotted lines). The main difference between the two is the truly diffuse scattering internal to the array.	162
Figure 8.4: Noise versus binning length in channel 1. To make this plot, the surface brightness was measured in nine regions across an object-masked mosaic. These regions are not near bright galaxies, stars, or diffuse plumes. The noise is defined as the standard deviation of those nine regions. The box size is incrementally increased until the box length is many hundreds of pixels. For reference the solid line shows the expected linear relation.	164
Figure 8.5: Similar to Figure 8.4 but for channel 2.	165
Figure 8.6: Noise as a function of exposure time (number of frames) in channel 1. The results from the warm mission data are shown with crosses and the expected behavior with the solid line. The results from the cryogenic mission are shown with open squares and the expected behavior with the dashed line.	166
Figure 8.7: Similar to Figure 8.6 but for channel 2.	167
Figure 8.8: Noise in electrons as a function of binning scale showing the relative strength of instrument systematics. Noise contributions from the source and background are shown as diagonal lines. Known instrumental systematics are shown as horizontal lines. For reference, also shown are the strengths of a hot Jupiter (1%) transit, 0.1% eclipse, and a 70 ppm super-Earth transit.	169
Figure 8.9: Channel 2 photometric gain versus diagonal sub-pixel position, based on a crude Gaussian model of the pixel. The vertical ranges show the amount of gain variation over about 0.2 pixels at the peak of gain (green) and near the corner of the pixel (red).	171
Figure 8.10: The map of intrapixel photometric gain, or “pmap” for channel 2 post-cryogenic data. This is the pmap built from data collected as of 2014/09/04. Note that gain is not symmetric around the center of the sweet spot and that the peak is not at the nominal center of the pixel.	172
Figure 8.11: Distribution of average noise pixels per AOR vs. exposure time. All ≈ 1300 staring mode AORs from the warm mission through June 2017 were used. Each of the gray shapes represents the distribution for the corresponding exposure time. Red lines show the median value per exposure time and are marked with that median noise pixel value. The total number of AORs per exposure time bin is printed at the top of the plot. We use 3σ clipping to remove outliers, such as those that fell far away from the sweet spot.	174
Figure 8.12: x , y , noise pixels, and flux values as a function of time over five simulated AORs. Note the noise pixel spikes at 16 and 30 hours which are seen in the noise pixel and flux plots, but not in the x and y position plots. This simulated dataset is of WASP 52.	175
Figure 8.13: Signal-to-noise ratio versus aperture size for the WASP-14b exoplanet, normalized to an aperture size of 2.5 pixels in radius.	176
Figure 8.14: Residual nonlinearity in warm mission channel 2 data. These plots show linearity-corrected aperture flux as a function of well depth (fluence) for a set of targets, measured on the “sweet spot” of Channel 2. Top: binned aperture flux measurements of three targets, normalized to the median of each target. Well depth was varied using instrument engineering requests (IERs) to vary the frame time and corrected with special dark frames obtained the same way. Data were binned by frame time. A 4th order polynomial fit to the data is overlaid as a dashed curve. Names of the stars are labeled, along with average flux densities. Bottom: Unbinned aperture flux vs. fluence data for 15 additional stars measured using AORs, color-coded by star. Frame times are labeled (in seconds) at the location of the median flux and fluence for a given frame time and star, with the qualifier “S” or “F” to denote full or sub-array readout mode. For comparison, we have overlaid the fit from the top plot. Measurements with perfectly corrected nonlinearity should lie on a straight horizontal line.	178
Figure 8.15: Peak pixel value in DN vs. distance from the sweet spot in channel 2. Sweet spot is defined here to be [15.12, 15.1] (when [0,0] is defined as the bottom left corner). These stars are all observed with	

multiple snapshots, and include the gain map calibration star itself taken with two different frame times. The second plot shows the different slope when using a 28 K source. 179

Figure 8.16: Bias Level in DN as a function of time. Bias level changes on long time scales (≈ 10 hours). Bias level as a function of time appears to not be repeatable from AOR to AOR. The data set used to make these plots consists of ten serendipitous staring mode AORs (five in each channel, 0.4 second frame time) in the off-field position, so theoretically empty of stars, although there are some stars in these observations. This bias change is not dependent on the frame delay (all frame delays show the change as a function of time). From these five AORs per channel, the maximum deviation is ≈ 2 DN in channel 1 and ≈ 0.5 DN in channel 2. These are binned over the whole BCD, so each point includes the mean from all 64 subframes. Only one amplifier is shown. Blue and black points show the different frame delays, for which there is no correlation with the shape of the long time scale change. Here we show two plots for each channel to demonstrate the range of level changes. 182

Figure 8.17: Channel 1 and 2 ensembles of primary calibrator fluxes as a function of time since the start of the mission. Black points show the ensemble of primary calibrators while green stars show the cosmic ray counts..... 185

Figure 8.18: Individual calibration stars as a function of time. There is no evidence for a single outlier star as the source of the flux degradation trend..... 186

Figure 8.19: A Monte Carlo simulation of calibration flux vs. time stamp slopes. This figure shows what the slopes would be if the time stamps for each data point were shuffled using a Fisher – Yates shuffle. The actual measured slope for channel 2 is shown with the dashed line. Because this measured slope is outside of 1σ , we take the slope to be significant..... 186

Figure 8.20: Skydark variations in channel 1 over the course of the warm mission. The y-axis is a difference of the flux density present in the darks after an average dark frame has been removed. 188

Figure 8.21: Eclipse depths for ten visits to XO-3b, as computed via various methods. The group of points for each epoch is separated to minimize confusion. Error bars in this plot are symmetric; in cases where the technique returned asymmetric uncertainties, we used the largest of the two values. We show the results for the separate visits to the left of the gray vertical line, and the average results to the right. Error bars on the separate visits are the uncertainties reported by the technique. Error bars on the averages are the uncertainties in the weighted mean, adjusted for “underdispersion” using the scatter in the group of measurements. The horizontal red lines display the grand mean for all the results, and its uncertainty.. 190

Figure 8.22: Similar to Figure 8.21. A blue horizontal line indicates the eclipse depth input to the simulations, 1875 ppm..... 191

Figure 8.23: Actual precision reached for published, single epoch, IRAC observations. Plots are normalized at a binning size of one. The dashed black line is photon noise limited. The dashed grey line is two (1.5) times the photon noise limit for channel 1 (2). The third plot is a zoom-in on channel 2. 193

Appendix I. Appendix List of Figures

Figure C.1: PRF fits vs. aperture photometry for selected IRAC calibration star CBCDs. The vertical axis is the fractional difference between the PRF fit and corrected aperture photometry. The aperture photometry for IRAC channels 3 and 4 is in a 3-pixel radius with a 12 – 20 pixel background annulus and an aperture correction factor from this Handbook. For IRAC channels 1 and 2, it is in a 10-pixel radius with the same annulus. Short black dashed lines are the expected annulus correction needed. Long blue dashed line is the offset estimated from a weighted average of the data. Note this is essentially the expected value for IRAC channels 3 and 4. But IRAC channel 1 (and IRAC channel 2 to a lesser extent) requires a pixel phase correction (see text).....	223
Figure C.2: Data from Fig. C.1, with IRAC channels 3 and 4 corrected for the annulus contribution, and IRAC channels 1 and 2 corrected for the pixel phase effect.....	224
Figure C.3: APEX PRF-fitted photometry in the Serpens test field, with array location-dependent PRFs vs. aperture photometry. The aperture has a 3 pixel radius, the background annulus is 12 – 20 pixels. The aperture fluxes have been corrected using the aperture corrections in Table 4.8. The IRAC channel 3 and 4 PRF fluxes have been corrected for annulus contribution.....	226
Figure C.4: APEX PRF-fitted photometry with a PRF Map vs. aperture photometry in the Serpens test field. PRF and aperture fluxes have been corrected as described in the text.....	227
Figure C.5: The 25 PRF positions on an IRAC BCD.....	231
Figure D.1: A BADTRIG problem in staring mode data. Left side vertical axis is for the grey lines and wheel speed RPM. The right-side vertical axis corresponds to x (blue) and y (green) centroids of the AOR as a function of sclk time. BADTRIG is set for the x-positions which have centroids of 14.5 after sclk time of 1.058017×10^9	235
Figure D.2: Background measured in electrons as a function of time for 0.02 second subarray data.....	237
Figure D.3: Same as Figure D.2, only now with each data point connected by a line, and zoomed in on the background modulation portion of the light curve.	237
Figure D.4: Same as Figure 4.13, except this AOR was during the 2013 anomaly. A wheel speed shift occurs at time 1.057755, but the centroids never return to their pre-wheel-shift positions.....	241
Figure D.5: x- and y-centroids as a function of time. The pointing history file changes just beyond sclk time 1.06246×10^9 , which changes the expected position of the star in the image, and therefore makes the centroiding algorithm essentially fail to find the target. This AOR has been re-processed and now no longer shows this problem.....	242
Figure D.6: x- and y-positions as a function of time for a WASP-15 AOR. The position points which do not follow the sawtooth pattern are caused by CRs.	243
Figure D.7: Strong horizontal dark stripes in a 6-second frame time raw image in channel 2.	245

Appendix J. List of Tables

Table 2.1: IRAC image quality properties. The second set of numbers for channels 1 and 2 are for the warm mission, and the rest of the numbers are for the cryogenic mission. Noise pixels are defined in Section 2.2.2.	8
Table 2.2: IRAC channel characteristics.	9
Table 2.3: IRAC read noise. The second set of numbers in channels 1 and 2 are for the warm mission.	13
Table 2.4: Useful quantities for IRAC sensitivity calculations. The second set of numbers in channels 1 and 2 are for the warm mission.	21
Table 2.5: Background brightness in IRAC channels. The second set of numbers in channels 1 and 2 are for the warm mission. $I_{\nu f_s}$ is the expected background brightness on the detectors, F_{ν}^{BG} is the flux density on each pixel due to the background brightness, and B is the background brightness on the detectors in electrons per second units, using the FLUXCONV values given in Section 4.3 of this Handbook, and the Gain values in Table 2.4.	21
Table 2.6: Fowler numbers for IRAC frames. The numbers in parentheses are for channels 1 and 2 in the warm mission if different from the cryogenic values. Wait ticks are defined in Section 2.4.3.	23
Table 2.7: IRAC High Dynamic Range (HDR) framesets.	24
Table 2.8: IRAC point-source sensitivity, based on Equation (2.6), low background (1σ , μJy). The second set of numbers in parentheses for channels 1 and 2 are for the warm mission.	25
Table 2.9: Same as Table 2.8 but for medium background (1σ , μJy).	26
Table 2.10: Same as Table 2.8 but for high background (1σ , μJy).	27
Table 2.11: Maximum unsaturated point source (in mJy), as a function of IRAC frame time. The second set of numbers in parentheses are for channels 1 and 2 are in the warm mission.	31
Table 3.1: Characteristics of the dither patterns.	37
Table 4.1: IRAC primary calibrator quoted flux densities and color corrections.	47
Table 4.2: The photometric calibration and zero magnitude flux densities for IRAC. Warm mission corrections are given as the second set of values in channels 1 and 2. Note that at the beginning of the warm mission the calibration was changing frequently. Different FLUXCONV values for these first months can be found on IRSA's IRAC web pages (under "Warm IRAC Characteristics").	48
Table 4.3: IRAC nominal wavelengths and bandwidths. R_{max} is the maximum spectral response.	52
Table 4.4: Color corrections for power-law spectra, $F_{\nu} \propto \nu^{\alpha}$	52
Table 4.5: Color corrections for blackbody spectra.	52
Table 4.6: Color corrections for zodiacal light spectrum.	53
Table 4.7: Color corrections for NGC 7023 (PAH-dominated) spectrum.	53
Table 4.8: Cryogenic and warm IRAC aperture corrections (warm corrections are given as the second set of values in channels 1 and 2). The radius is in native (≈ 1.2 arcsecond) pixels. To get arcseconds, multiply these numbers by the pixel size from Table 2.1.	59
Table 4.9: Pointing uncertainties.	73
Table 5.1: Bandwidth correction coefficients.	98
Table 6.1: Sample IRAC file names.	117
Table 7.1: Definition of bits in the pmask. The pipeline used all the bits.	125
Table 7.2: Definition of bits in the "imask." The pipeline used bits 3 and 8–14.	126
Table 7.3: Fluence thresholds required for warm mission channel 2 residual image flagging.	140
Table 7.4: Warm mission residual image durations.	140
Table 7.5: Coefficients for channel 1 and 2 ghost locations.	150
Table 8.1: IRAC extended source photometric correction coefficients.	163
Table 8.2: IRAC surface brightness correction factors.	163
Table 8.3: Approximate levels of the residual fluxes as a function of channel and frame time.	188

Appendix K. Appendix List of Tables

Table C.1: Correction factors for PRF flux densities.....	222
Table D.1: Examples of datasets with known noise pixel spikes.	238

Appendix L. Version Log

Version 4.0 (Final), 2021 September:

Added information about superboresight pointing keyword changes into Section 5.3.2.
Added information about the first frame effect into Section 5.1.10. Added the DOI into Section 1.1.

Version 3.0.1, 2021 January:

Updated uncertainty values in Table 4.2.

Version 3, 2020 December:

Rearranged large parts of the document, added high precision photometry and warm mission information.

Version 2.1.2, 2015 November:

S18.18 warm mission information added to Appendix A. Typo in equation in Section 2.2.2 corrected.

Version 2.1.1, 2015 October:

S19.2 added to Appendix A.

Version 2.1, 2015 February:

Added information about the warm mission to several sections and updated the aperture corrections.

Version 2.0.3, 2013 February:

Typo in Table 4.7 fixed: the 3.6 μm infinite value should have been 0.944 instead of 0.994.

Version 2.0.2, 2012 March:

S18.24 added to Appendix A.

Version 2.0.1, 2011 June:

Reference to Krick et al. added to Section 4.11.5.

Version 2.0, 2011 April:

Discussion about artifact mitigation was added to Chapter 5 (5.3).

A new processing version S18.18 BCD FITS header replaced the old header file in Appendix D.

Discussion of a few new header keywords, including timing keywords and bad data value keywords, was added in Section 6.2.

The file names in Table 6.1 were updated.

Added information about warm mission persistent images and edited the information on the cryogenic mission persistent images in Section 7.2.8.

Added information about the effect of very deep surface brightness level observations in Section 4.11.

Added an Index at the end of the document.

Version 1.0, 2010 February:

The first version of the IRAC Instrument Handbook, which includes information from the old IRAC Data Handbook, the old IRAC Pipeline Description Document, the cryogenic Spitzer Observer's Manual (SOM), and Spitzer Science Center web pages.

Bibliography

- Ábrahám, P., et al. (1997). Search for brightness fluctuations in the zodiacal light at 25 MU M with ISO. *Astronomy and Astrophysics*, 328, 702.
- Anderson, J. & King, I. R. (2000). Toward High-Precision Astrometry with WFPC2. I. Deriving an Accurate Point-Spread Function. *PASP*, 112, 1360.
- Arendt, R. et al. (2008). The Mid-Infrared Colors of the Interstellar Medium and Extended Sources at the Galactic Center. *The Astrophysical Journal*, 682, 384.
- Arendt, R. G., Fixsen, D. J., & Moseley, S. H. (2000). Dithering Strategies for Efficient Self-Calibration of Imaging Arrays. *Astrophysical Journal*, 536, 500.
- Ballard, S. et al. (2010). A Search for a Sub-Earth-Sized Companion to GJ 436 and a Novel Method to Calibrate Warm Spitzer IRAC Observations. *PASP*, 122, 1341.
- Beichman, C. A., Neugebauer, G., Habing, H. J., Clegg, P. E., Chester, T. J. . (1988). *Infrared Astronomical Satellite (IRAS) Catalogs and Atlases. Volume I: Explanatory Supplement*.
- Bertin, E. & Arnouts, S. (1996). SExtractor: Software for source extraction. *Astronomy & Astrophysics Supplement*, 117, 393.
- Blommaert, J., et al. (2003). *CAM – The ISO Camera ISO Handbook, Vol. 2, Ver 2.0*. Retrieved from http://iso.esac.esa.int/manuals/HANDBOOK/cam_hb/
- Buzasi, D. L. et al. (2015). Serendipitous science from the K2 mission. *arXiv:1511.09069*.
- Carey, S. J., et al. (2012). Absolute Photometric Calibration of IRAC - Lessons Learned Using Nine Years of Flight Data. 8442, p. Z1. SPIE.
- Charbonneau, D., et al. (2005). Detection of Thermal Emission from an Extrasolar Planet. *ApJ*, 626, 523.
- Charbonneau, D., et al. (2008). The Broadband Infrared Emission Spectrum of the Exoplanet HD 189733b. *Astrophysical Journal*, 686, 1341.
- Cohen, M., Megeath, S. T., Hammersley, P. L., Martín-Luis, F., Stauffer, J. (2003). Spectral Irradiance Calibration in the Infrared. XIII. “Supertemplates” and On-Orbit Calibrators for the SIRTf Infrared Array Camera. *AJ*, 125, 2645.
- Deming, D. et al. (2015). Spitzer Secondary Eclipses of the Dense, Modestly-irradiated, Giant Exoplanet HAT-P-20b Using Pixel-level Decorrelation. *ApJ*, 805, 132.
- Demory, B.-O., et al. (2016). A map of the large day-night temperature gradient of a super-Earth exoplanet. 532, p. 207. Nature.
- Estrada, A. D., et al. (1998). Si:As IBC IR Focal Plane Arrays for Ground-Based and Space-Based Astronomy. 3354, p. 99. SPIE.
- Evans, T. M. et al. (2015). A uniform analysis of HD 209458b Spitzer/IRAC light curves with Gaussian process models. *MNRAS*, 451, 680.
- Fazio, G. G., et al. (2004). The Infrared Array Camera (IRAC) for the Spitzer Telescope. *ApJS*, 154, 10.
- Fixsen, D. J., Moseley, S. H., Arendt, R. G. (2000). CALIBRATING ARRAY DETECTORS. *Astrophysical Journal*, 128, 651.
- Fraine, J. et al. (2013). Spitzer Transits of the Super-Earth GJ1214b and Implications for its Atmosphere. *ApJ*, 765, 127.
- Franceschini, A. et al. (1991). Galaxy counts and contributions to the background radiation from 1 μ m to 1000 μ m. *A&AS*, 89, 285.
- Fruchter, A. G. & Hook, R. N. (2002). Drizzle: A Method for the Linear Reconstruction of Undersampled Images. *PASP*, 114, 144.

- Gillon, M. et al. (2010). The thermal emission of the young and massive planet CoRoT-2b at 4.5 and 8 μm . *A&A*, *511A*, 3.
- Grillmair, C., et al. (2014). Improving our understanding of the Spitzer Space Telescope's pointing drifts. *Proc. SPIE*, (pp. Vol 9143, 59G).
- Hauser, M. G., et al. (1998). *COBE Diffuse Infrared Background Experiment (DIRBE) Explanatory Supplement*. Retrieved from http://lambda.gsfc.nasa.gov/product/cobe/dirbe_exsup.cfm
- Hoffmann, W. F., Hora, J. L., Fazio, G. G., Deutsch, L. K., & Dayal, A. (1998). MIRAC2: a Mid-Infrared Array Camera for Astronomy. *3354*, p. 24. SPIE.
- Hoffmann, W. F., Hora, J. L., Mentzell, J. E., Marx, C. T., Eisenhardt, P. R., Carey, S. J., Megeath, S. T., & Schwenker, J. T. (2004). Determination of Spitzer Space Telescope Focus from IRAC Images Without A Focus Slew. *5487*, p. 86. SPIE.
- Hora, J. L., et al. (2004). In-Flight Performance And Calibration of the Infrared Array Camera (IRAC) for the Spitzer Space Telescope. *5487*, p. 244. SPIE.
- Hora, J. L., et al. (2008). Photometry Using the Infrared Array Camera on the Spitzer Space Telescope. *PASP*, *120*, 1233.
- Ingalls, J. G. et al. (2016). Repeatability and Accuracy of Exoplanet Eclipse Depths Measured with Post-cryogenic Spitzer. *AJ*, *152*, 44.
- Knutson, H. A. et al. (2011). A Spitzer Transmission Spectrum for the Exoplanet GJ 436b, Evidence for Stellar Variability, and Constraints on Dayside Flux Variations. *ApJ*, *735*, 27.
- Knutson, H. A. et al. (2012). 3.6 and 4.5 μm Phase Curves and Evidence for Non-equilibrium Chemistry in the Atmosphere of Extrasolar Planet HD 189733b. *ApJ*, *754*, 22.
- Krick, J. e. (2018). Using the Spitzer IRAC science archive for instrument trending. *SPIE Proceedings*, *10698*, p. 106985Y.
- Krick, J. E. et al. (2016). Spitzer IRAC Sparsely Sampled Phase Curve of the Exoplanet Wasp-14B. *824*, 27.
- Krick, J., et al. (2011). Spitzer IRAC Low Surface Brightness Observations of the Virgo Cluster. *ApJ*, *735*, 76.
- Lacy, M., et al. (2005). The Infrared Array Camera Component of the Spitzer Space Telescope First Look Survey. *ApJS*, *161*, 41.
- Lauer, T. R. . (1999). The Photometry of Undersampled Point-Spread Functions. *PASP*, *111*, 1434.
- Lewis, N. K. et al. (2013). Orbital Phase Variations of the Eccentric Giant Planet HAT-P-2b. *ApJ*, *766*, 95.
- Lowrance, P. J. et al. (2016). Spitzer Infrared Array Camera (IRAC) Pipeline: final modifications and lessons learned. *Proceedings of the SPIE*, *9904*, p. 5Z.
- Makovoz, D. & Khan, I. (2005). Mosaicking with MOPEX. In M. B. P. Shopbell (Ed.), *ASP Conf. Series*. *347*, p. 81. San Francisco: PASP.
- Makovoz, D. & Marleau, F. (2005). Point-Source Extraction with MOPEX. *PASP*, *117*, 1113.
- Mighell, K. J., Glaccum, W., Hoffmann, W. . (2008). Improving the Photometric Precision of IRAC Channel 1. *7010*, p. 70102W. SPIE.
- Morello, G. et al. (2015). Revisiting Spitzer Transit Observations with Independent Component Analysis: New Results for the GJ 436 System. *ApJ*, *802*, 117.

- Quijada, M. A., Marx, C. T., Arendt, R. G., & Moseley, S. H. (2004). Angle-of-Incidence Effects in the Spectral Performance of the Infrared Array Camera of the Spitzer Space Telescope. *5487*, p. 244. SPIE.
- Reach W. T. et al. (2005). Absolute Calibration of the Infrared Array Camera on the Spitzer Space Telescope. *PASP*, *117*, 978.
- Reach W. T., Morris, P., Boulanger, F., & Okumura, K. (2003). The Mid-infrared Spectrum of the Zodiacal and Exozodiacal Light. *Icarus*, *164*, 384.
- Schuster, M. T., Marengo, M., & Pattern, B. M. . (2006). IRACproc: a software suite for processing and analyzing Spitzer/IRAC data. *6270*, p. 20. SPIE.
- Shupe, D., Moshir, M., Li, J., Makovoz, D., Narron, R., Hook, R. N. (2005). The SIP Convention for Representing Distortion in FITS Image Headers. *ASP Conf. Series*. *347*, p. 491. San Francisco: PASP.
- Stevenson, K. B. et al. (2012). Transit and Eclipse Analyses of the Exoplanet HD 149026b Using BLISS Mapping. *ApJ*, *754*, 136.
- Stevenson, K. B. et al. (2014). Transmission Spectroscopy of the Hot Jupiter WASP-12b from 0.7 to 5 μm . *AJ*, *147*, 161.
- Zellem, R. T. et al. (2014). The 4.5 μm Full-orbit Phase Curve of the Hot Jupiter HD 209458b. *ApJ*, *790*, 53.

Index

- 2MASS*, 73, 109, 113, 118, 120, 122, 146, 193, 194, 200, 202, 204, 205, 229
- anneal*, 48, 126, 138, 140, 208, 209
- AORKEY*, 2, 119, 121, 122, 128, 131, 132, 133, 134, 138, 142, 143, 149, 151, 153, 154, 224, 227, 229, 234, 238, 240, 241
- aperture correction*, 58, 59, 70, 157, 159, 160, 162, 163, 199, 211, 213, 215, 216, 220, 222, 223, 225, 226, 302
- extended source, 160, 161, 163
- infinite aperture, 159, 219
- aperture photometry*, 3, 20, 46, 66, 67, 85, 135, 149, 157, 158, 160, 162, 173, 180, 181, 183, 187, 197, 198, 199, 212, 213, 214, 216, 217, 220, 221, 223, 225, 226, 227, 228, 229, 239, 244, 245, 246
- extended source, 59, 135, 158, 160
- optimal size, 175, 176
- point source, 54, 58, 135, 157, 211
- APEX*, 64, 67, 196, 197, 199, 214, 217, 218, 219, 220, 221, 225, 226, 227, 229, 230
- array location-dependent photometric correction*, 7, 44, 46, 54, 56, 58, 72, 85, 105, 127, 157, 158, 183, 198, 212, 213, 215, 225, 226, 230, 246
- artifact correction*, 2, 198, 200
- astrometry*, 37, 70, 71, 72, 74, 113, 193, 200, 205, 217, 241
- Astronomical Observation Request (AOR)*, 2, 34, 36, 75, 99, 101, 108, 113, 114, 116, 119, 121, 123, 125, 139, 140, 170, 173, 174, 176, 177, 181, 182, 193, 199, 200, 201, 202, 203, 204, 205, 220, 240, 241, 242, 244
- Astronomical Observation Template (AOT)*, 2, 22, 32, 33, 35, 72
- average image*, 119, 208
- background*, 1, 3, 10, 19, 20, 21, 22, 24, 25, 26, 27, 28, 29, 31, 40, 42, 44, 46, 48, 52, 54, 55, 58, 66, 67, 85, 101, 102, 103, 104, 105, 108, 110, 111, 112, 113, 114, 120, 123, 124, 125, 127, 129, 135, 139, 140, 141, 144, 145, 154, 157, 159, 160, 162, 166, 167, 168, 175, 181, 187, 194, 197, 198, 199, 202, 205, 207, 209, 211, 212, 213, 214, 217, 220, 221, 223, 226, 228, 229, 230, 231, 235, 236, 237, 239, 244
- estimation, 197
- modulation, 236, 237
- banding*, 108, 109, 110, 126, 134, 148, 149, 151, 199, 203, 204, 210, 224
- bandpass*, 7, 9, 11, 54
- bandwidth effect*, 68, 124, 126, 132, 133, 151, 211, 214
- barrel shift*, 93, 95, 240
- Basic Calibrated Data (BCD)*, 2, 3, 10, 13, 17, 33, 34, 40, 46, 55, 58, 66, 68, 71, 76, 89, 91, 92, 99, 105, 106, 107, 108, 109, 111, 113, 114, 116, 117, 119, 120, 122, 123, 124, 125, 127, 129, 130, 131, 134, 146, 147, 150, 154, 155, 157, 159, 176, 180, 181, 182, 193, 194, 195, 196, 197, 198, 200, 201, 202, 203, 204, 206, 207, 208, 212, 213, 218, 220, 224, 226, 229, 231, 232, 234, 235, 236, 240, 247, 303
- orientation, 106, 116
- uncertainty image, 195, 196, 200, 212, 214
- battery heater*, 82, 83, 170
- beamsplitter*, 5, 6, 7, 9, 10, 105, 151
- binning*, 164, 168, 178, 182, 183, 191, 193
- large scales, 165
- medium scales, 165
- small scales, 165
- temporal, 167
- boresight*, 152, 169, 205
- calibration, 73, 107
- pointing history file, 107, 113, 120, 208
- bright target*, 28, 33, 67, 87, 108, 109, 110, 111, 112, 120, 123, 129, 130, 131, 132, 133, 134, 135, 136, 138, 139, 140, 146,

147, 148, 152, 153, 155, 170, 187, 194,
 199, 203, 204, 206, 209, 210, 211, 227
calibration, 1, 4, 5, 7, 15, 18, 33, 35, 36, 40,
 41, 44, 46, 47, 48, 49, 50, 55, 58, 64, 67,
 68, 71, 82, 86, 87, 89, 99, 101, 102, 103,
 104, 105, 106, 107, 112, 116, 118, 120,
 122, 126, 138, 145, 159, 160, 162, 163,
 166, 196, 205, 206, 207, 208, 209, 211,
 212, 213, 214, 216, 217, 219, 220, 221,
 228, 230, 234, 282
absolute, 45, 46, 158
 accuracy, 46
 extended source, 158
 repeatability, 46
star, 3, 8, 15, 40, 45, 46, 58, 59, 60, 62,
 64, 68, 84, 85, 120, 157, 158, 179, 183,
 186, 199, 201, 213, 216, 217, 220, 221,
 223
 primary, 46, 47, 84, 183, 185
 secondary, 46, 84
 zero magnitude flux density, 48
centroid, 34, 46, 75, 76, 80, 157, 172, 220,
 230, 232, 235, 238, 240, 241, 242, 245
channel. *See* *detector:channel*
chromatic aberration, 7
cold electronics, 98, 101
cold stops, 5
color correction, 10, 46, 47, 48, 49, 50, 51,
 52, 53, 198, 213, 215, 230
 spectral line, 53
column pull-down, 108, 110, 126, 131, 133,
 134, 143, 148, 156, 200, 203, 204, 224
column pull-up, 148
columns, 9, 35, 93, 102, 110, 121, 123, 124,
 130, 132, 133, 134, 148, 149, 197, 199,
 205
Command & Data Handling (C&DH), 5, 18,
 79, 170
confusion noise, 24, 29, 197
contributed software, 204
convolution, 158, 218
coolant
 depletion, 5
corrected BCD (CBCD), 2, 3, 33, 34, 40, 55,
 66, 71, 108, 109, 110, 112, 114, 117, 121,
 122, 123, 127, 128, 129, 131, 132, 150,
 194, 196, 197, 198, 200, 201, 202, 203,
 211, 212, 213, 214, 216, 220, 221, 223,
 225, 229, 230, 232
correlated noise, 76, 170, 171, 172, 188,
 189, 191
 removal techniques, 188
cosmic rays, 75, 87, 97, 106, 116, 123, 133,
 149, 154, 155, 156, 183, 185, 193, 210,
 216, 242
crosstalk, 123, 126, 135, 136
cryogenic assembly (CA), 4, 5, 96
Cryogenic Assembly (CA), 5
cryogenic mission, 2, 5, 8, 12, 13, 15, 18, 22,
 23, 25, 26, 27, 28, 29, 32, 33, 35, 40, 44,
 45, 48, 55, 56, 57, 59, 64, 65, 66, 67, 69,
 74, 105, 124, 127, 136, 137, 140, 158,
 166, 183, 194, 198, 200, 219, 246, 303
Cryogenic Telescope Assembly (CTA), 5
dark, 20, 24, 41, 43, 96, 99, 100, 102, 103,
 104, 116, 123, 126, 160, 166, 178, 187,
 196
 offset, 48
 superdark, 180
dark current, 40, 98, 101, 123, 124, 125,
 159, 198, 228
darkdrift, 102, 204, 205
data
 units, 19, 20, 53, 70, 71, 104, 106, 115,
 117, 120, 129, 158, 159, 211, 212, 214,
 220, 230
Data Collection Event (DCE), 2, 89, 91,
 107, 108, 117, 119, 121, 122, 126, 206,
 208, 239
data collection rate, 18
data number (DN), 15, 16, 21, 48, 92, 93,
 94, 95, 96, 97, 98, 102, 103, 105, 106,
 107, 109, 117, 120, 124, 128, 129, 133,
 135, 176, 179, 182, 201, 208
DCENUM, 119, 122
detector, 5, 9, 10, 16, 20, 24, 71, 94, 103,
 105, 149, 182
 array, 13
 bias, 5, 8, 40, 85, 87, 102, 168, 180, 182,
 194, 198, 205
 channel, 5, 6, 7, 8, 9, 10, 11, 12, 13, 19,
 20, 21, 22, 24, 25, 29, 30, 31, 33, 34,

42, 48, 52, 53, 56, 57, 58, 59, 60, 65,
 66, 67, 69, 70, 73, 74, 92, 95, 97, 101,
 102, 103, 104, 105, 106, 107, 109, 111,
 112, 113, 116, 119, 121, 122, 123, 124,
 125, 127, 129, 130, 131, 132, 133, 134,
 135, 136, 137, 138, 139, 142, 144, 147,
 148, 149, 150, 151, 152, 153, 156, 160,
 163, 164, 165, 166, 167, 168, 178, 179,
 183, 185, 187, 188, 194, 195, 199, 200,
 204, 205, 206, 207, 208, 209, 212, 213,
 219, 220, 221, 223, 224, 225, 226, 227,
 239, 244
 Fowler, 16, 17, 20, 22, 23, 33, 90, 92, 95,
 96, 98, 102, 104, 107, 119, 124, 129,
 130, 177
 full-well, 103
 linearity, 176
 residual nonlinearity, 177, 178
 readout, 14, 17, 22, 33, 96, 97, 101, 102,
 103, 104, 111, 112, 131, 205
 size, 5
 temperature, 5, 8, 10, 14, 15, 48, 87, 101,
 102, 136
 well depth, 178
diffuse emission, 163
diffuse scattering, 158
distortion, 7, 8, 12, 13, 37, 54, 70, 71, 107,
 115, 118, 200, 205, 219
 color dependency, 7
dithering, 10, 20, 21, 22, 32, 33, 34, 35, 36,
 37, 38, 39, 44, 55, 59, 60, 61, 62, 67, 72,
 73, 80, 105, 121, 127, 135, 136, 139, 143,
 147, 154, 180, 183, 196, 198, 209
 pattern, 35, 36, 37, 38, 39, 109
documentation
 website, 3
doublet lens, 5, 6, 7
drizzle, 37, 114
eclipse depth, 189, 190, 191
electronic interference, 244
electronics, 16
exposure time, 17, 19, 22, 23, 33, 60, 80, 92,
 98, 166, 173, 174, 177
extended source, 20, 29
faint sources, 199
fault protection, 18
fiducial frame, 114
field of view, 5, 6, 7, 10, 33, 35, 44, 54, 64,
 71, 74, 105, 107, 109, 114, 123, 135, 153,
 159, 165, 170, 202
filters, 5, 9, 10, 105
first-frame effect, 98, 99, 100, 116, 124, 164,
 165, 167, 187, 194, 199, 202, 205, 206,
 224
fixed target, 89
flagging, 126, 128, 129, 139, 140, 152, 193,
 199, 203, 204
flat-field, 7, 20, 21, 22, 24, 35, 44, 54, 71,
 96, 99, 105, 106, 116, 123, 126, 127, 144,
 196, 198, 200, 201, 205, 207, 208, 209,
 210
 superskyflat, 22, 205, 207
fluence, 103, 123, 140, 176, 178
flux calibration, 5, 106, 220
flux conversion. *See*
 header:keyword:FLUXCONV
focal plane, 6
focal plane assembly (FPA), 5, 18, 205, 209
focus, 8
 star, 9
FOV. *See field of view*
frame repeats, 22, 34, 67, 73, 119
frame time, 17, 20, 22, 23, 25, 27, 28, 29,
 31, 33, 42, 43, 59, 60, 61, 76, 77, 78, 92,
 103, 116, 124, 178, 179, 188
full array, 10, 11, 16, 17, 22, 23, 24, 26, 28,
 31, 33, 34, 35, 59, 60, 61, 62, 85, 89, 92,
 116, 119, 128, 140, 183, 205, 206, 207
full-array pull-up, 135
gain, 21, 44, 54, 96, 107, 120, 246
 extended source, 54
 point source, 54
ghost, 64, 96, 101, 108, 123, 126, 150, 151,
 204
 beamsplitter, 151
 filter, 150, 151
 photometry, 152
 pupil, 152
gyros, 72, 113
header, 71, 89, 92, 93, 99, 106, 107, 114,
 116, 119, 120, 122, 160, 194, 196, 200,

201, 203, 204, 205, 206, 208, 212, 214,
 235, 303
 keyword, 17, 71, 89, 99, 104, 116, 119,
 120, 127, 201, 203, 206, 207, 208, 212,
 234, 240
 ABADDATA, 201, 234
 BUNIT, 106, 120
 CD matrix, 71, 107, 113, 203
 CDELTA, 203
 CRPIX, 71, 107, 212
 CRVAL, 73, 74, 107, 113, 120, 205,
 212, 241
 DECRFND, 113, 120, 194, 205
 EXPID, 119, 122, 154
 EXPTIME, 92, 119, 120, 212, 214
 FLUXCONV, 21, 48, 106, 120, 201,
 212, 214
 FRAMTIME, 92, 119
 HDRMODE, 120, 207
 ORIG_DEC, 113, 120, 205
 ORIG_RA, 113, 120, 205
 RARFND, 113, 120, 194, 205
 USEDDBPHF, 120, 208
high dynamic range (HDR), 22, 23, 24, 25,
 26, 27, 33, 67, 68, 76, 99, 107, 113, 114,
 116, 118, 119, 126, 128, 129, 201, 204,
 206, 207, 208, 210, 224
high precision photometry, 34, 74, 76, 167,
 176, 182, 184, 245
horizontal striping. *See pattern noise*
housing
 main assembly, 5
 structure, 5
 IDL, 116, 157, 219, 232, 233
image
 artifacts, 2, 108, 109, 110, 111, 123, 152,
 198, 211, 214, 224, 229, 303
 orientation, 105
in-flight measurements, 8, 12, 15, 16, 64, 71,
 103
in-flight system, 9
InfraRed Science Archive (IRSA), 1, 2, 3, 4,
 10, 36, 40, 44, 51, 55, 57, 60, 63, 64, 68,
 71, 108, 122, 134, 172
 helpdesk, 3
In-Orbit Checkout (IOC), 4, 10, 13, 19, 29,
 137, 156, 291
InSb, 5, 6, 7, 13, 14, 92, 93, 94, 101, 109,
 124, 127, 128, 130, 283, 284
Instrument Engineering Request (IER), 120,
 126, 177, 178
intrapixel sensitivity variation, 34, 37, 46,
 57, 85, 155, 157, 158, 168, 170, 172, 176,
 183, 187, 213, 215, 218, 219, 220, 221,
 223, 224, 225, 226, 231, 245, 246
 map, 172, 176, 177, 180, 182
IRAC Warm Instrument Characterization
(IWIC), 4, 5, 15, 19
IRAF, 69, 116, 211, 219
jailbar effect. *See darkdrift*
labdark, 99, 101, 118, 123, 124, 130, 206
latent images. *See residual images*
lenses, 9
Level of data products, 2
limited cable bandwidth correction, 96
linearization, 14, 15, 16, 30, 94, 99, 101,
 103, 104, 116, 118, 123, 126, 129, 200,
 205, 207
mapping, 5, 32, 33, 35, 36, 55, 72, 87, 164,
 165, 203, 204
masks, 33, 109, 115, 124, 125, 126, 147,
 165, 195, 203, 204, 214
 dmask, 202
 fatal bit pattern, 126
 imask, 106, 108, 109, 110, 111, 115, 117,
 125, 126, 137, 146, 152, 156, 200, 201,
 202, 204, 240
 pmask, 115, 118, 125, 126, 201
 rmask, 125, 154, 195, 212, 214, 229
median image, 119, 208
mirrors, 9
missing data, 126, 127, 128
MOPEX, 64, 67, 71, 113, 114, 115, 126,
 154, 194, 197, 203, 211, 212, 214, 217,
 220, 229, 230
 namelist, 194, 195, 196, 212, 230
 source detection, 197
 source extraction, 197
mosaic, 37, 55, 58, 67, 68, 70, 74, 108, 109,
 112, 113, 114, 115, 116, 117, 131, 135,
 146, 147, 152, 153, 154, 166, 193, 194,

195, 196, 197, 199, 202, 203, 204, 207,
 208, 210, 211, 212, 213, 214, 225, 226,
 229, 230
mosaicking, 2, 55, 114, 155, 165, 193, 194,
 195, 197, 204, 212, 213, 225, 229
 coverage map, 115, 196, 212, 214
 drizzle, 196
 fiducial frame, 194, 195
 moving target, 89, 196
 subarray, 33
 uncertainty map, 196
Multiple Instrument Chamber (MIC), 5
 Adapter Plate, 5
multiplexer, 123
 glow, 124
mux. See *multiplexer*
muxbleed, 101, 102, 109, 111, 112, 118,
 123, 124, 126, 130, 131, 132, 156, 203,
 204, 210
 correction, 102
 warm mission, 102
muxstriping, 68, 108, 111, 112, 123, 124,
 130, 202
namelist, 154, 195, 212, 230
NASA Goddard Space Flight Center
(GSFC), 4
noise
 as a function of exposure time, 166
 confusion, 228
 correlated, 168
noise pixels, 8, 9, 19, 29, 64, 66, 173, 174
 spikes, 173, 238
noise reduction techniques, 171
non-linearity, 168
operability, 14
optical banding, 149, 151
optics, 6, 7, 184
optics housings, 5
outlier detection, 195
outlier rejection, 44, 68, 105, 107, 115, 123,
 135, 136, 147, 154, 195, 196, 197, 211,
 212, 214, 229
 strategies, 195
overlap correction, 131, 193, 194, 207, 211,
 214
paper acknowledgment, 3
pattern noise, 244, 245
PCRS peak-up, 34, 74, 170, 200
 guide star, 74
pedestal sample, 17, 67, 68, 124, 130
persistent images. See *residual images*
photometric calibration, 10, 45, 48
 absolute, 106, 196, 200, 201
 absolute calibration, 235
 point source, 158, 209
photometric stability, 84
photometric variations, 59, 145
photometry, 172
 accuracy, 2
 crowded fields, 197
 point source, 3, 157, 198
 time series, 167
pickoff mirrors, 5, 6, 210
pinstriping. See *muxstriping*
pipeline, 1, 2, 15, 33, 40, 44, 55, 59, 85, 86,
 89, 92, 94, 96, 99, 104, 105, 107, 108,
 110, 112, 113, 114, 115, 116, 117, 118,
 120, 122, 123, 125, 126, 127, 129, 131,
 132, 134, 135, 136, 137, 139, 140, 145,
 146, 148, 149, 152, 153, 154, 158, 176,
 180, 193, 194, 195, 196, 199, 202, 203,
 204, 205, 206, 207, 208, 209, 210, 211,
 212, 214, 220, 229, 234, 236, 242, 282
 artifact correction, 108, 111
 BCD, 125
 calibration, 89
 darkdrift, 203
 post-BCD, 116, 125, 193
 version, 122
pitch angle, 34, 80, 81, 169
pixel level decorrelation (PLD), 177, 189
pixel phase. See *intrapixel sensitivity*
 variation
pixel scale, 6, 70
pixel size, 3, 8, 14, 58, 59, 70, 115
pixel solid angle, 71, 212
pixels
 bad, 87, 88, 120, 124, 126, 200, 204, 214,
 216
 dead, 88, 115, 124
 hot, 48, 88, 95, 102, 111, 115, 124, 130
 noisy, 88

variable, 124
pmap. See *intrapixel sensitivity*
variation:map
point response function (PRF), 8, 20, 62, 64, 65, 67, 119, 152, 196, 197, 202, 214, 217, 218, 219, 222, 223, 225, 226, 229, 230, 231, 232
 core, 66, 221
 FWHM, 8, 9
 undersampled, 9, 109
point source extraction, 193
point source realization (PSR), 218, 219, 233
point spread function (PSF), 7, 57, 58, 62, 67, 75, 109, 129, 137, 150, 158, 160, 162, 173, 196, 198, 199, 202, 209, 217, 221, 228, 230
 extended, 67, 68, 69, 199
 FWHM, 8, 175
 undersampled, 168, 172
pointing, 22, 34, 72, 73, 76, 77, 78, 107, 113, 117, 120, 168, 194, 199, 202, 205, 206, 208
 accuracy, 205
 drift, 34, 72, 73, 74, 75, 76, 79, 168, 169, 170
 long-term, 76, 79, 80, 83, 170
 short-term, 76, 79, 80, 82
 glitches, 75
 history, 82, 241, 242
 history file, 113
 jitter, 73, 75, 76, 77, 82, 129, 169, 170, 218
 refinement, 73, 113, 114, 118, 193, 194, 200, 202, 205
 uncertainties, 73
 variations, 84
 wobble, 73, 75, 82, 169, 170
Pointing Calibration Reference Sensor (PCRS), 74
pointing control system (PCS), 72, 74, 78, 240
post-BCD, 73, 107, 112, 113, 114, 116, 117, 125, 126, 156, 193, 197, 199, 202, 203, 207
pre-flight measurements, 4, 14, 15, 24, 103, 129, 131
PRF fitting, 64, 66, 67, 157, 197, 199, 212, 214, 219, 220, 221, 225, 226, 227, 228, 229
projection system, 71
PSF-fitting, 67
quantum efficiency, 9, 10, 14, 19, 20, 24, 57
radhit. See *radiation hit*
radiation hit, 87, 123, 126, 156, 195
raw image, 2, 33, 103, 116, 117, 127, 128
 header, 120
Rayleigh-Jeans, 44, 54, 55, 56, 198
reaction wheel, 75, 170, 240
 speed shift, 240, 241
read noise, 13, 14, 16, 20, 22, 24, 85, 86, 95, 168, 196, 200, 205, 207
readout channel, 102, 103
readout mode, 22, 23, 32, 33, 60, 89, 92
residual images, 108, 123, 126, 135, 136, 137, 138, 139, 140, 141, 142, 143, 156, 168, 181, 187, 200, 209, 303
 slew residuals, 136, 138, 142, 143, 199
rows, 24, 35, 103, 110, 112, 121, 123, 125, 130, 131, 133, 134, 148, 149, 199
saturation, 9, 14, 15, 29, 30, 31, 67, 68, 87, 94, 95, 107, 108, 109, 110, 123, 124, 125, 126, 128, 129, 131, 132, 133, 139, 140, 148, 151, 198, 199, 200, 201, 202, 204, 206, 211, 214
scattered light, 20, 108, 109, 118, 123, 126, 127, 144, 145, 146, 147, 149, 152, 204, 208, 209
 ring, 152, 153
 splotches, 153, 154
Science Validation (SV), 4, 10, 13, 19, 29
self-calibration, 36
sensitivity, 5, 19, 21, 24, 28, 85, 86
 extended emission, 29
 point source, 19, 24, 25, 26, 27, 28, 29, 209
settle, 72, 73, 76, 77, 169
shutter, 5, 16, 18, 20, 40, 41, 43, 48, 89, 99, 104, 124, 180, 198
Si:As, 5, 6, 7, 14, 94, 98, 109, 110, 124, 128, 132, 148, 149, 156

signal sample, 17
skew, 70, 71
skydark, 34, 40, 41, 42, 43, 44, 59, 60, 85, 86, 87, 88, 100, 104, 106, 116, 118, 120, 124, 130, 138, 180, 188, 199, 202, 206, 207, 208, 235, 240, 244
 subtraction, 104
 superdark, 187
slew, 72, 73, 75, 76, 77, 169, 180
Smithsonian Astrophysical Observatory (SAO), 4, 13
source extraction, 66, 67, 196, 199
spectral lines, 53
spectral response, 7, 9, 10, 11, 49, 50, 51, 52, 54, 198, 213, 215
Spitzer Heritage Archive (SHA), 1, 2, 40, 46, 58, 59, 116, 136, 213, 216
star tracker, 72, 73, 74, 107, 113, 169, 170
staring mode, 34, 59, 61, 62, 74, 75, 76, 77, 79, 80, 82, 84, 120, 173, 174, 176, 180, 182, 235, 241
 skydark, 180
stellar mode, 22, 23, 25, 26, 27, 31, 33, 206
stellar photometry mode. *See stellar mode*
subarray, 10, 11, 17, 22, 23, 24, 25, 26, 27, 31, 33, 34, 35, 37, 58, 59, 60, 61, 62, 76, 77, 78, 85, 89, 92, 99, 102, 104, 114, 116, 117, 118, 128, 140, 170, 180, 187, 199, 203, 205, 208, 237, 239, 240
 58th frame, 105, 239
 58th plane, 199
 timing, 239
sub-pixel sampling, 37
superboresight, 113, 114, 194, 205, 229
 pointing correction, 73
superskyflat, 44, 45, 105, 118
surface brightness, 3, 48, 69, 70, 71, 115, 129, 150, 152, 153, 158, 159, 160, 161, 163, 164, 198, 303
 correction, 163
 sky, 160
sweet spot, 34, 62, 74, 170, 172, 174, 177, 178, 179
target acquisition accuracy, 74
throughputs, 9, 10, 19, 20, 21, 127, 159
timing, 238, 303
 Barycentric Dynamical Time (TDB), 238
 ephemeris time, 238
 Julian date, 239
 latency, 239
 UTC, 238
transmission, 9, 10, 11
transmission calibrator, 5
uncertainty image, 33, 96, 124, 196, 197
vignetting, 127
wait period, 92
wait ticks, 23
warm electronics, 18, 96, 123, 129
Warm Electronics Assembly (WEA), 5
warm mission, 2, 5, 8, 12, 13, 14, 15, 18, 21, 22, 23, 25, 26, 27, 28, 29, 31, 32, 33, 35, 40, 44, 45, 48, 55, 56, 57, 59, 64, 68, 69, 80, 82, 83, 86, 87, 99, 105, 127, 128, 136, 139, 140, 164, 168, 173, 174, 181, 183, 188, 194, 198, 201, 219, 242, 246, 302
 linearity, 15
 start, 5
wavefront error, 7
wavelength
 nominal, 48, 49, 50, 51, 52, 53
well depth, 14, 15, 30
zero magnitude flux density, 69, 70
zmag, 69
zodiacal background, 7, 20, 30, 31, 41, 44, 52, 53, 54, 55, 58, 86, 99, 101, 104, 105, 120, 127, 145, 159, 160, 161, 166, 181, 198, 207, 209, 230